The Structure-Function Relationship of Atheroprotective ApoA-I Mutants in High-Density Lipoproteins

This thesis is submitted in fulfilment of the requirements for the degree of Doctor of Philosophy in the

Department of Chemistry

Lancaster University

by

Sophie Lau

July 2021

Abstract

The Structure-Function Relationship of Atheroprotective ApoA-I Mutants in High-Density Lipoproteins

By Sophie Lau for the degree of Doctor of Philosophy.

In atherosclerosis cholesterol accumulation in arterial walls forms plaques which lead to associated cardiovascular diseases. High-density lipoprotein (HDL) nanoparticles known as “good cholesterol” transport cholesterol from arterial plaques to the liver for excretion. Therefore, HDL and its components have been targeted for tackling atherosclerosis treatment. Significantly, carriers of the R173C or L144R mutation in the major HDL protein apolipoprotein A-I (apoA-I) have low levels of HDL with a low atherosclerosis incidence. This suggests the mutations are atheroprotective as wild-type (WT) apoA-I carriers have a higher risk of atherosclerosis with low HDL levels. However, the mechanism for the mutants atheroprotective function is unknown.

This work compares the molecular structure of reconstituted HDL (rHDL) nanoparticles containing the apoA-I variants using biophysical techniques. To determine if the rHDL structure affects the nanoparticle function and aid atherosclerosis treatment development.

The expression and purification of unlabelled and uniformly [$^{13}C/^{15}N$]-labelled recombinant apoA-I variants was established. rHDL nanoparticles were prepared containing POPC, ±cholesterol, and apoA-I using detergent-mediated dialysis and density-based ultracentrifugation. The rHDL nanoparticle size and morphology were

analysed with techniques such as NativePAGE gradient gel electrophoresis and transmission electron microscopy (TEM).

A novel morphology characterisation was developed using ^{31}P solid-state NMR spectroscopy of oriented rHDL nanoparticles on glass substrates. Three distinct rHDL nanoparticle morphologies were identified that were inaccessible by TEM. The rHDL-L144R nanoparticles showed a different surface curvature when compared to the rHDL-WT and R173C nanoparticles. Subtle differences in the protein secondary structure were identified by circular dichroism and high-resolution 2D ^{13}C-^{13}C NMR spectra of PEG-precipitated rHDL-WT and L144R nanoparticles. Consequently, the different rHDL nanoparticle morphologies detected could be connected to the atheroprotective functional properties of the rHDL-L144R nanoparticles. The morphology characterisation technique was applied to a plasma HDL sample which provides a framework for application to clinical samples.

Declaration

This thesis has not been submitted in support of an application for another degree at this or any other university. It is the result of my own work and includes nothing that is the outcome of work done in collaboration except where specifically indicated. Many of the ideas in this thesis were the product of discussion with my supervisor Professor David Middleton.

Excerpts of this thesis have been published in the following academic publication.

Lau, S. & Middleton, D. A. (2020) Sensitive morphological characterization of oriented high-density lipoprotein nanoparticles using ^{31}P NMR spectroscopy. Angew Chem Int Ed Engl.

Acknowledgements

Firstly, I would like to thank my supervisor Prof. David Middleton for guidance, insightful ideas, and support throughout my PhD. I am grateful for the belief in me when he suggested the research proposal and for acquiring the PhD funding.

Thank you to my computational supervisor Prof. Jamshed Anwar for his support, introducing me to molecular dynamics simulations with useful discussions and explanations of concepts. I would like to thank Dr. Sarah Allinson for training and collaborating with me to work with cells in her lab and for the helpful discussions about the experiment setups. In the lab, I am grateful to Dr. Eleri Hughes and Dr. David Townsend, both of whom have helped me greatly with expertise and training me with lab techniques in my dissertation and PhD.

I extend my thanks to the Chemistry Department for their technical and friendly support creating a great environment to work in. I thank the Biological Life Sciences Department for collaborating with our lab there which was key for my PhD work.

Finally, I want to thank my partner Tash for keeping me going throughout my PhD and always providing me with laughter regardless of how many experiments didn't work! Thank you to my Mum for inspiring me to learn "how things work" from a young age, I wouldn't be here without her constant support. Thank you to my friends as we have supported each other in our PhD journeys, Abbie for your happiness in the lab and Lisa with our virtual office sessions.

This work was funded by a PhD studentship awarded by the British Heart Foundation.

Contents

List of Tables

List of Figures

List of Abbreviations

AAMD	All atom molecular dynamics	**LF**	Lipid-free
ABCA1/ G1	ATP binding cassette transporter A1/ G1	**m-β-CD**	methyl-β-cyclodextrin
ApoA-I	Apolipoprotein A-I	**MFI**	Mean fluorescence intensity
ApoA-I L144R	Apolipoprotein A-I Zaragoza	**MSP**	Membrane scaffold protein
ApoA-I R173C	Apolipoprotein A-I Milano	**MW**	Molecular weight
BODIPY -CE	BODIPY® FL C_{12} cholesteryl ester	**Native-PAGE/NDGGE**	Non-denaturing polyacrylamide gradient gel electrophoresis
CD	Circular dichroism	**NMR**	Nuclear magnetic resonance
CEs	Cholesteryl esters	**PdI**	Polydispersity index
CETP	Cholesteryl ester transfer protein	**PEG**	Polyethylene glycol
CGMD	Coarse grained molecular dynamics	**PISEMA**	Polarisation inversion spin exchange at the magic-angle
CP-MAS	Cross polarisation magic angle spinning	**PMA**	phorbol 12-myristate 13-acetate
CSA	Chemical shift anisotropy	**POPC**	1-palmitoyl-2-oleoyl-glycero-3-phosphocholine
CVD	Cardiovascular disease	**RCT**	Reverse cholesterol transport
DARR	Dipolar-assisted rotational resonance	**rHDL**	Reconstituted HDL
dHDL	Discoidal HDL	**SANS**	Small angle neutron scattering
DLS	Dynamic light scattering	**SDS-PAGE**	Sodium dodecyl sulphate polyacrylamide gel electrophoresis
E. coli	*Escherichia coli*	**SEC**	Size exclusion chromatography
EPR	Electron paramagnetic resonance spectroscopy	**SG-UTC**	Step gradient NaBr density ultracentrifugation
ESI-TOF MS	Electrospray ionisation time-of-flight mass spectrometry	**SLIM-PCR**	Site ligase-independent mutagenesis polymerase chain reaction
Fl-UTC	Flotation ultracentrifugation	**SSC-W/A**	Side scatter-Width/ Area
FSC-W/A	Forward scatter-Width/ Area	**SSE**	Secondary structure estimation
GAG	Glycosaminoglycan	**SS NMR**	Solid-state NMR
HDL/-C	High-density lipoprotein /-cholesterol	**SR-B1**	Scavenger receptor B1
HDX	Hydrogen-deuterium exchange	**TCEP**	Tris (2-carboxyethyl) phosphine hydrochloride
IMAC	Immobilised metal ion affinity chromatography	**TEM**	Transmission electron microscopy
IPTG	Isopropyl-β-D-thiogalactoside	**ThT**	Thioflavin T
LCAT	Lecithin: cholesterol acyltransferase	**T_m**	Melting temperature
LDLs	Low-density lipoproteins	**WT**	Wild-type

List of Appendices

1 Introduction

Atherosclerosis and associated cardiovascular disease are one of the major causes of death in the UK (British Heart Foundation (BHF) statistics factsheet August 2019). A low level of high-density lipoprotein cholesterol (HDL-C) is associated with an increased risk of atherosclerosis (Lewis and Rader, 2005). Apolipoprotein A-I (apoA-I) is the major protein component at 70 % of the total protein content in HDL (Brouillette et al., 2001; Vance and Vance, 2002). HDL nanoparticles transport cholesterol from the tissues to the liver for excretion in the reverse cholesterol transport (RCT) system (Fisher et al., 2012).

ApoA-I Milano (apoA-I R173C) (Weisgraber et al., 1980) and apoA-I Zaragoza (apoA-I L144R) (Recalde et al., 2001) are considered to be atheroprotective mutations of apoA-I, i.e. the mutations are hypothesised to confer protective functional capabilities to protect against the accumulation of cholesterol in the arterial wall. This is exhibited in the phenotype of the respective mutants carriers that have low levels of HDL-C and importantly a low incidence of atherosclerosis (Franceschini et al., 1980; Recalde et al., 2001).

Therefore, the two mutations are of interest to investigate the underlying structure-function relationship of the atheroprotective mutants compared to wild-type apoA-I (apoA-I WT). Carriers of the atheroprotective mutations show the opposite effect to HDL containing apoA-I WT as carriers have naturally low levels of HDL-C without the associated increased risk of atherosclerosis. This suggests the mutations affect the development of atherosclerosis or transport of cholesterol in the RCT system.

This research aims to establish methodologies for the routine production of the atheroprotective apoA-I proteins and reconstituted HDL (rHDL) nanoparticles to enable the first detailed comparison of the structural and functional properties of rHDL nanoparticles containing apoA-I WT, R173C or L144R. In particular, the molecular structure and organisation of the lipids, cholesterol and apoA-I protein in HDL combined with functional analysis of the rHDL nanoparticles.

1.1 Atherosclerosis

Atherosclerosis is a systemic inflammatory disease of the arterial wall, in which there is a build-up of lipids and fibrous components (Lusis, 2000). In atherogenesis plaques develop called atheromas in the endothelial cells, the inner lining, of the arteries (Libby et al., 2011). The process of atherogenesis is simplified in **Figure 1.1**.

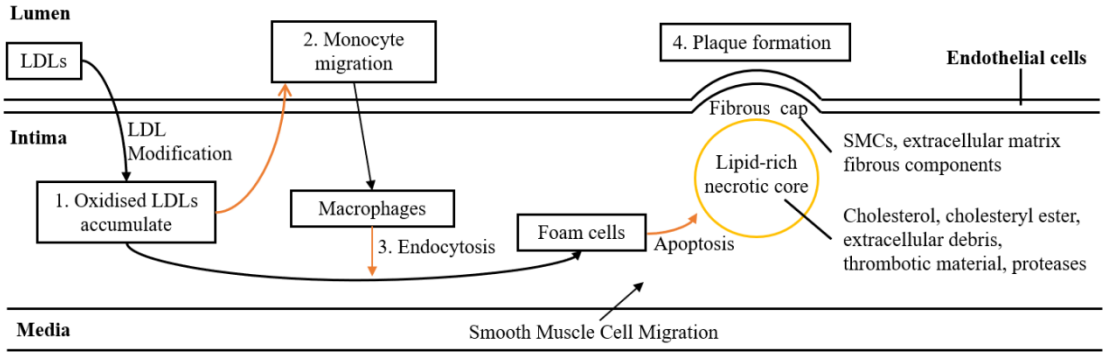

Figure 1.1. The simplified process of atherogenesis in an artery. Adapted from Lusis *et al.* (Lusis, 2000).

At branch points and major curved regions of arteries blood flow disturbances can occur leading to vulnerable regions where atherosclerotic lesions can form (Gimbrone, 1999). The subendothelial matrix composition of the arterial wall is altered and the endothelial permeability of the arterial wall in the vulnerable regions increases. This allows the accumulation of apolipoprotein B (apoB)-containing low-density lipoproteins (LDLs) in the subendothelial matrix of the intima layer to occur (Gimbrone, 1999; Lusis, 2000; Tabas et al., 2007). The apoB-containing LDLs interact with matrix proteoglycans on the subendothelial cell surface (Tabas et al., 2007). LDLs trapped in the subendothelial intima layer become oxidised through several mechanisms *in vivo* such as oxidative vascular cell waste and enzymes like myeloperoxidase and lipoxygenase (Lusis, 2000; Yoshida and Kisugi, 2010). The build-up of oxidised LDLs initiates the recruitment of leukocytes known as white blood cells (monocytes, lymphocytes), via the production of pro-inflammatory molecules by the endothelial cells (Lusis, 2000). The monocytes migrate from the endothelial cells to the subendothelial space in the intima and differentiate to form both macrophages and dendritic-like cells (Galkina and Ley, 2009; Libby et al., 2011; Tabas et al., 2007). The differentiated cells ingest highly oxidised

LDLs by phagocytosis forming lipid/cholesterol-laden macrophages called foam cells (Libby et al., 2011; Lusis, 2000; Tabas et al., 2007).

As the early lesion progresses the foam cells die, for example by apoptosis, and the dead cells are efficiently cleared until the lesion becomes advanced (Tabas, 2010). The removal of apoptic cells by efferocytes, a class of phagocytic cells, is known as efferocytosis (Tabas, 2010). In advanced lesions insufficient efferocytosis furthers the build-up of extracellular lipids and cell debris causing secondary necrosis (Tabas, 2005; Tabas, 2010). This accumulation produces the lipid-rich necrotic core, a hallmark of advanced atherosclerotic plaques (Lusis, 2000). The necrotic core also contains cholesterol crystals, cholesterol ester, proteases, thrombotic material, and extracellular debris (Lusis, 2000; Tabas et al., 2007).

The accumulation of cholesterol is highly pathogenic as there is no direct treatment for removing the cholesterol accumulated in arterial wall plaques, only prevention of further accumulation with drugs such as statins which act to reduce the levels of LDL cholesterol (Ward et al., 2019). Further accumulation of cholesterol in the arterial plaques leads to the following pathogenic complications and cardiovascular disease.

Smooth muscle cells (SMCs) transfer from the media into the intima layer of the arterial wall (Lusis, 2000). The SMCs produce extracellular matrix fibrous components such as collagen and elastin, that contribute to the formation of fibrous plaques, facilitated by macrophages and T-cells (Libby et al., 2011; Lusis, 2000; Tabas et al., 2007). A fibrous cap forms surrounding the necrotic core and contains SMCs and extracellular matrix components in the intima layer of the artery (Libby et al., 2011; Lusis, 2000; Tabas et al., 2007).

Small vessels in the lesion can haemorrhage as the plaque progresses, and calcification of the plaque and ulceration can occur at the surface of the lumen (Lusis, 2000). Advanced atherosclerotic plaques can rupture or erode, and the fibrous cap can become thinner (Tabas et al., 2007). Therefore, the ruptured plaques usually contain less SMCs and are macrophage-rich, whilst the fibrous cap is thin and contains less collagen (Libby et al., 2011). Plaque growth causes flow-limiting stenosis, the narrowing of the artery restricting blood flow resulting in tissue ischaemia (Libby et al., 2011).

Acute thrombotic vascular complications can occur from thrombosis when thrombi (blood clots) block blood vessels causing myocardial infarction and stroke (Libby et al., 2011; Lusis, 2000; Tabas et al., 2007). Thrombi are formed when a fibrous lesion ruptures and/or the thin fibrous cap fractures, which releases necrotic core and macrophage pro-coagulant components that interact with blood coagulant proteins in the arterial lumen (Libby et al., 2011; Lusis, 2000). Further complications such as dysfunctional arterial wall repair and the development of aneurysms are caused by elevated tension in the plaque affected arterial wall, known as hypertension (Libby et al., 2011).

1.2 Apolipoproteins and HDL

Apolipoproteins are serum proteins embedded in the lipid surface of lipoprotein particles, including LDL and HDL (von Eckardstein et al., 2001). HDL particles are heterogeneous as the particles can have different compositions, size, charge, and density (Rosenson et al., 2011). The HDL particles in addition to apoA-I (~70 %) contain other proteins such as apolipoprotein A-II (apoA-II) (~20 – 25 %), whilst the bulk body of the particle consists of phospholipids, as well as cholesterol, cholesteryl ester (CE), and triglycerides (Brouillette et al., 2001; Lewis and Rader, 2005). The chemical structures

of the bulk body components are in **Figure 1.2.** The CE, triglyceride, and phospholipid structures each contain long hydrophobic hydrocarbon tails and the cholesterol molecule is predominantly hydrophobic. The phospholipid molecule is amphipathic due to the hydrophilic glycerol-phosphocholine headgroup. The structural arrangement of these HDL constituents and apoA-I is described in **section 1.6.2**.

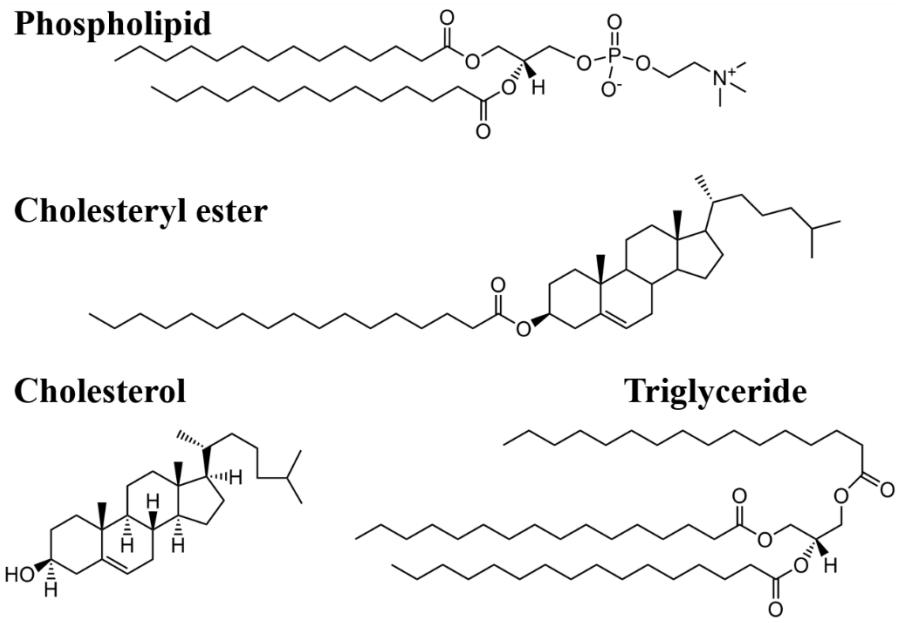

Figure 1.2. The chemical structures of a phospholipid (14:0 PC, 1,2-dimyristoyl-*sn*-glycero-3-phosphocholine, DMPC), 17:0 cholesteryl ester (cholest-5-*en*-3β-yl heptadecanoate), cholesterol, and a triglyceride (1,2,3-trihexadecanoyl-glycerol). Obtained from Avanti® polar lipids and (Sud et al., 2007)**.**

Accumulation and transport of cholesterol, triglycerides, and phospholipids in the blood stream is mediated by the protein-lipid complexes (von Eckardstein et al., 2001). Raised levels of HDL-C, also known as 'good cholesterol', has an atheroprotective effect protecting from the development of atherosclerotic coronary heart disease (Fisher et al., 2012). As there is an inverse correlation between HDL-C and cardiovascular disease

(CVD), i.e., low levels of HDL-C correlate with higher incidences of atherosclerosis and CVD, and vice-versa (Fisher et al., 2012).

Reverse cholesterol transport is the main role of HDL which involves the transport of cholesterol from tissues to the liver for excretion mediated via HDL particles (Fisher et al., 2012; von Eckardstein et al., 2001). The apoA-I bearing HDL particles are considered to be atheroprotective as the particles can stimulate cholesterol efflux from cells in atherosclerotic lesions for cholesterol transport and excretion (Fisher et al., 2012; von Eckardstein et al., 2001). This transport of cholesterol by HDL particles is considered to be atheroprotective as this prevents the build-up of excess pathogenic cholesterol in the arterial wall which accumulates in arterial plaques (Fisher et al., 2012; Lusis, 2000; von Eckardstein et al., 2001). Additionally, HDL particles can inhibit LDL oxidation and inflammatory events in atherogenesis (Fisher et al., 2012).

1.3 HDL synthesis and reverse cholesterol transport

Reverse cholesterol transport is the major process in which HDL containing apoA-I transports cholesterol from peripheral tissues or foam cells in atherosclerotic plaques, to the liver for recycling in lipoproteins, transport to steroidogenic tissues, catabolism, and biliary excretion (Fielding and Fielding, 1995; Fisher et al., 2012). The processes of HDL synthesis and RCT are summarised in the following sections.

1.3.1 The processes of HDL nanoparticle formation

Initially, apoA-I is secreted into the plasma from the intestines and liver, and approximately 5-10 % is lipid-free apoA-I, or apoA-I can interact with lipids to become small lipid-poor pre-β-HDL particles, whilst the majority of apoA-I is in a lipid-bound state in lipid-rich α-HDL particles (Brouillette et al., 2001; Del Giudice et al., 2011; von Eckardstein et al., 2001) (**Figure 1.3**).

Next, ATP binding cassette transporter A1 (ABCA1), a membrane protein, interacts with lipid-free apoA-I and lipid-poor pre-β-HDL particles, referred to as "HDL precursors" (Sahoo et al., 2004; von Eckardstein et al., 2001). This is an ATP-dependent process which regulates cellular cholesterol transport and lipid efflux from the cell membrane forming nascent phospholipid-rich cholesterol-poor discoidal HDL (dHDL) particles, as the pre-β-HDL and lipid-free apoA-I accumulate lipids and cholesterol (Duong et al., 2008; Lewis and Rader, 2005; Sahoo et al., 2004).

The apoA-I lipidation/relipidation process through interactions with hepatic ABCA1 is significant in preventing deterioration of lipid-poor apoA-I before mature α-HDL particles are formed (Lewis and Rader, 2005), as well as protecting against cholesteryl ester build-up in macrophages (Del Giudice et al., 2011).

The larger lipid-rich spheroidal α-HDL (sHDL, HDL_3 and HDL_2) particles have a hydrophobic CE-enriched core, and form when the HDL precursors obtain phospholipids and cholesterol as the particles circulate in the plasma (Lewis and Rader, 2005; von Eckardstein et al., 2001). The HDL_2 and HDL_3 notations refer to the two major subclasses of HDL nanoparticles (**see section 1.4**).

The hydrophobic core is surrounded by lipids and the particles can contain between 2 – 5 apoA-I molecules (Duong et al., 2008; Huang et al., 2011) and approximately two-thirds of HDL can contain apoA-II as they become more complex (Lewis and Rader, 2005). Initially smaller HDL_3 particles are formed and through the following processes form larger HDL_2 particles (Lewis and Rader, 2005).

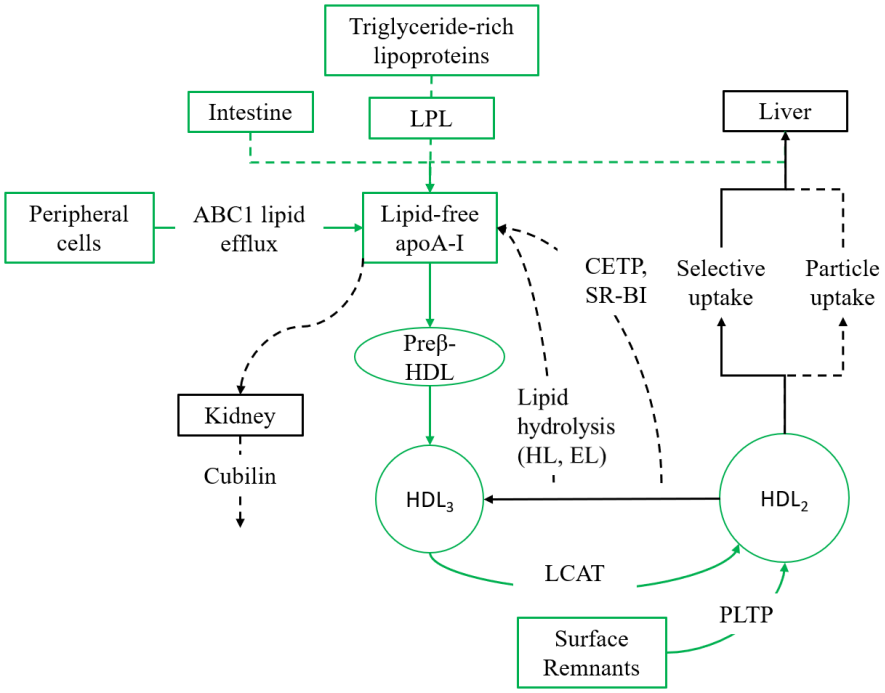

Figure 1.3. The processes of HDL synthesis (green). The dashed and solid arrows indicate the movement of protein and lipids, respectively. Adapted from (von Eckardstein et al., 2001).

The formation of cholesteryl ester is driven by lecithin: cholesterol acyltransferase (LCAT) which catalyses the esterification of cholesterol in the sHDL particles, therefore most plasma HDL-C is esterified (Lewis and Rader, 2005; von Eckardstein et al., 2001). The cholesteryl esters are hydrophobic and move into the particle core in mature sHDL particles (Lewis and Rader, 2005). In addition to LCAT, phospholipid transfer protein (PLTP) transfers plasma and surface triglyceride phospholipids to HDL, as well as facilitating HDL_3 particle fusion to form larger HDL_2 particles and the by-product of lipid-poor apoA-I (Lewis and Rader, 2005; von Eckardstein et al., 2001).

Furthermore, lipoprotein lipase (LPL) is an enzyme bound to endothelial cell surface heparan sulphate proteoglycans (Lewis and Rader, 2005). LPL hydrolyses triglycerides in triglyceride-rich lipoproteins, such as chylomicrons and very low-density

lipoproteins, resulting in the release of surface cholesterol, phospholipids, and apolipoproteins to the HDL precursors for the formation of larger HDL particles (Lewis and Rader, 2005).

1.3.2 Catabolism of HDL nanoparticles

In the RCT system (**Figure 1.4**), the mature α-HDL particles are affected indirectly by cholesteryl ester transfer protein (CETP), and the lipid and triglyceride hydrolysis enzymes hepatic lipase (HL) and endothelial lipase (EL) (von Eckardstein et al., 2001).

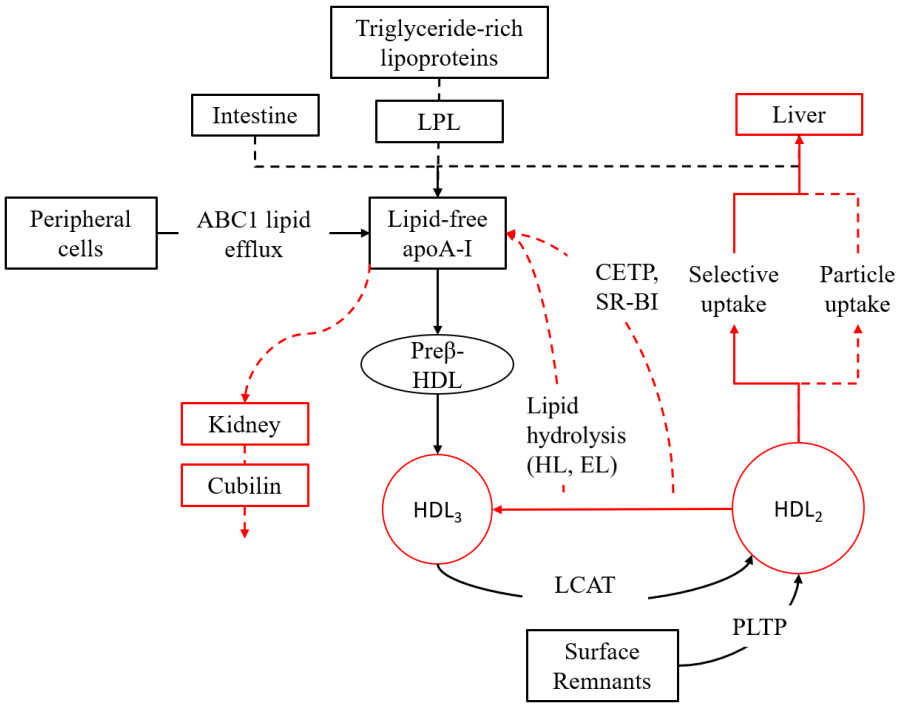

Figure 1.4. The processes of HDL catabolism and reverse cholesterol transport (red). The dashed and solid arrows indicate the movement of protein and lipids, respectively. Adapted from (von Eckardstein et al., 2001).

HL is a hepatic cell enzyme that converts larger HDL_2 particles into smaller HDL_3 particles and HDL precursors through hydrolysis of triglycerides and phospholipids in

HDL, with triglyceride lipase and phospholipase A1 activity, respectively (Lewis and Rader, 2005; von Eckardstein et al., 2001).

Endothelial cells produce EL which hydrolyses phospholipids in HDL, with phospholipase A1 activity like HL, producing fatty acids at the vascular endothelial surface (Lewis and Rader, 2005; von Eckardstein et al., 2001). CETP reduces the size of HDL_2 to HDL_3 particles by mediating the transfer of CE from HDL to triglyceride-rich apoB-containing lipoproteins, whilst transferring triglycerides to HDL from these lipoproteins (Lewis and Rader, 2005; Rigotti and Krieger, 1999; von Eckardstein et al., 2001).

The direct HDL catabolism pathways are scavenger receptor B1 (SR-B1) mediated lipid, cholesterol and CE uptake from HDL particles, and apolipoprotein E and apoA-I receptors mediated holoparticle uptake of HDL for further processing (von Eckardstein et al., 2001). The HDL binds to the SR-B1 receptor with high affinity allowing the transfer of HDL-C to hepatocytes in the liver and steroidogenic tissues without endocytosing the HDL particles and proteins (Lewis and Rader, 2005; von Eckardstein et al., 2001).

Additionally, some of the lipid-free apoA-I and pre-β-HDL particles are processed by glomerular filtration and apoA-I is reabsorbed in the proximal tubulus lumen in the kidney facilitated by cubilin (von Eckardstein et al., 2001).

Importantly, the RCT process is relevant to atherosclerosis as the ATP binding cassette transporters (ABCA1, ABCG1), and SR-B1 are present in macrophage foam cells and interaction with lipid-free apoA-I promotes cholesterol efflux to HDL particles (Fisher et al., 2012; Lewis and Rader, 2005; Yvan-Charvet et al., 2010; Zhou et al., 2015).

1.3.3 Summary

Overall, HDL has a direct role in reverse cholesterol transport, in mediating cholesterol efflux and the transport of cholesterol to the liver for excretion and recycling. This indicates that HDL is a primary target for gaining a greater understanding of how to tackle atherosclerosis treatment. To establish structural differences between the atheroprotective apoA-I mutants an understanding of HDL structure is required. The following sections describe the plasma HDL distribution, structural characterisation techniques, and current models of lipid-free apoA-I and HDL nanoparticles. This is followed by introducing the atheroprotective apoA-I mutant characteristics, a summary of rHDL-infusion therapies and experimental structural techniques that have been used to analyse rHDL nanoparticles.

1.4 Characterisation of HDL

The function of HDL is determined by the apolipoprotein content, mainly apoA-I and by the lipid content of the HDL particle (Vance and Vance, 2002). The properties of HDL have been reviewed extensively (Martin et al., 2014; Rosenson et al., 2011; Vance and Vance, 2002). Specifically, the characterisation and distinctions between the different subclasses of the heterogenous plasma HDL particles using various measurement techniques, summarised in **Table 1.1** (Martin et al., 2014; Rosenson et al., 2011).

Overall, the HDL particles have densities between approximately 1.063 – 1.21 g/ml, and diameters between 7.2 – 12.9 nm as determined by density gradient ultracentrifugation (UTC) and non-denaturing gradient gel electrophoresis (NDGGE) (Rosenson et al., 2011; Vance and Vance, 2002). Using NDGGE and density gradient UTC the major subclasses HDL_2 and HDL_3 can be further separated into HDL_{2a} and

HDL_{2b}, as well as HDL_{3a}, HDL_{3b} and HDL_{3c}, respectively (Chapman et al., 1981; Rosenson et al., 2011; Vance and Vance, 2002).

HDL particles of different size and charge can also be separated using 2-dimensional gel electrophoresis and classified as pre-β- or α-HDL, with the respective diameter ranges indicated in **Table 1.1** (Asztalos et al., 2000; Rosenson et al., 2011). There are also large pre-β_2 migrating HDL (12.0-14.0 nm), and pre-α-HDL with similar diameters to the α-HDL particle subclasses (Rosenson et al., 2011; Vance and Vance, 2002; Zhou et al., 2015). However, the pre-α particles relative to the α-HDL particles exist at a low concentration in human plasma (Asztalos et al., 2005; Rosenson et al., 2011).

The dHDL particles α-4 and pre-β_1-HDL particles contain lipids and apoA-I with and without cholesterol, respectively (Asztalos et al., 2005; Rosenson et al., 2011). In addition to the dHDL components the sHDL α-1 to α-3 particles contain cholesteryl esters and triglycerides in the hydrophobic core, the α-2 and α-3 particles also contain apoA-II, whereas the α-1 particles contain low concentrations of apoA-II (Asztalos et al., 2005; Rosenson et al., 2011).

Table 1.1. HDL particle subfractions categorised by physical properties and analysis technique. Adapted from (Rosenson et al., 2011).

	Very Large HDL	**Large HDL**	**Medium HDL**	**Small HDL**	**Very Small HDL**
Density Range (g/ml)	1.063 – 1.087	1.088 – 1.110	1.110 – 1.129	1.129 – 1.154	1.154 – 1.21
Size Range (nm)	12.9 - 9.7	9.7 – 8.8	8.8 – 8.2	8.2 – 7.8	7.8 – 7.2
Density Gradient Ultracentrifugation	HDL_{2b}	HDL_{2a}	HDL_{3a}	HDL_{3b}	HDL_{3c}
Density Range (g/ml)	1.063 – 1.087	1.088 – 1.110	1.110 – 1.129	1.129 – 1.154	1.154 – 1.170
Gradient Gel Electrophoresis	HDL_{2b}	HDL_{2a}	HDL_{3a}	HDL_{3b}	HDL_{3c}
Size Range (nm)	12.9 – 9.7	9.7 – 8.8	8.8 – 8.2	8.2 – 7.8	7.8 – 7.2
2D Gel Electrophoresis	α-1	α-2	α-3	α-4	Pre-β-1
Size Range (nm)	11.2 – 10.8	9.4 – 9.0	8.5 – 7.5	7.5 – 7.0	6.0 – 5.0
NMR	Large HDL particle	Medium HDL particle		Small HDL particle	
Size Range (nm)	12.9 – 9.7	9.7 – 8.8	8.8 – 8.2	8.2 – 7.8	7.8 – 7.2
Ion Mobility	HDL_{2b}	HDL_{2a} and HDL_3			
Size Range (nm)	14.5 – 10.5	10.5 – 7.65			

1.5 Antiatherogenic properties of HDL

It has been suggested that HDL has additional anti-atherogenic properties associated with the antioxidant and anti-inflammatory properties of HDL acting upon and aiding the prevention of atherosclerotic plaque formation (Barter et al., 2004). This further emphasises the atheroprotective nature of the HDL particles in addition to cholesterol transport in the RCT system.

The antioxidant functionality of HDL could be due to the inhibition of the oxidation of LDLs and transferring oxidation products of LDL to the liver for removal (Barter et al., 2004; Bowry et al., 1992; Okura et al., 2010). The accumulation of oxidised LDLs triggers the recruitment of monocytes leading to the formation of foam cells in atherosclerotic plaques (Galkina and Ley, 2009; Lusis, 2000; Tabas et al., 2007). The antioxidant properties of HDL can also be attributed to the proteins associated with HDL, specifically apoA-I, as well as apolipoprotein A-II and paraoxonase, in the transport and breakdown of lipid hydroperoxides (Barter et al., 2004; Bowry et al., 1992).

The anti-inflammatory functionality of HDL reduces the recruitment and migration of monocytes into the arterial wall through inhibiting the expression of MCP-1, a signalling protein involved in recruitment of monocytes, and endothelial cell adhesion proteins (Barter et al., 2004; Navab et al., 1991). Additionally, the formation of pro-inflammatory proteolytic peptides called granulins was inhibited by apoA-I and/or HDL binding to a macrophage-derived secretory factor complex containing progranulin, the precursor protein of the granulin peptides (Okura et al., 2010).

1.6 HDL nanoparticle structure

The following sections describe the structural models of lipid-free apoA-I WT followed by the structural models of discoidal HDL nanoparticles. It is necessary to characterise the lipid-free and lipid-bound structure of the apoA-I protein to determine if there are structural similarities and/or differences in the protein structure that are related to its function.

1.6.1 Lipid-free apoA-I

It is important to understand the structure of apoA-I as this relates to its interactions with lipids, cholesterol and enzymes, and therapeutic properties. Human apoA-I is a 243 residue protein that exists in lipid-free, lipid-poor or lipid-bound states (Silva et al., 2008). The mature protein is formed in the liver and intestine and has a molecular weight of ~28 kDa (1-24 signal sequence, residues 25-267) and mature apoA-I is produced after cleavage of the signal sequence *pre*- and *pro*- peptides, with the amino acid sequence shown in **Figure 1.5** (Brouillette et al., 2001; Del Giudice et al., 2011; Law and Brewer, 1984).

ApoA-I is a predominantly α-helical protein, which adopts different tertiary structures dependent upon the protein is lipid-free or lipid-bound. Various techniques have been used to analyse the structure of lipid-free apoA-I (see Oda *et al*. for a review) (Oda, 2017), however structural analysis of lipid-bound apoA-I particles due to its size and resistance to forming crystals are more problematic (see later).

The apoA-I protein sequence in the exon-4 encoded region (44 – 243) contains 22 amino acid repeats consisting of two 11 amino acid sequences, referred to as 11-mer/22-mer or as A and B, which form amphipathic helices (Li et al., 1988; Mei and Atkinson, 2011; Segrest et al., 1974; Segrest et al., 1992). The amphipathic alpha helices in apoA-I have

a polar face containing charged hydrophilic residues interacting with the aqueous environment and lipid headgroups, whilst the nonpolar hydrophobic face associates with lipid acyl tails or intramolecularly self-associates with the nonpolar faces of other helices in a lipid-free environment (Li et al., 1988; Segrest et al., 1974).

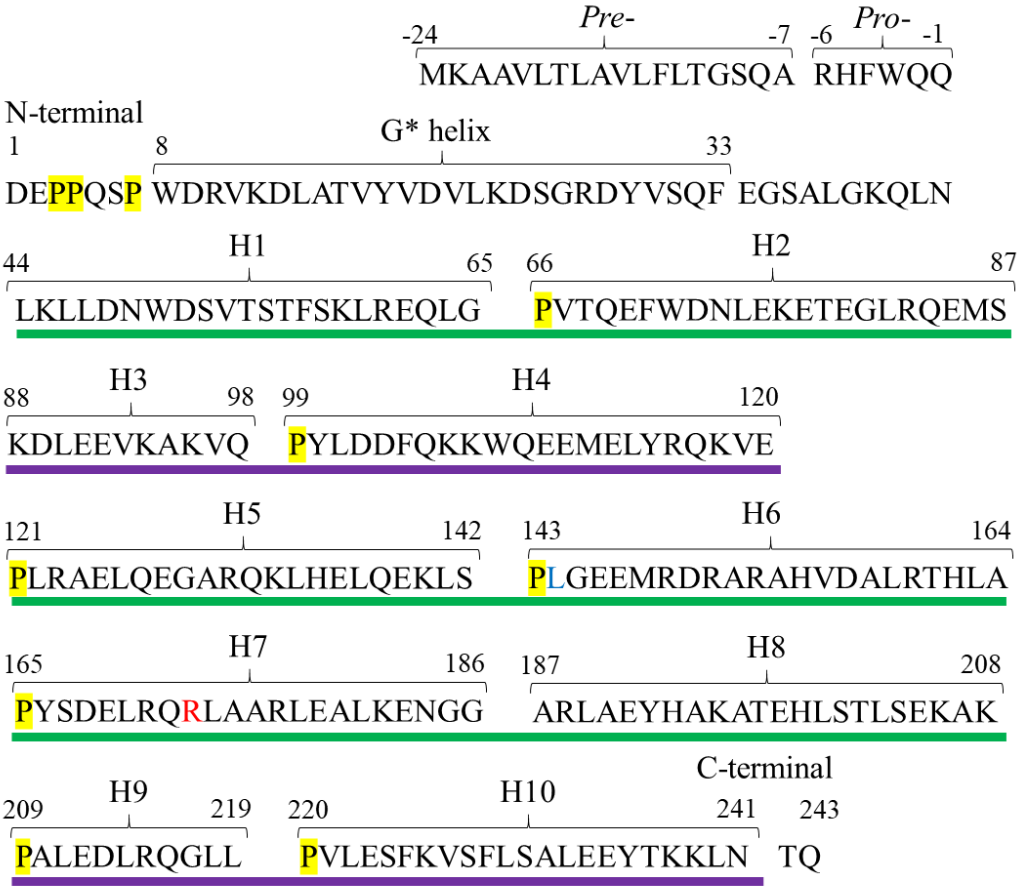

Figure 1.5. Human apoA-I WT amino acid sequence with the *pre*- and *pro*- signal peptides (Law and Brewer, 1984). The full-length protein (1 – 243) predicted secondary structure α-helices (H1-H10) are indicated (Li et al., 1988; Nolte and Atkinson, 1992). The G* N-terminal helix is labelled, and the type A and Y helices are underlined in green and purple, respectively (Segrest et al., 1992). The proline residues are yellow, and residues L144 and R173 are in blue and red, respectively. The figure is adapted from (Law and Brewer, 1984; Oda, 2017; Roberts et al., 1997; Segrest et al., 1992).

In Segrest *et al*.'s proposed theory the charged residues follow a pattern with the cationic residues (Lys, Arg) on either side of the polar face edges meeting the nonpolar face, whilst the anionic residues (Glu, Asp) were centred in the polar face (Segrest et al., 1974). The "Snorkel" model was suggested in which the cationic residues are described as amphipathic and are situated with the charged amine group(s) towards the hydrophilic lipid headgroups, and the hydrophobic acyl chains of the residues are associated with the hydrophobic lipid acyl chains (Segrest et al., 1992).

The amphipathic helices of apoA-I were separated into different classes called A, Y and G* (Segrest et al., 1992). The alpha helices described with the charge distribution as above are class A (Segrest et al., 1992). The class G* helix is encoded by exon-3, and the polar face contains randomly distributed positively and negatively charged residues (Segrest et al., 1992). Whereas, in the class Y amphipathic helix polar face the charged residues are clustered, alternating positive to negative regions, and distributed radially containing a total of three positive regions interspersed with two negative regions (Segrest et al., 1992). The helices were determined in ascending order of hydrophobicity as class A < Y < G, and suggested to facilitate protein-lipid interactions, a mix of both interaction types, and protein-protein interactions, respectively (Segrest et al., 1992).

There are two apoA-I crystal structures produced by Borhani *et al*. of N-terminally truncated apoA-I Δ(1-43) (Borhani et al., 1997), whilst Mei and Atkinson produced a structure of C-terminally truncated apoA-I Δ(185-243) (Mei and Atkinson, 2011). The N-terminally truncated lipid-bound tetrameric twisted-ring apoA-I Δ(1-43) crystal structure at 4 Å resolution is thought to represent lipid-bound apoA-I (Borhani et al., 1997). Each chain forms a nearly continuous α-helical secondary structure with proline residues throughout the chain causing kinks in the α-helical structure (**Helices 1-10,**

Figure 1.6, left) (Borhani et al., 1997). The individual apoA-I molecules in each dimer are arranged in an antiparallel conformation, with hydrophobic residue interactions between the nonpolar faces (Borhani et al., 1997).

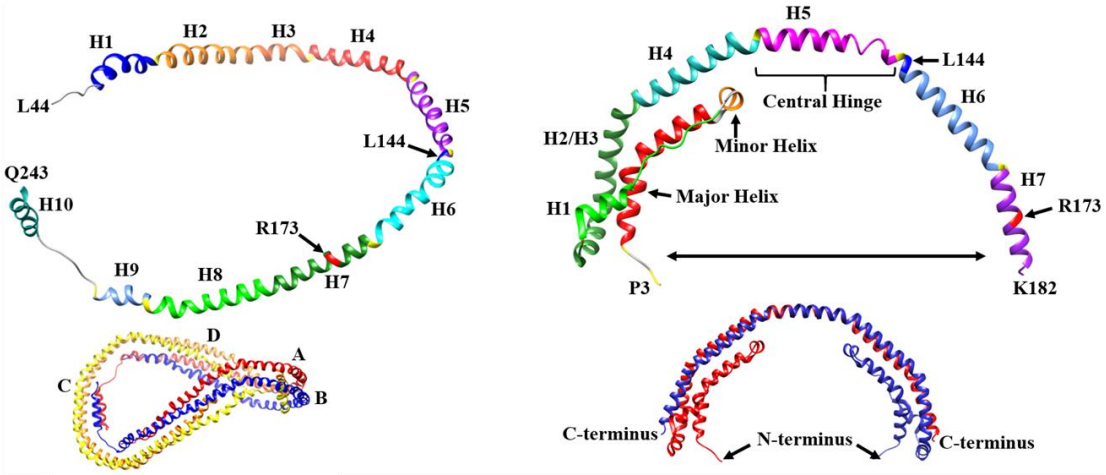

Figure 1.6. The crystal structure of apoA-I Δ(1-43) chain A (left) and Δ(185-243) (right) adapted from (Borhani et al., 1997) and (Mei and Atkinson, 2011), respectively. The monomer structures are labelled with the helices (e.g., H1), the residues L144 (blue), R173 (red), and the prolines (yellow). The apoA-I Δ(1-43) tetramer (chains A-D) and the apoA-I Δ(185-243) dimer conformation are both shown below the respective monomers.

Mei and Atkinson produced a higher resolution 2.2 Å crystal structure of C-terminally truncated apoA-I (Δ185-243) consisting of ~80% α-helical secondary structure (**Figure 1.6**, **right**) (Mei and Atkinson, 2011). Two antiparallel apoA-I (Δ185-243) half circle monomers produced a dimer with a diameter of 11.0 nm and height of 1.7 nm (Mei and Atkinson, 2011). Each monomer consists of 7 major helices and a minor helix, at the junctions between helices are proline residues which cause kinks in the structure similar to the apoA-I (Δ1-43) structure (Borhani et al., 1997; Mei and Atkinson, 2011).

The central hinge region contains a “leucine-like zipper” between hydrophobic leucine residue functional groups in the H5/5 helices (**Figure 1.7**), and without stabilising salt bridges suggesting flexibility, indicated by the arrow in **Figure 1.6** (Mei and Atkinson, 2011). It is suggested that at low apoA-I concentrations in solution that apoA-I will convert between monomeric and dimeric conformations, with monomeric apoA-I as a closed structure, with the hinge-region allowing the C-terminus to fold forming a monomeric apoA-I helical bundle (Mei and Atkinson, 2011). Lipid-free ApoA-I is suggested to have two structural domains consisting of an N-terminus helix bundle connected to a less structured carboxyl terminus structure containing alpha-helices (Alexander et al., 2009; Saito et al., 2003).

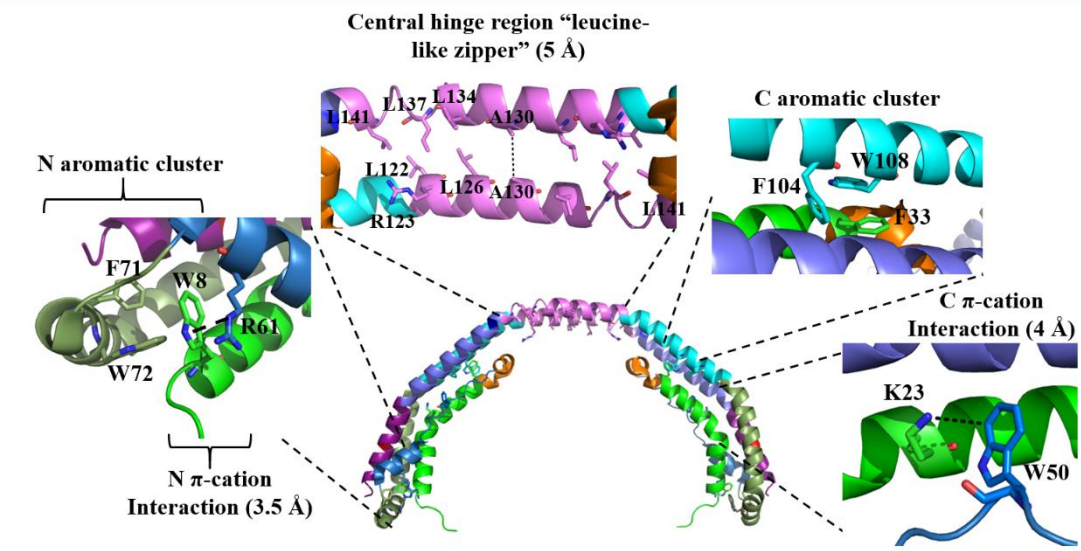

Figure 1.7. The intermolecular and intramolecular regions that stabilise the apoA-I Δ(185-243) dimer: The hydrophobic N- and C- terminal clusters and π-cation interactions with the corresponding distances in Å. The central hinge region "leucine-like" zipper. The α-helical residues are coloured as in the helical assignments of **Figure 1.5**: G* helix (green), residues 33 – 43 (orange), H1 (metallic blue), H2/3 (dark green), H4 (cyan), H5 (pink), H6 (violet), and H7 (dark purple). Residues L144 and R173 are in blue and red, respectively. Adapted from (Mei and Atkinson, 2011).

The apoA-I dimer is stabilised with intermolecular and intramolecular hydrophobic aromatic residue clusters at either end of the helix bundle (N and C termini), including π-π interactions at each cluster further stabilising the bundle at either end (**Figure 1.7**). At the C-terminus cluster the interaction is weaker suggesting a susceptibility to lipid disruption of the protein structure. Furthermore, π-cation interactions stabilise the helical bundle as well as intra- and inter-molecular salt bridges stabilising the backbone of the dimer (Mei and Atkinson, 2011).

Both crystal structures support that the hydrophobic interfaces between monomers of apoA-I are key to dimerization and form the apoA-I helical to lipid binding interface

providing a backbone in determining the size of HDL particles (Mei and Atkinson, 2011). The formation of a tetramer of apoA-I (Δ1-43) is suggested to form due to interacting hydrophobic surfaces of the dimers exposed due to the lack of residues 1-43 in the apoA-I structure, suggested to stabilise the lipid-free apoA-I structure and prevent the hydrophobic surface interacting and producing tetramers (dimer-dimer) interactions (Mei and Atkinson, 2011).

Borhani *et al*. suggested that the tetramer formed in the crystal structure is not necessarily indicative of apoA-I structure bound to lipids (Borhani et al., 1997). In which, the leucine and valine sidechains of each apoA-I monomer are unable to bind lipid as they are in the core of the 4-helix bundle formed in the tetramer, and the apoA-I dimers associate due to lack of lipids and form the tetramer through interaction of the respective dimers hydrophobic faces (Borhani et al., 1997).

There is further evidence that lipid-free apoA-I has a range of structures (Oda, 2017) from a two-state equilibrium between a 4- and 2-helix bundle at lower temperatures (Roberts et al., 1997; Rogers et al., 1998b) and multiple states at physiological temperatures including a molten globular state (Gursky 1996).

In the 4-helix bundle suggested structure the C-terminal residues (190-243) are in a less structured flexible conformation attached to the N-terminal residues (8-189) in compact helices (Roberts et al., 1997). The change in structure between the compact 4-helix bundle to the elongated 2-helix hairpin in equilibrium was suggested to be through a hinge mechanism and associated with apoA-I changing conformation for lipid binding (Roberts et al., 1997; Rogers et al., 1997; Rogers et al., 1998a; Rogers et al., 1998b).

Further research indicated that the N-terminal residues 1-98 are associated with structural stability in lipid free apoA-I due to conformational changes in N-terminally

truncated apoA-I mutants in particular Δ(1–43) (Rogers et al., 1998a). In contrast, the C-terminal truncation mutant overall structure was similar to the full-length conformation (Rogers et al., 1997; Rogers et al., 1998b). Both N- Δ(1–65) and C-terminal Δ(187–243) truncation mutations compared to full-length apoA-I showed reduced and greatly reduced lipid affinity, respectively (Rogers et al., 1998a). Rogers *et al*. also suggested that helix 3 could be associated with stabilising the lipid-free apoA-I conformation due to significant loss in alpha helicity and stability in a helix 3 Δ(88–98) internal deletion mutant (Rogers et al., 1998b).

The molten globular state at physiological temperature suggested the apoA-I secondary structure was well-defined with highly flexible alpha helices due to weak interhelical tertiary interactions (Gursky and Atkinson, 1996). This implied that the flexibility of the molten globular protein could aid in lipid binding in the formation of HDL particles (Gursky and Atkinson, 1996). More recent lipid-free apoA-I structural models are based upon using multiple techniques (Oda, 2017) such as mass spectrometry (MS), homology modelling and cross-linking (Pollard et al., 2013; Silva et al., 2005a), electron paramagnetic resonance spectroscopy (EPR) (Lagerstedt et al., 2012), combined crystal structures and molecular dynamics simulations (MDS) with cross-linking and MS (Segrest et al., 2014).

Silva *et al*. utilised 17 experimentally determined lysine cross-link distance restraints combined with homology modelling to produce an all atom lipid-free apoA-I structure (**Figure 1.8A**) (Silva et al., 2005a). The structure consists of a multiple helical bundle with a hydrophobic core including two helices in the C-terminal domain (215-225) which was spatially close to the N-terminus (Silva et al., 2005a). Another similar model (**Figure 1.8B**) with different overall structure and structural element arrangement due

to differences in cross-links formed compared to Silva *et al*. (Silva et al., 2005a) produced a structure which contained N-terminal residues 1-43, a 4-helix bundle between residues 44-186 (H1-7), and C-terminal helices (H8–10) (Pollard et al., 2013). In both cross-linking models the termini are in close proximity to each other and the helical bundle (Pollard et al., 2013; Silva et al., 2005a).

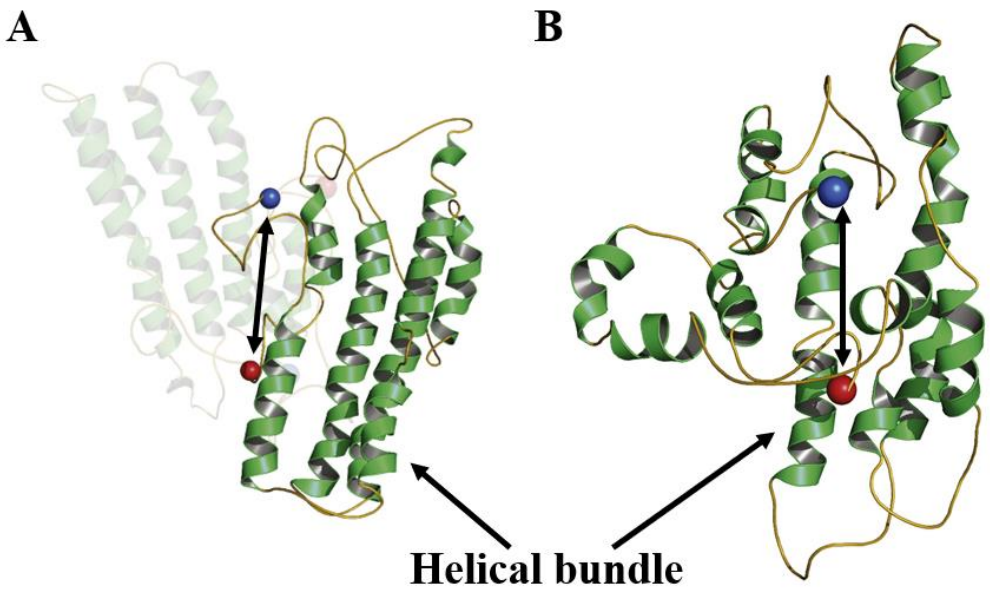

Figure 1.8. The lipid-free apoA-I structures produced by cross-linking (A) (Silva et al., 2005a) and (B) (Pollard et al., 2013). The double headed arrows indicate the N- (blue) and C- (red) termini proximity, the alpha helices (green), random coil (yellow) and the corresponding dimer of structure A is shown faded. Adapted from (Oda, 2017).

The "beta-clasp" mechanism describes destabilisation of the helical bundle due to C-terminal conformational changes in apoA-I during lipid binding (Lagerstedt et al., 2012; Oda et al., 2003). The C-terminal secondary structure was determined for residues 163-241, in which the secondary structure was α-helix (163-187), random coil (188-208) containing a flexible loop between residues 188-205, β-sheet (209-219), and α-helix/random coil (221/241) (Oda et al., 2003). In rHDL nanoparticles the flexible loop

and β-sheet regions converted to an ordered alpha helical structure suggesting the rearrangement of the apoA-I molecule to the "double belt model" conformation was initiated by these structural changes during lipid binding (Oda et al., 2003). Specifically, the change in conformation of the β-sheet occurred due to the energy provided by the conversion of residues 189-200 from random coil to α-helix during lipid binding (Lagerstedt et al., 2012; Nagao et al., 2014; Oda, 2017; Oda et al., 2003).

The "beta-clasp" mechanism was further investigated with EPR to produce a model of full-length lipid-free apoA-I structure (**Figure 1.9**) containing a central loop, an alpha helix bundle with a hydrophobic core of four anti-parallel β-strands in the N- and C-termini (Lagerstedt et al., 2012). The flexible central loop at residue 139 was suggested to be formed by the paired β-strands at residues 102-115 and 130-148, and the β-strands at residues 20–25 and 214-220 were suggested to stabilise the respective termini in close proximity to the overall protein structure (Lagerstedt et al., 2012).

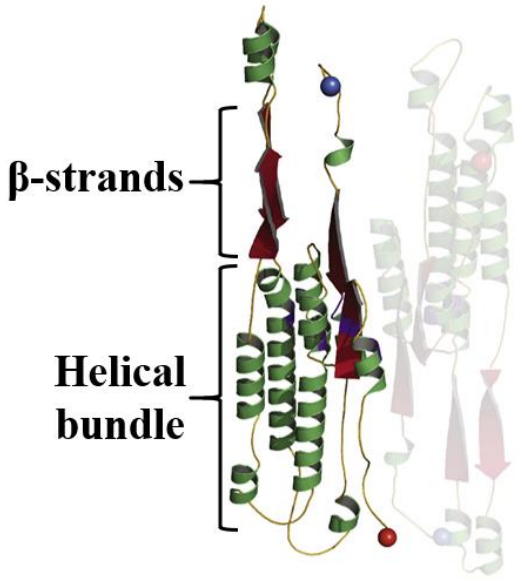

Figure 1.9. The "beta-clasp" model of lipid-free apoA-I. The termini are spheres N- (blue) and C- (red), α-helices (green), β-strands (red), random coil (yellow), the EPR spin-coupled residues (violet). the corresponding dimer is shown faded. Adapted from (Oda, 2017).

Segrest *et al*. produced a "chimera" structure (**Figure 1.10**) from the C-terminal residues 183-243 of apoA-I Δ(1-43) oriented in the hydrophobic cleft present throughout the closed hinge form of apoA-I Δ(185-243) (Oda, 2017; Segrest et al., 2014). The 15 ns MDS structure was described as a molten globule state structure and was the best fit to experimental data and models (Chetty et al., 2009; Lagerstedt et al., 2012; Pollard et al., 2013; Segrest et al., 2014; Silva et al., 2005a).

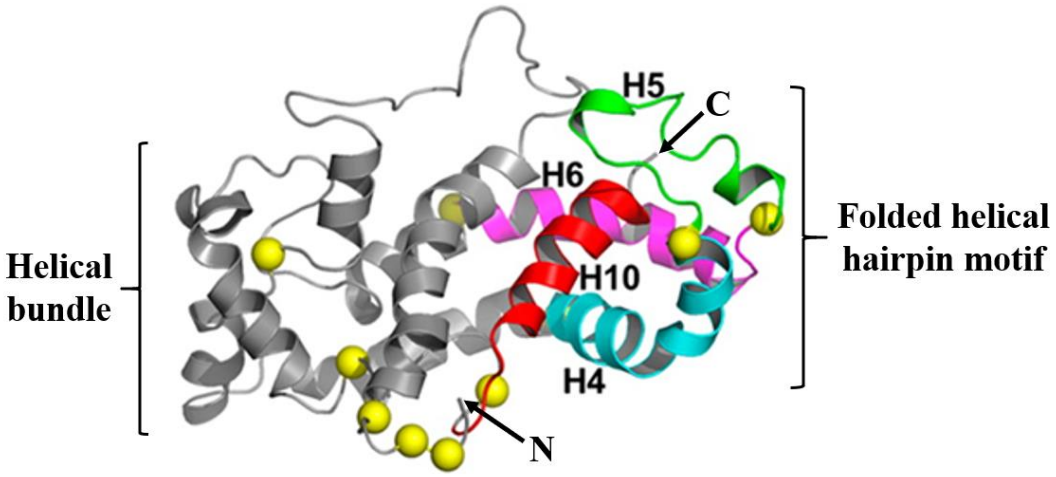

Figure 1.10. The "chimera" lipid-free apoA-I 15 ns structural model. The N- and C-termini are indicated with arrows, H4 (cyan), H5 (green), H6 (magenta), H10 (red), helical bundle helices H1-3 and H7-9 (grey), proline residues (yellow spheres), and the helical bundle and folded helical-hairpin motif are indicated. Adapted from (Segrest et al., 2014).

The structure contains termini in close proximity similar to previous models discussed, and 10 alpha helices (H1-H10) of varied sizes connected by regions of random coil (Segrest et al., 2014). The helical-hairpin motif contains H4 (100-120) in an antiparallel conformation with H6 (144-164) connected by H5, which contains two short alpha helices (126-129 and 137-141) and random coil (**Figure 1.10**) (Segrest et al., 2014). At 15 ns the motif is in a closed conformation compared to a more open helical-hairpin motif at later stages in the simulation (Segrest et al., 2014). The more open helical hairpin structure suggested a possible conformation for lipid binding in HDL formation or protein dimerization, with the movement of H5 outwards from above the enclosed C-terminal H10 (226-239) (Segrest et al., 2014).

The lipid-free apoA-I structures have similarities such as the amphipathic helical bundle and association of the N- and C- termini, and differences such as the helical spatial arrangements and assignment of secondary structure elements in the N- (1-43) and C- (190-243) terminal residues β-strands (Oda, 2017). Therefore, the lipid-free apoA-I structure is dynamic which is suggested to be due to various conformations required for the functions of apoA-I *in vivo* (Oda, 2017). Overall an understanding of how the lipid-free apoA-I structure relates to the protein function in HDL nanoparticles could inform how the atheroprotective mutations influence the apoA-I structure and in turn the HDL particle function.

1.6.2 HDL nanoparticle structure

It is difficult to study the structure of HDL nanoparticles and apoA-I in HDL directly by experimental techniques such as X-ray crystallography and NMR, due to the inhomogeneity in particle size and compositions (Phillips et al., 1997). Therefore, a combination of experimental (Gogonea, 2016) and computational molecular dynamics (MD) simulations (Pan and Segrest, 2016) have been used to determine the structure of discoidal and spheroidal HDL particles to various extents. The large size of rHDL nanoparticles has been an issue in X-ray crystallography and NMR studies and obtaining detailed structural information has remained a problem despite recent advances in solution state NMR truncated apoA-I structural determination (Bibow et al., 2017). The experimental structural techniques used to study the structure of rHDL nanoparticles are summarised in **section 1.8**.

The MD simulation types are briefly described below, and studies of HDL structure are a mixture of MD simulations and experimental data (Pan and Segrest, 2016). In all-atom MD (AAMD) each atom in every molecule in the system is represented

individually with respect to the force field used and individual atom behaviour is shown throughout the simulation (Pan and Segrest, 2016). Whereas, in a coarse-grained MD (CGMD) simulation the individual atoms are grouped so that each CG bead contains multiple atoms (≤10 atoms) compromising structural precision for increased simulation times and decreased computational cost (Pan and Segrest, 2016). In an MD simulated annealing (MDSA) simulation multiple structural conformations may be produced during the simulation as the system undergoes increases in temperature, using temperature jumps to surpass energy barriers, before cooling (Pan and Segrest, 2016).

1.6.3 Discoidal HDL nanoparticle structure

Earlier models of dHDL particles consisted of different apoA-I conformations in either a "picket fence", "hairpin" or "double belt" conformation whilst the lipids were in an oblate ellipsoid (discoidal), i.e. a lipid bilayer nanodisc (Gogonea, 2016). When apoA-I interacts with lipids the hydrophobic areas of the various proposed apoA-I dimers interact with the hydrophobic lipid regions, and vice-versa for the hydrophilic regions of the protein and the polar head groups of the lipids are exposed and interact with the aqueous phase (Borhani et al., 1997; Mei and Atkinson, 2011; Nath et al., 2007; Wu et al., 2009). Hagn *et al*. produced phospholipid nanodiscs smaller than 9 nm in diameter for structural analysis using high resolution solution-state NMR, with good quality spectra of an integral membrane protein embedded in the phospholipid nanodisc matrix, suggesting that the structure of apoA-I could be analysed using similar methods (Hagn et al., 2013).

The "picket-fence" (**Figure 1.11A**) model depicts two apoA-I molecules in which the alpha helices alternate in an antiparallel "fence-like" pattern with the helix normal parallel with the lipid bilayer nanodisc normal, the respective termini of each monomer

are associated either N- to N-terminus, or N to C-terminus (Gogonea, 2016; Jonas et al., 1989; Nolte and Atkinson, 1992; Phillips et al., 1997; Wald et al., 1990). This model has been discredited in the light of subsequent experimental data.

The "hairpin" model (**Figure 1.11B**) consists of antiparallel apoA-I monomers with each monomer folded back on itself at helix 5 (Rogers et al., 1998a; Silva et al., 2005b; Tricerri et al., 2001). The model was suggested to be able to accommodate up to 4 molecules of apoA-I in a dHDL particle compared to the belt model (Tricerri et al., 2001). The salt bridge interactions in both the "double-belt" and "hairpin" models are the same, however the protein-protein interactions are inter- and intramolecular, respectively (Martin et al., 2006; Silva et al., 2005b).

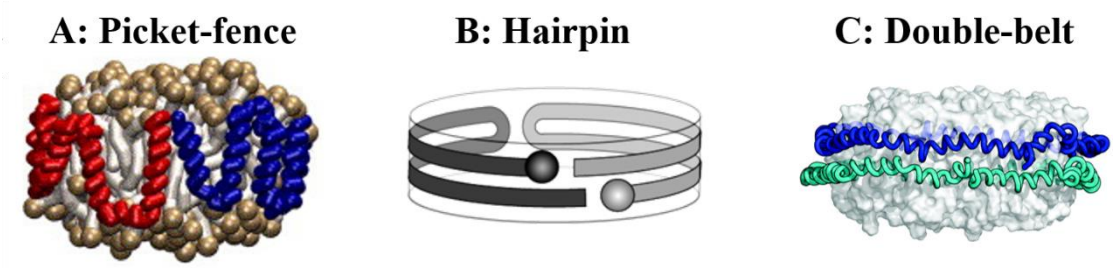

Figure 1.11. Structural models of discoidal HDL. **A)** The "picket-fence" model obtained from (Shih et al., 2007b). The apoA-I monomers (red, blue), lipid headgroups are spheres and lipid tails are white. **B)** The "hairpin" model of apoA-I monomers around a nanodisc lipid bilayer shape with the N-terminal residues as a sphere. Obtained from (Silva et al., 2005b). **C)** The "double-belt" model with antiparallel apoA-I Δ(1-43) monomers (blue, cyan) wrapped around a lipid bilayer nanodisc (white), obtained from (Nath et al., 2007).

However, experimental data and MD models indicated evidence for the "double belt" (**Figure 1.11C**) model with apoA-I Δ(1-43) monomers in a dimer that are antiparallel relative to each other, and the alpha helix normal is perpendicular to the lipid membrane normal (160 POPC molecules) in the dHDL particles (Bibow et al., 2017; Martin et al., 2006; Nath et al., 2007; Segrest et al., 1999). The "double-belt" model was supported by the crystal structure of apoA-I Δ(1-43) which was suggested to represent the lipid-bound structure of apoA-I (Borhani et al., 1997). The apoA-I Δ(1-43) N-terminally truncated protein is also referred to as a membrane scaffold protein 1 (MSP1) (Bayburt et al., 2002).

CGMD simulations supported the "double belt" model including a simulation starting with the protein in the "picket fence" conformation showing the protein conformation was unstable over a 1 μs timescale (Shih et al., 2007a; Shih et al., 2007b). The alignment of the antiparallel apoA-I monomers contained the helix 5 registry between the two monomers, where helix 5 of one monomer was aligned with helix 5 of the second monomer referred to as LL5/5 (Segrest et al., 1999). Additionally, the hydrophobic face of the amphipathic helices faces the lipid acyl chains whilst the polar face is exposed to the aqueous media (Segrest et al., 1999).

In further support of the belt model, Silva *et al*. showed that in dHDL (9.6 and 7.8 nm diameter) the apoA-I dimer contained the LL5/5 registry in the "double-belt" model and did not fit the "hairpin" model through comparison of inter- and intra-molecular cross-links and MS (Silva et al., 2005b). As well as, an alternative LL5/2 registry where the monomers in the dimer are moved with respect to each other, with helix 5 associated with helix 2 of the second monomer shown by intermolecular cross-links (Silva et al., 2005b). They also suggested that an apoA-I monomer in the hairpin conformation could

exist in particles with a dimer in the "double-belt" model conformation (Silva et al., 2005b).

Additional dHDL models contain specific secondary structure conformations for residues as random coil loop structures such as the "looped belt" and "solar flares" models. Martin *et al.* in the "looped belt" model of dHDL found evidence for continuous alpha helical secondary structure with a loop segment between residues 133-146 in lipid-bound apoA-I (**Figure 1.12A**), with predominantly intermolecular protein to protein monomer interactions supporting the "double-belt" model (Martin et al., 2006). The central loop in the "looped belt" model of HDL is a structural feature in the "beta-clasp" model of lipid-free apoA-I (Lagerstedt et al., 2012). The central loop in apoA-I was suggested to allow for changes in particle size between 7.2, 9.4 and 10.5 nm diameter dHDL particles by increasing or decreasing the size of the loop region (Martin et al., 2006).

Previously, Li *et al*. suggested the helices (H5/5) in lipid-bound apoA-I protruded outwards from the nanodisc edge in a "hinge-domain" (Brouillette et al., 1984; Li et al., 2004). This led to a proposed mechanism for increasing the particle size with a decrease in hinge size from 9.8 to 10.6 nm diameter, followed by the incorporation of the N-terminal domain (residues 1-43) helices in 11 residue increments as the particle size changed between 11.0, 11.4 and 12.0 nm diameter (Li et al., 2004).

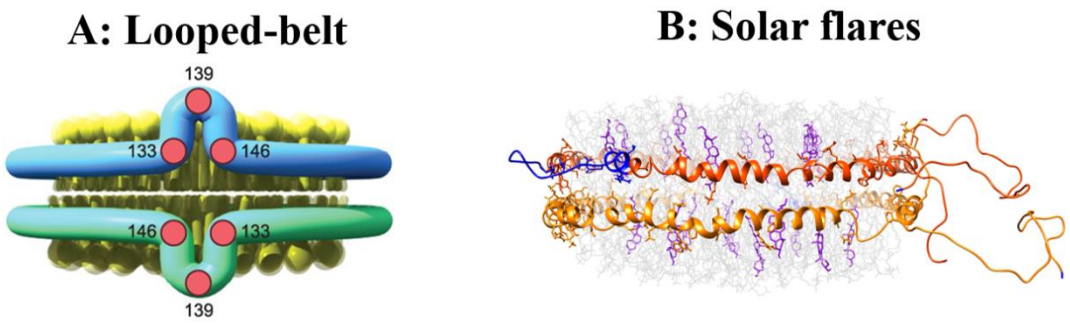

Figure 1.12. Further structural models of discoidal HDL. **A)** The "looped belt" model, apoA-I monomers (blue, cyan), lipid nanodisc (yellow). Obtained from (Martin et al., 2006). Residues 133-146 of the loop region are indicated with the central residue 139. **B)** The "solar flares" model, POPC:cholesterol:apoA-I 200:20:2, 9.6 nm diameter, POPC (light grey), cholesterol (purple), apoA-I chains (dark orange, orange), solar flare regions (blue), N- and C-termini residues (blue and red, respectively). Adapted from (Wu et al., 2007).

Another model called the "solar flares" model of dHDL (**Figure 1.12B**) was produced using hydrogen-deuterium exchange (HDX) MS, MS combined with cross-linking, and energy minimisation MD of the structure (Wu et al., 2007). The differences between this model and the "double-belt" model were the use of full-length apoA-I residues 1-243 including the N-terminal residues 1-43, and the "solar flare" random coil loop regions between residues 159-180 on each apoA-I monomer (Wu et al., 2007). The residues 159-170 were shown to be an LCAT interaction site in the lipid-bound apoA-I molecules (Wu et al., 2007). However, the "solar flare" model was subjected to 10 ns atomistic MD simulation in which the stabilising salt bridges of the solar flare regions were shown to collapse and suggested that further investigation was required by Wu *et al.* to test the stability of the atomistic dHDL model (Shih et al., 2008).

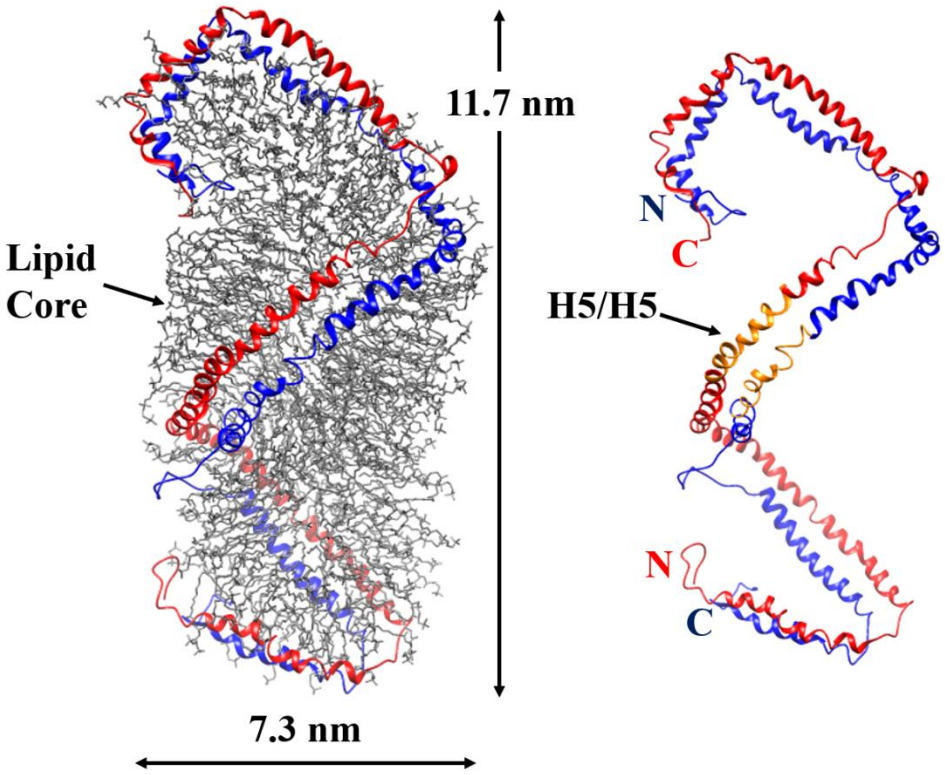

Figure 1.13. The anti-parallel double super-helix embedded around an ellipsoidal shaped lipid core (left) and without lipids (right). The N- and C- termini are indicated in the corresponding colour to the monomers, and the H5/H5 registry is indicated in orange. Adapted from (Wu et al., 2009).

An alternative model of lipid-bound apoA-I is the "double superhelix" (DSH) model (**Figure 1.13**) of nascent HDL (POPC:cholesterol:apoA-I 200:20:2 (M/M)) containing apoA-I in an anti-parallel double super-helix embedded around micellar lipids in a prolate ellipsoidal shape with the helix 5 registry (Gogonea et al., 2010; Wu et al., 2009). The model contains the "solar flare" regions between residues 159-180 and was produced using low-resolution small angle neutron scattering (SANS) with contrast variation and previous experimental data constraints (Wu et al., 2009). It was suggested that the DSH model shows a more flexible conformation of the nascent HDL particle allowing for maturation of the nascent HDL particles (Wu et al., 2009).

The thermodynamic stability of the DSH model was tested using various types of MD simulations with opposing results (Gogonea, 2016), as thermodynamically stable particles with solar flare regions containing fluctuating salt bridges (AAMD 60 ns) (Gogonea et al., 2010; Wu et al., 2009), and later suggesting the salt bridges could be viewed as "transient constructs" (Gogonea, 2016). However, this is in contrast to Jones *et al.*'s study that suggested the particle was not thermodynamically stable due to particle collapse to an oblate ellipsoid (CGMD 60 μs and MDSA 60 ns) (Jones et al., 2010).

Further study of dHDL produced the "Turtle" model using SANS with contrast variation with HDX-MS and cross-linking MS (Gogonea, 2016; Gogonea et al., 2013). The lipids are not in a bilayer as in the "double-belt" model but contained mainly lamellar lipids in an approximately discoidal shape, with the dimer of antiparallel helix 5 registry apoA-I in an open conformation as the dimer termini ends are spaced apart with micellar lipids in between (Gogonea et al., 2013).

The hairpin extended from the main discoidal lipids contained in chain A helices 2 and 3, 4, 5 (residues 66-143) aligned with helices 7, 6, and 5 (residues 121-194) in chain B, respectively, in particles without cholesterol (DMPC:apoA-I, 160:2, mol/mol) (Gogonea et al., 2013). The hairpin was suggested to allow for particle expansion such as incorporating lipid and cholesterol as the hairpin was absent in the particles containing cholesterol (DMPC:cholesterol:apoA-I, 172:18:2, mol/mol) (Gogonea et al., 2013). As the DSH and turtle models contained different open protein conformations this was suggested to be due to the particle composition, i.e. the use of DMPC or POPC, or the lipid:cholesterol:apoA-I molar ratios (Gogonea, 2016).

A recent experimentally determined model of truncated apoA-I Δ(1-54, 121-142) in discoidal rHDL-like nanodiscs (DMPC:protein 100:2 (M/M)) was produced using high resolution solution state NMR restraints combined with EPR spectroscopy (Bibow et al., 2017). The anti-parallel dimer conformation was stabilised by interhelical π-cation cluster interaction between H4 and H6 (**Figure 1.14**). Additionally, salt bridges were proposed such as the interhelical (H9 and H10) and intrahelical salt bridge interactions (H2 – 4) which could have stabilised the dimer (**Figure 1.14**) (Bibow et al., 2017).

Helices 4 and 6 are aligned in the LL5/5 registry in the lipid-free apoA-I WT Δ(1-43) crystal structure which is thought to represent lipid-bound apoA-I similar to the "double-belt" model (Borhani et al., 1997). However, this model does not contain full-length apoA-I WT therefore it may not accurately represent the apoA-I WT conformation in plasma or rHDL nanoparticles. Additionally, there is the absence of phospholipid structural information with this solution state NMR method. This is explored further in **Chapter 6**.

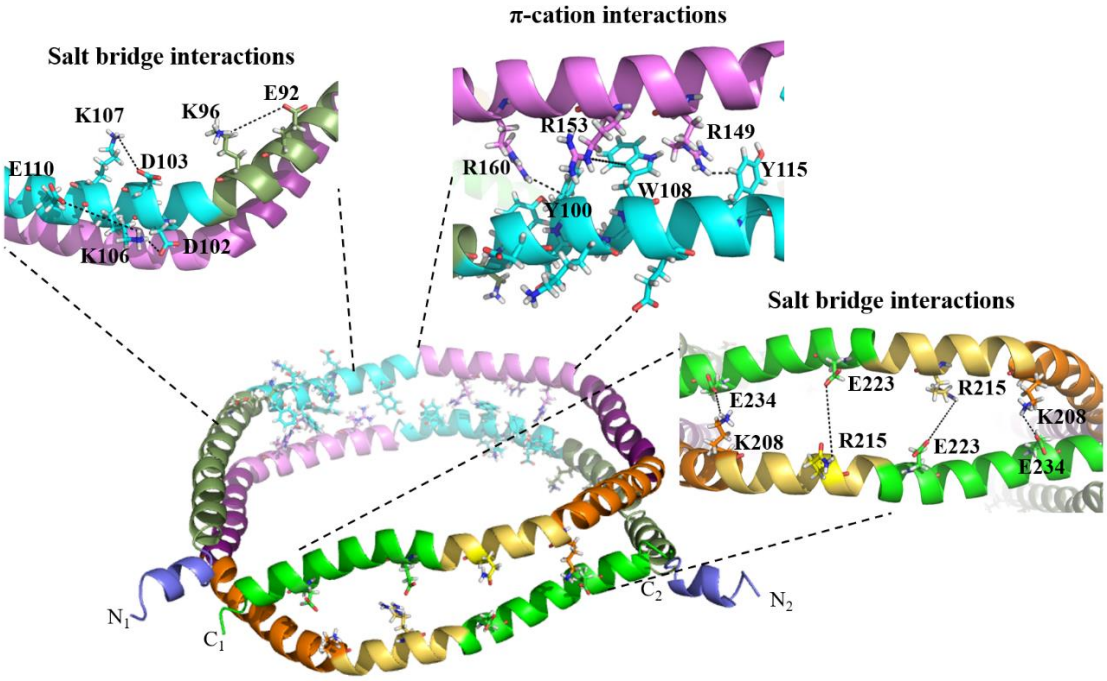

Figure 1.14. The structural model of apoA-I truncated apoA-I Δ(1-54, 121-142) in discoidal rHDL-like nanodiscs (DMPC:protein 100:2 (M/M). The stabilising π-cation interactions and proposed salt bridges are shown. The H1 (residues 55-65, violet), H2/3 (dark green), H4 (cyan), H6 (pink), H7 (dark purple), H8 (orange), H9 (yellow) and H10 (green). The monomer termini are labelled as N_1/C_1 and N_2/C_2. Adapted from (Bibow et al., 2017).

More recent studies have found further variation of the "double-belt" model to accommodate the different compositions of nascent HDL particles using experimental and atomistic MD simulations with longer timescales. In particular, nascent dHDL particles containing POPC:cholesterol:apoA-I molecule ratios of 160:24:2 (10 nm) and 200:20:2 (11 nm) were simulated for prolonged times using AAMD for 20 and 10 μs, respectively (Pourmousa et al., 2018). The protein monomers showed different conformations with respect to each other, and previous dHDL models in which the dimers have an approximately symmetrical conformation of both monomers, e.g. **Figure 1.12A-B** (Pourmousa et al., 2018).

The common feature of the helix 5 registry was retained in the simulations including the structure of helices 2-7 (Pourmousa et al., 2018), whilst some of the key differences are further outlined. The C-terminal region (**Figure 1.15A**, C_2) was shifted to the particle surface because of the position of the "hinge" region (**Figure 1.15**, N_1, yellow) in the 160:24:2 particle (Pourmousa et al., 2018). The secondary structural changes are indicated as helical bends and turns (**Figure 1.15**, blue, cyan), which became folded domains in both the N_2 and C_1 regions in the 160:24:2 particle, as well as the N-termini helix association stabilised by salt bridges in both particles (**Figure 1.15**, red) (Pourmousa et al., 2018).

Additionally, the nanodiscs do not have strictly planar bilayers, this is more prominent in the 160:24:2 particle, as the upper leaflet has a convex face compared to the lower leaflet concave face, to adapt to the lipid-protein circumference mismatch (Pourmousa et al., 2018). A non-planar nanodisc shape was described as "saddle shaped" HDL particles, with a more pronounced curvature of the lipids and increased protein twisting as the lipid:apoA-I or lipid:cholesterol:apoA-I molar ratio decreased below 160:2 and 160:24:2, respectively (Catte et al., 2006; Gu et al., 2010; Miyazaki et al., 2009).

The structures of dHDL produced have developed over numerous studies, and the particles are approximately discoidal in shape containing lipid, cholesterol and two apoA-I WT molecules. The nascent HDL structures produced by Pourmousa *et al*. (Pourmousa et al., 2018) have the advantage of comparatively longer simulation times, and demonstrate the versatility of apoA-I conformation in HDL particles, and the significant role apoA-I has in maintaining the structure of dHDL and adapting to forming various particles of different sizes (Pourmousa et al., 2018).

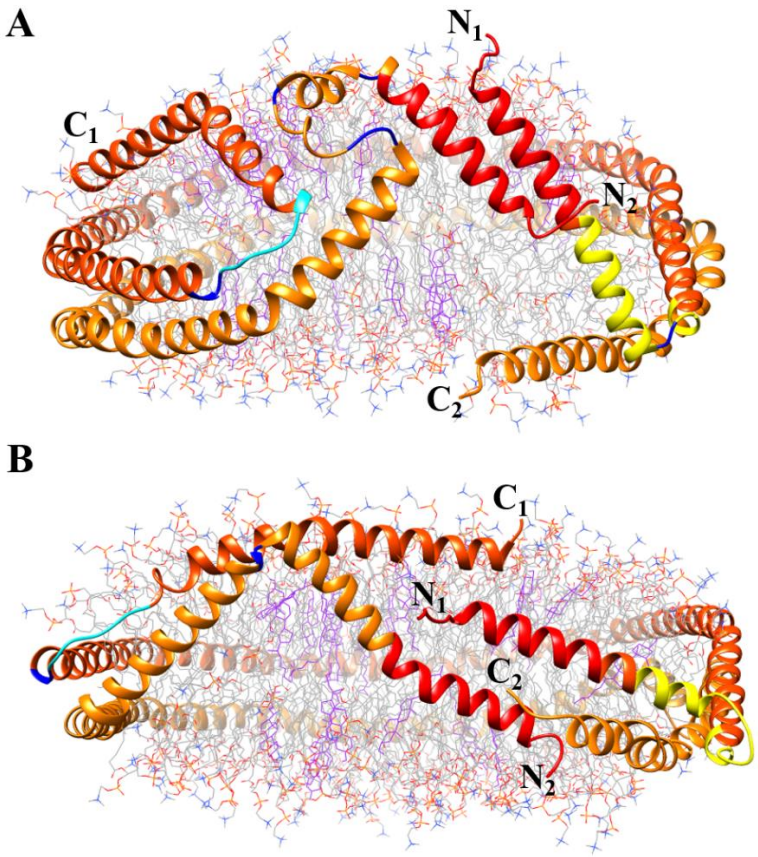

Figure 1.15. The AAMD simulation structures of nascent HDL containing POPC:cholesterol:apoA-I at ratios of **A)** 160:24:2 after 20 μs, and **B)** 200:20:2 HDL particle structure after 10 μs. Adapted from (Pourmousa et al., 2018). POPC headgroups (coloured by heteroatom), lipid tails (grey), cholesterol (purple), apoA-I chains (dark orange, orange), termini labelled N_1 C_1 and N_2 C_2, for chain 1 and 2, respectively. Structural features are helical bends and turns (blue), N-terminal residues 1-21 (red), hinge region residues 26-43 (yellow), and C-terminal bend residues 197-202 (cyan).

1.6.4 Spheroidal HDL nanoparticle structure

The structure of sHDL has been researched to a lesser extent than dHDL particles and is briefly described as understanding the structure of reconstituted discoidal HDL particles with the atheroprotective mutants was the primary focus in this research (see

reviews (Gogonea, 2016; Pan and Segrest, 2016) for more detail). The sHDL particles have a hydrophobic core containing triglycerides, cholesterol, cholesteryl ester and free cholesterol, surrounded by lipids with apoA-I molecules on the particle surface (Pan and Segrest, 2016). Various conformations of the apoA-I molecules have been proposed containing between 2-5 apoA-I molecules such as the "trefoil" model (Huang et al., 2011; Silva et al., 2008), the "helical-dimer-hairpin" model (Wu et al., 2011), and the "double-belt hairpin" model (Segrest et al., 2013). **Figure 1.16 A, B and C** show the general conformations of the apoA-I molecules in each model, respectively.

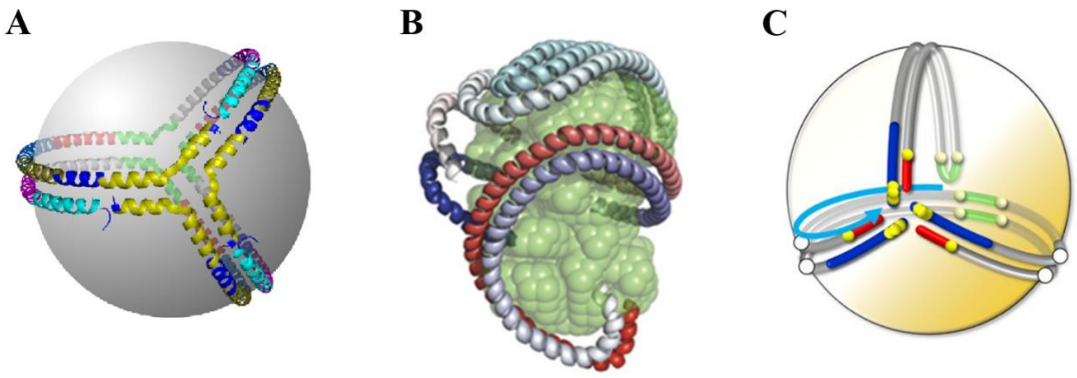

Figure 1.16. Structural models of sHDL. **A)** The "trefoil" model, 3 symmetrical helical apoA-I molecules surrounding a hypothetical lipid sphere, obtained from (Silva et al., 2008). **B)** The "helical-dimer-hairpin" model. The SANS lipid shape (green), apoA-I dimer (red, blue) and "folded-back hairpin" monomer (cyan), obtained from (Wu et al., 2011). **C)** The "double-belt-hairpin" model, the apoA-I dimer and hairpin monomer are wrapped around a hypothetical lipid sphere, obtained from (Segrest et al., 2013).

1.7 Atheroprotective apoA-I mutants

ApoA-I R173C (Milano) and apoA-I L144R (Zaragoza) are both considered to be atheroprotective mutants of apoA-I as carriers of either apoA-I mutant have low levels of HDL-C without cardiovascular disease or atherosclerosis (Franceschini et al., 1980;

Recalde et al., 2001). There are significantly more studies of the apoA-I R173C mutant compared to apoA-I L144R. The difference in amino acid structure in each atheroprotective mutant is shown in **Figure 1.17** for apoA-I R173C and L144R. These single amino acid changes affect the apoA-I structure in different ways, for apoA-I R173C the formation of cysteine-cysteine disulphide bonded dimers (Weisgraber et al., 1980). ApoA-I L144R may have different monomeric or lipid-bound conformation(s) (Fiddyment et al., 2011) possibly by additional intra- or intermolecular interactions due to the additional positive charge of the arginine residue.

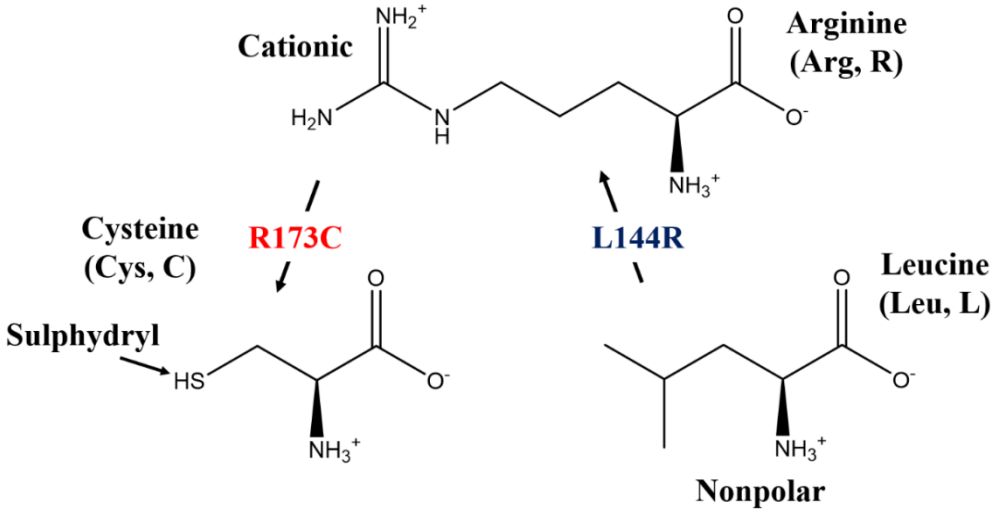

Figure 1.17. The structures of the amino acids arginine, cysteine, and leucine with the functional group (R) differences indicated as cationic, sulphydryl and nonpolar, respectively. The amino acid changes are indicated by the labelled arrows for apoA-I R173C (red) and L144R (blue).

The apoA-I Milano (R173C) mutation was discovered by Franceschini *et al*. in an Italian family from Northern Italy in 3 heterozygous carriers with hypertriglyceridemia (Franceschini et al., 1980), with the point mutation identified as R173C by Weisgraber *et al*. characterisation of the isolated mutated plasma apolipoprotein A-I (Weisgraber et al., 1980; Weisgraber et al., 1983). The plasma apoA-I R173C monomer molecular

weight was determined as ~28 kDa, a cysteine disulphide bond linked dimer ~55 kDa, and a mixed disulphide heteromer with apoA-II ~35 kDa (Weisgraber et al., 1980). Gualandri *et al*. determined that 33 carriers with ages between 2-81 years old were heterozygous carriers of the apoA-I R173C autosomal dominant trait (Gualandri et al., 1985). Additionally, the proportion of plasma apoA-I WT to apoA-I R173C in the mutation carriers was approximately 25 and 75 %, respectively (Weisgraber et al., 1983).

Recently, in a Spanish family 4 heterozygous carriers of the apoA-I Zaragoza variant were discovered between the ages of 13-37, a single amino acid missense point mutation at the 144th residue from leucine (L) to arginine (R) (L144R) (Recalde et al., 2001). The characteristics of the apoA-I R173C and L144R carrier phenotypes compared to apoA-I WT carriers are summarised in **Table 1.2**.

Both atheroprotective mutants exhibit phenotypes with reduced levels of plasma HDL, apoA-I, HDL-C and HDL CE, and increased HDL triglyceride (Franceschini et al., 1982; Franceschini et al., 1980; Recalde et al., 2001). The plasma HDL L144R particles were smaller than the control HDL particles (Recalde et al., 2001), whereas the HDL R173C particles also contained larger 12.0 nm diameter particles compared to 9.4 nm diameter measured by TEM (Franceschini et al., 1980). Further analysis of the plasma HDL R173C particles showed less HDL_2 particles and more HDL_3 particles with diameters between approximately 8.8-11.7 nm, compared to normal particle proportions (Franceschini et al., 1982). Enhanced CETP activity was suggested as a possible reason for the triglyceride enrichment and CE depletion of the HDL L144R particle core, and changes in the HDL composition overall (Recalde et al., 2001).

Table 1.2. The characteristics of the atheroprotective apoA-I R173C (Franceschini et al., 1982; Franceschini et al., 1980; Weisgraber et al., 1980; Weisgraber et al., 1983) and L144R (Recalde et al., 2001) carriers relative to apoA-I WT (normal) carriers. The ↑ and ↓ arrows indicate an increased or reduced level compared to normal apoA-I carriers, respectively. Triglycerides (TRL). Where available, the numbers are the percentage of the "normal" carrier levels the factor was reduced to, or approximate increase x2 i.e. 2-fold increase.

	Level/amount relative to apoA-I WT carriers in human carriers					
apoA-I mutation	**Plasma HDL**	**HDL Size**	**ApoA-I**	**HDL-C**	**CE**	**TRL**
R173C	↓	↓	↓	↓	↓	↑
L144R	↓	↓	↓ 60%	↓ 40%	↓ 65%	↑ x2

The phenotype characteristics of 4 carriers between ages 43-62, of the apoA-I L144R mutation from the Copenhagen City Heart Study were measured and consistent with Recalde *et al.*'s findings of lower levels of total cholesterol, HDL-C, apoA-I levels and increased triglycerides compared to apoA-I WT carriers (Haase et al., 2011). This was supported by apoA-I L144R expression in apoA-I deficient mice showing low HDL-C levels, and the mouse plasma HDL particles were characterised as predominantly small HDL_3 (pre-β- and α4-HDL) in the approximately 5-7.5 nm diameter range (Haase et al., 2011).

This suggested a decrease in LCAT activity due to a reduced ratio of cholesteryl ester: total cholesterol in the apoA-I L144R expressing mice (Haase et al., 2011), which

Recalde *et al*. observed in human carriers but they concluded that as the LCAT activity was normal this was unlikely (Recalde et al., 2001). ApoA-I L144R and LCAT expressing apoA-I deficient mice showed a similar ratio of cholesteryl ester: total cholesterol and a HDL particle size distribution (pre-β-, α1- to α4-HDL) to apoA-I WT expressing mice (Haase et al., 2011). The deletion of helix 6 (residues 143-164) in apoA-I WT resulted in a significantly inhibited LCAT activation (~97%) showing this region is important for LCAT activation (Sorci-Thomas et al., 1993). Therefore, further research could be required to conclusively determine if HDL L144R interacts differently with LCAT compared to HDL WT.

Helix 7 (residues 165-186) was deleted from apoA-I WT producing a ~98% LCAT activation inhibition suggesting the apoA-I R173C containing region of residues could also affect LCAT activation (Sorci-Thomas et al., 1993). Reconstituted HDL R173C relative to rHDL-WT particles had a decreased capability in LCAT activation, 40 and 70% reduction for 7.8 and 12.5 nm diameter rHDL, respectively, suggested to be a result of an altered conformation in the disulphide bond region in the rHDL-R173C particles (Calabresi et al., 1997a).

The apoA-I R173C mutation cysteine residue was suggested to destabilise the helix bundle domain conformation (**Figure 1.8-9**), as the cationic arginine residue may form an intrahelical salt bridge with the anionic glutamic acid residue 169 in apoA-I WT in the lipid-free or lipid-bound states (Alexander et al., 2009; Mei and Atkinson, 2011). There are also intermolecular salt bridges (D89-R173-E92) between the N-terminal helix bundle residues (D89, E92) and helix 7 (R173) of the respective monomers in the dimeric apoA-I Δ(185-243) crystal structure (**Figure 1.6**) (Mei and Atkinson, 2011). The apoA-I R173C mutation was suggested to prevent the formation of dimeric apoA-

I in a similar conformation to the lipid-free apoA-I WT Δ(185-243) dimer crystal structure due to destabilisation of the salt bridges (Mei and Atkinson, 2011).

Dimeric apoA-I R173C was suggested to affect rHDL particle size distribution with only dimers or multiple dimers associating with the HDL, so there could be limits upon the possible conformations of dimeric apoA-I R173C compared to apoA-I WT (Alexander et al., 2009; Calabresi et al., 1997b). A "double-belt" model of dimeric apoA-I R173C Δ(1-43) protein conformation was described as "locked" in a shifted helix-helix registration compared to the lipid-bound apoA-I WT LL5/5 registration, by the intermolecular covalent disulphide bond between adjacent monomer cysteine residues (Klon et al., 2000). The R173 residue was mutated to cysteine in both apoA-I monomers using PyMol software (Schrodinger, 2015) to visualise the shifted registry between the disulphide bonded monomers (**Figure 1.18**). It can clearly be observed that the interhelical registry of the apoA-I R173C monomers changes which could result in structural perturbations when the protein is lipid-free or rHDL-bound.

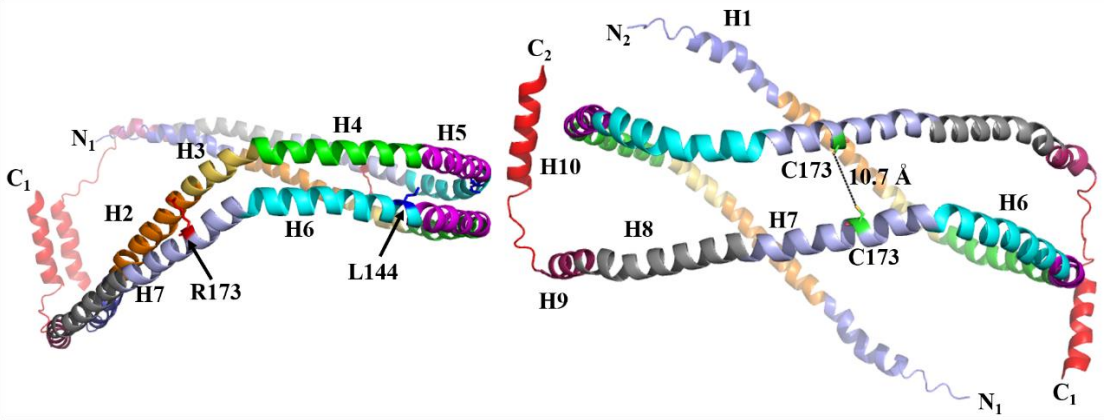

Figure 1.18. (Left) The apoA-I WT Δ(1-43) crystal structure monomers, chains A and B (1AV1 PDB) (Borhani et al., 1997). Selected helices are labelled to indicate the LL5/5 registry in apoA-I WT with the L144 (blue) and R173 (red) residue positions indicated. **(Right)** The R173 residue was mutated to cysteine in both of the apoA-I WT Δ(1-43) monomers and oriented with the C173 residues in anti-parallel proximity relative to each other. The distance between the -SH groups of the cysteine residues is indicated to show where the disulphide bond would align the monomers.

Significantly, the carriers of HDL R173C and L144R have a low incidence of atherosclerosis or CVD, with an altered HDL particle composition and size (Recalde et al., 2001; Weisgraber et al., 1980). This could be due to enhanced RCT, however the mechanism through which this could occur, or if the particles have a different structure affecting the particle functional capabilities (e.g., interactions RCT enzymes, cell receptors) compared to HDL WT particles is yet to be completely understood. This in turn, could be applied to future development of HDL-infusion therapies to treat atherosclerosis.

The structure of dimeric lipid-bound apoA-I R173C Δ(1-43) has been predicted with molecular modelling (Klon et al., 2000) based upon the belt model of apoA-I WT Δ(1-43) (Segrest et al., 1999). Structural models have been proposed for discoidal HDL

nanoparticles containing dimeric apoA-I R173C structure based upon lysine cross-linking combined with mass spectrometry distance restraints of 7.8 and 12.5 nm diameter rHDL-R173C nanoparticles has been studied (Bhat et al., 2010). Structural "double belt" apoA-I HDL models based upon this data (Bhat et al., 2010) and the apoA-I WT Δ(185-243) crystal structure (Mei and Atkinson, 2011) have been proposed for HDL R173C nanoparticles (Gursky et al., 2013).

Although, structural models have been proposed for the apoA-I R173C dimer conformation in discoidal rHDL nanoparticles there is a lack of high-resolution structural information from techniques such as solid-state NMR.

Little is known about the structural conformation of lipid-free or lipid-bound apoA-I L144R, with minimal studies demonstrating the feasibility of producing rHDL POPC:cholesterol:apoA-I L144R 200:20:2 (M/M) nanoparticles (Fiddyment et al., 2011). Therefore, there is a need to address the lack of structural information of the lipid-free apoA-I L144R protein and in rHDL nanoparticles. The advantageous phenotype observed in carriers of the apoA-I L144R mutation suggests that the apoA-I L144R protein could have better functional properties relative to apoA-I WT in the search for better rHDL-infusion therapy treatments.

1.8 Structural techniques used to study rHDL nanoparticles

This section briefly summarises the experimental techniques that have been used to characterise rHDL nanoparticles. **Table 1.3** shows the structural information provided by the experimental technique and the limitations with example references indicated.

Previous experimental techniques have focussed upon determining the apoA-I protein structure. However, the lipid and cholesterol component organisation within the rHDL nanoparticles could affect the particle function. A thorough comparison of the rHDL nanoparticle constituents could provide clues to determine why the apoA-I mutants are atheroprotective.

A lack of high-resolution solid-state NMR studies of full-length apoA-I proteins in rHDL nanoparticles indicated that further study of apoA-I WT and the mutants was required. The apoA-I proteins can be uniformly labelled with $^{15}N/^{13}C$ to produce solid-state 2D ^{13}C-^{13}C CP-MAS dipolar correlation and ^{1}H-^{15}N PISEMA spectra to study the apoA-I protein conformations. ^{31}P oriented solid-state NMR could be used to study the lipid organisation within the rHDL nanoparticles.

Table 1.3. A summary of the structural techniques used to characterise rHDL apoA-I WT nanoparticles.

Technique	Structural Information	Limitations	References
Circular dichroism	Average secondary structure estimations, thermal stability	Not residue secondary structure assignment specific	(Giudice et al., 2017)
Cross-linking with mass spectrometry	Inter- and intrahelical distance restraints	Cross-linker arm length	(Silva et al., 2005b)
EPR spectroscopy	Tertiary and secondary structure information		(Martin et al., 2006)
Solution NMR	High-resolution protein structural restraints, secondary and tertiary conformations	Truncated apoA-I Δ(1-54, 121-142), limited by HDL particle size	(Bibow et al., 2017)
Solid state NMR	Overall secondary structure conformation, some residue-specific information	Truncated apoA-I Δ(1-43), an abundance of cross-peaks due to large protein size	(Li et al., 2006)
X-ray crystallography	High resolution secondary structure assignment	Truncated lipid-free proteins, limited by apoA-I and HDL particle size	(Borhani et al., 1997)
DLS	Hydrodynamic diameter	Assumes an ideal spherical particle shape	(Wu et al., 2009; Wu et al., 2007)
NDGGE	Hydrodynamic diameter	Broad bands lead to estimated diameters	(Cavigiolio et al., 2008)
TEM	Diameter	Dried nanoparticles, limited morphology detection	(Zhang et al., 2011)
Cryo-em	Morphology	Limited contrast	(Zhang et al., 2011)
SANS	Average protein and lipid conformations	Low-resolution, time-averaged conformation	(Wu et al., 2009)

1.9 rHDL infusion therapy

Currently, there are no direct treatments for patients with atherosclerosis to remove accumulated cholesterol and induce plaque regression. There is an inverse relationship between HDL-C levels and the risk of cardiovascular disease (Lewis and Rader, 2005). There has been considerable interest in the development of HDL-infusion therapies (Darabi et al., 2016; Kingwell et al., 2014), which are the intravenous injection of reconstituted HDL nanoparticles to increase HDL-C levels to increase RCT and reduce arterial plaque size (Darabi et al., 2016; Kingwell et al., 2014).

Importantly, the development of an rHDL-infusion therapy could have the potential to directly treat atherosclerotic plaques, and it is of great interest to analyse the structure-function relationship of the rHDL constituents to inform the production of future atherosclerosis treatments.

There are rHDL-infusion therapies that have progressed from animal models to clinical trials in human patients (Darabi et al., 2016; Kingwell et al., 2014) which are discussed in the following sections for apoA-I WT and R173C rHDL-infusion therapies. The rHDL-infusion therapies differ in phospholipid composition, apoA-I type (plasma or recombinant apoA-I WT or recombinant apoA-I R173C), and the lipid:apoA-I molar ratio. Due to the abundance of phosphatidylcholine (PC) containing lipids in plasma HDL, lipids such as POPC and soy-PC have been predominantly used to form rHDL for infusion therapy studies (Darabi et al., 2016).

1.9.1 ApoA-I WT infusion therapy

An earlier study directly infused plasma HDL-VHDL into cholesterol-fed rabbits and induced the regression of atherosclerotic lesions, specifically aortic fatty streaks, and

lipid deposits. This was suggested to be through stimulation of RCT by the infused HDL particles (Badimon et al., 1990). A magnetic resonance imaging (MRI) clinical trial study of statin-treated patients undergoing existing atherosclerosis treatment with nicotinic acid over a year found a statistically significant elevation of HDL-C levels and reduction in LDL-cholesterol with reduced atherosclerosis progression (Lee et al., 2009). The nicotinic acid was used to increase the plasma HDL-C levels of the patients. This highlighted in a human study that elevated levels of HDL-C can reduce the progression of atherosclerosis.

The main clinical intravenous rHDL apoA-WT formulations are CSL111 and CSL112 from CSL Behring (Australia). CSL111 contained rHDL prepared from soy-PC:human apoA-I WT at a 300:2 molar ratio. rHDL-infusion treatments were trialled in human patients with acute coronary syndrome (ACS) (Tardif et al., 2007), peripheral vascular disease (Shaw et al., 2008), type 2 diabetes (Calkin et al., 2009; Patel et al., 2009), and in a mouse model (Chen et al., 2012). Positive differences in plaque morphology were observed such as a decrease in lipid content, macrophage-containing lipids cell size and inflammation of CSL111 treated plaques (Shaw et al., 2008), despite no significant decrease in the atheroma plaque volume (Tardif et al., 2007).

In comparison, the CSL112 rHDL formulation formed from soy-PC:plasma apoA-I WT at the 110:2 molar ratio rHDL-infusion therapy has been extensively researched (2013 – ongoing) from pre-clinical testing in animals (Diditchenko et al., 2013), to clinical trials in human patients (Easton et al., 2014; Gibson et al., 2019; Gille et al., 2018; Gille et al., 2019; Gille et al., 2014; Tricoci et al., 2015). The most recent trials are the large phase 2 AEGIS-I trial (Gibson et al., 2016) and a large phase 3 AEGIS-II trial

(NCT03473223, ongoing patient recruitment, expected completion 2022) (Karalis and Jukema, 2018).

CSL112 increases ABCA1 mediated cholesterol efflux (Diditchenko et al., 2013) for the treatment of ACS and post-ACS cardiovascular events in patients with stable atherosclerotic disease (Tricoci et al., 2015). In the various studies and clinical trials there was an increase in reverse cholesterol transport, apoA-I levels, and pre-β-HDL formation (Easton et al., 2014; Gille et al., 2014; Tricoci et al., 2015).

1.9.2 ApoA-I R173C infusion therapy

The primary rHDL-infusion therapy formulations containing apoA-I R173C are called ETC-216 (Esperion, USA) and MDCO-216 (Medicines Company, USA). The ETC-216 rHDL infusions contained POPC:recombinant apoA-I R173C at a 1:1 weight ratio (Kingwell et al., 2014). ETC-216 infusions showed significant regression in atheroma plaque volume in patients with ACS (Nissen et al., 2003), and in rabbits with advanced aortic lesions (Ibanez et al., 2008). Further study in rabbits with atherosclerosis showed the ETC-216 and apoA-I WT complexes produced similar plaque regression, but the apoA-I R173C rHDL showed greater anti-inflammatory, plaque stabilising, and antioxidant effects, as well as a decreased plaque macrophage density (Ibanez et al., 2012). Ibanez *et al*. suggested the changes in the "molecular footprint" of the atherosclerotic lesions produced a more stable phenotype with differences in the protein and gene expression in the aortic lesions treated with ETC-216 (Ibanez et al., 2008). Therefore, the apoA-I R173C complexes could produce rapid regression and atherosclerotic plaque stabilisation.

Manufacturing problems, side-effects and expensive production costs affected the ETC-216 and CSL111 rHDL formulations halting further studies (Darabi et al., 2016; Karalis

and Jukema, 2018; Kingwell et al., 2014). The ETC-216 manufacturing was optimised to reduce the side-effects observed in clinical trials (Karalis and Jukema, 2018; Reijers et al., 2017), and further researched as MDCO-216 in monkeys (Kempen et al., 2013) and human patient trials (Kallend et al., 2016; Kempen et al., 2016a; Kempen et al., 2016b; Nicholls et al., 2018) with each trial indicating MDCO-216 was well-tolerated. The results suggested MDCO-216 could potentially be used to treat patients with atherosclerosis as suggested by the increase in pre-β-1 HDL levels and ABCA1 mediated cholesterol efflux, and lipoprotein composition changes (Kallend et al., 2016; Kempen et al., 2016a; Kempen et al., 2016b; Nicholls et al., 2018). However, the drug was discontinued by the Medicines company due to the lack of clinical efficacy in the regression of atherosclerotic plaques (Nicholls et al., 2018) despite the complex being well tolerated in animals and human patients (Li et al., 2019).

1.9.3 Adaptations of rHDL infusion therapy composition

Optimisation of rHDL based upon the structure function relationship of the components within the formulation has been called “smart” rHDL therapy to optimise the atheroprotective effects of rHDL (Darabi et al., 2016). Different lipids or lipid ratios could affect the particle function, such as in CER-001 egg-sphingomyelin:DPPG in a wt ratio of 97:3 combined with recombinant human apoA-I at protein:lipid wt ratio of 1: 2.7 (Barbaras, 2015; Tardif et al., 2014), similar to how changing the apolipoprotein could affect the particle function.

For example, sphingomyelin lipids have a high affinity to cholesterol, stabilise rHDL particles, regulate plasma HDL enzymes, and are a substrate for potent signalling mediators (Darabi et al., 2016). PC containing lipids stabilise rHDL, are a substrate for potent signalling mediators, have anti-inflammatory and anti-apoptic effects, ABCA1

mediated cholesterol uptake, and modulate particle uptake and clearance (Darabi et al., 2016). Additionally, phosphatidylglycerol containing lipids have similar effects to PC lipids, without anti-inflammatory/anti-apoptic effects, and aid in the regulation of apoA-I level and function, and regulation of plasma HDL enzymes (Darabi et al., 2016).

An interesting approach to rHDL formulations was as a dual-therapy with statin-loaded rHDL nanoparticles in apoE knockout mice with atherosclerosis (Duivenvoorden et al., 2014). The discoidal rHDL complexes were 25-30 nm diameter and contained lipids (lyso-PC, DMPC): human apoA-I: simvastatin at a ratio of 80.7: 7.7: 11.6 wt % of the nanoparticle (Duivenvoorden et al., 2014). The complexes *in vitro* had an anti-inflammatory effect in J774 macrophages and accumulated in plaques with a decreased macrophage plaque content *in vivo* in the mice model (Duivenvoorden et al., 2014).

Another study demonstrated that rHDL nanoparticles with approximately 10 nm diameter were combined with an MRI imaging agent which binds to collagen to monitor changes in arterial plaques in a mouse model (Chen et al., 2013). The use of statins and an imaging agent in the rHDL nanoparticles demonstrates further possibilities of rHDL-infusion therapies (Di Bartolo et al., 2018).

1.9.4 Limitations of rHDL-infusion therapies

The studies of rHDL infusion therapies discussed have limits such as small study population sizes, the short time period of assessment following treatment, and a need to assess how plaque vulnerability is affected by rHDL infusions which atheroma volume does not include (Kingwell et al., 2014). As well as improvements in choosing primary efficacy end points, and choice of patients as the trials focussed on potent statin treated patients with ACS which could have affected the effectiveness of the HDL infusions

due to the improved prognosis of ACS patients treated with these statins (Karalis and Jukema, 2018).

1.9.5 Summary

Overall, there is evidence of pre-clinical atheroprotective functions and properties in rHDL-infusion therapies despite the mixed results of clinical trials suggesting a greater understanding is required of HDL functionality and properties in stimulation of RCT compared to only increasing the HDL-C levels (Karalis and Jukema, 2018). Additionally, the combined approach of determining plaque stability, factors which affect plaque vulnerability, and the use of multiple imaging techniques could allow for greater characterisation than plaque size and regression to determine the success of an rHDL therapy in the treatment of atherosclerosis (Di Bartolo et al., 2018).

Taken together, there is evidence for both apoA-I WT and R173C rHDL-infusion therapy atheroprotective effects indicated by the regression in the size of atheroma plaques in animal models and human patient studies. Therefore, there is a benefit to continuing research which could provide mechanistic information informing the development of future rHDL-infusion treatments. A greater understanding of the differences and comparison of the molecular features which enhance the atheroprotective properties of rHDL containing apoA-I WT, apoA-I R173C and apoA-I L144R could inform future rHDL therapy approaches.

Furthermore, the adaptation of the rHDL nanoparticle compositions and the potential as a combined therapy for atherosclerosis for cholesterol efflux and as a drug delivery system demonstrate that rHDL-infusion therapy is versatile with many options to explore.

1.10 Aims

The overall aim of this thesis is to understand how the structure of the apoA-I R173C and L144R mutants is related to their atheroprotective function. This is key to understanding how the HDL nanoparticles *in vivo* can transport cholesterol effectively to gain an enhanced understanding of the low atherosclerosis incidence in the mutant carriers. Importantly, the direct structural comparison between rHDL nanoparticles containing the atheroprotective apoA-I mutants and apoA-I WT will inform possible rHDL-infusion treatments for atherosclerosis.

To establish if there are significant differences or similarities in the respective particle structure that affect the HDL particle function in cholesterol transport, through the following objectives:

- To implement a methodology for the expression of the atheroprotective apoA-I mutants with a sufficient yield for the routine expression of unlabelled, and dual or mono-isotopically (^{13}C and/or ^{15}N) labelled protein for NMR studies.

- Establish a working protocol for preparing rHDL nanoparticles incorporating apoA-I WT and the atheroprotective mutations for biophysical characterisation. This will enable the detection of structural differences or similarities that could affect the rHDL nanoparticle function.

- Use a combination of characterisation techniques, solid-state NMR, combined with computational modelling, to examine the molecular structure and organisation within the particles of the protein, phospholipid, and cholesterol constituents. To produce structural models of the respective rHDL nanoparticles

and search for molecular level structural clues to establish a structure-function relationship.

- To test the capability of the lipid-free and lipid-bound apoA-I proteins in rHDL nanoparticles to induce cholesterol efflux *in vitro* from cholesterol-loaded macrophages.

2 Theory

This chapter is an introduction to the main techniques used for analysis of the reconstituted HDL (rHDL) nanoparticles. Both circular dichroism (CD) and solid-state NMR (SS NMR) were used to examine the structure of apoA-I within the rHDL nanoparticles. SS NMR was also used to characterise the structure of the lipids in the rHDL nanoparticles.

2.1 Circular dichroism

CD is a widely used technique to study the overall secondary structure conformations and thermal stability of proteins (Greenfield, 2006a; Greenfield, 2006b). The definition of CD is the "unequal absorption of left-handed and right-handed circularly polarised light" (Greenfield, 2006b). At the wavelength λ with the left-handed (ε_L) and right-handed (ε_R) circularly polarised light extinction coefficients, this is represented by (Sreerama and Woody, 2004a):

$$\Delta\varepsilon(\lambda) = \varepsilon_L(\lambda) - \varepsilon_R(\lambda) \qquad \textbf{[1]}$$

The following units are typically used for CD called molar CD (M^{-1} cm^{-1}) and can be interconverted with molar ellipticity [θ] (deg cm^2 $dmol^{-1}$) (**Equation [2]**) (Sreerama and Woody, 2004a).

$$\Delta\varepsilon = \frac{[\theta]}{3298} \; and \; [\theta] = \frac{100 \cdot \theta}{C \cdot l} \qquad \textbf{[2]}$$

The concentration (C) in g/L of the sample is taken into account with the pathlength l in cm (Sreerama and Woody, 2004a). The difference between the absorption of the two

opposing circularly polarised light beams occurs when there are chiral centres present in the sample molecule(s) (Wallace and Janes, 2009).

To understand how chiral centres in a molecule enable CD signal detection the electric vector model is shown in **Figure 2.1**. Where the opposing beams of circularly polarised light are of equal magnitude and form a plane polarised light beam (Wallace and Janes, 2009). When the polarised light passes through an achiral sample no CD signal is detected as $\varepsilon_L(\lambda) = \varepsilon_R(\lambda)$ which results in a linear path of the vector (**Figure 2.1**, **left**).

A CD signal occurs, either positive or negative as in **Figure 2.2**, when the sample contains chiral centre(s) which absorb left- or right-handed circularly polarised light in varied amounts at different wavelengths in the far UV range (180 – 250 nm) (Greenfield, 2006b; Wallace and Janes, 2009). This absorption changes the magnitude of the vectors with respect to each other, e.g. greater absorption of the right-handed circularly polarised light in **Figure 2.1 (right)**, and results in an elliptically polarised light beam (Wallace and Janes, 2009). The ellipticity angle θ by definition is $\tan\theta = \frac{minor\ elliptical\ axis}{major\ elliptical\ axis}$ (Wallace and Janes, 2009).

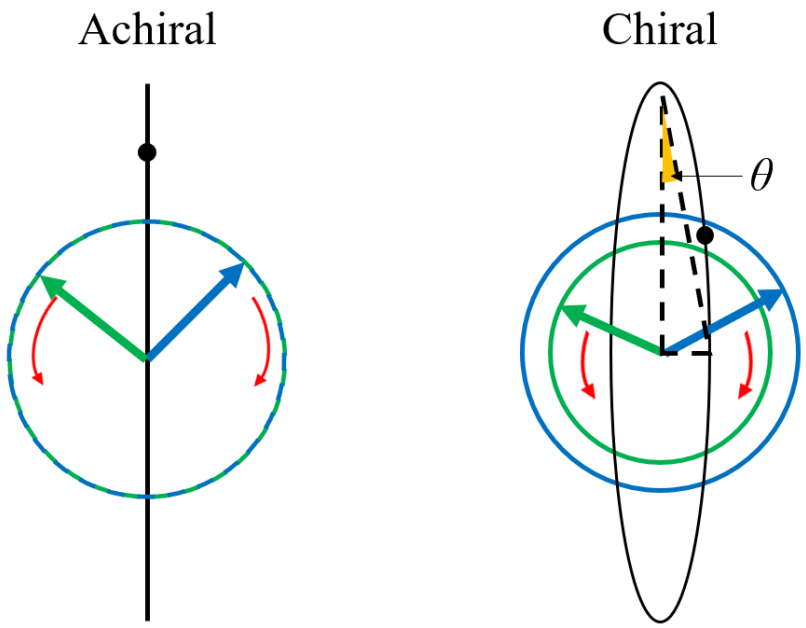

Figure 2.1. A comparison of circularly polarised light absorption in an achiral and a chiral centre containing sample, the field of view is down the direction of the light source (Wallace and Janes, 2009). Left- (blue) and right- (green) handed circularly polarised light vectors and the individual rotations (red arrows). The resultant linear and elliptical vectors (black) for the achiral and chiral samples, respectively. The ellipticity angle θ (orange). Adapted from (Wallace and Janes, 2009).

The primary chiral chromophores in proteins are peptide bonds in the polypeptide backbone that have specific electronic transitions that enable structural studies of proteins with CD (Wallace and Janes, 2009; Whitmore and Wallace, 2008). The transitions in the peptide bond chromophore are between the $n \rightarrow \pi^*$ and $\pi \rightarrow \pi^*$ electron molecular orbitals with the maximum absorption wavelengths at approximately 220 and 190 – 200 nm, respectively (**Figure 2.2**) (Wallace and Janes, 2009; Whitmore and Wallace, 2008).

Characteristic CD spectra (**Figure 2.2**) are produced when analysing proteins as the chromophores become aligned in specific arrangements in secondary structures such as α-helices or β-sheets (Greenfield, 2006b). In a protein with a predominantly α-helical

structure, such as apoA-I, the $\pi \rightarrow \pi^*$ transition produces two negative minima at ~222 and 206 nm, and the $n \rightarrow \pi^*$ transition has a positive maxima at ~190 nm (Holzwarth and Doty, 1965).

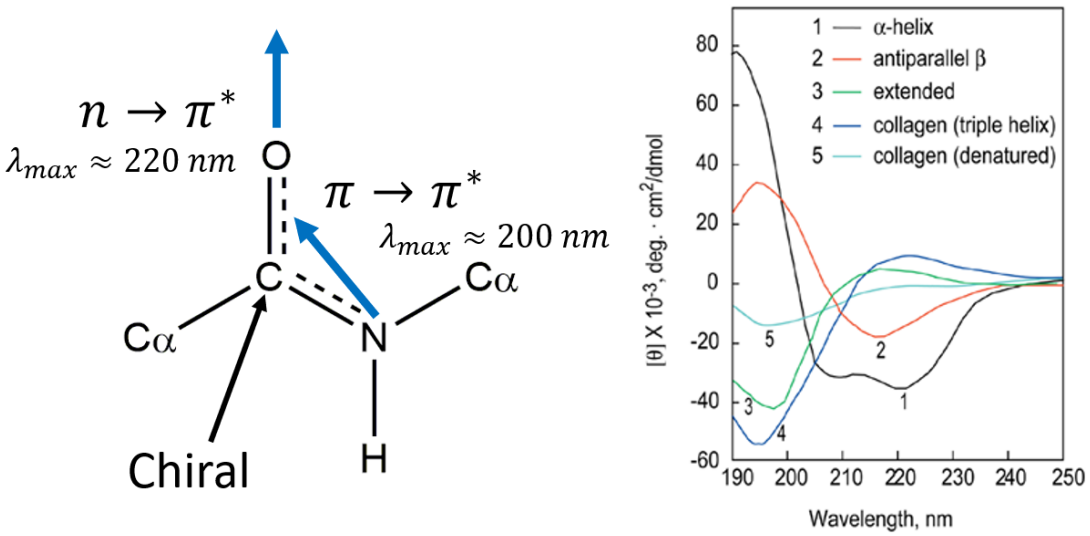

Figure 2.2. (Left) The peptide bond chiral chromophore electronic transitions which occur when circularly polarised light is absorbed during CD. The transition dipoles of the $\boldsymbol{n} \rightarrow \boldsymbol{\pi}^*$ and $\boldsymbol{\pi} \rightarrow \boldsymbol{\pi}^*$ molecular orbital transitions (blue arrows). Adapted from (Whitmore and Wallace, 2008). **(Right)** Example characteristic secondary structure CD spectra obtained from (Greenfield, 2006b). Poly-L-lysine, (1) α-helical at pH 11.1, (2) anti-parallel β-sheet at pH 11.1, and (3) extended conformation (random coil) at pH 5.7. Placental collagen, (4) triple-helix native, and (5) denatured.

The secondary structure components in a protein sample can be estimated with various deconvolution algorithms combined with fitting to a reference data set including proteins with known structures (Greenfield, 2006b; Sreerama and Woody, 2004a; Wallace and Janes, 2009). Therefore, CD spectroscopy can be used to determine the molecular structure of proteins. Furthermore, changes in the CD spectra can be used to determine important thermal stability and denaturation properties (Greenfield, 2006a).

2.2 Solid-state NMR

Important aspects of SS NMR analyses are focussed upon that were used to observe high-resolution spectra such as magic-angle spinning, cross-polarisation, proton decoupling and broadline SS NMR. To understand these concepts the basic principles of primarily SS NMR are briefly explained.

Nuclei have intrinsic angular momentum called spin (I) which produces a nuclear magnetic moment (μ) and the ratio between I and μ is called the gyromagnetic ratio (γ) (Apperley et al., 2012). In this study, I = ½ nuclei were observed in apoA-I and POPC (i.e., ^{15}N, ^{13}C, and ^{31}P), and the following description will therefore be limited to spin ½ nuclei. Nuclear spins precess about the magnetic field at an angular frequency $\omega = \gamma B_0$, called the Larmor precession frequency, where $\omega/2\pi$ is in the MHz (radiofrequency (RF)) range for typical magnetic field strengths of 7 – 20 T.

The nuclear magnetic moment can exist in $2I+1$ projections on an axis and the magnetic component quantum number (m_I) defines the number of spin states under B_0 (Apperley et al., 2012). In terms of energy levels, spin ½ nuclei can exist in two energy states where m_I equals +½ or -½ known as the α and β states, respectively. The splitting into energy levels in the presence of a magnetic field is called the Zeeman effect with the nuclear magnetic moments in a low (α) or high (β) energy state aligned with or opposing B_0 (Apperley et al., 2012). A slight excess in the population of spins in the low energy state gives rise to bulk magnetization, which can be represented by a vector. The energy difference between the two states is given by $\Delta E = h\omega/2\pi$.

The vector model can be used to describe what occurs during an NMR experiment. The nuclei in a sample possess an overall net magnetisation of the nuclear magnetic moments under an applied magnetic field (B_0) at equilibrium, and the magnetisation

vector is aligned along B_0, which corresponds to the z-axis in the laboratory frame (**Figure 2.3**). A perturbation of the nuclear spins away from equilibrium occurs when oscillating electromagnetic radiation is applied at frequencies close to the Larmor frequency.

In the vector model, this perturbation is represented as a rotation of the bulk magnetization (M) about either the x-axis or y-axis. An RF pulse of defined duration and strength is applied. In order to observe an NMR signal, a pulse of sufficient length and strength is required to rotate the magnetization into the x-y, or transverse, plane; this is called a 90° or $\pi/2$ pulse, referring to the tip-angle of the magnetisation. The magnetisation vector then precesses in the transverse plane about the z-axis at the Larmor frequency and generates an oscillating signal in the RF coil, which is detected as a free- induction decay (FID) (Keeler, 2010).

The frequency domain spectrum is produced when the time domain FID signal is converted to the frequency domain by Fourier transformation. The precession frequencies of spins in different chemical environments is determined by chemical shielding of the nuclei by the circulating electrons, which may enhance or reduce the overall magnetic field experienced by the nuclei. Chemical shielding is anisotropic, but for small molecules undergoing rapid reorientation in the magnetic field the shielding effect around each nucleus is averaged to produce a single isotropic chemical shift. Nuclear spins also couple to one another through bonds (J-coupling) or through space as a result of the interactions between the nuclear dipoles.

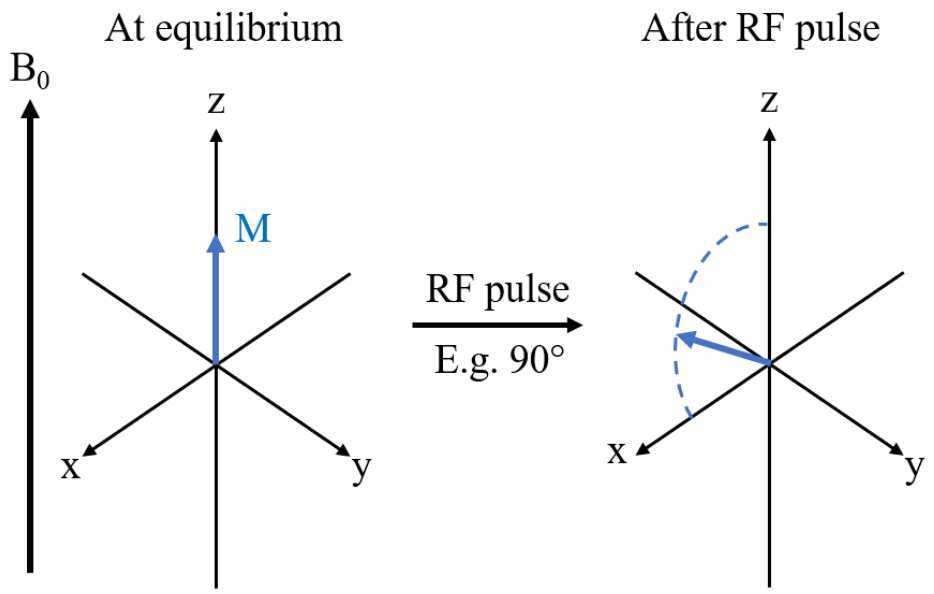

Figure 2.3. The vector model of an NMR experiment. The direction of the bulk magnetisation (M) of the nuclei in a sample at equilibrium under B_0 (left). After an RF pulse is applied, e.g., 90° or $\pi/2$ radians, the bulk magnetisation moves outwards as indicated by the dashed line towards the xy-plane. Adapted from (Keeler, 2010).

After the RF pulse the magnetisation vector of the nuclei reverts to the overall net magnetisation aligned with B_0 at the equilibrium position, this is known as relaxation (Keeler, 2010). There are two types of relaxation called longitudinal (T_1) and transverse (T_2) relaxation. T_2 relaxation concerns the loss of coherence of the spins, which dampens the oscillating signal. T_1 relaxation concerns the re-establishment of the Boltzmann distribution.

An example pulse sequence of a ^{13}C NMR experiment with proton decoupling is shown in **Figure 2.4**. The nuclei in a sample are initially at equilibrium under B_0. A radiofrequency pulse is applied, e.g., at 90° or 180° in t_p. The following period t_{acq} is when the FID signal is acquired with simultaneous proton decoupling (Keeler, 2010). This pulse sequence is repeated multiple times to improve the signal-to-noise ratio and each repeat is known as a transient. A delay t_r, called the recycle delay, between each

pulse-acquisition step is required to allow the spins to relax to their equilibrium populations. The transients are averaged before conversion of the FID to an NMR spectrum using Fourier transformation (Keeler, 2010).

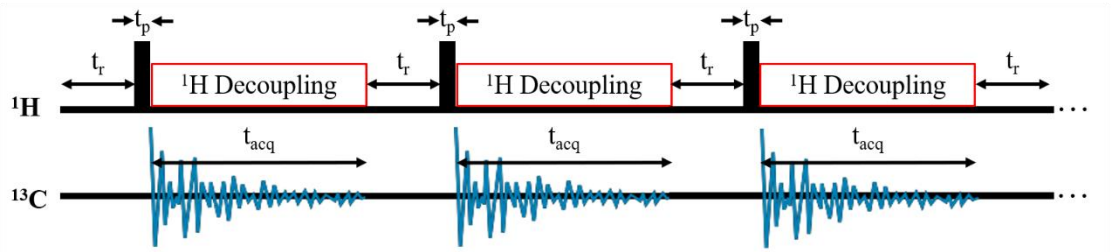

Figure 2.4. An example NMR experiment pulse sequence for ^{13}C nuclei with ^{1}H decoupling. The period the nuclei in a sample reach equilibrium is the relaxation delay t_r. The RF pulse is applied during t_p and the FID is acquired in the acquisition period (t_{acq}). During t_{acq} proton decoupling is applied. The ellipses represent *n* repeats of the pulse sequence. Adapted from (Keeler, 2010).

2.2.1 Magic-angle spinning

In the solution NMR analysis of small-to-medium size molecules (100-20,000 Da), effects from dipolar coupling and chemical shift anisotropy (CSA), i.e. orientation dependence of the chemical shielding, are observed minimally due to the rapid isotropic tumbling of molecules in solution (Duer, 2004). During the timescales used in solution NMR this results in an averaging of the CSA orientation dependence to zero (Duer, 2004). In solids, or semi-solid materials, these effects are not averaged to zero and can result in broad lineshapes in the NMR spectrum (Bothwell and Griffin, 2011). The lineshapes contain information about molecular dynamics and can provide orientational information as will be shown later. However, it is often necessary to apply measures to narrow the NMR lines in order to obtain high-resolution spectra.

Magic-angle spinning (MAS) is frequently used in SS NMR to produce high-resolution spectra with narrow lineshapes by removing the effects of the CSA and heteronuclear dipolar coupling (Duer, 2004). Typically, the sample is packed into a zirconium rotor and rotated at high frequencies (2 kHz to > 100 kHz) around the spinning axis (**Figure 2.5**). The spinning axis is at the magic-angle θ_R = 54.736° relative to B_0 (Duer, 2004). The shielding tensor principal z-axis orientation relative to B_0 is described by the angle θ (**Figure 2.5**) and the molecular orientation dependence is defined as $3\cos^2\theta - 1$ (Duer, 2004). The principal z-axis and the spinning axis are separated by angle β (Duer, 2004).

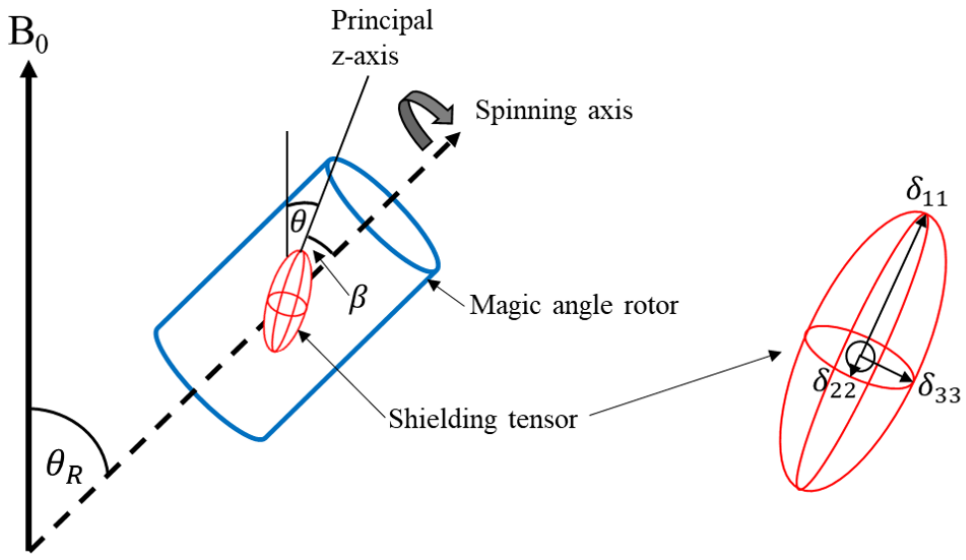

Figure 2.5. The magic-angle spinning experiment (left), at the magic-angle θ_R = 54.7° relative to B_0, the rotor is spun rapidly about the spinning axis (Duer, 2004). The shielding tensor principal z-axis is oriented at angle θ and β relative to B_0 and the spinning axis, respectively. The chemical shift shielding tensor components (right). An ellipsoid representation of the chemical shielding tensor with the separate components δ_{11}, δ_{22} and δ_{33}. Adapted from (Duer, 2004).

The principle of MAS can be explained with a powder sample containing all molecular orientations where θ and β can be all possible values. The interaction tensor for each molecule in a solid sample is in a fixed position with multiple molecules in different orientations in the sample (Duer, 2004). The angle θ changes with time as the solid sample is rapidly spun at θ_R. The average of the nuclear spin interaction orientation dependence ($3\cos^2\theta$) with the angles θ, β, and θ_R as described above (Duer, 2004) is:

$$\langle 3\cos^2\theta - 1\rangle = \frac{1}{2}(3\cos^2\theta_R - 1)(3\cos^2\beta - 1) \qquad \textbf{[3]}$$

At the magic-angle $3\cos^2\theta_R - 1 = 0$, hence the average interaction anisotropy $\langle 3\cos^2\theta - 1\rangle = 0$ and only the isotropic component of the chemical shielding is observed (Duer, 2004). This produces SS NMR spectra which have narrow bands and removes the effects of anisotropic lineshape broadening (Bothwell and Griffin, 2011; Duer, 2004). A centre band is flanked on either side by spinning side-bands, separated by the MAS frequency. If the MAS frequency exceeds the CSA, then a single peak at the isotropic chemical shift is observed (Duer, 2004).

2.2.2 Dipolar coupling and proton decoupling

In solution NMR the J-coupling ("through bond"), provides bond connectivity information in a molecule and is observed as multiplets in the spectrum (Apperley et al., 2012; Keeler, 2010). Indirect spin-spin coupling occurs through the polarisation of electrons in the bond between the connected nuclei (Mlynarik, 2017). However, J-coupling is not usually observed in SS NMR as it is small relative to dipolar coupling in solid samples, e.g. <1 kHz for light elements (Apperley et al., 2012). Dipolar coupling is anisotropic and has the $3\cos^2\theta - 1$ dependence on the magnetic field, where in this

case θ is the angle between the vector linking the positions of two dipolar coupled nuclei and B_0.

Dipolar ("through space") coupling between two nuclei is important in SS NMR and results in significant line broadening (Apperley et al., 2012; Bechinger et al., 2004). It is the interaction between two magnetic dipole moments of the nuclei μ_i and μ_s, separated by the internuclear distance r (**Figure 2.6A**) (Apperley et al., 2012; Duer, 2004). The dipolar interaction strength is affected by the orientation of the spins with respect to B_0 (**Figure 2.6B**), and the internuclear distance by $\frac{1}{r^3}$ (**Equation [4]**) (Duer, 2004).

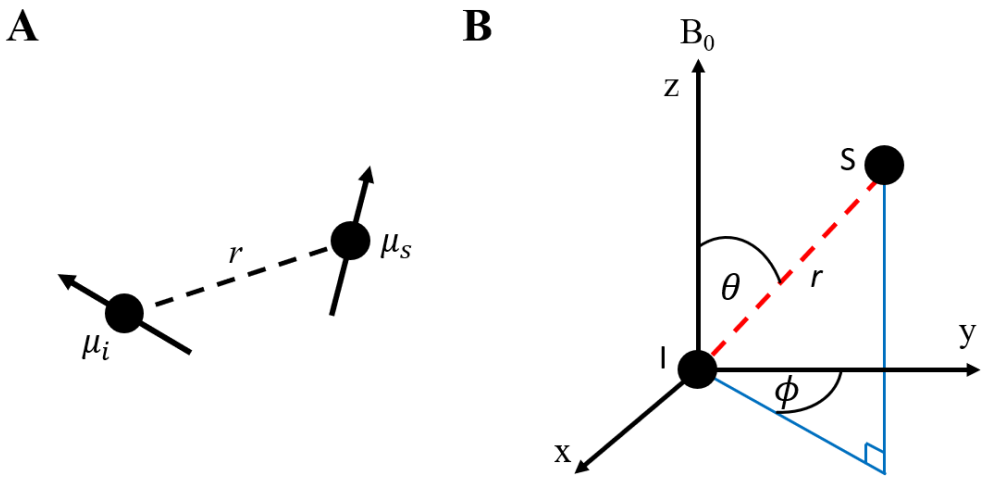

Figure 2.6. A) A representation of two nuclei I and S with magnetic moments μ_i and μ_s separated by the internuclear distance r. Obtained from (Apperley et al., 2012). **B)** The internuclear vector (red dashed line) between nuclei I and S, with the angles θ and ϕ defining the vector orientation relative to B_0. Adapted from (Duer, 2004).

The dipolar coupling constant can be calculated with

$$D_{zz} = \left(\frac{\mu_0}{4\pi}\right)\frac{\gamma_I\gamma_S\hbar}{r^3}(3\cos^2\theta - 1) \qquad \textbf{[4]}$$

where $\hbar$ is Planck's constant/2π, μ_0 is the vacuum permeability constant, r is the internuclear distance, and the nuclei gyromagnetic ratios are γ_I and γ_S (Bechinger et al., 2004; Duer, 2004). In organic solids, ^{1}H-^{1}H dipolar coupling constants can exceed 70 kHz, whereas ^{15}N-^{1}H bonds can have a dipolar coupling interaction between approximately $-20 \leq \Delta\nu \leq 10$ kHz (Bechinger et al., 2004).

Dipolar coupling between nuclei complicates and broadens the NMR spectrum (Apperley et al., 2012). To obtain a high-resolution spectrum, the sample must be rotated at frequencies much greater than the dipolar coupling constant (Duer, 2004). This is straightforward for weaker couplings (e.g., ^{13}C-^{13}C), but technically more demanding for removing stronger (e.g., ^{1}H-^{1}H) couplings (Apperley et al., 2012). Consequently, many NMR experiments on organic solids rely on the observation of ^{13}C or ^{15}N signals whilst removing heteronuclear couplings (^{13}C-^{1}H, ^{15}N-^{1}H) with either continuous wave or a broadband decoupling sequence, which is used to irradiate the protons in a sample (Apperley et al., 2012; Keeler, 2010).

The continuous wave irradiation at the Larmor frequency of the protons in a sample removes the heteronuclear dipolar coupling between the measured nuclei and the protons, such as ^{15}N and ^{13}C in the sample (Keeler, 2010). A broadband decoupling sequence is a set of pulses with specific phases and flip angles with continuous irradiation of protons in the sample (Keeler, 2010). An example of a broadband decoupling sequence for SS NMR samples is called small phase incremental alternation

containing 64 steps (SPINAL-64) which was developed by Fung *et al*. (Fung et al., 2000).

2.2.3 Cross-polarisation

An important method in SS NMR for increasing sensitivity and reducing measurement times is cross-polarisation (CP) at the Hartmann-Hahn condition. CP is mediated by the heteronuclear dipolar interaction and is the transfer of magnetisation from an abundant and sensitive nuclei to less abundant, less sensitive nuclei (X) in a sample, such as ^{1}H to ^{13}C or ^{15}N (Apperley et al., 2012; Duer, 2004).

CP improves the spectrum signal-to-noise ratio for the measured FID of the less abundant nuclei, and reduces the overall experiment time (Duer, 2004). The experiment time is reduced as the relaxation time (T_1) is dependent on the ^{1}H nuclei magnetisation which has a more rapid recovery of equilibrium magnetisation compared to nuclei X (Apperley et al., 2012). This is due to the presence of both strong homonuclear and heteronuclear dipolar interactions for the protons in the sample. Whereas, nuclei X has predominantly weaker heteronuclear dipolar interactions which result in longer relaxation times (Duer, 2004). The X nuclei such as $^{13}C/^{15}N$ have relatively low natural abundance compared to ^{1}H in proteins. Therefore, CP is used to increase the signal intensity of the observed X nuclei (Apperley et al., 2012).

The basic pulse sequence for a CP NMR experiment is shown in **Figure 2.7**. Firstly, the ^{1}H nuclei magnetisation moves to the -y axis with a 90°_{x} pulse (Duer, 2004). Next, the ^{1}H magnetisation is maintained due to the formation of the spin-lock field with an on-resonance ^{1}H contact pulse (-y) (Apperley et al., 2012; Duer, 2004). At the same time the contact pulse (-y) at the X nuclei frequency is applied (**Figure 2.7**) (Apperley et al.,

2012; Duer, 2004). The contact time is the period in which the contact pulses are applied and the magnetisation transfer occurs (Apperley et al., 2012).

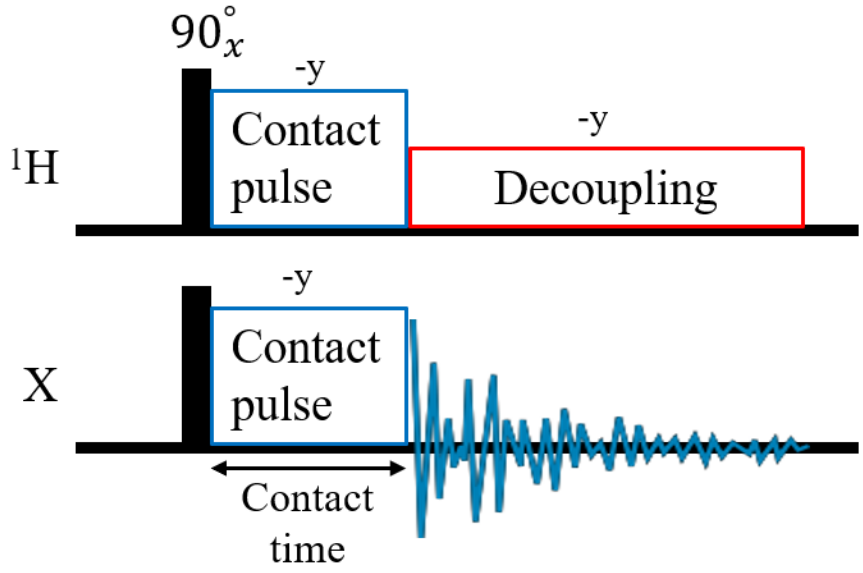

Figure 2.7. An example of the CP pulse sequence. After the RF pulse ($\mathbf{90^{\circ}_{x}}$) CP occurs when the contact pulses are applied. During the X nuclei signal acquisition proton decoupling is applied. Adapted from (Duer, 2004), example FID from **Figure 2.4**.

To achieve CP the amplitudes of the contact-pulses are changed to meet the Hartmann-Hahn match condition (Duer, 2004), originally discovered by (Hartmann and Hahn, 1962), defined as:

$$\gamma_H B_1(^1H) = \gamma_X B_1(X) \qquad \textbf{[5]}$$

This results in CP when both nuclei have equal energy gaps between the nuclei spin states described as equal nuclei nutation frequencies (Apperley et al., 2012; Duer, 2004). The theoretical enhancement of the signal from nucleus X by cross-polarisation from H is γ_H/γ_X, although this is rarely achieved in practice because of nuclear relaxation (Apperley et al., 2012).

2.2.4 Homonuclear decoupling experiments

Two-dimensional (2D) correlation cross-polarisation magic-angle spinning (CP-MAS) NMR experiments between ^{13}C-^{13}C nuclei can be used to produce spectra containing site-specific cross-peaks, which indicate nuclei close in space and can be used in protein structural analyses (Duer, 2004; Takegoshi et al., 2001). To obtain higher resolution spectra the sample is spun at the magic-angle to remove dipolar coupling before re-establishment of the dipolar coupling with a recoupling sequence (Duer, 2004), such as dipolar-assisted rotational resonance condition (DARR) recoupling (Takegoshi et al., 2001).

The DARR recoupling can be used to recouple the ^{13}C-^{13}C nuclei mediated by the ^{13}C-^{1}H heteronuclear dipolar interaction (Takegoshi et al., 2001). During MAS, continuous wave proton irradiation re-establishes the heteronuclear dipolar coupling with a ^{1}H RF field intensity under the DARR condition (Takegoshi et al., 2001). The rotational resonance condition is when the proton RF field intensity is equal to the sample rotation field intensity multiplied by an integer (n = 1 or 2) (Oas et al., 1988; Takegoshi et al., 2001).

In the mixing period of the pulse sequence the magnetisation is transferred between the proton and ^{13}C nuclei (Duer, 2004). Proton homonuclear and heteronuclear dipolar interactions broaden the spectrum, which produces an heteronuclear dipolar coupling pattern (Takegoshi et al., 2001). The heteronuclear dipolar coupling pattern of a ^{13}C spin and another ^{13}C spin spinning sideband overlap (Takegoshi et al., 2001) to form cross-peaks in the spectrum when the nuclei are close in space (Duer, 2004).

2.2.5 NMR of oriented molecules

As stated earlier, the nucleus is surrounded by electrons that produce a secondary opposing field to B_0 which shields the nucleus and affects the chemical shift detected (Duer, 2004; Mlynarik, 2017). The extent of chemical shielding and therefore a decrease in the resonance frequency of the nuclei depends on the chemical environment of the nuclei, i.e. the surrounding atoms in the molecule (Mlynarik, 2017).

The CSA interaction is a second rank tensor that contains three principal components referred to as σ_{11}, σ_{22} and σ_{33} and shows that the chemical shielding is not homogeneous around a nucleus (**Figure 2.5**) (Bechinger et al., 2004). The CSA in a static sample is therefore orientation dependent and the measurable chemical shielding constant σ of a nucleus can be calculated from the tensor components relative to B_0 (Bechinger et al., 2004) using

$$\sigma = \sigma_{11} sin^2\Theta cos^2\Phi + \sigma_{22} sin^2\Theta sin^2\Phi + \sigma_{33} cos^2\Phi \qquad \textbf{[6]}$$

The position of B_0 relative to the principal axes of the chemical shift tensor is defined by the angles Θ and Φ as in **Figure 2.8C** (Bechinger et al., 2004; Duer, 2004). To convert to the chemical shift $\delta_{aa} = \sigma_{ref} - \sigma_{aa}$ for each interaction tensor component separately where aa = 11 or 22 or 33 (Duer, 2004). The chemical shift is measured relative to a reference compound such as tetramethylsilane (TMS) and calculated from the measured nuclei shielding constant σ relative to σ_{ref} as described above (Duer, 2004).

If a molecule has a restricted range of orientations relative to B_0, such as a single crystal or a protein in an oriented lipid bilayer, the chemical shift tensors (δ_{11}, δ_{22} and δ_{33}) can be readily used in **Equation [6]** to determine relevant interaction tensor orientations such as the amide bond (N-H) for residues in a protein (Bechinger et al., 2004). The ^{15}N

chemical shift (δ_i) can be calculated for the amide (i) groups in a protein backbone with **Equation [7]**

$$\delta_i = \delta_{11} sin^2\Theta cos^2\Phi + \delta_{22} sin^2\Theta sin^2\Phi + \delta_{33} cos^2\Theta \qquad \textbf{[7]}$$

The amide ^{15}N chemical shift tensor can be described by the main components δ_{11}, δ_{22} and δ_{33} which have the chemical shift values of 60, 75 and 222 ppm, respectively (Bechinger et al., 2004). The isotropic chemical shift is defined as $\delta_{iso} = (\delta_{11} + \delta_{22} + \delta_{33})/3$ and the tensor components are defined as $(\delta_{33} - \delta_{iso}) \geq (\delta_{11} - \delta_{iso}) \geq (\delta_{22} - \delta_{iso})$ (Apperley et al., 2012; Duer, 2004). δ_{33} is directed along the plane of the peptide bond at ~18° from the N-H bond in an α-helical protein which are aligned along the helix axis (**Figure 2.8A**) (Bechinger et al., 2004).

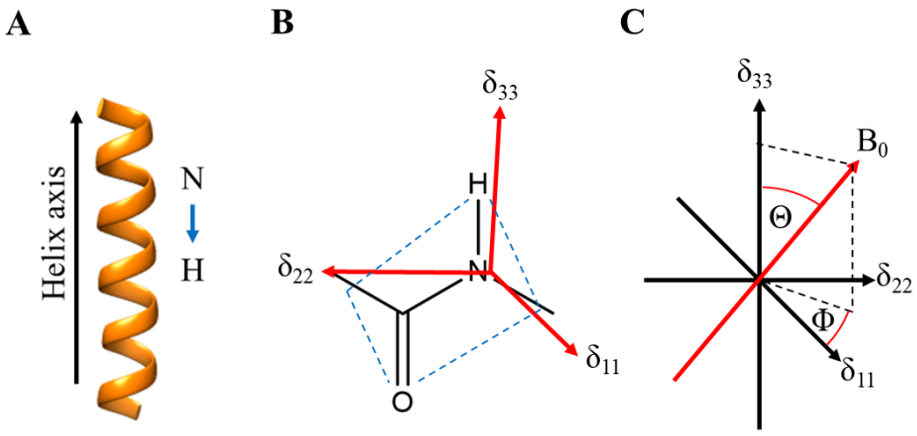

Figure 2.8. A) The alignment of N-H bonds throughout a right-handed alpha helix with the main helix axis indicated. **B)** The ^{15}N chemical shift tensors (δ_{33}, δ_{22} and δ_{11}) in relation to the peptide bond and B_0. δ_{33} is aligned in the peptide bond plane (dashed blue outline). **C)** The Φ and Θ angles represent the position of B_0 relative to the ^{15}N chemical shift tensors. Adapted from (Bechinger et al., 2004).

The ^{1}H-^{15}N dipolar coupling constant (D_i) for each residue (i) can be calculated using **Equation [8]** (Chen and Tjandra, 2012), as dipolar coupling occurs between the N and H nuclei in the N-H bond (**Figure 2.8B**) (Bechinger et al., 2004).

$$D_i = D_{max}(3cos^2\theta - 1)/2 \qquad \textbf{[8]}$$

The N-H bond vector and B_0 are separated by the angle θ, and the largest dipolar coupling value is D_{max} (Chen and Tjandra, 2012).

An example of α-helical protein alignment with respect to an oriented lipid bilayer has been shown with [^{15}N]-labelled Vpu, an 81 residue protein associated with HIV-1 (Marassi et al., 1999) in **Figure 2.9**. The observed ^{15}N chemical shifts at ~200 and 70 ppm indicated alignment of the N-H bond within the helices (**Figure 2.8A**) as parallel and perpendicular to the bilayer normal, respectively (**Figure 2.9**) (Marassi et al., 1999).

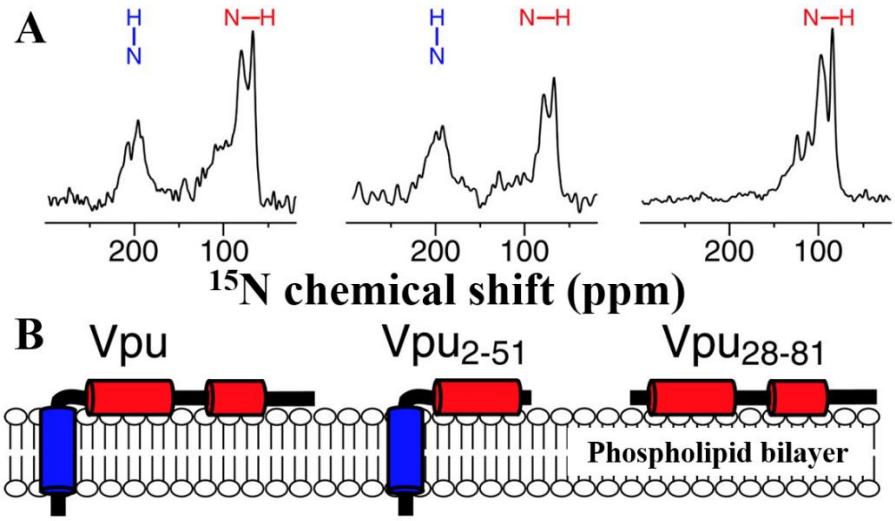

Figure 2.9. The ^{15}N NMR spectra of [^{15}N]-labelled Vpu and truncated Vpu (residues 2-51 and 28-81) in oriented phospholipid bilayers **(A)**. The α-helix N-H bond alignment is indicated as parallel (blue) or perpendicular (red) to the bilayer normal. The position of the corresponding amphipathic (red) and hydrophobic (blue) Vpu helices is shown in **(B)**. Obtained and adapted from (Marassi et al., 1999).

2.2.6 PISEMA

The 2D SS NMR methods used in this study are described further such as polarisation inversion spin exchange at the magic-angle (PISEMA) (Wu et al., 1994) and the 2D ^{13}C-^{13}C CP-MAS spectrum.

To obtain site-specific information from a SS NMR experiment dipolar couplings which can cause significant line broadening need to be taken into account (Ramamoorthy et al., 1999). PISEMA acts to decrease the spin-diffusion effects between ^{1}H nuclei, i.e. homonuclear dipolar couplings, without an increase in heteronuclear dipolar coupling utilising the spin-lock phase (Ramamoorthy et al., 1999; Yamamoto et al., 2005). Therefore, PISEMA can be used to produce high resolution spectra in the heteronuclear dipolar frequency dimension (Ramamoorthy et al., 1999; Wu et al., 1994).

PISEMA can be applied to [^{15}N]-labelled proteins in oriented phospholipid bilayers to determine the protein orientation relative to B_0 (Marassi et al., 1997; Ramamoorthy et al., 1999). This utilises the heteronuclear dipolar coupling between ^{15}N-^{1}H in the amide bonds present in the protein backbone as described earlier, and the respective nuclei chemical shift frequencies (Marassi et al., 1997; Ramamoorthy et al., 1999).

In the SEMA phase (**Figure 2.10**) double (or triple) resonance pulse sequences with spin-exchange at the magic angle are used (Ramamoorthy et al., 1999). At the magic angle (θ_m) an effective field is formed through application of off-resonance RF ^{1}H irradiation in the t_1 period, i.e., the ^{1}H magnetisation spin-lock for magnetisation transfer (Ramamoorthy et al., 1999; Yamamoto et al., 2005). The suppression of the ^{1}H homonuclear dipolar couplings is achieved with the flip-flop Lee-Goldburg (LG) pulse sequence (Lee and Goldburg, 1965). During this the effective field is phase- (X to -X), and frequency-switched at each 2π rotation (**Figure 2.10**) (Ramamoorthy et al., 1999).

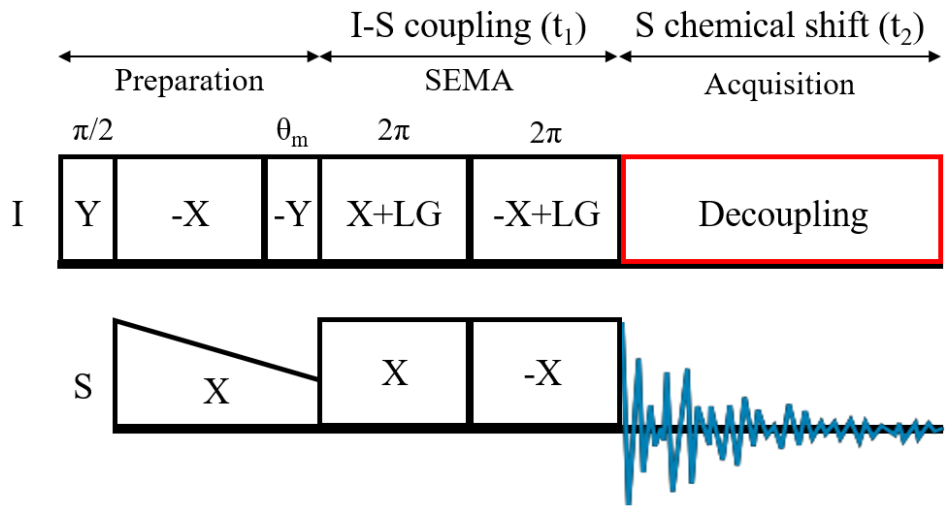

Figure 2.10. The stages of the PISEMA SS NMR experiment. The preparation stage: The initial 90° pulse (π/2). The quadrature phases are represented by X, -X, Y, -Y. The SEMA stage: The LG condition frequencies are shown as positive (+LG) and negative (-LG), and the θ_m is the magic-angle pulse at 54.74°. (Ramamoorthy et al., 1999). Proton decoupling is applied during the FID acquisition phase. Adapted from (Yamamoto et al., 2005), and example FID from **Figure 2.4**.

A 2D PISEMA spectrum is produced with the ^{1}H-^{15}N dipolar couplings correlated with the ^{15}N chemical shifts. The cross-peaks in the PISEMA spectra correspond to individual amide sites (N-H) in the protein studied (Marassi et al., 1999). In the Vpu protein example, a 2D PISEMA Vpu experimental spectrum contained a "wheel-like" pattern in the transmembrane α-helix region (**Figure 2.11A**) (Marassi et al., 1999). The transmembrane α-helix of Vpu (**Figure 2.9**, **blue**) was suggested to have a tilt of ~15° relative to B_0 as the observed Vpu cross-peaks were similar to the simulated α-helix 2D PISEMA spectrum peaks (**Figure 2.11B**, **D**) (Marassi et al., 1999).

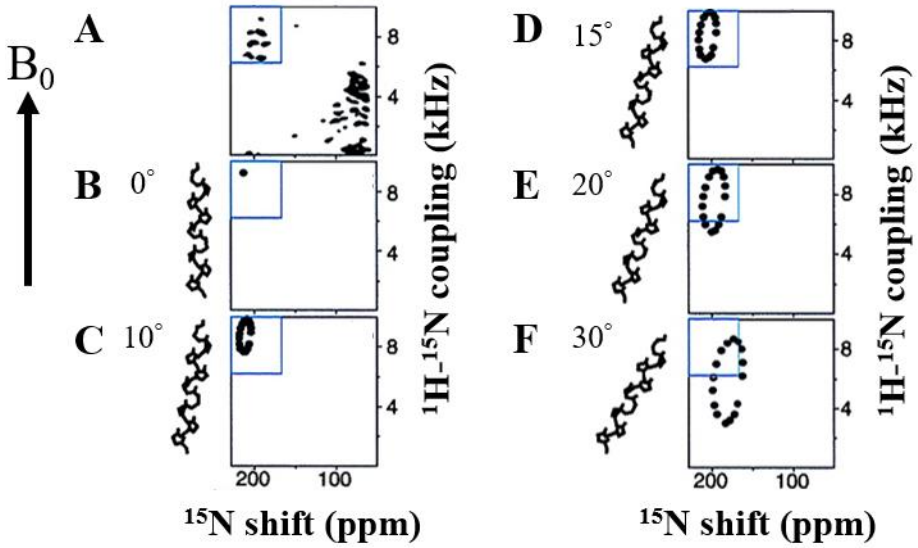

Figure 2.11. (A) The experimentally observed 2D PISEMA spectrum of [^{15}N]-labelled Vpu. **(B-F)** The simulated 2D PISEMA spectra of an α-helix containing 17 amino acid residues with tilt angles between 0 – 30° with respect to the bilayer normal/B_0. The transmembrane α-helix region is highlighted by the blue box. Obtained and adapted from (Marassi et al., 1999).

This is a powerful technique in SS NMR as the orientation of a protein in a phospholipid bilayer can be determined, as well as helical residue secondary structure assignment (Marassi and Opella, 2000). The α-helix wheel pattern can be shown by the pattern of resonances in the PISEMA spectrum (**Figure 2.11**) (Marassi and Opella, 2000). This is aided by narrow spectrum lines due to the reduction of the heteronuclear dipolar coupling in the SEMA period by 18.4 % (Yamamoto et al., 2005). Additionally, several factors influence the resonance frequencies such as the α-helix orientation, the CSA of the amide tensor, the amide bond length, and the backbone dihedral angles (Marassi and Opella, 2000).

3 Atheroprotective apoA-I mutant expression and characterisation

3.1 Introduction

This section (**3.1.1-3.1.3**) gives an overview of the strategy for expressing recombinant apoA-I WT and the atheroprotective mutants, apoA-I R173C and L144R.

3.1.1 Recombinant protein expression

E. coli cells are used widely to express recombinant proteins for further study in a variety of cell types such as BL21(DE3) cells that are used for initial protein expression tests (Rosano and Ceccarelli, 2014). In this work, BL21(DE3) cells are used for the development and optimisation of recombinant protein expression, and XL1-Blue cells are used to store the expression vector.

XL1-Blue cells do not express Endonuclease I due to the *endA1* mutation in the *E. coli* cell genotype. This mutation increases the quality of the plasmid preparations for sequencing by reducing the amount of nonspecific cellular plasmid DNA digestion (Samuelson, 2011) (Agilent).

The stability of plasmid inserts is improved due to the *recA1* mutation in the XL1-Blue cell genotype which removes homologous DNA recombination (Samuelson, 2011; Studier et al., 1990) (Agilent). Additionally, the BL21 (DE3) cells were used for

recombinant protein expression as the *recA1* mutation can slow cell growth (Samuelson, 2011).

Previously, recombinant his_6-tagged apoA-I WT (E2D) was expressed to a yield of 100 ±20 mg/L of cell culture media in BL21(DE3)pLysS *E. coli* cells. The pNFXex vector contained an optimised apoA-I cDNA sequence for expression in *E. coli* cells (Ryan et al., 2003) with further details in **section 3.2.1**. The expression was further optimised to produce the apoA-I WT (E2D) protein with a yield up to 100 mg/L of culture media (Townsend, 2016). Therefore, this expression method was used to express apoA-I WT (E2D) to provide enough apoA-I to study as a comparison to the atheroprotective apoA-I mutant proteins, in the lipid-free and lipid-bound protein rHDL nanoparticle structure.

Laboratory protein recombinant apoA-I protein expression can produce yields as low as 0.1 ug/L up to 100 mg/L of cell culture media (Brouillette and Anantharamaiah, 1995; Panagotopulos et al., 2002; Pyle et al., 1996; Ryan et al., 2003; Schmidt et al., 1995; Townsend, 2016). In comparison an industrial scale batch-fed expression of apoA-I R173C has produced a yield of 2 - 4.9 g/ L of culture media (Calabresi et al., 1994; Caparon et al., 2010).

Briefly, the his-tagged apoA-I (E2D) protein expression was induced using isopropyl-β-D-thiogalactoside (IPTG) in the BL21(DE3) cells (**section 3.2.5**), and immobilised metal ion affinity chromatography (IMAC) was used to separate the fusion protein from *E. coli* proteins after cell lysis. Before the cleavage of the his_6-tag using formic acid to produce apoA-I WT (3-243).

3.1.2 Atheroprotective mutant recombinant protein expression

The development of procedures to express the atheroprotective mutants of apoA-I Milano (R173C) and apoA-I Zaragoza (L144R) to a sufficient yield and purity was required to produce the proteins for further study. The aim was to produce the atheroprotective mutants on a similar scale to apoA-I WT, up to 100 mg/L of cell culture media. Methods development was also required for producing rHDL nanoparticles. The scale of recombinant protein expression required for the characterisation of the rHDL nanoparticles is discussed further in **Chapter 4, section 4.3.4.2**. The atheroprotective apoA-I mutant expression was adapted for apoA-I R173C whilst apoA-I L144R was expressed under similar conditions as apoA-I WT (E2D). Dimeric apoA-I R173C can form through formation of a disulphide bond between two apoA-I R173C cysteine residues (Weisgraber et al., 1980). Therefore, it is important to confirm if the recombinant apoA-I R173C can also form dimeric apoA-I R173C.

3.1.3 Labelled protein expression

For expression of apoA-I WT and the atheroprotective apoA-I mutants for solid-state NMR analyses it is necessary to uniformly ^{13}C and/or ^{15}N label the protein. The apoA-I WT (E2D) minimal media expression conditions (Townsend, 2016) were used to produce dual [^{13}C,^{15}N]-labelled apoA-I R173C and L144R. Additionally, dual-labelled apoA-I WT, [^{13}C]-apoA-I WT and [^{15}N]-apoA-I WT were expressed for solid-state NMR analyses. To achieve this, apoA-I R173C and L144R apolipoproteins were expressed in *E. coli* using a minimal growth medium containing either ^{13}C glucose or ^{15}N NH_2Cl as the sole carbon and nitrogen sources, or both sources for dual-labelled [^{13}C,^{15}N]-protein expression.

This chapter discusses the first application of expressing unlabelled and dual-labelled recombinant apoA-I L144R using the established apoA-I WT expression method. As well as adaptation of the apoA-I WT methodology with a TCEP reduction stage to form a mixture of monomeric and dimeric disulphide bonded apoA-I R173C.

3.1.4 Aims

This chapter describes the methodology developed to express the atheroprotective apoA-I Milano (R173C) and apoA-I Zaragoza (L144R) proteins to a sufficient yield and purity for structural and functional analyses.

3.2 Materials and methods

3.2.1 Plasmid design

Previously, Dr. M. Oda of the Children's Hospital Oakland Research Institute USA, kindly provided the pNFXex vector for apoA-I (E2D) expression stated earlier (Oda et al., 2001; Ryan et al., 2003; Townsend, 2016). Oda *et al*. altered the human cDNA of apoA-I WT to include a his_6-tag for affinity chromatography protein purification and a proteolytic cleavage site (**Appendix 1A**).

The bacterial expression vector phAIex was formed by subcloning the altered WT apoA-I cDNA into the pET-20b+ bacterial expression vector. The phAIex expression plasmid was transformed into BL21(DE3)pLysS *E. coli* cells for his-tagged apoA-I recombinant protein expression (Oda et al., 2001). To optimise the bacterial expression of apoA-I WT Ryan *et al.* altered the cDNA of human apoA-I in the pBluescript KS (+) vector (Stratagene) using site-directed mutagenesis (Oda et al., 2001; Ryan et al., 2003).

The E2D mutation was produced to form an acid labile D-P peptide bond between residues 2 and 3 to allow formic acid cleavage of the N-terminal his_6-tag after affinity

column chromatography (Ryan et al., 2003). Additionally, silent mutations were used to mutate the cDNA sequence for proline, arginine, leucine, and glycine amino acids to more abundant codons (frequency per one thousand) present in *E. coli* cells to optimise the apoA-I (E2D) protein expression. For example, the arginine 188 codon AGA at 2.7 frequency per thousand was mutated to CGC with a 21.1 frequency per thousand. Further silent mutations were introduced to produce 13 new restriction endonuclease sites for further changes to the protein sequence if required (Ryan et al., 2003).

After the cDNA manipulations were confirmed via sequencing the apoA-I (E2D) cDNA sequence was subcloned into the high copy number pET20b+ plasmid to form the pNFXex expression vector (Ryan et al., 2003). The pNFXex vector contains an ampicillin resistance gene and an IPTG-inducible promoter for IPTG induced protein expression (Ryan et al., 2003). The pET20b+ plasmid and recombinant his-tagged apoA-I (E2D) modified cDNA and amino acid sequence are in **Appendix 1**.

3.2.2 Atheroprotective mutant construct production using SLIM-PCR

The site-directed ligase-independent mutagenesis polymerase chain reaction (SLIM-PCR) method is used for rapid and efficient mutagenesis to form sequence modifications such as insertion, deletion and substitution (Chiu et al., 2004). Previously, the apoA-I R173C protein was expressed (Townsend, 2016), consequently the apoA-I R173C plasmid was isolated and sequenced again as outlined below. However, the apoA-I R173C nucleotide sequence compared to the apoA-I WT (E2D) sequence was a 477/579 nucleotide 82 % match producing an inconclusive amino acid sequence (**Appendix 1**). Therefore, the SLIM-PCR reaction was repeated to produce the apoA-I R173C mutant plasmid. To form the apoA-I R173C and apoA-I L144R point mutations

the following primers were designed with the desired mutation on complementary overhangs (**Figure 3.1**).

Figure 3.1. ApoA-I R173C (Townsend, 2016) and apoA-I L144R SLIM-PCR forward (F) and reverse (R) primer designs. The primers were produced by Sigma-Aldrich®. The sequences are 5' to 3', the 5' adaptor sequence of the tailed primer complementary nucleotide overhang (red), and the mutated nucleotides are also shown in red.

The respective mutations for apoA-I R173C and apoA-I L144R were formed by changing the nucleotides coding R173 from CGC to TGC (C173), and nucleotides coding L144 from CTG to CGC (R144). The respective codons were chosen with a relatively high abundance in *E. coli* cells following the process of Ryan *et al*. (Ryan et al., 2003). A comparison of the codon frequency per thousand for cysteine and arginine residues in *E. coli.* from various sources is summarised in **Table 3.1**. There was a marginal difference between the frequency of cysteine codons in *E. coli* from either source therefore the cysteine codon TGC was used. The most abundant codons for arginine in *E. coli* are CGC and CGT with varied difference between sources for both

codons (**Table 3.1**). The codon CGC was used as this was the most abundant arginine codon used in the pNFXex vector apoA-I WT (E2D) cDNA sequence (Ryan et al., 2003).

Table 3.1. The relative abundance (frequency per thousand) of the most abundant cysteine and arginine codons in *E. coli* cells.

		Abundance in *E. coli* cells (frequency per thousand)		
Amino acid	***Codon***	(GenScript, 2019)	(Komar, 2016; Nakamura et al., 1999)	(Ryan et al., 2003)
Cysteine	TGC	6.1	5.5	
	TGT	5.2	5.9	
Arginine	CGC	19.7	14.0	21.1
	CGT	20.0	15.9	20.7

3.2.3 SLIM-PCR reaction

Initially, the original expression PNFXex vector for apoA-I WT (E2D) was isolated from the XL1-Blue plasmid storage cells and a mutation was induced using the SLIM-PCR method (Chiu et al., 2004).

The SLIM-PCR reaction is described in **Figure 3.2** (Chiu et al., 2004). The L144R and R173C forward tailed (F_T) primer and reverse short (R_S) primer were added to a PCR tube labelled as L144R and R173C reaction 1, respectively. The L144R and R173C reverse tailed (R_T) primer and short forward (F_S) primer were added to a separate PCR tube labelled as L144R and R173C reaction 2, respectively. The remaining reaction reagents were prepared as a master mix and aliquoted together into each primer reaction mix, and the control reaction.

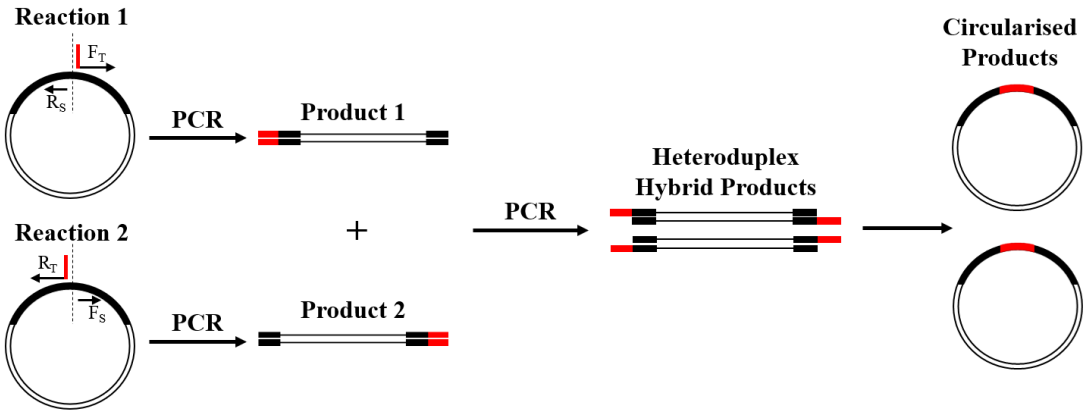

Figure 3.2. The process of SLIM-PCR reactions 1 and 2 for both atheroprotective mutant plasmid DNA formation, adapted from (Chiu et al., 2004).

In the first PCR reaction the primers annealed to the denatured plasmid DNA (double stranded to single stranded) and formed mixed PCR products with the required mutation in the complementary overhangs. The second PCR cycle combined the products of reaction 1 and 2 in which the DNA was denatured and reannealed to form heteroduplex hybridised double stranded PCR products. The heteroduplex products with the respective complementary overhangs spontaneously circularised to form the plasmid DNA containing the R173C and L144R mutations, respectively.

Each 25 µL reaction contained 5 µL of Phusion HF buffer (Mg^{2+} concentration of 1.5 mM, Thermo Scientific™), 200 µM dNTP's (2 µL of 2 mM stock, Novagen), 2.5 µL betaine, ~10 pmol (0.5 µM) of the respective primers (0.5 µL of 25 µM stocks), ~1 ng of template plasmid pNFXex ApoA-I (E2D) DNA, 1 U (0.5 µL) of Phusion™ Hot Start II High-Fidelity DNA Polymerase (Thermo Scientific™), and 12.5 µL Milli-Q® Ultrapure (MQ) H_2O to a final volume of 25 µL. The control reaction mix contained 1 µL of MQ H_2O instead of 2x 0.5 µL of the two primers in the reaction mixes.

In the PCR amplification cycle the PCR machine plate was preheated to 98°C for 2 minutes (step 1). The following cycle was used, with initial denaturation at 98°C for 30 seconds (step 2), at 61°C for 30 seconds (step 3), at 72°C for 8 minutes (step 4), 35 cycles of steps 2-4 (step 5), a final extension at 72°C for 5 minutes (step 6) and held at 4°C (step 7). After the first PCR cycle 5 µL of each reaction was run on a 0.8% (w/v) agarose gel with a 1 kb DNA ladder (NEB®, Thermo Scientific™). If the PCR was successful a strong band would appear at approximately 4.5 kb on the agarose gel corresponding to the plasmid. DpnI a restriction enzyme, used to digest the methylated template DNA, was added to each reaction (1 µL of 20 U stock concentration, NEB®) and incubated at 37°C for 1 hour. To stop the DpnI digestion 30 µL of H-buffer (300 mM NaCl, 50 mM tris, pH 9.0, 20 mM EDTA, pH 8) was added to each PCR reaction.

Before SLIM hybridisation was initiated the PCR products from reaction 1 and 2 were combined for each mutation L144R and R173C. The second PCR cycle began with an initial denaturation at 99°C for 3 minutes (step 1), 65°C for 5 minutes (step 2), 30°C for 15 minutes (step 3), 2 cycles of steps 2-3 (step 4) and held at 4°C (step 5). After the SLIM hybridisation PCR cycle a 5 µL sample of each reaction was run on a 0.8 % (w/v) agarose gel. The PCR products were stored at -20°C prior to XL1-Blue cell transformation.

3.2.4 Gel electrophoresis

3.2.4.1 Agarose gel electrophoresis

To prepare a 0.8 % (w/v) agarose gel, 0.8 g of agarose was dissolved in 100 mL of TAE buffer and 10 µL of SYBR™ Safe DNA stain (Invitrogen™) was added to the solution. The gel was poured into the gel cast and allowed to set with a 1.5 mm 10 well gel comb. To 5 µL aliquots of each sample for both SLIM-PCR reactions 1 µL of 6x sample buffer

was added. The samples run in the 0.8% (w/v) agarose gels were the control, L144R 1 and 2, R173C 1 and 2, L144R PCR products and the R173C PCR products. Both the GeneRuler 1 kb DNA Ladder (Thermo Scientific™) and the 1 kb DNA ladder (NEB®) were diluted and used to the appropriate concentration for 1.5 mm wells following the manufacturer's instructions (**Figure 3.3**). In each agarose gel 1.8 µL of marker was loaded per well.

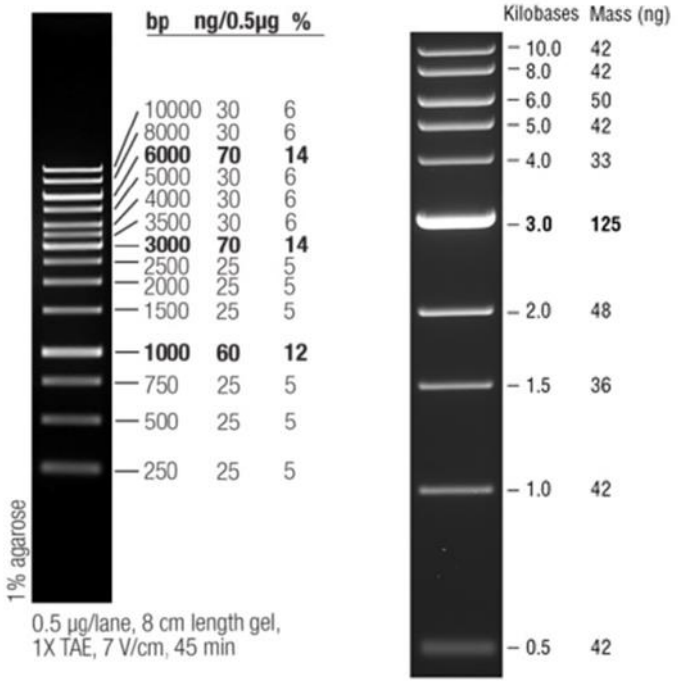

Figure 3.3. GeneRuler 1 kb DNA Ladder (Thermo Scientific™) (left). 1 kb DNA Ladder (NEB®), ethidium bromide staining on a 0.8% TAE agarose gel. Mass values 0.5 µg/lane (Right). Images obtained from Thermo Scientific™ and NEB®, respectively.

After the samples were loaded into the respective wells, 1x TAE buffer (10x stock 0.4 M tris base, 12.1 mL acetic acid, 10 mM EDTA) was used to fill the buffer dam and the gels were run at 100 V until the dye front had run past the halfway point of the total gel

length for band separation. The gels were imaged using the Molecular Imager® ChemiDoc™ XRS+ Imaging System and the Image Lab™ 4.0 Software (Bio-Rad).

3.2.4.2 SDS-PAGE electrophoresis

To analyse the protein content of samples throughout the apoA-I WT, R173C and L144R protein expressions sodium dodecyl sulphate polyacrylamide gel electrophoresis (SDS-PAGE) was used. SDS, an anionic detergent, was added to samples to break down the tertiary structure of proteins combined with a heat shock at 95°C to denature and linearize the protein structure. The negatively charged proteins under a constant voltage migrated towards the anode and were compared to a marker with bands corresponding to known molecular weights (**Figure 3.4**).

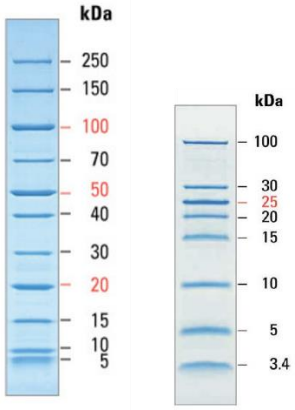

Figure 3.4. PageRuler™ Broad Range (left) and Low Range (right) Protein Ladders (ThermoFisher Scientific) on a 4 – 20 % tris-glycine gel and an 18 % tris-tricine gel, respectively. Image obtained from ThermoFisher Scientific.

The SDS-PAGE gels were prepared with a 15% resolving gel and a 4 % stacking gel. The 15 % resolving gel contained 3.75 mL of 40 % solution of acrylamide: bis-acrylamide 37.5:1 (Fisher Scientific™), 2.5 mL of 1.5 M tris HCl buffer pH 8.8, 3.6 mL of dH_2O and 100 µL of 10% (w/v) SDS solution. The 4 % stacking gel contained 1 mL of 40% solution of acrylamide: bis-acrylamide 37.5:1, 2.5 mL of 0.5 M tris HCl

buffer pH 6.8, 6.3 mL of dH_2O, and 100 µL of 10% (w/v) SDS solution. Just prior to pouring 75 µL of 10% (w/v) APS and 7.5 µL of TEMED were added to the resolving and stacking gel solutions.

The gel plates were cleaned using methanol and placed into the gel casting frames. The 15% resolving gel solution was prepared and pipetted to just below the 10-well comb mark. A layer of water saturated *n*-butanol was pipetted onto the upper resolving gel surface to produce an even gel surface. Once the gel was set the butanol was rinsed away with dH_2O before the 4% stacking gel was pipetted above the resolving gel. The 10-well comb was inserted into the stacking gel and allowed to set. The SDS-PAGE gels in the plates were rinsed with dH_2O and stored at 4°C wrapped in water saturated paper towel until used. The 1x running buffer contained 100 mL of 10x running buffer diluted to 1 L with dH_2O. The 10x running buffer contained 250 mM tris base, 1.92 M glycine, and 1% (w/v) SDS.

The 'fix' solution contained 25% (v/v) isopropanol, and 10% (v/v) acetic acid made up to 250 mL with dH_2O. The 'stain' solution contained 10% (v/v) acetic acid and 0.006% (w/v) Coomassie Blue R250 made up to 500 mL with dH_2O. The 'destain' solution contained 10% (v/v) acetic acid and 40% (v/v) methanol made up to 250 mL with dH_2O. The SDS-PAGE gel was inserted into the buffer dam with 1x running buffer in the buffer dam. For each SDS-PAGE gel 5 µL of the PageRuler™ Broad Range Protein Ladder marker (**Figure 3.4**) was loaded into the gel using a micro-syringe (Hamilton). Each SDS-PAGE sample was mixed with 10x sample buffer (SB) to a final ratio of 1x SB, vortexed and heated at 95°C for 5 minutes. The samples were loaded into the stacking gel wells using a micro-syringe with a total volume of 20 µL. The sample volumes and concentrations loaded into the SDS-PAGE gels were sample dependent.

The gels were run at 200 V using the Mini-PROTEAN® Tetra Cell and PowerPac™ Basic Power Supply (Bio-Rad) until the dye front approached the end of the gel. The SDS-PAGE gel was removed from the glass slides and placed in 'fix' solution for 30 minutes, 'stain' solution overnight and 'destain' on a rotary shaker until the background stain was removed. The gels were imaged using the same imaging system as described for the agarose gels.

3.2.4.3 Non-denaturing gradient gel electrophoresis

Non-denaturing gradient gel electrophoresis (NDGGE) was used to examine the formation of dimeric apoA-I R173C. The 4-16% NativePAGE™ bis-tris protein gels (Invitrogen™) were used, and the marker was the High Molecular Weight (HMW) calibration kit for native electrophoresis (Amersham™, GE Healthcare) (Cavigiolio et al., 2008; Dalla-Riva et al., 2015). The HMW marker kit contains thyroglobulin 669 kDa, ferritin 440 kDa, catalase 250 kDa, lactate dehydrogenase 140 kDa and bovine serum albumin 66 kDa. The corresponding protein Stokes' diameters are 17.0 nm, 12.2 nm, 10.0 nm, 9.2 nm, and 7.1 nm, respectively (Cavigiolio et al., 2008; Suurkuusk and Singh, 2000).

The samples were prepared to contain 1x NativePAGE™ sample buffer (4x stock, Invitrogen™) and pipetted into the respective sample wells. The NativePAGE™ anode and cathode running buffers were prepared from the 20x running buffer and cathode additive (Invitrogen™). The gels were run at 150 V until the dye front approached the end of the gel in the Bolt Mini Gel Tank (Novex Life Technologies). InstantBlue™ (Expedeon) stain was used to stain the gels for 1 hour and the gels were imaged as described previously.

3.2.5 Plasmid transformation into *E. coli* cells

The features of various types of *E. coli* competent cells used for protein expression are summarised by Rosano and Ceccarelli (Rosano and Ceccarelli, 2014). BL21(DE3) *E. coli* competent cells are the most widely used strain for protein expression and initial protein expression tests (Rosano and Ceccarelli, 2014). The BL21 strain of *E. coli* cells is derived from the parental B strain B834 which contains the mutation *hsd*SB to prevent DNA methylation, DNA degradation and loss of the plasmid from the cells (Rosano and Ceccarelli, 2014).

In the BL21(DE3) chromosome the λDE3 prophage was inserted into the genome containing the genes for the *lac*UV5 promoter and T7 RNA polymerase (RNAP) for protein expression (Rosano and Ceccarelli, 2014; Studier et al., 1990). IPTG initiates T7 RNAP production by inhibiting the *lac* repressor repression of the *lac*UV5 promoter in the BL21(DE3) genome (Studier et al., 1990). The T7 RNAP can then transcribe the recombinant protein gene sequence as the pET20b+ vector contains the T7 promoter system (Rosano and Ceccarelli, 2014; Studier et al., 1990). Additionally, BL21(DE3) cells do not contain the genes for *OmpT* (Grodberg and Dunn, 1988) and *lon* (Gottesman, 1996) proteases which degrade extracellular and non-native proteins, respectively.

To explore the possibility of expressing predominantly dimeric apoA-I R173C and tuneable IPTG induced expression, the R173C plasmid was transformed into Origami™ B(DE3) competent cells which have the features of BL21(DE3), Tuner™ (*lacZY* mutant, *lac* permease) and Origami™ (*trxB/gor* mutations) cells (Novagen). The *lac* permease *lacY* deletion mutation enables IPTG induced concentration dependent protein expression as the IPTG enters the cell homogeneously across the cell population

without *lac* permease (Khlebnikov and Keasling, 2002; Rosano and Ceccarelli, 2014). In cells without the mutation the amount of lac permease membrane proteins per cell can vary resulting in non-homogenous IPTG induction as IPTG enters the cell with and without *lac* permease (Khlebnikov and Keasling, 2002; Rosano and Ceccarelli, 2014).

The cytoplasm in *E. coli* cells is a reducing environment therefore proteins expressed intracellularly in the cytoplasm are usually present in their reduced form (Bessette et al., 1999; Stewart et al., 1998). In the context of cysteine residues this refers to a free thiol (SH) group preventing the formation of disulphide bonds (R-S-S-R) in proteins expressed intracellularly (Bessette et al., 1999; Derman et al., 1993). The thioredoxin and glutaredoxin pathways in *E. coli* cells are involved in reducing disulphide bonds of proteins expressed in the cytoplasm (Prinz et al., 1997). Consequently, the *trxB* and *gor* mutations aid disulphide bond formation in cytoplasmic proteins corresponding to the deletion mutations of genes for the expression of the enzymes thioredoxin reductase and glutathione reductase, respectively (Derman et al., 1993; Stewart et al., 1998).

3.2.5.1 Plasmid transformation protocol

The plasmid was initially transformed into XL1-Blue competent *E. coli* cells (Agilent Technologies) for plasmid storage and any further DNA manipulation required if SLIM-PCR was unsuccessful. After cDNA sequence confirmation to confirm the presence of the L144R and the R173C mutations the respective plasmids were transformed into BL21(DE3) competent *E. coli* cells (Agilent Technologies) for protein expression. Both types of competent cells follow the transformation protocol provided by Agilent Technologies described below.

LB agar, total volume of 500 mL was autoclaved and cooled to below 55°C before 500 µL of 10 % (w/v) ampicillin was added to a final concentration of 100 µg/mL ampicillin.

Under sterile conditions the LB agar containing 100 µg/mL ampicillin was poured into petri dishes and allowed to set for approximately 30 mins. The LB agar plates containing 100 µg/mL ampicillin were stored inverted at 4°C and pre-warmed at 37°C for at least 1 hour prior to the cell transformation.

Sterile SOB medium was prepared containing 5.0 g tryptone, 1.25 g yeast extract and 0.125 g NaCl. The volume was adjusted to 250 mL with dH_2O and autoclaved. After the solution was autoclaved, 2.5 mL of 1 M $MgCl_2$ and 2.5 mL of 1 M $MgSO_4$ were filter sterilised using a 0.22 µm syringe filter into the 250 mL SOB medium before use. A 20 % (w/v) glucose solution was filter-sterilised and prepared just before use, with a total volume of 10 mL. To prepare the sterile SOC media with a total volume of 1 mL per aliquot, 200 µL of the filter-sterilised 20 % (w/v) glucose was added to 0.8 mL of SOB media.

The SOC media 1 mL aliquots were pre-heated to 42°C in a water bath and sterile eppendorfs were pre-chilled on ice. The competent cells were thawed on ice. The cells were gently mixed and 100 µL was aliquoted into the sterile Eppendorf tubes for each PCR product reaction L144R, R173C and for the positive control plasmid pUC18. To each aliquot 1.7 µL of β-mercaptoethanol was added and the tubes were swirled gently and incubated on ice for 10 minutes. The tubes were swirled every 2 minutes. Aliquots of 2 and 5 µL of the R173C and L144R PCR products were added to individual 100 µL cell aliquots. To the positive control cell aliquot 1 µL of pUC18 control DNA was added. The various aliquots were named apoA-I M2 and M5, and apoA-I Z2 and Z5.

The cells were incubated on ice for 30 minutes. After the incubation on ice the cells were heat shocked at 42°C for 45 seconds. The cells were incubated on ice for 2 minutes. To each cell aliquot 900 µL of pre-heated SOC media was added drop-by-

drop. The cells were incubated at 37°C for 1 hour at 200 rpm. Under sterile conditions 100 µL of each respective cell aliquot was spread onto separate LB agar plates containing 100 µg/mL carbenicillin. The plated cell cultures were inverted and incubated at 37°C overnight. A single colony from each plate was selected and overnight cell cultures were prepared using approximately 15 mL of sterile LB media containing 100 µg/mL carbenicillin. The cell cultures were incubated overnight at 37°C with shaking. The GenElute™ Plasmid Miniprep Kit (SIGMA®) was used to isolate the respective plasmid DNA for cDNA sequencing. The plasmid samples were sent to Source Bioscience Lifesciences for sequencing.

Glycerol stocks were prepared from the overnight cell cultures to store the cells containing the apoA-I R173C and L144R plasmids. Glycerol was diluted to form a 50 % (v/v) solution with dH_2O and filter-sterilised with a 0.22 µm syringe filter before use under sterile conditions. In cryogenic storage vials 500 µL of 50 % (v/v) glycerol and 500 µL of overnight cell cultures (XL1-Blue or BL21(DE3)) for apoA-I R173C and L144R, were mixed and frozen at -80°C to preserve the *E. coli* cells for future use.

During optimisation of the apoA-I R173C protein expression, the R173C plasmid was transformed into Origami™ B(DE3) (Novagen) cells to facilitate the formation of disulphide bonds during protein expression (Prinz et al., 1997; Rosano and Ceccarelli, 2014) using the following transformation protocol as provided by Novagen.

The Origami™ B(DE3) cells were thawed on ice in 20 µL aliquots for up to 5 minutes and gently mixed before pipetting into pre-chilled 1.5 mL Eppendorf tubes. The R173C plasmid (1 µL of 10 ng/µL stock) and the positive control plasmid (1 µL of 0.2 ng/µL stock) were added to the respective 20 µL cell aliquots, gently mixed, and incubated on ice for 5 minutes. The cells were heat-shocked at 42°C for 30 seconds in a water bath

and the cells were incubated on ice for 2 minutes. Pre-heated SOC medium was slowly added to each cell aliquot whilst on ice until 80 µL SOC medium was added. The cells were incubated at 37°C for 1 hour at 250 rpm before plating onto pre-warmed LB agar plates containing 100 µg/mL carbenicillin. The following plates were incubated overnight at 37°C; a negative control plate without cells, 10 µL of the test plasmid plated, and two plates with 25 and 50 µL of the R173C plasmid test cells plated. Overnights were prepared from a single colony as described earlier of the R173C plasmid containing cells and after an overnight incubation glycerol stocks were prepared.

3.2.6 Expression of apoA-I WT (E2D)

3.2.6.1 Cell growth and induction

The following recombinant apoA-I WT (E2D) expression protocol was established (Townsend, 2016) and adapted from the previous expression methods (Oda et al., 2001; Ryan et al., 2003). LB media was prepared with 25 g of LB (Millers) in 1 L of dH_2O and autoclaved to sterilise. Once the LB cooled to less than 55°C, 1 mL of 10 % (w/v) carbenicillin was added to 1 L of LB to a final concentration of 100 µg/mL. Under sterile conditions overnight cultures of the BL21(DE3) cells containing the apoA-I WT (E2D) plasmid were prepared by inoculating 15-20 mL of LB media containing 100 µg/mL ampicillin with a scraping of the BL21(DE3) apoA-I WT glycerol stocks. The cell cultures were incubated overnight at 37°C with shaking at 200 rpm.

The overnight cell culture was used to inoculate 1 L of LB containing 100 µg/mL ampicillin and incubated at 37°C at 200 rpm until the $OD_{600} \geq 0.6$ indicating cell growth in the logarithmic phase. Protein expression was induced by the addition of 1 mL of 1 M IPTG to a final concentration of 1 mM to the cell culture (1 L). The induced cell

culture was incubated at 37°C for 5 hours at 200 rpm to allow protein expression. A 1 mL pre-induction sample was taken prior to IPTG addition and a 1 mL post-induction sample was taken for SDS-PAGE. The SDS-PAGE samples were centrifuged at 13.4 krpm for 3 minutes. The supernatant was discarded, and the pellet was resuspended in 1 mL dH_2O.

3.2.6.2 Cell lysis

The cells were centrifuged at 5000 x g for 20 minutes at 4°C. The growth media was discarded, and the pelleted cells were resuspended in minimal volume of lysis buffer (6 M guanidine HCl, 20 mM $NaPO_4$, 0.5 M NaCl) pH 7.4, and frozen at -20°C overnight. For example, a maximum of 10 mL lysis buffer for a 1 L protein expression. The cells were sonicated on ice for 5 cycles of 15 seconds on, 60 seconds off, at an amplitude of approximately 20 microns. Phenylmethylsulphonyl fluoride (PMSF) at a stock concentration of 200 mM was added before and after sonication to a final overall concentration of 1 mM. The lysed cells were centrifuged at 43 000 x g for 30 minutes at 4°C. The lysis supernatant was retained, and the pellet discarded. The lysis supernatant was diluted by adding an equal volume of lysis buffer pH 7.4 before further purification. A 100 µL supernatant and a pellet sample were taken for SDS-PAGE.

3.2.6.3 His-trap chromatography

The apoA-I WT (E2D) protein amino acid sequence contains a hexahistidine (his_6) tag used to isolate the fusion protein apoA-I (E2D) using his-trap chromatography. The column used was the 5 mL HisTrap FF™ pre-packed Ni Sepharose column (GE Healthcare). The his_6-tag in the fusion protein has a high binding affinity for the Ni^{2+} metal ions and binds to the column resin. Imidazole competes with the fusion protein his_6-tag for binding to the nickel ions, as the imidazole binds at a higher affinity. The concentration of imidazole was increased to remove non-specific binding proteins in

wash steps and to elute the fusion protein. The ÄKTA Start chromatography system and UNICORN™ Start 1.0 software (GE Healthcare) were used for the separation of the fusion protein from the cell lysis proteins.

An example to show the process of IMAC is shown in **Figure 3.5**, the Ni^{2+}-nitriloacetic acid (Ni^{2+}-NTA) matrix is attached to a support resin, usually cross-linked agarose beads, and the Ni^{2+} metal ion has 4 coordinate bonds with the NTA matrix atoms (Bornhorst and Falke, 2000). As the lysis sample flows through the column the his-residues in the poly-histidine fusion protein tag form 2 coordinate bonds with the Ni^{2+} ion immobilising the protein attached to the matrix in the resin (Bornhorst and Falke, 2000).

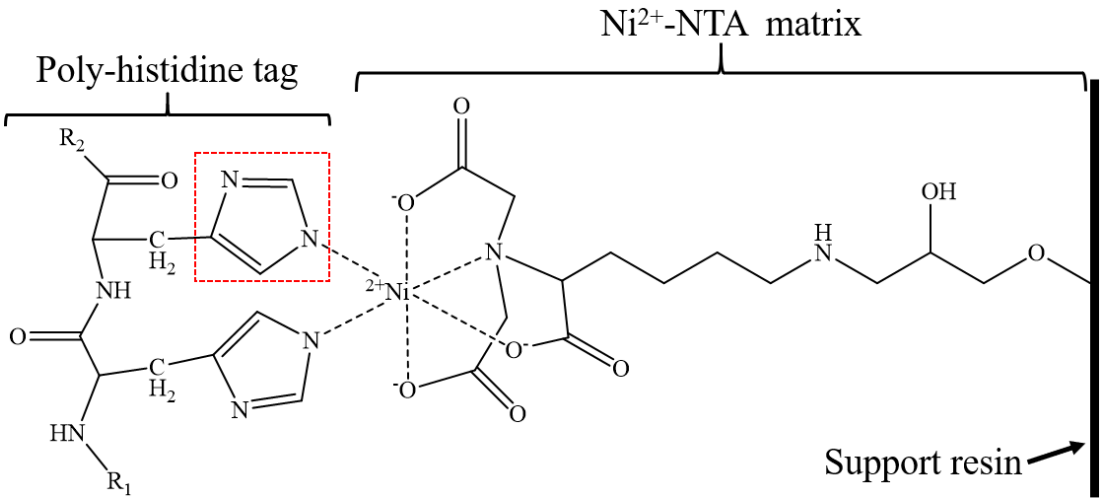

Figure 3.5. An example of interactions between the poly-histidine tag of a fusion protein and the Ni^{2+}-NTA matrix attached to a support resin inside a chromatography column during IMAC. The R_1 group indicates the additional histidine residues in the poly-histidine tag, e.g., a His_6-tag contains 6 histidine residues in total. The R_2 group represents the link to the recombinant protein. The red box outlines the structure of imidazole. Adapted from (Bornhorst and Falke, 2000).

Imidazole is an analogue of the histidine residue R group structure (**Figure 3.5**, red) and competitively binds to the IMAC resin Ni^{2+} metal ion with a higher affinity than the poly-histidine residues to displace and elute the fusion protein at high imidazole concentrations (≥100 mM for Ni^{2+}-NTA) (Bornhorst and Falke, 2000). As the post-induction cell lysis sample contains expressed *E. coli* proteins and his_6-tagged-apoA-I (E2D), the his_6-tag is an important addition to the apoA-I cDNA sequence enabling the isolation of the fusion protein from the *E. coli* protein impurities (Oda et al., 2001; Ryan et al., 2003).

All buffers and solutions used for his-trap chromatography were filtered and degassed using a vacuum pump prior to use with the column. The column was stored in 20 % (v/v) ethanol and prepared by washing the column with dH_2O at a flow rate of 5 mL/min until the UV and conductivity were constant values which indicated the column was equilibrated with dH_2O. The column was equilibrated with lysis buffer pH 7.4 at a flow rate of 5 mL/min.

Fractionation was started, and 10 mL fractions were collected unless stated otherwise. The diluted lysis supernatant sample was loaded at a flow rate of 1 mL/min and the volume loaded per chromatography purification run was equivalent to half a litre of cell culture. The column was washed with lysis buffer pH 7.4, to remove any non-specific binding proteins at a flow rate of 3 mL/min.

To further remove non-specific binding proteins the imidazole concentration was increased using a step gradient. The column was washed with binding buffer (20 mM $NaPO_4$, 0.5 M NaCl, 20 mM imidazole) pH 7.4, at a flow rate of 3 mL/min. At a flow rate of 3 mL/min, the column was washed with 95 % binding buffer pH 7.4, and 5 % elution buffer (20 mM $NaPO_4$, 0.5 M NaCl, 500 mM imidazole) pH 7.4, with a final

concentration of 45 mM imidazole. The fusion protein was eluted with 100 % elution buffer pH 7.4, 500 mM imidazole concentration, and 1 mL fractions were collected at a flow rate of 1 mL/min. In-between runs the column was washed with dH_2O then lysis buffer, pH 7.4. For storage the column was washed with dH_2O then 20 % (v/v) ethanol at 5 mL/min.

The 1 mL elution fractions samples corresponding to the protein peak on the chromatogram protein concentrations were tested using the Nanodrop™ 2000c (Thermo scientific™) protein A_{280} measurement. Fractions with a protein concentration above 1 mg/mL were pooled for dialysis. A 100 µL SDS-PAGE sample was taken of the flow-through, lysis buffer wash, 20 mM imidazole wash, and the 45 mM imidazole wash. A 50 µL pooled fusion protein elution sample was also taken for SDS-PAGE. The samples in lysis buffer contained guanidine hydrochloride which required ethanol precipitation as the guanidine hydrochloride interferes with running the samples in an SDS-PAGE gel.

3.2.6.4 His-tag formic acid cleavage

The pooled his-tagged apoA-I column fractions were incubated at 55°C with 45 % (v/v) formic acid for 5 hours in a water bath to cleave the his-tag from the apoA-I via the acid labile D2-P3 bond. The formic acid and his-tag were removed by dialysis over 2 days with 1 buffer change at 4°C in 50 mM tris base, 1 mM EDTA, 1 mM benzamidine, pH ≥ 8.0. After dialysis a 50 µL post-cleavage apoA-I (E2D) sample was taken for SDS-PAGE to check the protein purity and concentration.

3.2.7 Atheroprotective apoA-I mutant expression

After confirmation of protein sequence via gene sequencing the apoA-I R173C and apoA-I L144R plasmids were transformed into BL21(DE3) cells for initial protein

expression tests. The apoA-I WT (E2D) protein expression conditions were used to express both apoA-I R173C and L144R to test if the conditions were sufficient and comparable to routinely express both proteins at acceptable yields and purity.

As described earlier BL21(DE3) cells are not tuneable to IPTG concentration dependent induction of protein expression (Rosano and Ceccarelli, 2014). Therefore, the protein expression levels were analysed using SDS-PAGE of hourly post-induction samples of a 0.5 L cell culture for each mutant under the apoA-I WT (E2D) conditions for cell growth and IPTG induction. A 1 mL pre-induction sample and post-induction samples at 2, 3, 4 and 5 hrs, and after the overnight incubation were taken for SDS-PAGE analysis.

Overall, the apoA-I WT (E2D) protocol was used as described previously in **section 3.2.6**, for protein expression, purification, and isolation to produce apoA-I R173C and apoA-I L144R post-his-tag cleavage.

3.2.7.1 ApoA-I R173C cysteine reduction

Mass spectrometry was used to analyse the post his-tag cleavage sample of apoA-I R173C, and the mass was greater than expected, under the conditions described in **section 3.2.7.3**. Additionally, NDGGE gels did not show evidence of dimer formation as expected via the 173rd cysteine residue. Dr. F. Benson (Faculty of Health and Medicine, Lancaster University) helpfully suggested that the cysteine residue could have a post-translational modification such as the glutathione modification in the protein expression by Sengupta and Udgaonkar (Sengupta and Udgaonkar, 2017). Therefore, the modification of the cysteine residue by glutathione preventing the formation of disulphide bonded dimeric apoA-I R173C was investigated.

Tris (2-carboxyethyl) phosphine hydrochloride (TCEP) (Sigma-Aldrich) was used to reduce the cysteine residue in apoA-I R173C and analyse the mass of monomeric and dimeric apoA-I R173C without the suspected glutathione modification (Li et al., 2012; Sengupta and Udgaonkar, 2017).

The method of TCEP removal and apoA-I R173C incubation time were tested. Initially, apoA-I R173C was incubated with 5 mM TCEP reducing agent for ≥ 12 hours at 4°C with inverting to mix. The glutathione and TCEP removal methods were tested using dialysis and a PD-10 desalting column (GE Healthcare). The apoA-I R173C pre-TCEP stock solution was 0.75 mg/mL in 50 mM tris base, 1 mM benzamidine, 1 mM EDTA, pH 8.0 buffer. The final protein concentration was 0.65 mg/mL containing 5 mM TCEP at 25°C for 24 hrs, total sample volume of 3 mL per sample.

To remove the TCEP 2.5 mL aliquots of the sample were dialysed with 2 buffer changes, dialysis and desalting (PD-10) column, and PD-10 column only. The samples were incubated at 37°C for 8 days with samples taken for NDGGE at 0, 24, 120 and 192 hours. After the initial TCEP removal tests, apoA-I R173C was incubated at 0.5 mg/ml with 5 mM TCEP at 37°C. After TCEP removal by dialysis as previously described and incubation at 37°C to form dimeric apoA-I R173C a sample for NDGGE analysis was taken every 24 hours and stored at -20°C. The samples were filtered using a 0.22 µm syringe filter (Corning®) to remove precipitated protein.

The following apoA-I R173C TCEP reduction conditions were used after optimisation tests. All incubation periods including dialysis and dimer formation were at 4°C at approximately 0.5 mg/mL to reduce protein precipitation. The post-formic acid cleaved apoA-I R173C (E2D) was incubated for 24 hours with 5 mM TCEP. The TCEP and cleaved glutathione were removed by dialysis over 2 days with at least 2 buffer changes.

To form apoA-I R173C dimer the protein was incubated for 48 hours post-TCEP removal.

3.2.7.2 Size exclusion chromatography for mass spectrometry

Before the apoA-I R173C post-TCEP incubation sample was loaded onto the column the protein concentration was increased using a Corning® Spin-X UF6 Concentrator Polyether sulfone (PES) membrane (Sigma-Aldrich). The spin concentrator was loaded with 6 mL of dH_2O to pre-rinse the membrane and spun at 3200 x g for 20 minutes at room temperature. The flow-through was discarded and the concentrator was loaded with 6 mL of apoA-I R173C at 0.8 mg/mL and centrifuged as above until the total volume was 1 mL. The expected apoA-I R173C concentration was 4.8 mg/mL in a 1 mL volume and the measured concentration was 3.16 mg/mL. Therefore, the concentrator yield was approximately 66 % of the total protein in the dilute stock solution.

Size exclusion chromatography (SEC) was used to separate apoA-I monomer and dimer for mass spectrometry analysis using the HiLoad™ 16/600 Superdex™ 75 pg, 120 mL column volume (CV), connected to the ÄKTA Start chromatography system and UNICORN™ Start 1.0 software (GE Healthcare). The SEC was washed at a flow rate of 1 mL/min with four CVs of dH_2O and equilibrated with four CVs of 10 mM tris base, 1 mM EDTA, 0.15 M NaCl, 1 mM NaN_3, pH 8.0. After the TCEP reduction and incubation to form apoA-I R173C dimer, a sample of 3.7 mg/mL with a total volume of 1 mL was loaded onto the column at a flow rate of 1.0 mL/min. The SEC buffer was run for 1 CV for dimer and monomer separation. When the protein UV absorbance increased above 5 mAU 1 mL fractions were collected and the concentration was measured using the Nanodrop™ 2000c. The fractions were run on an NDGGE gel as described earlier to determine the purity and amount of separation.

3.2.7.3 Mass spectrometry of atheroprotective mutants

The samples were outsourced to Liverpool University where the initial protein samples were run, and the data was deconvoluted by Mr M. Prescott at the Institute of Integrative Biology using electrospray ionisation time-of-flight mass spectrometry (ESI-TOF MS) using the Q-ToF Micro mass spectrometer (Waters/Micromass). The SEC separated apoA-I R173C monomer and dimer samples were run, and data was deconvoluted by Dr. P. Brownridge at the Centre for Proteome Research using C4 based reversed phase liquid chromatography (LC) ESI-TOF MS for full-length intact mass analysis. The SEC fractions were confirmed to contain only monomer or dimer using NDGGE.

The apoA-I R173C and apoA-I L144R samples were sent as 100 µL stock solutions in 30 % (v/v) acetonitrile in MQ H_2O at 1 mg/mL each for ESI-TOF MS. The apoA-I R173C monomer and dimer samples analysed by C4 based reversed phase LC-MS were in 10 mM tris, 1 mM EDTA, 1 mM NaN_3, pH 7.4 containing 5 % (v/v) acetonitrile. The monomer sample also contained 5 mM TCEP to ensure reducing conditions and prevent dimer formation before the sample was analysed. The apoA-I R173C monomer and dimer (fractions T50/51) stock concentrations were 100 µL at 1.6 and 1.8 mg/mL, respectively.

3.3 Results

3.3.1 Evidence of plasmid mutations using SLIM-PCR

3.3.1.1 Plasmid construct PCR products

The SLIM-PCR reaction was used to generate mutations in the apoA-I WT (E2D) sequence for expression of the atheroprotective mutants, apoA-I L144R and R173C. Therefore, it was necessary to confirm the estimated mass of the plasmids following the SLIM-PCR reaction before sequencing the plasmid cDNA recombinant protein

sequence. The PCR amplification (**Figure 3.6**) and the SLIM hybridisation (**Figure 3.7–3.8**) agarose gels contained strong bands labelled as the PCR products at approximately 4.5 kb which corresponded to the approximate number of bases as the apoA-I (E2D) pNFXex vector. The SLIM-PCR products were transformed into XL1-Blue cells and the respective plasmids were isolated from overnight cultures grown from single colonies of the transformed cells. The purified plasmids were sequenced prior to protein expression tests.

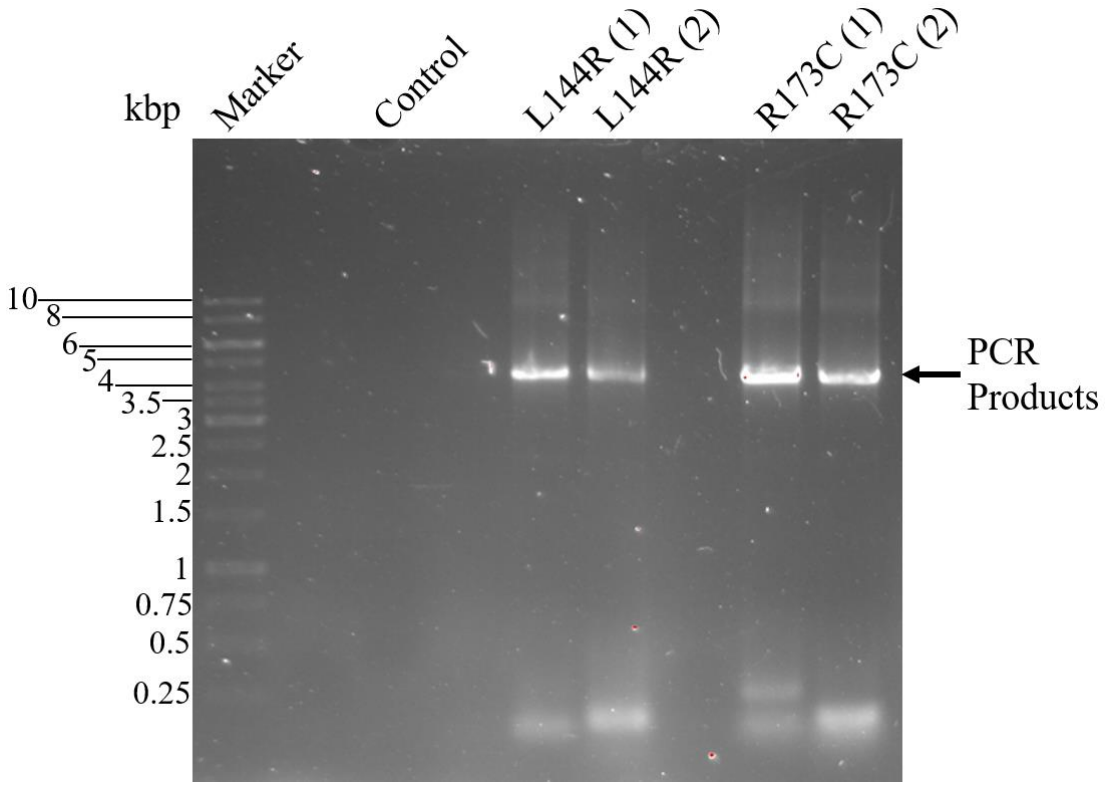

Figure 3.6. The SLIM-PCR amplification products from the L144R and R173C reactions 1 and 2 in a 0.8 % (w/v) agarose gel including a control PCR sample.

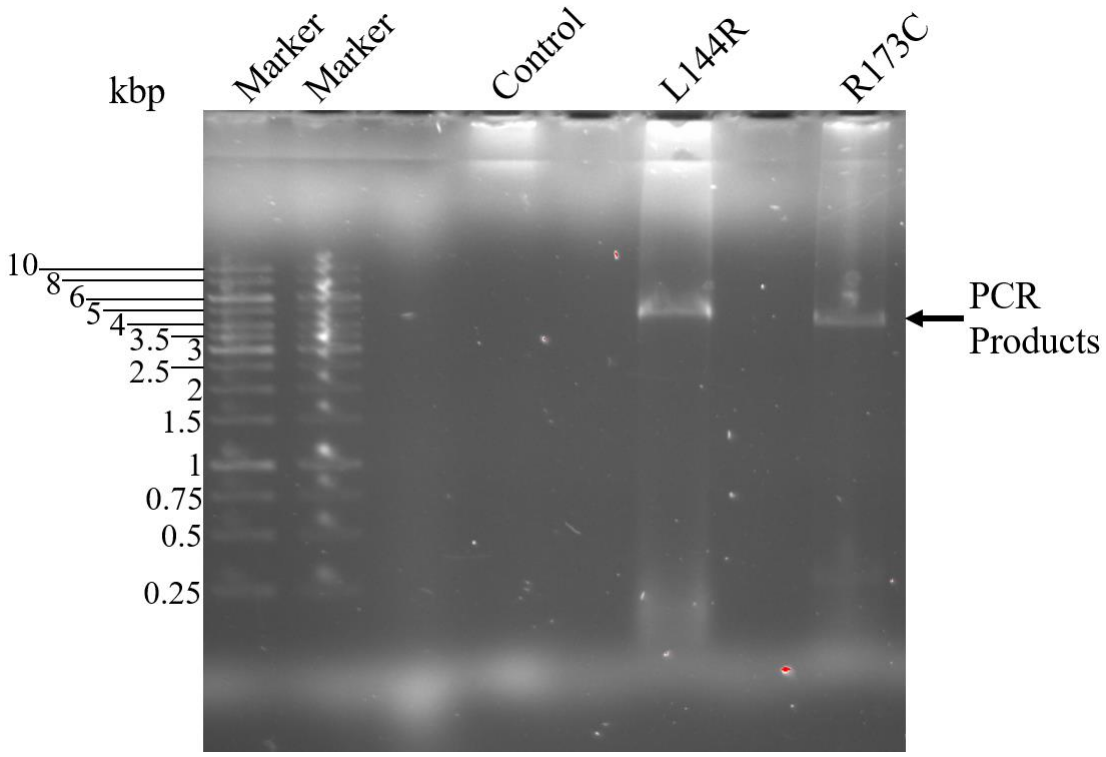

Figure 3.7. The SLIM-PCR hybridisation products from both the L144R and R173C reactions in a 0.8 % (w/v) agarose gel including a control PCR sample.

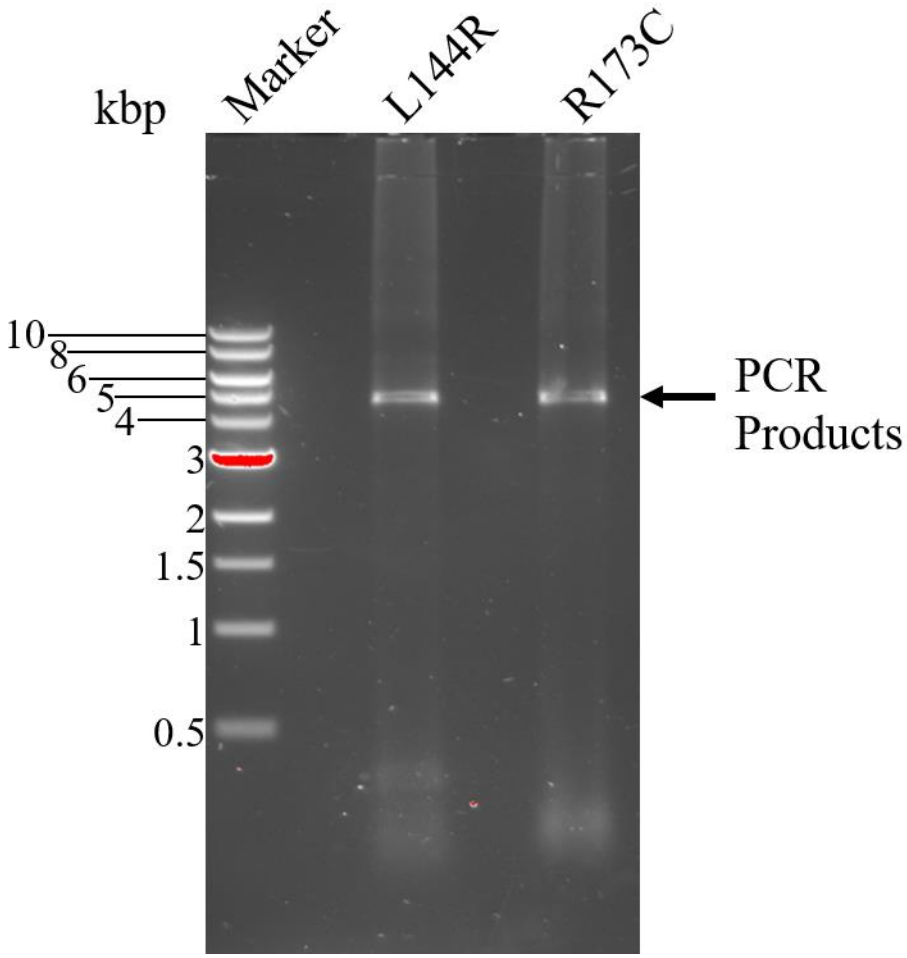

Figure 3.8. The SLIM-PCR hybridisation products from both the L144R and R173C reactions in a 0.8 % (w/v) agarose gel.

3.3.1.2 Gene sequencing

After confirmation of the estimated plasmid masses for apoA-I R173C and L144R by agarose gel electrophoresis, the plasmids were sequenced to confirm the mutation of the 173rd and 144th residues occurred, respectively. The expected cDNA nucleotide sequence of apoA-I WT (E2D) is shown in **Appendix 1B**. The sequence of the mutated plasmids containing the expected R173C and L144R mutation respectively were compared to the apoA-I WT (E2D) cDNA sequence to confirm the presence of the mutation in the plasmid DNA before protein expression tests using BLAST® blast-n

suite (Zhang et al., 2000). The ExPASy Translate tool was used to convert the cDNA nucleotide sequence to amino acids (Artimo et al., 2012).

The cDNA sequences of both the R173C and L144R mutants (**Appendix 1**) were compared to the apoA-I WT cDNA sequence using BLAST® sequence and showed the expected nucleotide changes of 1 and 2 nucleotides, respectively. As the BLAST® data showed a 99 % match for both R173C at 776/777 (CGC to TGC) nucleotides and L144R at 775/777 (CTG to CGC) nucleotides indicating that the codon mutations specified in the SLIM-PCR primers occurred. The nucleotide sequence when converted to amino acid sequence also showed the R173C and L144R mutations at the correct residue number in the protein sequence.

3.3.2 ApoA-I (E2D) and atheroprotective mutant protein expression and purification

3.3.2.1 Protein expression

To confirm the overexpression of the fusion proteins of apoA-I WT, R173C and L144R, SDS-PAGE gels were used to determine the relative amount and estimate the molecular weight (MW) of the fusion protein compared to the *E. coli* proteins. The fusion protein N-terminally his_6-tagged apoA-I (E2D) has a molecular weight of 29798.57 Da (~30 kDa) as calculated by inputting the amino acid sequence (**Appendix 1B**) into the ExPASy Compute pI/MW tool (Artimo et al., 2012). The approximate molecular weight of 28 kDa is used for the fusion protein as the migration of the fusion protein in the gel compared to the marker bands indicates the band is less than approximately 30 kDa (**Figure 3.9**).

In each SDS-PAGE gel for the pre- and post-induction protein expression samples of apoA-I WT (**Figure 3.9**), R173C (**Figure 3.10**) and L144R (**Figure 3.11**), the pre-

induction sample does not have a strong band at approximately 28 kDa. This suggests that basal expression of the fusion protein does not occur allowing the cells to grow to an optimal density before IPTG is added, as basal 'leaky' expression of recombinant proteins can lead to slow cell growth rates (Rosano and Ceccarelli, 2014). After IPTG addition overall *E. coli* protein expression occurred as indicated by the bands over the range of 10 – 250 kDa. The fusion protein at approximately 28 kDa for each mutant and apoA-I WT was expressed after 2-5 hours and overnight post-induction incubation at 37°C.

The expression of apoA-I WT increased from 2 – 5 hours post-induction (**Figure 3.9**). The apoA-I R173C expression increased from 2 – 4 hours, with a similar intensity expression band at 5 hours to 3 hours post-induction (**Figure 3.10**). After an overnight induction there was a decrease in the apoA-I R173C expression. The apoA-I L144R expression increased over time with no significant increase after an overnight induction period (**Figure 3.11**).

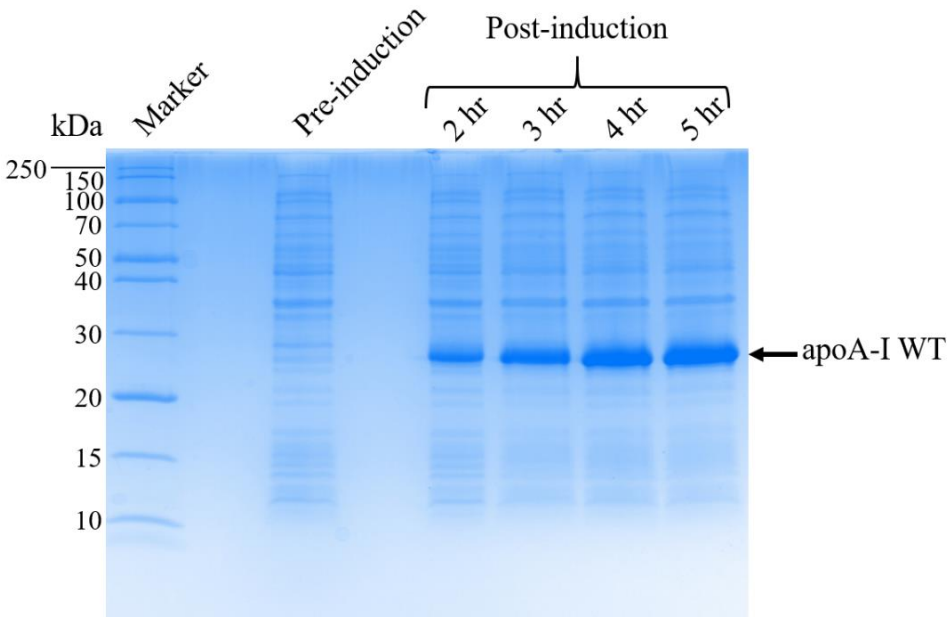

Figure 3.9. ApoA-I WT (E2D) pre- and post-induction hourly samples over 2 – 5 hours on a 15 % SDS-PAGE gel.

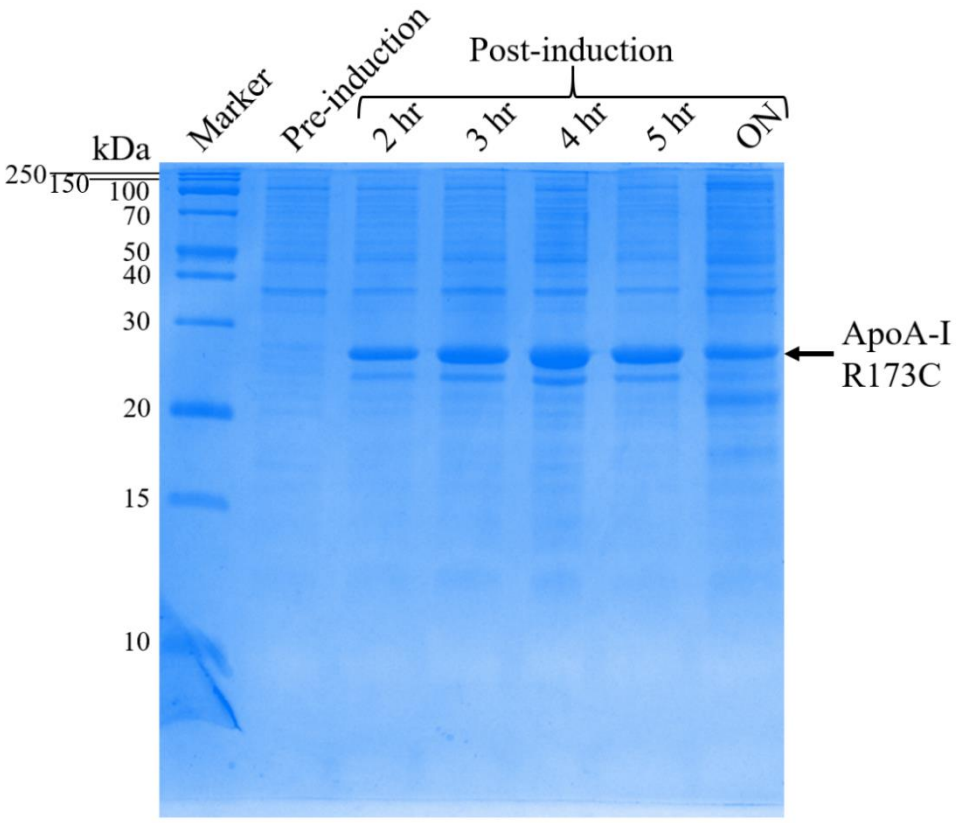

Figure 3.10. ApoA-I R173C pre- and post-induction hourly samples (2-5 hours) and overnight (ON) sample on a 15 % SDS-PAGE gel.

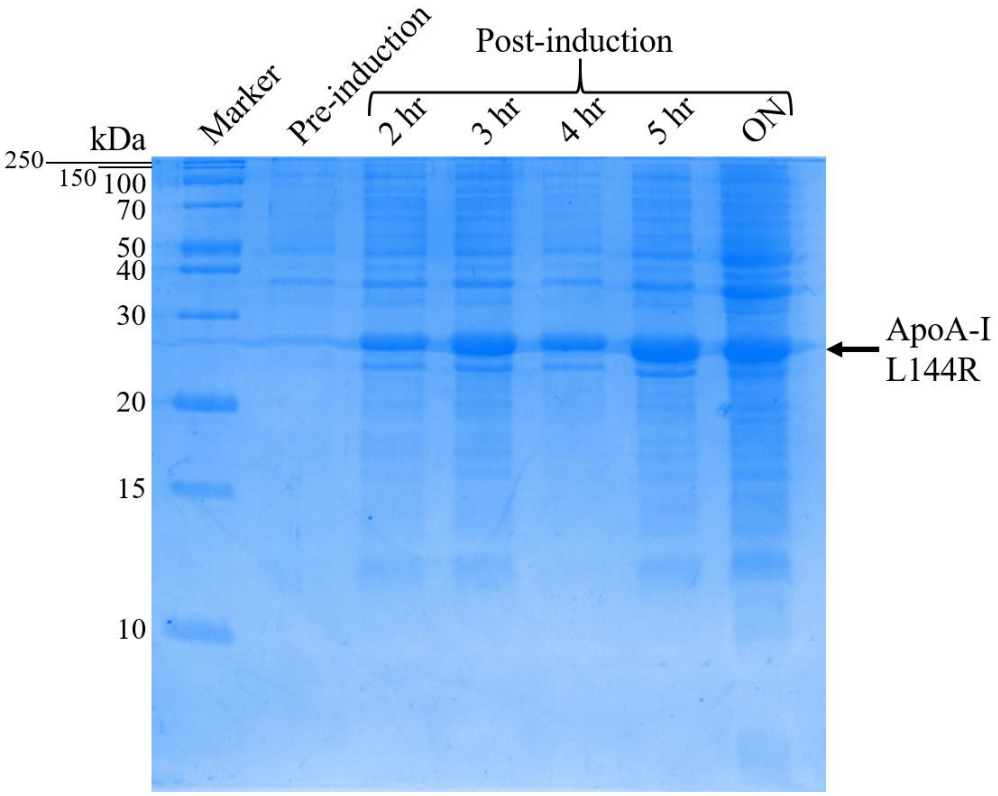

Figure 3.11. ApoA-I L144R pre- and post-induction hourly samples (2-5 hours) and ON sample on a 15 % SDS-PAGE gel.

3.3.2.2 Nickel ion affinity chromatography

To separate the fusion protein from the proteins expressed by the *E. coli* cells nickel ion affinity chromatography was used and the samples at each wash step were visualised on an SDS-PAGE gel to check for the removal of impurities. In **Figure 3.12**, the apoA-I WT +his-tag protein band is indicated on the SDS-PAGE gel and the fusion protein band is present in the post-induction, lysis supernatant, and final elution (500 mM imidazole) lanes.

In the corresponding chromatogram a peak in the UV absorbance indicated the presence of protein eluted from the nickel column. The flow-through (FT), lysis buffer (wash 1), 20 mM, 45 mM and 500 mM imidazole washes are as indicated. In the purification for apoA-I WT the wash 1 and 45 mM imidazole bands are faint with a band at

approximately 28 kDa indicating that minimal amounts of the fusion protein were eluted at these stages. The bands are faint due to low concentration as indicated on the chromatogram at 45 mM imidazole with a minimal increase in UV absorbance at approximately 130 mL. The wash 1 and 20 mM imidazole samples were prepared through EtOH precipitation to remove the protein from guanidine HCl which interferes with samples running effectively in an SDS-PAGE gel. It appears the guanidine was not completely removed and/or the precipitated protein did not fully resuspend therefore only some faint impurity bands are visible.

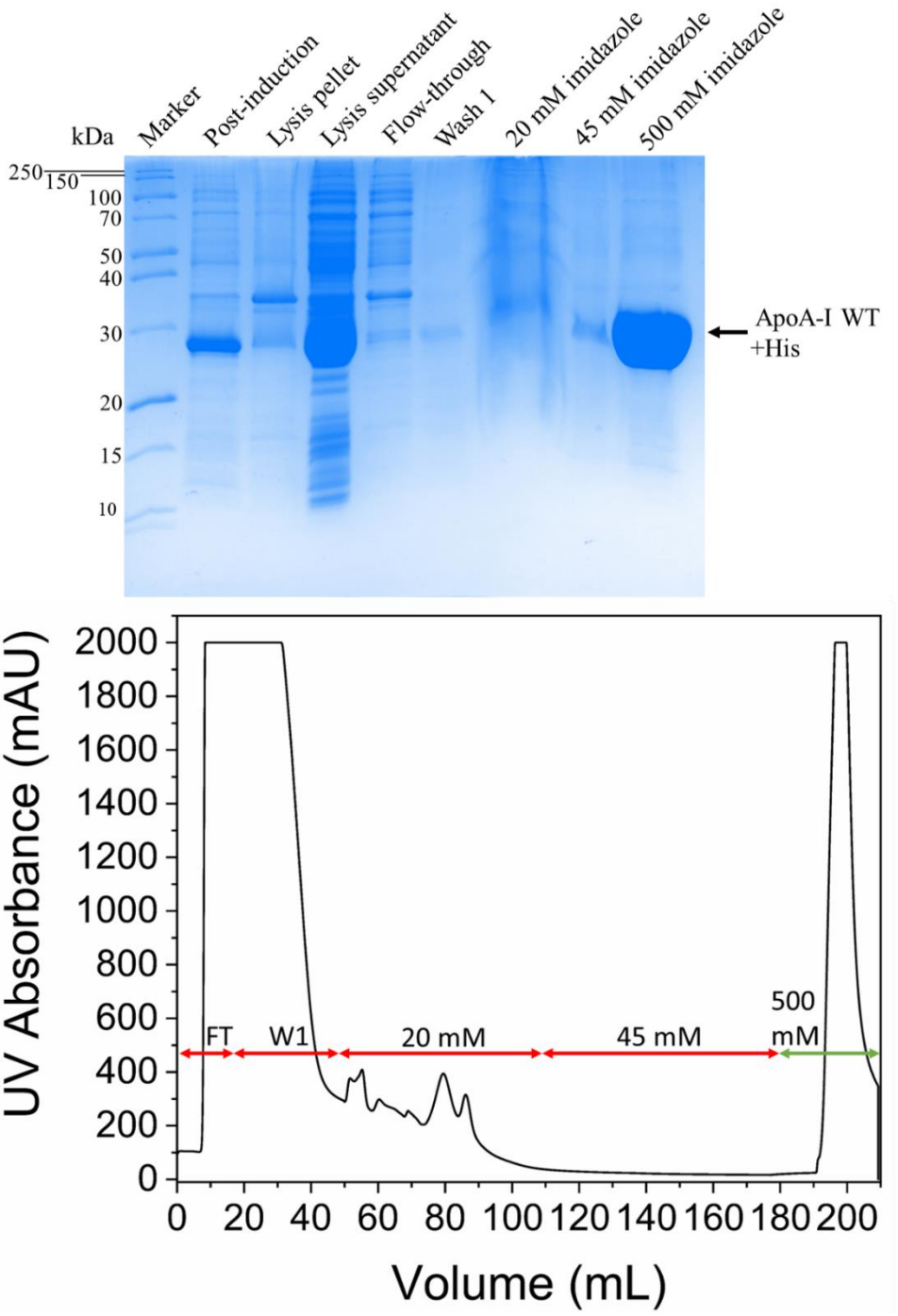

Figure 3.12. 15 % SDS-PAGE gel of the apoA-I WT lysis pellet, lysis supernatant, flow-through (FT), wash 1 (W1), 20 mM imidazole, 45 mM imidazole, 500 mM imidazole fractions. The UV protein absorbance chromatogram of His-trap chromatography purification of apoA-I WT.

The peaks on the chromatogram confirmed the removal of non-specific binding proteins in the flow-through and wash 1 fractions, and the binding of the majority of the fusion protein to the nickel resin. The fusion protein in the 500 mM imidazole lane is indicated as a large band at approximately 28 kDa with some faint impurities only present at a high concentration as the sample was > 1.5 mg/mL on the gel. The chromatogram peak at 500 mM imidazole also shows a high UV absorbance up to the maximum of 2000 mAU indicating protein elution.

ApoA-I L144R was purified under the same conditions with each lysis and wash step shown in the SDS-PAGE gel (**Figure 3.13**). The lysis supernatant contained a larger amount of fusion protein at approximately 28 kDa compared to the lysis pellet and post-induction sample. The flow-through, wash 1, 20 mM and 45 mM imidazole samples in the chromatogram (**Figure 3.13**) show UV absorbance peaks indicating the elution of non-specific binding *E. coli* proteins.

However, similar to the apoA-I WT 20 and 45 mM imidazole wash steps (**Figure 3.12**) the apoA-I L144R fusion protein band in the corresponding samples was faint (**Figure 3.13**). The eluted fusion protein at 500 mM imidazole at this high concentration at approximately 1 mg/mL shows some smaller impurities indicated by faint bands comparable to apoA-I WT and R173C. The elution fusion protein peak also reached a maximum of 2000 mAU.

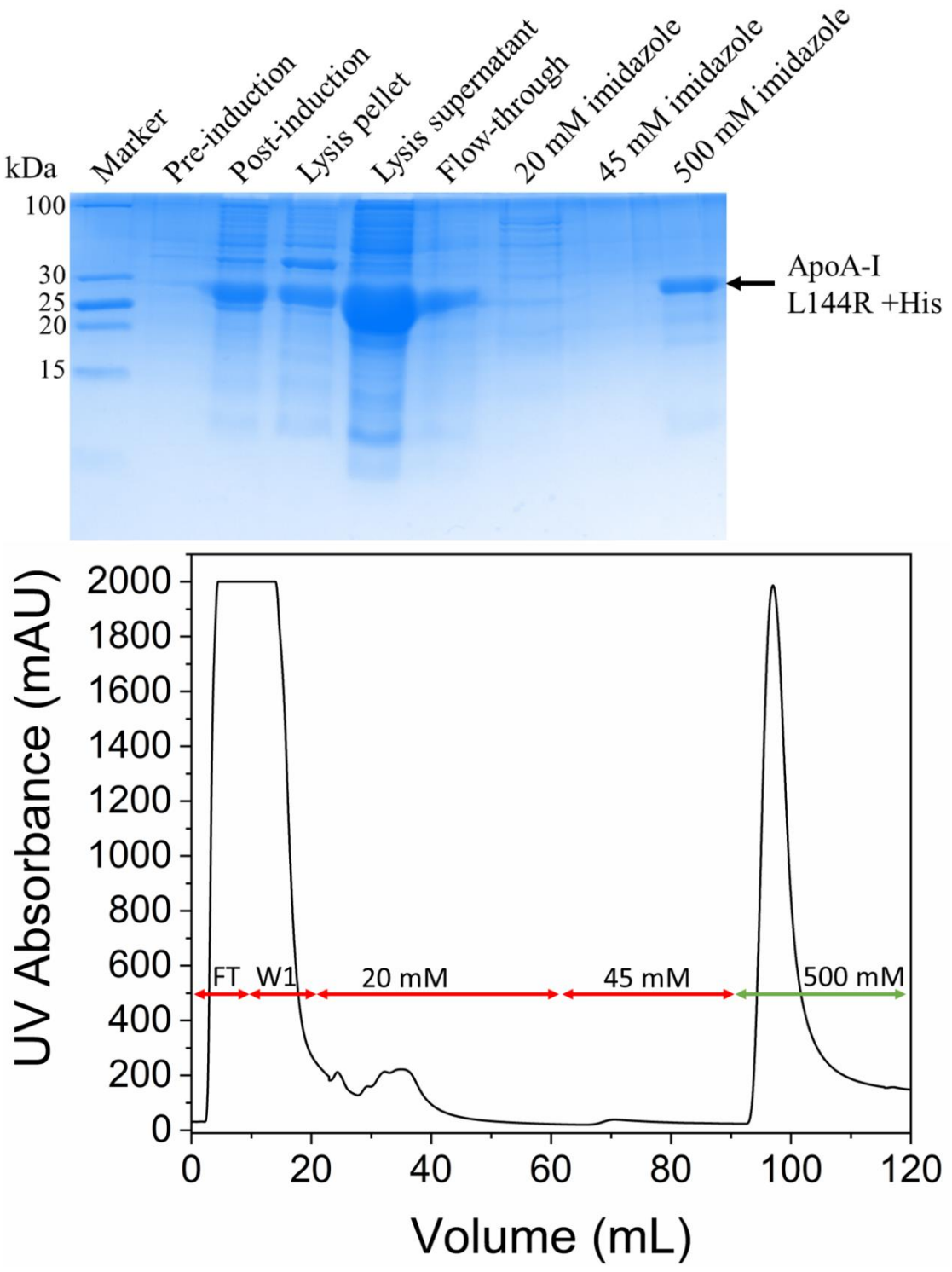

Figure 3.13. 15 % SDS-PAGE gel of the apoA-I L144R pre-induction, post-induction, lysis pellet, lysis supernatant, FT, 20 mM imidazole, 45 mM imidazole, 500 mM imidazole fractions. The UV protein absorbance chromatogram of His-trap chromatography purification of apoA-I L144R.

ApoA-I R173C expressed in BL21(DE3) cells fractions are shown at each stage in the chromatogram (**Figure 3.14**) whilst the fusion protein expressed with Origami™ B(DE3) cells is shown with the respective chromatogram (**Figure 3.15**). The SDS-PAGE gel of apoA-I R173C BL21(DE3) chromatogram fractions indicated fusion protein in the lysis supernatant, flow-through, and 500 mM elution (**Figure 3.14**). The flow-through and wash stages (wash 1, 20 mM and 45 mM imidazole) show peaks in the UV absorbance in the chromatogram indicating the removal of non-specific binding proteins, like apoA-I WT and L144R. The SDS-PAGE imidazole wash steps only show faint bands on the gel. The elution fraction at 500 mM imidazole is comparable with the apoA-I WT and L144R with faint impurities below the concentrated 1-2 mg/mL apoA-I R173C +his-tag band. The overall apoA-I R173C +his-tag fusion protein elution peak maximum was lower than apoA-I WT and L144R at approximately 1200 mAU.

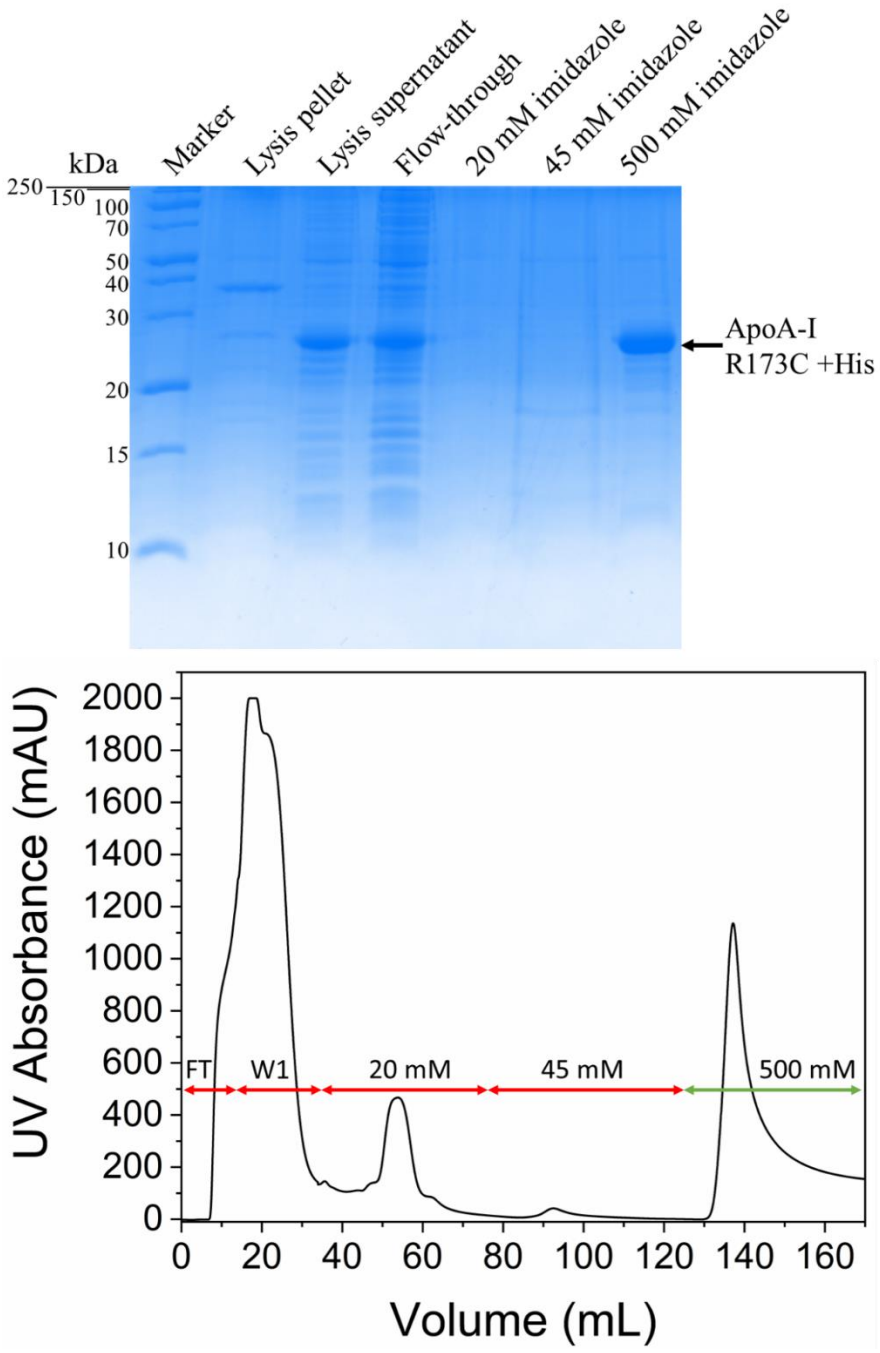

Figure 3.14. 15 % SDS-PAGE gel of the apoA-I R173C lysis pellet, lysis supernatant, FT, W1, 20 mM imidazole, 45 mM imidazole, 500 mM imidazole fractions. The UV protein absorbance chromatogram of His-trap chromatography purification of apoA-I R173C.

The apoA-I R173C fusion protein expressed with Origami^{TM} B(DE3) cells was purified and an SDS-PAGE gel was run of the final elution fraction for mass spectrometry

(**Figure 3.15**). The eluted fusion protein had a peak maximum at approximately 600 mAU and no impurity bands as indicated on the SDS-PAGE gel. The wash stages contained peaks similar to the chromatograms of apoA-I WT, L144R and R173C (BL21(DE3)) indicating the removal of non-specific binding proteins.

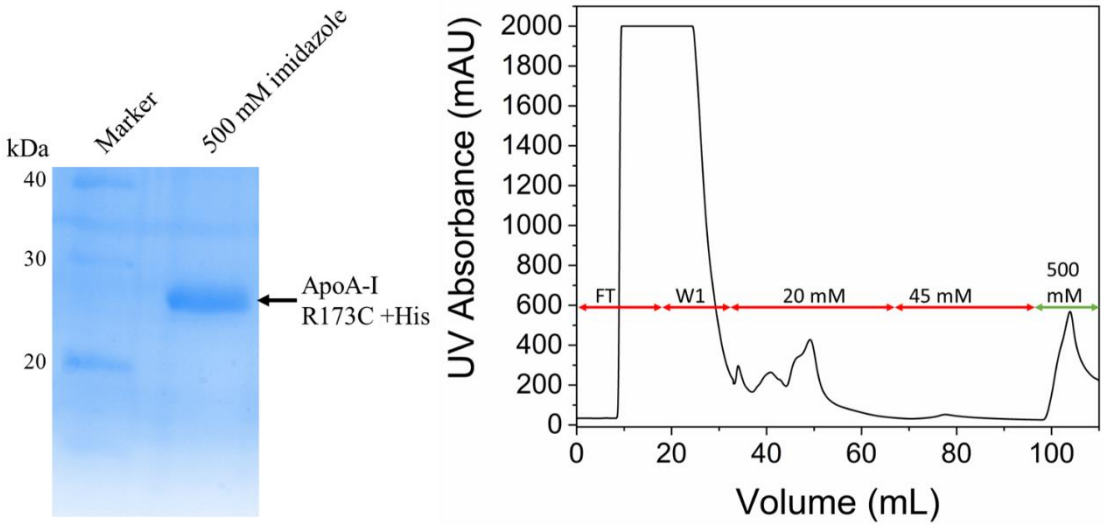

Figure 3.15. 15 % SDS-PAGE gel of the pooled apoA-I R173C + His-tag elution fraction protein expressed with Origami^{TM} B(DE3) *E. coli* cells. The UV protein absorbance chromatogram of His-trap chromatography purification of apoA-I R173C expressed with Origami^{TM} B(DE3) *E. coli* cells.

3.3.2.3 His-tag cleavage and protein dialysis

After separation of the fusion protein for apoA-I WT, R173C and L144R expressed with BL21(DE3) cells the his-tag was cleaved during incubation with formic acid. The SDS-PAGE gels in **Figure 3.16** correspond to apoA-I WT (A), R173C (B) and L144R (C). Each gel shows only the fusion protein band at approximately 28 kDa (apoA-I +his-tag) in the pre-cleavage sample lane and a lower molecular weight post-his-tag cleavage protein band in the post-cleavage lane.

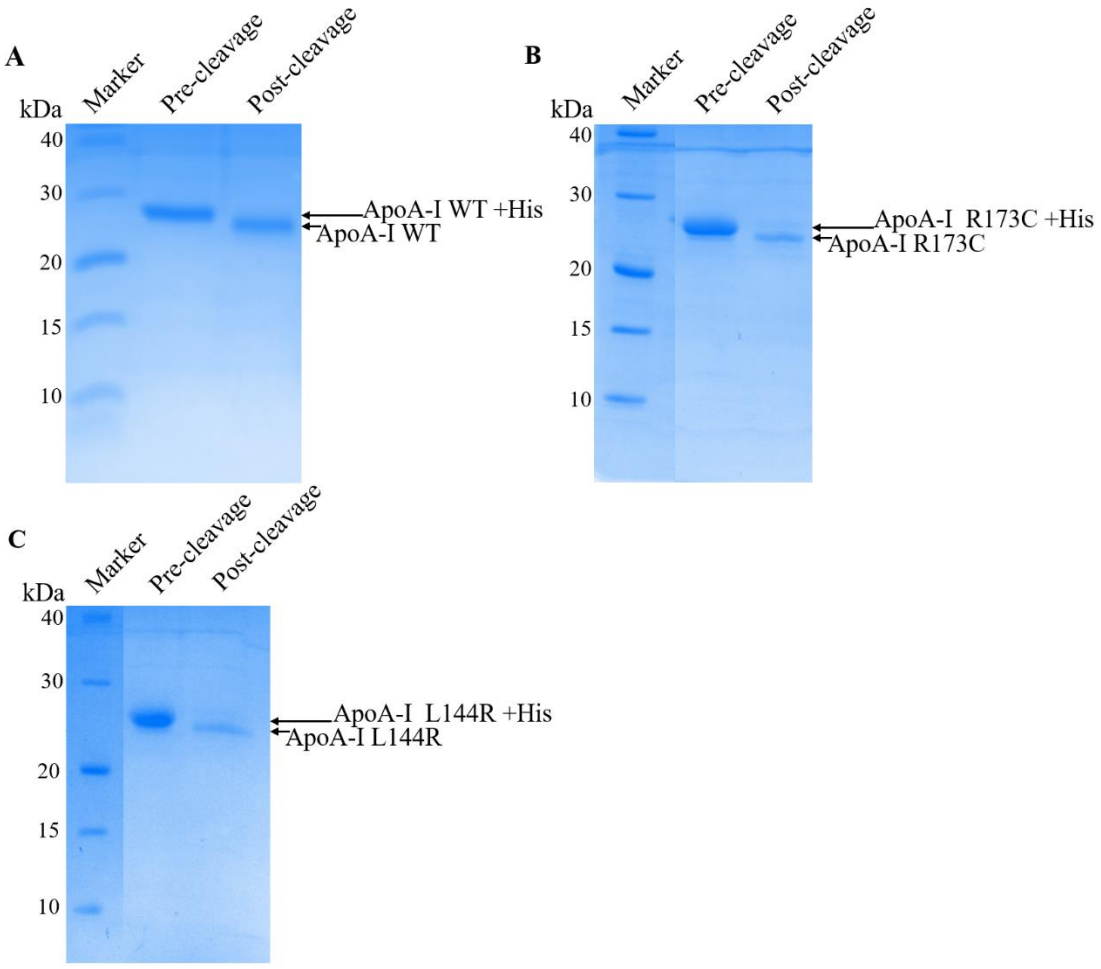

Figure 3.16. 15 % SDS-PAGE gels of the pre- and post-His-tag cleavage of **A)** apoA-I WT, **B)** apoA-I R173C and **C)** apoA-I L144R, at 0.2 mg/mL protein per lane. For the purposes of showing the pre- and post-his-tag cleavage samples for apoA-I L144R and R173C, empty lanes and duplicate samples were cropped from the gel images, and the gels without cropping are in **Appendix 1**.

3.3.3 Protein identification

3.3.3.1 Confirmation of protein mass

The purified post-cleavage protein samples of the atheroprotective apoA-I mutants were analysed by mass spectrometry to confirm their molecular masses. Initially, apoA-I R173C and L144R post-cleavage proteins expressed with BL21(DE3) cells were

analysed using ESI-TOF MS. The expected masses of apoA-I WT, R173C and L144R proteins residues 3-243 (post-his-tag cleavage) were predicted using the ExPASy compute pI/MW tool (Artimo et al., 2012) for comparison to the observed masses from ESI-TOF MS sample analysis.

The expected and observed molecular masses, and the adducts for each protein are summarised in **Table 3.2**. Previously, the mass of the apoA-I WT (E2D) protein was in close agreement with the expected mass (Townsend, 2016). Similarly, the apoA-I L144R observed mass (27878 Da, **Figure 3.17**) is the expected mass of apoA-I L144R +1H atom (**Table 3.2**).

The apoA-I R173C mass (28088 Da, **Figure 3.18**) was greater than expected by 307 Da, therefore further investigation was required to produce the protein with the expected molecular mass. Before the identification of the glutathione adduct the apoA-I R173C +his-tag fusion protein was expressed with Origami™ B(DE3) cells and analysed by ESI-TOF MS (**Figure 3.19**). The measured masses were below the expected mass of the apoA-I R173C fusion protein suggesting that the protein expressed was modified at some stage in the expression.

Table 3.2. The expected and observed masses of apoA-I WT (Townsend, 2016), L144R and R173C as analysed by ESI-TOF MS.

E. *coli*	**ApoA-I (E2D)**	**Expected mass (Da)**	**Observed mass (Da)**	**Mass difference (Da)**	**Adduct**
BL21(DE3)	WT	27834	27837	3	3H
	L144R	27877	27878	1	1H
	R173C	27781	28088	307	glutathione
Origami™ B(DE3)	R173C +His	29614	24693	4921	
			27272	2342	
			28284	1330	

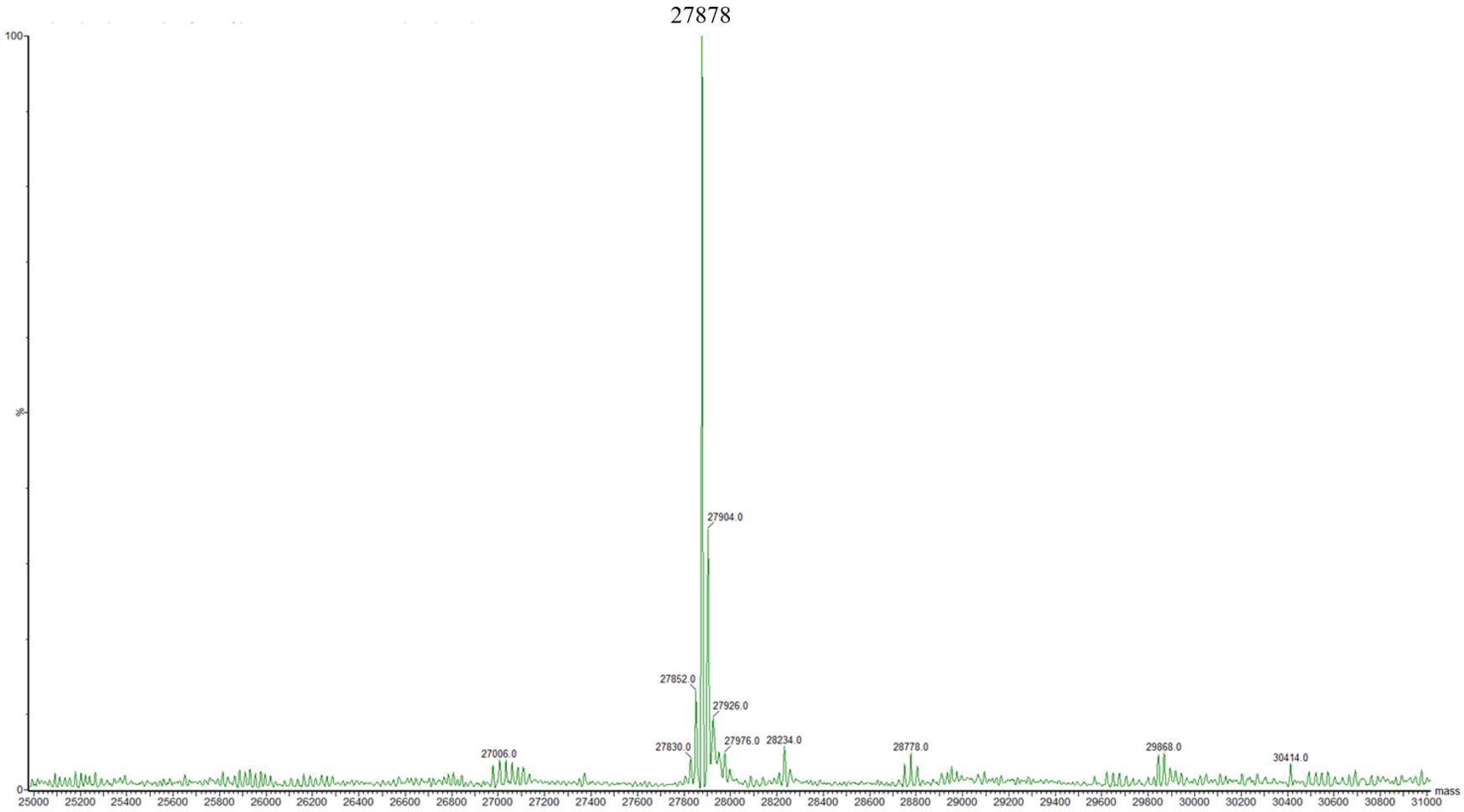

Figure 3.17. The mass spectrum of apoA-I L144R by ESI-TOF MS, observed mass 27878 Da.

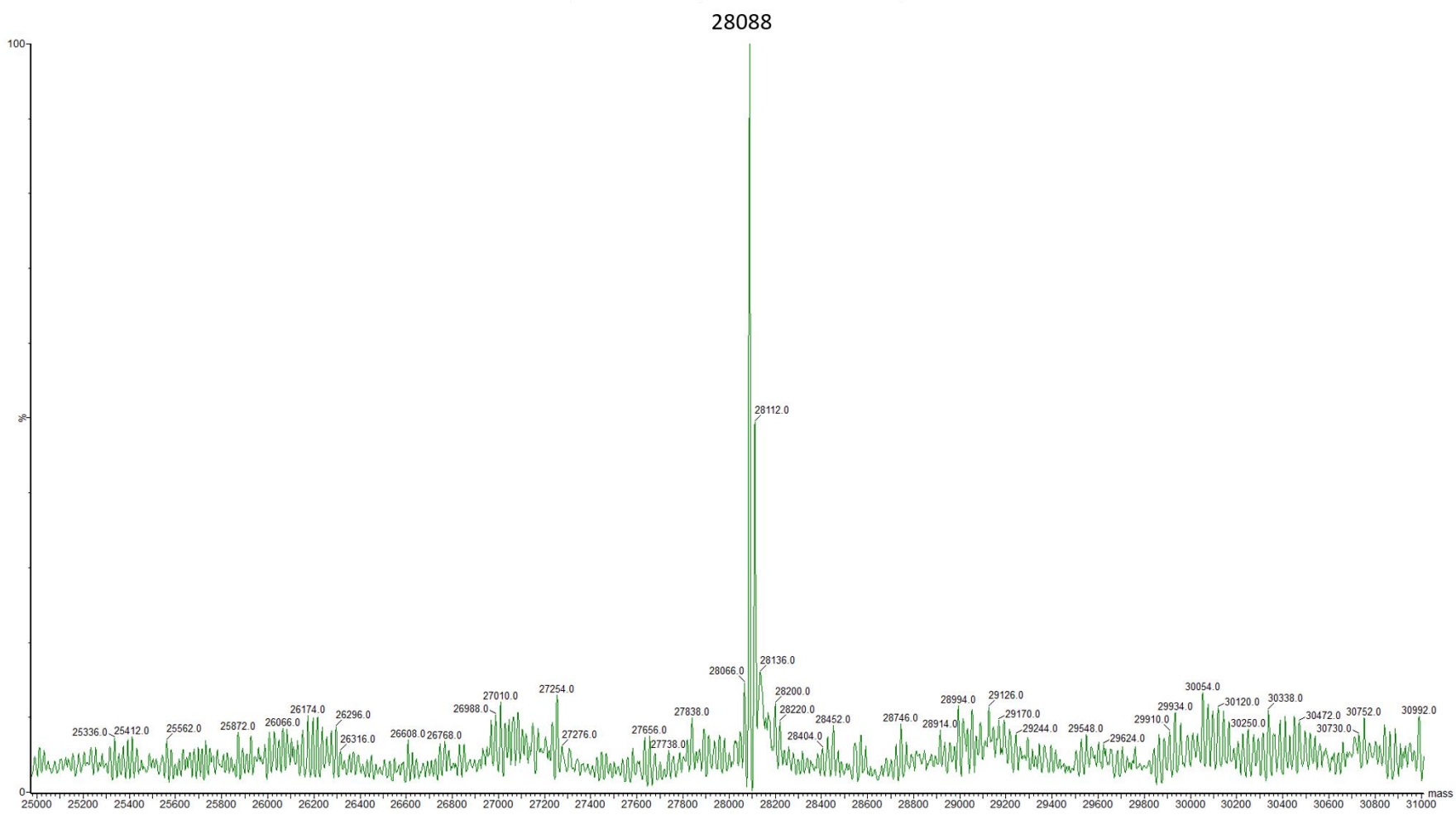

Figure 3.18. The mass spectrum of apoA-I R173C + glutathione cysteine modification by ESI-TOF MS, observed mass 28088 Da.

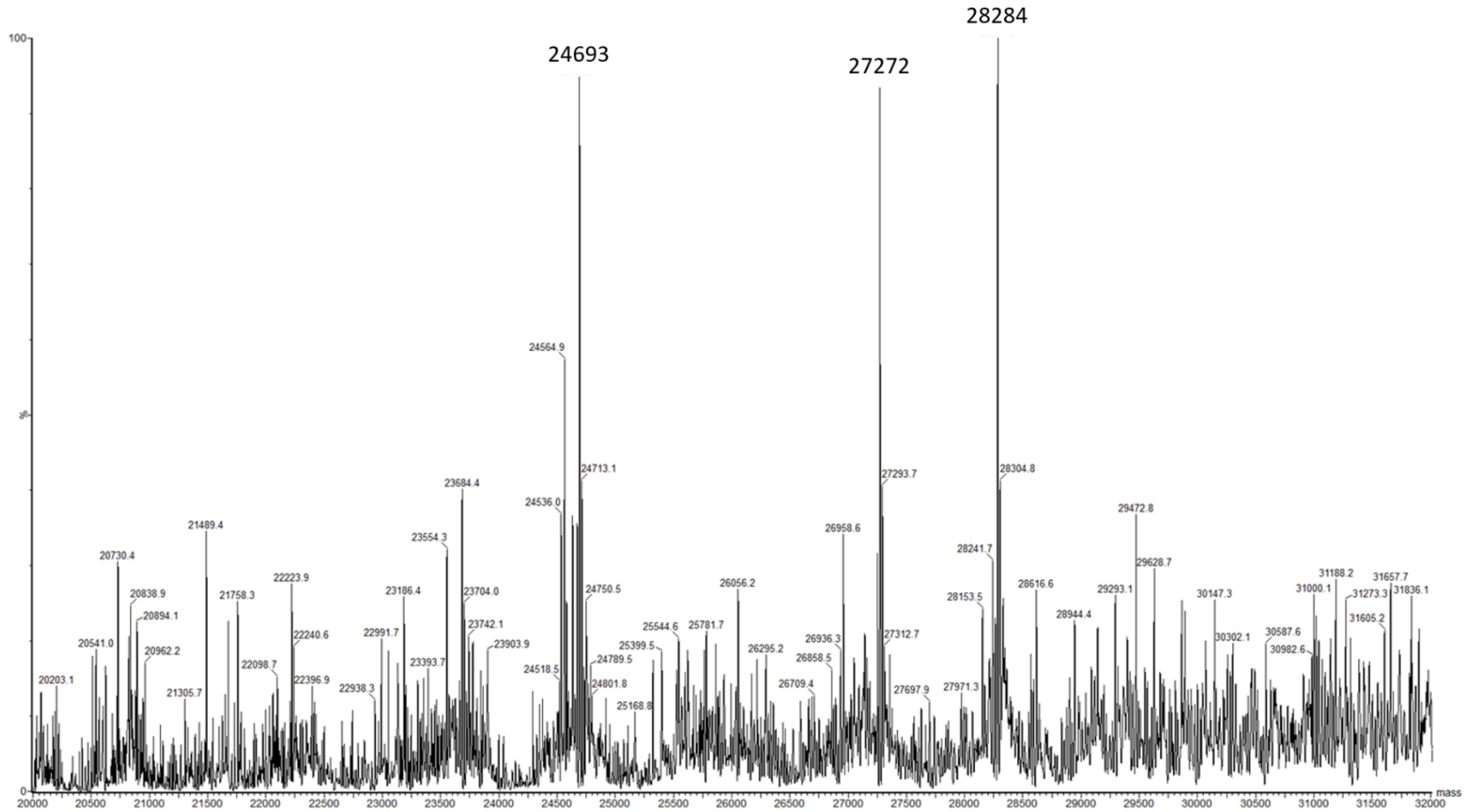

Figure 3.19. Mass spectrum of apoA-I R173C +His (Origami^{TM} B(DE3) cells), by ESI-TOF MS , observed masses 24693, 27272, and 28284 Da.

3.3.3.2 Identification and cleavage of the apoA-I R173C glutathione moiety

The observed mass of the apoA-I R173C post-his-tag cleavage protein was greater than the expected mass by 307 Da, so it was suspected that the free cysteine thiol groups were modified with glutathione. Therefore, the apoA-I R173C protein was reduced using TCEP to remove any post-translational modifications via the reduction reaction in **Figure 3.20**. ApoA-I WT does not contain cysteine residues and so the mutation allows for dimerization of the protein through intermolecular disulphide bridge formation (Weisgraber et al., 1980). This may be responsible for the atheroprotective properties of this mutant, and so it was necessary to regenerate free thiol groups for subsequent disulphide formation.

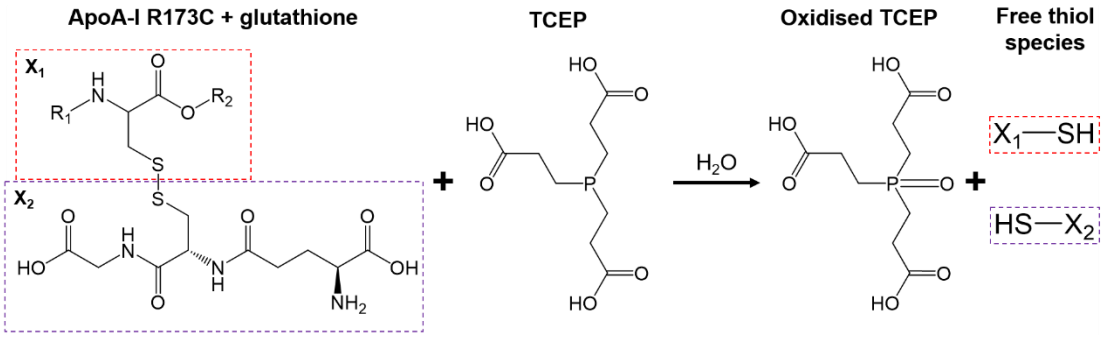

Figure 3.20. The TCEP disulphide bond reduction reaction of apoA-I R173C + glutathione moiety. The apoA-I R173C cysteine (X_1, red) contains residues 3-172 and 174-243 in R_1 and R_2, respectively, and is bonded through a disulphide bond to the glutathione moiety (X_2, purple). The reduction reaction oxidises TCEP and regenerates the cysteine and glutathione thiol (-SH) groups.

After reduction, three methods were tested for removal of TCEP: dialysis only, dialysis and desalting (PD-10) column, and PD-10 column only. The samples were taken of apoA-I R173C + 5 mM TCEP at 0 and 192 hours, post-TCEP removal for each method at 0, 24, 120 and 192 hour incubation periods (**Figure 3.21**). Successful removal of

glutathione could be monitored by mass spectrometry (see later) and inferred by the formation of dimeric protein. Both apoA-I R173C samples in the presence of the reducing agent showed a singular band at approximately 28 kDa for apoA-I R173C monomer. Similarly, the presence of only monomeric apoA-I R173C is indicated at each timepoint for the samples using dialysis and the PD-10 column, and only the PD-10 column for TCEP removal. The apoA-I R173C dimer and monomer bands are indicated in the TCEP dialysis only removal method.

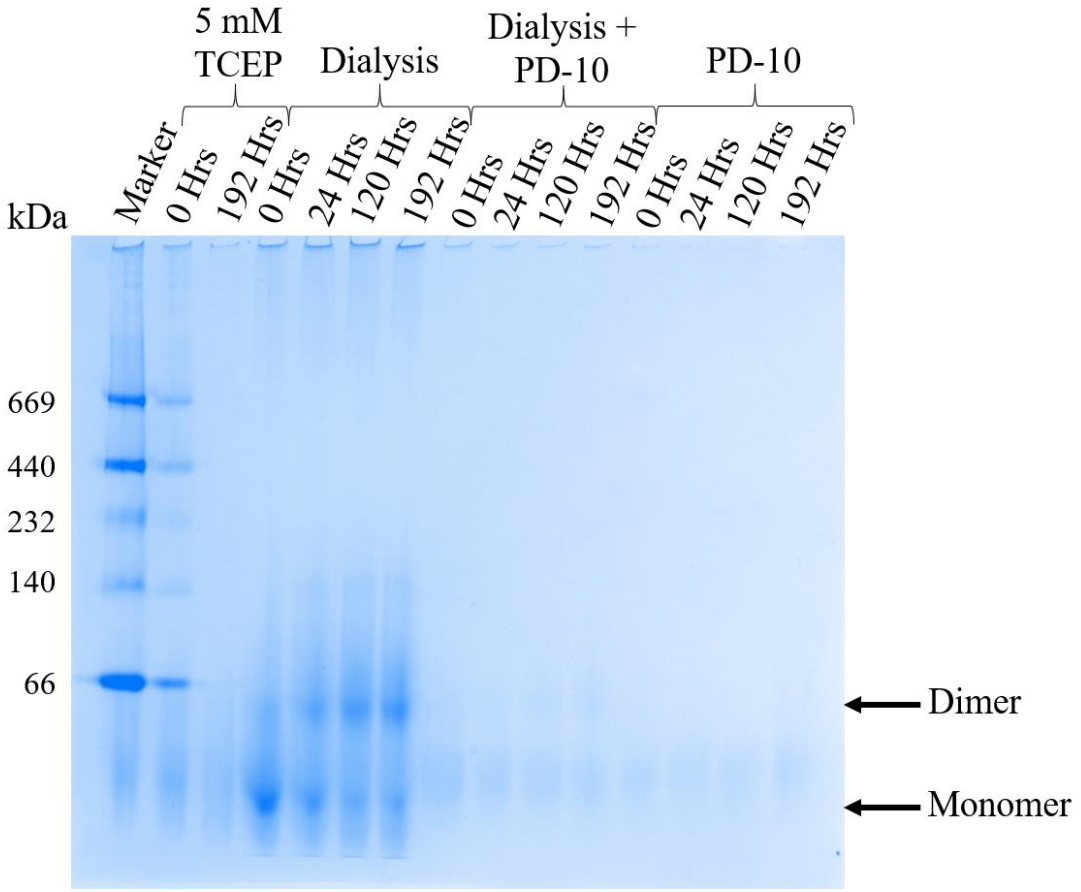

Figure 3.21.A 4 – 16 % NativePAGE gel of apoA-I R173C samples +5 mM TCEP and without TCEP removed by three different methods: dialysis, dialysis and PD-10, and PD-10 only at 0, 24, 120 and 192 hours.

The TCEP was removed by dialysis and a sample was taken at 24 hour intervals over 7 days (**Figure 3.22**). ApoA-I R173C dimer and monomer were present at relatively equal amounts at each time point except for 0 hr after TCEP removal, at approximately 56 and 28 kDa, respectively. The apoA-I R173C sample containing 5 mM TCEP also contained dimeric and monomeric apoA-I R173C possibly due to formation of dimer in the presence of TCEP in an equilibrium or partial oxidation of the TCEP reducing agent.

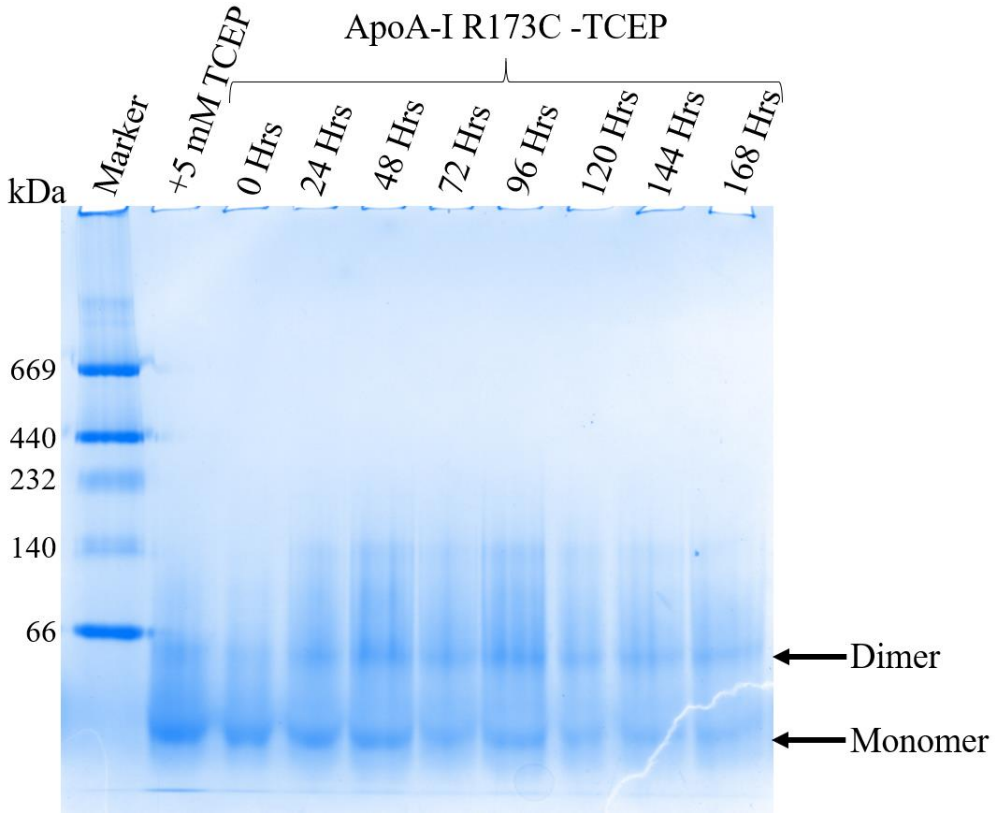

Figure 3.22. A 4-16 % NativePAGE gel of ApoA-I R173C with 5 mM TCEP and without TCEP incubated at 37°C for 7 days, with samples taken at 24-hour intervals.

Size exclusion chromatography fractions run on a NativePAGE gradient gel of the separation of apoA-I R173C monomer and dimer post-TCEP reduction and the UV absorbance chromatogram are in **Figure 3.23**. The fractions labelled in the gel were eluted during the SEC and correspond to peak 1 (blue) and peak 2 (green) in the chromatogram. Fractions T47 – T54 show a band at approximately 56 kDa indicating dimeric apoA-I R173C only. Monomeric apoA-I R173C was in fractions T56 – T60 at approximately 28 kDa. Fractions T47-48 and T55 contained a lower concentration of dimeric apoA-I R173C than T49-T54 shown by the faint band intensity. The SEC was used to separate monomeric and dimeric apoA-I R173C protein for mass spectrometry analysis only and the separation was not further optimised.

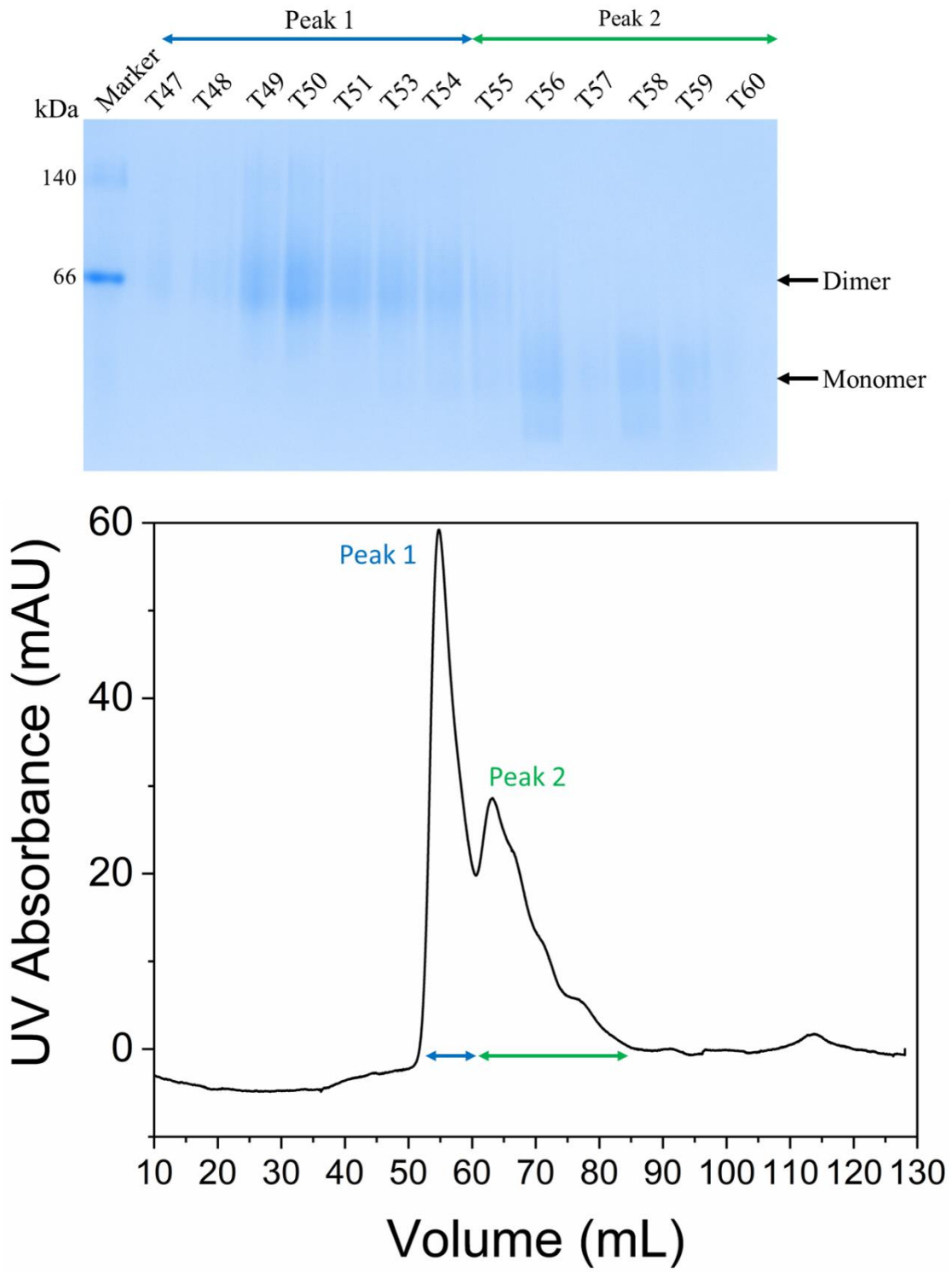

Figure 3.23. A 4 – 16 % NativePAGE gradient gel of post-TCEP apoA-I R173C SEC fractions T47-T54 (peak 1, blue) and T55-T60 (peak 2, green) indicated in the UV protein absorbance chromatogram.

The post-TCEP treated apoA-I R173C monomer and dimer SEC separated samples were analysed using mass spectrometry to confirm the molecular masses and if the suspected glutathione adduct was removed. The expected and observed masses are in **Table 3.3** of the apoA-I R173C post-TCEP treated monomer and dimer, and the previous pre-TCEP monomer mass for comparison.

Table 3.3. The expected and observed masses of apoA-I R173C monomer and dimer pre- and post-TCEP reduction as analysed by C4 based reversed phase LC-MS for intact mass samples.

ApoA-I R173C	Expected mass (Da)	Observed mass (Da)	Mass difference (Da)	Adduct
Pre-TCEP	27781	28088	307	glutathione
Monomer	27781	27783	2	2H
Dimer	55560	55563	3	3H

After TCEP treatment post-glutathione cleavage apoA-I R173C monomer and dimer separated by SEC expected masses are 27781.37 and 55560.74 Da, respectively. The measured mass of monomeric apoA-I R173C was 27783.45 Da (**Figure 3.24**) and dimeric apoA-I R173C was 55563.43 Da, with another peak at lower intensity at 27781.21 Da (**Figure 3.25**). The smaller mass at 27781.21 Da despite the similar mass to monomeric apoA-I R173C was probably a processing artefact as the NativePAGE gel of fractions T50/51 combined for MS indicated that only dimeric apoA-I R173C was present in the sample (**Figure 3.23**). The mass difference of apoA-I R173C monomer and dimer was 2 and 3 Da, corresponding to +2H and +3H atoms, respectively. Therefore, the MS masses confirmed the correct masses of apoA-I R173C monomer and dimer protein expressed.

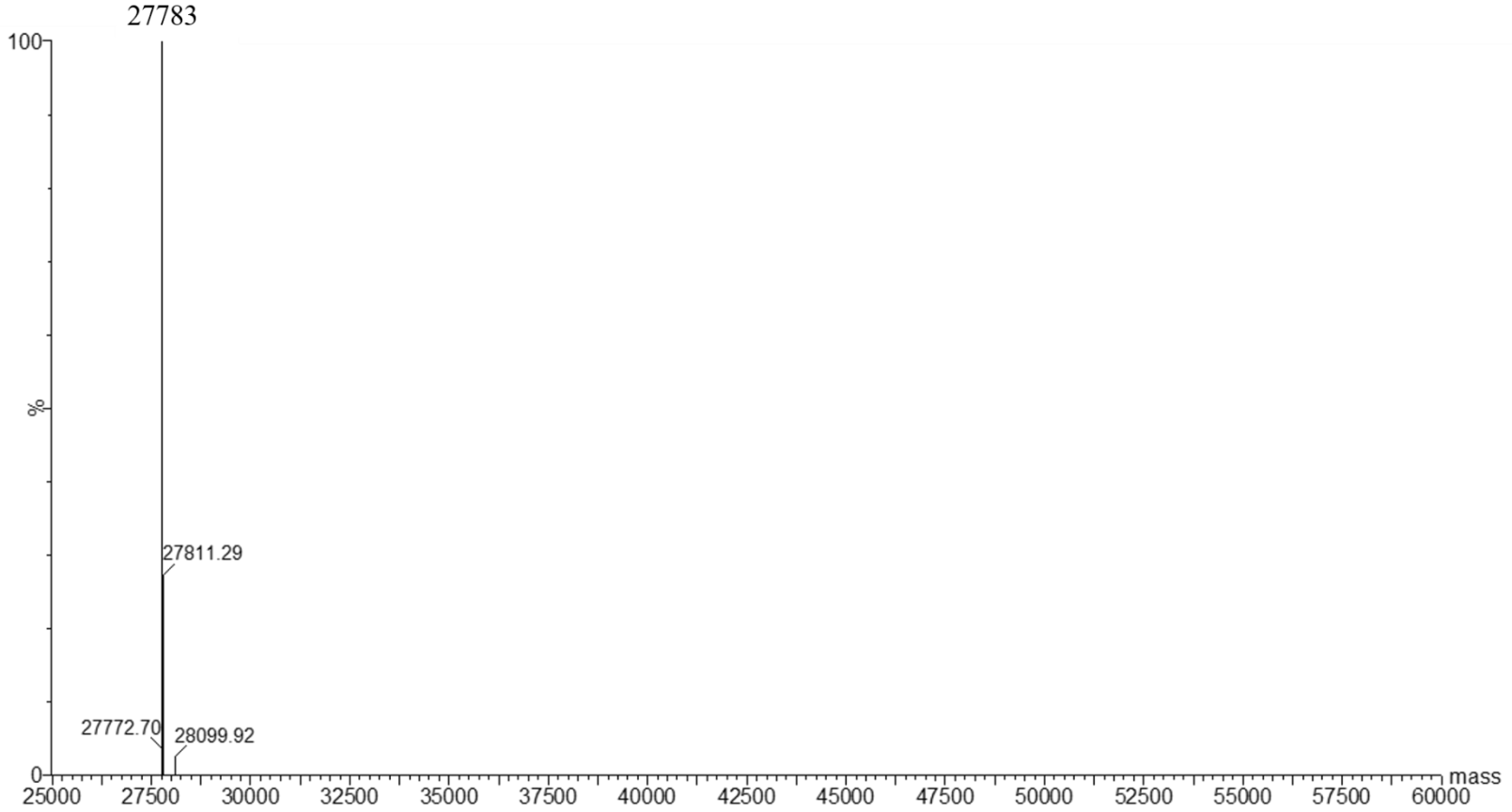

Figure 3.24. ApoA-I R173C monomer mass spectrum deconvoluted mass 27783.45 Da using C4 based reversed phase LC-MS for intact mass samples.

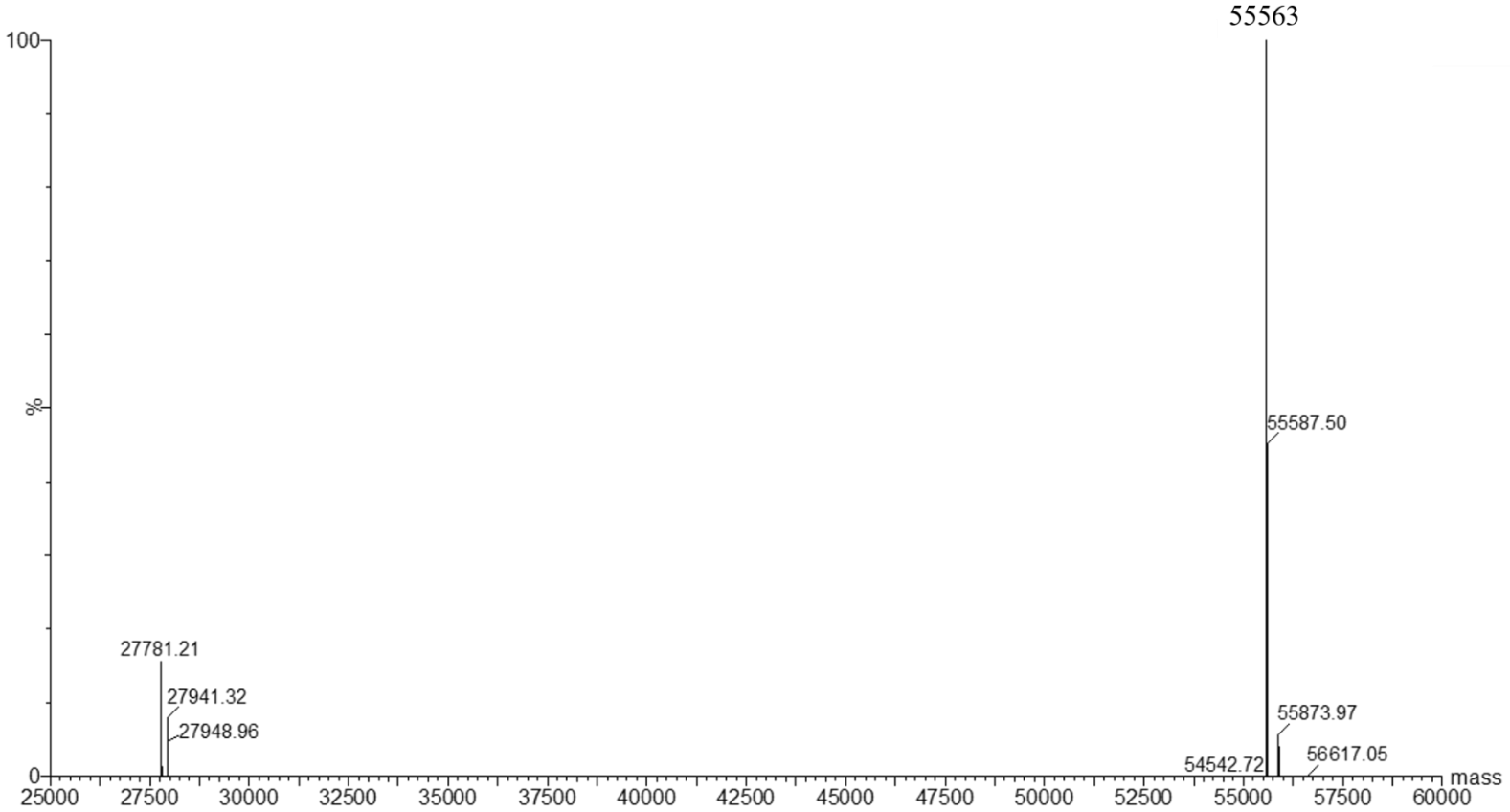

Figure 3.25. ApoA-I R173C dimer mass spectrum, deconvoluted mass of 55563.43 Da using C4 based reversed phase LC-MS for intact mass samples.

The apoA-I WT, R173C and L144R proteins were run on a NativePAGE gradient gel (**Figure 3.26**) to confirm if monomeric or dimeric protein was present in the stock protein solutions (>2.0 mg/mL). Each protein contained monomer and dimer at approximately 28 and 56 kDa, respectively.

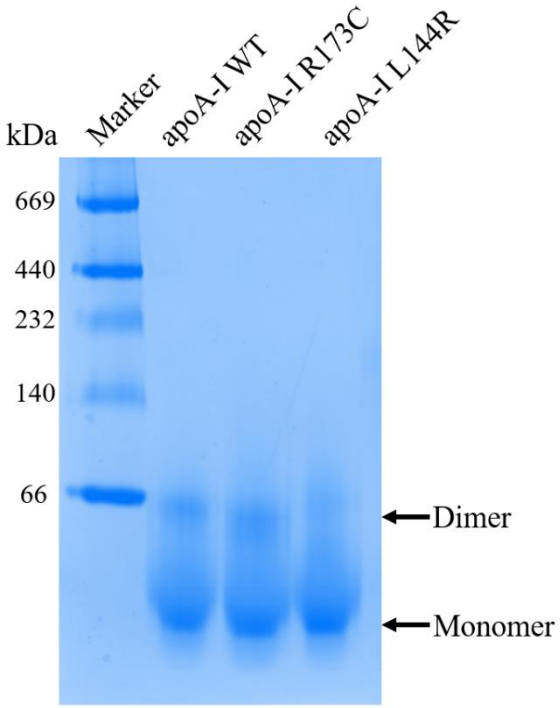

Figure 3.26. A 4 – 16 % NativePAGE gradient gel of lipid-free apoA-I WT, R173C and L144R under non-denaturing conditions at 8 ug protein per lane (0.4 mg/mL), with dimeric and monomeric protein bands indicated.

This suggests that the apoA-I WT and L144R mutant do not require a cysteine residue to form dimers, as the dimers cannot form through the formation of an intermolecular disulphide bond like apoA-I R173C. This can be expected as the apoA-I proteins have the capability to form dimers for discoidal HDL nanoparticle formation (Fiddyment et al., 2011; Giudice et al., 2017). Lipid-free apoA-I WT structural models show the formation of dimeric apoA-I due to the intermolecular interactions between monomers (Oda, 2017). ApoA-I dimers can form at > 0.1 mg/mL concentrations as lipid-free

apoA-I multimer formation is concentration dependent (Davidson et al., 1996; Giudice et al., 2017; Oda, 2017; Petrlova et al., 2016). Additionally, a comparison of the observed masses (**Table 3.2-3.3**) for each apoA-I protein shows that only the apoA-I R173C forms a stable dimer under MS conditions. Taken together, this suggests that the formation of an intermolecular covalent bond in the apoA-I WT and L144R dimers is not critical to dimer formation but that the disulphide bond in dimeric apoA-I R173C could stabilise the apoA-I R173C dimer under MS conditions.

3.3.3.3 Protein expression yield

The average unlabelled and labelled protein expression yields for apoA-I WT, R173C and L144R are given in **Table 3.4**. ApoA-I WT expressions had the highest average yield at 56 mg/L. Whereas apoA-I R173C and L144R average yields were similar to each other but lower than achieved for apoA-I WT, being 33 and 32 mg/L respectively. The dual-labelled apoA-I L144R had a high yield of 53 mg/L in comparison to apoA-I WT at 19 mg/L but the yield of dual-labelled apoA-I R173C was considerably lower at 7 mg/L post-TCEP treatment. The singular isotopically labelled [^{13}C]- and [^{15}N]-apoA-I WT protein yields were 24 and 29 mg/L, respectively. Further optimisation of the expression on minimal media was not attempted as sufficient quantities of protein were obtained for NMR analysis.

Table 3.4. ApoA-I WT, R173C and L144R average protein expression yield (mg per Litre of LB) ±SD, the number of expressions averaged = n, and the range (mg/L).

Protein	Average Yield (mg/L) ±SD	Range (mg/L)
apoA-I WT	55.6 ±25.8	23.1 – 99.0 (n = 6)
apoA-I R173C	33.4 ±8.2	24.5 – 44.4 (n = 4)
apoA-I L144R	32.3 ±13.2	21.1 – 49.0 (n = 4)
[^{13}C, ^{15}N]-apoA-I WT	19.2	(n = 1)
[^{13}C]-apoA-I WT	24.4	(n = 1)
[^{15}N]-apoA-I WT	29.0	(n = 1)
[^{13}C, ^{15}N]-apoA-I R173C	7.3 ±0.4	7.0 – 7.7 (n = 2)
[^{13}C, ^{15}N]-apoA-I L144R	52.5	(n = 1)

The protein expression range is shown as an indicator of a low yield compared to a high yield for the unlabelled protein expressions. Each expression minimum yield was at least 20 mg/L indicating a usable yield if an anomalous expression occurred. Whilst the maximum yields of apoA-I R173C, L144R and WT were 44, 49 and 99 mg/L indicating that the protein yields over these ranges were sufficient for routine use.

3.4 Discussion

3.4.1 Comparison of expression conditions of native and atheroprotective apoA-I

The conditions for expressing atheroprotective apoA-I mutants were identical to those used for apoA-I WT (E2D) expression, except that apoA-I R173C required the additional reduction step to remove the glutathione moiety from the cysteine residue to form disulphide bonded dimeric apoA-I R173C. This is the first use of TCEP as a reducing agent to form dimeric apoA-I R173C. The apoA-I R173C and L144R plasmid masses at approximately 4.5 kb were at the expected number of bases of the pNFXex

vector. Additionally, the protein cDNA gene sequences were determined to be 99 % accurate compared to apoA-I WT (E2D) indicating a single residue mutation for both R173C and L144R cDNA sequences within the pNFXex vector.

The apoA-I R173C expression presented some difficulties in determining the post-translational modification glutathione moiety and removal with an adaptation of the TCEP reduction method of a prion protein with the glutathione adduct (Sengupta and Udgaonkar, 2017). The Origami^{TM} B(DE3) cells were used containing the apoA-I R173C pNFXex vector, however the mass spectrum of apoA-I R173C +his-tag indicated the presence of multiple incorrect molecular species with masses below the expected mass, therefore the expression using Origami^{TM} B(DE3) cells was not further optimised.

To confirm the masses of the monomeric and dimeric apoA-I R173C SEC was used to separate the monomer and dimer post-glutathione cleavage (**Figure 3.23**) for mass spectrometry analysis. The minor mass differences between the expected and measured masses of the monomer and dimer confirmed the masses to be correct of the expressed recombinant protein apoA-I R173C monomer and dimer.

Both apoA-I R173C and L144R expressions were optimised with similar yields and purity to apoA-I WT for comparative structural and functional studies at 33 and 32 mg/L of culture media, respectively. Additionally, apoA-I L144R was expressed with similar purity and yield to Fiddyment *et al*. at approximately 30 mg/L of culture media (Fiddyment et al., 2011).

The minimal media expression of dual-labelled apoA-I R173C required optimisation indicated by the low yield of 7 mg/L of media. The dual-labelled apoA-I WT minimal media expression produced 19 mg/L. In comparison, the dual-labelled apoA-I L144R

yield was as high as the maximum expression yield for unlabelled apoA-I L144R at 52 mg/L and 49 mg/L, respectively. The labelled apoA-I R173C protein yield was low due to precipitation during the TCEP incubation and dialysis stages to remove the reducing agent and incubation to form dimeric apoA-I R173C. However, improvements were made to the unlabelled apoA-I R173C TCEP protocol with a maximum protein concentration of 0.5 mg/mL used to reduce the protein precipitation during the TCEP reduction and dimer formation.

The purified apoA-I proteins when run on a NativePAGE gel at a concentration of 0.4 mg/mL showed monomeric and dimeric apoA-I diluted from concentrated stock solutions > 2.0 mg/ml. This in agreement with previous studies on apoA-I in solutions at a concentration > 0.1 mg/ml has been shown to form multimers (dimeric, tetrameric or greater) as the protein concentration increased (Davidson et al., 1996; Giudice et al., 2017; Oda, 2017; Petrlova et al., 2016). Therefore, the apoA-I WT and L144R proteins formed an approximately similar ratio of monomeric to dimeric apoA-I as apoA-I R173C.

The apoA-I R173C in the presence of TCEP did not form approximately equal amount of dimer and monomer as shown in the NativePAGE gels (**Figure 3.21-3.22**) whilst samples without TCEP after 24 hours showed approximately equal amounts of monomeric and dimeric apoA-I R173C. This suggests that the formation of apoA-I R173C dimer was a result of the formation of a disulphide bond between two monomer cysteine residues rather than a concentration dependent effect of dimer/multimer formation.

Overall, a combination of the protein yields of the atheroprotective apoA-I mutants at approximately 30 mg/L, the high level of protein purity as assessed by SDS-PAGE gels

and the confirmation of accurate mass using mass spectrometry indicated that expression and purification conditions developed here were suitable for providing the proteins as required throughout the study.

The apoA-I R173C and L144R mutants yields at ~30 mg/L of culture media were 3-fold less than comparative apoA-I WT yields of up to 120 mg/L (Del Giudice and Lagerstedt, 2018; Ryan et al., 2003; Townsend, 2016). As a comparison early bacterial expressions of apoA-I WT produced low yields between 0.1 – 650 µg/L, and relatively higher yields up to 5 – 20 mg/L (Brouillette and Anantharamaiah, 1995; Panagotopulos et al., 2002; Pyle et al., 1996; Schmidt et al., 1995).

In a laboratory scale expression ~100 mg/L of culture media for apoA-I WT is a high amount of protein for routine expression needs. A direct comparison of laboratory-scale recombinant apoA-I R173C yields was not available at this time. Previous industrial-scale batch-fed *E. coli* expressions of the apoA-I R173C mutant yielded between 2 – 4.9 g/L of culture media (Calabresi et al., 1994; Caparon et al., 2010). The large-scale expression demonstrated it is feasible to produce higher yields of apoA-I R173C. Further optimisation of the apoA-I R173C and L144R expression methodology would be required to optimise the expression yields on a non-industrial scale. For example, another optimised expression protocol high-cell density culture system produced yields of unlabelled ~ 17 - 34 mg and [^{13}C,^{15}N, ^{2}H]-labelled apoA-I WT 14 – 25 mg/ 50 mL of culture media (Sivashanmugam et al., 2009).

Recent reviews have discussed progress of recombinant protein expression in *E. coli* cells such as the strain genotype, plasmid design, expression on an industrial scale, and selection of overexpressing cells to obtain optimal yields (see reviews for more detail and refs therein) (Rosano et al., 2019; Tripathi and Shrivastava, 2019). Therefore, there

are other options to consider for future optimisation of the expressions of apoA-I R173C and L144R to obtain a similar or higher yield to apoA-I WT (~100 mg/ L).

4 Production of reconstituted High-Density Lipoproteins

4.1 Introduction

A protocol for producing rHDL nanoparticles comprising phospholipids and apoA-I with and without cholesterol for structural and functional comparisons of rHDL containing WT and mutant proteins was required. The following section is a summary of the process of rHDL nanoparticle formation. Henceforth, rHDL particles containing WT apoA-I will be referred to as rHDL-WT, and likewise rHDL containing the mutant proteins will be termed rHDL-R173C and rHDL-L144R.

4.1.1 Discoidal rHDL nanoparticle formation

Discoidal rHDL nanoparticles are similar in shape to nascent plasma HDL nanoparticles as in the "double-belt" model (Segrest et al., 1999). The rHDL nanoparticles are prepared *in vitro* using the now widely-used detergent-mediated reconstitution method with physiologically relevant lipids containing unsaturated bonds such as egg-PC and saturated DPPC established by Matz and Jonas (Jonas, 1986; Matz and Jonas, 1982).

The sodium cholate detergent-mediated dialysis method is described in the methods **section 4.2.1** for rHDL nanoparticle formation (Jonas, 1986). The temperature at each stage of the sodium cholate dialysis method is close to and above the lipid gel to liquid phase transition temperature (T_c) to improve rHDL formation. The T_c of DMPC is 24°C and for POPC T_c is -2°C, and preparation temperatures of 25°C and 4°C, have been reported (Jonas, 1986; Pownall et al., 1978). The detergent is removed by extensive

dialysis in excess of 500-fold buffer (Jonas, 1986). During dialysis the concentration of the detergent molecule decreases to below the critical micellar concentration (CMC) which results in the dissociation of detergent micelles to detergent monomers for removal (Seddon et al., 2004). The CMC is the minimum concentration of a molecule, lipid or detergent, required to form a micelle (Seddon et al., 2004).

The lipid/detergent mixed micelles and amphipathic apoA-I interact to form discoidal rHDL nanodiscs. The hydrophobic interactions in the lipid-lipid and protein-lipid interface are principally formed by the hydrophobic effect and are a major factor in the assembly and stability of rHDL nanoparticles as shown in previous discoidal HDL self-assembly coarse grained molecular dynamics (CGMD) simulations (Shih et al., 2007a; Shih et al., 2007b), and in the discoidal HDL "double-belt" model (Nath et al., 2007). The hydrophobic effect acts upon the hydrophobic groups to minimise the exposure to the aqueous environment, i.e., the hydrocarbon lipid tails, referred to as the attractive force enabling aggregation/association of the nonpolar groups in an amphiphile (Luckey, 2014; Tanford, 1973). There is also a repulsive force between the polar groups of the amphiphile, i.e. the same charge on the lipid headgroup(s) causes ionic electrostatic repulsion and limits size in amphiphile micelle formation (Tanford, 1973).

Cholesterol can be incorporated into discoidal rHDL in the reconstitution process by adding cholesterol in the initial lipid drying and resuspension of the lipid film (Jonas, 1986). In discoidal rHDL the majority of cholesterol is not in the boundary layer of lipids interacting with apoA-I (Jonas, 1986), but is located in the central region of the bilayer leaflet similar to the model of nascent HDL containing POPC:cholesterol:apoA-I molar ratios of 160:24:2 and 200:20:2 produced by Pourmousa *et al.* (Pourmousa et al., 2018). The cholesterol molecules in the model are oriented with the hydroxyl moiety

facing the aqueous solution with the lipid headgroups, and the cholesterol molecules are intercalated between lipids in the nanodisc lipid bilayer (Pourmousa et al., 2018).

4.1.2 The structure of lipids, cholesterol, and sodium cholate

Phospholipids are amphipathic containing the hydrophobic hydrocarbon fatty acid tails connected to a hydrophilic glycerol-phospho-choline or phosphatidylcholine head group (**Figure 4.1**). The lipid used to prepare rHDL nanoparticles was 1-palmitoyl-2-oleoyl-glycero-3-phosphocholine (16:0-18:1 PC or POPC) as this lipid is physiologically relevant (**Figure 4.1**) (Jonas, 1986; Matz and Jonas, 1982). Additionally, the majority of phospholipids in native HDL particles contain PC at approximately 33-45 wt% of total HDL lipid, including POPC (Kontush et al., 2013; Wiesner et al., 2009). The 16:0-18:1 ratio refers to the fatty acid acyl chain length: the number of unsaturated bonds within the tail at positions *sn*-1 and *sn*-2, and *sn* refers to the stereospecific numbering (**Figure 4.1**).

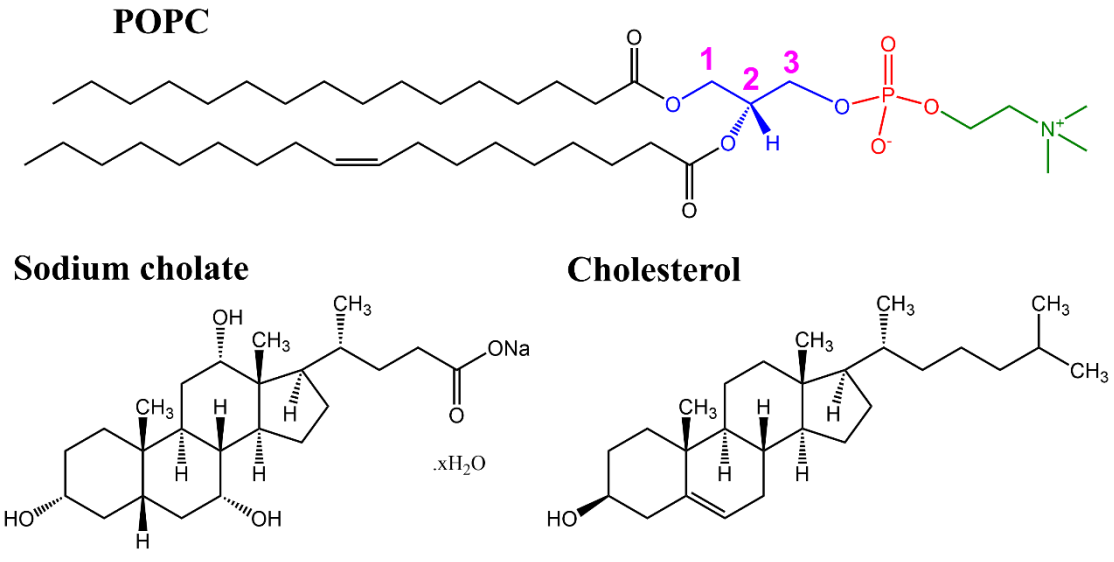

Figure 4.1. The structure of POPC (16:0-18:1 PC) with *sn* numbers 1-3 (magenta), the hydrophobic fatty acid hydrocarbon tails (black), and the hydrophilic glycerol-phospho-choline (blue-red-green). The structures of sodium cholate (bile salt), and cholesterol.

Cholesterol is similar in structure to sodium cholate with a rigid steroid ring and a single hydroxyl group (**Figure 4.1**). Sodium cholate is a bile salt commonly used to form rHDL and consists of rigid steroid rings with 3 hydroxyl groups, attached to an acyl carboxyl chain (**Figure 4.1**). In comparison to sodium cholate cholesterol is considerably less polar and therefore more hydrophobic. Sodium cholate is also ionic, readily soluble in aqueous buffers, and a mild non-denaturing detergent (Seddon et al., 2004).

4.1.3 Size fractionation of HDL

Reconstituted HDL nanoparticles are heterogeneous in particle size, and restricted size ranges can be separated using size exclusion chromatography (SEC) or the particle density using density gradient ultracentrifugation (UTC) (Jonas, 1986). Native HDL particles have a density between 1.063 – 1.21 g/mL and can be separated based upon the particle density by flotation UTC (Fl-UTC) to separate from lipid-free apoA-I (Jonas et al., 1984; Schumaker and Puppione, 1986), or gradient density UTC (linear or discontinuous) to separate the rHDL particles from liposomes and free apoA-I (Cavigiolio et al., 2008; Jonas, 1986; Kelley and Kruski, 1986).

Non-denaturing gradient gel electrophoresis (NDGGE) with NativePAGE gels are used to estimate the rHDL particle size (Cavigiolio et al., 2008; Dalla-Riva et al., 2015). Negative stain transmission electron microscopy (TEM) (Cavigiolio et al., 2008; Zhang et al., 2011) and dynamic light scattering (DLS) (Del Giudice et al., 2017; Schwendeman et al., 2015; Wu et al., 2009; Wu et al., 2007) have also been used to measure particle size. In this work the rHDL particle separation techniques were compared, and the particle size was measured using NDGGE, TEM, and DLS (**Figure 4.2**).

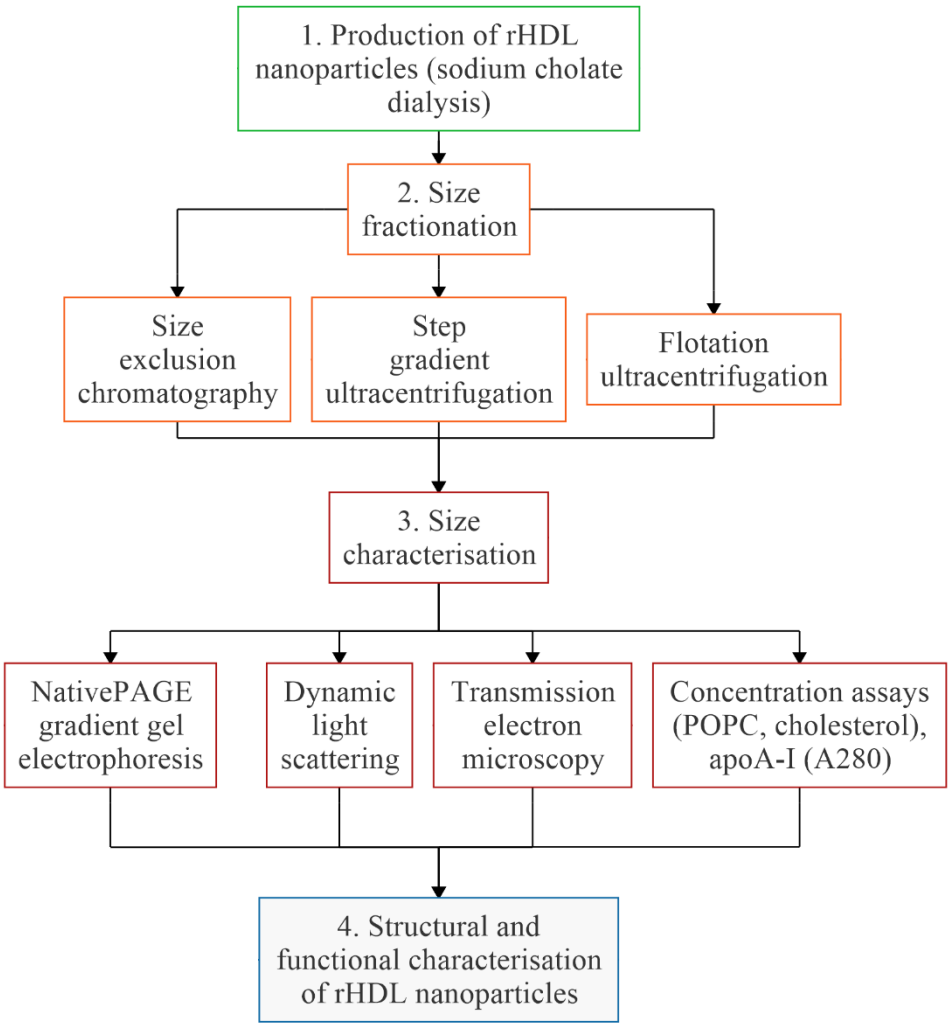

Figure 4.2. The stages of rHDL nanoparticle preparation for further structural and functional characterisation. **1**. Sodium cholate dialysis. **2**. rHDL nanoparticle size fractionation with SEC or density-based ultracentrifugation (step gradient or flotation). **3**. Size characterisation by NDGGE, DLS, or TEM. The final rHDL nanoparticle component compositions were determined with concentration assays.

4.1.4 Plasma HDL nanoparticle molar ratios

In this section the size distributions of plasma HDL nanoparticles of previous *in vitro* and *in vivo* studies are described for each apoA-I protein. A comparison of the different plasma HDL sizes informed the decision to produce rHDL nanoparticles with a predominant diameter between 8-11 nm in this work.

The plasma HDL WT nanoparticle subclasses (**see Chapter 1**, **Table 1.1**), as characterised by NDGGE are HDL_{3c} (7.2-7.8 nm), HDL_{3b} (7.8-8.2 nm), HDL_{3a} (8.2-8.8 nm), HDL_{2a} (8.8-9.7), and HDL_{2b} (9.7-12.9 nm) (Nichols et al., 1986). Native HDL WT nanoparticles formed *in vitro* by incubation of apoA-I with various cell types and in human or murine plasma have diameters between ~7.3-12.2 nm (**Table 4.1, see references therein**), with major particles in each NDGGE subclass.

Additionally, the all atom MD (AAMD) model of Pourmousa *et al*. (2018) had particle molar ratios and diameters of 160:24:2 (10 nm) and 200:20:2 (11 nm) similar to the nascent HDL particles characterised by Duong *et al*. at ~196:24:2 (9 nm) from J774 macrophages and ~190:16:2 (11 nm) from HSFs (Duong et al., 2006; Pourmousa et al., 2018).

Table 4.1. Nascent HDL WT, R173C and L144R particle hydrodynamic diameter with major particles in bold (SEC, NDGGE and 2D-NDGGE), and diameter by TEM. The cell line *in vitro* models are J774 (murine) or THP-1 (human) macrophages, human skin fibroblasts (HSF) or Chinese hamster ovary (CHO) cells. The subject plasma types are human or murine with the protein(s) expressed *in vivo* indicated.

Diameter (nm)				
SEC	**TEM**	**NDGGE**	**Model**	**Reference**
apoA-I WT				
9 ±0.5 12 ±0.4	9 ±2 12 ±2	**8.5**, **12,** 14 (2D)	J774	(Duong et al., 2006)
8 ±0.4 11 ±0.6		**7.5**, **11**, 13 (2D)	HSF	
		7.4, 9-9.2, 10.8-11	THP-1	(Bielicki et al., 1999)
	13.6 ±2.9	**7.3 ±0.05** **9.3 ±0.08** **11.1 ±0.09** 14.2 ±0.16 and 16.3 ±0.12	CHO	(Forte et al., 1995)
	9.4 ±1.7	7.9 ± 0.02 **8.4 ±0.07** **10.3 ±0.3**	human	(Franceschini et al., 1987; Franceschini et al., 1980)
		7.8, 8.5-13 (2D antibody)	human	(Favari et al., 2007)
		8.8-12.9 7.9, **8.7, 9.4, 10.0**	apoA-I/A-II murine	(Bielicki et al., 1997)
apoA-I R173C				
8.8-11.7 10.3 ±0.4	12 ±2.5	**8.0 ±0.03**, **8.6 ±0.1** 9.9 ±0.2	human	(Franceschini et al., 1987; Franceschini et al., 1982; Franceschini et al., 1980)
		7.8, 8.5-13 (2D)	human	(Favari et al., 2007)
		10, 12	murine	(Alexander et al., 2009)
			murine	
		7.6, 8.3 (55%) 9.5 (45 %)	R173C/A-I WT/A-II	(Bielicki et al., 1997)
		7.6, 8.5, 9.5	R173C/A-II	
apoA-I L144R				
		5-6 and 7-7.5(2D) **7.8-8.2, 8.2-8.8** 8.8-9.7	murine	(Haase et al., 2011)

In comparison, the atheroprotective mutants have a shifted plasma HDL distribution compared to plasma HDL WT particles, with reduced HDL_2 (8.8-12.9 nm) particles in human carriers for apoA-I R173C (Franceschini et al., 1987; Franceschini et al., 1982) and a reduced overall size in human apoA-I L144R carrier plasma (Recalde et al., 2001) and in a mouse model for apoA-I L144R (Haase et al., 2011). Therefore, rHDL infusion therapy has focussed on smaller rHDL nanoparticles which mediate ABCA1 cholesterol efflux with lower lipid:apoA-I molar ratios such as CSL112 soy-PC:apoA-I WT at 110:2 (M/M) with a 7.5-8.0 nm in diameter (Diditchenko et al., 2013) and MDCO-216 POPC:apoA-I R173C at 78:2 (M/M) with an 8 nm particle diameter (Kempen et al., 2013).

However, there is evidence of larger rHDL nanoparticles between 8.5-13 nm in diameter in the HDL_2 subclasses as detected in human apoA-I R173C plasma (Favari et al., 2007), and in murine mouse models (Alexander et al., 2009; Bielicki et al., 1997). The major 7.6 nm diameter HDL nanoparticle in an apoA-I R173C/A-II murine model suggested an increase in apoA-I R173C dimer formation without apoA-I WT decreased the particle size population (Bielicki et al., 1997).

Additionally, the murine plasma HDL L144R particle distribution contained minor populations of larger particles between 8.8-9.7 nm in diameter (Haase et al., 2011). An established human plasma HDL distribution for apoA-I L144R carriers has yet to be established to the extent of apoA-I WT or R173C carriers. Moreover, larger rHDL nanoparticles were utilised for diversifying rHDL infusion therapy, for example, as a statin carrier (25-30 nm) (Duivenvoorden et al., 2014) and as an MRI plaque imaging agent carrier (~10 nm) (Chen et al., 2013). Therefore, this chapter has focused upon

producing discoidal rHDL atheroprotective mutant particles with a similar diameter to the nascent HDL WT nanoparticles between approximately 8 – 11 nm.

4.1.5 Discoidal rHDL nanoparticle size and molar ratios

Discoidal rHDL nanoparticles prepared with POPC:±cholesterol:apoA-I form different sizes of rHDL nanoparticles based upon the molar ratio of the components used (Jonas, 1986). The rHDL nanoparticle sizes from previous studies are summarised in the discussion for a direct comparison to rHDL nanoparticles produced in this work (**see section 4.4.2**, **Table 4.9**, **and references therein**). The range of rHDL nanoparticles was between ~7.3-17.0 nm dependent upon the start molar ratio (**Table 4.9**).

This study focused on the POPC:apoA-I WT 100:1 molar ratio to produce rHDL apoA-I WT (rHDL-WT) nanoparticles as the predominant band in the rHDL nanoparticle preparations was between 9.7-10.2 nm diameter and appeared to form regardless of the molar ratio used (Chen et al., 2009; Gu et al., 2010; Sparks et al., 1992b). Hereafter, the discoidal rHDL nanoparticle molar ratios will be referred to as POPC:±cholesterol: 2 apoA-I molecules per nanoparticle, e.g. 200:2. This is based on current knowledge of chemical cross-linking of apoA-I in discoidal rHDL nanoparticles within the diameter range of ~8-11 nm (Cavigiolio et al., 2008; Han et al., 2005; Silva et al., 2005b; Silva et al., 2008).

rHDL nanoparticles containing cholesterol can form between ~7.8-17.0 nm in diameter at various molar ratios (**Table 4.9**). Cavigiolio *et al*. produced particles with average diameters within the five subclasses of plasma HDL nanoparticles (Cavigiolio et al., 2008). The intermediate particle size between 9.2-10.0 nm (182:8:2 mol/mol) is similar in size and molar ratio to the 200:20:2 molar ratio, which as discussed earlier resembles nascent plasma HDL WT nanoparticles (Duong et al., 2006; Pourmousa et al., 2018).

Wu *et al.* produced rHDL nanoparticles prepared at the 200:20:2 molar ratio with an average diameter of ~9.6 nm by NDGGE and produced the discoidal HDL solar flare (Wu et al., 2007) and DSH HDL models (Wu et al., 2009).

rHDL-WT nanoparticles previously prepared at the 200:20:2 molar ratio were used in functional studies with binding via apoA-I WT to the murine SR-B1 cell receptor *in vitro* (Xu et al., 1997), and in mediating ABCA1- (Chroni et al., 2003) and ABCG1- (Daniil et al., 2013) mediated cholesterol efflux *in vitro* from murine J774 macrophages.

Reconstituted HDL R173C nanoparticles prepared at the 190:10:2 molar ratio were between 9.8-10.0 nm in diameter with a final molar ratio of 100 ±10: 5: 1 and infusion resulted in lesion regression in an atherosclerotic mouse model (Cho and Kim, 2009). Additionally, rHDL-WT nanoparticles produced at the 190:10:2 molar ratio were used as LCAT enzyme reaction substrates which demonstrated the particles can be used to determine cholesteryl ester formation (Han et al., 2005).

The previous literature of functional studies with rHDL nanoparticles at these molar ratios indicated that further study combined with structural characterisation of the rHDL bearing the atheroprotective mutants could provide mechanistic information in how these particles transport cholesterol or interact with enzymes in reverse cholesterol transport. To determine if the atheroprotective mutant containing rHDL nanoparticles are atheroprotective due to the presence of the mutant protein(s) only rHDL nanoparticles of comparable size and composition were prepared to the rHDL-WT nanoparticles.

To show the current scale of rHDL nanoparticle yields, the preparation of rHDL-C WT 160:8:2 nanoparticles is briefly described. The rHDL-C nanoparticles of various sizes were prepared using the sodium cholate dialysis method followed by ultracentrifugation

and size exclusion chromatography purification (Cavigiolio et al., 2008). The rHDL-C WT 160:8:2 nanoparticles had a diameter of ~9.6 nm and the highest yield at ~32.8 ±11.3 % relative to the starting apoA-I concentration. In comparison the rHDL-C ~8.4 and 12.2 nm diameter particle yields were ~8.2 – 9.2 %. Whereas the 7.8 and 17.0 nm diameter particle yields were ~19.1 and 12.5 %, respectively (Cavigiolio et al., 2008). The less than 50 % and varied yields suggested that there are improvements required to optimise the yield of rHDL nanoparticle production.

This work is the first preparation of rHDL-L144R nanoparticles for routine production and further characterisation. As well as a direct comparison between the rHDL nanoparticles containing apoA-I WT, R173C or L144R produced using the sodium cholate dialysis method. Three different methods were tested for the purification of the rHDL nanoparticles size exclusion chromatography, flotation, and step-gradient density ultracentrifugation.

4.1.6 Aims

It was necessary to develop a reliable method to produce rHDL nanoparticles bearing apoA-I WT of defined composition and size. After the method was developed rHDL particles containing the atheroprotective mutants apoA-I R173C and L144R were produced for direct comparison to the rHDL-WT particles. The rHDL nanoparticles of known composition and size were produced for further characterisation in later chapters.

4.2 Materials and methods

4.2.1 Production of rHDL via sodium cholate dialysis

Initially, lipids are dissolved in chloroform and the solvent is evaporated with a stream of nitrogen to form a thin lipid film. Mixed micelles of lipid and sodium cholate are formed when the film is resuspended in buffer containing sodium cholate up to a lipid: sodium cholate molar ratio of 1:2. After the formation of mixed micelles of lipid and sodium cholate as indicated by the change from an opaque to translucent solution (Walter et al., 1991), apoA-I is added to the solution and incubated for at least 12 hours (Jonas, 1986).

Sodium cholate detergent mediated dialysis was used to form rHDL with the more physiologically relevant phospholipid POPC adapted from the method described and implemented by Jonas *et al*. (Jonas, 1986; Matz and Jonas, 1982). To form a concentrated POPC/sodium cholate stock solution to form rHDL with apoA-I, typically > 30 mg of POPC was weighed into a round bottom flask and dissolved in chloroform in a fume hood. A thin lipid film was formed in the flask by evaporation of the chloroform under a stream of N_2 whilst rotating the flask. The lipid film was placed under high vacuum for a minimum of 4 hours or overnight before resuspending in aqueous buffer. The sample buffer was 10 mM tris HCl, 1 mM EDTA, 1 mM NaN_3, pH 7.4. Henceforth this is referred to as rHDL buffer. A minimum volume of 0.5 mL rHDL buffer, pH 7.4, was used to resuspend the lipids.

Sodium cholate (bovine) was dissolved in rHDL buffer pH 7.4, to a final concentration of 232.2 mM (100 mg/mL) to form a concentrated stock solution. Initially, the sodium cholate was added to the lipid film at an equimolar concentration to a final volume of 0.5 mL. The POPC/sodium cholate 1:1 (M/M) was incubated above the T_c of POPC (-

2°C) at 4°C for 1-2 hours until the solution became clear indicating the formation of POPC/sodium cholate micelles. If the solution remained turbid, sodium cholate was added up to a 1:2 lipid: sodium cholate molar ratio with the sample volume increased to 1 mL.

Samples were prepared to the final POPC/ apoA-I molar ratio of 200:2 (M/M) with apoA-I WT, apoA-I R173C and apoA-I L144R, expressed and purified as described in **Chapter 3**, **section 3.2.6**. Some samples were prepared with uniformly [^{13}C, ^{15}N]-labelled apoA-I for NMR analysis. The initial lipid concentration was typically 3 or 5 mM dependent upon the protein stock concentration used as this limited the maximum lipid concentration. After protein expression the protein concentration was usually between 1 – 2 mg/mL, which is equivalent to 36 – 72 µM for WT apoA-I, apoA-I R173C and apoA-I L144R. Therefore, to minimise the protein volume added a concentrated protein solution was prepared as described below, usually ≥ 6 mg/mL equivalent to 0.22 mM.

Initially lyophilisation was used to concentrate the apoA-I protein solutions. The proteins were dialysed at 4°C using the 12-14 kDa molecular weight cut-off (MWCO) membrane dialysis tubing into 50 mM ammonium bicarbonate, pH 8.0, with at least 1 buffer change over 2 days. The protein was aliquoted and flash frozen using liquid N_2 over a large surface area such as a round bottom flask and lyophilised for 24 hours in a freeze-dryer. The cycle was repeated if the solvent was not completely sublimated and lyophilised protein. The protein was then resuspended in a smaller volume of sample buffer to ≥ 6 mg/mL.

However, there were issues with precipitation of the protein during dialysis and incomplete resuspension after lyophilisation. Therefore, to concentrate the protein or

buffer exchange, Corning® Spin-X UF 6 PES membrane spin concentrators were used as described previously to prepare a concentrated apoA-I solution at ≥ 6 mg/mL for rHDL nanoparticle formation. An example of a typical rHDL sample POPC, sodium cholate and apoA-I stock concentrations (conc.) and volumes used is shown in **Table 4.2**.

Table 4.2. Typical rHDL sample preparation conditions. The preparation of the POPC/sodium cholate mixed micelle stock solution concentrations, and apoA-I addition to the mixed micelles.

Stock Conc. (mM)	Sample component	Volume (µL)	Final Conc. (mM)	Molar ratio
-	POPC	Film	78.9	1:1
232.2	Sodium cholate	170.0	78.9	
	rHDL buffer, pH 7.4	330.0		
	Total volume (µL)	500		
Incubation period for lipid/detergent micelle formation				
78.9	POPC/sodium cholate	63.4	5	200:2
0.22	apoA-I WT	227.3	0.05	
	rHDL buffer, pH 7.4	709.4		
	Total volume (µL)	1000		

The POPC/apoA-I 200:2 (M/M) sample was incubated for at least 12 hours (overnight) at 4°C with mixing. To remove the sodium cholate the rHDL sample was extensively dialysed against rHDL buffer pH 7.4 (500-fold excess), using 12 – 14 kDa MWCO dialysis tubing, with at least 5 buffer changes over 3 days. The samples were then run on a 4 – 16 % NativePAGE gel to determine if rHDL formed at this molar ratio of

lipid/apoA-I and were further purified using SEC or density gradient ultracentrifugation.

4.2.2 Production of rHDL containing cholesterol

The detergent mediated sodium cholate dialysis method used to produce discoidal rHDL containing cholesterol was the same as described previously, except for the initial steps up to the solvent evaporation with N_2 to form a lipid/cholesterol film. POPC and cholesterol were weighed and resuspended in chloroform separately to form stock solutions. Aliquots of POPC and cholesterol were transferred to a round bottom flask to a final molar ratio of POPC: cholesterol 10:1 (M/M). ApoA-I was added to the final POPC/ apoA-I molar ratios of 160:2, 200:2, 240:2, and 300:2. Samples were also prepared at a start POPC:cholesterol:apoA-I molar ratio of 190:10:2 for apoA-I WT, L144R and R173C. After sodium cholate removal by dialysis, the samples were analysed by NDGGE. The cholesterol quantitation kit (MAK043, Sigma-Aldrich®) was used to measure the cholesterol concentration in duplicate.

4.2.3 Purification of rHDL nanoparticles

4.2.3.1 Sodium bromide density ultracentrifugation

Two types of NaBr density UTC were used to separate the rHDL nanoparticles from liposomes and lipid-free apoA-I to restrict the size distribution of the nanoparticles. The discontinuous step gradient sodium bromide density ultracentrifugation (SG-UTC) method was previously used in the separation of plasma lipoproteins (Chapman et al., 1981; Kelley and Kruski, 1986) and rHDL nanoparticles to separate the rHDL from free apoA-I, lipids, and heterogenous rHDL nanoparticles (Jonas, 1986). Sequential flotation UTC has been used as method to separate plasma HDL (Schumaker and

Puppione, 1986) and single-step flotation UTC was used to separate rHDL nanoparticles from lipid-free apoA-I (Cavigiolio et al., 2008; Jonas et al., 1984).

The approximate NaBr density in g/mL was calculated by interpolation of the salt table data (**Appendix 2**) as suggested by Schumaker and Puppione (Schumaker and Puppione, 1986). The interpolated values were used to determine the corresponding mass in grams for each density layer of NaBr used (**Appendix 2**). The buffer used throughout UTC was rHDL buffer, pH 7.4.

In SG-UTC, in a 13.2 mL Ultraclear tube (Beckman Coulter), the NaBr density (g/mL) solutions were under-layered, a total volume of 2.5 mL per layer, starting with the 1.04 g/mL solution, in increasing density order, with the following layers 1.09, 1.15, and 1.21 g/mL (**Figure 4.3**). The sample density was increased to > 1.21 g/mL by mixing 1.5 mL of 38 % (w/v) NaBr solution with 0.5 mL of the rHDL sample post sodium cholate removal by dialysis. If a control balance tube was used the final 1.5 mL layer was 1.30 g/mL density NaBr instead of sample. The tube was gently filled up to approximately 2-3 mm of the tube opening before UTC with the density layers of NaBr solution.

After the sample was under-layered below the 1.21 g/mL density layer, the sample was centrifuged at 41 krpm for 24 hrs at 4°C in the SW41 Ti rotor (Beckman Coulter) at the slowest acceleration rate and no brake setting for deceleration. Immediately after the run ended 0.5 mL samples were carefully taken, to avoid disturbing the layers, from the top of the tube. The fractions were dialysed to remove the NaBr and analysed by NDGGE. The fractions containing the rHDL were pooled and concentrated using an Amicon Ultra-4 device with a 10 kDa MWCO (Merck). The spin concentrator was pre-

rinsed with dH_2O before the sample was loaded (up to 4 mL) and centrifuged at 4000 x g for 30 minutes.

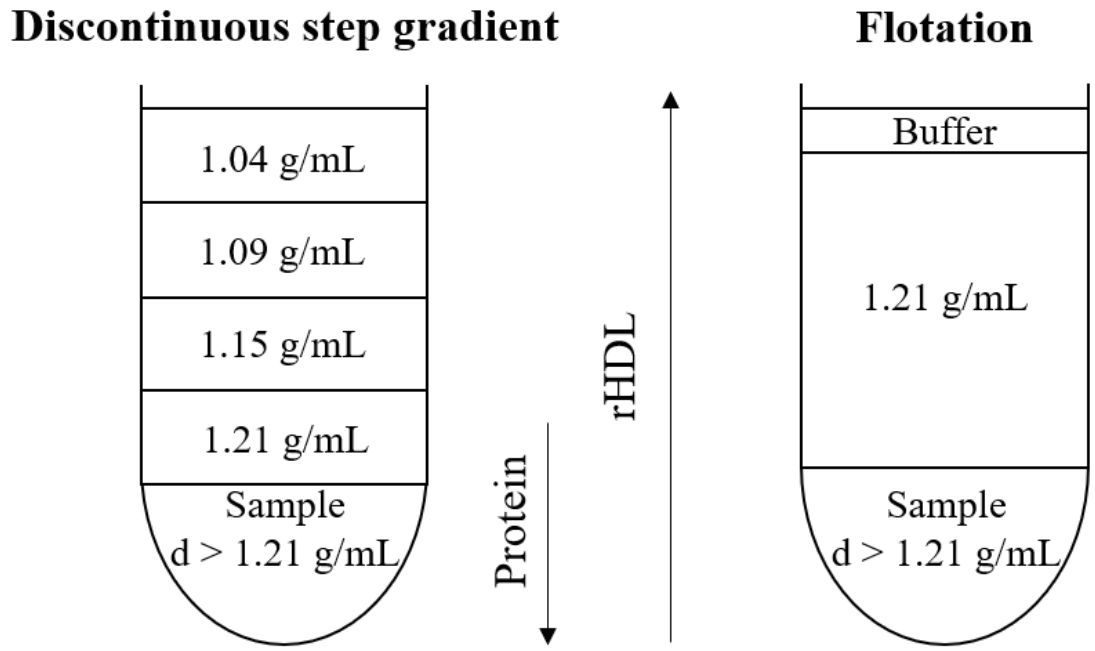

Figure 4.3. A diagram of the density layers in discontinuous SG-UTC NaBr (left) and Fl-UTC (right). The NaBr density is indicated in each layer in g/mL, and the arrows indicate the direction of separation of the rHDL nanoparticles and protein during UTC.

Flotation UTC is a single NaBr density layer, in which the sample was prepared the same as in step gradient UTC, and the solutions were under-layered as before. In a 10.4 mL polycarbonate centrifuge tube with a cap (Beckman Coulter), 0.5 mL rHDL buffer was layered, then 7.9 mL of 1.21 g/mL density NaBr solution, and finally the sample density > 1.21 g/mL (0.5 mL sample + 1.5 mL 38 % (w/v) NaBr), with the layers shown in **Figure 4.3**. The prepared rHDL sample Fl-UTC tubes were centrifuged at 65 krpm for 22 hrs at 4°C in a 70.1 Ti rotor (Beckman Coulter). A total volume of 2.5 mL was collected from the top of the tube in 0.5 mL fractions, and dialysed at 4°C against rHDL buffer, pH 7.4, with two buffer changes over 2 days to remove the NaBr. As before the

fractions were analysed by NDGGE before the fractions were pooled and concentrated for analyses and characterisation.

Further purification of rHDL from free lipids and free apoA-I, and size-fractionation of rHDL were undertaken using size exclusion chromatography. In SEC the HiPrep 16/60 Sephacryl S-300 HR column (S-300 SEC) was used connected to the ÄKTA Start chromatography system and UNICORN™ Start 1.0 software (GE Healthcare). This size exclusion column was compatible with the chromatography system and had been used to purify rHDL previously (Wu et al., 2009).

4.2.3.2 Size exclusion chromatography of rHDL nanoparticles

SEC was explored as an alternative method for size fractionation. The S-300 SEC manual showed a separation of a 0.5 mL sample containing the protein standards, IgG 160 000 Da, BSA 67 000 Da, β-lactoglobulin 35 000 Da, cytochrome C 12 400 Da and cytidine 240 Da. The peaks of interest in relation to apoA-I are β-lactoglobulin eluting at ~85 mL, and cytochrome C at ~95 mL. Therefore, lipid-free apoA-I with a 28 kDa MW would be expected to elute between 85 – 95 mL running buffer volume if present in the sample. The S-300 SEC was equilibrated with filtered and degassed dH_2O, before equilibrating the column in 10 mM tris base, 1 mM EDTA, 1 mM benzamidine, 0.15 M NaCl, pH 7.0.

The rHDL was prepared using the detergent-mediated dialysis method as described earlier and the initial rHDL sample concentration was POPC/apoA-I WT sample 200:2, 13.3/0.13 mM (M/M) (+sodium cholate), 1 mL total volume. After dialysis to remove sodium cholate, the sample volume was approximately 2 mL and a 20 µL sample was taken for NDGGE. The POPC/WT apoA-I 200:2 (M/M) rHDL post-sodium cholate removal sample was centrifuged for 10 minutes at 13.4 krpm to remove any unreacted

or precipitated POPC. The sample was loaded onto the column at a flow rate of 1.6 mL/min and a total volume of 1.6 mL, and 1 mL fractions were collected over 1 CV of running buffer. The fractions were stored at 4°C until further analysis for protein concentration and NDGGE.

4.2.4 Particle size analysis

4.2.4.1 Native PAGE gradient gel electrophoresis

The rHDL samples were run under the conditions described in **Chapter 3**, **section 3.2.4.3**. FIJI software (Schindelin et al., 2012) was used to determine the relative mobility (R_f) values of the standard molecular weight marker and sample bands. The R_f is the migration distance of the unknown band divided by the migration distance of the dye front. The log(diameter) vs the R_f values of the standards were plotted and values were interpolated to produce a standard curve and fitted with an exponential fitting function for the estimated diameter using OriginPro 2018 following the method of Cavigiolio *et al*. (Cavigiolio et al., 2008).

4.2.4.2 Dynamic light scattering

The rHDL nanoparticle samples were measured post-sodium cholate removal with DLS to determine the particle diameter with a Zetasizer Nano ZSP (Malvern) at B23 Diamond Light Source, Oxford, UK. Prior to measurement the samples were centrifuged at 2000 x g for 10 minutes to remove precipitated lipids or MLVs. The 50 µL rHDL samples were scanned in triplicate at 25°C and a 173° scattering angle in a ZEN0040 micro cuvette cell. The protein concentration was 36 µM (1 mg/mL) in rHDL buffer, pH 7.0. The intensity-weighted population distribution was used to determine the mean particle size, and the volume-weighted population distribution was used to represent the major particles present in the sample. This is explained further in the results **section 4.3.1.1**.

Note – The DLS measurements of the rHDL-R173C samples were performed before the glutathione adduct of apoA-I R173C was identified in **Chapter 3**. This could explain why the rHDL-R173C 200:2 (M/M) DLS measurement did not show particles, or this could be due to a low particle concentration.

4.2.4.3 Transmission electron microscopy

Transmission electron microscopy (TEM) has been used to determine the diameter of rHDL nanoparticles (Zhang et al., 2011). Here, TEM using two different staining methods was employed to visualise the rHDL nanoparticles.

Initially, phosphotungstic acid (PTA) was used to negatively stain and image rHDL nanoparticles. A 10 µL aliquot of post sodium cholate removal rHDL POPC/WT apoA-I 200:2 (M/M) was pipetted onto a carbon coated copper grid and the excess was blotted after 3 minutes. To stain the rHDL 5 µL of 2 % (w/v) PTA pH 7.0 was pipetted onto the grid and incubated for 2 minutes, blotted, and dried before imaging. The sample was kindly imaged by Dr. N. Fullwood (Biomedical and Life Sciences, Lancaster University, UK) using a Jeol JEM-1010 transmission electron microscope and further developed in the dark room by Dr. D. Townsend (Chemistry, Lancaster University, UK).

To further optimise the protocol and promote the formation of individual rHDL nanoparticles as opposed to rouleaux, a method was adapted from the optimised negative staining method of rHDL developed by Zhang *et al.* (Zhang et al., 2011). Before the sample was pipetted onto the TEM grid, 3 drops at 35 µL each of dH_2O were pipetted next to 3 drops of 2 % (w/v) uranyl acetate (UA) on parafilm in a line. The sample, 3 µL, was pipetted onto a glow-discharged carbon coated copper grid (Agar scientific) and after 2 minutes clean filter paper was used to blot the excess sample.

The grid was quickly washed by inverting and blotting in sequence along the 3 drops of dH_2O to remove buffer salts. The rHDL particles on the TEM grid were negatively stained by two quick stain and blot steps on the UA drops followed by a 2-minute incubation on the final UA drop. The excess stain was blotted, and the sample grid was left to dry under a heat lamp. The samples were imaged, and the materials were provided at the Astbury Centre for Structural Molecular Biology at the University of Leeds, UK. The microscope used was the FEI Tecnai T12 transmission electron microscope with a 120 keV Lab6 electron source, and a Gatan US4000/SP 4 k x 4 k CCD camera. The microscope was funded by the Wellcome Trust (090932/Z/09/Z). The images were processed using FIJI software (Schindelin et al., 2012).

Initially, the rHDL sample protein concentration was varied of POPC:apoA-I WT 200:2 (M/M) rHDL to see if the stacking/formation of rouleau was affected by sample concentration, of a concentration range between 9 – 36 µM (0.25 – 1.0 mg/mL). TEM samples of POPC:apoA-I R173C and POPC:apoA-I L144R were imaged at 9 and 36 µM, respectively. The rHDL nanoparticles with the start molar ratio of POPC:cholesterol:apoA-I of 190:10:2 (M/M) containing apoA-I WT or R173C were imaged with TEM. FIJI software was used to measure 150 nanoparticles, comprised of 50 random particles measured three times, for a particle size distribution in the sample when the particles were definable.

4.2.5 Sample concentration determination

The molar ratios of protein, lipid and where appropriate, cholesterol were determined at different stages of the procedure. To determine the protein concentration of the rHDL samples the NanoDrop^{TM} 2000c (ThermoFisher Scientific) (Desjardins et al., 2009) was used with minimal contribution of the lipids to light scattering. If light scattering

occurred, as shown by a noisy UV absorbance signal at 260/280 nm, the sample was centrifuged to remove unreacted or precipitated lipids and diluted to decrease the effect of the light scattering.

To measure the lipid concentration of the rHDL samples a phospholipid quantification assay kit was used (CS0001, Sigma-Aldrich) following the protocol provided in a colorimetric 96-well plate assay. The assay uses the enzyme phospholipase D which releases choline from the lipid head group which is oxidised by the enzyme choline oxidase. The oxidation reaction produces hydrogen peroxide which reacts with the substrates in the development mix and probe for detection at 570 nm. The phosphocholine standards and samples were assayed in duplicate. The rHDL samples were run in various dilutions to produce an absorbance value within the standard curve.

The cholesterol quantitation kit (MAK043, Sigma-Aldrich®) was used to measure the rHDL sample cholesterol concentration in duplicate following the protocol provided in a colorimetric 96-well plate assay. The assay measured the total cholesterol in a sample through a coupled enzyme assay similar to the lipid assay kit, the reaction product reacts with the cholesterol probe for detection at 570 nm (MAK043, technical bulletin, Sigma-Aldrich®).

4.3 Results

4.3.1 Sodium cholate detergent mediated analysis

Reconstituted HDL WT nanoparticles were produced using the sodium cholate dialysis method (Jonas, 1986). The rHDL-WT nanoparticles were used to compare the different methods of size fractionation of SEC, SG-UTC and Fl-UTC. After selecting the best procedure, the rHDL nanoparticles containing apoA-I R173C or L144R were prepared. The rHDL POPC:apoA-I WT 200:2 (M/M) particles were run on a NativePAGE gel

and compared to lipid-free apoA-I WT to determine if rHDL particles had formed after sodium cholate removal by dialysis (**Figure 4.4**).

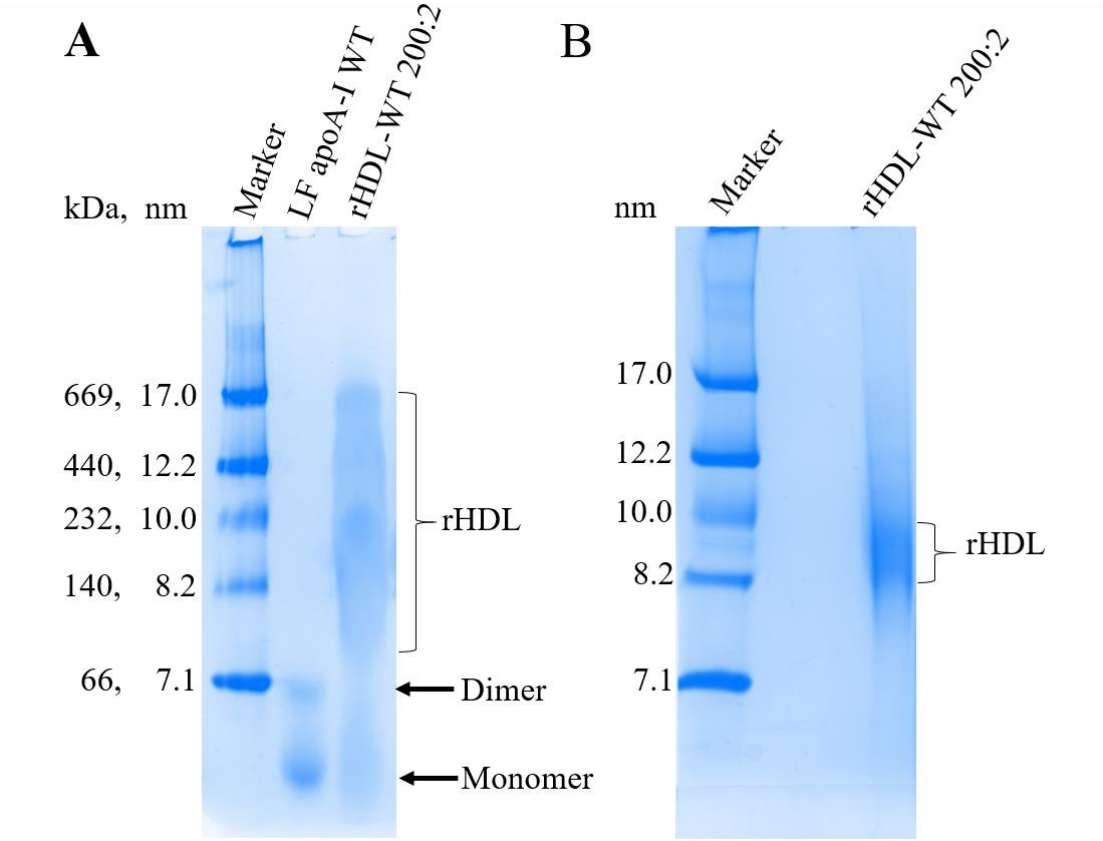

Figure 4.4. A 4-16% NativePAGE gradient gel of **A)** Lipid-free (LF) apoA-I WT and rHDL-WT POPC:apoA-I WT after sodium cholate removal, ~1 mg/mL apoA-I. **B)** rHDL-WT post-sodium cholate removal at a concentration < 1 mg/mL apoA-I.

The lipid-free apoA-I WT lane indicated the presence of apoA-I monomers and dimers, the latter probably formed as a result of the concentrated protein stock solutions used to prepare the rHDL nanoparticles (**see section 3.3.3.2**, **section 3.4**). The overloaded rHDL sample (apoA-I WT 1 mg/mL) showed rHDL nanoparticles indicated by the broad protein stain between approximately 7.5 – 17.0 nm diameter, most intense at around 10 nm (**Figure 4.4A**), and a broad band below 66 kDa showing unreacted LF apoA-I WT.

The rHDL-WT 200:2 sample was diluted to a protein concentration < 1 mg/mL and the predominant band indicated rHDL nanoparticles between 8.2 – 10.0 nm in diameter (**Figure 4.4B**). The size range of rHDL-WT nanoparticles detected required further size fractionation to produce a homogenous rHDL nanoparticle population for structural characterisation.

4.3.1.1 Dynamic light scattering of crude rHDL nanoparticles

DLS diffusivity measurements were taken of the rHDL nanoparticle samples to determine the particle hydrodynamic diameter. The translational diffusion constant of a particle is inversely related to its hydrodynamic radius according to the Stokes-Einstein relation, assuming the particle is spherical. The intensity percentage indicates the mean particle size in a sample, but larger particles can be overrepresented as the major particle in the sample as the intensity percentage scales with the size of the particle (Stetefeld et al., 2016). The volume percentage population distribution for each measurement is shown to indicate the proportion of the particles represented in the sample (Stetefeld et al., 2016).

Each sample was measured between a 0 – 10000 nm diameter scale, however larger particles (which represent a small fraction of the total population) are not shown above 50 nm, as the region of interest for the rHDL nanoparticles is between 0 – 50 nm. The peaks above 50 nm in the intensity-weighted distribution "disappeared" in the volume-weighted distribution indicating the particles above 50 nm were present in insignificant proportions to the main particle size peak in the sample (Stetefeld et al., 2016). The polydispersity index (PdI) was used to determine if the sample was suitable to be measured using DLS and is indicated in the figure description. If the PdI was > 0.7 the sample is more polydisperse with a broad particle size distribution. A PdI < 0.7 indicates

a sample approaching a monodisperse particle distribution at < 0.1 (Stetefeld et al., 2016).

The DLS measurements determined the average particle diameter and PdI as an average of 3 scans. The rHDL-WT 200:2 (M/M) nanoparticle post-sodium cholate dialysis size distribution is shown in **Figure 4.5**. The full diameter range of 0 – 10000 nm is shown in both the intensity- and volume-weighted distributions to show the negligible contribution of the large intensity particle size peaks.

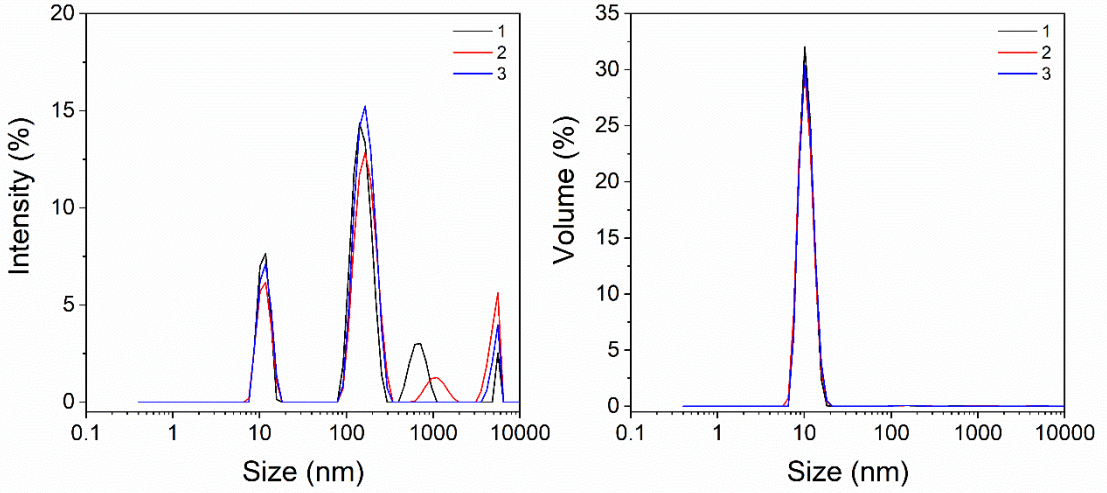

Figure 4.5. The intensity- and volume-weighted particle population distributions of rHDL-WT nanoparticles at the POPC:apoA-I WT 200:2 molar ratio. The average particle diameter was 11.3 ±0.2 nm with a PdI of 0.55 ±0.02.

The predominant rHDL-WT particle size was 11.3 nm according to the intensity-weighted peak (**Figure 4.5**).

The large peaks above approximately 100 nm were not present in the volume distribution and therefore the large particles could be liposomes or contaminants such as dust, but these did not represent a significant number of particles in the sample. Additionally, the particle peak at approximately 10 nm is similar in both particle

distributions indicating the homogeneity of the particles between the two different distributions (Stetefeld et al., 2016). Hereafter the DLS particle size measurement figures will show only the volume-weighted distribution with a linear scale between 0-50 nm, the intensity-weighted mean particle size and PdI.

Overall, the range of possible rHDL particle sizes in the overloaded gel lane and the presence of LF apoA-I WT (**Figure 4.4A**) prompted further separation of the particles produced to form a more homogenous particle population for rHDL particle characterisation. It was particularly important to remove LF apoA-I WT for solid-state NMR studies in **Chapter 5** using labelled protein to ensure any protein signals were from lipid-bound apoA-I only. The purpose of the fractionation was to isolate the predominant rHDL nanoparticle band discussed in **section 4.1.5** between approximately 9.7 – 10.2 nm.

Different methods were compared to separate the rHDL-WT nanoparticles from LF apoA-I WT and different rHDL nanoparticle sizes: size-exclusion chromatography, step gradient UTC, and flotation UTC. Henceforth, the rHDL-WT nanoparticles post-sodium cholate dialysis are referred to as unfractionated whilst the further purified particles are described as fractionated with respect to the technique used. The size exclusion chromatography, step gradient UTC and flotation UTC separation techniques will be abbreviated to SEC, SG-UTC, and Fl-UTC fractionated, respectively.

4.3.2 Size exclusion chromatography

Size exclusion chromatography of unfractionated rHDL POPC:apoA-I WT 200:2 (M/M) nanoparticles was tested to see if the rHDL could be separated by size and from LF protein and liposomes.

The peaks in the UV absorbance chromatogram of the SEC-fractionated rHDL-WT 200:2 (M/M) nanoparticles (**Figure 4.6**) corresponded to protein in the 1 mL elution fractions. The LF and lipid-bound apoA-I WT tryptophan and tyrosine aromatic amino acids absorbed UV light at the 280 nm wavelength as the sample was eluted from the size exclusion column and flowed through the UV detector. This is similar to the NanoDrop™ 2000c which utilises the Trp and Tyr residue 280 nm UV light wavelength absorbance to determine the protein concentration (Desjardins et al., 2009).

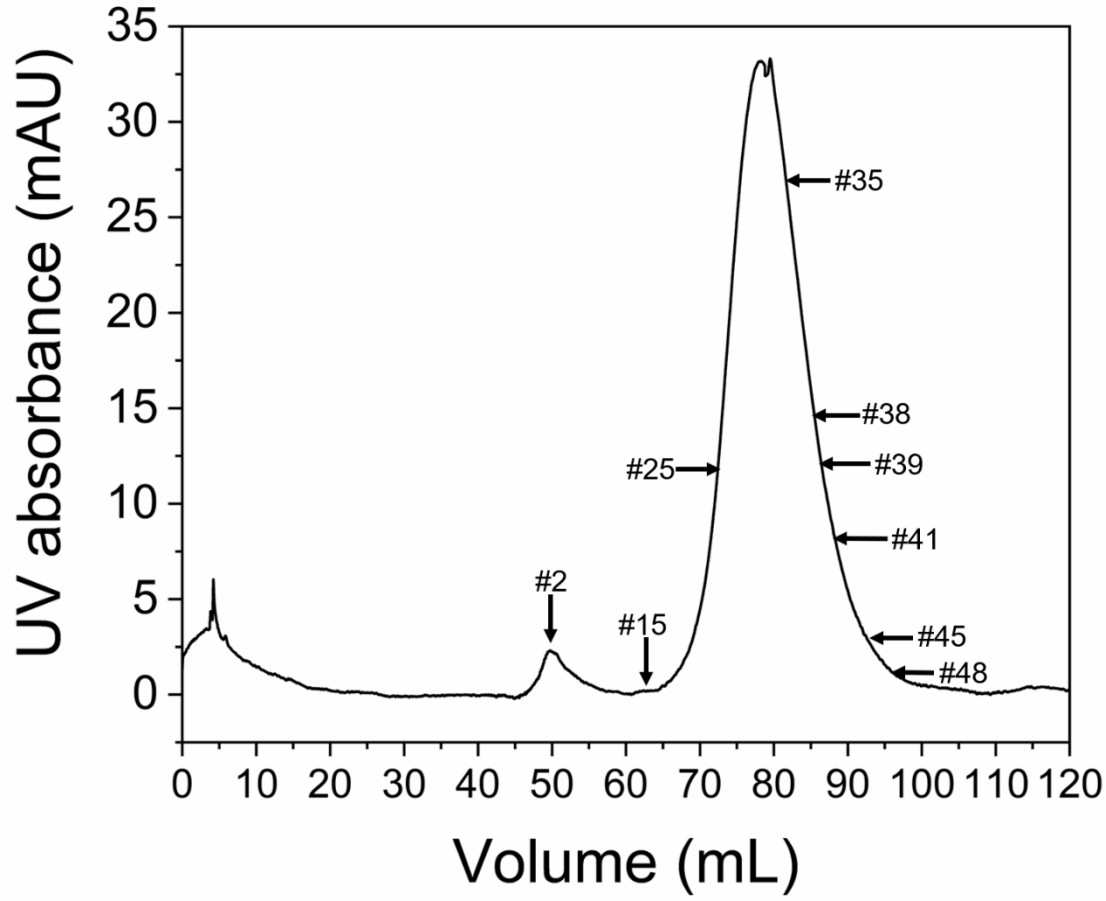

Figure 4.6. UV absorbance chromatogram of the SEC separation of rHDL-WT 200:2 (M/M) nanoparticles. The approximate positions of the 1 mL fractions measured with DLS are labelled and indicated with the black arrows.

In the UV chromatogram the main peak was at an elution volume between 65 – 100 mL with a peak maximum at approximately 32.5 mAU. The 1 mL fractions indicated in **Figure 4.6** were examined by DLS measurements to determine if the particles were separated by size.

The protein concentration of the crude rHDL-WT 1.6 mL sample loaded onto the column was ~65 µM, equivalent to a total mass of 2.9 mg. However, only ~48 % of the protein mass was detected in fractions 24-36 in a total volume of 13 mL. The difference in protein mass was unlikely to be accounted for by fractions 1-24 due to the low absorbance values (<12 mAU), i.e., the concentration of the 1 mL fraction 25 was 0.061 mg/mL (2.2 µM) at ~12 mAU. Furthermore, the protein mass in fraction 35 near the peak maximum was ~0.1 mg. Hence, the total mass of the fractions 1-24 and 37-48 would not equate to 1.5 mg of apoA-I WT.

The loss of sample could be due to possible protein aggregation with lipids in the centrifugation step prior to column loading. Therefore, the overall yield of fractions containing protein and hence rHDL nanoparticles was low under these SEC conditions as the sample was diluted across a large volume at low concentrations overall.

4.3.2.1 Dynamic light scattering of size exclusion chromatography fractions

SEC fractions 2-48 were measured using DLS and examples are shown in **Figure 4.7**. The intensity-weighted average particle sizes and PdI values are in **Table 4.3.** After 50 mL, the void volume, the SEC column fraction 2 indicated particles with an average hydrodynamic diameter of ~11.3 nm. This suggested a relatively small loss in the separation yield as the small UV absorbance at 2.5 mAU corresponded to a ~0.2 µM apoA-I concentration.

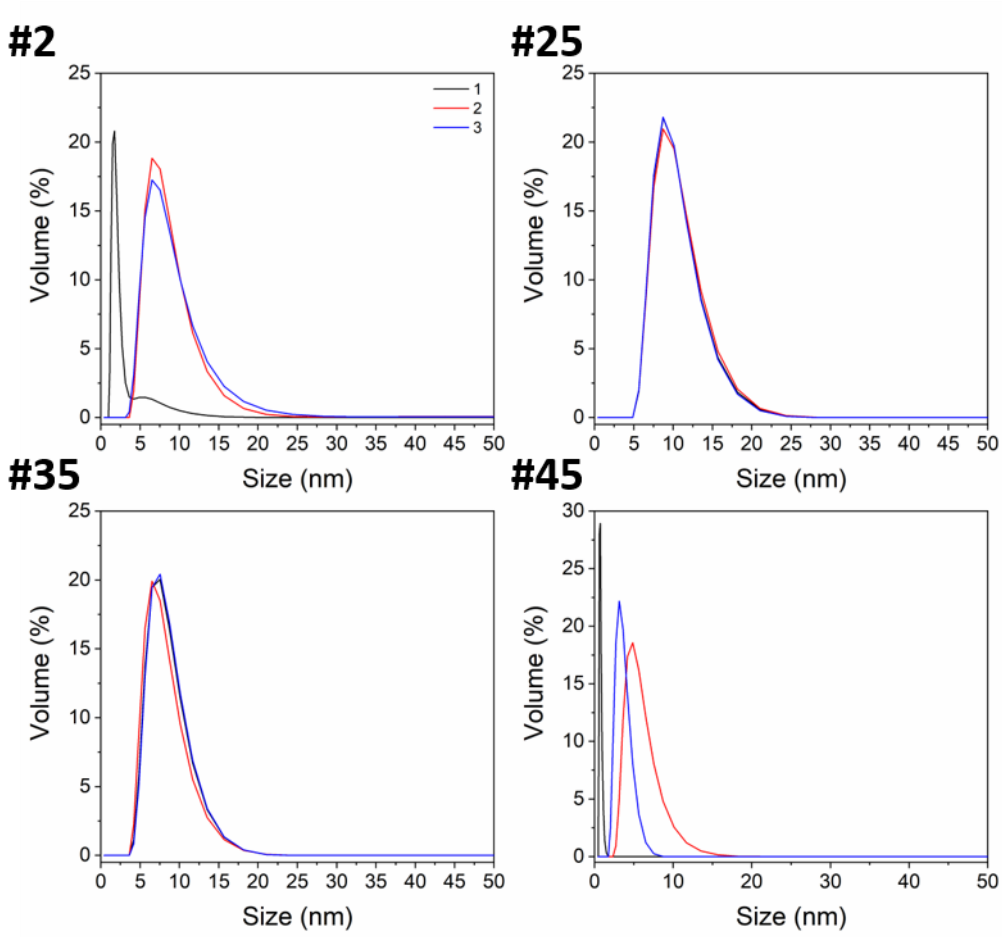

Figure 4.7. DLS volume-weighted particle population distributions of SEC fractions 2, 25, 35, and 45, scans 1-3, corresponding to the peaks in the SEC chromatogram (**Figure 4.6**). The average particle hydrodynamic diameter (nm) and PdI values are in **Table 4.3**.

Fraction 25 contained particles with a hydrodynamic diameter of 12.3 nm. Whilst the fractions 35, 38, 39 and 41 showed particles with a hydrodynamic diameter of 10.1, 9.6, 9.9, and 10.9 nm, respectively. The standard deviation (SD) of the particle size measurements was within the range of each respective measurement which suggested the predominant particle size was approximately ~10 nm between the elution volume 83-89 mL. The progressive decrease in particle hydrodynamic diameter from ~12 nm (#25), to ~10 nm (#35-41), to ≤ 7.8 nm (#45) combined with the corresponding increase

in the UV absorbance in the SEC chromatogram suggested the separation of particles of different sizes.

Table 4.3. The intensity-weighted (%) distribution of the particle population in the unfractionated rHDL-WT 200:2 (M/M) sample and 1 mL SEC fractions. Each measurement was an average of 3 scans, the average PdI and particle size are ±SD. The individual peak particle sizes for fractions 2, 45 and 46 are indicated, as the DLS measurements were dissimilar in scans 1-3.

Fraction #	Particle size (nm)	PdI
Unfractionated	11.3 ± 0.2	0.55 ± 0.02
2	2.3 and 9.9, 10.9, 13.0	0.47 ±0.20
15	815.7 ±46.3	0.13 ±0.02
25	12.3 ±0.2	0.36 ±0.05
35	10.1 ±0.3	0.49 ±0.24
38	9.6 ±0.4	0.56 ±0.03
39	9.9 ±0.4	0.26 ±0.06
41	10.9 ±1.7	0.43 ±0.09
45	0.8, 7.8, 4.2	0.30 ±0.20
48	460.8, 0.9, 0.8,	0.37 ±0.22

The polydispersity index values were < 0.7 (**Table 4.3**) of the unfractionated (PdI 0.55) and the SEC 25-41 fractions (PdI 0.26-0.56) suggesting the particles were suitable for DLS measurements (Malvern Instruments Ltd, 2011; Stetefeld et al., 2016). However, fraction 41 had a large SD with a range between 9.2-12.6 nm and a similar PdI (0.43) to fractions 35-39 (0.49, 0.56, 0.26) which indicated the particles may not have eluted completely in size order, i.e., larger particles have a shorter retention time in the size exclusion column and are eluted first.

The two important limitations of the SEC separation were low sample recovery and sample dilution. Therefore, individual fractions would require spin concentration before screening by DLS and NativePAGE gels to confirm particle size and separation from lipid-free apoA-I. Furthermore, there was a limited availability of the DLS equipment, and the NativePAGE gel protocol was not optimised at this point. Therefore, it was difficult to determine if the SEC rHDL-WT nanoparticle was successful with DLS measurements alone.

However, the range of SEC fraction(s) nanoparticle hydrodynamic diameters measured by DLS (7.8 – 12 nm) confirmed the presence of various sizes of rHDL-WT nanoparticles. This provided additional evidence of nanoparticle characterisation for future experiments.

4.3.3 Density-based ultracentrifugation rHDL purification

NaBr or KBr density-based ultracentrifugation methods are routinely used to isolate plasma HDL particles (Chapman et al., 1981; Huang et al., 2011; Kelley and Kruski, 1986; Rosenson et al., 2011; Schumaker and Puppione, 1986). In the plasma HDL density-based particle separation the various HDL subclasses have defined density ranges between 1.063 – 1.21 g/mL (Chapman et al., 1981; Rosenson et al., 2011), (**see Chapter 1**, **Table 1.1**). Examination of the methods used to purify plasma HDL and rHDL nanoparticles of different sizes and from lipid-free apoA-I indicated that SG-UTC or Fl-UTC can be used (Cavigiolio et al., 2008; Chapman et al., 1981; Jonas, 1986; Jonas et al., 1984; Kelley and Kruski, 1986; Schumaker and Puppione, 1986). Therefore, the purification of rHDL-WT nanoparticles using SG-UTC and Fl-UTC was tested.

4.3.3.1 Step-gradient density ultracentrifugation

For discontinuous SG-UTC, multiple layers of NaBr solution were layered above the sample (> 1.21 g/mL) at the densities of 1.21, 1.15, 1.09 and 1.04 g/mL as in **Figure 4.3**, to separate the rHDL particles based upon the particle density. After ultracentrifugation 0.5 mL fractions were dialysed to remove NaBr and analysed by DLS and NativePAGE to confirm the presence of protein and rHDL nanoparticles.

DLS was used to measure the particle diameter of the rHDL POPC:WT apoA-I 200:2 (M/M) nanoparticles in the pooled fractions of the 1.09, 1.15 (**Figure 4.8**) and 1.21 g/ml NaBr density layers (2.5 mL total volume). The sample PdI and mean peak diameters are in **Table 4.4**. The DLS peaks for the pooled 1.09 and 1.21 g/mL fractions are not shown as the particle diameters were very large at 414 and 304 nm, respectively, which suggested the presence of liposomes. The 1.15 g/mL fractions major particles average diameter was 12.8 ±0.9 nm, indicating a particle size range between 11.9 – 13.7 nm (**Figure 4.8**).

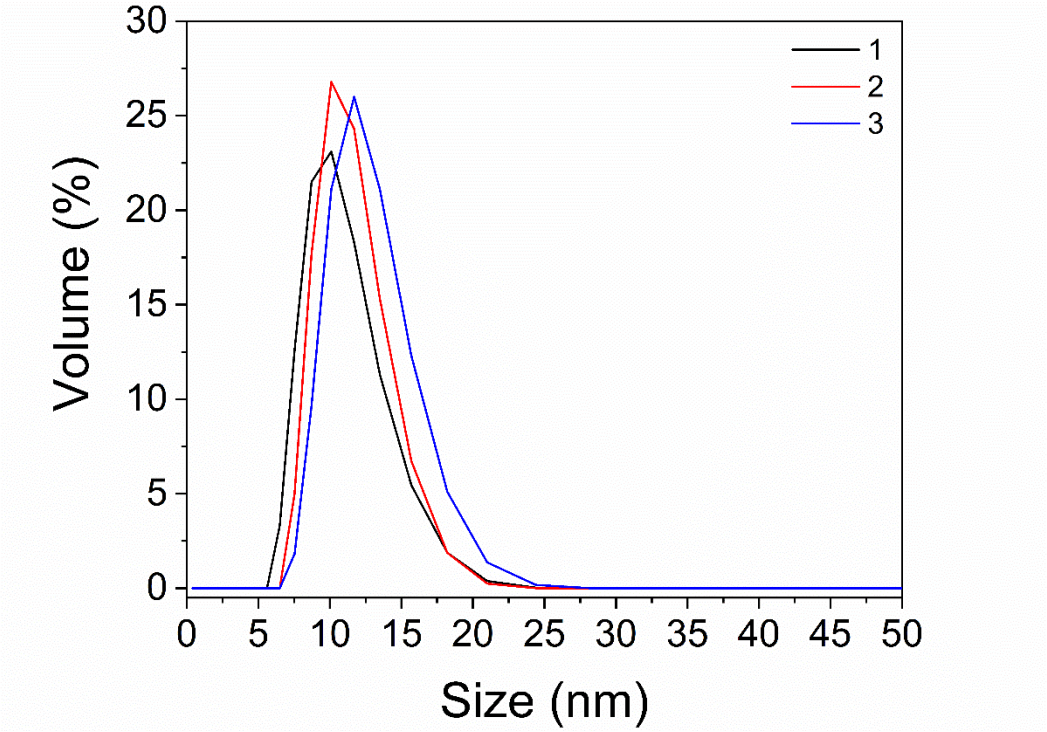

Figure 4.8. DLS volume-weighted particle population distributions of pooled 1.15 g/mL fractions of rHDL POPC/WT 200:2 (M/M) nanoparticles. The average particle hydrodynamic diameter (nm) and PdI values are in **Table 4.4**.

Table 4.4. Intensity DLS measurements of the rHDL POPC/apoA-I 200:2 (M/M) fractions separated by discontinuous SG-UTC. The PdI and mean particle diameter (nm) ±SD for each sample DLS intensity peak.

Density fraction	Particle size (nm)	PdI
Post-dialysis	11.3 ±0.2	0.55 ±0.02
1.09 g/mL	414.2 ±13.2	0.27 ±0.03
1.15 g/mL	12.8 ±0.9	0.42 ±0.09
1.21 g/mL	304.3 ±14.9	0.34 ±0.07

NativePAGE gradient gels were used to determine the hydrodynamic diameters of the unfractionated and SG-UTC fractionated rHDL nanoparticles. The SG-UTC fractions were pooled by density layer (2.5 mL) or as 0.5 mL fractions and run on a NativePAGE gradient gel in **Figure 4.9** and **Figure 4.10**, respectively. In the NativePAGE gels the rHDL nanoparticle sizes in each lane are indicated by the arrows followed by the approximate particle size as determined using the relative mobility of the particle bands. For example, the predominant particle band in the 1.15 g/mL 2.5 mL pooled fractions sample lane (**Figure 4.9**) indicated the presence of particles with a diameter of 9.1 nm and is labelled as rHDL-9.1 WT.

In **Figure 4.9** the major rHDL band appears between the 8.8 – 11.5 nm in the unfractionated sample lanes with and without sodium cholate, and pre-UTC. The pre-UTC bands showed staining indicating rHDL nanoparticles with diameters at ~7.4-8.8, 12.1 and 16.2 nm.

The rHDL-12.1 and -16.1 nm diameter particles in the 1.09 g/mL fraction lane indicated some separation of the larger rHDL particles from the predominant rHDL-9.1 WT particles. Faint bands in the 1.15 g/mL pooled rHDL at ~ 12.2 and 17.0 nm in the 1.15 g/ml fraction indicated partial separation from the rHDL-9.1 nm particle. The rHDL-9.1 WT particles were separated from the rHDL-7.4-8.8 nm particles which showed bands only in the 1.21 g/mL pooled fractions.

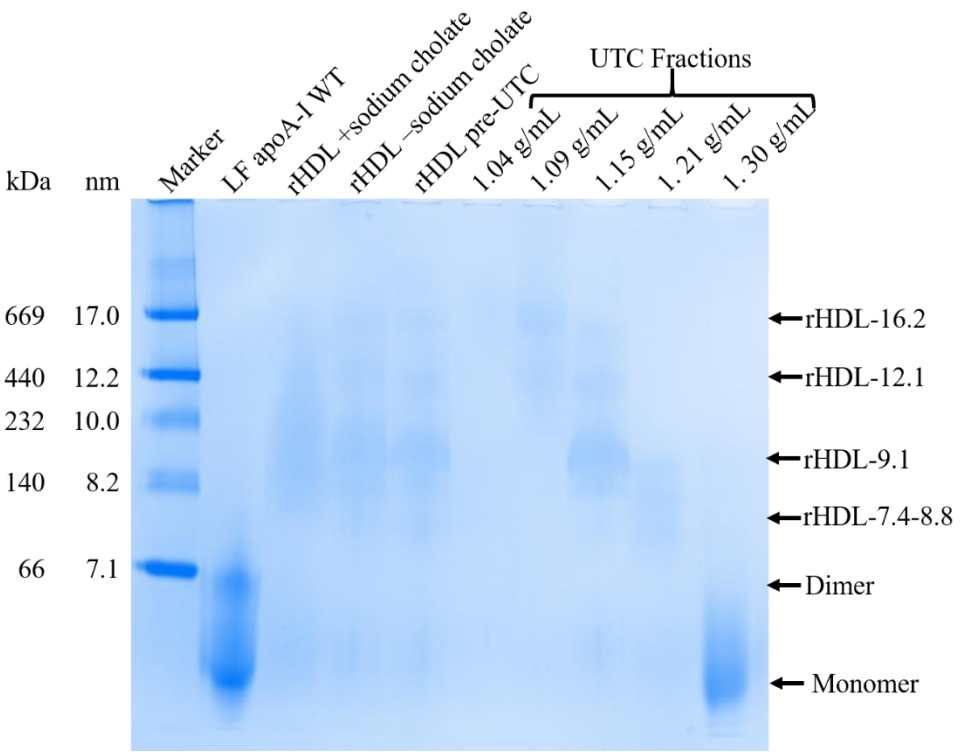

Figure 4.9. A 4-16 % NativePAGE gradient gel of the different stages of the rHDL nanoparticle POPC:apoA-I WT 200:2 (M/M) preparation using SG-UTC. The sample lanes contain: LF apoA-I WT, rHDL containing sodium cholate, rHDL without sodium cholate, rHDL pre-UTC after storage at 4°C, and each 2.5 mL pooled NaBr SG-UTC fractions at 1.04, 1.09, 1.15, 1.21 and 1.30 g/mL density. The labels indicate the bands corresponding to monomeric and dimeric lipid-free WT apoA-I, and rHDL particles 7.4-8.8, 9.1, 12.1 and 16.2 nm in diameter.

The 1.30 g/mL fractions contained a strong intensity band of monomeric lipid-free apoA-I. This suggested the ultracentrifugation conditions separated LF apoA-I from the rHDL nanoparticles. The relative position (8.6-9.8 nm) of the predominant rHDL-9.1 WT nanoparticle band in the 1.15 g/mL lane remained similar to the unfractionated sample band which suggested the lipid-free apoA-I WT band in the 1.30 g/mL lane was not due to loss of apoA-I from the rHDL nanoparticles but due to unreacted apoA-I.

To further separate the rHDL-9.1 WT particles the 0.5 mL fractions were examined by NativePAGE before pooling together for further characterisation (**Figure 4.10**). Representative fractions of layers 1.04, 1.09 and 1.21 g/mL NaBr density did not show bands for rHDL particles or LF apoA-I WT. The 1.15 g/mL fractions 11-14 showed a prominent band at ~8.7 nm. If a fraction contained additional bands, such as fraction 14 at ~8.0 nm, it was not pooled for further characterisation. The isolated 0.5 mL fractions rHDL-8.7 nm particles (**Figure 4.10**) was similar to the approximate diameter of the 1.15 g/mL (2.5 mL) fraction major band between 8.6-9.8 nm (**Figure 4.9**).

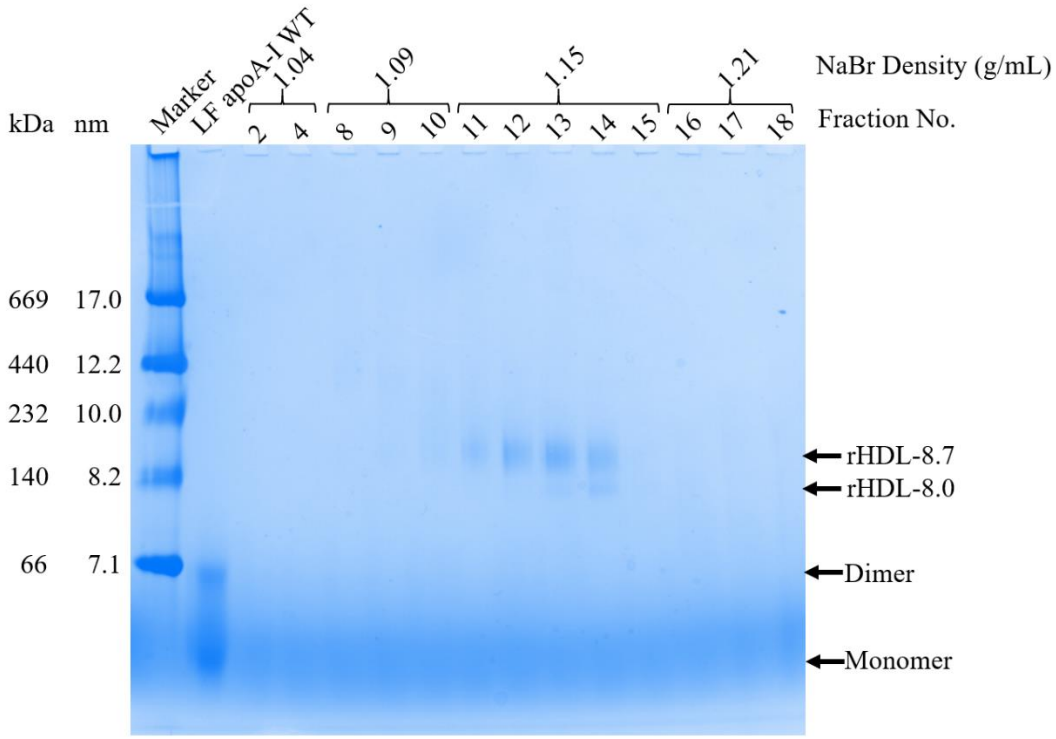

Figure 4.10. A 4-16 % NativePAGE gradient gel of the different stages of the rHDL POPC/WT 200:2 (M/M) preparation using SG-UTC. The sample lanes contain: LF apoA-I WT, and separate 0.5 mL fractions from the NaBr density gradient layers at 1.04, 1.09, 1.15, and 1.21 g/mL density. The labels indicate the bands corresponding to monomeric and dimeric LF apoA-I WT and rHDL nanoparticles.

The apoA-I concentrations of the pooled (2.5 mL) density layers at 1.04, 1.09, 1.21, 1.30 g/mL NaBr density were 0.2, 8.5, 4.9, and 7.7 µM, respectively. The 1.15 g/mL fractions containing the predominant rHDL-9.1 WT had a concentration of 15.9 µM. An approximate mass of protein 3.5 mg was in the unfractionated rHDL sample, and the total protein mass of the SG-UTC fractions was ~2.4 mg. The loss in sample could be due to precipitation of protein with lipids and interaction with the spin concentrator membrane pre-UTC, or dilution of the sample during UTC and NaBr removal dialysis.

Both NativePAGE gels (**Figure 4.9-4.10**) showed a predominant particle with a diameter of ~8.7-9.1 nm, whereas the DLS measurements of the unfractionated rHDL-WT sample and pooled 1.15 g/mL (2.5 mL) fractions indicated particles with a larger diameter of 11.3 and 12.8 nm, respectively. This difference could be due to the DLS measurement of the pooled 1.15 g/mL density layer rather than selected 0.5 mL fractions. In the DLS measurement the 1.15 g/mL pooled fraction rHDL-12.1 particle faint band (**Figure 4.9**) could produce an increase in the intensity-weighted average particle diameter.

The absence of bands in the 0.5 mL fractions for the rHDL-12.1 and -16.2 WT particles in **Figure 4.10** in the 1.04 and 1.09 g/mL density layers and the lack of DLS particle detection in the 1.09 g/mL layers (**Table 4.4**) suggested the use of these density layers may not be necessary for isolation of the rHDL-9.1 WT particles. Therefore, the use of single-step flotation density ultracentrifugation was tested.

4.3.3.2 Flotation density ultracentrifugation

Flotation density ultracentrifugation was used to determine if particle separation and separation from lipid-free apoA-I could be achieved compared to SG-UTC. In Fl-UTC the sample (> 1.21 g/mL density) was layered beneath a 1.21 g/mL NaBr density layer,

with a 0.5 mL layer of rHDL buffer, pH 7.4 (**Figure 4.3**). After centrifugation fractions were taken from the tube (0.5 mL each) from low to high density. The fractions 8-14 and 20-21 were pooled as rHDL-9.1 WT nanoparticles were not expected in these fractions due to the SG-UTC fraction results (**Figure 4.9-4.10**). The rHDL nanoparticles had a density > 1.21 g/mL therefore were expected to be in the upper layers "floated".

In **Figure 4.11** fractions 1, 4 and 5 showed a band for rHDL-8.1 and -9.1 nm WT particles, which were similar to the diameter of the particles isolated in the 0.5 mL SG-UTC 1.15 g/mL fractions (**Figure 4.10**). Fractions 2 and 3 showed only the 9.1 nm diameter particles and were pooled for further analyses. The rHDL-9.1 WT predominant band particle diameter range was between ~8.7-9.5 nm. The Fl-UTC fraction 1-3 lanes appeared to contain faint staining above 10 nm which could indicate the presence of larger rHDL nanoparticles. Fraction 1 also contained a partial band at ~8.1 nm indicating a degree of incomplete separation of particles in the fractions. The Fl-UTC conditions were sufficient for the separation of unreacted apoA-I WT as indicated by the monomer apoA-I WT band in the final fractions 20-21.

The protein concentrations of fractions 1, 2, 3, 4 and 5 were 6.7, 6.5, 6.5, 5.2, and 5.4 µM, respectively. Fraction 1 contained a faint band for the rHDL-8.1 WT particles at the same protein concentration (6.7 µM) as fractions 2 and 3 (6.5 µM), which indicated that with Fl-UTC as in SG-UTC the 0.5 mL fractions should be checked by NDGGE. The unfractionated sample protein mass in 0.5 mL was ~1.4 mg and the Fl-UTC fraction concentrations of fractions 1-21 contained a total mass of apoA-I of ~1.3 mg. Therefore, based upon the protein mass the loss of sample during the protocol was reduced compared to SEC and SG-UTC.

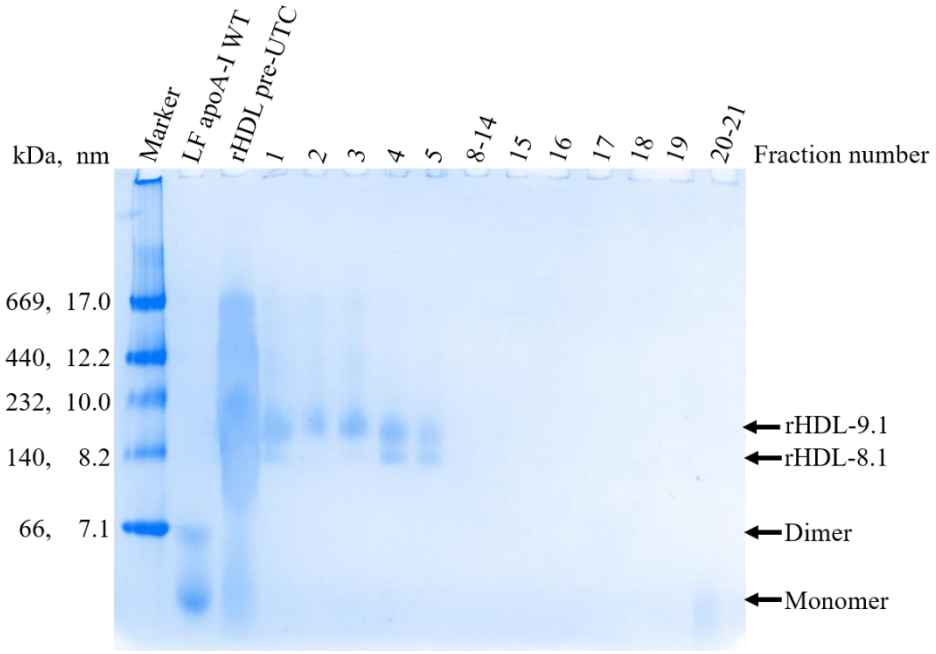

Figure 4.11. A 4-16 % NativePAGE gradient gel of the different stages of the rHDL POPC/WT 200:2 (M/M) Fl-UTC fractions. The sample lanes contain: LF apoA-I WT, and separate 0.5 mL fractions shown by the fraction number. The labels indicate the bands corresponding to monomeric and dimeric LF apoA-I WT and rHDL-8.1 and -9.1 nm WT particles.

4.3.4 Transmission electron microscopy of rHDL-WT

Initially, rHDL POPC/apoA-I WT 200:2 nanoparticles post-sodium cholate removal were negatively stained with 2 % (w/v) PTA for TEM (**Figure 4.12**). The rHDL nanoparticles are indicated by the black arrows, and are in the well-known rouleaux formation (Silva et al., 2008).

The rouleaux commonly form when the rHDL nanoparticles are negatively stained with phosphotungstic acid and are considered to be an artefact of the TEM sample preparation (Chen et al., 2009; Duong et al., 2006; Zhang et al., 2011). The particles stack with the lipid headgroups of the nanoparticles facing the headgroups of the next

rHDL nanoparticle, with the disc face perpendicular to the TEM grid plane (**Figure 4.12**). However, the sample staining background significantly obscured the rHDL nanoparticles to sufficiently measure the nanoparticle diameter, as well as the sample concentration as the rouleau are layered upon other rouleau.

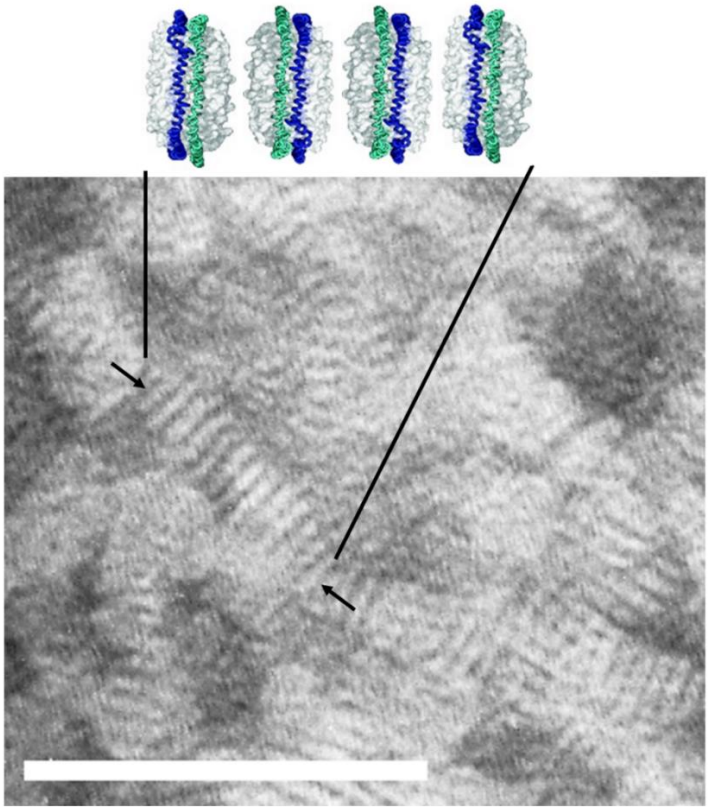

Figure 4.12. A TEM image at x 80 k magnification of POPC:apoA-I WT 200:2 (M/M) unfractionated rHDL nanoparticles post-sodium cholate removal stained with 2 % (w/v) PTA. The scale bar is 100 nm, and the black arrows indicate stacked rouleau of rHDL nanoparticles. The discoidal rHDL nanoparticle model image was obtained from (Nath et al., 2007).

Due to the lack of individual particles using the PTA stain, a protocol was adapted from the optimised negative stain method produced by Zhang *et al*. (Zhang et al., 2011) and used to image the rHDL POPC:apoA-I 200:2 (M/M) nanoparticles after Fl-UTC at the

protein concentrations of 9 (**Figure 4.13**) and 36 µM (**Figure 4.14**). At 9 µM the nanoparticles were imaged as separate nanodiscs with the lipid headgroups of the disc associated with the TEM grid surface and did not show rouleau formation.

Fifty particles were measured in triplicate for a total of 150 particle measurements to check the reproducibility of using FIJI to measure the particle diameter in the TEM images. The average diameter of the nanoparticles was 10.7 ±2.3 nm. The distribution of the particle diameters is shown by the histogram in **Figure 4.13B**.

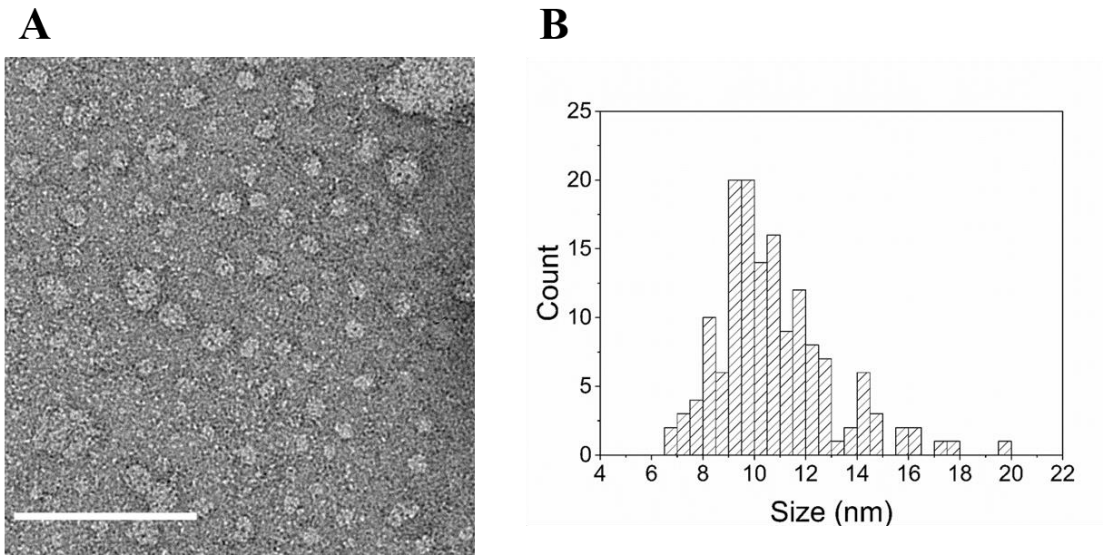

Figure 4.13. A) A TEM image at x 68 k magnification of POPC/apoA-I WT 200:2 (M/M) rHDL, 9 µM protein concentration, post-flotation UTC stained with 2 % (w/v) UA. The scale bar is 100nm. **B)** A histogram of 150 rHDL-WT nanoparticle diameter measurements at 9 µM apoA-I concentration.

At 36 µM protein concentration the rHDL nanoparticles were more concentrated and closely packed together (**Figure 4.14A**), with randomly distributed particles in shorter rouleaux compared to the extended rouleaux in **Figure 4.12**. The advantage of the 36 µM concentration of particles was that the edges of the particles were visible, enabling the particle thickness to be determined. The concentrated regions of rHDL nanoparticles

at the 36 µM protein concentration provided more particles to measure **Figure 4.14A**. The average diameter of 150 nanoparticles was 10.7 ±2.0 nm. The average thickness was 5.6 ±0.7 nm.

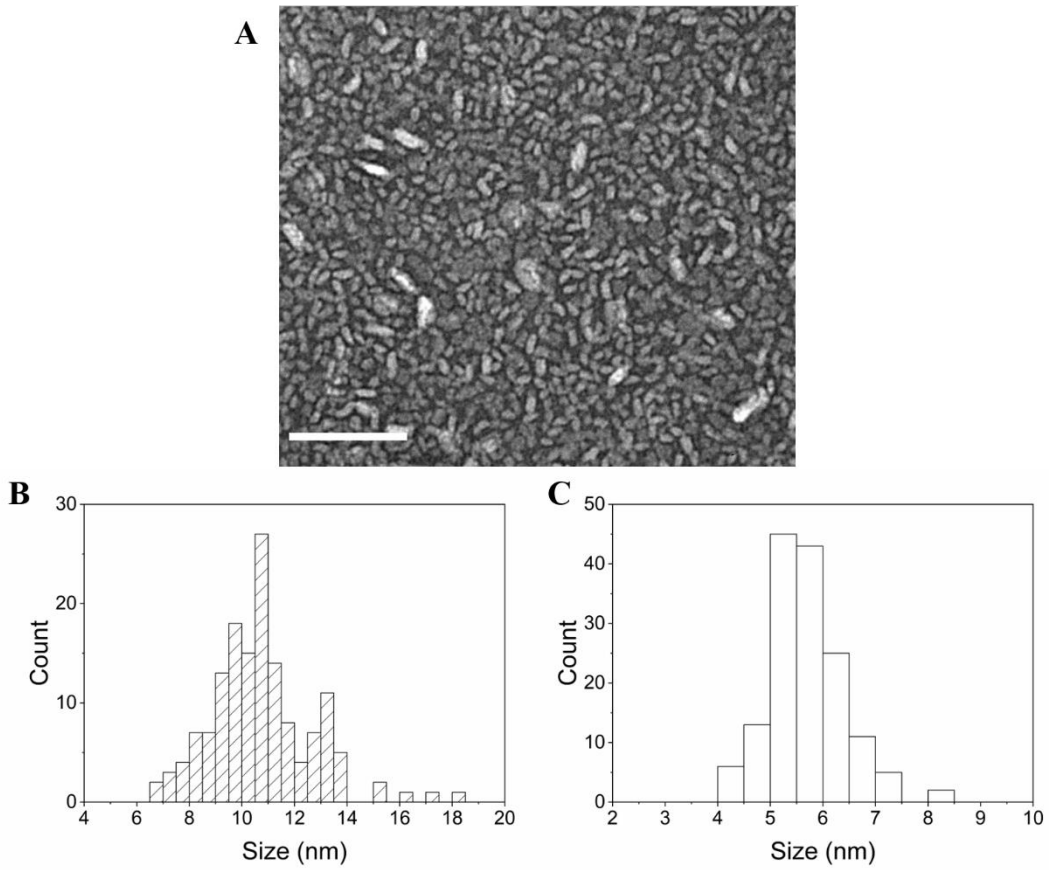

Figure 4.14. A) A TEM image at x 68 k magnification of POPC/apoA-I WT 200:2 (M/M) rHDL, 36 µM protein concentration, post-flotation UTC stained with 2 % (w/v) UA. The scale bar is 100 nm. The corresponding histograms of 150 rHDL-WT nanoparticle **(B)** diameter and **(C)** thickness measurement.

The thickness (~5.6 nm) of the particles was greater than that of a lipid bilayer ~4 nm (Kucerka et al., 2005) suggesting there was systematic error in the measurements or overestimation of the particle measurements. This could include user error in measuring the TEM images using FIJI software in defining the particle edge for each measurement.

Additionally, DLS and NDGGE measure the hydrodynamic diameter of the particles whilst TEM measures negatively stained dried particles.

At both protein concentrations the majority of particles were between 8 – 13 nm diameter at 81 and 83 % of the 150 particles at 9 and 36 μM, respectively. Therefore, the Fl-UTC fractionated POPC:apoA-I WT rHDL sample showed a similar size distribution with some heterogeneity in particle diameter.

The DLS average rHDL-WT diameter particle of the SG-UTC 1.15 g/mL pooled fractions was 12.8 ±0.9 nm compared to the pre-UTC diameter of 11.3 ±0.2 nm. The Fl-UTC rHDL-WT nanoparticle TEM diameter measurements (10.7 ±2.0 nm) were within the ranges of the pre-UTC measurements and the SG-UTC pooled fractions.

However, the TEM measurements indicated that the Fl-UTC rHDL-WT sample contained nanoparticles of various sizes despite appearing as the predominant rHDL-9.1 WT band on the NativePAGE gel (**Figure 4.11**) in fractions 2 and 3. This could be due to low concentrations of the particles in the sample or low sample concentration loaded into the gel resulting in minor particle populations below the detection limit of the NativePAGE gel protein stain. Therefore, the samples showed some variability in the nanoparticle diameter and were not completely homogenous, but Fl-UTC was successful in the removal of lipid-free apoA-I WT.

4.3.4.1 A comparison of the rHDL-WT fractionation methods

SEC and density-based UTC were compared to determine which method best isolated the major rHDL-WT nanoparticles between 8.2 – 10 nm in diameter as observed by NDGGE (**Figure 4.4).** The percentage yield and sample recovery were estimated for each fractionation method (**Table 4.5**). Overall, the SG-UTC method had higher fraction concentrations and yield compared to SEC and Fl-UTC. The Fl-UTC method

had the highest sample recovery which suggested the reduced number of density layers could have minimised the sample losses during the protocol stages.

Table 4.5. The percentage yield of the rHDL-9.1 WT particles purified by SEC, Fl-UTC and SG-UTC, i.e., the mass of apoA-I in the pooled fractions relative to the start mass (mg) in parentheses, the fractions used, total fraction volume, apoA-I WT mass (mg) and concentration (conc. in μM) are indicated.

Method	Fractions	Fraction volume (mL)	ApoA-I mass in fractions (mg)	Conc. (μM)	Yield (%)	Recovery (%)
SEC (2.9 mg)	35-40	6.0	0.39	2.3	13.4	66.3
Fl-UTC (1.4 mg)	2-3	1.0	0.18	6.5	13.0	87.4
SG-UTC (3.5 mg)	11-15	2.5	1.11	15.9	31.9	68.1

The SEC fractionated particles showed size separation by DLS only and had limitations such as dilute fractions and lower sample recovery. The SG-UTC and Fl-UTC methods were characterised with NativePAGE which confirmed the separation of rHDL from lipid-free apoA-I WT. The removal of lipid-free apoA-I by ultracentrifugation was highly important for labelled apoA-I solid-state NMR rHDL samples and secondary structure analysis by circular dichroism.

It was concluded that the particles isolated by Fl-UTC were reasonably homogenous for further study based upon the average TEM rHDL-WT diameter (~10.7 nm) and the predominant NDGGE band of rHDL-9.1 WT nm particles. The NativePAGE gel bands of the rHDL-8.7-9.1 WT particles between the UTC methods were similar (**Figure 4.10-4.11**) and suggested the SG-UTC and Fl-UTC methods isolated similar sized particles.

Additionally, the SG-UTC method separated some of the larger diameter particles (12.2 and 17.0 nm) from the rHDL-8.7-9.1 WT 1.15 g/mL density layer (**Figure 4.9**).

Henceforth, the SG-UTC and Fl-UTC methods were used for isolating the rHDL-8.7-9.1 nm nanoparticles dependent upon the structural characterisation technique used. The SG-UTC method had benefits such as the high sample yield and separation from the larger diameter rHDL nanoparticle. In comparison, the Fl-UTC method isolated nanoparticles of a similar size with a greater sample recovery and simpler preparation procedures.

4.3.4.2 Scale of rHDL nanoparticle preparation for characterisation techniques

This is an approximate guide to scale the rHDL nanoparticle preparation using the SG-UTC fractionation method for the three main characterisation techniques used in this work: CD, SS NMR of oriented and polyethylene glycol (PEG)-precipitated samples. An example starting sample POPC/apoA-I concentration was ~5/0.05 mM (**Table 4.2**) and contained ~6.76 mg of apoA-I in 4 mL rHDL buffer, pH 7. The concentration of apoA-I was used as an indicator of yield at each stage of the preparation as the protein concentration was routinely estimated using the A_{280} UV absorbance.

The apoA-I concentration required for circular dichroism was 0.1 mg/mL in a total volume of 300 µL. The final oriented SS NMR samples contained an apoA-I concentration of 0.21 mg/mL in 1 mL total volume. Therefore, the sample preparation for the CD (~14-fold dilution) and SS NMR oriented samples (~7-fold dilution) required dilution after SG-UTC. Hence, the single unlabelled apoA-I WT and mutant(s) protein expression yields at approximately 56 and 32 mg /L of culture media, respectively, were suitable for preparation of the circular dichroism and oriented ^{31}P SS NMR samples.

In comparison, the PEG-precipitated rHDL samples required a scaled preparation as a minimum pellet mass of 5 mg was desirable. The obtained PEG-precipitated rHDL mass was between 2 – 5 mg for the samples in this work. The final mass of apoA-I in the example sample in **Table 4.6** (in bold) was ~1.1 mg. Therefore, to produce a final PEG-precipitated rHDL apoA-I mass between 2 – 5 mg, a starting mass of apoA-I between 12.2 – 30.5 mg was required. The [^{13}C, ^{15}N]-labelled apoA-I WT/R173C/L144R protein expression yields were ~19, 7, and 53 mg/L of culture media, respectively. Therefore, multiple labelled apoA-I WT and R173C expressions were required to prepare the PEG-precipitated samples.

This provides an estimate of the amount of apoA-I and POPC that is required using the SG-UTC rHDL nanoparticle protocol for the three different characterisation methods.

Table 4.6. Example sample preparation of rHDL-WT 200:2 nanoparticles. The apoA-I concentration is indicated at each stage including the percent protein compared to the starting apoA-I mass. *spin-concentrated samples.

Stage of rHDL preparation	ApoA-I concentration (mg/mL)	Total sample volume (mL)	ApoA-I protein mass (mg)	ApoA-I retained in rHDL (%)
Start	1.69	4	6.76	-
After sodium cholate removal	1.39	3.5	4.87	72.0
Before SG-UTC*	7.20	0.5	3.60	53.2
After SG-UTC* 1.15 g/mL fractions	4.44	0.25	**1.11**	16.4

Overall, 16.4 % of apoA-I was retained in the rHDL-WT 200:2 nanoparticles between ~8 – 10 nm in diameter as determined by NDGGE. The total percentage of apoA-I detected in the 1.04 – 1.09 and 1.21 – 1.30 g/mL NaBr density fractions at ~18.8 % did not account for the remaining apoA-I. The possible causes of apoA-I loss could be apoA-I interaction with the cellulose membrane during the spin concentration, precipitation during dialysis or high protein concentration precipitation.

4.3.5 Preparation of rHDL-R173C and rHDL-L144R nanoparticles

Detergent mediated dialysis method followed by SG-UTC or Fl-UTC was chosen as the best method for size fractionation of the rHDL-WT nanoparticles and separation from lipid-free apoA-I (**see section 4.3.4.1**). Therefore, the same method was applied to isolate rHDL nanoparticles with a similar diameter to the rHDL-9.1 WT nanoparticles containing apoA-I R173C or L144R at the molar ratio of POPC:apoA-I mutant 200:2 (M/M). DLS, NDGGE and TEM were used as before to determine if rHDL nanoparticles were formed. It was important to produce the atheroprotective mutant nanoparticles at a similar size to the rHDL-WT nanoparticles to compare structural features.

4.3.5.1 rHDL-R173C nanoparticles

In the following sections, as with the rHDL-9.1 WT nanoparticles, the apoA-I mutant particles are referred to by the predominant diameter size in nm, such as rHDL-9.4 R173C or rHDL-8.9 L144R.

The rHDL-R173C nanoparticles prepared at the POPC:apoA-I R173C 200:2 molar ratio were analysed by NativePAGE. Before fractionation the major band was between ~9.1 – 9.7 nm, the rHDL-9.4 R173C nanoparticles (**Figure 4.15**). Faint bands for separate minor particle populations at ~7.5-8.8 nm and 12.2 nm were also observed (**Figure 4.15**,

rHDL pre-UTC). After SG-UTC, in the 1.15 g/mL layer, the major particle population diameter was between ~8.8-10.1 nm (**Figure 4.15**, **2.5 mL pooled fractions**) and ~8.6-9.2 nm (**Figure 4.16**, **0.5 mL fractions**). The rHDL-9.4 R173C band indicated particles with an equivalent diameter to the purified rHDL-9.1 WT particles (**Figure 4.9**).

A comparison of the three pooled density layers 1.09 – 1.21 g/mL sample lanes showed partial separation of the predominant rHDL-9.4 R173C particle population from the rHDL-7.5-8.8 and -12.2 R173C nanoparticles (**Figure 4.15**). The 1.09 g/mL fractions contained very faint staining between 12.2 – 17.0 nm, and the 1.21 g/mL fractions contained a faint broad band between 7.5-8.8 nm (**Figure 4.15**). The 1.15 g/mL pooled fractions (2.5 mL) contained the predominant rHDL-9.4 R173C particle population. As well as faint bands that indicated the presence of minor rHDL-R173C nanoparticle populations at ~12.2 nm and between 7.5-8.8 nm.

The 1.30 g/mL fraction sample lane did not show clearly defined bands but there was some staining indicating the presence of monomeric lipid-free apoA-I R173C and rHDL-7.5 R173C particles. The LF apoA-I R173C showed bands indicating the presence of monomeric and dimeric protein. This was expected as apoA-I R173C can form a disulphide bonded dimer confirmed by mass spectrometry and in the presence of a reducing agent (TCEP) was monomeric (**see Chapter 3**).

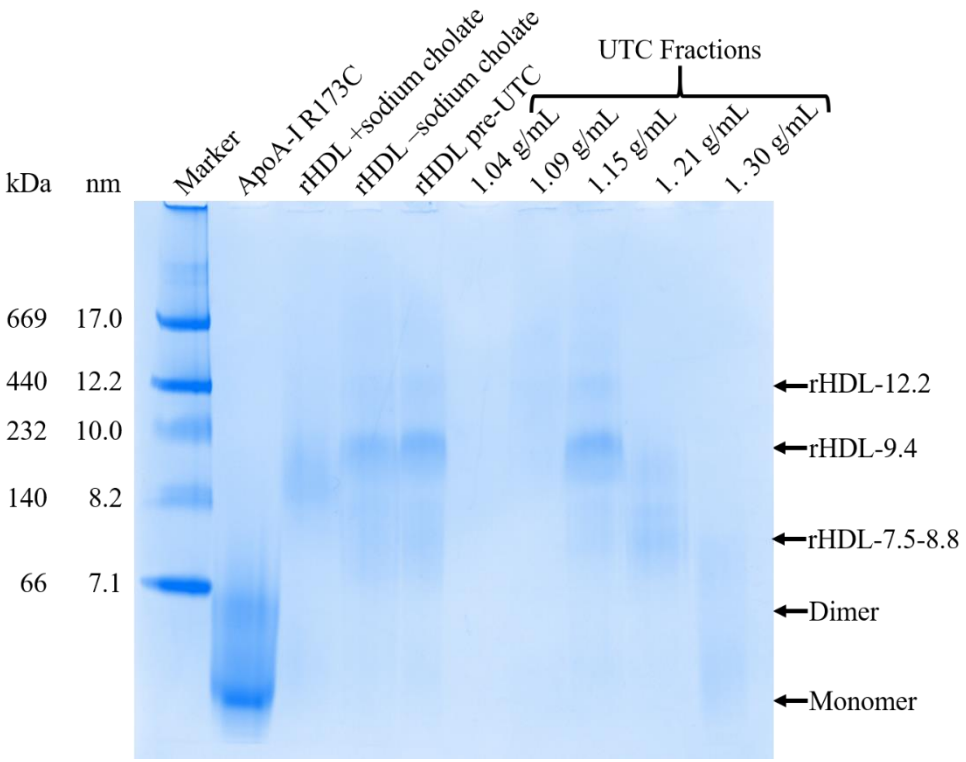

Figure 4.15. A 4 – 16% NativePAGE gradient gel of rHDL POPC:apoA-I R173C 200:2 (M/M) preparation using SG-UTC. The sample lanes contain: LF apoA-I R173C, rHDL containing sodium cholate, rHDL without sodium cholate, rHDL pre-UTC after storage at 4°C, and each 2.5 mL pooled NaBr SG-UTC fractions, at 1.04, 1.09, 1.15, 1.21 and 1.30 g/ml density. The labels indicate the bands corresponding to monomeric and dimeric lipid-free apoA-I R173C, and rHDL between 7.5 – 12.2 nm diameter.

It was expected that upon TCEP and glutathione removal the monomeric apoA-I R173C which contained reduced cysteine residues would become fully oxidised to form disulphide bonded dimeric apoA-I R173C. The presence of monomer suggested that the apoA-I R173C was not completely converted to dimer. The monomer could be in equilibrium with the dimer formation after TCEP removal. The apoA-I R173C lipid-free conformation is unknown however apoA-I WT has exhibited a variety of lipid-free structures (**see section 1.6.1**). Therefore, the cysteine residue in the monomer may not be completely accessible to form the disulphide bonded dimer.

The individual 1.15 g/mL (0.5 mL) fractions 12-14 (**Figure 4.16**) showed rHDL-R173C particles with an ~8.9 nm diameter similar to the 0.5 mL rHDL-8.7 WT particle fractions at the same NaBr density (**Figure 4.10**), and a diameter range of ~8.6-9.2 nm. This suggested that before pooling together for further characterisation the individual fractions should be analysed by NativePAGE.

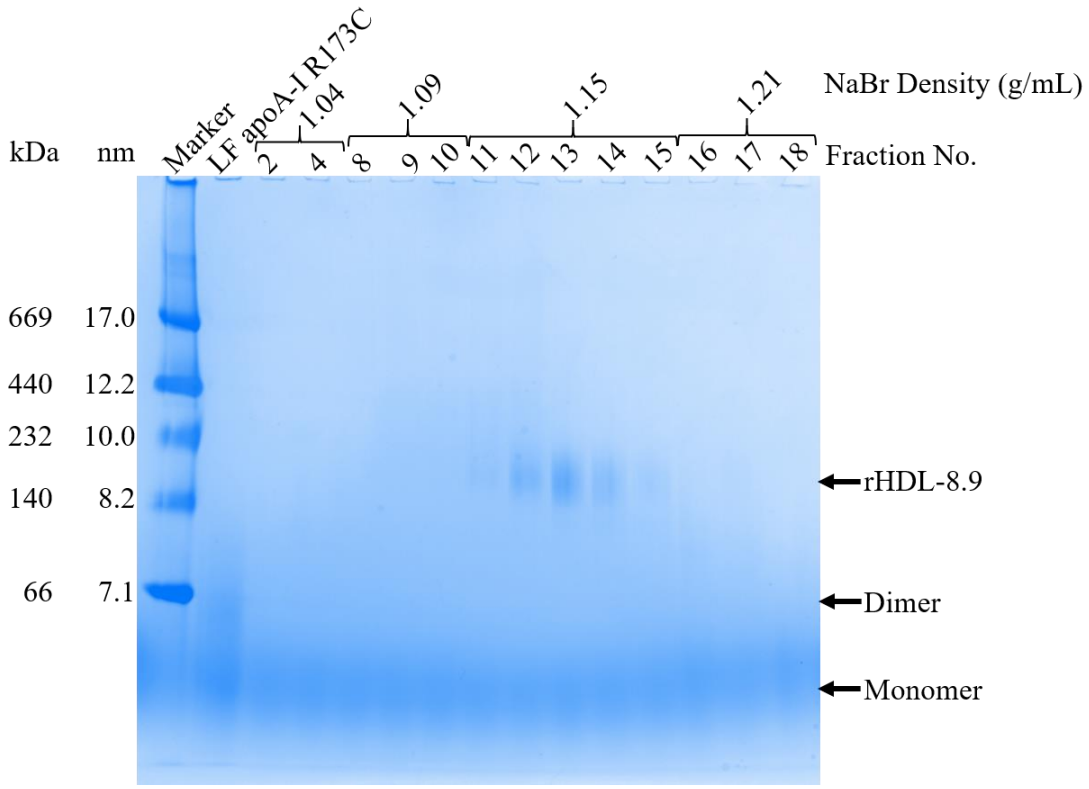

Figure 4.16. A 4-16 % NativePAGE gradient gel of the different stages of the rHDL POPC/R173C 200:2 (M/M) SG-UTC fractions. The sample lanes contain: LF apoA-I R173C, and separate 0.5 mL fractions shown by the fraction number at the NaBr density layers of 1.04, 1.09, 1.15, and 1.21 g/mL density. The labels indicate the bands corresponding to monomeric and dimeric LF apoA-I R173C and rHDL-8.9 R173C particles.

The DLS measurement of the 1.15 g/mL pooled 2.5 mL layer of rHDL-R173C nanoparticles was an average of 2 scans as the PdI of scan 1 was ~0.79 and therefore

not included. The average particle diameter was 13.8 ±0.30 nm and a PdI of 0.57 ±0.01 nm, with the volume-weighted distribution in **Figure 4.17B**. The DLS rHDL-R173C average particle diameter at 13.8 nm was larger compared to rHDL-WT 1.15 g/mL fractions at 11.3 nm and the rHDL-8.9-9.4 R173C NativePAGE diameter particles. The intensity-weighted diameter DLS measurement was affected by impurities present within the 50 nm diameter range which could cause the intensity peak average to shift higher (**Figure 4.17A**).

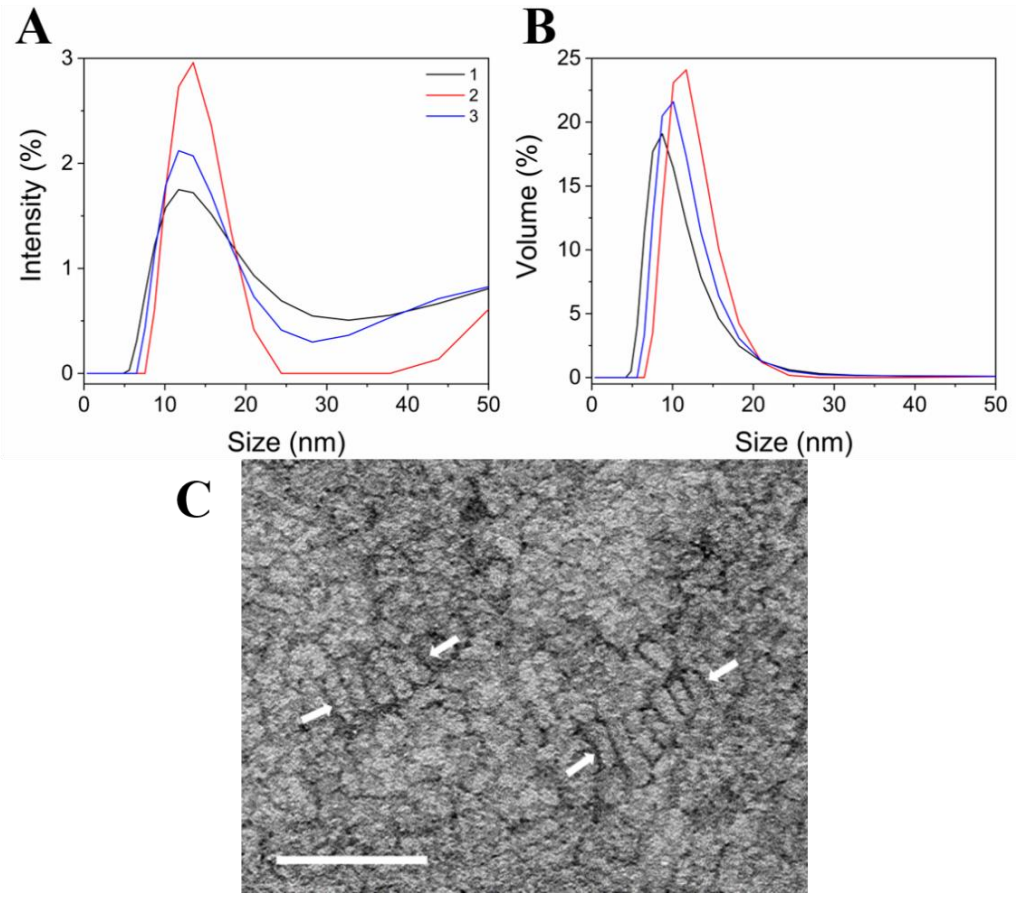

Figure 4.17. rHDL-R173C POPC:apoA-I 200:2 (M/M) nanoparticles SG-UTC fractionated DLS **A)** intensity- and **B**) volume-weighted particle population distributions between 0 – 50 nm. **C)** A TEM image at x 98 k magnification of Fl-UTC fractionated rHDL-R173C nanoparticles at the 9 µM protein concentration and stained with 2 % (w/v) UA. The scale bar is 50 nm.

An attempt was made to image the POPC/apoA-I R173C 200:2 (M/M) rHDL nanoparticle sample at 9 µM protein concentration (**Figure 4.17C**) to obtain planar particles with the lipid bilayer parallel to the TEM grid surface as with rHDL-WT nanoparticles at the 9 µM apoA-I concentration (**Figure 4.13**). The image showed the characteristic rouleaux of the rHDL nanoparticles as indicated by the arrows. However, the image resolution was not sufficient to measure the particle diameter as it appears the particles did not disperse across the TEM grid surface but appeared concentrated with the stain. Due to time constraints the resolution and sample imaging could not be improved, and the sample was not imaged at the 36 µM protein concentration.

4.3.5.2 rHDL apoA-I L144R nanoparticles

The rHDL-L144R nanoparticles were prepared at the POPC:apoA-I L144R 200:2 molar ratio using the same methods as described for the rHDL-WT and R173C nanoparticles. The SG-UTC fractionation NativePAGE gel of the 2.5 mL pooled density layer fractions (**Figure 4.18**) showed LF apoA-I L144R contained monomeric and dimeric protein similar to apoA-I WT and R173C.

The major unfractionated rHDL-L144R nanoparticle population was between 8.2 – 10.0 nm with sodium cholate, and ~8.8 – 9.0 nm without sodium cholate (**Figure 4.18**). The presence of faint bands also showed nanoparticle populations at ~11.6 nm and between ~7.6–8.3 nm. The major nanoparticle population in the SG-UTC fractionated rHDL-L144R 200:2 (M/M) sample was at ~9.0 nm with a range between 8.8 – 9.4 nm (**Figure 4.18**, **1.15 g/mL sample lane**). The rHDL-9.0 L144R nanoparticle population was similar in size to the rHDL-9.1 WT and rHDL-9.4 R173C nanoparticle populations.

The rHDL-7.6-8.3 L144R particle population was separated from the major rHDL-9.0 L144R particles population as indicated by a broad band between 7.6 – 9.0 nm in the

1.21 g/mL density layer (**Figure 4.18**). Additionally, the separation of lipid-free apoA-I L144R by SG-UTC from the rHDL-L144R nanoparticles was indicated by the broad stain in the 1.30 g/mL density layer.

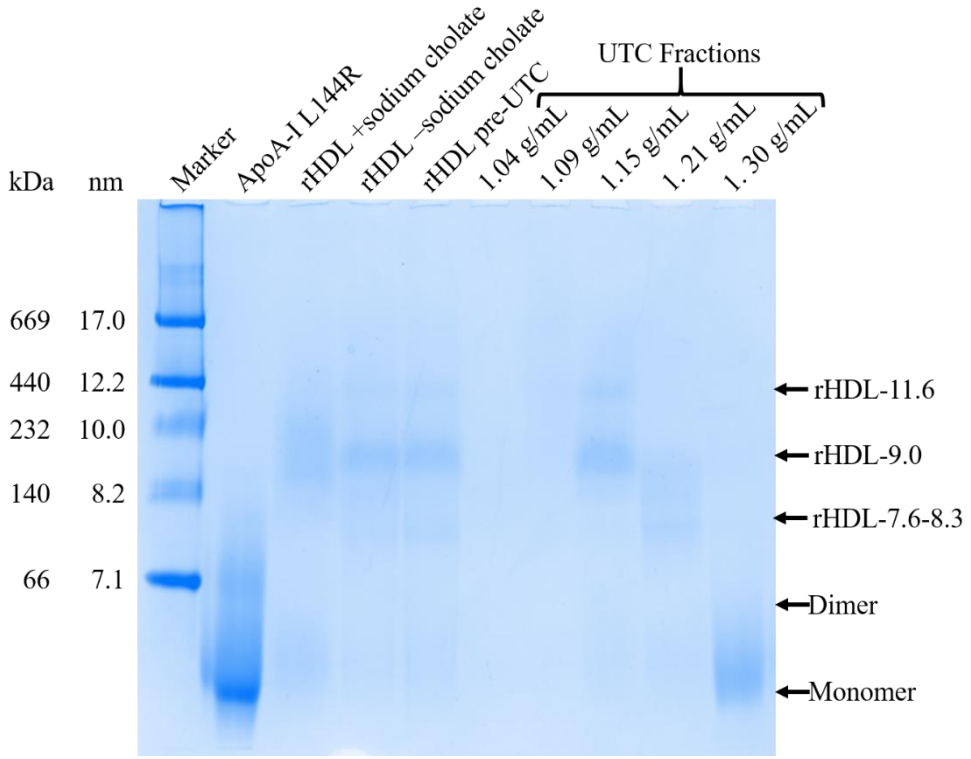

Figure 4.18. A 4 – 16% NativePAGE gradient gel of rHDL POPC:apoA-I L144R 200:2 (M/M) nanoparticle preparation. The sample lanes contain: LF apoA-I L144R, rHDL containing sodium cholate, rHDL without sodium cholate, rHDL pre-UTC after storage at 4°C, and each 2.5 mL pooled NaBr SG-UTC fractions, at 1.04, 1.09, 1.15, 1.21 and 1.30 g/ml density. The labels indicate the bands corresponding to monomeric and dimeric lipid-free apoA-I L144R, and rHDL particles with a diameter between 7.6 – 11.6 nm.

The separate 0.5 mL fractions were run on a NativePAGE gel and at the 1.15 g/mL density layer fractions 12 and 13 faint bands showed particles with a diameter of ~8.9 nm (**Figure 4.19**). The gel was stained for an extended period but the rHDL-L144R

bands appeared faintly and did not image well. Therefore, the gel contrast after imaging was altered (not shown) to view the rHDL bands before the fractions were pooled. The bands appeared at approximately the same diameter as the rHDL-8.7-9.1 WT and rHDL-8.9-9.4 R173C samples. The lipid-free apoA-I L144R band was faint compared to the dark blue staining at the dye front with the approximate position of the monomeric protein indicated in **Figure 4.19**.

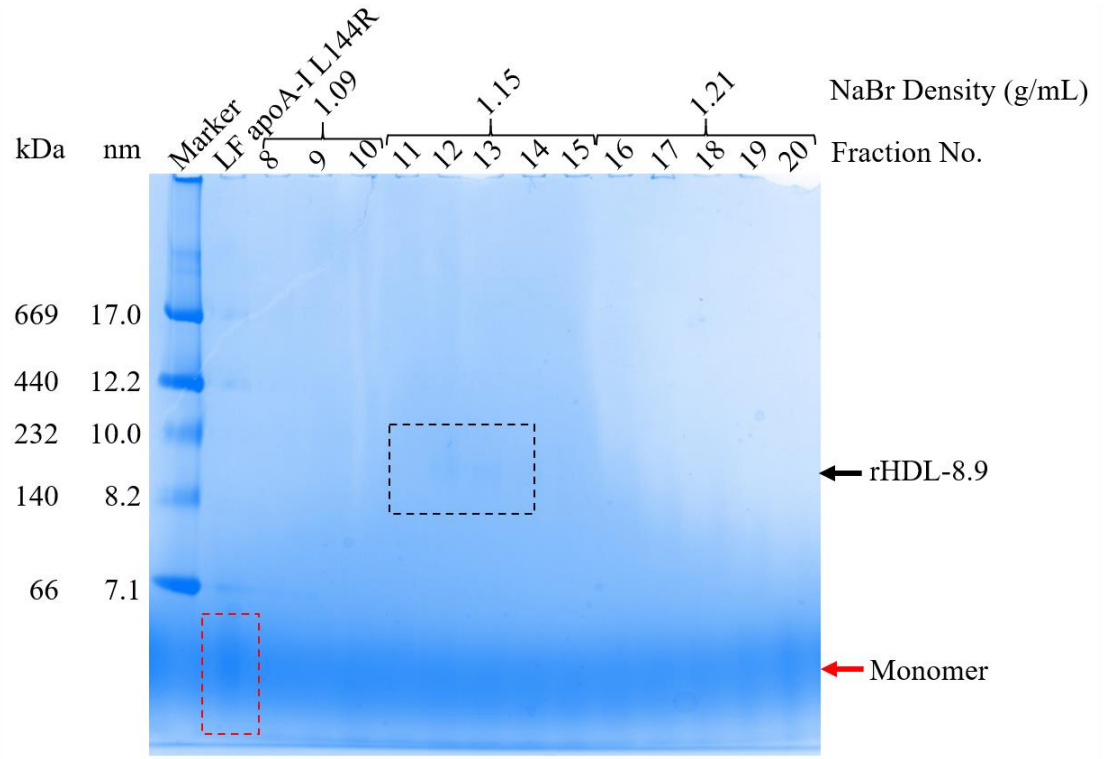

Figure 4.19. A 4-16 % NativePAGE gradient gel of the different stages of the rHDL POPC/L144R 200:2 (M/M) SG-UTC fractions. The sample lanes contain: LF apoA-I L144R, and separate 0.5 mL fractions shown by the fraction number for the NaBr density layers 1.09, 1.15 and 1.21 g/mL. The labels indicate the bands corresponding to monomeric LF apoA-I L144R and rHDL-L144R nanoparticles. The dashed box (black) outlines the position of the faint rHDL bands in fractions 12 and 13. The dashed box (red) indicates the approximate position of monomeric lipid-free apoA-I L144R.

The rHDL POPC:apoA-I L144R 200:2 (M/M) sample particle size was measured using DLS of the unfractionated nanoparticles (**Figure 4.20A**) but not the 1.15 g/mL pooled fractions due to samples produced at the time of DLS equipment availability. The average intensity-weighted particle diameter was 6.2 ±0.45 nm with a PdI of 0.78 ±0.04. This was significantly smaller in comparison to the NDGGE major particle band between 8.8-9.4 nm. The PdI of each measurement was >0.7 indicating the sample was quite polydisperse and not as suitable for DLS measurements as the SG-UTC fractionated nanoparticles of rHDL-WT and R173C. The larger PdI may be due to possible liposome formation at approximately 100 nm and dust contamination at approximately 5000 nm in the intensity-weighted particle distribution.

The TEM image of the rHDL-L144R fractionated Fl-UTC nanoparticles at the 36 µM protein concentration showed short rouleaux formation in a concentrated region of rHDL nanoparticles for diameter and thickness measurements (**Figure 4.20B**). The average diameter and thickness of the total 150 nanoparticles was 11.8 ±1.9 nm (**Figure 4.20C**) and 5.6 ±0.7 nm (**Figure 4.20D**), respectively.

The majority of the rHDL-L144R nanoparticles showed 74 % of particles between 8-13 nm in diameter, which was slightly lower than the rHDL-WT particle diameter distribution (81-83 %). The rHDL-L144R diameter histogram (**Figure 4.20C**) indicated a shifted distribution of larger rHDL particles 7.0-17.0 nm compared to the rHDL-WT of 6.5-14.0 nm. The thickness of the rHDL-L144R nanoparticles at 5.6 ±0.6 nm was the same as the rHDL-WT nanoparticles at 5.6 ±0.7 nm.

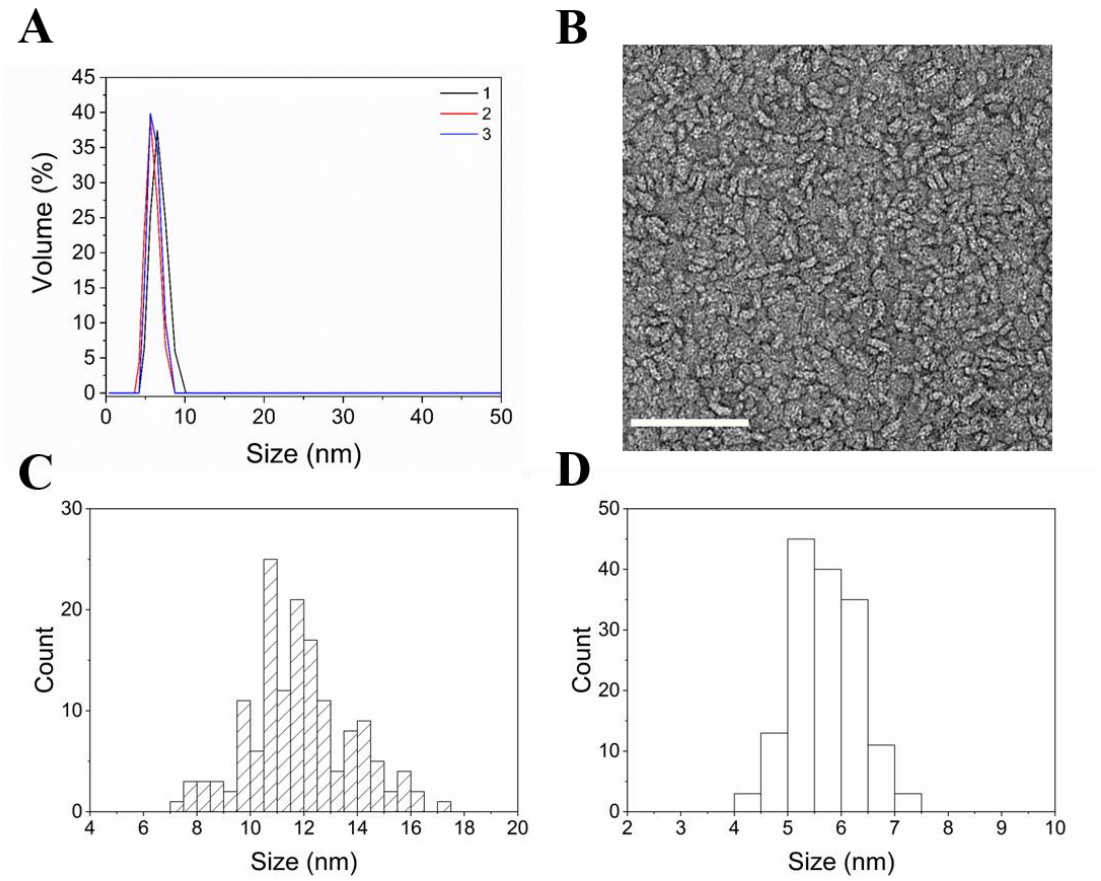

Figure 4.20. rHDL-L144R nanoparticle size measurements at the POPC:apoA-I L144R molar ratio of 200:2 (M/M). **A)** DLS of unfractionated rHDL nanoparticles, scans 1-3 of the volume-weighted particle distribution. **B)** A TEM image at 36 µM protein concentration of Fl-UTC fractionated nanoparticles stained with 2 % (w/v) UA. The scale bar is 100 nm at x 68 k magnification. Histograms of 150 rHDL-L144R nanoparticle **C)** diameter and **D)** thickness measurements at the 36 µM apoA-I concentration.

The diameter DLS measurement of the unfractionated rHDL-L144R was significantly smaller at ~6.2 nm. As the sample was unfractionated this could have contributed to a different particle diameter, but there was no observed band in the NativePAGE gel <7.6 nm diameter. The overall major rHDL-L144R nanoparticle distribution as imaged by

NDGGE (8.8-9.4 nm) and TEM (11.8 nm) showed similar particle sizes to the rHDL-WT NDGGE (8.6-9.8) and TEM (10.7 nm).

4.3.6 rHDL nanoparticles containing cholesterol

Discoidal rHDL-WT nanoparticles containing cholesterol (rHDL-C) were reconstituted with an initial POPC:cholesterol molar ratio of 10:1 (M/M), and varied POPC:apoA-I WT molar ratios of 300, 240, 200, and 60:2. The rHDL-C particles were characterised by NDGGE and cholesterol content was confirmed by a cholesterol concentration assay and calculated as the mol % of the total lipid in the sample.

The rHDL-C nanoparticles were characterised using NativePAGE to determine the particle sizes after sodium cholate removal (**Figure 4.21**). Across the various phospholipid:cholesterol:apoA-I WT ratios five different rHDL-C nanoparticles were produced and are indicated by the average diameter for each band. At each lipid:apoA-I ratio 300-160:2 the rHDL-C-9.7 WT nanoparticle population was predominant despite an increase in the total lipid + cholesterol:apoA-I ratio. The diameter range of the major rHDL-C-9.7 WT nanoparticle population was between ~9.0-10.1 nm.

Each lane was absent of lipid-free apoA-I indicating the apoA-I WT in each sample was completely lipid-bound. The higher lipid:cholesterol:apoA-I WT ratios 300:30:2 and 240:24:2 showed faint bands indicating the presence of rHDL-C-17.4 and -12.7 WT particle populations. In comparison, the lower phospholipid:apoA-I ratios at 200:20:2 and 160:16:2 showed the rHDL-C-8.4 WT nanoparticle population, whilst the 160:16:2 molar ratio also showed a faint band for the rHDL-C-7.5 WT nanoparticle population.

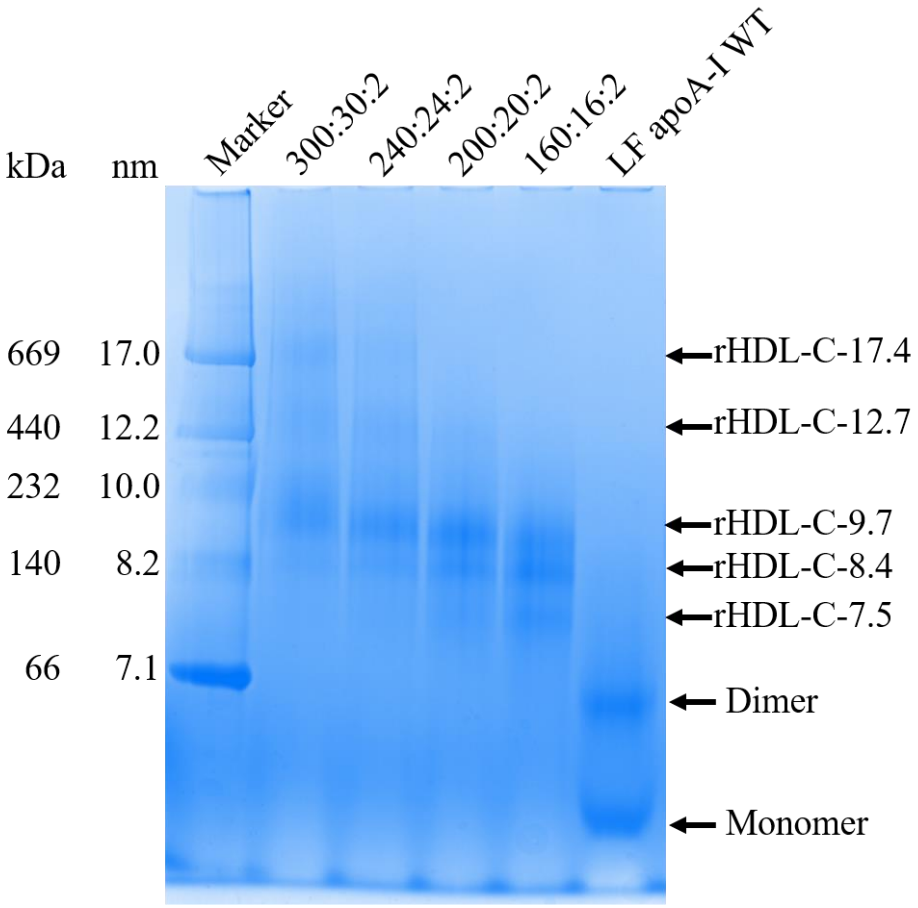

Figure 4.21. A 4-16% NativePAGE gradient gel of unfractionated POPC:cholesterol:apoA-I WT at the start molar ratios of 300:30:2, 240:24:2, 200:20:2, and 160:16:2 (M/M). The rHDL-C nanoparticles formed are indicated with the corresponding diameter (nm), and the lipid-free apoA-I WT monomer and dimer.

Unfractionated rHDL-C L144R and WT particles at the molar ratio of POPC:cholesterol:apoA-I of 200:20:2 were produced and analysed by NativePAGE (**Figure 4.22**). Both rHDL-C nanoparticle preparations with apoA-I WT and L144R showed bands at ~8.3 and 9.1 nm diameter. The major rHDL-L144R and WT nanoparticle band diameter range was between ~8.8-9.4 nm.

The lipid-free apoA-I WT protein showed approximately equal monomer to dimer shown by the comparable band size and band intensity. In comparison the LF apoA-I

L144R protein appeared predominantly monomeric with less intense dimer band staining relative to the apoA-I WT dimer band. Both proteins were stored at concentrations above 1.0 mg/mL which for apoA-I WT results in the formation of predominantly dimeric protein (Davidson et al., 1996; Giudice et al., 2017; Oda, 2017; Petrlova et al., 2016). This suggested that the apoA-I L144R may not have as strong a concentration dependent multimer formation relative to apoA-I WT. This was not explored further because this did not affect the rHDL nanoparticles formed which were comparable to the apoA-I WT and R173C rHDL nanoparticles.

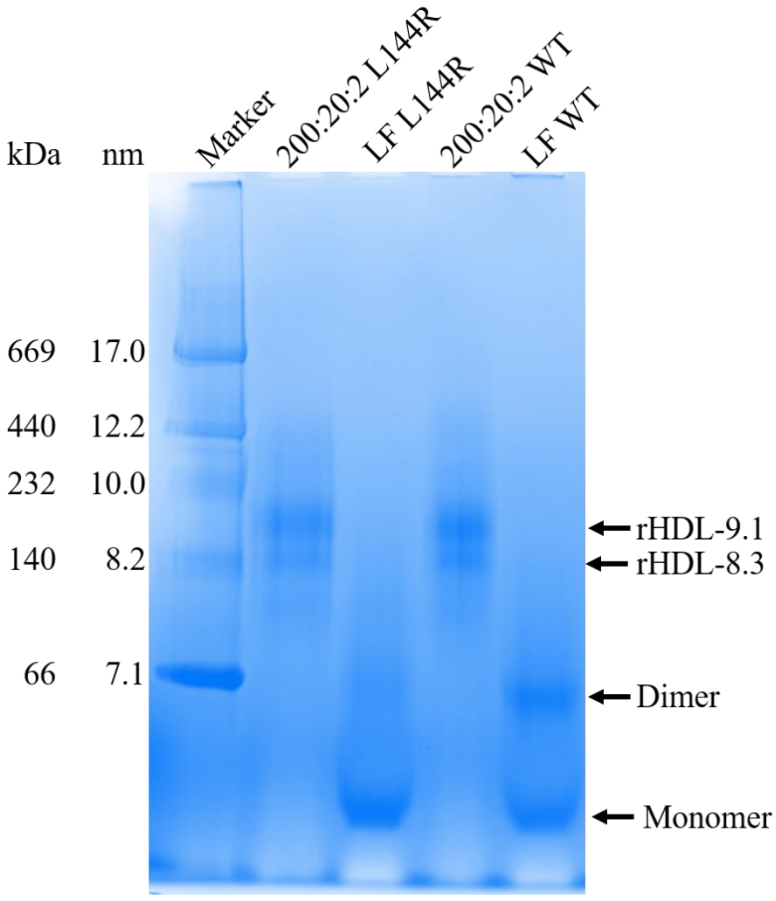

Figure 4.22. A 4-16% NativePAGE gradient gel of unfractionated POPC:cholesterol:apoA-I L144R/WT at the start molar ratio of 200:20:2 (M/M). The rHDL-C nanoparticles formed are indicated with the corresponding diameter (nm), and lipid-free monomeric and dimeric apoA-I WT and L144R.

The POPC:cholesterol:apoA-I molar ratio of 190:10:2 (M/M) (5 mol % cholesterol) was used to prepare rHDL-C WT, R173C and L144R nanoparticles and the particle size was analysed by NDGGE (**Figure 4.23**). The unfractionated rHDL-C WT 190:10:2 (M/M) sample showed rHDL with a major band at ~9.3 nm, with a diameter range of 8.8-9.6 nm. Minor faint bands indicated possible larger rHDL-WT nanoparticles at ~17.4 and 12.0 nm and a smaller particle at ~8.3 nm. The rHDL-C L144R sample contained rHDL of similar sizes and band intensity to rHDL-C WT, with the major rHDL-C L144R band between 8.7-9.3 nm. The rHDL-C R173C sample did not show any strongly stained bands suggesting the sample concentration was too low for NDGGE analysis but SG-UTC fractionation showed bands indicating rHDL-C nanoparticles were formed (**Figure 4.26A**).

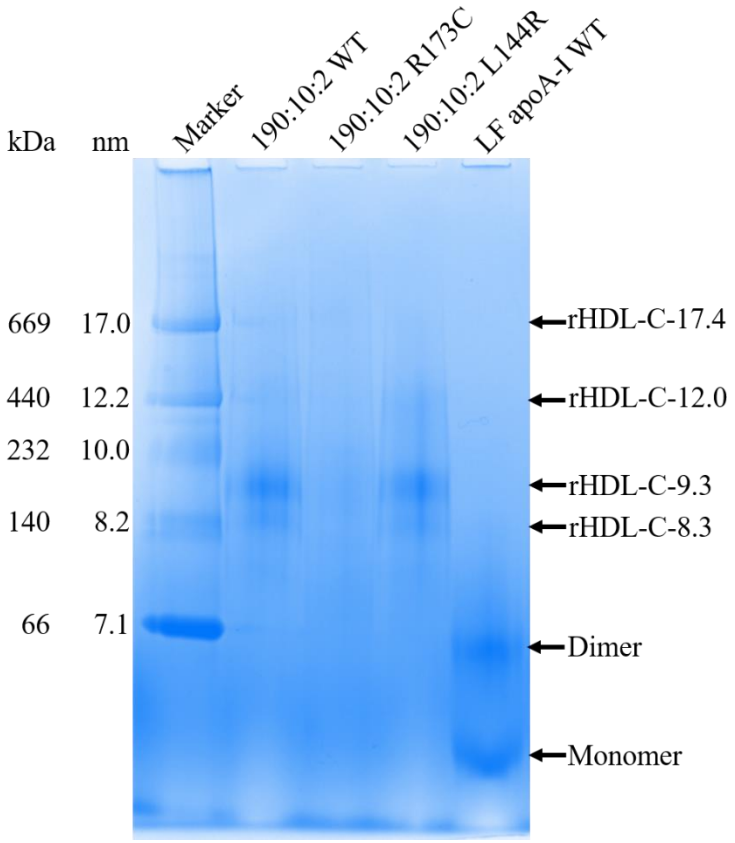

Figure 4.23. A 4-16% NativePAGE gel of unfractionated POPC:cholesterol:apoA-I WT/R173C/L144R at the molar ratio of 190:10:2 (M/M) post-sodium cholate removal, and lipid-free apoA-I WT.

Each sample was fractionated with SG-UTC and the separation of the particles showed rHDL-C-9.1 WT particles in the 1.15 g/mL density fractions between 8.6-9.4 nm in diameter (**Figure 4.24**). Fractions were pooled (11-12) for further analyses which did not contain the rHDL-C-8.1 WT particles indicated by a faint band in fractions 13-14.

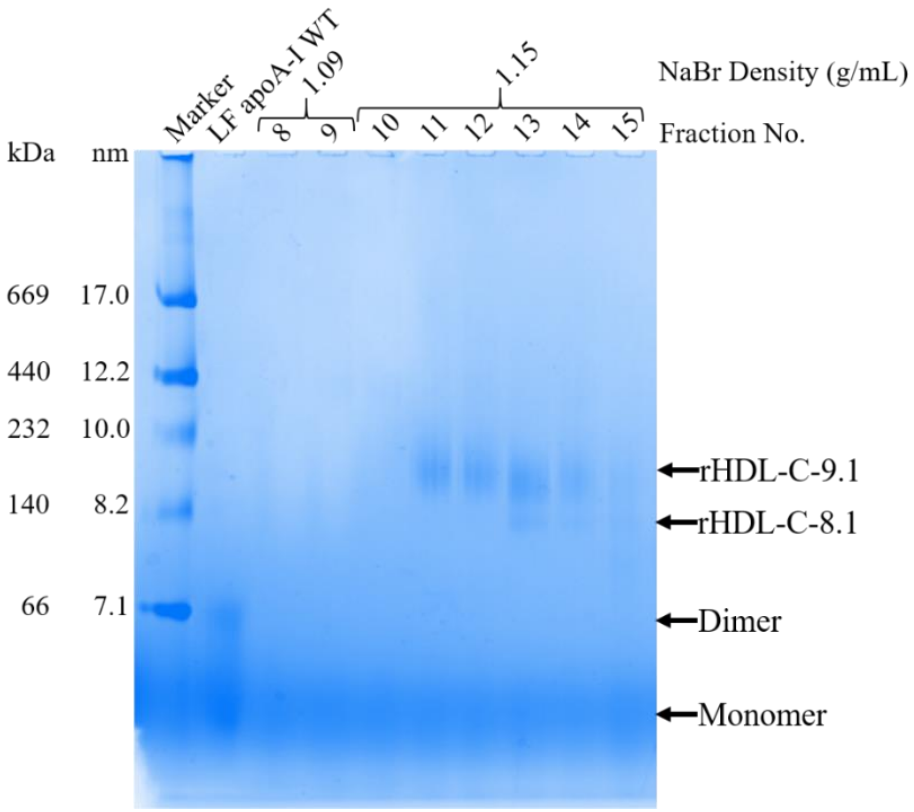

Figure 4.24. A 4-16 % NativePAGE gradient gel of the different stages of the rHDL POPC:cholesterol:apoA-I WT 190:10:2 (M/M) 1.09 and 1.15 g/mL SG-UTC fractions (0.5 mL). The labels indicate the bands corresponding to LF apoA-I WT monomer and dimer, and the rHDL-C-8.1 and -9.1 nm WT particles in the fractions.

The rHDL-C WT 190:10:2 (M/M) nanoparticles post-Fl-UTC at 36 µM protein concentration (**Figure 4.25A**) were analysed by TEM and showed the rHDL-C WT nanoparticles in concentrated dense regions. The rHDL-C WT nanoparticle average diameter and thickness were 11.8 ±1.8 nm and 5.8 ±0.7 nm, respectively. The size distribution indicated rHDL-C nanoparticles between ~8.5-15 nm diameter and ~4-8 nm thickness. The majority of particles were between 8-13 nm at 78 % of the total particles measured. The TEM diameter size distribution of the Fl-UTC fractionated rHDL-C WT nanoparticles suggested the sample contained the minor particle population at ~12.0 nm detected by NativePAGE before UTC (**Figure 4.23**). The

particles in TEM were larger than those indicated by NativePAGE analysis (**Figure 4.24**) due to difficulties in defining particle edges which could have led to an overestimation of the nanoparticle diameter. As a result of limited time, only the rHDL-C WT 190:10:2 nanoparticles were visualised by TEM.

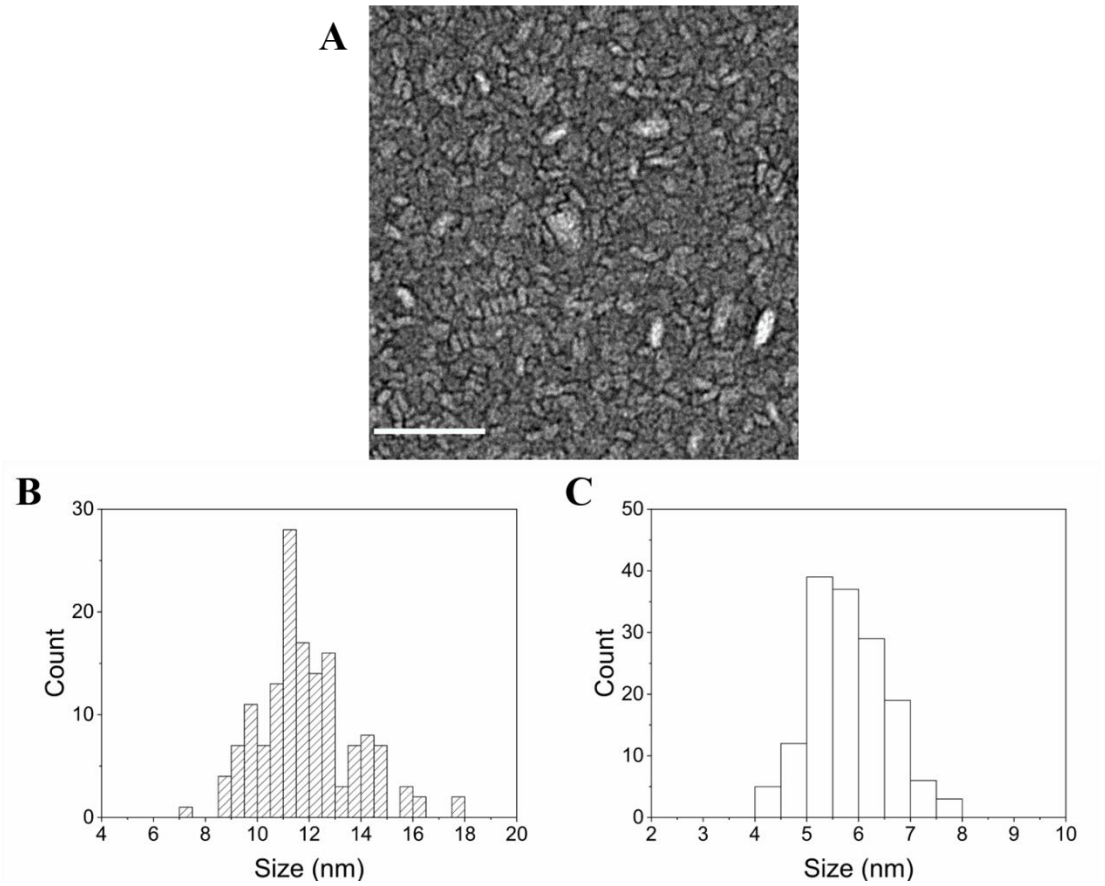

Figure 4.25. Fl-UTC pooled (2.5 mL) rHDL-C nanoparticles at the molar ratio of POPC:cholesterol:apoA-I WT 190:10:2 (M/M), **A)** A TEM image at x68 k magnification and 36 µM protein concentration. The corresponding diameter (**B**) and thickness (**C**) rHDL-C WT nanoparticle histograms of a total of 150 nanoparticles.

The NativePAGE gels of the 190:10:2 rHDL-C nanoparticles with apoA-I R173C (**Figure 4.26A**), and L144R (**Figure 4.26B**) show the predominant species in the 1.15 g/mL 0.5 mL fractions as rHDL-C-9.3, respectively. The major band particle diameter range for rHDL-C-9.3 R173C was between 8.7-9.7 nm and the rHDL-C-9.3 L144R

diameter range was between 8.7-9.3 nm. The 1.15 g/mL fractions showed faint bands of ~11.5 nm rHDL-C R173C particles, whilst the rHDL-C L144R fractions also contained particles ~15.9 nm in diameter. This suggested that with the 5 mol % cholesterol rHDL-R173C and L144R preparations the separation of fractions was not as defined in the 1.15 g/mL layer and in future the 1.21 g/mL fractions could contain more fractions to pool for rHDL-C-9.3 L144R particles.

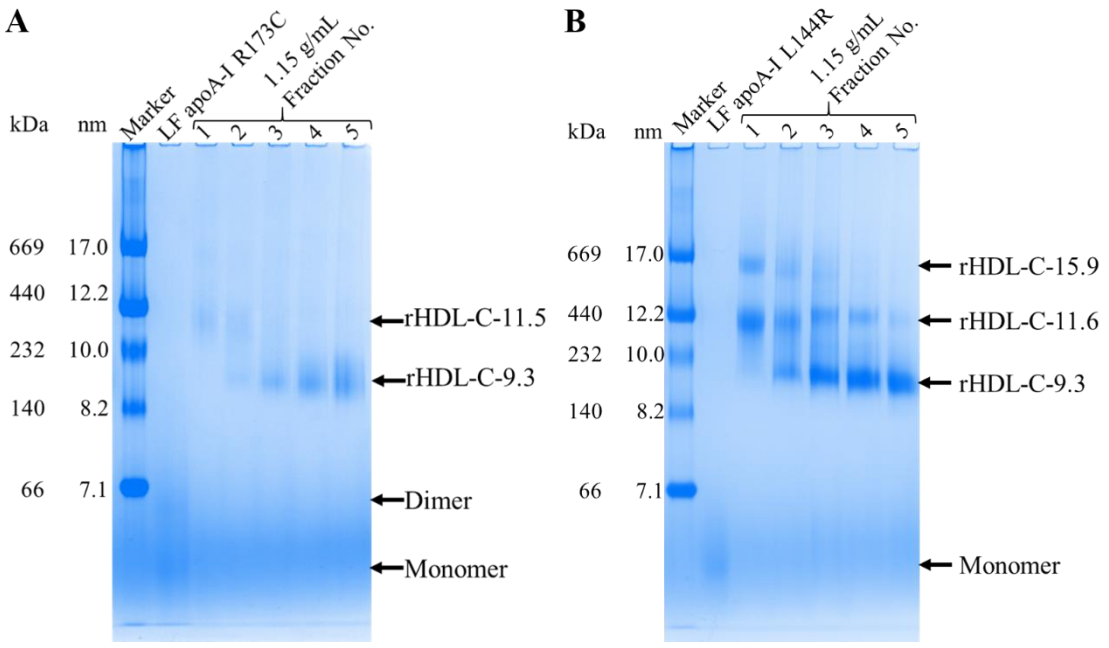

Figure 4.26. A 4-16 % NativePAGE gradient gel of the different stages of the rHDL particles at the molar ratio of POPC:cholesterol:apoA-I 190:10:2 (M/M) 1.15 g/mL SG-UTC fractions 1-5 (0.5 mL). **A)** apoA-I R173C with bands for LF apoA-I R173C monomer and dimer, and the rHDL-C-9.3 and -11.5 nm R173C particles in the fractions. **B)** apoA-I L144R with bands for LF apoA-I L144R monomer, and the rHDL-C-9.3, -11.6 and 15.9 nm L144R particles in the fractions.

4.3.7 Sample concentration of rHDL nanoparticles

The POPC:apoA-I 200:2 (M/M) rHDL protein and lipid concentration were measured before and after sodium cholate removal by dialysis, and after SG-UTC isolation of the predominant particles in each preparation in the 1.15 g/mL pooled fractions (**Table 4.7**). The start and final POPC:cholesterol:apoA-I molar ratios are in **Table 4.8** for the unfractionated rHDL-C WT, R173C and L144R nanoparticles. The lipid and cholesterol concentrations of the rHDL and rHDL-C nanoparticles were quantified using enzyme concentration assays measured in duplicate. The protein concentration was determined in triplicate using the NanoDrop^{TM} A_{280} absorbance measurements.

For the rHDL-WT, and L144R nanoparticle POPC:apoA-I 200:2 (M/M) samples the final molar ratios were similar before and after sodium cholate removal (**Table 4.7**). In comparison, the rHDL-R173C 200:2 sample molar ratio after dialysis was significantly lower at 44.7 ±2.3: 2 (M/M). Additionally, after SG-UTC and spin concentration the rHDL-WT and R173C 200:2 sample POPC measurements had a large relative standard deviation at 186.6 ±27.0 and 268.0 ± 107.0, respectively.

The respective NativePAGE gels did not detect a change in the estimated diameter range of the rHDL-WT, R173C or L144R nanoparticles between ~8.6 – 10.1 nm at each stage in the rHDL protocol (**see sections 4.3.3.1 and 4.3.5**). Therefore, the fractionated rHDL-WT and rHDL-R173C molar ratios, and post-dialysis rHDL-R173C values were considered anomalous. Whereas the rHDL-L144R 200:2 nanoparticle POPC molar ratio showed a lower POPC:apoA-I molar ratio with a smaller relative SD at 140.5 ±4.7: 2.

The final POPC:apoA-I molar ratios with the lowest relative SD were used as the overall estimated molar ratio for the rHDL-WT, R173C and L144R samples. Henceforth, the

rHDL-WT, R173C and L144R samples will be referred to as the estimated molar ratio at ~200:2 for reference.

Table 4.7. The rHDL-WT/R173C/L144R 200:2 (M/M) POPC: apoA-I sample concentrations (mM) and final molar ratios ± relative SD. The POPC sample concentration (n = 2) ± SD and the apoA-I concentration (n = 3) SD were all ≤0.001.

Sample	Concentration (mM) ±SD		Molar ratio (M/M) ± relative SD
	POPC	apoA-I	
apoA-I WT			
Before dialysis	6.0 ±0.059	0.061	197.7 ±2.1:2
After dialysis	5.0 ±0.032	0.050	202.2 ±3.6:2
1.15 g/mL spin conc.	14.9 ±2.151	0.159	186.6 ±27.0 :2
apoA-I R173C			
Before dialysis	5.0 ±0.009	0.051	197.5 ±0.9:2
After dialysis	1.0 ±0.052	0.045	44.7 ± 2.3:2
1.15 g/mL spin conc.	14.4 ±5.754	0.108	268.0 ± 107.0:2
apoA-I L144R			
Before dialysis	5.3 ±0.037	0.052	202.9 ±2.1:2
After dialysis	4.7 ±0.027	0.045	207.6 ±1.7 :2
1.15 g/mL spin conc.	9.4 ±0.312	0.134	140.5 ±4.7:2

The unfractionated rHDL-C WT, R173C and L144R nanoparticle final POPC:cholesterol:apoA-I molar ratios and mol % cholesterol are summarised in **Table 4.8**.

Table 4.8. The rHDL-C WT/R173C/L144R nanoparticle POPC and cholesterol concentration (mM) (n = 2) are ±SD post sodium cholate removal by dialysis. The apoA-I protein concentration (n = 3) SD for each sample was ≤0.001. The cholesterol mol % is in parentheses.

		Concentration (mM) ±SD			
ApoA-I	**Start molar ratio (M/M)**	**POPC**	**Cholesterol**	**ApoA-I**	**Final molar ratio (M/M) ± relative SD**
WT	300:30:2 (10)	2.9 ±0.127	0.41 ±0.086 (14.2)	0.022	264.7 ±12.1: 37.6 ±8.0: 2
	240:24:2 (10)	3.7 ±0.030	0.41 ±0.052 (11.0)	0.031	241.6 ±2.1: 26.5 ±3.4: 2
	200:20:2 (10)	3.8 ±0.140	0.51 ±0.012 (13.5)	0.041	186.1 ±6.9: 25.2 ±0.6: 2
	160:16:2 (10)	3.2 ±0.035	0.36 ±0.074 (11.2)	0.043	149.9 ±1.9: 16.8 ±3.5: 2
R173C	190:10:2 (5)	4.4 ±0.195	0.37 ±0.013 (8.5)	0.045	193.6 ±8.9: 16.4 ±0.6: 2
L144R	190:10:2 (5)	1.1 ±0.163	0.06 ±0.007 (5.4)	0.014	166.3 ±24.4: 8.9 ±1.0: 2
	190:10:2 (5)	3.9 ±0.333	0.31 ±0.003 (7.9)	0.038	205.6 ±17.4: 16.3 ± 0.2: 2
	200:20:2 (10)	4.1 ±0.004	0.56 ±0.043 (13.7)	0.047	172.4 ±2.6: 23.7 ± 1.9: 2

In the 10 mol % cholesterol rHDL-C WT sample the final POPC:cholesterol:apoA-I WT molar ratio decreased from ~265:38:2 to 150:17:2 as the start POPC:cholesterol:apoA-I WT molar ratio decreased (300:30:2 to 160:16:2). This coincided with a decrease in the predominant rHDL-C WT nanoparticle diameter range as estimated by NDGGE from 9.3 – 10.1 nm to 8.7 – 9.3 nm (**Figure 4.21-4.22**). The rHDL-C L144R 200:20:2 (10 mol % cholesterol) final molar ratio of 172.4 ±2.6: 23.7 ± 1.9: 2 was slightly lower than the rHDL-C WT 186.1 ±6.9: 25.2 ±0.6: 2 final molar ratio. The rHDL-C WT and L144R 200:20:2 samples both contained ~13.5 mol % cholesterol, with a slightly lower overall POPC content in the rHDL-C L144R nanoparticles.

In the rHDL-C WT and L144R 190:10:2 (5 mol % cholesterol) samples the final molar ratios were similar at 193.6 ±8.9: 16.4 ±0.6: 2 (8.5 mol % cholesterol) and 205.6 ±17.4: 16.3 ± 0.2: 2 (7.9 mol % cholesterol), respectively. However, the rHDL-C R173C final molar ratio was 166.3 ±24.4: 8.9 ±1.0: 2 which suggested the rHDL-C R173C nanoparticles contained less cholesterol at ~5.4 mol %. The differences detected in the rHDL-C WT, R173C and L144R 190:10:2 nanoparticle final molar ratios did not reflect a change in the predominant diameter detected by NDGGE of crude and fractionated samples between 8.6 – 9.7 nm (**Figure 4.23, 4.24, 4.26**).

Similar to the rHDL samples without cholesterol the rHDL-C nanoparticles in this work will be referred to by the estimated start molar ratio such as 200:20:2 for reference in further chapters.

4.4 Discussion

The primary purpose of this chapter was to develop a method to produce homogenous rHDL nanoparticles of similar size containing apoA-I WT, R173C or L144R at the molar ratios of POPC:±cholesterol:apoA-I of 200:2, 200:20:2 and 190:10:2.

4.4.1 rHDL nanoparticle fractionation

The reliability of two methods for preparing size-fractionated rHDL particles, density-based UTC and SEC, were assessed, using the POPC:apoA-I WT 200:2 molar ratio as the test system. To isolate the predominant rHDL-WT nanoparticles between ~8.6-9.8 nm according to NDGGE.

SEC was limited by the relatively low rHDL apoA-I WT protein concentrations recovered in fractions, which prevented size measurements by NDGGE. The predominant rHDL-WT population SG-UTC yield was approximately 2-fold higher than the Fl-UTC and SEC fractionation methods. Whereas Fl-UTC fractionation had the highest overall sample recovery at ~20 % higher than both SEC and SG-UTC, due to the reduction in density layers in the preparation.

rHDL-C WT 160:8:2 nanoparticles of a similar diameter at ~9.6 nm have been produced with a yield of ~32.8 % relative to starting apoA-I concentration (Cavigiolio et al., 2008). In this work, the yield of rHDL nanoparticles was ~13 % using both the Fl-UTC and SEC purification methods. Interestingly, the SG-UTC purified rHDL nanoparticle yield was similar to the literature comparison at ~32 %. However, it is clear from this yield that further optimisation would be beneficial to scaling up rHDL nanoparticle preparation for further characterisation.

The density-based UTC fractionation of the rHDL-WT 200:2 nanoparticles indicated the successful removal of unreacted lipid-free apoA-I from the rHDL nanoparticles. This was important for future characterisation as lipid-free apoA-I could interfere with labelled-protein NMR measurements or lipid-bound protein secondary structure analyses such as circular dichroism. Therefore, it was decided that rHDL nanoparticles preparation by sodium cholate detergent mediated dialysis, followed by SG- or Fl-UTC, was the more efficient method.

A challenge of the rHDL nanoparticle preparation was the loss of apoA-I in the rHDL SG-UTC method (**section 4.3.4.2**), specifically for the preparation of ^{13}C-CP-MAS SS NMR PEG-precipitated rHDL samples containing dual-labelled apoA-I. Stages during which sample loss could occur were sample spin concentration or during dialysis. Alternatives to spin concentration could be lyophilisation or a buffer exchange column to remove sodium cholate and unreacted lipids initially, or NaBr after SG-UTC. Additionally, optimisation of the unlabelled and labelled protein expression yields would be beneficial to scale up the rHDL nanoparticle sample preparation.

4.4.2 Evaluation of the rHDL nanoparticle size

The unfractionated and UTC fractionated rHDL (200:2 POPC:apoA-I) size distributions with and without cholesterol are summarised in **Table 4.10** and **Table 4.11**, respectively. The previously published rHDL/rHDL-C WT diameters, as analysed by NDGGE and TEM, are summarised in **Table 4.9** for a direct comparison to the rHDL nanoparticles produced in this work.

The unfractionated rHDL containing apoA-I WT or the atheroprotective apoA-I mutants R173C and L144R showed a similar rHDL nanoparticle size range according to NDGGE with a major band between 8.2 – 10.0 nm in diameter in each case. The

NativePAGE gels indicated the presence of minor rHDL populations between approximately 7.4 – 8.8, ~11.6-12.2 and 16.2 nm, and the presence of lipid-free apoA-I.

Previously, rHDL-R173C nanoparticles produced with 100 % dimeric apoA-I R173C produced particles 7.8 and 12.5 nm in diameter only (Calabresi et al., 1997b). In this study, the recombinant apoA-I R173C expression was a mixture of monomer and dimer as determined by NativePAGE (**see Chapter 3**, **section 3.3.3.2**, **Figure 3.26**) which suggested the major rHDL-R173C nanoparticles formed could be between 7-12 nm, rather than predominantly small particles or at the restricted sizes of 7.8 or 12.5 nm.

The rHDL-WT nanoparticle diameters were similar to previously published particle diameters at the POPC:apoA-I WT 200:2 molar ratio measured by NDGGE of ~9.8 nm and 10.2 nm (**Table 4.9**) (Chen et al., 2009; Gu et al., 2010).

The TEM measurements of the rHDL-WT and L144R nanoparticle average diameters and thicknesses were ~11 and 5.6 nm, respectively. The rHDL-R173C nanoparticles were not measured by TEM as the nanoparticles appeared concentrated with the stain which resulted in low image resolution. Additionally, rouleaux formation occurred at the higher rHDL-WT protein concentration of 36 µM, and a lower concentration (9 µM) was necessary to observe individual particles with their faces exposed. This suggested the rHDL-WT nanoparticles stained with uranyl acetate form rouleaux dependent upon the rHDL sample concentration (Lau and Middleton, 2020). This observation will be central to the interpretation of the NMR results in **Chapter 6**.

Table 4.9. The range of previous discoidal rHDL-WT nanoparticle sizes produced in sample preparations containing POPC:±cholesterol:apoA-I WT at different molar ratios. In preparations of mixed particles, the major band by NDGGE is highlighted in bold.

POPC:±cholesterol:apoA-I WT		Diameter (nm)		Reference
Start	**Final**	**NDGGE**	**TEM**	
58:2	64:2	9.4 ±0.5	9.3 ±1.5	(Sparks et al., 1992b)
118:2	130:2	9.8 ±0.5	9.9 ±1.5	
202:2	160:2	10.2 ±0.5	11.2 ±1.5	
314:2	256:2	10.6 ±0.5	12.1 ±1.5	
160:2		7.6	7.6 ±1.6	(Chen et al., 2009)
		9.8	9.8 ±1.7	
200:2		9.8		
50-100:2		7.3, 9.3-9.5, **10.2**		(Gu et al., 2010)
140-180:2	-	9.3-9.5, **10.2**	-	
200-300:2		**10.2**, 12.2, 17.0		
60: 4: 2	68: 4: 2	7.8 ±0.1	6.9 ±0.9	(Cavigiolio et al., 2008)
	105: 6: 2	8.4 ±0.4	8.0 ±1.1	
160: 8: 2	181: 8: 2	9.6 ±0.4	9.4 ±0.9	
320:16:2	281: 9: 2	12.2 ±0.8	12.2 ±0.8	
	348: 13: 2	17.0 ±1.6	17.0 ±1.6	
200: 20: 2	172: 18: 2	**10.0**, 12.2		(Daniil et al., 2013)
		9.6-10.4, 11.8-12.2		(Xu et al., 1997)
200: 20: 2	218: 17: 2	9.6	(DLS) 10.8	(Wu et al., 2007)
	210: 15: 2	9.6 ±0.1	11.3 ±0.2	(Wu et al., 2009)
190:10:2	200: 10: 2	**9.6-9.7**, 12.2-17.0		(Han et al., 2005)

The standard deviation of the TEM measurements indicated the rHDL nanoparticles fractionated by Fl-UTC contained greater heterogeneity than the size range indicated on the NativePAGE gel between 8.7 – 9.5 nm in diameter (**Table 4.10**). The TEM

measurements of dried nanoparticles were probably an overestimate as the particle thickness was greater than an average hydrated POPC bilayer at ~4.1 nm (Kucerka et al., 2005; Lau and Middleton, 2020). In NDGGE the estimated Stokes diameter was calculated from the relative mobility of globular (i.e., spherical) protein standards which has been suggested to result in an underestimated diameter as the rHDL nanoparticle shape is discoidal (Forte et al., 1995).

Table 4.10. The unfractionated and SG-UTC fractionated major particle size diameters of the POPC: apoA-I WT/R173C/L144R rHDL nanoparticles prepared at the 200:2 molar ratio. The TEM rHDL particles were Fl-UTC fractionated particles.

ApoA-I	Diameter (nm)				
	Unfractionated		Fractionated		
	NDGGE	DLS	NDGGE	DLS	TEM
WT	8.2 – 10.0	11.3 ±0.2	8.6 – 9.8	12.8 ±0.9	10.7 ±2 x 5.6 ±0.7
R173C	8.8 – 10.0		8.6 – 10.1	13.8 ±0.3	
L144R	8.8 – 9.0	6.2 ±0.45	8.8 – 9.4		11.8 ±1.9 x 5.6 ±0.7

The rHDL-WT 200:2 nanoparticle DLS average diameter at ~11 nm was similar to the TEM measured diameter and greater than the NDGGE estimated diameter range. The rHDL-WT 200:2 nanoparticle hydrodynamic diameter range according to NDGGE was between 8.2 – 10 nm (**Table 4.10**). In comparison the hydrodynamic diameter determined by DLS was 11.3 nm. A difference in the hydrodynamic diameter of rHDL measured by NDGGE versus DLS has been observed elsewhere (Wu et al., 2009; Wu

et al., 2007), rHDL-C WT 200:20:2 nanoparticles had diameters of 9.5 – 9.7 nm according to NDGGE and 10.8 – 11.5 nm determined by DLS.

The rHDL-L144R DLS hydrodynamic diameter was ~6.2 nm which was significantly smaller than both TEM (11.8 nm) and NDGGE (8.8 – 9.4 nm) measured diameters of the same particles and the rHDL-WT/R173C nanoparticles. The reason for this difference in the rHDL-L144R nanoparticle size measured by DLS is unclear, but, as will be shown in **Chapter 6**, is probably related to the shapes of the particles in the two preparations.

The rHDL-C WT nanoparticles containing 10 mol % cholesterol between the molar ratios of POPC:apoA-I WT of 300-160:2 showed a similar major particle size distribution between 8.7 – 10.1 nm overall (**Table 4.11**). The rHDL-WT/L144R nanoparticles at the 200:20:2 molar ratio produced major rHDL nanoparticles of similar diameter between ~8.8 – 9.7 nm. This was analogous to the ~9.5 – 9.7 nm diameter of the rHDL-C WT 200:20:2 nanoparticles produced by Wu *et al*. (Wu et al., 2009; Wu et al., 2007).

Additionally, the 190:10:2 rHDL-C WT/R173C/L144R nanoparticles NDGGE diameters showed similar diameters with respect to the different apoA-I protein (8.7 – 9.7 nm). The rHDL-C 190:10:2 nanoparticle diameters were comparable to previous study rHDL-C WT nanoparticle diameters with similar molar ratios of 9.2 – 10.0 nm and 9.6 – 9.7 nm (Cavigiolio et al., 2008; Han et al., 2005).

In the rHDL nanoparticle preparations there was a degree of heterogeneity in the unfractionated and UTC fractionated rHDL nanoparticles detected by DLS and TEM. The NativePAGE gel diameter range estimates showed the major rHDL nanoparticles with and without cholesterol particle populations were comparable.

Table 4.11. The unfractionated major particle size diameters by NDGGE of the POPC:cholesterol:apoA-I WT/R173C/L144R rHDL-C nanoparticles prepared at the molar ratios indicated. [a]SG-UTC, [b]TEM Fl-UTC fractionated.

POPC: cholesterol: apoA-I (M/M)	Diameter (nm)		
	apoA-I WT	L144R	R173C
300:30:2	9.3 – 10.1		
240:24:2	9.0 – 9.7		
200:20:2	9.0 – 9.7	8.8 – 9.4	
160:16:2	8.7 – 9.3		
190:10:2	8.8 – 9.6, 8.6 – 9.4[a] 11.8 ±1.8 x 5.8 ±0.7[b]	8.8 – 9.6, 8.7 – 9.3[a]	8.7 – 9.7[a]

This variation was expected to an extent as previous studies of density-based UTC fractionated rHDL-WT particles prepared at similar molar ratios (200:2, 160:2) diameters were 11.2 ± 1.5 nm (Sparks et al., 1992b) and 9.8 ±1.7 nm (Chen et al., 2009). Both studies utilised these discoidal rHDL nanoparticles (**Table 4.9**) for solution state NMR apoA-I WT structural studies of the lysine conformation "microenvironment" variation (Sparks et al., 1992b) and tertiary apoA-I conformation differences (Chen et al., 2009).

In contrast, previous studies of nanodisc diameters determined with TEM of DMPC:MSP1D1 (apoA-I Δ(1-54)) 160:2 (mol/mol) and DMPC:MSP1ΔH5 100:2 (mol/mol) rHDL nanoparticles were 9.5 ±1.1 and 8.2 ±0.6 nm, respectively, after SEC fractionation (Hagn et al., 2013). The latter particles were characterised by solution-state NMR to produce a discoidal nanodisc structure model (**Figure 1.14**) (Bibow et al.,

2017). This suggested the heterogeneity could be further reduced by SEC however due to limited time this method was not tested further.

4.4.3 Summary

In conclusion, the rHDL and rHDL-C WT/R173C/L144R nanoparticle major diameters (**Table 4.10** and **Table 4.11)** were similar to the literature plasma HDL WT and rHDL-WT nanoparticle diameters (**Table 4.1** and **Table 4.9**). The SG-UTC fractionated rHDL nanoparticles by NDGGE showed separation from lipid-free apoA-I with partial separation of the particle sizes outside of the major band range (~8 – 10 nm). The TEM particle diameter measurements confirmed partial separation from the minor nanoparticle sizes. Furthermore, the yield of the rHDL nanoparticle preparation required further optimisation.

Overall, the formation of rHDL nanoparticles of a similar size distribution containing the apoA-I R173C and L144R mutants allowed for a direct comparison to rHDL-WT nanoparticles. The nanoparticles were suitable for further structural and functional characterisation as previous solution-state NMR studies contained a similar level of heterogeneity, and the UTC fractionation separated the rHDL nanoparticles from lipid-free apoA-I. Additionally, this is the first preparation of rHDL-L144R nanoparticles for structural analyses at the POPC:±cholesterol:apoA-I L144R molar ratios of 200:2 and 200:20:2, with only a NativePAGE gel previously run of rHDL-L144R nanoparticles at the 190:10:2 molar ratio (~10 nm) (Fiddyment et al., 2011). Hence the molar ratios of rHDL-WT were used as a basis for producing rHDL-L144R nanoparticles of similar size and composition in this study.

5 ApoA-I structure in rHDL

5.1 Introduction

The atheroprotective apoA-I mutants, L144R and R173C, could contain structural differences in the apoA-I conformation compared to apoA-I WT in rHDL nanoparticles. The mutation in apoA-I R173C enables the formation of disulphide bonded dimers and has been suggested to exist in a "locked" shifted registry in rHDL-R173C nanoparticles (Klon et al., 2000). ApoA-I L144R contains an additional positive residue compared to apoA-I WT in the residue region 143-164 suggested to be key to interactions with the enzyme LCAT in RCT (Sorci-Thomas et al., 1993). Therefore, structural differences in the rHDL nanoparticle protein constituent could affect functionality in reverse cholesterol transport, e.g., in cholesterol incorporation/transport, and interaction with enzymes.

This chapter focuses on the apoA-I structural comparison of the rHDL nanoparticles characterised in **Chapter 4**, by varying the lipid:protein molar ratio e.g., 200:2, the respective apoA-I protein WT, R173C or L144R, and introducing cholesterol rHDL-C. The aim of the work is to find molecular clues, either in the structure of apoA-I or in the morphology (**Chapter 6**) of the rHDL particles, that may explain the functional differences between apoA-I WT and the atheroprotective mutants.

There have been a variety of experimental techniques used to analyse the structure of apoA-I WT in rHDL nanoparticles as described in **Table 1.3** (**Chapter 1**, **section 1.8**) such as CD, solution and SS NMR. In comparison, experimental structural analysis of apoA-I R173C in solution and HDL has been limited to lysine cross-linking with MS,

HDX MS and CD (Bhat et al., 2010; Calabresi et al., 1997b; Chetty et al., 2012; Giudice et al., 2017). Furthermore, the structure of apoA-I L144R in rHDL nanoparticles has not been studied by structural techniques such as SS NMR or CD. At the time of writing, a structure-function study comparing LF apoA-I WT to L144R and respective rHDL 200:20:2 nanoparticles was published containing comparative CD data (Gkolfinopoulou et al., 2020).

Earlier solution NMR studies of apoA-I WT in discoidal rHDL nanoparticles of different sizes focussed on lysine residue conformation (Sparks et al., 1992b). The discoidal rHDL lysine residue conformations were suggested to be in different "microenvironments" such as in a nonpolar or polar α-helix face dependent on particle size 9.3 - 12.1 nm diameter (Sparks et al., 1992b). Additionally, ^{1}H-^{15}N apoA-I cross-peak differences were observed in 2D solution NMR spectra of apoA-I residues in 7.8 and 9.8 nm diameter discoidal rHDL nanoparticles (Chen et al., 2009). This suggested the overall tertiary apoA-I conformation differed between the nanoparticles of different sizes (Chen et al., 2009).

Solution NMR has been used for structural analysis of membrane proteins embedded in membrane scaffold protein 1 (MSP1) or apoA-I Δ(1-43), and truncations of MSP1 nanodiscs (Bayburt et al., 2002), which mimic a membrane environment (Hagn et al., 2013). Interestingly, Bibow *et al*. produced an advanced structural model of lipid-bound apoA-I Δ(1-54, and 121-142) in nanodiscs using high resolution solution NMR with EPR (Bibow et al., 2017) (**see Chapter 1**, **section 1.6.3**, **Figure 1.14**). This included residue-specific truncated apoA-I secondary structure assignment with inter- and intramolecular distance constraints (Bibow et al., 2017). However, solution NMR studies of rHDL with full-length apoA-I are challenging because the larger size of the

particles, and slower rotational diffusion, gives rise to line broadening and loss of resolution. Higher resolution can be obtained using ^{13}C and ^{15}N SS NMR with magic-angle spinning.

SS NMR has been used to analyse the structure of truncated apoA-I in PEG-precipitated nanodiscs, with analysis by CP-MAS 2D ^{13}C-^{13}C correlation spectra (Li et al., 2006; Mors et al., 2013). The PEG-precipitated nanodiscs have been established as a viable option for structural studies of embedded proteins such as human CYP3A4 (Kijac et al., 2007) and proteorhodopsin (Mors et al., 2013). CP-MAS SS NMR and the corresponding 2D ^{13}C-^{13}C correlation spectra of dual-labelled MSP1 (apoA-I Δ(1-43)) can be used to determine the overall protein secondary structure in large molecular weight nanodiscs (Li et al., 2006).

The solution and SS NMR studies have focussed on the structure of truncated apoA-I WT rather than discoidal rHDL nanoparticles containing full-length apoA-I WT. Therefore, high-resolution SS NMR of full-length apoA-I in rHDL nanoparticles could validate previous HDL models based on lipid-free truncated apoA-I crystal structures (**e.g. see Chapter 1**, **section 1.6.1**-**1.6.2**) (Bhat et al., 2010; Gursky, 2013; Gursky et al., 2013).

Another technique that has been used to analyse apoA-I secondary structure in rHDL is CD spectroscopy (**see Chapter 2**, **section 2.1)**. The secondary structure and thermal stability of LF and rHDL bound apoA-I WT and R173C have been estimated using CD spectroscopy (**see Table 5.4 – 5.5**, **and refs therein**). Interestingly, Giudice *et al*. used synchrotron radiation CD (SRCD) to examine the secondary structure and thermal stability of ~9.6 nm diameter ~200:2 (M/M) DMPC WT and R173C rHDL nanoparticles (Giudice et al., 2017). SRCD has a significantly better signal-to-noise

ratio at wavelengths below 200 nm (Giudice et al., 2017; Wallace and Janes, 2009). Therefore, the SRCD analysis was used as a comparison for the SSE and melting temperatures measured for the rHDL nanoparticles prepared in this work.

Another aspect to consider is the prolonged atomistic MD simulations of nascent HDL at the POPC:cholesterol:apoA-I WT 200:20:2 and 160:24:2 molar ratios on multi-microsecond timescales (10 and 20 μs) (Pourmousa et al., 2018). The simulations revealed deviations from a strictly planar discoidal lipid bilayer and belt-like apoA-I morphology (**see Chapter 1**, **Figure 1.15**) (Pourmousa et al., 2018), but experimental verification is needed.

To summarise, knowledge of the intact protein structure of WT apoA-I in HDL particles is incomplete. The effective combination of experimental and computational studies could aid in understanding the structure of rHDL nanoparticles. Furthermore, less is known about the structural origins of the atheroprotective properties of the L144R and R173C apoA-I mutants. Therefore, it was necessary to compare the apoA-I WT with the apoA-I mutants structure to search for structural evidence of the atheroprotective function.

5.1.1 Aims

The aim of the work described in this chapter is to detect structural differences in apoA-I WT, L144R and R173C when incorporated into rHDL nanoparticles. This was addressed using CP-MAS SS NMR and CD to determine structural properties of the rHDL nanoparticle apoA-I proteins. To search for hints in the atheroprotective apoA-I protein structures which could affect the rHDL nanoparticle functions.

5.2 Material and methods

The rHDL nanoparticles characterised in this chapter were prepared as described in **Chapter 4**. The following methods for rHDL nanoparticle apoA-I structural characterisation are published in (Lau and Middleton, 2020).

5.2.1 CD of lipid-free and rHDL bound apoA-I

The lipid-free (LF) and fractionated rHDL apoA-I WT/R173C/L144R sample protein secondary structure was investigated using CD with a Chirascan plus qCD spectrometer (Applied Photophysics). In each sample loaded into a quartz cuvette (Starna scientific) the apoA-I concentration was 3.6 µM with a total volume of 300 µL in rHDL buffer, pH 7.4. The following conditions were used for measurement: temperature 37^{o}C, path length 1 mm, bandwidth 1 nm, time per point 0.5 s, step size 1 nm, and wavelength range of 180 – 260 nm.

The background CD signal scans in triplicate (n = 3) were subtracted from CD spectra before sample analysis. The rHDL and LF sample backgrounds were POPC small unilamellar vesicles diluted to the sample lipid concentration in rHDL buffer pH 7.4 or rHDL buffer only, respectively. Preliminary scans (n = 3) at varied protein concentration (1.8, 3.6, 7.2, 18 µM) determined the appropriate apoA-I sample concentration was 3.6 µM to detect a CD signal whilst minimising noise (data not shown).

Preparations of rHDL containing apoA-I WT or R173C or L144R, and the lipid-free proteins were incubated with agitation at 3.6 µM protein concentration for 24 hours at 37°C. The protein concentration was taken before and after to determine the amount of apoA-I precipitation. CD spectra were taken at 0 and 24 hours at 37°C. However, after

24 hours the protein concentration was below 3.6 μM and resulted in too much noise therefore only the before incubation spectra are shown.

Each sample was scanned in triplicate for secondary structure estimation (SSE). To determine if the samples were stable for multiple UV measurements the samples were scanned 50 times. The CDApps software was generously provided by Drs G. Siligardi, R. Hussain, and T. Javorfi at B23, Diamond Light Source (Oxford, UK) (Hussain et al., 2015) to analyse the CD spectra for SSE. In the SSE analysis the CONTINLL algorithm (Provencher and Gloeckner, 1981; Sreerama and Woody, 2000) with the SMP56 (43 soluble + 13 membrane proteins) basis set was used between the wavelength range 190 – 240 nm. Note – the rHDL-L144R 190:10:2 sample SSE was also analysed using the CDSSTR algorithm and SMP56 basis set due to anomalous SSE with the CONTINLL algorithm.

Thermal CD spectra of the samples were collected as the temperature was increased in 1°C increments from 25 to 95°C at a rate of 1°C/min with a tolerance of 0.1°C, and a final CD spectra collected once the sample cooled to 25°C (Giudice et al., 2017). The Global 3 thermal global analysis software (Applied Photophysics) was used to determine the melting temperature(s) (T_m) from the collected thermal CD spectra and has previously been used for thermal CD analysis of lipid-free apoA-I WT (Townsend et al., 2017). The thermodynamic analysis uses sigmoidal unfolding curve fitting across multiple wavelengths based upon the Gibbs-Helmholtz (**Equation [9]**) (Greenfield, 2006a) (Applied Photophysics).

$$\Delta G = \Delta H\left(\frac{1-T}{T_m}\right) - \Delta C_p\left((T_m - T) + T ln\left(\frac{T}{T_m}\right)\right) \qquad \textbf{[9]}$$

Where, in the thermal transition from a folded to an unfolded protein state, ΔG is the Gibbs free energy, ΔH is the van't Hoff enthalpy, ΔC_p is the change in heat capacity, T is the temperature (K), T_m is the melting temperature (K) (Greenfield, 2006a) (Applied Photophysics).

To confirm the number of transitions, i.e. T_m's, the unfolding curves at 222 nm and the unfolding curve first derivatives were plotted between 25 – 95°C (Greenfield, 2006a). A peak maximum in the first derivative plot corresponds to a T_m which in turn corresponds to the midpoint T_m of the inflection in a sigmoidal unfolding curve (Greenfield, 2006a). The T_m(s) from each analysis were similar with respect to each other. This revealed the number of transitions as monophasic (lipid-free apoA-I) or biphasic (rHDL apoA-I) during the thermal temperature ramp. The OriginPro 2018 software Boltzmann (sigmoidal) and BiDoseResponse (double sigmoidal) fitting functions were used to fit the respective unfolding curves. The r^2 values of the sigmoidal fitting for the monophasic unfolding curves of lipid-free apoA-I WT, R173C and L144R were 0.9976, 0.9991, and 0.9987, respectively. The biphasic unfolding curve double sigmoidal fitting r^2 values were 0.9991, 0.9988, and 0.9982 for rHDL-WT, R173C and L144R, respectively.

The CD data was too noisy below 200 nm in the thermal denaturation samples to analyse for SSE using the CONTINLL algorithm and SMP56 basis set. For example, CONTINLL SMP56 basis set (190-240 nm) SSE analysis for LF apoA-I WT at 25°C was 48.5 % α-helix (α), 5.9 % β-strand (β), 17.3 % turns (T), 28.2 % unordered (U), and at 95°C was 75.6 % α-helix and 24.4 % β-strand. At 95°C this contradicted the thermal CD spectra which was characteristic of a shift from α-helical to predominantly random coil.

Therefore, the approximate α-helical content was estimated using the molar ellipticity [θ] at 222 nm [θ_{222}] from the observed CD data in the following equation (Morrisett et al., 1973):

$$alpha\ helix\ \% = 100\left(\frac{-[\theta_{222}] + 3000}{3000 - (-36000)}\right) \qquad \textbf{[10]}$$

Equation [10] is an approximation as it assumes the secondary structure in the protein consists of α-helix and random coil, and the α-helix estimated error was ~7.7 % as determined from [θ_{222}] = 0. The molar ellipticity at 222 nm values of a 100 % α-helical or random coil protein (poly-L-lysine) used were -36000 and 3000 deg cm^2 $dmol^{-1}$, respectively, (Greenfield and Fasman, 1969; Morrisett et al., 1973), and have previously been used to approximate the α-helical content of apoA-I WT and R173C (Alexander et al., 2009; Fang et al., 2003b; Suurkuusk and Singh, 2000).

5.2.2 rHDL nanoparticle PEG precipitation

For solid-state NMR analysis, the rHDL nanoparticles were precipitated using PEG-6000 for ^{13}C CP-MAS NMR (Mors et al., 2013). A 40 % (w/v) PEG-6000 stock solution was prepared and added to the rHDL samples to a final concentration of 24 % (w/v). To allow for rHDL precipitation the samples were incubated for 48 hours at 4°C and inverted to mix. After the rHDL PEG precipitate formed the samples (0.8 mL) were centrifuged in an SW 55 Ti rotor (Beckman Coulter) at 41 krpm, 4°C for 2 hours. The supernatant was removed, and the rHDL nanoparticle precipitate was stored at 4°C before transferring to a 3.2 mm diameter magic-angle spinning rotor.

5.2.3 Oriented rHDL nanoparticle preparation

Glass cover slips (Paul Marienfeld GmbH & Co. KG, Germany; 8 x 22 mm, thickness No. 0 (0.08-0.12mm)) were cleaned with successive rinses of MeOH, EtOH and MilliQ grade water before the slides were dried over 24 – 48 hours at 37°C. A 1 mL sample of rHDL-WT 200:2 nanoparticles in rHDL buffer (10 mM tris, 1 mM EDTA, 1 mM NaN_3) pH 7.4 was pipetted in equal aliquots onto 24 glass cover slips and placed in a desiccator until the sample was completely dried (≥12 hours). The dried sample was rehydrated at 99 % humidity for 16 hours inside a glass desiccator chamber containing 100 mL MQ H_2O placed inside a 37°C incubator. Just prior to NMR analysis the hydrated sample glass slides were stacked and wrapped in cling film.

5.2.4 Solid-state NMR of apoA-I in rHDL nanoparticles

A Bruker Avance 400 spectrometer was used to perform the SS NMR measurements using an 89 mm bore magnet at a magnetic field strength of 9.3 T and a temperature of 25°C. The stacked oriented rHDL [^{15}N]-apoA-I WT 200:2 nanoparticle sample was placed into the coil (9 x 3 x 3 mm) of a double resonance (H/F and X, the latter tuned to 161 MHz for ^{31}P observation) static flat-coil probe (Bruker).

The pulse sequence for the ^{1}H-^{15}N PISEMA spectrum was as described by Wu *et al.* (Wu et al., 1994), and began with a 2.5 µs 90° pulse on ^{1}H. Then ramped cross-polarisation (^{1}H to ^{15}N) was used with a time period of 2 ms and at the proton nutation frequency of 40 kHz. Subsequently, frequency-switched Lee-Goldburg cross-polarisation was used at the magic-angle to obtain spin-exchange between ^{1}H to ^{15}N nuclei with the ^{1}H and matched ^{15}N fields of 62.5 and 76 kHz, respectively. This was followed by the signal acquisition period with simultaneous proton decoupling at a field

of 62.5 kHz. Each increment contained an average of 10 000 transients in a total of 32 t_1 increments in the indirect dimension which represents the ^{1}H-^{15}N dipolar coupling.

The precipitated rHDL [^{13}C]-labelled apoA-I samples were packed into a 3.2 mm zirconium rotor. A HFXY probe in double-resonance mode and a magic-angle spinning frequency of 8 kHz were used to obtain the 2D ^{13}C-^{13}C spectra. Before signal acquisition Hartmann-Hahn cross-polarisation with a contact time of 2 ms was used. Throughout signal acquisition at 63 kHz SPINAL-64 ^{1}H decoupling was applied (Fung et al., 2000). This was followed by a mixing time of 100 ms in which the dipolar-assisted rotational resonance DARR condition (Takegoshi et al., 2001) was satisfied by changing the ^{1}H nutation frequency to the MAS frequency of 8 kHz, and the spectra were recorded. Each increment contained an average of 400 – 600 transients in a total of 480 t_1 increments in the indirect dimension. The detection in the indirect dimensions was phase-sensitive as the States-TPPI (time proportional phase incrementation) method was used. The measurement period for each sample was between 2 – 7 days due to differences in rotor packing efficiency. Each chemical shift in the spectra was relative to the reference compound tetramethylsilane.

5.2.5 Two-dimensional NMR spectra calculations

SS NMR spectra of the AAMD-simulated POPC:cholesterol:apoA-I 200:20:2 nascent HDL nanoparticle model (Pourmousa et al., 2018) were calculated including ^{1}H-^{15}N PISEMA and 2D ^{13}C-^{13}C NMR spectra (Lau and Middleton, 2020). The atomic coordinates of the HDL particle were rotated in the final frame of the MD simulation so I_z^{HDL} was aligned with B_0 for the PISEMA spectrum. The ^{15}N chemical shift (δ_i) was calculated for the amide (i) groups in the apoA-I protein backbone with **Equation [7] (Chapter 2**, **section 2.2.5)**. The amide ^{15}N chemical shift tensor can be described by

the main components δ_{11}, δ_{22} and δ_{33} and the chemical shift values used were 60, 75 and 222 ppm, respectively (Lau and Middleton, 2020). The ^{1}H-^{15}N dipolar coupling constant (D_i) for each residue (i) was calculated using **Equation [8]** (**Chapter 2**, **section 2.2.5**), as dipolar coupling occurs between the N and H nuclei in the N-H bond, as described earlier. The observed D_{max} at 11 kHz was the maximum value of the dipolar coupling (Lau and Middleton, 2020).

The protein coordinates from the final frame of the AAMD 200:20:2 simulation in a PDB file (Pourmousa et al., 2018) were submitted to the SHIFTX2 server (Han et al., 2011) which used the protein secondary structure to predict the ^{13}C chemical shifts (Lau and Middleton, 2020). The backbone amide carbon (C') and Cα chemical shifts were correlated with the chemical shifts for Cβ and further sidechain carbon atoms to produce the 2D spectrum from the predicted frequencies (Lau and Middleton, 2020). The purpose of the simulated spectrum was to predict the position of cross-peaks only. Therefore, every cross-peak and diagonal peak had the same intensity, as factors that can affect the cross-peak intensity like the dipolar coupling strength and spin-diffusion were not considered.

In both dimensions the time domain signal with the appropriate frequencies were produced. An exponential line broadening function of 25 Hz was combined with Fourier transformation to generate the spectrum (Lau and Middleton, 2020). Both types of simulated spectra, the ^{1}H-^{15}N PISEMA and 2D ^{13}C-^{13}C NMR spectra were generated with C programs written by Prof. David Middleton for this purpose (Lau and Middleton, 2020).

5.3 Results

5.3.1 CD analysis of apoA-I secondary structure

The UV stability of LF and lipid-bound apoA-I WT, R173C and L144R was tested by 50 repeat scans at 37°C. The repeated scans were used to determine if the apoA-I WT or atheroprotective mutant structure denatured under the CD experiment conditions. All samples have a spectrum characteristic of a high α-helical content, as evident in the maxima at ~190 nm and the two minima at ~206 and 222 nm (**Figure 5.1**) (Holzwarth and Doty, 1965). The lipid-free and rHDL-bound apoA-I proteins were stable and did not denature under multiple UV scans. This is shown by the reproducibility of the CD scans in each sample between ~195 – 240 nm. Therefore, the proteins retained their predominantly α-helical conformations, and the samples were analysed further using CD spectroscopy.

Another test of the LF and lipid-bound apoA-I WT protein stability compared to the atheroprotective mutants was incubation of the samples at 37°C for 24 hours (**Table 5.1**). To determine if precipitation of the protein occurred the protein concentration was taken before and after incubation. The LF and rHDL-WT and R173C samples showed similar amounts of protein aggregation. The LF and rHDL-L144R samples aggregated approximately 18 – 23 % and 25 % more, respectively than the apoA-I WT/R173C samples. This suggested the apoA-I L144R protein was less stable and more prone to aggregation. The protein concentration after 24 hours was below 3.6 μM therefore the secondary structure was estimated for the 0 hr time point samples only.

Table 5.1. The average concentration (μM) after incubation and percent precipitation of LF and lipid-bound apoA-I WT/R173C/L144R in rHDL POPC:apoA-I 200:2 (M/M) nanoparticles. The 3.6 μM samples were incubated for 24 hours at 37°C.

Sample	Average concentration (μM)	% precipitated
apoA-I WT	2.3	36.0
apoA-I R173C	2.1	41.3
apoA-I L144R	1.5	59.0
rHDL-WT 200:2	3.0	17.3
rHDL-R173C 200:2	3.0	16.3
rHDL-L144R 200:2	2.1	41.7

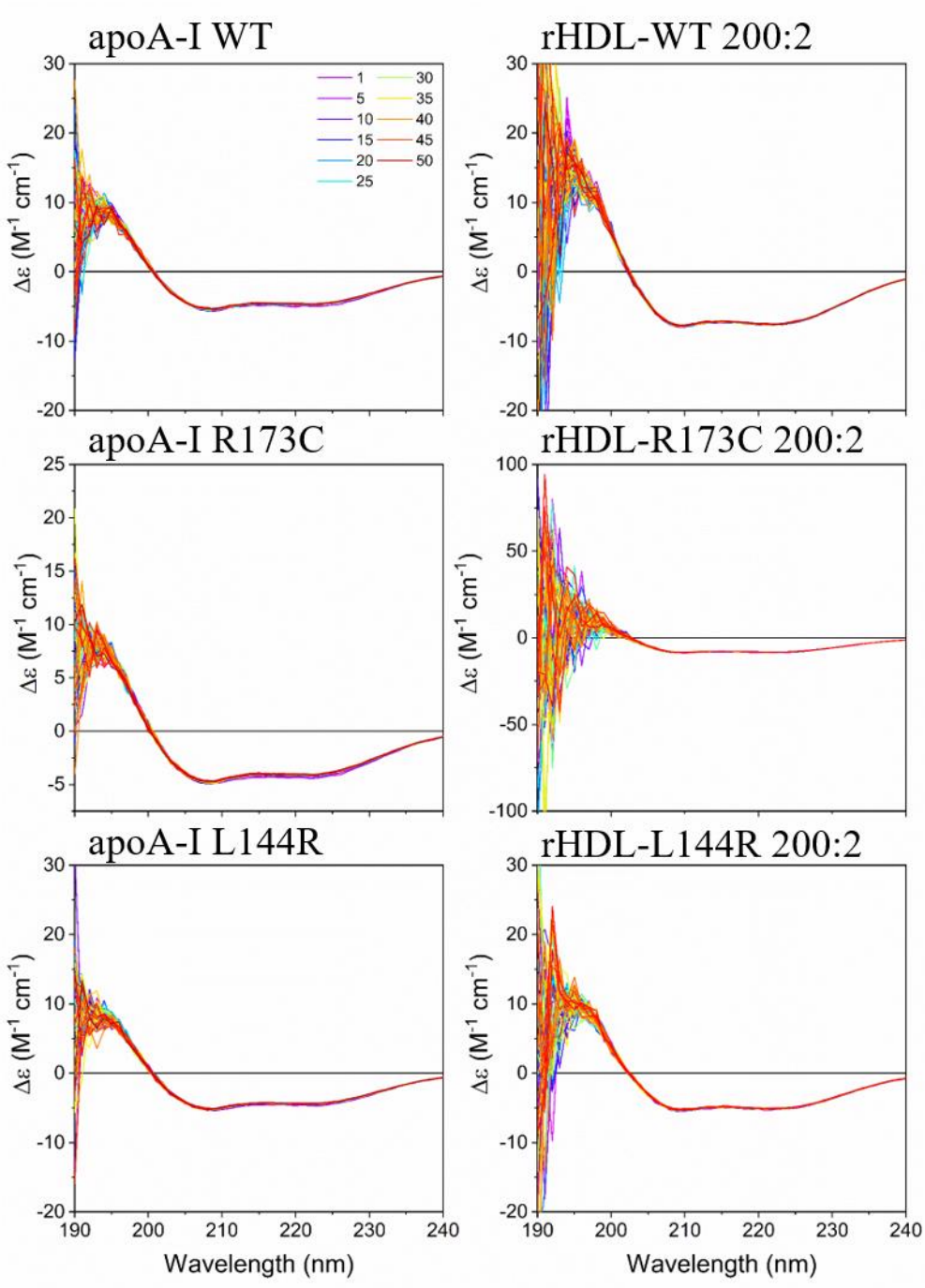

Figure 5.1. UV stability CD spectra of lipid-free apoA-I (left) and rHDL POPC: apoA-I WT/R173C/L144R 200:2 (M/M) (right) samples. Each spectrum shows a total of 50 repeat scans at 37°C, and 3.6 µM protein concentration.

The CD spectra for the LF and rHDL POPC:±cholesterol:apoA-I 200:2 (**Figure 5.2**) and rHDL-C 190:10:2 WT/R173C/L144R samples (**Figure 5.3**) showed the characteristic CD spectrum for a predominantly α-helical protein.

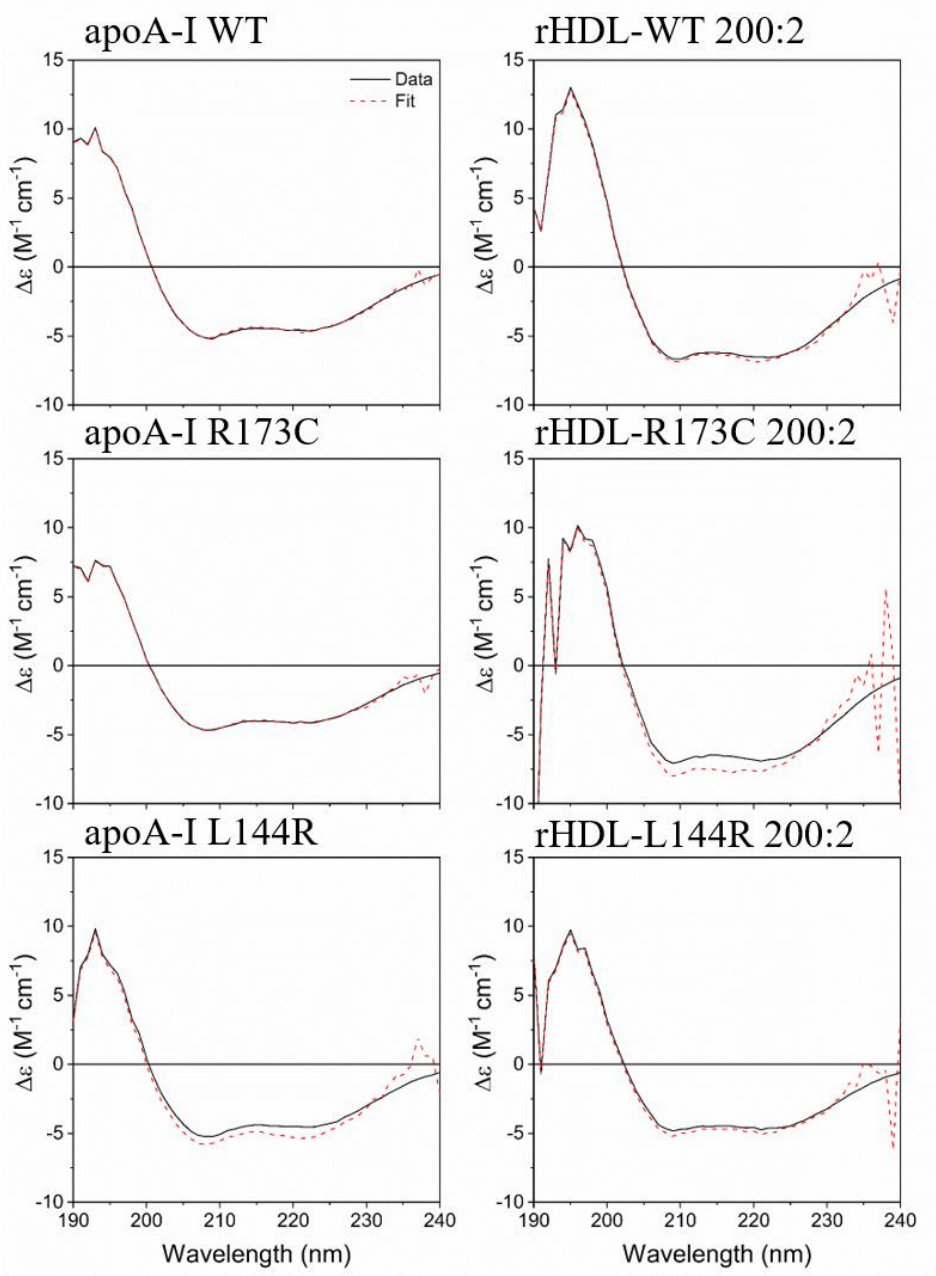

Figure 5.2. The average CD spectra (n = 3) of LF (left) and rHDL POPC:apoA-I WT/R173C/L144R 200:2 (M/M) (right) samples. At 37°C and 3.6 μM apoA-I concentration. The measured data (black line) and the CONTINLL algorithm and SMP56 basis set fit (dashed red line).

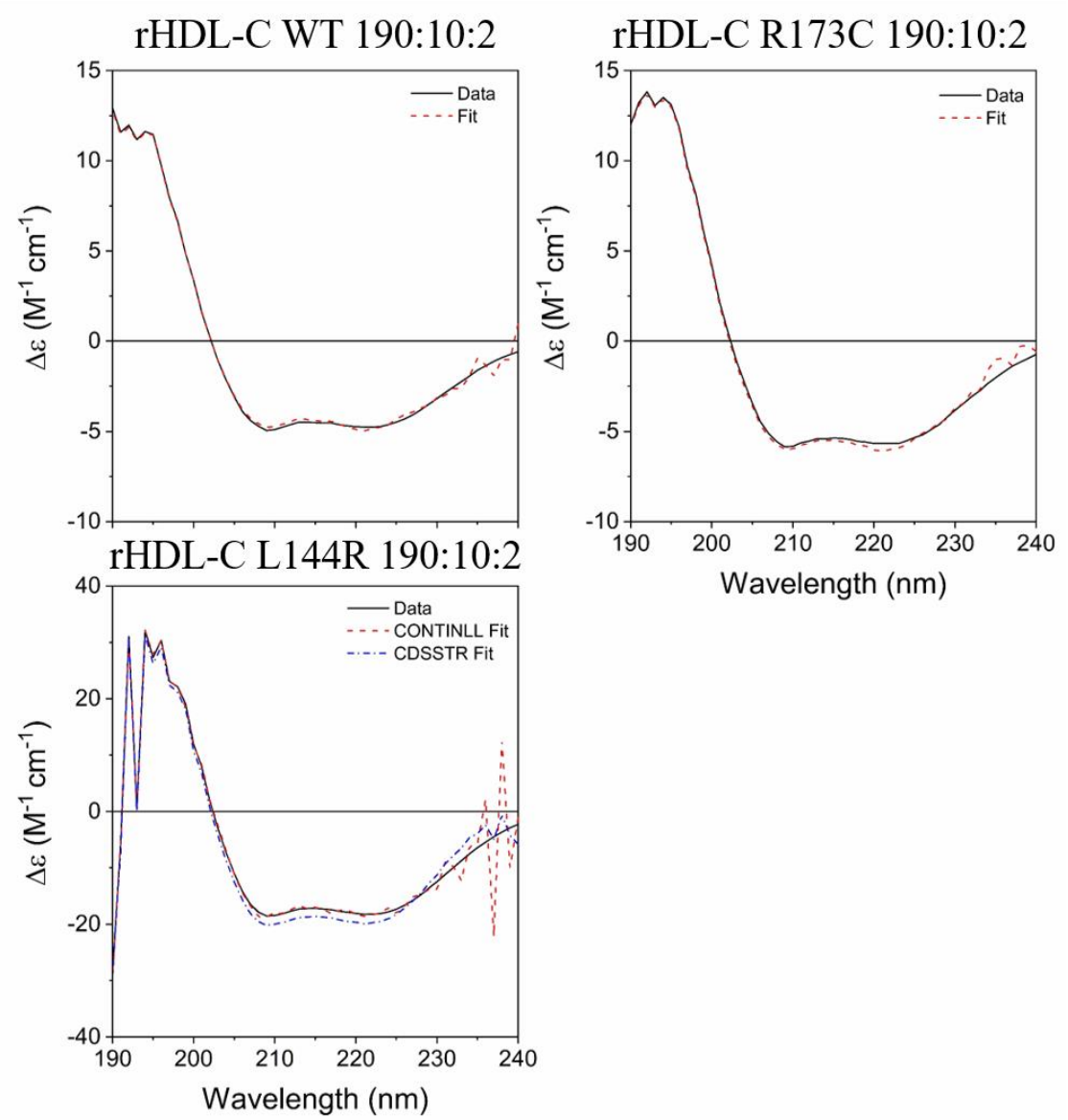

Figure 5.3. The average CD spectra (n = 3) of the rHDL-C WT/R173C/L144R 190:10:2 (M/M) samples. At 37°C and 3.6 µM apoA-I concentration. The measured data (black line) and the CONTINLL algorithm and SMP56 basis set fit (dashed red line). The rHDL-C L144R sample CDSSTR SSE fit is in blue (dashed-dot line).

To determine the reason for the noise in the CONTINLL algorithm spectra fits between ~230 – 240 nm (**Figure 5.2–5.3**) the residuals and SSE for the rHDL-WT 200:2 nanoparticle sample were compared for the CONTINLL, SELCON3, and CDSSTR SSE algorithms. Each algorithm produced a CD spectrum fit for a predominantly α-

helical protein between 190 – 240 nm with the maxima at ~190 nm, and minima at ~206 and 222 nm (**Figure 5.4**).

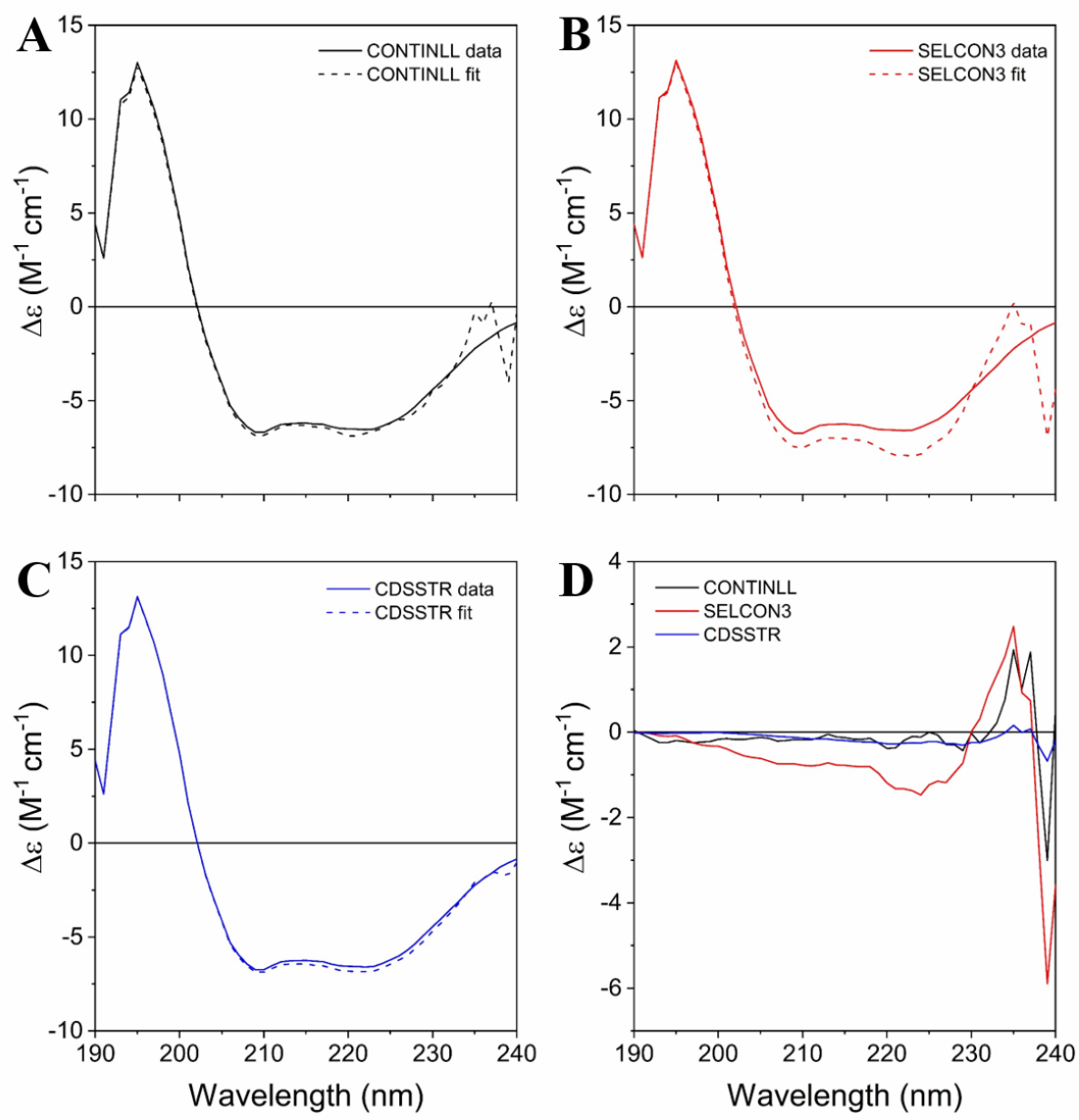

Figure 5.4. A comparison of SSE analysis of the rHDL-WT 200:2 sample. The average CD spectra (n = 3) at 37°C and 3.6 µM apoA-I concentration. The measured data (black line) and the (**A**) CONTINLL (**B**) SELCON3, and (**C**) CDSSTR algorithm and SMP56 basis set fit (dashed lines). (**D**) The residuals for each algorithm.

The RMSD and residuals (**Figure 5.4D, Table 5.2**) were used as an indicator for the "goodness of fit" between the SSE fit and the observed CD data (Whitmore and

Wallace, 2008). The SELCON3 SSE algorithm was not used due to the larger overall difference in the residuals between 190 – 240 nm, hence a larger overall RMSD (~0.22). This was observed in the difference between the experimental spectra and the SELCON3 fit (**Figure 5.4B**).

Table 5.2. The corresponding SSEs of rHDL-WT 200:2 (M/M) SSE algorithm comparison estimated with the SMP56 basis set, including normalised mean residual standard deviation (NMRSD).

Algorithm	**Secondary structure estimation (%)**					
	α-helix	**β-strand**	**turns**	**unordered**	**Total**	**NRMSD**
CONTINLL	66.6	1.9	11.1	20.3	99.9	0.103
SELCON3	61.1	4.1	15.3	21.2	101.7	0.218
CDSSTR	77.7	8.1	9.4	5.4	100.6	0.031

The CDSSTR algorithm fit was the most similar to the experimental spectrum (**Figure 5.4C**) with the corresponding low RMSD (0.031) value. In comparison the CONTINLL SSE algorithm fit contained noise between ~230 – 240 nm with an RMSD of ~0.1 (**Figure 5.4A**). The differences in the 230-240 nm region between CONTINLL and CDSSTR were observed in the residual plot (**Figure 5.4D**). This suggested the CDSSTR algorithm was the most "ideal" for SSE of the lipid-bound apoA-I based upon the RMSD and residuals.

The higher resolution SRCD analysis of apoA-I WT in rHDL 200:2 nanoparticles produced an SSE estimation of α - 69 %, β - 4.5 %, T - 8% and U - 18 % (Giudice et al., 2017) (**see section 5.4.1, Table 5.5**). ApoA-I is a primarily α-helical protein when lipid-free or lipid-bound (**see section 1.6, and refs therein**). The CONTINLL algorithm provided the most similar SSE (±2 – 3 %) for each secondary structure component when compared to the SRCD SSE (**Table 5.2**). In comparison the CDSSTR SSE values compared to the SRCD SSE were α - +8.7, β - +3.6, T - +1.4, and -12.6 % - U. This suggested that despite the lower RMSD value the CDSSTR SSE was overestimated. Furthermore, the CDSSTR usually produces a low RMSD due to differences in SSE fit calculations compared to the CONTINLL algorithm fits (Greenfield, 2006b; Whitmore and Wallace, 2008).

In the CONTINLL analysis the noise in the 230 – 240 nm region could be due to the type of reference protein(s) and the corresponding reference CD spectra in the SMP56 basis set. The SMP56 basis set contained 43 soluble proteins and 13 membrane proteins (Sreerama and Woody, 2004b). In comparison lipid-bound apoA-I is in a discoidal nanodisc shape wrapped around the lipid nanodisc bilayer (**see section 1.6.2**). Therefore, the reference proteins CD spectra in this region compared to experimental spectra from conventional CD may not truly represent the lipid-bound apoA-I in the 230 – 240 nm region.

Overall, the SSE was similar to the high-resolution SRCD data for rHDL-WT 200:2 nanoparticles, which suggested the noise in the 230 – 240 nm region of the CONTINLL fits did not interfere with the SSE of lipid-bound apoA-I. It appeared that the reference proteins used to calculate the SSE with CONTINLL do not completely fit the experimental spectra between 230 – 240 nm.

The region of interest for calculating the SSE in particular the α-helix content at 222 nm using CONTINLL or **Equation [10]** was suitable for determining the apoA-I SSE when compared to the literature SRCD CONTINLL SSE. Therefore, the CONTINLL and SMP56 basis set were used for each sample in this work despite the noise present in the SSE fit between 230 – 240 nm.

The secondary structure was estimated for each sample at 37°C (**Table 5.3**) using the CONTINLL algorithm and SMP56 basis set. The LF apoA-I samples each contained similar SSEs overall. The rHDL-WT and R173C α-helical content was greater than the respective LF protein structure estimations. In apoA-I R173C this appears to be due to conversion of the unordered content to β-strand and α-helix when lipid-bound. The rHDL-WT SSE indicated smaller structural changes following a similar pattern except for a decrease in β-strand content. Surprisingly, the LF and lipid-bound apoA-I L144R α-helical content was very similar with an increase in unordered protein content when lipid-bound.

Table 5.3. The corresponding SSEs of LF apoA-I and rHDL-WT/R173C/L144R 200:2 (M/M), and rHDL-C 190:10:2 samples estimated using the CONTINLL algorithm and SMP56 basis set, including normalised mean residual standard deviation (NMRSD). *CDSSTR algorithm

Sample	Secondary structure estimation (%)				
	α-helix	β-strand	turns	unordered	NMRSD
apoA-I WT	51.6	6.1	15.7	26.6	0.035
apoA-I R173C	46.2	5.3	17.9	30.6	0.052
apoA-I L144R	54.9	6.3	18.3	20.5	0.171
rHDL-WT 200:2	66.6	1.9	11.1	20.3	0.103
rHDL-R173C 200:2	73.8	19.1	7.1	0	0.296
rHDL-L144R 200:2	54.3	3.1	12.1	30.6	0.223
rHDL-C WT 190:10:2	60.7	8.5	8.4	22.4	0.051
rHDL-C R173C 190:10:2	64.7	4.4	10.5	20.4	0.047
rHDL-C L144R 190:10:2	0	0	100	0	0.224
rHDL-C L144R 190:10:2*	43.5	25.8	15.5	15.0	0.095

The rHDL-C WT 190:90:2 apoA-I SSEs contained relatively small structural changes compared to the rHDL-WT 200:2 nanoparticles. There was only a small decrease in α-helical content (-5.9 %) with an increase in the β-strand secondary structure (+6.6 %). The rHDL-C R173C 190:90:2 nanoparticles apoA-I contained a large increase in unordered secondary structure content (+20.4 %) compared to the rHDL-R173C 200:2 nanoparticles. This corresponded with a decrease (-14.7 %) in β-strand content. The rHDL-C R173C 190:90:2 SSEs were similar to the rHDL-WT 200:2 SSE nanoparticles.

This suggested the apoA-I R173C protein could adopt an overall similar secondary structure conformation in rHDL-C 190:90:2 nanoparticles despite the shifted registry of the disulphide bonded monomers.

The rHDL-C L144R 190:10:2 SSEs suggested the apoA-I L144R structure was comprised of 100 % turns when analysed using the CONTINLL algorithm. This was considered an anomalous SSE as the CD spectrum (**Figure 5.3**) was characteristically α-helical.

Therefore, the rHDL-C L144R 190:10:2 secondary structure was estimated with the CDSSTR algorithm. The SSE results were treated with caution due to the overestimation of α-helical content in the rHDL-WT 200:2 sample (**Table 5.2**). The CDSSTR SSE for lipid-bound apoA-I L144R predicted a predominantly α-helical protein (~43.5 %) which agreed with the characteristic spectrum (**Figure 5.3**).

However, the β-strand content (~25.8 %) was relatively high compared to the rHDL-C WT/R173C 190:10:2 samples. Furthermore, the intensity of the CD signal -20 to 30 M^{-1} cm^{-1} was disproportionate relative to all other samples at the same apoA-I concentration. This could be due to incomplete separation from lipid-free apoA-I L144R or a lower stability of the protein leading to precipitation or dissociation from the rHDL-C nanoparticles.

5.3.1.1 CD analysis of thermal stability

The thermal stability of the different rHDL formulations with WT and mutant proteins may reflect their stability and/or resistance to denaturation *in vivo*. The CD spectra for the lipid-free and rHDL bound proteins show a typical α-helical spectrum at 25°C (**Figure 5.5**). The peak minima at 208 and 222 nm decreased as the temperature increased. The protein structure became less α-helical and more characteristic of a

random coil spectrum. The isodichroic point at approximately 205 nm suggested for LF and rHDL bound apoA-I proteins a two-state thermal unfolding model (monophasic) (**Figure 5.5**). However, the thermal unfolding curves of the molar ellipticity (**Figure 5.6**) and the first derivative of the unfolding curve at 222 nm (**Figure 5.7**) suggested the rHDL nanoparticles thermal unfolding was a three-state model (biphasic). This was in agreement with the findings of Giudice *et al*. using high resolution SRCD of rHDL-WT and R173C nanoparticles (Giudice et al., 2017).

Global analysis was used to determine the melting temperature(s) (T_m's) of the samples, and the unfolding curves of the molar CD at 222 nm with the corresponding first derivatives of the plots (**Figure 5.6-5.7**) were used to determine the number of transitions as the temperature increased. Both the unfolding curves and first derivatives show the raw data and the calculated global CD data. The LF protein monophasic unfolding curves were fitted with a Boltzmann sigmoidal fit and the rHDL protein unfolding curves were fitted with a BiDoseResponse double sigmoidal fit (**Figure 5.6**). The peak maxima of the first derivatives of the unfolding curves approximately correspond to the T_m's determined using the Global data analysis in **Table 5.4**.

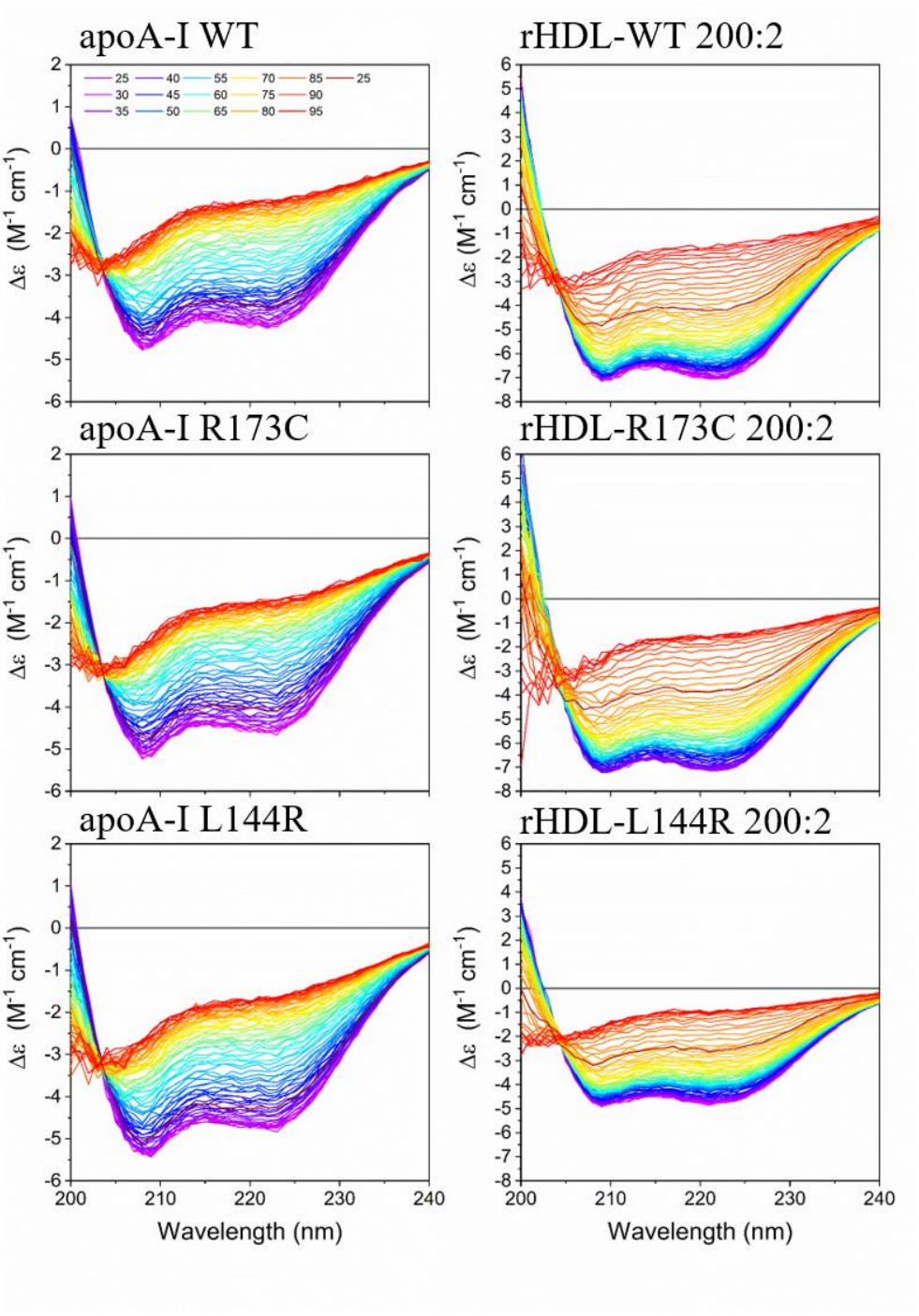

Figure 5.5. Thermal CD spectra of LF and rHDL-WT/R173C/L144R 200:2 (M/M) nanoparticles in rHDL buffer, pH 7.4 over the temperature range of 25 – 95°C. The protein concentration was 3.6 μM.

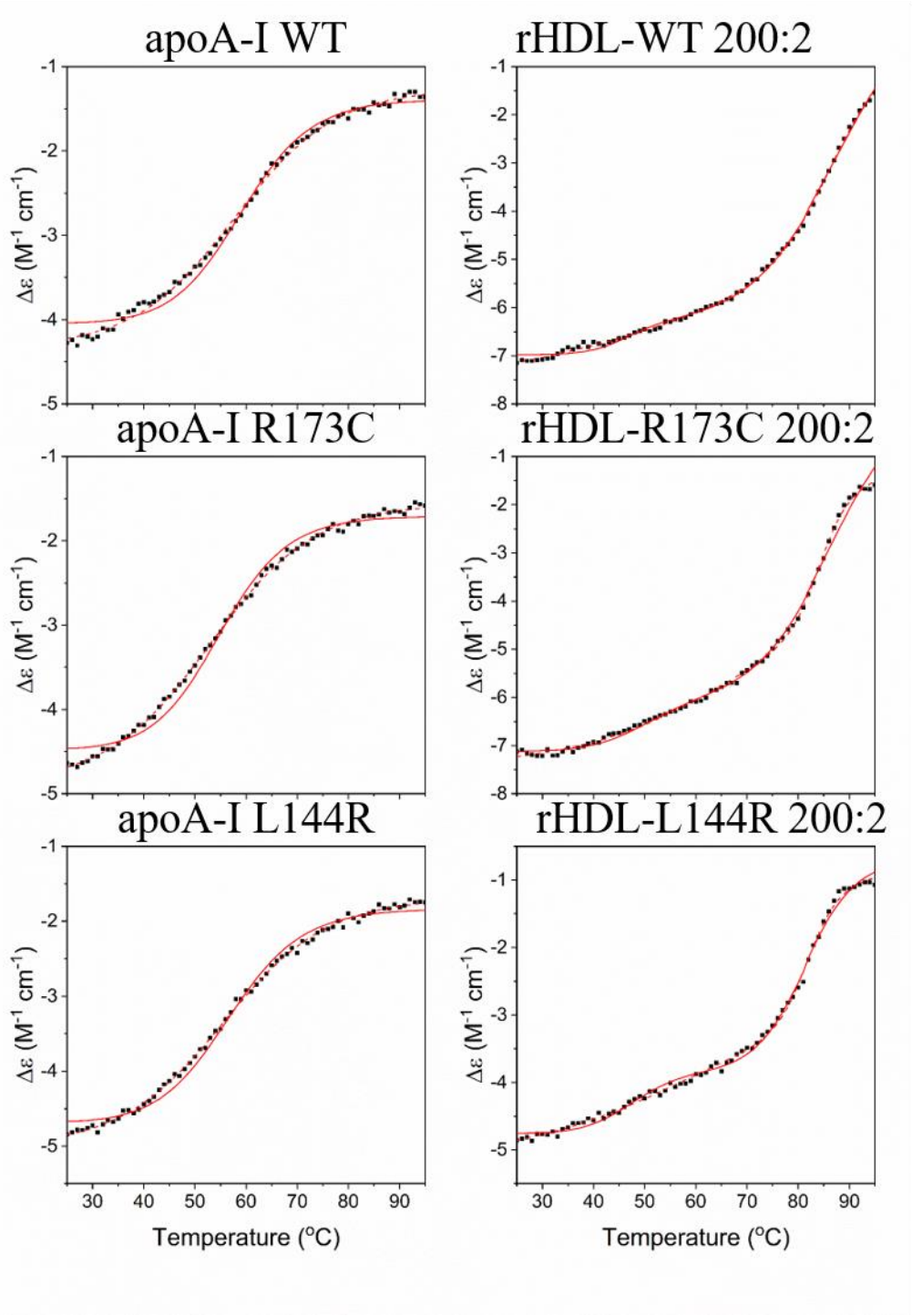

Figure 5.6. The thermal CD transition analyses for LF and rHDL-WT/R173C/L144R 200:2 (M/M) samples. The unfolding curves, Δε at 222 nm: raw data (black) and fit (dashed red line), and Global analysis calculated fit (solid red line) (Lau and Middleton, 2020).

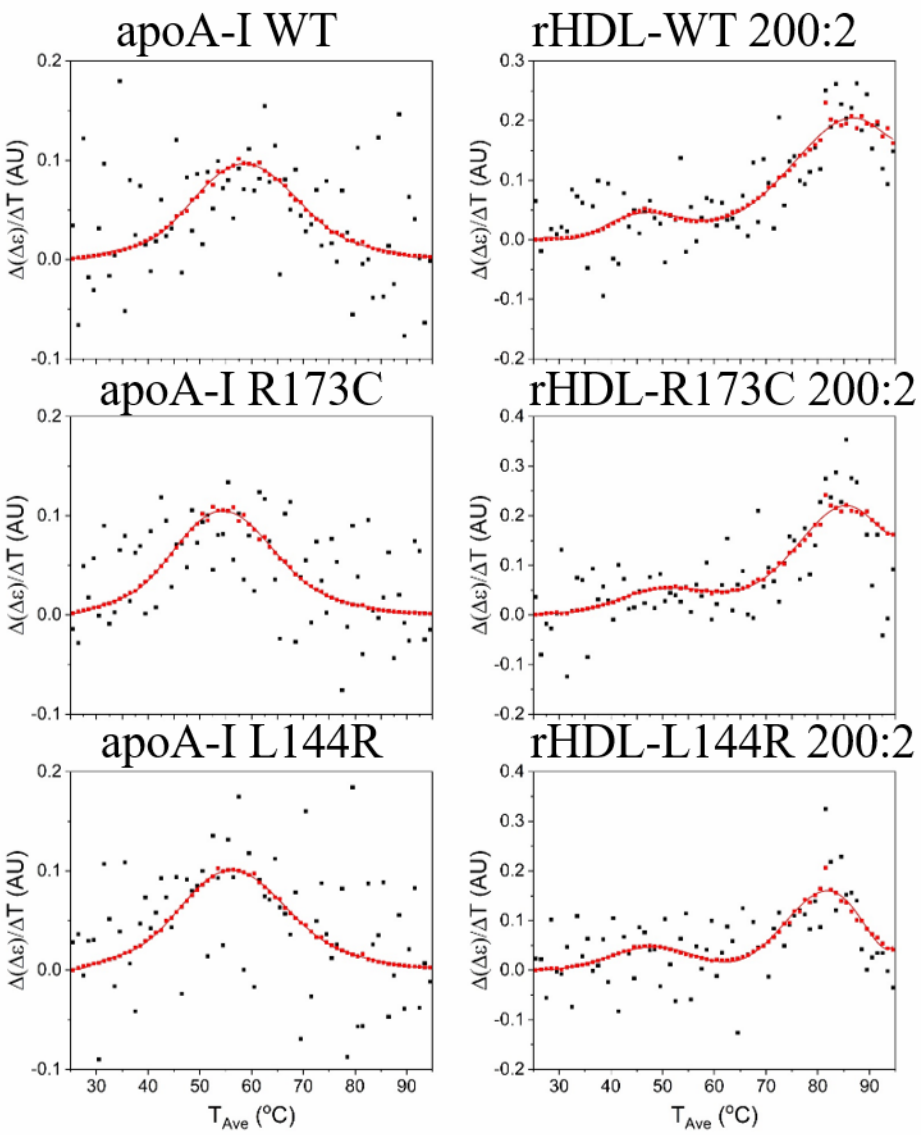

Figure 5.7. The corresponding first derivatives of the thermal CD transition analyses for the LF and rHDL-WT/R173C/L144R 200:2 (M/M) samples. The raw data derivative (black), Global calculated data derivative (red) and polynomial fit (solid red line) (Lau and Middleton, 2020).

The T_m's determined for LF apoA-I WT and R173C are in good agreement with previously measured values (**Table 5.4**). The LF apoA-I L144R T_m showed a similar trend to Gkolfinopoulou *et al.*'s values with a lower LF apoA-I L144R T_m relative to apoA-I WT at the 3.6 µM protein concentration (Gkolfinopoulou et al., 2020). Overall,

the ~2 – 4°C difference between the LF apoA-I T_m's suggested a minor decrease in the thermal stability of the solution state apoA-I mutants relative to apoA-I WT.

Table 5.4. The observed melting temperatures of the lipid-free and rHDL-WT/R173C/L144R 200:2 (M/M) samples compared to literature T_m's ±standard error.

Sample	Observed T_m (°C)		Literature T_m (°C)
	T_m 1	**T_m 2**	**T_m 1**
apoA-I WT	55.1 ± 0.1	-	55.3±0.5 (Del Giudice et al., 2016) 55.9±1.4 (Petrlova et al., 2014) 56.0 (Townsend et al., 2017) 57.3±0.4 (Dalla-Riva et al., 2015) 59±1.0 (Fang et al., 2003a) 60.0 ±2.0 (Fang et al., 2003b) 60±1.5 (Saito et al., 2003) 61±1.0 (Mei and Atkinson, 2011) ~57.5 (Gkolfinopoulou et al., 2020)
apoA-I R173C	51.4 ± 0.1	-	50.9±1.4 (Petrlova et al., 2014)
apoA-I L144R	53.2 ± 0.1	-	~55 (Gkolfinopoulou et al., 2020)
rHDL-WT	43.4 ± 0.3	82.9 ± 0.4	46.6±3.6 and 78.8±0.2 (Giudice et al., 2017)
rHDL-R173C	47.0 ± 0.4	81.0 ± 0.4	55.9±5.0 and 72.15±0.4 (Giudice et al., 2017)
rHDL-L144R	44.6 ± 0.2	76.3 ± 0.1	No published data

The rHDL apoA-I protein thermal stability in order of least stable for T_m1 was apoA-I WT (43.4°C) < L144R (44.6°C) < R173C (47.0°C). This could suggest structural changes in the protein whilst bound to lipids (Giudice et al., 2017) or some disassociation from the lipid nanodisc bilayer as the temperature approaches the LF protein T_m. The disulphide bond in the apoA-I R173C dimer could stabilise the protein in this first transition. In comparison, the lipid-bound apoA-I L144R was marginally more stable than rHDL apoA-I WT.

The second transition at higher temperatures has been suggested to be due to dissociation of the protein from the lipid bilayer nanodisc (Giudice et al., 2017). This is supported by the loss of α-helical secondary structure (**Figure 5.8**) and transition to a denatured protein random coil type spectrum in each rHDL sample (**Figure 5.5**). The difference in the observed T_m1 and 2 values compared to Giudice *et al.*'s could be due to sample conditions such as buffer, protein concentration, particle homogeneity, or lipid used in rHDL formation.

The T_m2 thermal stability in order of least stable was apoA-I L144R (76.3°C) < R173C (81.0°C) < WT (82.9°C). This indicated that the R173C protein may have similar thermal stability due to the intramolecular disulphide bond in the second transition to apoA-I WT in rHDL. Whereas apoA-I L144R had a lower thermal stability than both apoA-I R173C and apoA-I WT in rHDL nanoparticles.

During a thermal CD experiment as the protein unfolds the number of melting temperatures indicates the number of protein conformations (Greenfield, 2006a). In a monophasic transition there are two species at 25 and 95°C respectively. In a biphasic thermal transition, there are three species before and after each T_m, i.e., an additional

intermediate species conformation. The estimated α-helical content of the protein conformation in each species conformation are indicated in **Figure 5.8**.

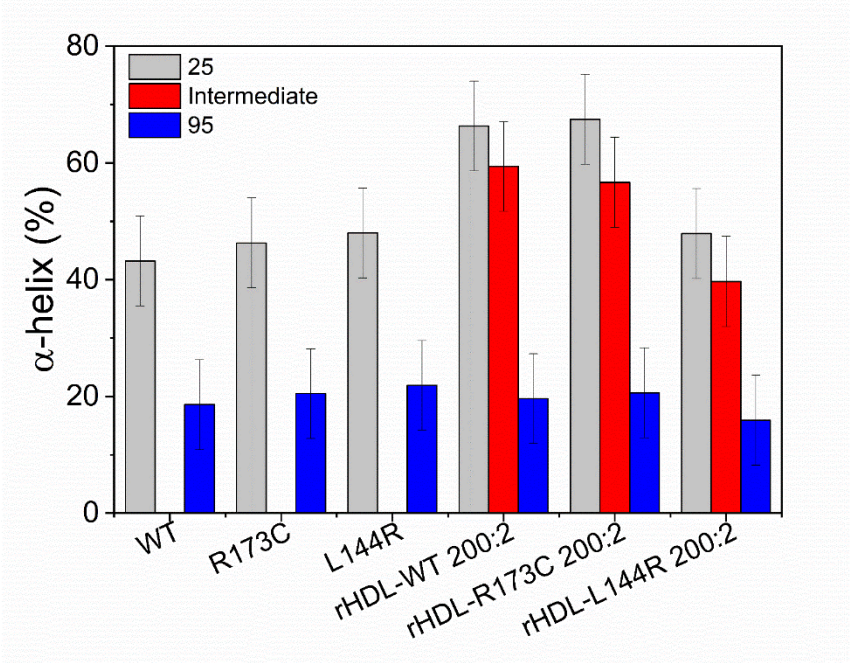

Figure 5.8. LF and rHDL-WT/R173C/L144R 200:2 sample estimated α-helical content ±7.7 % error using **Equation [10]** before and after each thermal transition. The LF sample species were pre- and post-T_m at 25 and 95°C, respectively. The rHDL sample species pre-T_m1 at 25°C, the intermediate species between T_m1 and T_m2 at 58 (WT), 63 (R173C), and 61°C (L144R), and species post-T_m2 at 95°C. The intermediate temperatures indicated were the temperatures most of the protein in the sample was in the intermediate conformation.

The LF apoA-I WT and mutants showed similar behaviour pre-T_m from 43 – 48 % α-helical to 19 – 22 % post-T_m which indicated denaturation of the α-helical protein structure. The rHDL-WT and R173C samples were ~67 % α-helical and rHDL-L144R was ~48 % α-helical at 25°C pre-T_m1. The rHDL apoA-I intermediate conformations showed a small decrease in α-helical structure (7 – 11 %) fluctuations within the error range of the start conformations (**Figure 5.8**). After T_m2 the rHDL-WT/R173C sample

α-helical content decreased to ~20 % and rHDL-L144R to ~16%. This suggested the apoA-I protein structure dissociated from the lipids as the α-helical content was similar to LF apoA-I at 95°C (**Figure 5.8**).

5.3.2 SS NMR apoA-I orientation in rHDL nanoparticles

To determine the rHDL nanoparticle apoA-I protein secondary structure and orientation with respect to the lipids rHDL nanoparticles were prepared with [^{13}C, ^{15}N]-labelled apoA-I WT. The PEG-precipitated rHDL-WT 200:2 nanoparticles were analysed by CP-MAS ^{13}C-^{13}C dipolar correlation SS NMR spectroscopy (**Figure 5.9**). The chemical shifts for alpha, beta and backbone amide carbons are highly sensitive to secondary structure and can distinguish amino acids in α-helices from those in β-sheet or unstructured regions. The resolution of the spectrum did not provide complete individual cross-peak secondary structure assignment from chemical shift reference data (**Appendix 3**) (Ulrich et al., 2007; Wang and Jardetzky, 2002).

The rHDL-WT 200:2 experimental spectrum was compared with a spectrum simulated from predicted chemical shifts for the predominantly α-helical structure of apoA-I in the model of Pourmousa *et al*. The similarity between the experimental and simulated HDL-C 200:20:2 model apoA-I WT spectra (**Figure 5.9**) indicated a predominantly α-helical structure as in **Figure 5.10B** (Pourmousa et al., 2018).

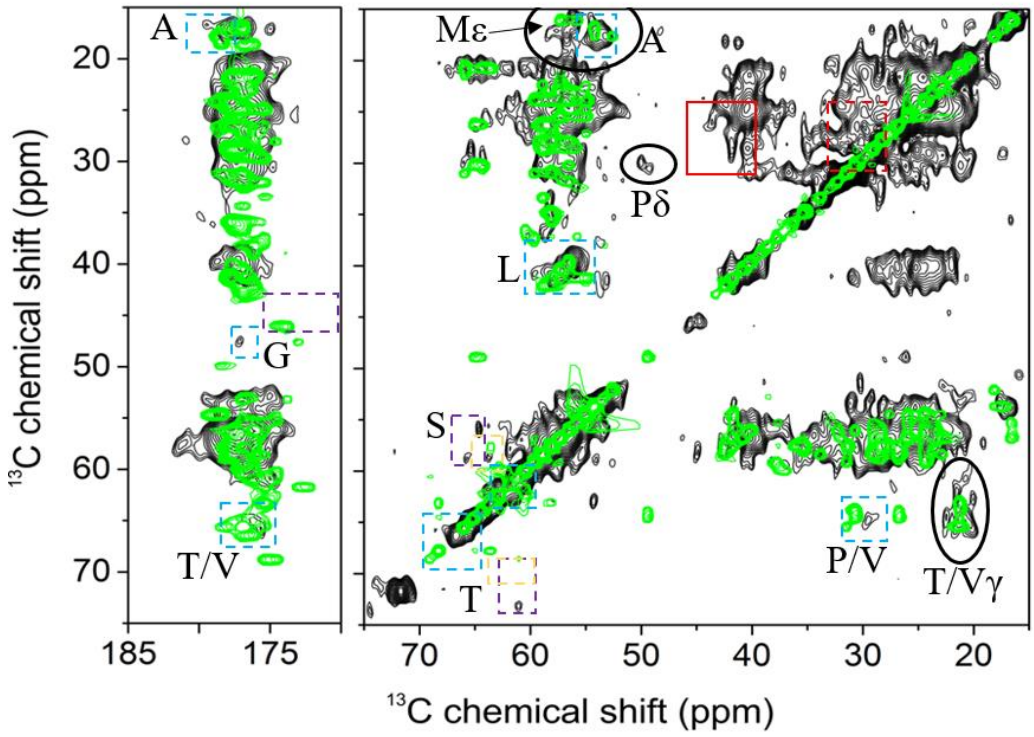

Figure 5.9 The 2D ^{13}C-^{13}C dipolar correlation spectrum of the PEG-precipitated rHDL [^{13}C]-WT 200:2 (M/M) nanoparticles. The spectrum was obtained at a frequency of 100.13 MHz, a DARR mixing time of 100 ms, and a MAS spinning frequency at 8 kHz (Lau and Middleton, 2020). The HDL-C WT 200:20:2 AAMD model (Pourmousa et al., 2018) simulated spectra is overlaid (green contours). The apoA-I WT chemical shifts were predicted by submission of the simulation protein coordinates to the SHIFTX2 server (Han et al., 2011). The cross-peaks (dashed boxes) which are very sensitive to structure were identified as α-helical (blue), β-sheet (purple) and random coil (yellow). Cross-peaks arising from possible long-range coupling are circled (black). Experimental arginine possible long-range couplings, Cδ-Cγ/Cβ-Cδ (red box), and Cβ-Cγ (dashed red box). Adapted from (Lau and Middleton, 2020).

In the rHDL-WT 200:2 spectra there were multiple cross-peaks in the Cα – Cβ region (~15 – 35 by ~15 -35 ppm), whereas the AAMD simulated spectra showed cross-peaks

in the central diagonal region only. Multiple amino acids (MLIQEKR) have side-chain cross-peak correlations in this region of the experimental spectrum. As an example the possible long range side-chain coupling(s) cross-peak regions for arginine are shown in **Figure 5.9** for Cδ-Cγ/Cβ-Cδ (red box), and Cβ-Cγ (dashed red box).

In the simulated spectrum factors such as the cross-peak intensity were not considered as the simulated spectra was used to predict the position of cross-peaks only. Therefore, the possible long-range couplings in the simulated HDL-C WT 200:20:2 apoA-I spectrum may not be similar to the experimental rHDL-WT 200:2 apoA-I spectrum in this region and does not reflect structural differences between the spectra.

An ^{1}H-^{15}N PISEMA spectrum was produced from an oriented rHDL-WT 200:2 sample where I_z^{HDL} (**Figure 5.10B**), the principal axis of inertia of the rHDL nanoparticles, was predominantly parallel to B_0 (**see Chapter 6 section 6.3.1.1**, **Figure 6.8**, **16 hr hydration**). The simulated ^{1}H-^{15}N PISEMA spectrum of the AAMD-HDL model apoA-I WT was overlaid relative to the experimental rHDL-WT 200:2 spectrum (**Figure 5.10A**).

In a ^{1}H-^{15}N PISEMA spectrum cross-peaks appear due to the alignment of the N-H bond vectors in α-helical proteins relative to the lipid bilayer normal/B_0 (**see Chapter 2**, **Figure 2.11**) (Marassi et al., 1999; Marassi and Opella, 2000). The ^{1}H-^{15}N dipolar coupling and ^{15}N chemical shift cross-peaks become disperse in a "wheel-like" pattern as the α-helix axis tilts with respect to the bilayer normal/B_0, i.e. towards perpendicular to the bilayer normal (Marassi et al., 1999; Marassi and Opella, 2000).

Marassi and Opella simulated ^{1}H-^{15}N PISEMA spectra for an α-helix containing 19 amino acids at angles between 0 – 90° relative to the bilayer normal, similar to **Figure 2.11** (Marassi et al., 1999; Marassi and Opella, 2000). The cross-peak regions for the

approximate upper and lower limits of the 0 – 40° and 50 – 90° tilt angles relative to the bilayer normal, and either extreme at 0° or 90° are in **Figure 5.10A**.

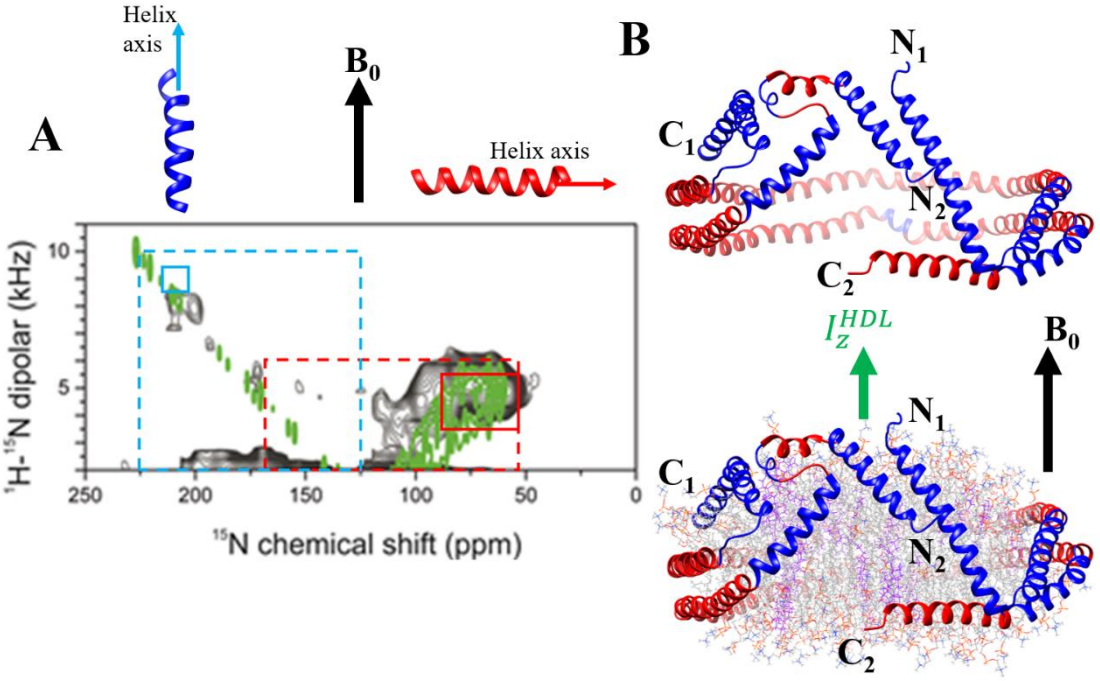

Figure 5.10. (A) The ^{1}H-^{15}N PISEMA spectrum of the oriented rHDL [^{15}N]-WT 200:2 (M/M) 16 hr rehydration nanoparticles oriented with $\boldsymbol{I_z^{HDL}}$ predominantly parallel to B_0. The dipolar couplings were calculated for the HDL-AAMD model apoA-I WT for the overlaid PISEMA spectrum (green) when $\boldsymbol{I_z^{HDL}}$ was parallel to the applied magnetic field. The estimated regions (dashed boxes) for α-helices tilted relative to B_0 between 0 – 40° (blue) and 50 – 90° (red). The regions for 0° (blue) and 90° (red) solid boxes. **(B)** $\boldsymbol{I_z^{HDL}}$/the nanodisc bilayer normal parallel to B_0 with the HDL-C WT 200:20:2 AAMD model, with α-helices tilted with respect to B_0 between 0 – 90° (blue) and perpendicular (~90°) relative to B_0 (red). POPC headgroups (coloured by heteroatom), lipid tails (grey), cholesterol (purple), apoA-I termini labelled N_1 C_1 and N_2 C_2, for chain 1 and 2, respectively. Adapted from (Lau and Middleton, 2020).

The similarities between the experimental and simulated rHDL nanoparticle spectra cross-peaks suggested the apoA-I α-helices were predominantly perpendicular to the lipid bilayer nanodisc normal (**Figure 5.10**, **red**) (Lau and Middleton, 2020). This was reflected in the AAMD model where the majority of the α-helices in the rHDL nanoparticle apoA-I chains were 61% perpendicular relative to B_0 (**Figure 5.10B**, **red**).

In HDL nanoparticles the hydrophobic effect acts to stabilise the interactions between the hydrophobic face of the apoA-I helices and the lipid acyl tails (Shih et al., 2007a; Shih et al., 2007b). Additionally, interhelical interactions such as salt bridges stabilise the interactions between the anti-parallel apoA-I chains (Bibow et al., 2017).

Furthermore, AAMD simulations of POPC, cholesterol, and short peptides comprised of 18 ELK amino acid residues exhibited different arrangements of the α-helices similar to the picket-fence model (**Figure 1.11A**) (Islam et al., 2018; Pourmousa and Pastor, 2018). This suggested the interhelical registry and interactions between the helices in the discoidal HDL apoA-I dimer are important to form the "double-belt" HDL model. Therefore, spectra cross-peak position changes due to further rearrangement of the apoA-I protein chains was not expected.

The cross-peaks in the 0 – 40° tilt angle region (**Figure 5.10A, blue**) also agree with the tilted α-helices in the AAMD-HDL model (**Figure 5.10B, blue**). This suggested the results of these combined 2D SS NMR spectra agree with the "double-belt" model of apoA-I in discoidal HDL nanoparticles (Bibow et al., 2017; Pourmousa et al., 2018) compared to the earlier "picket-fence" model (Jonas et al., 1990; Phillips et al., 1997).

The diagonal cross peaks (~140 – 230 ppm by ~2 – 10 kHz) in the 0 – 40° tilt angle region correspond to the apoA-I residues tilted with respect to B_0 in both spectra (**Figure 5.10A**, **blue**). As the tilt angle increased towards 40° the cross-peaks shift

diagonally towards the right side of the blue region, i.e. towards 125 ppm. This is visualised in **Figure 5.10B** where the α-helices (blue) show varied tilt angles with respect to B_0.

5.3.2.1 Atheroprotective apoA-I L144R structure in rHDL nanoparticles

Investigation of the differences between the rHDL-WT and atheroprotective apoA-I L144R and R173C 200:2 nanoparticle protein conformation was required. This was implemented by PEG-precipitation of the rHDL-L144R nanoparticles and compared to the rHDL-WT 2D high resolution ^{13}C-^{13}C dipolar correlation spectrum. The highlighted regions of the spectra (**Figure 5.11**) indicated small differences between the apoA-I WT and L144R protein conformations in rHDL nanoparticles (Lau and Middleton, 2020). This suggested the apoA-I L144R was also predominantly α-helical. However, differences in the chemical shifts for specific amino acids, which may indicate local structural differences cannot be pinpointed without selective isotope labelling of apoA-I.

An example of an identified residue region was alanine in the rHDL-WT and L144R proteins between ~53 – 58 ppm to ~16 – 19 ppm for C_α and C_β, respectively (Li et al., 2006; Wang and Jardetzky, 2002). This indicated the presence of alanine residues in an α-helical or random coil conformation (Li et al., 2006). The reference α-helical alanine chemical shifts are between approximately C_α at 53.9 – 55.8 ppm and C_β at 17.2 – 19.4 ppm. Whilst the random coil alanine shifts are at 50.9 – 54.4 ppm, and 17.8 – 20.3 ppm (**Appendix 3**) (Wang and Jardetzky, 2002). The regions indicated in **Figure 5.11** contain predominantly α-helical secondary structure residue cross-peaks. This was by comparison with the average chemical shifts (**Appendix 3**) (Wang and Jardetzky, 2002), and to previous spectra of truncated apoA-I (MSP1) in PEG-precipitated nanodiscs (Li et al., 2006), and LF apoA-I WT (Townsend et al., 2017).

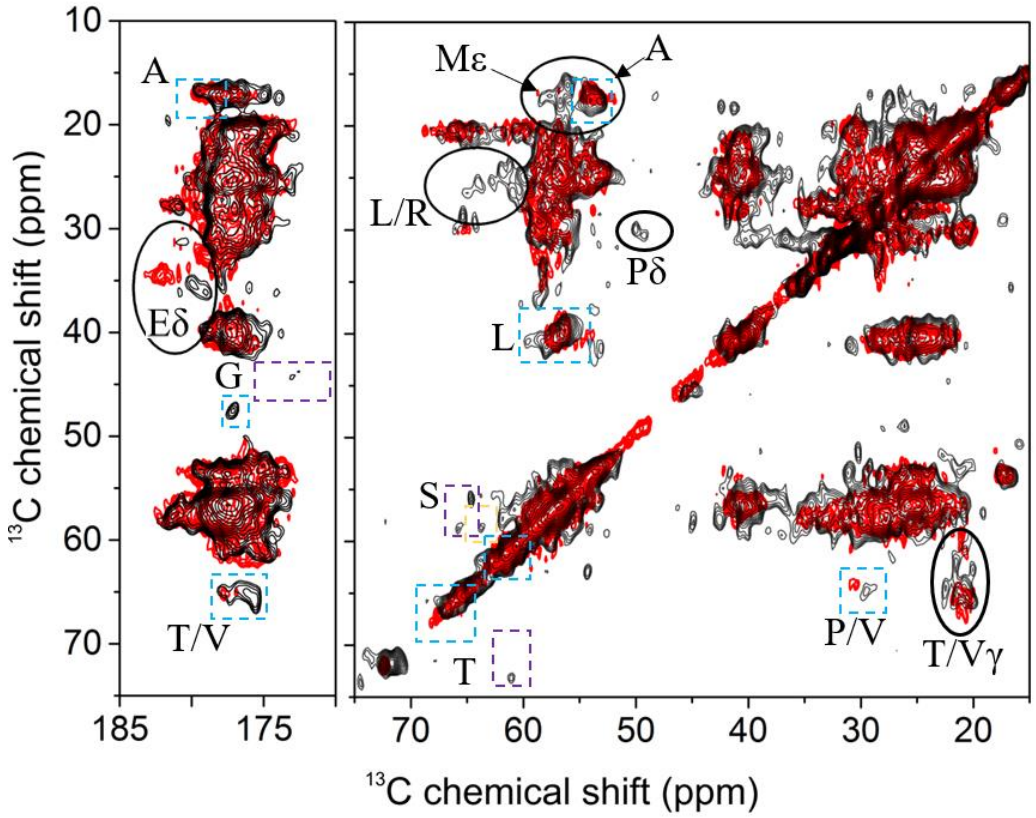

Figure 5.11. The expanded 2D ^{13}C-^{13}C dipolar correlation spectra of the PEG-precipitated rHDL [^{13}C]-WT (black) and L144R (red) 200:2 (M/M) nanoparticles. The spectrum was obtained at a frequency of 100.13 MHz, a DARR mixing time of 100 ms, and a MAS spinning frequency at 8 kHz (Lau and Middleton, 2020). The cross-peaks (dashed boxes) which are very sensitive to structure were identified as α-helical (blue), β-sheet (purple) and random coil (yellow). Cross-peaks arising from possible long-range coupling are circled (black).

The rHDL-L144R spectrum suggested there could be an increased mobility of residues such as methionines, and/or changes in the double belt interhelical registry. This was suggested by the absence of cross-peaks assigned to the methionine methyl groups and inter-residue long-range couplings (**Figure 5.11**, **Mε**) compared to the rHDL-WT spectrum.

Interestingly, the rHDL-L144R Glu carboxyl ^{13}C chemical shifts are perturbed relative to rHDL-WT (**Figure 5.11**, **Eδ**). The L144R point mutation occurs in α-helix 6 (H6) of apoA-I in which there are multiple native acidic and basic side chains ideally placed for interhelical salt bridge formation (**Figure 5.12A**) (Borhani et al., 1997). The arginine residue in apoA-I L144R H6 could change the Glu-Arg and Asp-Arg salt-bridge patterns in H6 (**Figure 5.12B**).

In the apoA-I WT Δ(1-43) crystal structure (Borhani et al., 1997) monomers are in an antiparallel alignment with the LL5/5 interhelical registry with α-helix 6 and 4 (H4) in registry with each other (**see Chapter 1**, **Figure 1.6**). In the H6/H4 alignment the L144 sidechain is facing inwards between the respective monomers in a cluster of hydrophobic residues. Therefore, the apoA-I L144R mutation could pose conformational constraints and prevent this alignment from forming in the LL5/5 registry.

To visualise the possible salt bridges, the L144 residue was mutated to arginine using the mutagenesis feature of the PyMol software (Schrodinger, 2015) in the LL5/5 registration of the apoA-I WT Δ(1-43) crystal structure (Borhani et al., 1997). This produced 25 suggested rotamer conformations in total. In this assumed LL5/5 registry of the apoA-I L144R dimer there was only one viable arginine rotamer which did not produce clashes (**Figure 5.12A**, **right**). The R144 residue is facing outwards on the hydrophilic face of H6 in proximity to Glu147. This could indicate the formation of a salt bridge between R144 and E147.

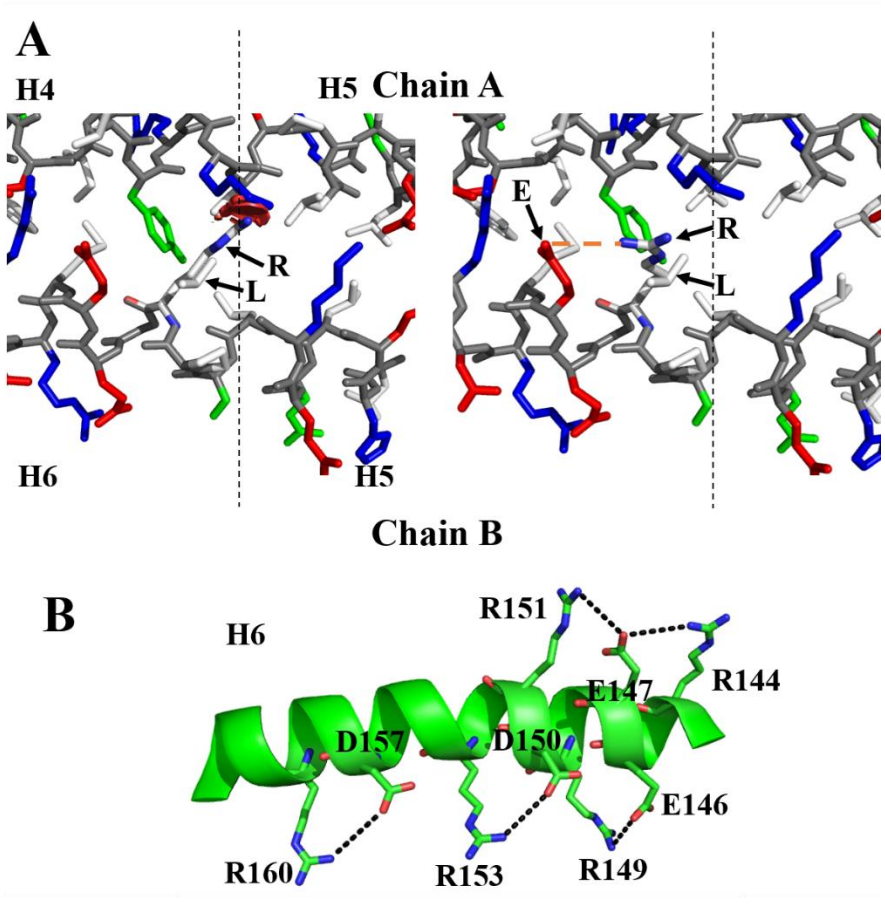

Figure 5.12. (A) A cross-section of apoA-I L144R H6 (chain B) and H4 (chain A). **Left)** The R144 rotamer example with spatial clashes (red discs). **Right)** The R144 rotamer conformation without clashes. The residues at position 144 are Leucine (L) and Arginine (R), and Glutamic acid (E) at position 147. The suggested E147 and R144 salt bridge (orange dashed line). The approximate margin between H4/H5 and H6/H5 is indicated by the dashed line. The amino acid sidechains are represented by polarity: nonpolar (white), polar (green), acidic (red, negative charge), basic (blue, positive charge), and backbone atoms (grey). **(B)** The possible salt bridge network in apoA-I L144R H6 with the Glu, Asp and Arg residues labelled.

The high resolution 2D ^{13}C-^{13}C dipolar correlation spectrum of apoA-I in rHDL-WT and R173C 200:2 nanoparticles were compared (**Figure 5.13**). Similar to the rHDL-

L144R apoA-I spectrum the spectra are broadly similar with an absence of major structural differences. The structural differences detected in the rHDL-bound apoA-I R173C protein are shown by some selective chemical shift differences such as Ala, Leu and Ser in the β-sheet regions (**Figure 5.13**). Further differences observed in the rHDL-R173C protein spectrum were a lack of assigned cross-peaks in the Thr/Val C'-Cα/Cβ (~177 by 65 ppm) and P/V Cβ-Cα (~28 by 65 ppm) α-helix regions.

Interestingly, the differences observed in the rHDL-R173C spectrum were not the same as the rHDL-L144R spectrum. The R173C mutation is in the apoA-I α-helix 7 (H7), which results in a shifted interhelical registry in the apoA-I R173C dimer due to the disulphide bonded "locked" conformation (Klon et al., 2000). This could explain the subtle structural differences in the rHDL-R173C apoA-I spectrum relative to the rHDL-WT spectrum.

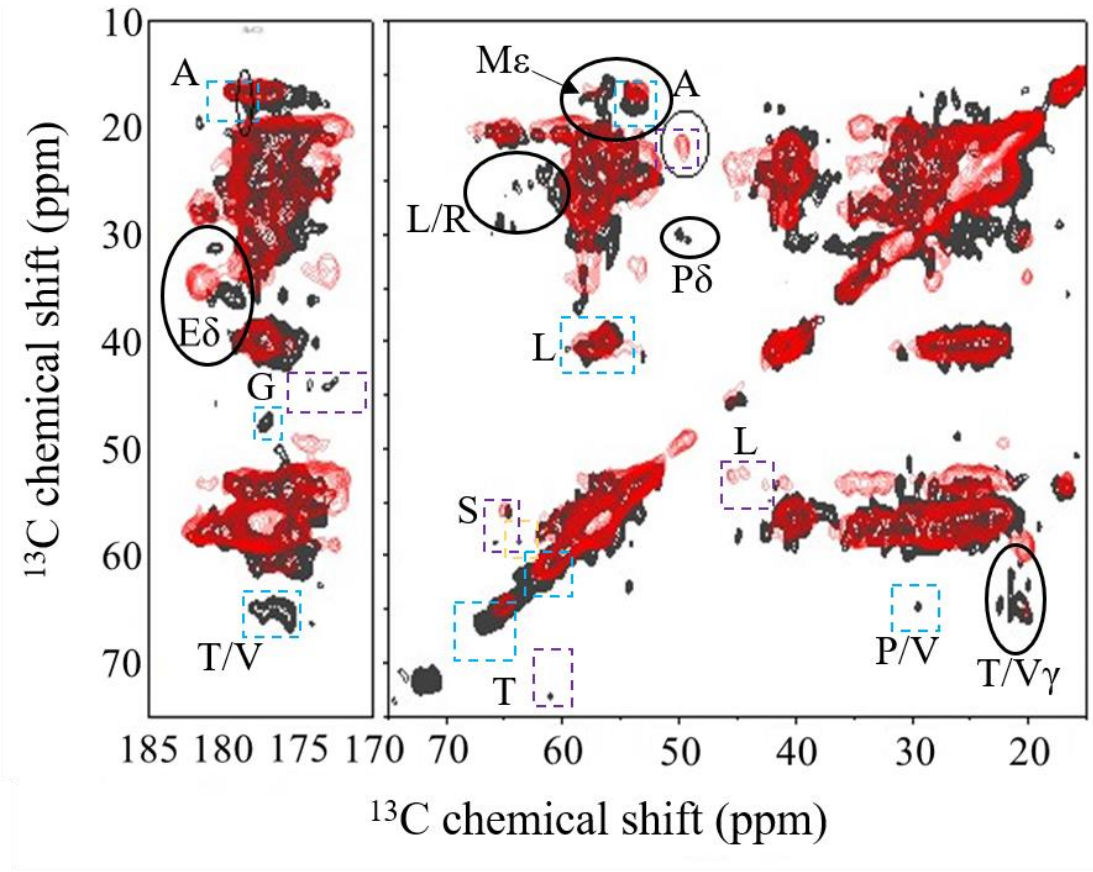

Figure 5.13. The expanded 2D ^{13}C-^{13}C dipolar correlation spectra of the PEG-precipitated rHDL [^{13}C]-WT (black) and R173C (red) 200:2 (M/M) nanoparticles. The spectrum was obtained at a frequency of 100.13 MHz, a DARR mixing time of 100 ms, and a MAS spinning frequency at 8 kHz (Lau and Middleton, 2020). The cross-peaks (dashed boxes) which are very sensitive to structure were identified as α-helical (blue), β-sheet (purple) and random coil (yellow). Cross-peaks arising from possible long-range coupling are circled (black).

Finally, the 2D ^{13}C-^{13}C dipolar correlation spectrum of PEG-precipitated lipid-free apoA-I WT was compared to the apoA-I rHDL-WT 200:2 spectrum (**Figure 5.14**). Similar to the previous spectra the structurally sensitive cross-peak regions are highlighted. The LF apoA-I WT and the rHDL-WT spectra are very similar with only small structural differences detected. Such as the Cα-Cβ cross-peaks assigned for lipid-

free apoA-I WT for the residues Ala, Thr, Pro/Val in random coil and β-sheet regions (**Figure 5.14**).

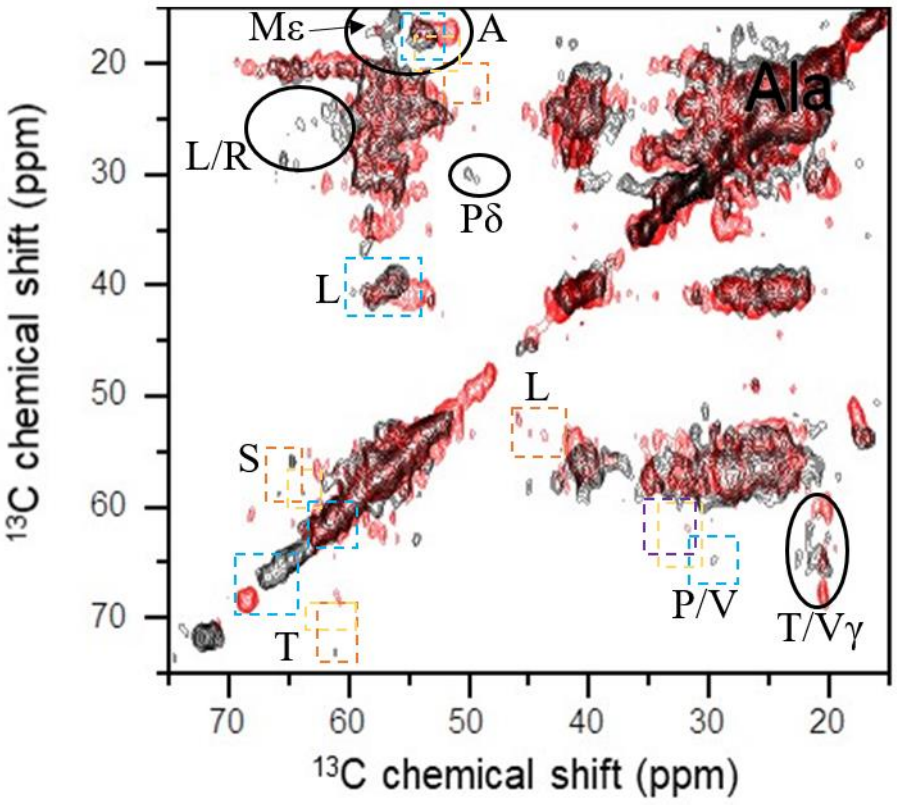

Figure 5.14. The expanded 2D ^{13}C-^{13}C dipolar correlation spectra of the PEG-precipitated rHDL [^{13}C]-WT 200:2 (M/M) nanoparticles (black) and lipid-free apoA-I WT (red). The spectrum was obtained at a frequency of 100.13 MHz, a DARR mixing time of 100 ms, and a MAS spinning frequency at 8 kHz (Lau and Middleton, 2020). The cross-peaks (dashed boxes) which are very sensitive to structure were identified as α-helical (blue), β-sheet (purple) and random coil (yellow). Cross-peaks arising from possible long-range coupling are circled (black).

Another aspect to consider was whether the differences in the PEG-precipitated lipid-free and rHDL-bound apoA-I sample spectra were due to differences in the protein side-chain dynamics. Amino acid side-chain rotation dynamics can occur on the micro- to

nanosecond timescale. This can affect the CP-MAS spectra by weakening the dipolar coupling strengths and relative signal intensity (Matlahov and van der Wel, 2018).

It is possible that the dynamics of the residue sidechains contributed to some of the small differences observed in the cross-peak regions of the lipid-free apoA-I WT spectrum. For example, the absence of a Pδ cross-peak for lipid-free apoA-I WT. Overall, the spectral differences were attributed to small structural differences as the cross-peak positions shifted from one site-specific secondary structure region to another. For example, the lipid-bound and lipid-free Thr cross-peaks were at the β-sheet to β-sheet/random coil regions, respectively.

5.4 Discussion

5.4.1 Lipid-bound apoA-I stability and secondary structure

CD SSE and thermal stability of the rHDL 200:2 nanoparticles were compared to determine if there were significant differences in the structures of the apoA-I mutants that confers greater or lower stability on the proteins. The rHDL nanoparticles had two thermal transitions. T_m1 could be a result of protein to protein conformation changes, whereas, protein dissociation from the lipids as the protein structure becomes fully denatured occurs during T_m2 (Giudice et al., 2017).

In the main protein-lipid dissociation transition the rHDL-L144R T_m2 was lower at 76.3°C than the rHDL-WT (82.9°C) and R173C (81.0°C) 200:2 nanoparticles. The changes in the lipid-bound apoA-I L144R SSE -12 % α-helix and +10 % unordered content could contribute to the lower thermal stability (T_m2) of lipid-bound apoA-I L144R compared to apoA-I WT in rHDL. The reduced stability of LF and rHDL apoA-I L144R could contribute to the different HDL metabolism and enhanced catabolism of

apoA-I/A-II *in vivo* (Gkolfinopoulou et al., 2020; Recalde et al., 2001), and the efficiency of *in vivo* lipid transfer (Lau and Middleton, 2020).

The LF apoA-I WT, R173C and L144R transition temperatures were in good agreement with previously published values (**Table 5.4**, **and refs therein**). Both atheroprotective mutants had a lower thermal stability compared to apoA-I WT. The LF apoA-I WT and R173C SSE's (α – 52, β – 6, T – 16, and U – 27 %) were similar to each other, and previous literature values at apoA-I concentrations close to 3.6 μM. The SSE's for apoA-I WT (α – 48, β – 8, T – 19, and U – 25 %) and R173C were similar in Giudice *et al*.'s study (Giudice et al., 2017), and for WT only (α – 49, β – 6, T – 17, U - ~28 %) (Sparks et al., 1992a).

Other studies estimated the α-helix content only of apoA-I WT between approximately 40 – 54 % (Alexander et al., 2009; Del Giudice et al., 2016; Han et al., 2005; Jonas et al., 1989; Mei and Atkinson, 2011; Petrlova et al., 2014). Previous LF apoA-I R173C of mixed monomer and dimer contained 55 ±1.3 % α-helix (7.2 μM) (Petrlova et al., 2014). The LF apoA-I R173C in this work has a lower α-helix content but this could be due to the lower sample concentration (3.6 μM) to avoid oligomerisation.

The rHDL-WT 200:2 SSEs (α – 67, β – 2, T – 11, and U – 20 %) were similar to literature values in **Table 5.5**. The secondary structure changes from LF to rHDL apoA-I WT support the "beta-clasp" model of lipid binding (**see Chapter 1**, **section 1.6.1**, **Figure 1.9**) (Lagerstedt et al., 2012; Oda et al., 2003). The LF apoA-I random coil (189-200) and β-sheet regions (209-219) are converted to α-helix during lipid-binding (Lagerstedt et al., 2012; Nagao et al., 2014; Oda, 2017; Oda et al., 2003) which correspond to approximately -4.5 and -4.1 % decreases in respective structure content.

This is similar to the structural changes observed from LF WT and rHDL-WT 200:2 observed by CD here, U is -6.3 % and β is -4.2 % (**Table 5.3**).

The increase in α-helix content in apoA-I WT upon lipid binding has been widely observed (**see Table 5.5**, **and refs therein**). The energy to bind lipids from α-helix formation has been suggested to be provided by the conversion of C-terminus random coil and β-sheet to α-helix (Lagerstedt et al., 2012; Nagao et al., 2014; Oda, 2017; Oda et al., 2003; Saito et al., 2004). The N-terminal domain, residues 1 – 43, of apoA-I WT have been shown to become lipid-bound in larger rHDL nanoparticles (11 – 12 nm) (Li et al., 2004). In the AAMD-HDL model of 200:20:2 nanoparticles these residues are predominantly helical (Pourmousa et al., 2018).

Table 5.5. Literature SSEs of rHDL nanoparticles with approximate molar ratios and nanoparticle diameters (nm). Lipids are POPC or *DMPC, rHDL-R173C and L144R are indicated by $^{R173C}_{or}{}^{L144R}$.

POPC:cholesterol :apoA-I	SSE (%)				~Size (nm)	References
	α	β	T	U		
200:2*	69, 71^{R173C}	4.5	8	18	9.6	(Giudice et al., 2017)
90:2, 152:2^{R173C}	61, 61^{R173C}				7.8	(Calabresi et al., 1997b)
~300:2	71, 62^{R173C}				12.5	
124:2	76				10	(Saito et al., 2004)
160:2	68.1				7.8, 9.8	(Chen et al., 2009)
64:2	58	5	8		9.3	(Sparks et al., 1992a)
130:2	63	8	19		9.9	
160:2	73	13	17		11.2	
256:2	74	12	11		12.1	
160:2	73 ±3				9.4	(Gu et al., 2010)
200:2	84 ±3				10.2	
156:2	78.0				9.6	(Silva et al., 2008)
170:2*	65 ±3				11.6	(Fang et al., 2003a)
190:10:2	74 ±2				9.7	(Han et al., 2005)
84:10:2	61				7.7	(Jonas et al., 1989)
144:12:2	72				8.6, 9.6	
164:38:2	58				10.9	
200:20:2^{L144R}	~57.5				~ 8.4 – 10.0	(Gkolfinopoulou et al., 2020)
200:20:2	~65.5					

The lipid-bound apoA-I R173C structure contained more residues in an ordered conformation (α – +7.2%, β – +17 % and -20% U) compared to rHDL-WT

nanoparticles. This contrasted with the rHDL-R173C 200:2 nanoparticle SSE from SRCD (Giudice et al., 2017). This suggested that dimeric disulphide bonded apoA-I R173C when lipid-bound in a "locked" shifted registry (Klon et al., 2000) may retain some regions with different conformations such as β-strand structure. The overall β-strand content in the LF apoA-I WT "beta-clasp" model was ~17 % in the N- and C-termini regions (Lagerstedt et al., 2012) suggesting potential regions of β-strand formation in rHDL apoA-I R173C (~19 % by CD).

Furthermore, the rHDL-C WT and R173C 190:10:2 nanoparticles (~8.8 – 9.6 nm diameter) contained similar secondary content to the corresponding apoA-I 200:2 nanoparticles. Previously, ~9.6 nm diameter rHDL-C WT 160:8:2 (M/M) nanoparticles examined by EPR spectroscopy detected 9 % β-strand content in apoA-I WT (Giudice et al., 2017; Oda et al., 2013). This is similar to the ~8.5% β-strand content observed in the rHDL-C WT 190:10:2 nanoparticles in this study.

Interestingly, a recent structure-function study showed analysis of rHDL-C ~200:20:2 (M/M) nanoparticles containing apoA-I WT or L144R with a diameter between ~ 8.4 – 10.0 nm (Gkolfinopoulou et al., 2020). The CD α-helix content (~57.5 vs. ~65.5 %) and thermal stability (~70 vs. 73°C) of lipid-bound apoA-I L144R were lower than apoA-I WT in the rHDL-C nanoparticles, respectively (Gkolfinopoulou et al., 2020). This is similar to the reduced thermal stability and α-helix content determined for the rHDL-L144R 200:2 (M/M) nanoparticles in this work. Additionally, the LF apoA-I L144R of ~52 % α-helix content was similar to this work (~55%) (Gkolfinopoulou et al., 2020).

5.4.2 rHDL apoA-I SS NMR structural analyses

This work focussed upon comparing the protein structures of apoA-I WT, R173C and L144R in PEG-precipitated rHDL nanoparticles detected using 2D ^{13}C-^{13}C dipolar CP-MAS SS NMR.

The 2D ^{13}C-^{13}C dipolar CP-MAS SS NMR spectra of rHDL-WT and L144R nanoparticles showed small differences between the predominantly α-helical lipid-bound proteins (Lau and Middleton, 2020). Interestingly, the differences detected in the rHDL-L144R protein assigned cross-peaks, suggested an increased mobility of residues and the possible altering of the salt bridge network in helix 6 and/or the interhelical registry.

The subtle differences in the spectra could reflect the increase in unordered (+10 %) and decrease in α-helical content (-12 %) in the rHDL-L144R apoA-I relative to the lipid-bound apoA-I WT (Lau and Middleton, 2020). The rHDL apoA-I L144R differences in the local structure detected by SS NMR and reduced stability indicated by T_m2 relative to apoA-I WT in rHDL suggest the conformation of the "double belt" dimer in the discoidal rHDL nanoparticles could be perturbed. Further experiments are required to understand if the subtle structural differences detected in lipid-bound apoA-I L144R results in these changes.

Another key aspect of this work was the comparison between the AAMD-HDL model and experimental rHDL-WT 2D ^{13}C-^{13}C CP-MAS correlation CP-MAS and ^{1}H-^{15}N PISEMA spectra. The AAMD-model deviates from the planar "double belt" model (Segrest et al., 1999) with the N- and C- terminal α-helices tilted away from the bilayer normal (Pourmousa et al., 2018). Cross-peaks were observed in the corresponding estimated regions for tilt angles between 0 – 90° from B_0 in a simulated α-helical

spectrum (Marassi and Opella, 2000). The intensity and distribution of the experimental rHDL-WT and AAMD-HDL protein cross-peaks in the perpendicular α-helical region (~50 – 125 ppm by ~0 – 6 kHz) was greater than the cross-peaks in the parallel orientation region (~125 – 225 ppm by 0 – 10 kHz) (**Figure 5.10**). This suggested the protein conformation of apoA-I in the rHDL-WT 200:2 nanoparticles and AAMD-HDL model were similar with the α-helices predominantly perpendicular to the bilayer normal.

Overall, the similarities between the two different types of SS NMR spectra supported the predominantly α-helical conformation and molecular belt model alignment of apoA-I relative to the lipids. However, further evidence is required to support the predominantly perpendicular orientation of the apoA-I WT protein α-helices with respect to the lipid bilayer/B_0, such as a simulated PISEMA spectrum in which the apoA-I protein is parallel to the bilayer normal. As well as experimental comparisons to oriented rHDL-WT, R173C and L144R nanoparticle protein ^{1}H-^{15}N PISEMA spectra using uniformly [^{15}N]-labelled proteins.

The CP-MAS spectra of apoA-I R173C in rHDL did not show the same differences as apoA-I L144R relative to apoA-I WT in rHDL nanoparticles. This suggested that although the interhelical registry of the apoA-I R173C dimer is shifted to align via H7 through the cysteine-cysteine disulphide bond that this does not cause major structural differences with respect to apoA-I. The lipid-bound apoA-I R173C dimer in the shifted registry spectrum contained different cross-peaks assigned to the β-sheet regions for Leu and Ala residues. In combination with the CD SSE this suggested that apoA-I R173C in HDL could contain a higher β-strand content compared to apoA-I WT.

Similarly, the lipid-free apoA-I WT CP-MAS spectrum indicated additional cross-peaks assigned to β-sheet and unstructured random coil regions. The structural models of lipid-free apoA-I WT are predominantly α-helical (**see Chapter 1**, **section 1.6.1**) with regions of unstructured random coil between α-helices. In the crystal structures of apoA-I Δ(1-43) between H9 and H10, and in the N-terminal helical region of apoA-I Δ(185-243) (Borhani et al., 1997; Mei and Atkinson, 2011), and cross-linking models of full-length apoA-I WT (Pollard et al., 2013; Silva et al., 2005a). The β-sheet content has been detected in the "beta-clasp" model of lipid-free apoA-I WT (Lagerstedt et al., 2012; Oda et al., 2003).

This is the first direct comparison of the thermal stability and secondary structure using CD and solid-state NMR of rHDL nanoparticles containing apoA-I WT, or the atheroprotective apoA-I mutants. Overall, the CD SSEs indicated apoA-I WT, R173C and L144R in rHDL nanoparticles was predominantly α-helical. Surprisingly, the apoA-I L144R protein did not increase in α-helix content when lipid bound but increased in unordered content. This could explain the lower thermal stability of the rHDL-L144R nanoparticles compared to rHDL apoA-I WT. Furthermore, the CP-MAS spectra comparison of precipitated rHDL-WT and L144R nanoparticles did not show major differences in the secondary structure. The comparisons of both experimental rHDL-L144R and R173C protein CP-MAS spectra compared to rHDL apoA-I WT suggested the proteins overall contain similar predominantly α-helical conformations.

The detection of selective differences in the structurally sensitive cross-peaks of the apoA-I L144R and R173C proteins in rHDL nanoparticles suggested there were subtle local structural differences. To identify the local differences in structure further SS NMR experiments are required with rHDL nanoparticles containing selectively labelled

proteins expressed using suitable E. *coli* auxotrophs (Lin et al., 2015; Monneau et al., 2016).

The absence of major structural differences detected in the respective apoA-I proteins suggested further investigation of possible morphological differences was necessary. For example, the rHDL nanoparticles could have different lipid and cholesterol distributions affecting the overall nanoparticle morphology. This was explored further in **Chapter 6** using oriented ^{31}P SS NMR. The rHDL nanoparticle morphology could affect how the particles interact with enzymes in RCT (Lau and Middleton, 2020), such as LCAT (Sorci-Thomas et al., 1993), CETP (Qiu et al., 2007) and cell receptors like ABCA1 (Sahoo et al., 2004).

6 rHDL nanoparticle morphology

6.1 Introduction

In the previous chapter the structure of apoA-I WT and atheroprotective apoA-I mutants in rHDL nanoparticles was analysed by CD and SS NMR. However, only subtle structural differences between the lipid-bound apoA-I WT and atheroprotective apoA-I mutants were found. This suggested the apoA-I structure may not be the only component of the rHDL nanoparticles that could explain the atheroprotective rHDL nanoparticle functional differences, and the lipid component may also play a role.

As discussed in **Chapter 5**, the experimental techniques used to study rHDL nanoparticle structure have focussed on the truncated apoA-I WT structure rather than the phospholipid or cholesterol constituents. There is also a need for techniques to establish the morphology of the particles, as the surface curvature could affect cholesterol cycling and how the rHDL nanoparticles interact with enzymes such as CETP (Qiu et al., 2007) in RCT. The shape of the particles modulates interactions with CETP and SR-B1, for example (Liadaki et al., 2000; Qiu et al., 2007). It is conceivable that the apoA-I mutants confer different morphologies on the HDL particles compared to apoA-I WT.

TEM is used routinely to confirm the discoidal shape of rHDL nanoparticles (Bibow et al., 2017; Chen et al., 2009; Sparks et al., 1992b; Zhang et al., 2011) and (**see Chapter 4**, **Table 4.1 and refs therein**). However, negative stain TEM is limited in resolution

and may miss subtle shape differences between rHDL nanoparticles that could have significant implications for the functional interactions with cholesterol cycling proteins. Additionally, the type of negative staining such as PTA was suggested to increase rouleaux formation of rHDL nanoparticles compared to uranyl formate (UF) (Zhang et al., 2011).

Previous solution and SS NMR studies have focussed on the structure of truncated apoA-I (Bibow et al., 2017; Li et al., 2006) or the structure of nanodisc embedded proteins (Hagn et al., 2013; Mors et al., 2013) rather than discoidal rHDL nanoparticles containing full-length apoA-I WT. The truncated apoA-I Δ(1-54, 121-142) structure was analysed by solution-state NMR to produce high-resolution structural models of discoidal rHDL-like nanoparticles to increase reorientation rates (Bibow et al., 2017; Lau and Middleton, 2020).

The ^{31}P CSA provides lipid headgroup curvature information, however, this cannot be obtained using this high-resolution solution NMR technique due to averaging of the ^{31}P CSA information from isotropic tumbling (Lau and Middleton, 2020). Under the applied magnetic field in solution NMR magnetic alignment of bicelles or larger macrodiscs (~30 nm in diameter) occurs and the ^{31}P CSA is preserved (Park et al., 2011). However, plasma HDL and rHDL particles have smaller diameters between ~7 – 17 nm (Cavigiolio et al., 2008; Chen et al., 2009; Rosenson et al., 2011; Sparks et al., 1992b) and do not align under B_0 (Lau and Middleton, 2020).

NMR structural studies of embedded membrane proteins in planar oriented phospholipid bilayers on glass slides is well established and has enabled the study of proteins associated with diseases and proteins with antibiotic activity (Bechinger et al., 2004; Hansen et al., 2015; Hughes and Middleton, 2014; Naito, 2009; Park et al., 2012;

Salnikov et al., 2009; Sharma et al., 2010). An oriented planar lipid bilayer can be prepared with or without protein on glass slide substrates such as microscope cover slips (Hughes and Middleton, 2014; Nicholson et al., 1987; Park et al., 2012; Salnikov et al., 2009; Sharma et al., 2010; Traaseth et al., 2006). The lipid/protein sample organic solvent is evaporated after deposition on the slides. Next the sample is rehydrated at a relatively high humidity and constant temperature (Naito, 2009).

In oriented phospholipid bilayer SS NMR studies, the membrane can be oriented with the bilayer normal perpendicular or parallel to the applied magnetic field (Bechinger et al., 2004; Huster, 2014). rHDL nanoparticles can form rouleaux which are stacks of particles where the lipid bilayer normal (I_z^{HDL}) is parallel to the surface of the TEM grid which formed as a function of concentration as indicated in **Chapter 4** with UA stained rHDL-WT 200:2 nanoparticles visualised by TEM. At the higher apoA-I concentration (36 μM) the rHDL-WT 200:2 nanoparticles formed rouleaux where I_z^{HDL} is perpendicular to B_0. Whereas, at the lower apoA-I concentration (9 μM) I_z^{HDL} was parallel to B_0 and formed discrete nanoparticles (**Figure 6.1**). Significantly this implied that the rHDL nanoparticles could adopt preferred orientations in a concentration dependent manner on glass slides for oriented SS NMR analyses (Lau and Middleton, 2020).

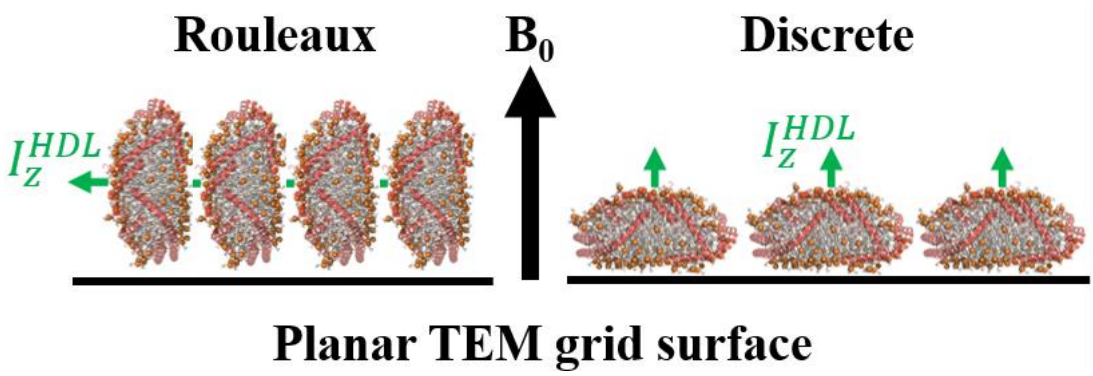

Figure 6.1. The orientations of rHDL nanoparticles on the planar TEM grid surface as stacks in rouleaux (**left**) and as discrete (**right**) particles, where the principal axis of inertia ($\boldsymbol{I_Z^{HDL}}$) of the HDL nanoparticle matrix, is oriented perpendicular and parallel relative to B_0, respectively. The lipid headgroups (orange spheres), lipid acyl tails (grey), and apoA-I WT molecules (red). The AAMD-HDL WT 200:20:2 model was obtained from (Pourmousa et al., 2018).

The two extreme orientations of I_Z^{HDL} relative to the applied magnetic field of 0° (parallel) and 90° (perpendicular) were considered for the simulated NMR line shapes as the rHDL nanoparticles could adopt a completely parallel or perpendicular orientation on the planar glass surface. The relationship between the dynamically averaged lipid orientation and the ^{31}P NMR lineshape relative to the applied magnetic field and how this affects the observed spectra is explained in **section 6.2.3.** It will be shown that the rHDL nanoparticles have specific orientations on the glass surface and that experimental and simulated ^{31}P line shapes are highly sensitive to the surface curvature of the lipid cargo, which defines the overall shape of the particles.

Furthermore, there is a distinct lack of NMR methods for determining the shape of rHDL nanoparticles containing full-length apoA-I or the atheroprotective apoA-I mutants. Therefore, this chapter focuses on analysing the novel application of oriented ^{31}P SS NMR for determining rHDL nanoparticle morphology. The oriented ^{31}P SS

NMR of lipids in rHDL nanoparticles could provide clues to differences in the nanoparticle morphology or lipid distributions not evident by experimental analyses that have focussed on the apoA-I structure.

6.1.1 Aims

The aim of the work described in this chapter is:

To compare the morphologies of the rHDL particles bearing the WT and mutant proteins. A ^{31}P NMR method was developed, which exploited the ability of rHDL to adopt preferred orientations on glass substrates held at a fixed angle in the magnetic field. Previous oriented studies of lipid bilayers demonstrated the feasibility of examining protein and lipid orientations with ^{15}N/^{13}C, and ^{31}P SS NMR, respectively (Bechinger et al., 2004; Das et al., 2013; Hughes and Middleton, 2014; Marassi and Crowell, 2003; Nakazawa et al., 2009; Salnikov et al., 2009).

6.2 Materials and methods

The rHDL nanoparticles characterised in this chapter were prepared as described in **Chapter 4**. The following methods for rHDL nanoparticle lipid and cholesterol structural characterisation are published in (Lau and Middleton, 2020).

6.2.1 Oriented rHDL nanoparticle preparation

The glass cover slips and dried rHDL nanoparticles on slides were prepared as described in **Chapter 5** (**see section 5.2.3**). The dried samples were rehydrated at 37°C and 99 % humidity for various time periods (3, 4, 6 and 16 hours), and wrapped in cling film before NMR analysis. The human plasma HDL sample (10 mg, Merck) contained ~5 mg protein in 150 mM NaCl, 0.01 % EDTA, pH 7.4 solution and was diluted to 1 mL before following the same preparation as the rHDL nanoparticle samples.

6.2.2 ^{31}P solid-state NMR of rHDL nanoparticles

A Bruker Avance 400 spectrometer was used to perform the SS NMR measurements using an 89 mm bore magnet at a magnetic field strength of 9.3 T and a temperature of 25°C. The stacked oriented rHDL nanoparticle sample was placed into the coil (9 x 3 x 3 mm) of a double resonance (H/F and X, the latter tuned to 161 MHz for ^{31}P observation) static flat-coil probe (Bruker), and ^{31}P NMR measurements were collected. Excitation of the ^{31}P spins was induced with a 3.5 µs 90° pulse followed by continuous wave proton decoupling at 20 kHz during the acquisition time period. A 2 s recycle delay was used and spectra contained 10 000 – 50 000 accumulated transients.

6.2.3 ^{31}P oriented rHDL nanoparticle lineshape calculations

6.2.3.1 Lipids in planar or spherical distributions

This section explains the relationship between the lipid orientation and the ^{31}P NMR lineshape relative to the applied magnetic field (B_0) in different lipid samples and how this affects the observed spectra. To explain NMR lineshape calculations used in this work for planar and spherical lipid distributions.

The lipid orientation within the planar bilayer relative to B_0 can be detected using ^{31}P SS NMR (Huster, 2014). The chemical shift tensor components of a phospholipid are represented by an ellipsoid as in **Figure 2.5** (**see Chapter 2**) where $\delta_{11} \geq \delta_{22} \geq \delta_{33}$ (Duer, 2004; Nakazawa et al., 2009). The orientation dependence of the CSA for lipids in different samples affects the observed spectra (**Figure 6.2**) (Huster, 2014). The isotropic chemical shift (δ_{iso}) in the simulated spectrum of lipids undergoing rapid motion in solution show a narrow Lorentzian lineshape at ~2 ppm as the CSA components average to zero (**Figure 6.2A**) (Huster, 2014). In experimental solution NMR spectra, the

detected isotropic chemical shift varies dependent upon the type of phospholipid and lipid headgroup (Puppato et al., 2007).

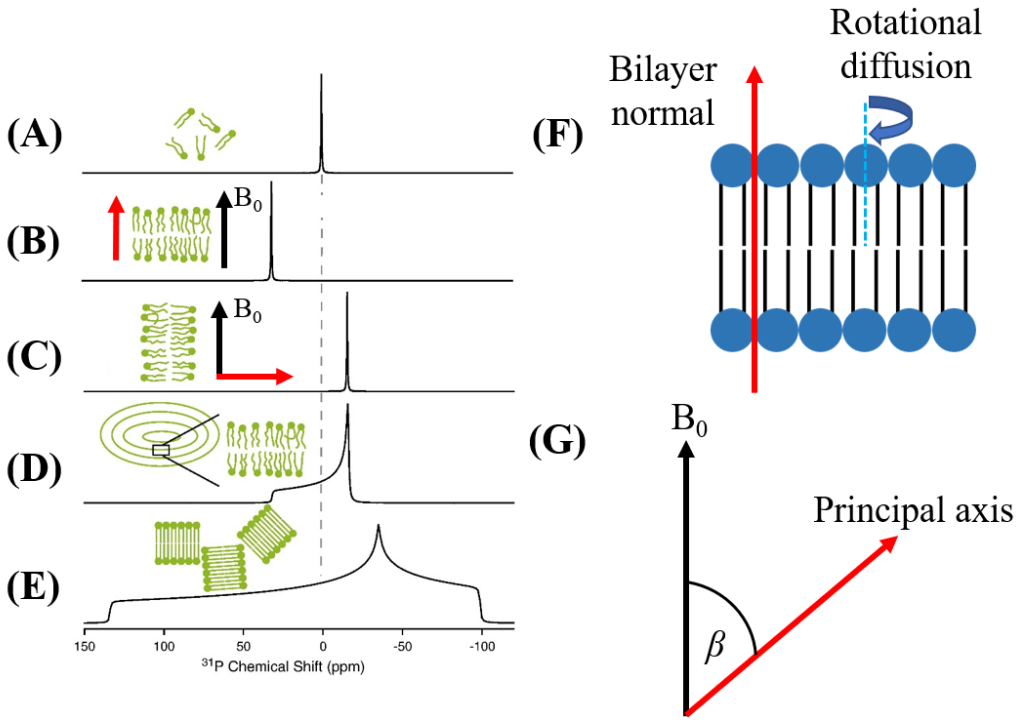

Figure 6.2. Simulated ^{31}P proton decoupled NMR spectra adapted from (Huster, 2014). **(A)** Lipids in solution undergoing isotropic motion at δ_{iso} at 2 ppm (dotted line). **(B)** A planar lipid bilayer at ~30 ppm with the principal axis (bilayer normal) parallel, **(C)** or perpendicular to B_0, at ~-15 ppm. **(D)** Lipids in a multilamellar vesicle with each chemical shift for all available lipid orientations in the vesicles. **(E)** A solid crystalline state lipid spectrum (Huster, 2014). **(F)** Rotational diffusion of a bilayer lipid (blue arrow) around the long molecular axis of the lipid (dashed blue line). The bilayer normal (red arrow), the lipid headgroups (blue) and fatty acid tails (black). **(G)** The principal axis of the rotationally averaged chemical shift tensor (red arrow) of a bilayer lipid relative to B_0 (black arrow), separated by the angle β.

The theoretical treatment in this work is based on previous work by Picard *et al*. for aqueous suspensions of liposomes and has been adapted for the specific case of rHDL

oriented on a planar substrate (Lau and Middleton, 2020; Picard et al., 1999). All simulations were performed using C programs written by Prof. D. Middleton. The simulated spectra for a 100 % planar or spherical lipid distribution were determined using **Equations [11]** and **[12]** of the measured lipid(s) ^{31}P NMR frequency and the spectral density, respectively.

A lipid experiences fast rotational diffusion around the long molecular axis in a lipid bilayer in the liquid crystalline phase state (**Figure 6.2F**) (Huster, 2014; Macdonald et al., 2013). The measured ^{31}P NMR frequency of a rapidly rotating lipid in a bilayer can be described with (Picard et al., 1999):

$$\omega = \Delta\delta_{av}\frac{(3cos^2\beta - 1)}{2} + \delta_{iso} \qquad \textbf{[11]}$$

The angle between B_0 and the principal axis of the chemical shift tensor is β (**Figure 6.2G**) (Picard et al., 1999). The isotropic chemical shift (δ_{iso}) is nearly zero (~2 ppm) for a lipid in a fluid bilayer with the corresponding rotationally averaged full CSA is 45 ppm, and $\Delta\delta_{av}$ is 30 ppm (Huster, 2014; Macdonald et al., 2013). When the lipid bilayer normal is parallel or perpendicular to B_0 the respective chemical shifts are 30 and -15 ppm, respectively (**Figure 6.2B-C**) (Huster, 2014).

A range of ^{31}P NMR frequencies dependent on the lipid orientation(s) (i.e., angle β) can be observed between 30 and -15 ppm. This results in a broad powder pattern lineshape, e.g., as seen for a multilamellar vesicle that contains multiple lipid orientations (**Figure 6.2D**) (Huster, 2014; Macdonald et al., 2013). In comparison the spectra of lipids in a solid crystalline state (**Figure 6.2E**) shows a very broad powder pattern lineshape (Huster, 2014). The continuous lineshape with less than three-fold symmetry is formed from overlapping lines at each frequency due to the presence of all available orientations

(Duer, 2004). This demonstrates the orientation dependence of the ^{31}P SS NMR signal in phospholipids.

Equation [12] describes the connection between the orientation distribution of the lipids which experience fast molecular motions and the sample molecules weighted-average NMR frequencies (Lau and Middleton, 2020; Picard et al., 1999). These are known as the spectral density, S(ω), and angular distribution, P(β), and affect the NMR spectrum lineshape. This is defined as (Picard et al., 1999):

$$S(\omega)|d\omega| = P(\beta)|d(\beta)| \qquad \textbf{[12]}$$

In a liposome the lipid molecules are in a 100 % spherical distribution and a spherically-averaged and axially symmetrical powder lineshape is produced as P(β) = sin(β) (**Figure 6.2D**) (Huster, 2014; Lau and Middleton, 2020). In comparison, β = 0° or 90° when a 100 % planar lipid bilayer normal (**Figure 6.2B and C**) is parallel or perpendicular to B_0, respectively. The narrow Lorentzian lineshapes are observed at 30 and -15 ppm for the 100 % parallel and perpendicular oriented lipid bilayers, respectively (Huster, 2014). This is a result of the limited random distribution of lipids about the β angles in the planar bilayers hence the term angular distribution P(β) (Lau and Middleton, 2020). The following calculation was used to determine the real part of the NMR signal as a function of time.

$$Re\big(S(t)\big) = \sum_{\beta=0}^{\frac{\pi}{2}} P(\beta)\cos(\omega t) \qquad \textbf{[13]}$$

The complex signal was Fourier transformed to produce the NMR lineshape with the broadening function (exp(-t/T_2)) used on all calculated signals (Lau and Middleton, 2020).

6.2.3.2 Calculations of expected lineshapes from the AAMD model

A ^{31}P NMR lineshape was simulated based on the AAMD structural model of nascent HDL containing POPC:cholesterol:apoA-I WT 200:20:2 (M/M) (**Figure 6.3**) (Pourmousa et al., 2018) for comparison with the lineshapes of the oriented rHDL nanoparticle samples. The three different types of motion the POPC molecules can experience within a bilayer leaflet are translational motion, local motional fluctuations, and as described before the rotation about the long molecular axis (Klauda et al., 2008; Lau and Middleton, 2020; Macdonald et al., 2013). The dominant motion of the POPC lipids was assumed to be the rotational diffusion about the long molecular axis i.e. angle β which in turn scales the ^{31}P CSA as shown in **Equation [11]** (**section 6.2.3.1**) (Lau and Middleton, 2020).

The dynamically averaged ^{31}P NMR frequency for each lipid in the final 1 μs of a 10 μs MD simulation trajectory was determined by calculating the average inclination angle (β_{av}) of each of the 200 lipids over this time period. Previous studies have calculated the axial rotational diffusion coefficient (D_R) of DPPC lipids in MD simulated fluid-phase bilayers between ~$1x10^7$ – $1.6x10^8$ s^{-1} (Essmann and Berkowitz, 1999; Klauda et al., 2008), and experimentally with electron spin resonance in DMPC/DMPG/cholesterol fluid membranes where the D_R values had a magnitude up to $x10^9$ s^{-1} (Ge and Freed, 2011; Sanderson, 2012). Therefore, the timescale of 1 μs was greater than the rotational diffusion timescale of each lipid in this timeframe (Lau and Middleton, 2020).

I_z^{HDL} the principal axis of inertia of the rHDL nanoparticle lipid matrix was therefore assumed to be either parallel or perpendicular to B_0, i.e. as separate discrete rHDL nanoparticles or as stacks in the rouleaux formation, respectively (**Figure 6.3**) (Lau and Middleton, 2020).

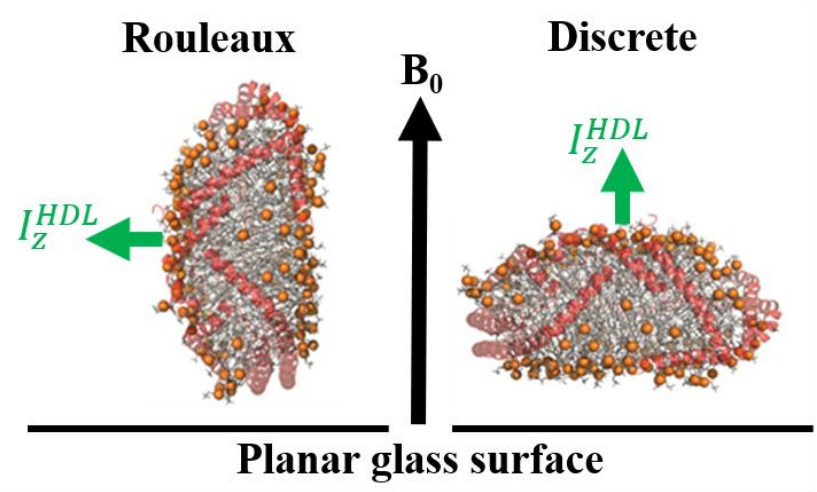

Figure 6.3. The orientation of the rHDL nanoparticles with $\boldsymbol{I_Z^{HDL}}$, the principal axis of inertia of the HDL nanoparticle matrix, oriented perpendicular (**left**) and parallel (**right**) to B_0, representations for stacked rouleaux or discrete nanoparticles relative to the planar glass surface. AAMD-HDL WT 200:20:2 model obtained from (Pourmousa et al., 2018). The lipid headgroups (orange spheres), lipid acyl tails (grey), and apoA-I WT molecules (red).

Across a total of 64 frames in the final 1 μs of the 10 μs MD simulation the angle β in each frame was calculated for all POPC molecules in the 200:20:2 HDL nanoparticle. β is the angle between each lipid(s) principal axis of inertia (I_Z^{POPC}) relative to B_0 (Lau and Middleton, 2020). Small changes in the root mean square deviation (RMSD) occur in the final 1 μs of the simulation and the overall assembly is assumed to have reached a stable state.

To calculate the time-averaged ^{31}P frequency of each lipid molecule the average inclination angle β_{av} over the final 1 μs was substituted into **Equation [11]** (Lau and Middleton, 2020). Another approach considered was motional averaging of the full CSA tensor of each lipid molecule in the HDL nanoparticle. However, the method

described above had greater sensitivity towards the lipid molecule(s) average orientations (Lau and Middleton, 2020).

6.2.3.3 Application to the hemispheroid shape

Picard *et al*.'s equation determined the density of probability for an ellipsoid (**Equation [14]**) (Picard et al., 1999). This applied to rHDL nanoparticles with lipid bilayer surface curvature which was approximated by a hemispheroid (concave or convex) (Lau and Middleton, 2020).

$$P(\beta) = \frac{2\pi b^2 \sin\beta}{[\sin^2\beta + r^2\cos^2\beta]^2} \qquad \textbf{[14]}$$

In **Equation [14]** r = b/a, where a and b are the minor and major hemispheroid axis, respectively, indicated in **Figure 6.4**. When a < b the shape is an oblate hemispheroid and was assumed to represent the surface curvature of the lipids.

As described previously, the rHDL nanoparticles can form rouleaux or exist as discrete particles on a planar surface. Therefore, the NMR lineshapes were calculated for the hemispheroid approximation where I_z^{HDL} was perpendicular or parallel to B_0. The NMR lineshape calculations for an oblate hemispheroid with axis a parallel or perpendicular to B_0 were different with respect to the angles available to the lipids in the nanoparticles. The NMR lineshape when axis a was parallel to B_0 (**Figure 6.4A**) was calculated using **Equations [11]**, **[12]** and **[14]**, with summation of every angle β from 0° to 90°. The angle β represents the available orientations of the lipids in discrete rHDL nanoparticles (Lau and Middleton, 2020).

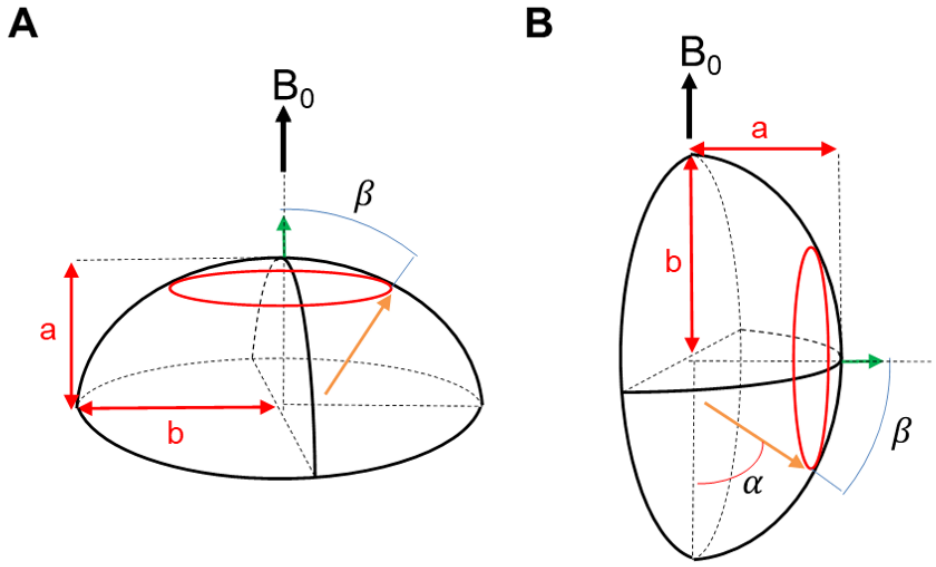

Figure 6.4. The hemispheroid representation of the surface curvature in an rHDL nanoparticle. The minor axis (a) and major axis (b) are indicated. $\boldsymbol{I_z^{HDL}}$ (green arrow) or axis a is parallel **(A)** or perpendicular **(B)** to the applied magnetic field (B_0). The angles α and β are indicated relative to B_0. Obtained from (Lau and Middleton, 2020).

In comparison for rouleaux rHDL nanoparticles axis a is perpendicular to B_0 and the lipids can also be oriented in a circular distribution at angle α with respect to angle β (**Figure 6.4B**). Therefore, the possible α values were from +(90°-β) to –(90°-β). All of the α and β angles were summated and α was substituted into **Equation [14]**, followed by the use of **Equations [11]**, and **[12]** to calculate the lineshape (Lau and Middleton, 2020).

6.2.3.4 Discoidal rHDL nanoparticle lineshape simulations

The rHDL-C nanoparticle lineshapes were simulated with a torus discoidal shape approximation. This approximation contained two components, a planar lipid bilayer inner circular core and the surrounding outer lipids distributed in a partial torus. The radius of the circular core is defined as *c*, and the partial torus width by *t* (**Figure 6.5A-B**) (Lau and Middleton, 2020).

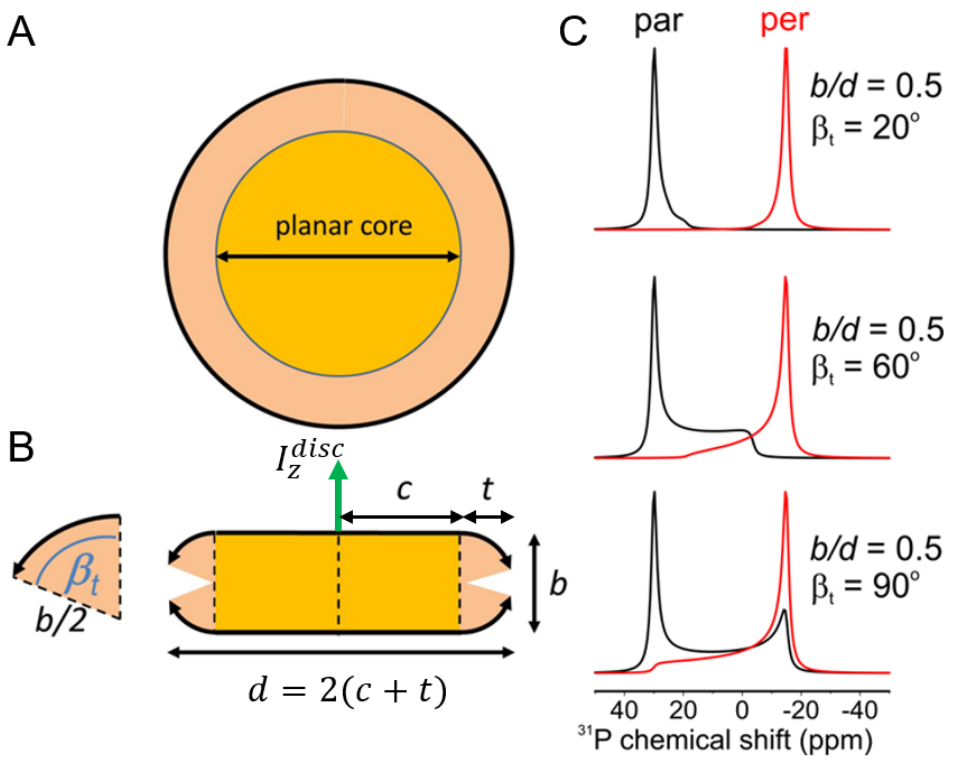

Figure 6.5. The discoidal rHDL morphology approximation **(A, B)**. The labels indicate the particle diameter *d*, thickness *b*, the partial torus width *t*, the radius of the planar core *c*, and the maximum tilt angle β_t of the lipids in the partial torus relative to $\boldsymbol{I_z^{disc}}$. **(C)** Simulated spectra when the disc normal is parallel (black) or perpendicular (red) to B_0. The maximum angle of β_t was increased from 20 to 90°. The constant value of b/d = 0.5 was used when the diameter and thickness of the rHDL nanoparticles was assumed to be 11 and 5.5 nm, respectively. Obtained from (Lau and Middleton, 2020).

The lipids in the partial torus are in various orientations tilted away from I_z^{HDL} which were described by the maximum tilt angle β_t. The particle diameter (*d*) and thickness (*b*) were 11 nm and 5.5 nm, respectively, based upon the rHDL nanoparticle TEM measurements in **Chapter 4**. The condition that the curvature of the partial torus lipids did not alter *d* or *b* was used (Lau and Middleton, 2020). Therefore, the inner core must

contract to maintain *d* and *b*, i.e., r will decrease as β_t increases. This is described by **Equation [15]**.

$$c = 0.5(d - b\sin\beta_t) \quad \textbf{[15]}$$

Equation [16] was derived in this work to describe the lipids in the partial torus, i.e., fraction of lipids (f_t). It follows that the fraction of lipids in the core is $\boldsymbol{f_c = 1 - f_t}$ (Lau and Middleton, 2020).

$$f_t = \frac{b(2\beta_t c + b\sin\beta_t)}{2c^2 + b(2\beta_t c + bsin\beta_t)} \quad \textbf{[16]}$$

The density of probability of lipids in the partial torus in discrete rHDL nanoparticles, i.e. when I_z^{HDL} was parallel to B_0, was calculated according to **Equation [17]** which was partially derived from Picard *et al*.'s equation for a full torus (Picard et al., 1999), where $0 \leq \beta \leq \beta_t$ (Lau and Middleton, 2020).

$$P_t(\beta) = 0.5\pi b(c + 0.5b\sin\beta) \quad \textbf{[17]}$$

The angular distributions were summated for the lipids in the planar bilayer core and partial torus when $\beta = 0°$ and $0 \leq \beta \leq \beta_t$, respectively. **Equations [15]**, **[16]** and **[17]** were used to calculate the NMR lineshape of the discoidal approximated particles (Lau and Middleton, 2020).

For rouleaux oriented rHDL nanoparticles where I_z^{HDL} is oriented perpendicular to B_0 a numerical approach was required. Separate unit vectors described the planar core and the partial outer torus lipid components. The β angles between these unit vectors and B_0 were used to calculate the NMR lineshape (Lau and Middleton, 2020). These calculations allowed the production of simulated ^{31}P NMR spectra fittings (**Figure**

6.5C) for measured rHDL nanoparticle spectra that contained a similar lineshape by varying β_t to determine the rHDL nanoparticle morphology.

6.3 Results

6.3.1 SS NMR of rHDL nanoparticles

6.3.1.1 Surface curvature of lipids detection by SS NMR

NMR spectra were simulated to determine if the ^{31}P NMR lineshape could in principle be affected by the rHDL nanoparticle morphology when rHDL is oriented on a planar substrate. The simulated spectra used the atomic coordinates of the POPC molecules from the AAMD simulated model of POPC:cholesterol:apoA-I WT 200:20:2 HDL nanoparticle simulated for 10 μs (Pourmousa et al., 2018). The calculations used to determine the simulated spectra and the lipid contributions at each orientation with respect to B_0 are discussed in **section 6.2.3.2**

When the HDL model principal axis of inertia (I_z^{HDL}) was parallel to B_0 (**Figure 6.6B**) the spectrum exhibits a continuous asymmetric lineshape between the upper and lower limits of the ^{31}P CSA in **Figure 6.6A**.

The lineshape reflects a proportion of the outer lipids that are perpendicular to B_0 (resulting in the 'spike' at -15 ppm) and a larger proportion of inner lipids with their long molecular axes distributed about the B_0 axis (Lau and Middleton, 2020). When I_z^{HDL} is perpendicular to B_0 most of the lipids were in the perpendicular orientation at -15 ppm with a smaller proportion towards the upper limit (**Figure 6.6C**). These lipid orientations can be observed in the AAMD model by the lipid headgroup positions (**Figure 6.6D**).

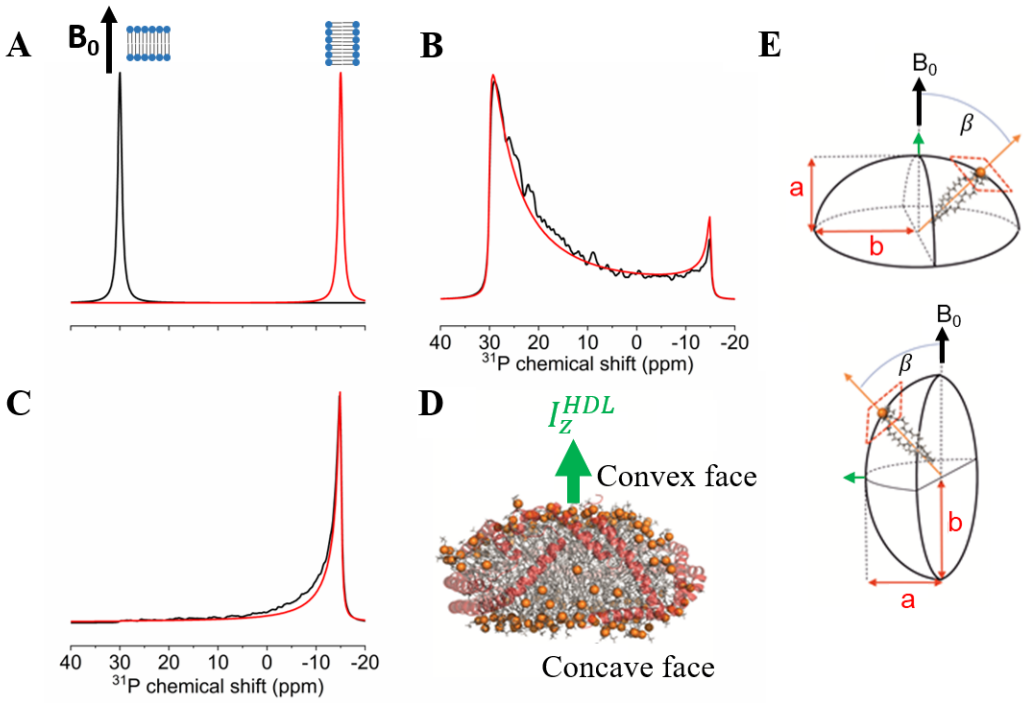

Figure 6.6. (A) The simulated spectra for a phospholipid bilayer with the lipid membrane normal parallel (black) and perpendicular (red) to B_0. The simulated MD model lineshapes (black) and hemispheroid approximation when a/b = 0.4 (short/long axis) (red) when the principal axis of inertia of HDL ($\boldsymbol{I_Z^{HDL}}$) is **(B)** parallel or **(C)** perpendicular to B_0. **(D)** The POPC:cholesterol:apoA-I WT 200:20:2 HDL nanoparticle structure after 10 μs of AAMD simulation obtained from (Pourmousa et al., 2018). ApoA-I molecules (red), lipid acyl chains (grey) and headgroups (orange spheres). **(E)** The hemispheroid representation of the surface curvature in an rHDL nanoparticle with minor axis (a), major axis (b), and $\boldsymbol{I_Z^{HDL}}$ (green arrow). The angle β indicates the lipid principal axis relative to B_0. Adapted from (Lau and Middleton, 2020).

It was considered whether the lineshapes based on the HDL model could be replicated by assuming a hemispheroid distribution of lipid orientation, as visual inspection of the model shape reveals convex and concave surfaces. Simulated spectra based on the hemispheroid approximation (**see section 6.2.3.3**), with the hemispheroid parallel and

perpendicular relative to B_0, fit the AAMD model NMR lineshapes well (**Figure 6.6B-C**). This revealed that the oblate hemispheroid approximation (**Figure 6.6E**) was a suitable representation of the HDL particle lipid surface curvature (Lau and Middleton, 2020). The normal to the tangent plane at any point on the hemispheroid surface (**Figure 6.6E**) represents the average lipid molecular orientation at that position (Lau and Middleton, 2020; Picard et al., 1999).

With the hemispheroid approximation it is straightforward to generate simulated ^{31}P lineshapes for different surface curvatures. The orientational distribution of the lipids (**Figure 6.7**) can be related to the surface curvature of the hemispheroid by a flattening factor $f = 1 - a/b$ between 0 to 1.0, i.e. as a decreases f will increase towards 1 (Lau and Middleton, 2020). As the surface curvature lessens the lineshapes became narrower and approach the planar lipid distribution lineshapes in **Figure 6.6A**.

The surface curvature lipid orientation relationship could then be applied to fit experimentally observed rHDL nanoparticle spectra. This is a valuable tool to determine if the lipid distribution in the rHDL nanoparticles contained surface curvature.

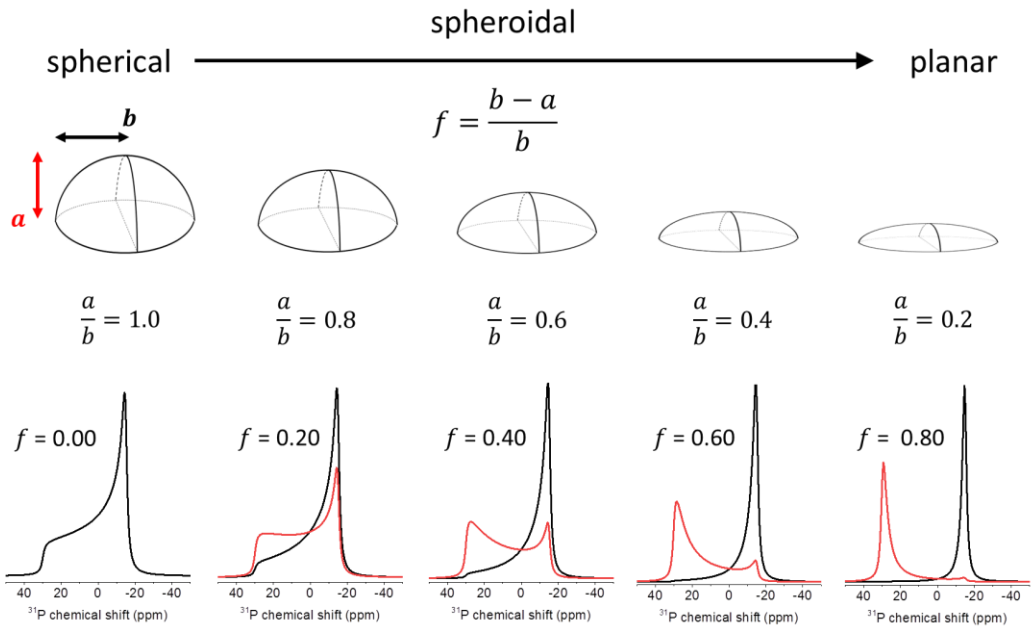

Figure 6.7. The simulated ^{31}P NMR spectra lineshape oblate hemispheroid (a < b) approximation of the lipid surface curvature in rHDL nanoparticles. The flattening factor (*f*) was increased from a completely spherical (*f* = 0) to planar (*f* = 1.0) lipid distribution when axis a was parallel (red) or perpendicular (black) relative to B_0. Each spectrum lineshape was normalised to the peak area, and across the assumed full 45 ppm averaged POPC CSA. Obtained from (Lau and Middleton, 2020).

6.3.1.2 ^{31}P NMR spectra of oriented rHDL nanoparticles at different hydration times

The rHDL-WT 200:2 samples were deposited on glass cover slips, dried, and then rehydrated for different lengths of time to test how the level of hydration can affect the ^{31}P NMR lineshape (**Figure 6.8**). Two symmetrical peaks were observed at the upper and lower limits of the ^{31}P CSA and indicated a mixture of particles oriented parallel (30 ppm) and perpendicular to (-15 ppm) to B_0. The best fits of the experimental spectra were Lorentzian lineshapes at the upper and lower limits of the CSA. Therefore, a fitting factor of 1.0 and the ratio (r_p) of particles either parallel or perpendicular to B_0 were used to fit the experimental peaks.

As the hydration time increased (3-16 hrs) the proportion of parallel to perpendicular oriented nanoparticles increased (as signified by the ratio of the peak areas), and the peak width became narrower (Lau and Middleton, 2020). This suggests that longer hydration times favour the formation of discrete (parallel to B_0) rather than rouleaux stacked (perpendicular to B_0) rHDL nanoparticles as the hydration level increased. An increased amount of moisture in the sample, after 16 hours, may have reduced the CSA indicated by the decrease in the separation between the two peaks to ~41 ppm. This could reflect an increase in the lipid mobility in the rHDL nanoparticles (Lau and Middleton, 2020).

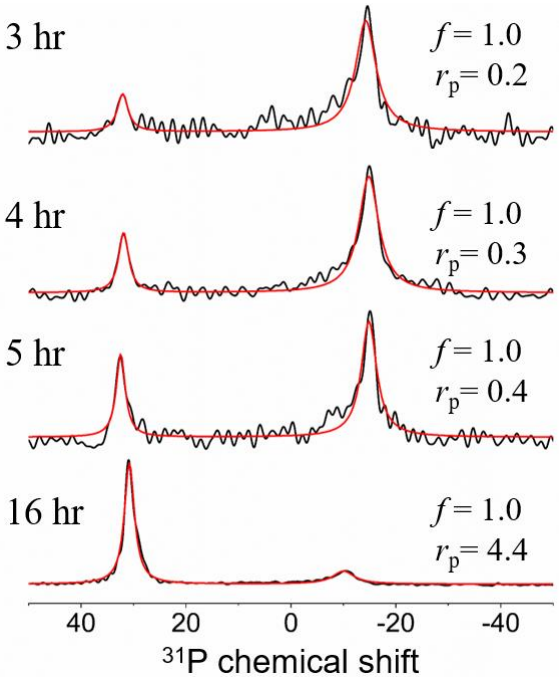

Figure 6.8. ^{31}P NMR spectra of rHDL-WT 200:2 nanoparticles at 3 mM POPC concentration with a hydration time of 3, 4, 5 and 16 hours at 37°C. The best fits (red) of the spectra are Lorentzian lineshapes considered as a ratio (r_p) of planar (f = 1.0) nanoparticles either parallel or perpendicular to B_0. Optimisation of the linewidths and peak areas was used to determine the best fits, and the peak areas were proportional to r_p. Adapted from (Lau and Middleton, 2020).

6.3.1.3 Atheroprotective apoA-I rHDL morphology

Oriented ^{31}P NMR rHDL 200:2 nanoparticle spectra, in triplicate to assess the reproducibility of the sample preparation, were obtained for separate samples containing either apoA-I WT, R173C or L144R. The sample lipid concentration was lower to try and form predominantly discrete rHDL nanoparticles, i.e., oriented with I_z^{HDL} parallel to B_0. Initial observations indicated the rHDL-WT (**Figure 6.9**) and R173C (**Figure 6.10**) lineshapes were distributions of nanoparticles oriented either parallel or perpendicular to B_0. The spectra were fitted with the planar bilayer morphology Lorentzian lineshape fitting with a value of f = 1.0, and a varied r_p value dependent on the orientation proportions in each spectrum (#1-3) (Lau and Middleton, 2020).

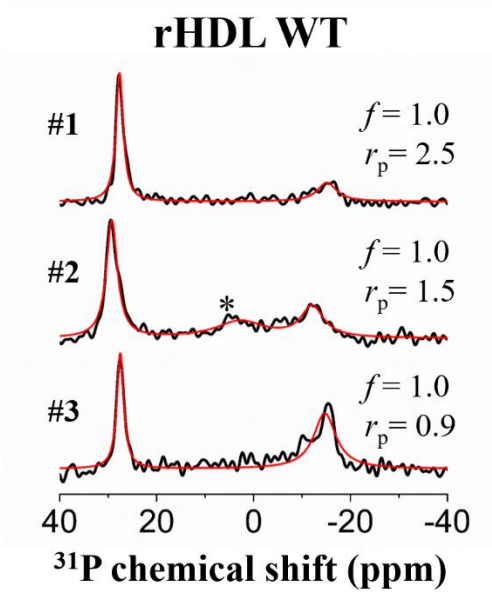

Figure 6.9. The oriented ^{31}P NMR spectra of rHDL-WT 200:2 nanoparticles. The POPC concentration after dialysis was ~0.76 mM. Each sample (#1-3) was rehydrated for 4 hours at 37°C. The experimental spectra (black) and simulated Lorentzian best fits (red). The fitting criteria included the f values, r_p ratio, and line broadening. The * indicates an additional peak not seen in any other spectrum and possibly from smaller, micellar-like structures.

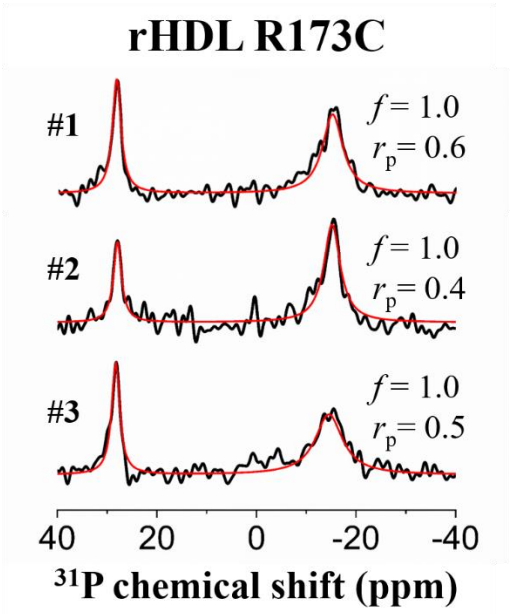

Figure 6.10. The oriented ^{31}P NMR spectra of rHDL-R173C 200:2 (M/M) nanoparticles. The POPC concentration after dialysis was ~0.15 mM. Each sample was rehydrated for 4 hours at 37°C. The experimental spectra (black) and simulated Lorentzian best fits (red). The fitting criteria included the f values, r_p ratio, and line broadening.

The rHDL-L144R lineshape (**Figure 6.11**) was significantly different from the results above and were more indicative of the lipid surface curvature seen in the MD model, as represented by the hemispheroid approximation. The *f* factor values of 0.5 and 0.6 indicated the lipid surface curvature of the rHDL-L144R nanoparticles was not a planar bilayer nanodisc as in **Figure 6.7**.

Although not clearly delineated as in the previous spectra, the lineshapes are consistent with two orientations of the particles, as before. Maxima occur at the two edges of the spectra, but some intensity is also present across the entire CSA range. Comparisons with simulated spectra of a mixture hemispheroid distributions in the two orientations, indicate that a larger proportion of rHDL-R173C nanoparticles formed rouleaux as

indicated by the lower r_p values. The rHDL-L144R r_p values were higher than both rHDL-WT and R173C nanoparticles indicating the morphology of the particles resulted in less rouleaux formation (Lau and Middleton, 2020).

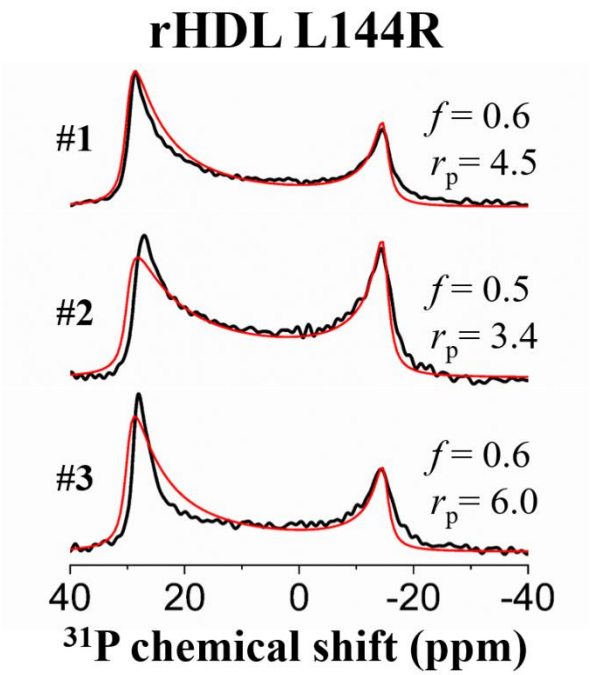

Figure 6.11. The oriented ^{31}P NMR spectra of rHDL-L144R 200:2 (M/M) nanoparticles. The POPC concentration after dialysis was ~0.70 mM. Each sample was rehydrated for 4 hours at 37°C. The experimental spectra (black) and simulated hemispheroid approximation best fits (red), and a broadening of 200 Hz was applied to the rHDL-L144R spectra. The fitting criteria included the f values, r_p ratio, and line broadening.

The application of these fitting functions to the NMR lineshapes of the oriented ^{31}P NMR spectrum has allowed the determination of similarities and differences in the rHDL nanoparticle morphology. The lipid surface curvature difference in the rHDL-L144R nanoparticle morphology could suggest a physical basis for the atheroprotective properties of this mutant (Lau and Middleton, 2020).

6.3.1.4 Oriented rHDL-C WT nanoparticles ^{31}P NMR analysis

To determine if cholesterol affected the NMR lineshape, samples were prepared at the POPC:cholesterol:apoA-I WT molar ratios indicated in **Figure 6.12**. Each sample contained 10 mol % cholesterol relative to the total POPC content. The curvature of the lower limit lipid distribution peak at -15 ppm increased as the lipid:cholesterol:apoA-I WT molar ratio increased (160:16:2 to 300:30:2) (Lau and Middleton, 2020). The lineshape distribution between the upper limit (30 ppm) and lower limit (-15 ppm) shows a change in the distribution of lipids in the rHDL nanoparticles relative to B_0. In the samples containing cholesterol the curvature increased towards the upper limit and the lineshape is quite distinct from that of a planar lipid distribution or a hemispheroid approximation. Another model was therefore sought to explain this observation.

A new fitting model was used for the spectra of rHDL nanoparticles containing cholesterol (**Figure 6.12A**) referred to as the torus disc distribution. In this model the planar lipid bilayer circular core is surrounded by lipids in a partial torus (**Figure 6.5**). The increase in the lipid content resulted in the outer lipids being moved further from the lipid bilayer normal, i.e. as β_t increased in the partial torus (Lau and Middleton, 2020). Summation of the I_z^{disc} components was used to calculate the torus disc experimental spectra fittings when I_z^{disc} was oriented parallel or perpendicular to B_0 (**see section 6.2.3.4**, **Figure 6.5C**) (Lau and Middleton, 2020).

Additionally, a comparative spectrum of POPC:apoA-I WT 300:2 nanoparticles in **Figure 6.12B** fitted the torus disc morphology without cholesterol. This suggested the morphology occurs when the total lipid concentration is increased. The rHDL nanoparticle lipid surface area may increase to adapt to the increased number of lipid

molecules which could reduce the exposure of the outer lipids to the aqueous medium (Lau and Middleton, 2020).

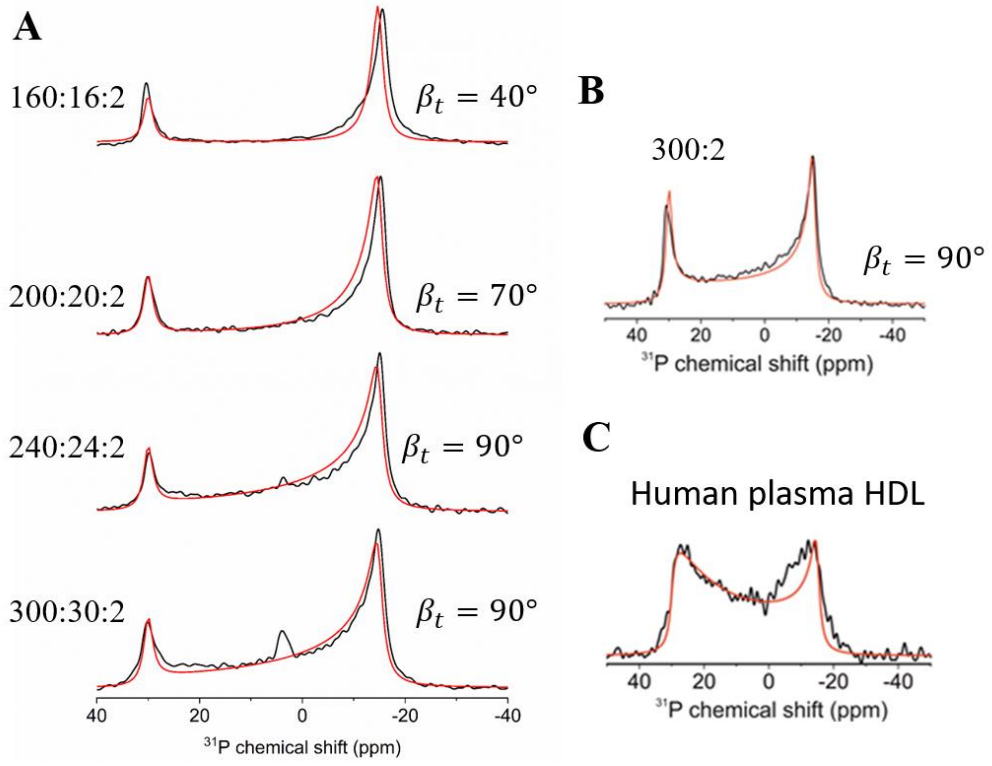

Figure 6.12. (A) The experimental (black) ^{31}P NMR spectra of rHDL-C WT nanoparticles at the molar ratios indicated. The lipid concentration was 3 mM and samples were rehydrated for 4 hours at 37°C. The torus disc model simulated fitted spectra (red). The maximum tilt angle of the lipids in the torus is indicated by β_t. **(B)** rHDL-WT 300:2 nanoparticle ^{31}P NMR spectrum (black) without cholesterol fitted with the torus disc distribution (red). **(C)** Unfractionated human plasma HDL ^{31}P NMR spectrum (black) fitted with the hemispheroid approximation (red). Adapted from (Lau and Middleton, 2020).

Furthermore, the spectrum of unfractionated human plasma HDL was fitted with the combined parameters in equal proportions of the hemispheroid morphology approximation and a 100 % spherical distribution. The morphology sensitive technique

was able to detect the presence of spherical mature and flatter nascent discoidal HDL particles (Lau and Middleton, 2020).

The possibility that the observed spectra were comprised of a superimposed powder spectrum and an oriented spectrum was considered. The rHDL nanoparticle morphology models were chosen with respect to the observed experimental spectra. For example, the rHDL-WT 200:20:2 nanoparticle spectra for the AAMD simulated spectrum fitted with the hemispheroid approximation model (**Figure 6.6B**) and the observed spectrum fitted with the torus disc model (**Figure 6.12A**).

The different rHDL morphology models explained the differences in the observed lineshape curvature. Whereas a superimposed powder and oriented spectra would not account for this. For example, the lineshape curvature in **Figure 6.12** rHDL-C nanoparticles spectra shifted towards the upper limit (~30 ppm) and was not accounted for by the hemispheroid or the planar morphology fittings.

6.4 Discussion

6.4.1 Discoidal rHDL nanoparticle morphology

The ^{31}P NMR lineshape of oriented rHDL nanoparticles is sensitive to the alignment of lipids within the rHDL nanoparticles with respect to B_0. Application of calculated fittings produced three distinct models of discoidal rHDL nanoparticle morphology, described as the hemispheroid approximation and planar disc (Picard et al., 1999), and the torus disc models (Lau and Middleton, 2020). Whilst other models may also describe the observed phenomena, the key finding of this work is that ^{31}P NMR is a useful new tool to assess the morphological differences between HDL preparations, either from reconstituted samples or from human plasma.

Another facet of this approach was the production of simulated NMR lineshapes using the AAMD-HDL 200:20:2 model (Pourmousa et al., 2018). This demonstrated how computational HDL models could be combined with or compared to experimental results using the ^{31}P SS NMR morphology tool.

In terms of the different rHDL nanoparticles in this study. The rHDL-WT and R173C 200:2 nanoparticles had a planar disc morphology. This fits the predominant discoidal HDL model in the literature of a planar lipid nanodisc surrounded by a belt of apoA-I (Bibow et al., 2017; Segrest et al., 1999; Sparks et al., 1992b). The rHDL-L144R 200:2 nanoparticle lineshape is consistent with greater lipid surface curvature, which may be approximated by a hemispheroid distribution of lipid orientations. The overall lipid surface curvature was similar to the AAMD-HDL 200:20:2 simulated model (Pourmousa et al., 2018). In **Chapter 5**, the 2D ^{13}C-^{13}C CP-MAS correlation and ^{1}H-^{15}N PISEMA spectra of the rHDL nanoparticles apoA-I spectra supported the predominantly α-helical conformation and molecular belt model alignment of apoA-I relative to the lipids (**section 5.3.2**, **Figure 5.9-5.10**).

In the AAMD-HDL model the apoA-I molecules are not strictly perpendicular to the bilayer normal to adapt to the lipid-protein circumference mismatch (**Figure 6.6D**), which causes bending of the lipid nanodisc to maintain contact between the lipid leaflets forming a convex and a concave face (Lau and Middleton, 2020; Pourmousa et al., 2018). The simulated lineshapes for the AAMD-HDL model, i.e. the lipid orientations, can be represented by the hemispheroid approximation, reflecting the lipid surface curvature in both orientations when I_z^{HDL} is parallel or perpendicular relative to B_0 (Lau and Middleton, 2020).

The absence of distortion from planarity of the lipid bilayer nanodisc suggested the lipids in the disc morphology of the rHDL-WT and R173C nanoparticles are sufficiently relaxed (Lau and Middleton, 2020). In comparison, the rHDL-L144R lipid surface curvature was represented by the hemispheroid approximation which suggested these nanoparticles have a convex and concave face. This surface curvature of the particles could have resulted in a higher proportion of discrete particles on the planar surface as indicated by the larger r_p values, i.e., the ratio of particles with I_z^{HDL} parallel: perpendicular relative to B_0.

The hemispheroid rHDL-L144R nanoparticle morphology lipid surface curvature could explain the reduced thermal stability at T_m2 and the different estimated secondary structure content of apoA-I L144R in rHDL, +10 % unordered and -12 % α-helical relative to rHDL-WT, determined by CD, when compared to the relaxed lipids in the planar disc rHDL-WT and R173C morphologies. The rHDL-WT and R173C apoA-I proteins also had a similar T_m2 at 82.9°C and 81°C, respectively, which suggested a similar stability of the proteins in the rHDL 200:2 nanoparticles, possibly related to the planar disc morphology.

In **Chapter 4**, the rHDL-L144R 200:2 DLS diameter measurement was significantly smaller at ~6.2 nm compared to ~11.3 nm for the rHDL-WT nanoparticles. The rHDL-L144R DLS diameter was considerably less than the rHDL-WT and L144R estimated NDGGE hydrodynamic diameter (~8.6 – 10.1 nm) and the TEM diameter of dried particles (~11 nm). The hydrodynamic diameter of non-spherical particles can be overestimated when measured using DLS, i.e., the non-spherical planar disc rHDL-WT morphology, which calculates the diameter based upon an ideal spherical particle morphology (Eiser, 2014; Lau and Middleton, 2020). The ^{31}P NMR tool detected the

rHDL-L144R hemispheroid morphology where the lipid surface curvature approaches that of an ideal spherical particle. This could explain the diameter measurement discrepancy, with the DLS measurement representing the actual rHDL-L144R particle diameter (Lau and Middleton, 2020).

In the last model, the rHDL-C WT nanoparticles containing 10 mol % cholesterol had a torus disc morphology. In comparison to the previous models the outer lipids move away from the bilayer normal as the particle cholesterol and lipid content increased (Lau and Middleton, 2020). This was observed in the ^{31}P NMR spectra line shape as a change in the lower limit (-15 ppm) peak curvature shifted towards the upper limit as the lipid and cholesterol content increased. The narrower Lorentzian line shapes of the rHDL-WT and R173C planar disc morphology and rHDL-L144R hemispheroid morphology line shapes shifted peak orientations towards the upper limit were distinct from the rHDL-C spectra lineshapes. A key feature of the rHDL-C WT torus disc morphology is the possibility of allowing for molecular crowding as the lipid content increases allowing for an increased lipid surface area to prevent exposure of the outer lipid hydrophobic acyl tails to the aqueous medium (Lau and Middleton, 2020).

6.4.2 Summary

This is the first application of oriented ^{31}P SS NMR to determine the morphology of rHDL nanoparticles. As well as a direct comparison between the rHDL-WT, R173C and L144R nanoparticle morphologies. The development of this technique has diversified the techniques used to characterise rHDL nanoparticles morphology. As it is necessary to use multiple approaches when characterising rHDL nanoparticle structure as seen by the differing measured diameters. The different morphologies identified here could reflect the dynamic nature of *in vivo* nascent discoidal HDL

nanoparticles. This in turn could affect how the particles interact with enzymes in RCT (Lau and Middleton, 2020), such as LCAT (Sorci-Thomas et al., 1993), CETP (Qiu et al., 2007) and cell receptors like ABCA1 (Sahoo et al., 2004). The functional aspects of the respective rHDL nanoparticles are explored further and discussed in **Chapters 7** and **8**.

Significantly, the proof of concept unfractionated human plasma HDL sample demonstrated how this morphology detection tool could be used to analyse fractionated HDL cardiovascular disease patient samples (Lau and Middleton, 2020). Furthermore, the morphological detection could be applied to experimental assays such as HDL particles formed *in vitro* (Duong et al., 2006).

7 Further investigations

7.1 Introduction

The work in this chapter lays the foundation for future work in analysing the rHDL nanoparticles function and structure computationally and experimentally. Preliminary coarse-grained MD simulations have examined the conditions required for self-assembly simulations of rHDL nanoparticles containing full-length apoA-I WT and R173C. In addition, experimental cellular assays have been developed to assess the capability of WT apoA-I and mutants to facilitate cholesterol efflux *in vitro*. Finally, the amyloidogenic potential of apoA-I WT and mutants are assessed.

7.1.1 Molecular dynamics simulations of HDL nanoparticles

Molecular dynamics simulations can be used to produce models of HDL nanoparticles. There are different types of MD simulations that can be combined with experimental data (**see Chapter 1**, **section 1.6.2**) and have been reviewed comprehensively (Pan and Segrest, 2016; Pourmousa and Pastor, 2018). The work in this chapter has focussed on coarse-grained MD simulations. The major advantage of CGMD simulations is the prolonged timescales, e.g. 10 - 42 μs (Debnath and Schäfer, 2015; Shih et al., 2007a), that can be sampled due to the 4 to 1 atom mapping in the MARTINI force field (Marrink et al., 2007; Monticelli et al., 2008).

The structure of apoA-I WT in CGMD HDL self-assembly simulations has focussed upon truncated apoA-I WT Δ(1 – 43), Δ(1 – 54) and Δ(1 – 65) also known as MSP1, MSP1 Δ(1 – 11) and MSP1Δ(1 – 22), respectively (Debnath and Schäfer, 2015; Shih et

al., 2006; Shih et al., 2007a; Shih et al., 2007b). The CGMD simulations observed the self-assembly process of HDL nanoparticles over timescales up to 10.0 μs (Shih et al., 2007a) and 42 μs (**Figure 7.1A**) (Debnath and Schäfer, 2015). Interestingly, Debnath and Schäfer utilised a feature in GROMACS (Abraham et al., 2015) called the backmapping algorithm which converts a CG structure to an all-atom model (Debnath and Schäfer, 2015; Rzepiela et al., 2010). The resultant AAMD structure was simulated for 500 ns and demonstrated the stability of the converted structure containing the truncated apoA-I proteins and lipids (**Figure 7.1B**).

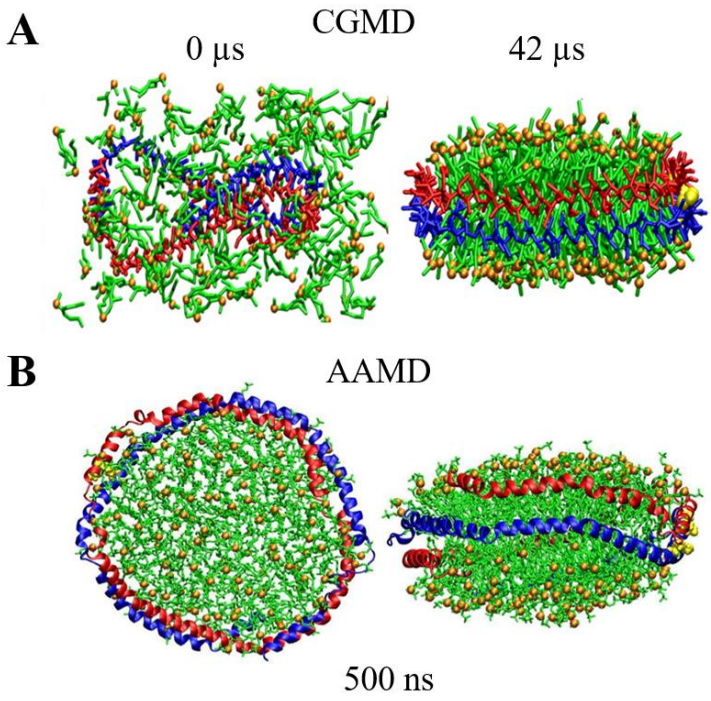

Figure 7.1. (A) The self-assembly CGMD simulation of a HDL nanoparticle containing 160 DMPC lipids (green acyl chains, gold spheres headgroups), and two apoA-I Δ(1 – 65) monomers (red, blue) at the start (0 μs) and end (42 μs) of the simulation. **(B)** The final structure of a backmapped AAMD simulated HDL nanoparticle for 500 ns. Obtained and adapted from (Debnath and Schäfer, 2015).

There was limited time in which to focus on the computational aspects of this work. Therefore, initial simulations aimed to produce HDL nanoparticles through self-assembly following a similar methodology to Shih *et al*. and Debnath and Schäfer. The previous CGMD self-assembly HDL simulations used truncated apoA-I WT therefore this work aimed to establish self-assembly of HDL nanoparticles containing full-length apoA-I WT and mutants. The CGMD assembled HDL nanoparticle structural models would provide further comparison between apoA-I WT and the atheroprotective mutants. To determine if structural differences are related to the atheroprotective apoA-I mutant function.

7.1.2 Macrophage cholesterol efflux

A key stage in atherosclerosis is the formation of foam cells leading to the development of atherosclerotic plaques (**see section 1.1**). Foam cells are macrophages that contain lipoprotein derived cholesterol and CEs (Libby et al., 2011; Tabas, 2010; Tabas et al., 2007).

Macrophages contain three different cell receptors involved in cholesterol efflux known as ABCA1, ABCG1, and SR-B1 (Shen et al., 2018). In RCT LF apoA-I and lipid-poor pre-β-HDL particles interact with ABCA1 initiating the major pathway for cellular lipid and cholesterol efflux (Sahoo et al., 2004; Sankaranarayanan et al., 2011; von Eckardstein et al., 2001). Mature HDL nanoparticles interact with the macrophage cell receptors SR-B1 and ABCG1 to mediate cholesterol efflux through passive diffusion and unidirectional efflux, respectively (Shen et al., 2018).

The significant pathogenicity of cholesterol accumulation in atherosclerotic plaque macrophages highlights the importance of understanding this stage in RCT (Libby et al., 2011; Lusis, 2000). *In vitro* cholesterol efflux assays from cholesterol-loaded

macrophages could provide insight into the effectiveness of the cholesterol acceptors containing apoA-I WT or the atheroprotective mutants in mediating cholesterol efflux.

The efflux of cholesterol from cells has been widely monitored using radiolabelled [^{3}H]- or [^{14}C]-cholesterol with cholesterol acceptors such as lipid-free apoA-I and rHDL containing apoA-I WT or R173C (Calabresi et al., 1999; Daniil et al., 2013; Sankaranarayanan et al., 2011; Zhu et al., 2005). Sankaranarayanan *et al*. demonstrated the effective use of BODIPY-cholesterol (**Figure 7.2A**) fluorescence detection as an alternative to radiolabelled cholesterol in a simplified ABCA1-mediated cholesterol efflux assay (Sankaranarayanan et al., 2011). Murine J774 macrophages loaded with BODIPY-cholesterol were incubated with lipid-free apoA-I WT or human HDL_3 as cholesterol acceptors (Sankaranarayanan et al., 2011). The ABCA1-mediated efflux was determined by the difference between BODIPY-cholesterol efflux from J774 macrophages incubated with or without cAMP prior to incubation with cholesterol acceptors (Sankaranarayanan et al., 2011).

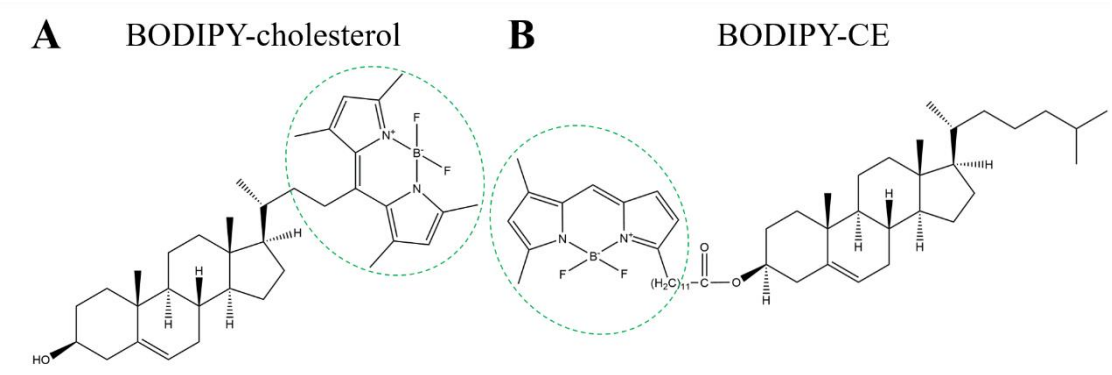

Figure 7.2. The structure of **(A)** BODIPY-cholesterol and **(B)** BODIPY-cholesteryl ester (-CE). The BODIPY fluorophore motif is circled (green).

The BODIPY-cholesterol efflux from murine J774 macrophages was measured by fluorescence detection in the filtered media rather than retained cholesterol in the cells

(Sankaranarayanan et al., 2011). In comparison, Liu *et al*. adapted the use of BODIPY-cholesterol for flow cytometry with BODIPY-cholesterol loaded THP-1 monocytes (Liu et al., 2014). Flow cytometry is a versatile technique that can detect and separate cells from cellular debris through laser light scattering and fluorescent molecule detection (McKinnon, 2018).

In this work preliminary experiments explored the experimental conditions for evaluating the cholesterol acceptor mediated efflux of BODIPY-CE (**Figure 7.2B**) from THP-1 macrophages using flow cytometry.

7.1.3 Amyloidogenic properties of apoA-I

This work aimed to compare the amyloidogenic potential of WT and mutant apoA-I. This may be a reason for the atheroprotective properties of the mutants.

ApoA-I can become amyloidogenic in pro-inflammatory conditions such as an acidic pH, in the presence of glycosaminoglycans (GAGs), including heparin, and oxidation of methionine residues (Ramella et al., 2011; Townsend et al., 2017; Wong et al., 2010). In atherosclerosis this results in deposition of misfolded aggregated apoA-I WT in the form of amyloid fibrils or apoA-I peptide fragments in atherosclerotic plaques (Mucchiano et al., 2001; Ramella et al., 2011; Rocken et al., 2006).

Heparin is a GAG polysaccharide comprised of linear chains containing the subunits L-iduronic acid 2-sulphate (IdoA,2S) and D-glucosamine N,6-sulphated (GlcNS,6S) (**Figure 7.3A**) (Casu et al., 2015; McLaurin et al., 1999). GAGs have been detected in atherosclerotic plaque deposits (Ramella et al., 2011; Teoh et al., 2011), and in other amyloidogenic protein deposits (Cohlberg et al., 2002; McLaurin et al., 1999). Interestingly, GAGs were suggested to aid amyloid-β peptide fibril formation by acting

as a supporting frame (McLaurin et al., 1999). Heparin is required for rapid fibril formation by apoA-I.

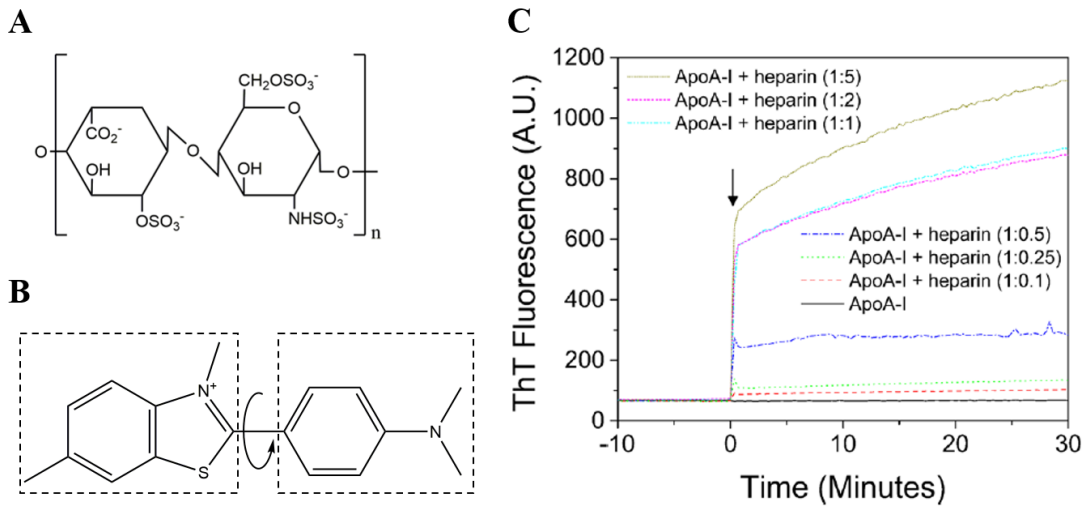

Figure 7.3. (A) The disaccharide unit of heparin containing the sequential subunits [IdoA2SO_3-GlcNS,6SO_3], adapted from (Casu et al., 2015). **(B)** The structure of ThT, a cationic fluorescent dye. The planar segments are outlined by the dashed boxes and can rotate about the C-C bond indicated with the arrow. Adapted from (Biancalana and Koide, 2010). **C)** An example ThT fluorescence assay of apoA-I WT (7 µM) with varied molar ratios of apoA-I: heparin 1:0.1 – 1:5 at pH 4. Arrow indicates the addition of HCl to change the pH to 4.0. Obtained from (Townsend et al., 2017).

The widely used thioflavin T (ThT) (**Figure 7.3B**) binding assay was used to detect the formation of amyloid fibrils *in vitro* (Khurana et al., 2005; LeVine, 1993). An increase in ThT fluorescence is observed when ThT binds to amyloid fibrils (LeVine, 1993). For example, apoA-I incubated with heparin under acidic conditions showed an enhanced rate of fibril formation indicated by the increased ThT fluorescence (**Figure 7.3C**) (Townsend et al., 2017). In this work, the ThT assay was used as a starting point to determine if the LF atheroprotective mutants were less likely to form amyloid fibrils.

7.1.4 Aims

The following aims of this chapter are described here:

1. To produce HDL nanoparticle structures containing full-length apoA-I WT or apoA-I R173C with coarse-grained molecular dynamics simulations. To provide further structural comparisons between apoA-I WT and mutants in HDL nanoparticles.
2. To use flow cytometry to monitor the cholesterol efflux from BODIPY-CE loaded THP-1 macrophages mediated by apoA-I and rHDL nanoparticles. The development towards the cholesterol efflux assay method is key to understanding if the rHDL bearing atheroprotective apoA-I mutants have a greater cholesterol efflux capacity.
3. To begin to assess the susceptibility of the atheroprotective apoA-I mutants to form amyloid fibrils. ApoA-I WT under the appropriate conditions can become amyloidogenic and contribute to the formation of atherosclerotic plaques (Arciello et al., 2016; Townsend et al., 2017).

7.2 Materials and methods

7.2.1 Molecular dynamics simulations

VMD (Humphrey et al., 1996) and PyMol (Schrodinger, 2015) software were used to produce figures and visualise trajectories. The production run simulations were run on the High-End Computing Cluster (HEC, Lancaster University, UK).

7.2.1.1 Full-length apoA-I structure

The full-length apoA-I structures were kindly produced by Dr. E. Hughes using Modeller 9.18 (Webb and Sali, 2016) to produce 5 model structures for apoA-I WT and with mutated residues L144R and R173C for the respective apoA-I mutants. The

alignment sequences used the truncated apoA-I Δ(1-43) (PDB 1AV1) (Borhani et al., 1997) crystal structure and the N-terminal residues 3 – 42 of the full-length solution SANS apoA-I structures (PDB 3K2S) (Wu et al., 2009). The protein structure model was selected with the lowest Discrete Optimised Protein Energy (DOPE) score (Shen and Sali, 2006).

7.2.1.2 Self-assembly molecular dynamics simulations

The following methods were adapted from (Debnath and Schäfer, 2015; Shih et al., 2007a; Shih et al., 2007b). The Martini FF version 2.2 (de Jong et al., 2013; Marrink et al., 2007; Monticelli et al., 2008) was used. The CG POPC, water and ion topology files were obtained from the Martini download source (http://cgmartini.nl/index.php/downloads) (Marrink, 2004; Wassenaar et al., 2015).

To form the apoA-I R173C dimer, the apoA-I R173C monomers were oriented anti-parallel with the cysteine residue sulphydryl groups 0.85 nm apart. The atomistic apoA-I protein structures were coarse-grained using the martinize.py script (de Jong et al., 2013). DSSP (Joosten et al., 2011; Kabsch and Sander, 1983) was used to assign the backbone secondary structure. The secondary structure of the protein backbone was predominantly α-helical as in the PDB structures (Borhani et al., 1997; Mei and Atkinson, 2011; Wu et al., 2009).

The CG protein was placed in the centre of a cubic box 1 nm from the box edge. Energy minimisation (EM) was performed with the steepest descent algorithm with up to 1000 steps *in vacuo*. Next 160 CG POPC lipids were added to the simulation box randomly followed by a second EM *in vacuo* under the same conditions. The system was solvated with CG water beads and EM. The first system contained the apoA-I R173C dimer (1074 CG beads), 160 POPC lipids (1920 CG beads), 31117 water beads and 16 Na^+

ion CG beads in a cubic box (16 x 16 x 16 nm). The second system contained the apoA-I WT Δ(1-43) chain A and B monomers (898 CG beads), 160 POPC lipids (1920 CG beads), 23049 water beads and 12 Na^+ beads in a cubic box (14.6 x 14.6 x 14.6 nm).

The molecular dynamics parameters (mdp) were adapted from the recommendations of de Jong *et al*. (de Jong et al., 2016) for the CGMD NVT, NPT, and production run ensembles. A 20 fs integration time step was used throughout these stages. Each system was equilibrated to 320 K (NVT) for 1 ns. This was followed by 1 ns NPT equilibrations until the average pressure was ~1 bar. In the NVT and NPT equilibrations the protein was under position restraints. The temperature coupling time constant (τ_T) was 1 ps with the v-rescale thermostat (Bussi et al., 2007). The pressure coupling time constant (τ_P) was 4 ps with a compressibility of $3x10^{-5}$ bar^{-1} for the isotropic Berendsen barostat conditions (Berendsen et al., 1984; Debnath and Schäfer, 2015).

The Coulomb electrostatics were treated with reaction-field electrostatics (Fukuda and Nakamura, 2012) with a cut-off of 1.2 nm, a relative dielectric screening constant (ε_{rel}) of 15, and the reaction-field dielectric constant was set to infinity (Barnoud and Monticelli, 2015; de Jong et al., 2016). The Coulomb potential was shifted smoothly to zero between 0 – 1.2 nm (Debnath and Schäfer, 2015). The LJ potential was smoothly decreased between 0.9 – 1.2 nm to zero with the vdW-modifier force-switch (Barnoud and Monticelli, 2015; Debnath and Schäfer, 2015). The Verlet cutoff scheme was used with a 1.4 nm cutoff and the neighbour list updated every 20 steps (de Jong et al., 2016; Debnath and Schäfer, 2015). Periodic boundary conditions were used in each direction (x, y, z).

The dynamic production MD run was simulated without position restraints on the protein from the NPT equilibrated system with coordinates saved every 0.5 ns. The

simulation progress was monitored to determine if it was necessary to the total time of 10 μs. The apoA-I R173C and WT Δ(1-43) simulations were stopped at ~6.6 and 8.9 μs, respectively, as the protein conformation did not alter significantly after the initial self-assembly into "HDL-like" nanoparticles.

7.2.2 Cholesterol efflux

The following methods for the BODIPY-CE efflux assay were adapted from (Liu et al., 2014; Sankaranarayanan et al., 2011). The following experiments were performed with the helpful guidance of Dr. S. Allinson (Biomedical and Life Sciences, Lancaster University, UK).

7.2.2.1 THP-1 cell culture and differentiation into THP-1 macrophages

The human THP-1 monocytes were generously gifted by Dr. L. Unterholzner and kindly initially cultured by PhD student Rebecca Barker (Biomedical and Life Sciences, Lancaster University, UK) from frozen cell stocks. The cell culture products were purchased from Thermo Fisher Scientific from Gibco® unless indicated otherwise.

The cell culture experiments, and preparation of sterile solutions were performed under sterile conditions in a laminar air flow hood. The THP-1 monocytes were grown in suspension in 75 cm^2 flasks at 37°C in 5% CO_2 in air (standard conditions). The cell culture media per 500 mL contained RPMI 1640 medium with 2 mM L-glutamine supplemented with 10 % (v/v) heat-inactivated foetal calf serum (FCS) and 100 units/mL penicillin and 100 ug/mL streptomycin (PS). The cells were split 1:2 or 3 (v/v) with fresh media approximately every 2 – 3 days to prevent the cell density rising above 1 $x10^6$ cells/mL.

Just prior to THP-1 monocyte differentiation microscope cover slips were placed into the sample wells for confocal microscopy. The THP-1 cells were counted with a haemocytometer and added to a final cell density of 6 $x10^5$ cells/mL per well in a 12 well plate with a maximum volume of 2 mL. Phorbol 12-myristate 13-acetate (PMA) (stock 1 mg/mL) was added to each well to a final concentration of 100 ng/mL and incubated for 48 hours under standard conditions to differentiate the cells to THP-1 macrophages. The differentiation of the cells was checked using a microscope as the THP-1 macrophages become adherent.

7.2.2.2 Preparation of the BODIPY-CE complex

Prior to incubation with the THP-1 macrophages the BODIPY-CE complex was prepared (Sankaranarayanan et al., 2011). MEM media, pH 7.4 supplemented with 10 mM HEPES was prepared by the syringe filter-sterilisation (0.22 µm) of 5 mL 1 M HEPES into 495 mL MEM media. The methyl-β-cyclodextrin (m-β-CD, Sigma) 20 mM stock solution was prepared by dissolving 211.5 mg of m-β-CD in 8 mL of MEM-HEPES.

A concentrated 109.4 mM stock solution of cholesterol (42.3 mg in 1 mL $CHCl_3$) was prepared in a 5 mL amber glass vial with a PTFE-lined lid (Avanti®). The BODIPY® FL C_{12} cholesteryl ester (BODIPY-CE, Invitrogen™), 1 mg was dissolved in 1.27 mL of $CHCl_3$ to produce a stock concentration of 1 mM and transferred to a 5 mL amber glass vial with a PTFE-lined lid (Avanti®) wrapped in foil.

The cholesterol and BODIPY-CE were aliquoted into a foil wrapped 25 mL round-bottomed flask and dried under N_2 in the dark to form a thin film and remove the organic solvent. The film was dried under a high vacuum for at least 4 hours before resuspension. M-β-CD (20 mM) in MEM-HEPES (4 mL) was added to resuspend the

dried film. The appropriate volumes of stock solutions were added at the respective stages to the final concentrations of BODIPY-CE/m-β-CD (BD-CE complex) of 0.05/0.2/20 mM. The BODIPY-CE was complexed with m-β-CD to increase the solubility in the cell culture media (Sankaranarayanan et al., 2011).

The BD-CE complex was sonicated at 37°C in a bath sonicator for 30 minutes. After sonication the BD-CE complex was incubated at 37°C with shaking for 3 hours and filter-sterilised with a 0.45 µm syringe filter. If the BD-CE complex was not used immediately it was stored at 4°C. Just prior to use the complex was sonicated under the same conditions as before and diluted with an equal volume of sterile MEM-HEPES media containing 2 ug/mL Sandoz 58-035 (Sigma) acyl-coenzyme A:cholesterol acyltransferase (ACAT) inhibitor (100 µg/mL stock in DMSO). The ACAT inhibitor is present in the MEM-HEPES media from this point forward at a final concentration of 1 ug/mL. The final molar concentrations of BODIPY-CE/cholesterol/m-β-CD were 0.025/0.1/10 mM.

7.2.2.3 THP-1 macrophage BODIPY-CE uptake

After THP-1 macrophage differentiation the RPMI cell culture media was removed, and the cells were washed with 1 mL of MEM-HEPES media. The cells were incubated under standard conditions for 1 hour with 2 mL per well of MEM-HEPES media containing the BD-CE complex (0.025/0.1/10 mM) and ACAT inhibitor at the final concentrations described above. The labelling media was removed, and the THP-1 macrophages were washed with 2 mL of MEM-HEPES media per well to remove the BD-CE complex not taken up into the cells. Next, the cells were incubated under standard conditions with RPMI containing 2 mg/mL fatty-acid free bovine serum albumin (BSA), 1 µg/mL Sandoz ACAT inhibitor, and ± 0.3 mM cAMP for 18 hours.

This will be referred to as the equilibration period. The cells were washed with MEM-HEPES before cholesterol acceptor incubation.

7.2.2.4 Incubation with cholesterol acceptors

The cholesterol acceptors in MEM-HEPES media were added to the cells at the concentrations described below with a total volume of 2 mL per well. The control wells contained THP-1 macrophages ±BD-CE complex without cholesterol acceptors. During the efflux incubation periods the controls were incubated with media only. The lipid-free apoA-I WT, R173C and L144R were lyophilised, resuspended in MEM-HEPES and filter-sterilised (0.22 µm) before addition to each well. The conditions tested are described in the next section.

After incubation with the respective cholesterol acceptors the cells were washed with 2 mL of MEM-HEPES media. Accutase® solution (Sigma) 0.55 mL was added to each well and the plate was incubated under standard conditions for 10 minutes. The solution was gently pipetted across the surface to ensure the cells were detached fully. The detached cells were transferred to individual round-bottomed flow cytometry tubes and kept on ice closed with parafilm until analysis. The cells in Accutase solution were directly analysed by flow cytometry as the solution contained Dulbecco's PBS (0.2 g/L KCl, 0.2 g/L KH_2PO_4, 8 g/L NaCl, and 1.15 g/L Na_2HPO_4), and 0.5 mM EDTA·4Na and 3 mg/L phenol red.

7.2.2.5 Flow cytometry

The CytoFlex flow cytometer (Beckman Coulter) and the CytExpert software (Beckman Coulter) were used for sample measurements and analysis. The sample flow rate was 60 µL/min and a total of 10000 events per sample were recorded. Initially, to determine the gating used for the THP-1 macrophages the cell nuclei were stained with

NUCLEAR-ID® Red DNA stain (Enzo life Sciences), at a 500-fold dilution in the resuspended cell media.

The BODIPY-CE has an excitation and emission maxima of ~502 nm and 511 nm, respectively. The respective excitation and emission peak ranges are between ~460 – 512 nm and ~500 – 570 nm, respectively (Fluorescence SpectraViewer, ThermoFisher Scientific). The fluorescence was recorded for each sample and shown in the PC5.5 and FITC channel ranges for the nuclear DNA stain (Enzo) and the BODIPY-CE, respectively. The DNA stain excitation and emission maxima are at ~566 and 650 nm (Enzo), respectively. The respective excitation and emission peak ranges are between ~450 – 650 nm, and 600 – 700 nm (Enzo).

The forward scatter (FSC) and side scatter (SSC) area plots were used to determine the THP-1 macrophage cell population gating (P2/P3) and separated the cellular debris (P1). The FSC-Width (FSC-W) vs. FSC area (FSC-A) plots in P2/P3 were used to confirm most of the compound fluorescence was measured in singlet cells. The nuclear dye (PC5.5-A) and BODIPY-CE (FITC-A) fluorescence area was compared using histograms between samples in P2/P3. A correlation area dot plot between the PC5.5 and FITC fluorescence detection was also included.

The percentage of BODIPY-CE retained in the cells after incubation was initially calculated using:

$$\%\ cholesterol\ retained = \frac{MFI_{acc.}}{MFI_{no\ acc.}} \cdot 100 \qquad \textbf{[18]}$$

The mean fluorescence intensity (MFI) of the BODIPY-CE detected in flow cytometry in cells incubated with ($MFI_{acc.}$) and without cholesterol acceptors ($MFI_{no\ acc.}$). The background MFI of cells without BODIPY-CE was subtracted from each MFI before

the % cholesterol retained was calculated. Therefore, the % cholesterol efflux = 100 - % cholesterol retained. This was similar to the method used by Liu *et al.* (Liu et al., 2014).

The control samples were THP-1 macrophages incubated ± BD-CE complex only, and ±0.3 mM cAMP in the equilibration period. Initial control samples contained the nuclei staining dye to gate the THP-1 macrophages. The apoA-I WT concentration range was tested at the following concentrations 10, 25, 50 and 100 µg/mL. The apoA-I WT and atheroprotective apoA-I mutants cholesterol efflux were tested at the excess concentrations of 120 and 600 µg/mL and incubated for 8 and 24 hours with the BODIPY-CE loaded cells at each concentration. To develop a method and establish background controls the effect of cAMP in the equilibration period before incubation with a cholesterol acceptor, and the background level of efflux without acceptors at 0, 1, 2, 4, 8 and 24 hours were tested.

In the final experiment comparing apoA-I WT and the atheroprotective apoA-I mutants as described above the cholesterol efflux was also calculated similar to Sankaranarayanan *et al*. (Sankaranarayanan et al., 2011). Before each MFI value was used the background (BGD) fluorescence of THP-1 cells without the BD-CE complex was subtracted. Additional control samples were included of BODIPY-CE loaded THP-1 macrophages without cholesterol acceptors measured at 0 (MFI_{t0}), 8 and 24 ($MFI_{no\ acc.}$) hrs post-equilibration period to calculate the BGD efflux as follows:

$$BGD\ efflux\ \% = \frac{MFI_{no\ acc.}}{MFI_{t_0}} \cdot 100 \qquad \textbf{[19]}$$

The % cholesterol efflux was calculated with **Equation [20]**:

$$\%\ cholesterol\ efflux = 100 - \left(\frac{MFI_{acc.}}{MFI_{t_0}} \cdot 100\right) - BGD\ efflux \quad \textbf{[20]}$$

The background efflux was subtracted for the respective 8 and 24 hr incubation periods, respectively.

7.2.2.6 Fluorescence microscopy

The microscope cover slips placed into the wells prior to THP-1 macrophage differentiation were removed from the wells after BD-CE complex uptake. The adherent cells were washed with 1 mL PBS and fixed in 4 % (v/v) paraformaldehyde for 20 minutes. Next the cells were washed with 1 mL of PBS and a droplet of DAPI was used to stain the cell DNA and mount the cover slips onto microscope slides. The slides were stored at 4°C. Initially, the THP-1 macrophages were viewed after incubation with the BD-CE complex with an Axiovert 35 fluorescence microscope (Zeiss) with the transmission and FITC channels.

The LSM 880 AxioObserver confocal microscope (Zeiss) and Zeiss software was used to confirm if the cells contained the BD-CE complex. The samples were viewed with the objective lens Plan-Apochromat dry 40x magnification/0.95 Korr, with the laser at 488 nm at 10 – 12.7 % power. The BODIPY-CE and DAPI stained nuclei fluorescence excitation/emission wavelengths are 488/541 and 405/447 nm, respectively. The images were viewed using the ZEN Lite (Zeiss) and FIJI (Schindelin et al., 2012) software.

7.2.3 Thioflavin T fluorescence assay

The following methods for the ThT fluorescence assay were adapted from (Townsend et al., 2017). The samples and stock solutions were prepared in McIlvaine buffer (165 mM Na_2HPO_4 and 17.6 mM citrate) at pH 7.0. The ThT (Sigma-Aldrich) and heparin ([IdoA(2S)-GlcNS(6S)] > 70 %, Iduron) stock solutions were prepared to a final concentration of 1 mM. The average MW of heparin was ~14 – 15 kDa. The lipid-free apoA-I WT/R173C/L144R stocks were prepared at concentrations > 72 µM.

The ThT assay fluorescence measurements used the FlexStation 3 microplate reader (Molecular Devices) and a 96-well clear bottomed black walled plate (Nunc®). The sample wells (n = 6) contained a total volume of 200 µL, with 7.2 µM apoA-I, 20 µM ThT, at pH 7.0 or pH ~4.6 ± 14.4 µM heparin. The control samples (n = 6) were ThT only and apoA-I WT/R173C/L144R without ThT.

The wavelengths used for ThT excitation and emission were 430 and 480 nm, respectively. A constant temperature of 37°C was used throughout the assay. The fluorescence readings were taken every minute with agitation every 30 seconds, and 10 seconds before the measurement was taken. The baseline fluorescence of all samples was established for 10 minutes at pH 7.0. After 10 minutes 2.6 µL of concentrated 37 % HCl was added to the relevant sample wells to decrease the pH to <5.0.

7.3 Results

7.3.1 Self-assembly G MD simulations

The CGMD simulations of 160 POPC lipids with full-length apoA-I R173C dimer and two apoA-I WT Δ(1-43) monomers are described in sections **7.3.1.1** and **7.3.1.2** respectively.

7.3.1.1 ApoA-I R173C CGMD simulation

Initially, before starting the CGMD simulation setup the apoA-I R173C dimer was prepared. The modelled all atom full-length apoA-I R173C structure monomers were oriented anti-parallel with the cysteine residue sulfhydryl groups in α-helix 7 (H7) approximately 8.5 Å apart (**Figure 7.4A**). The H7 representations show the reduced number of atoms in the CG representation (**Figure 7.4B** vs. **C**). The disulphide bond was formed when the AA structure was converted to the CG structure (**Figure 7.4B to C**). The disulphide bond was relaxed to ~2.4 Å during energy minimisation *in vacuo* before further setup of the CGMD system.

After the addition of 160 POPC lipids, 16 Na^+ ions and solvation with water the system was equilibrated to a temperature and pressure of 323 K and 1 bar, respectively. The apoA-I R173C dimer CGMD system (**Figure 7.5**, **0 ns**) was simulated for a total time of 6.6 μs. The POPC molecules aggregated and formed micelles during the equilibration stages and the dynamics run due to the hydrophobic effect.

Further interactions driven by the hydrophobic effect occurred between the lipids and amphipathic protein α-helices within 105 ns (**Figure 7.5**). Interestingly, the termini α-helices (red, blue) acted as “anchors” for the lipids and were originally extended outwards before joining the overall elongated lipid micelle/bilayer (**Figure 7.5**, **5 – 95 ns**).

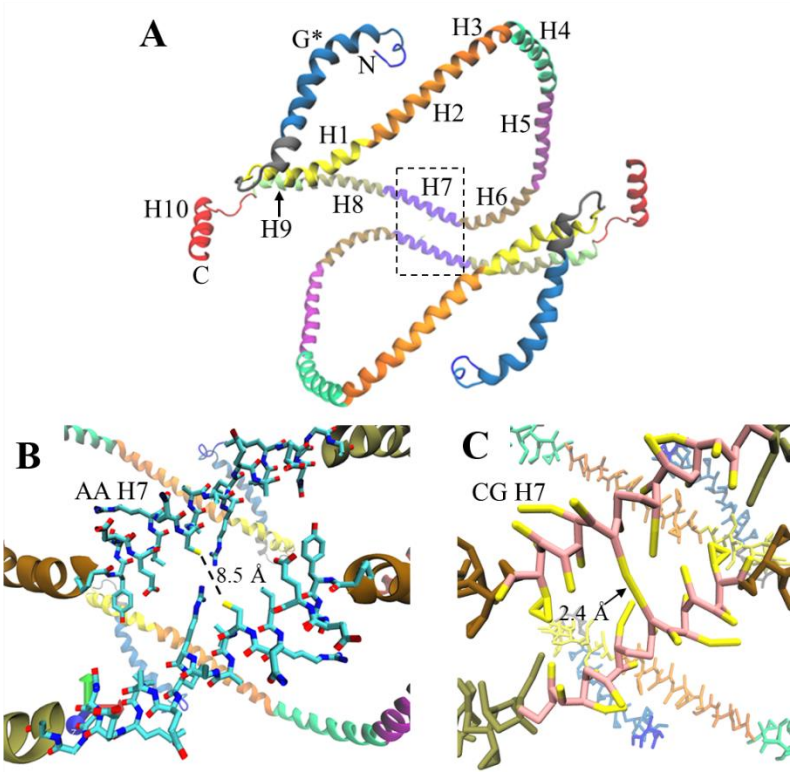

Figure 7.4. The all-atom anti-parallel full-length apoA-I R173C monomers orientations prior to disulphide bond formation, chain 1 and 2. The secondary structure is as described in **Chapter 1**, **section 1.6**, **Figure 1.5–1.6**. The N-termini (N) G* helix (blue), and the α-helices are coloured as H1 (yellow), H2 (orange), H3 (light orange), H4 (green), H5 (purple), H6 (brown), H7 (violet), H8 (light brown), H9 (light green) and the C-termini H10 (C, red). H7 in the all-atom (**A**) and coarse-grained (**B**) representations. The respective monomer cysteine residues were positioned ~8.5 Å apart (**A**) and the disulphide bond was relaxed to ~2.4 Å in an energy minimisation *in vacuo* (**B**).

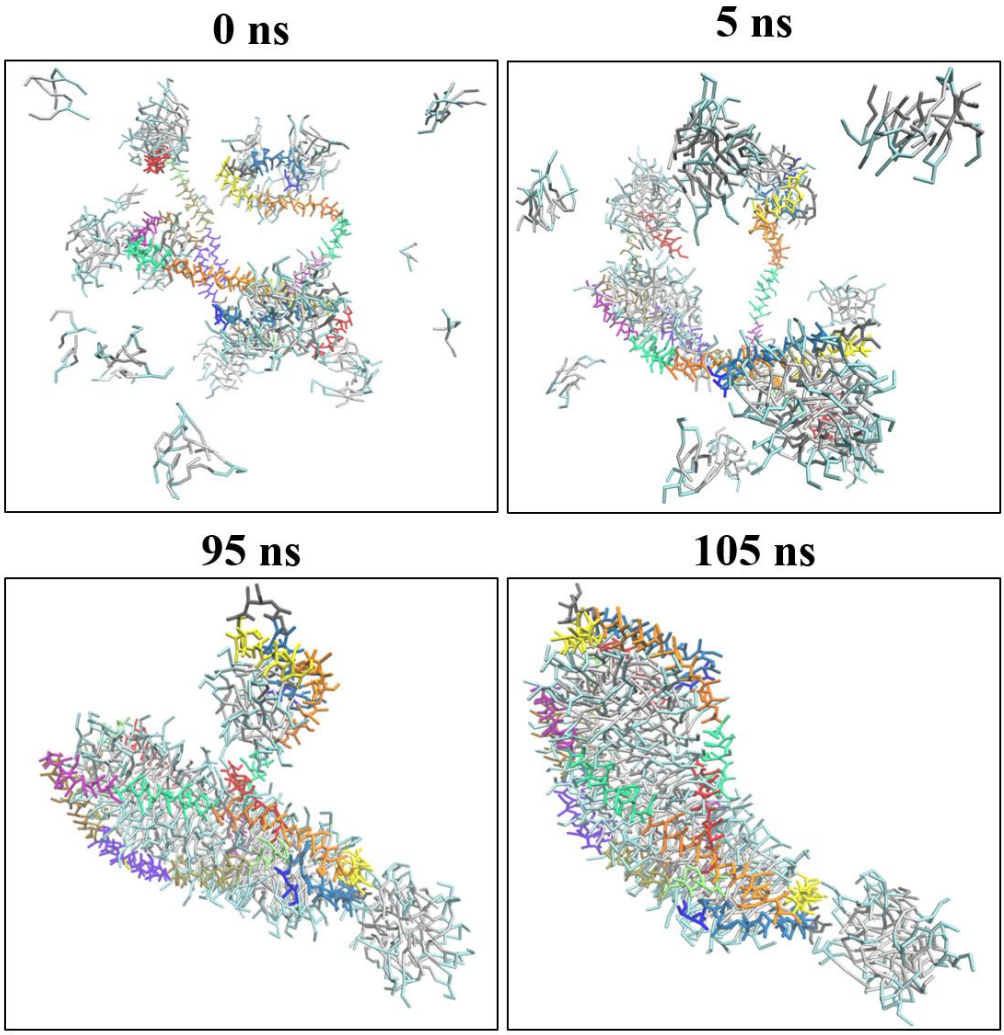

Figure 7.5. Snapshots of timepoints (0, 5, 95 and 105 ns) during the 6.6 μs self-assembly simulation of full-length dimeric apoA-I R173C with 160 POPC lipids.

The POPC lipids were in an approximate elongated bilayer disc shape between ~138 ns to 6.6 μs (**Figure 7.6**). The overall final "HDL-like" nanoparticle conformation was approximately 12.9 nm x 6.8 nm in diameter with a thickness between 4.3 – 4.6 nm.

The apoA-I R173C dimer chains 1 and 2 (**Figure 7.4**) did not wrap around the POPC bilayer to form an interhelical registry, except at the position of the disulphide bond in H7 (**Figure 7.6**). The apoA-I R173C chain 1 primarily formed interhelical interactions within the same chain and folded back at H5/6 (**Figure 7.6D**) to form the N- and C-termini α-helix cluster (**Figure 7.6A**). Chain 2 did not wrap around the bilayer completely due to self-association between the N-terminal region and H2/3 (**Figure 7.6B-C**).

The apoA-I R173C dimer interacted predominantly with the lipid acyl tails whilst exposed POPC areas without the protein contained the POPC headgroups facing outwards (**Figure 7.6C**). Furthermore, the relative mean standard deviation (RMSD) and radius of gyration of the apoA-I R173C dimer during the simulation indicated relatively small changes in the protein conformation after the incorporation of the POPC lipids into the bilayer (~138 ns) (**Appendix 4**).

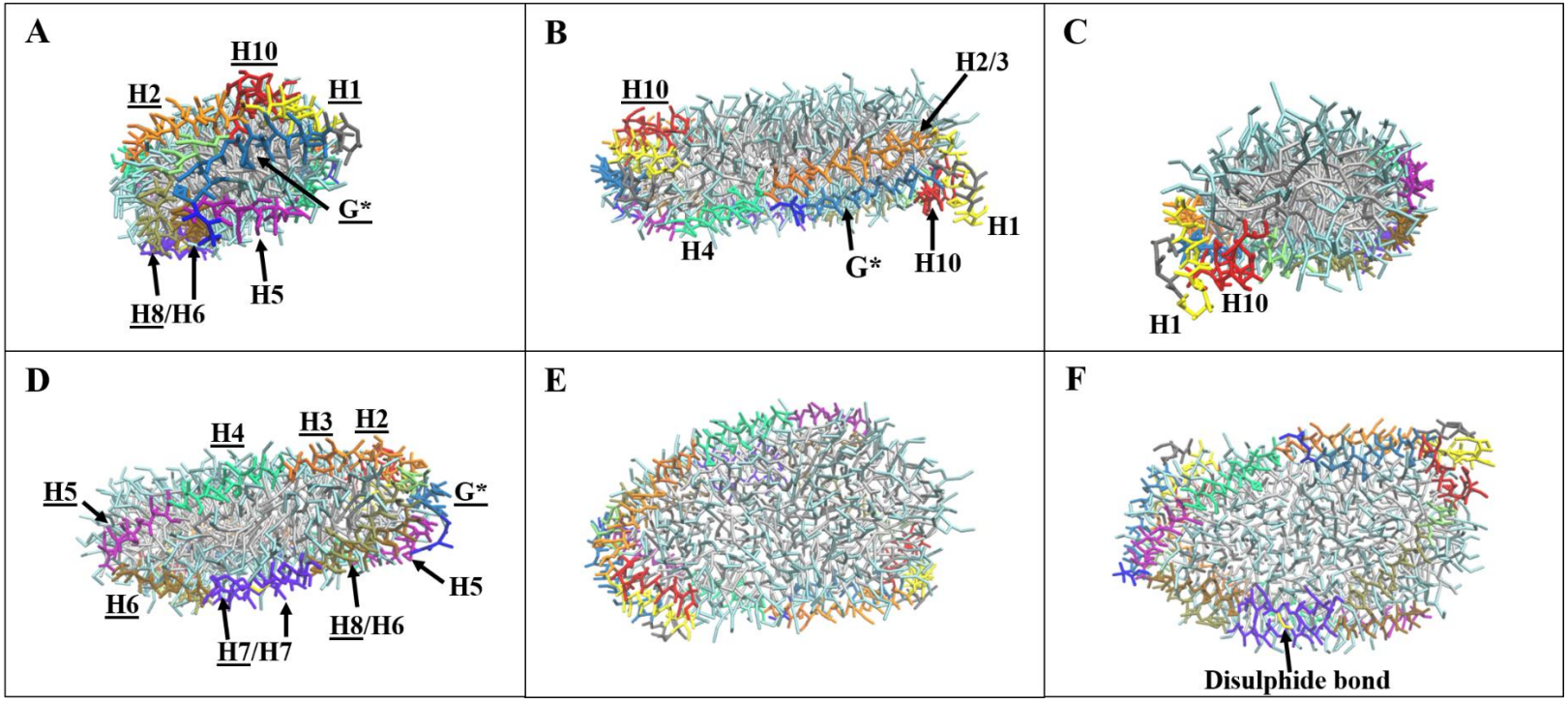

Figure 7.6. The full-length dimeric apoA-I R173C with 160 POPC lipids self-assembly HDL CGMD simulation final conformation **(A-D)** side-views and **(E-F)** top views at ~6.6 μs. The apoA-I R173C dimer helices are coloured as in **Figure 7.4**. The POPC headgroups are blue and acyl tails are silver. The labels for chain 1 α-helices are underlined to distinguish these from chain 2 α-helices in the apoA-I R173C dimer.

7.3.1.2 Self-assembly apoA-I WT Δ(1-43) CGMD simulation

A control CGMD simulation of the apoA-I WT Δ(1-43) crystal structure (Borhani et al., 1997) and 160 POPC lipids under the same conditions as above was performed (**Figure 7.7**). To determine if the MD parameters used could reproduce results similar to previous nanodisc simulations with truncated apoA-I WT (Debnath and Schäfer, 2015; Shih et al., 2007b).

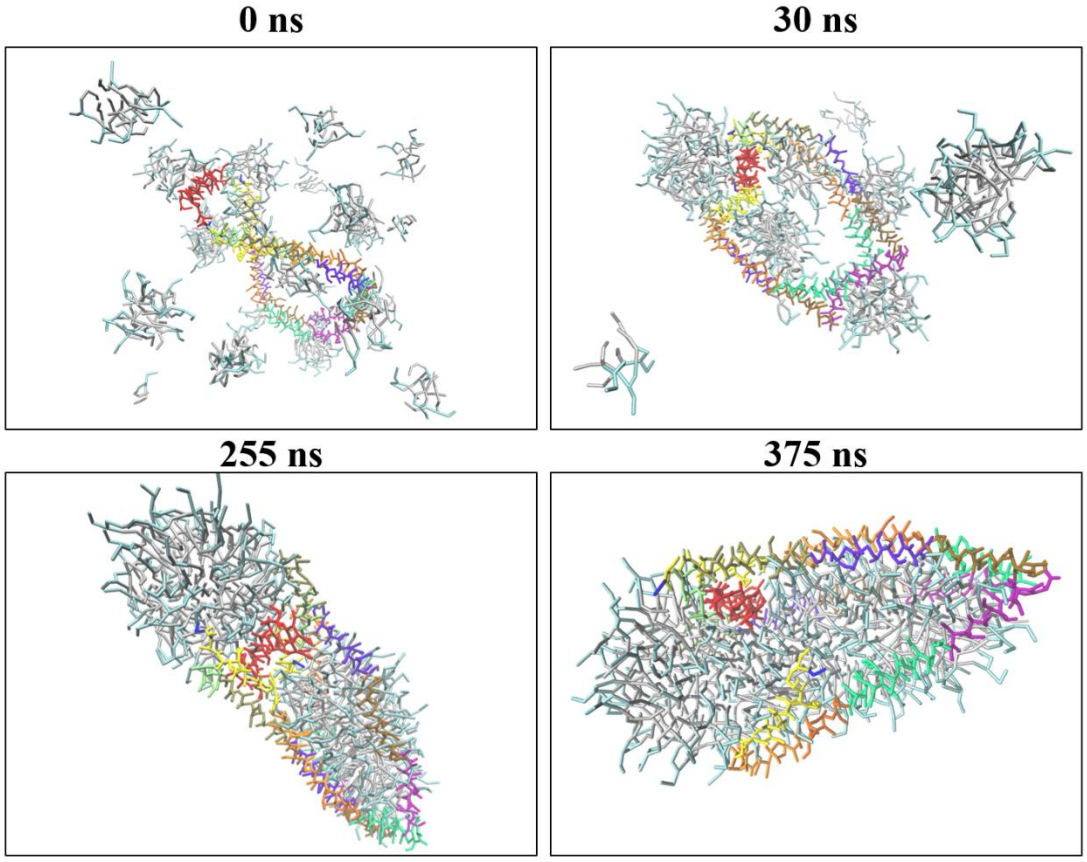

Figure 7.7. Snapshots of timepoints (0, 30, 255 and 375 ns) during the 8.9 μs self-assembly simulation of two apoA-I WT Δ(1-43) monomers with 160 POPC lipids, the CGMD WT simulation.

The starting conformation of the apoA-I WT Δ(1-43) monomer chains A and B at 0 ns were as in **Chapter 1**, **Figure 1.6** (Borhani et al., 1997). In the apoA-I WT Δ(1-43)

CGMD simulation the POPC molecules interacted with the monomer residues through the hydrophobic effect. The protein monomer conformations remained similar up to 375 ns (**Figure 7.7**), e.g., at 255 ns the C-termini of chain A interacted with H1 of chain B and vice versa. At 375 ns chain A is wrapped around the outside in a V-shape as the C-termini helices (**Figure 7.7**, **red**) of both monomers and chain B H1 (**Figure 7.7**, **yellow**) folded back to allow the POPC micelle to form an elongated bilayer with a micellar end containing all of the lipids. The inter- and intrahelical interactions are more clearly observed in the final conformation of the "HDL-like" nanoparticle (**Figure 7.8A**) at 8.9 μs. The nanoparticle was approximately 11.9 x 9.1 – 9.9 nm, with a thickness between 4.2 – 5.1 nm.

The H5/H5 registry of the apoA-I WT Δ(1-43) crystal structure was disrupted at ~40 ns when POPC molecules separated the chains. At ~6.5 μs chain B began to move back towards the chain A H5 which brought the helices into close proximity (**Figure 7.8D**). The CGMD simulation did not achieve a conformation similar to the "double belt" model as chain B was folded back across the planar face of the POPC lipid bilayer (**Figure 7.8E** and **H**). The apoA-I WT Δ(1-43) CG monomer backbone conformation changes were observed in the RMSD and radius of gyration (**Appendix 4**). The protein was not wrapped around the lipid bilayer therefore the final conformation contained exposed areas of the lipid bilayer with some lipids facing outwards (**Figure 7.8B-C**).

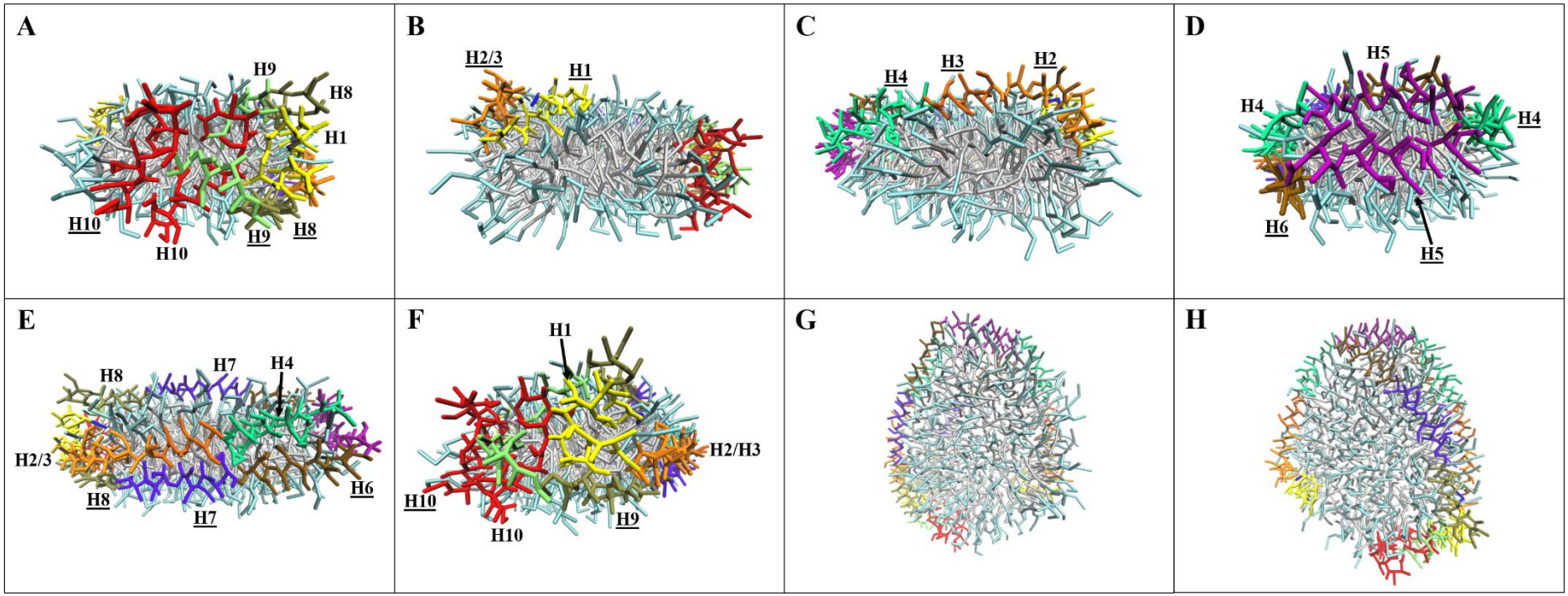

Figure 7.8. WT CGMD conformation at 8.9 μs. The apoA-I Δ(1-43) chains A and B (Borhani et al., 1997) with 160 POPC lipids self-assembly HDL CGMD simulation final conformation **(A-F)** side-views and **(G-H)** top views at ~8.9 μs. The α-helices are coloured as in **Figure 7.4**. The POPC headgroups are blue and acyl tails are silver. The labels for chain A α-helices are underlined to distinguish these from the chain B α-helices.

7.3.2 BODIPY-cholesteryl ester uptake

The following sections describe the different sample conditions used in the THP-1 macrophage BODIPY-CE uptake and efflux flow cytometry assay.

7.3.2.1 Fluorescence microscopy

Initially the THP-1 macrophage uptake of the BD-CE complex was tested using a standard fluorescence microscope (data not shown). There was some photobleaching of the cells during imaging, therefore confocal microscopy was used to confirm the uptake of BODIPY cholesterol. The incubated THP-1 macrophages showed intake of the BD-CE complex detected as bright green fluorescence spots in the cytoplasm as lipid droplets (Ghosh et al., 2010) or close to/in the cell membrane (**Figure 7.9B-C**). This suggested the THP-1 macrophage incubation conditions with the BODIPY-CE/cholesterol/m-β-CD complex (0.025/0.1/10 mM) were successful for flow cytometry.

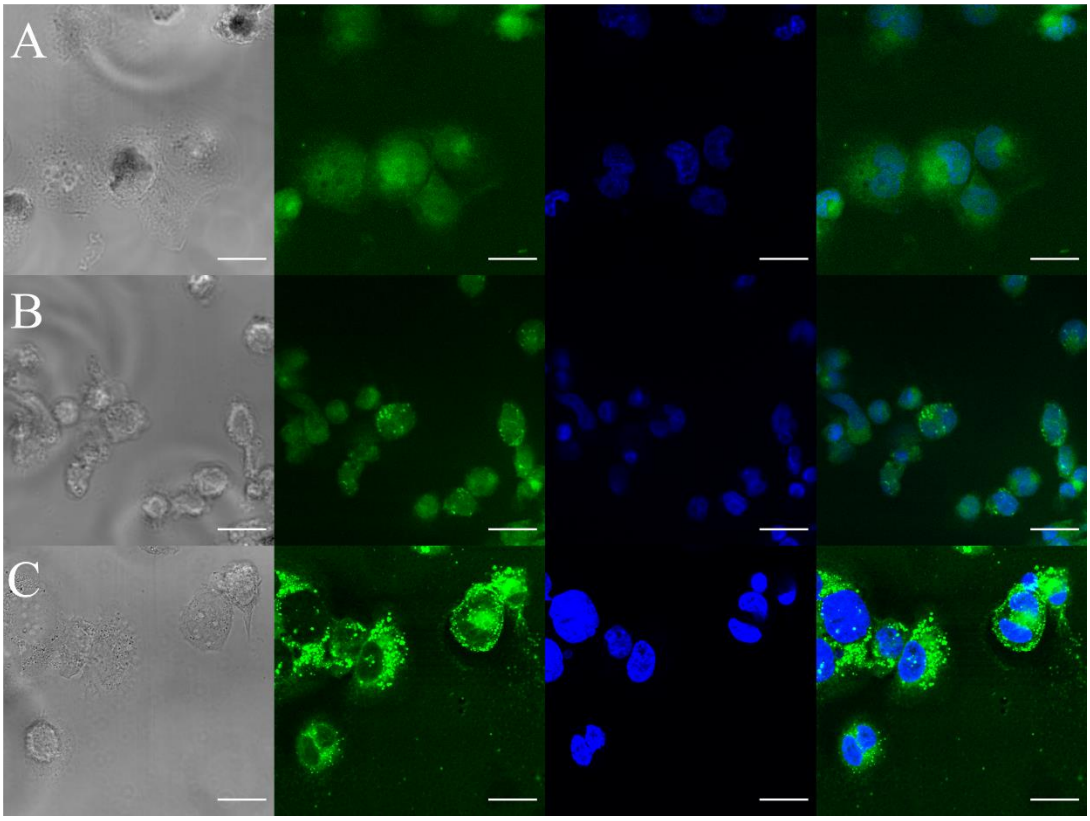

Figure 7.9. THP-1 macrophages incubated without the BD-CE complex **(A)** and with the BD-CE complex **(B)** imaged under the same conditions. **(C)** Another example of cells incubated with the BD-CE complex. The sample was viewed under different microscope settings to enhance the fluorescence detected. The scale bar represents 20 µm. The different confocal microscope channels shown (left to right) are the non-fluorescent transmission, FITC (493 – 589 nm) for BODIPY-CE detection, and the DAPI-stained nuclei channel (410 – 483 nm), with a final overlay of the FITC and DAPI channel images.

7.3.2.2 Flow cytometry of BODIPY-CE in THP-1 macrophages

To further confirm the intake of the BD-CE complex into THP-1 macrophages flow cytometry was used. The preliminary flow cytometry experiment examined the difference in fluorescence between THP-1 macrophages incubated with and without the BD-CE complex. The fluorescence was detected after the 18 hour incubation period.

The THP-1 macrophages (P2) were separated from cellular debris (P1) with the gating in **Figure 7.10A-B**. After data collection analysis of the FSC-width versus FSC-A showed the majority of the cells which contributed to the fluorescence detected in P2 were singlets in the indicated regions (**Figure 7.10A-B)**. The greater fluorescence detected in the THP-1 macrophages (**Figure 7.10C**, **FITC-A**) clearly indicated the cells with BODIPY-CE retained the fluorophore. Furthermore, the correlation between the nuclear staining dye (PC5.5-A) and the FITC-A BODIPY-CE detected fluorescence indicated the P2 gated cells contained both fluorescent compounds (**Figure 7.10C**). The background fluorescence of the THP-1 only cells in the FITC region did not overlap significantly with the BODIPY-CE fluorescence detected.

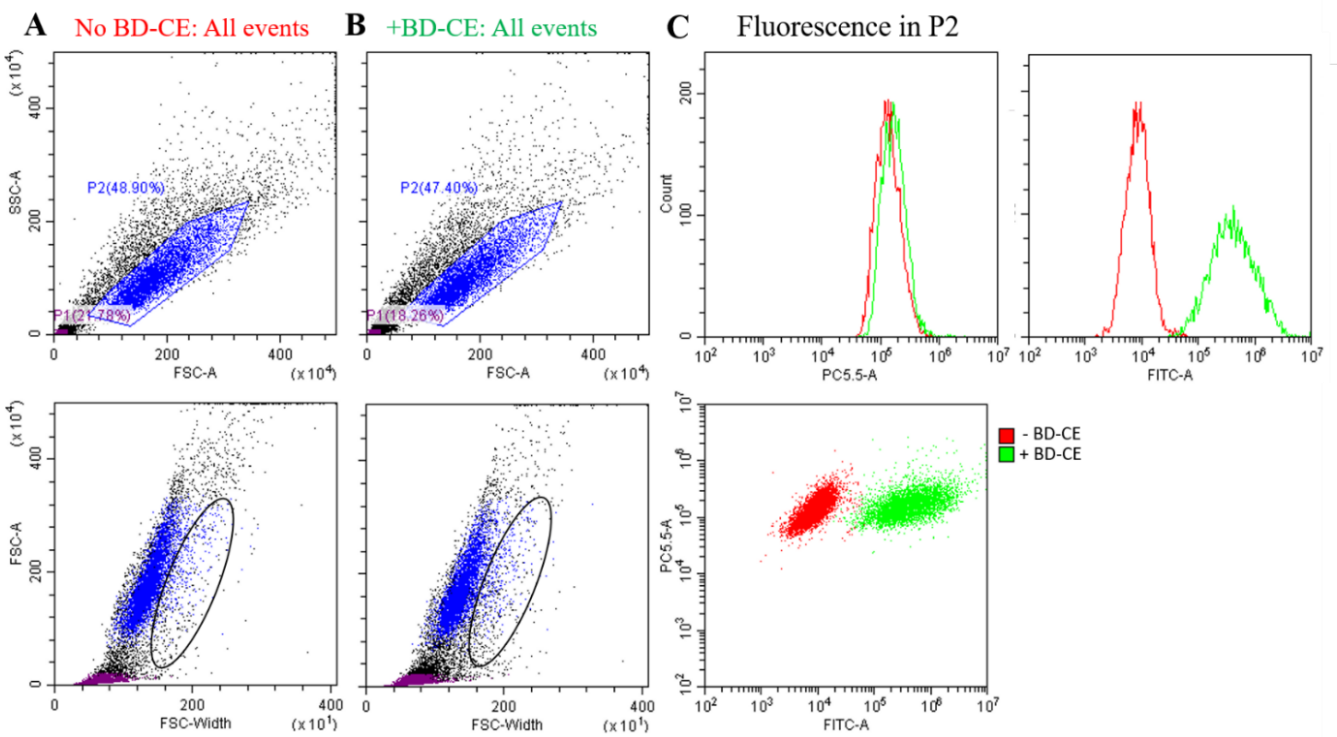

Figure 7.10. Flow cytometry of THP-1 macrophages ±BD-CE after a 4-hr incubation in media. A total of 10000 events (P1+ P2) were recorded. **(A**, **B)** In the FSC vs. SSC area plots the cells were gated in P2 (blue) and separated from the cell debris in P1 (purple). P1 and P2 are shown in the corresponding post-gated FSC-W vs. FSC-A dot plots with the doublet region circled. (C) The fluorescence histograms and dye correlation plot for cells -BD-CE complex (red) and +BD-CE complex (green) for the nuclear dye (PC5.5-A), and the BODIPY-CE (FITC-A).

7.3.3 Development of the BODIPY-CE efflux assay

Next, BD-CE loaded THP-1 macrophages were incubated with lipid-free apoA-I WT at various protein concentrations to determine if apoA-I could mediate cholesterol efflux from the cells (**Figure 7.11**).

Interestingly, the cells incubated without cAMP showed no cholesterol efflux until a 10-fold increase in apoA-I WT concentration with only 4 % efflux overall. The relatively large ~20 – 32 % cholesterol efflux in the samples incubated with cAMP before incubation with apoA-I WT for 4 hours suggested the media and time period were suitable for cholesterol efflux detection. Additionally, the cholesterol efflux at concentrations of apoA-I WT above 25 µg/mL appeared to plateau at approximately 25 % cholesterol efflux (**Figure 7.11**). However, the results for each sample required repeats to determine if the controls for the background cholesterol efflux and experimental conditions for cholesterol efflux were suitable.

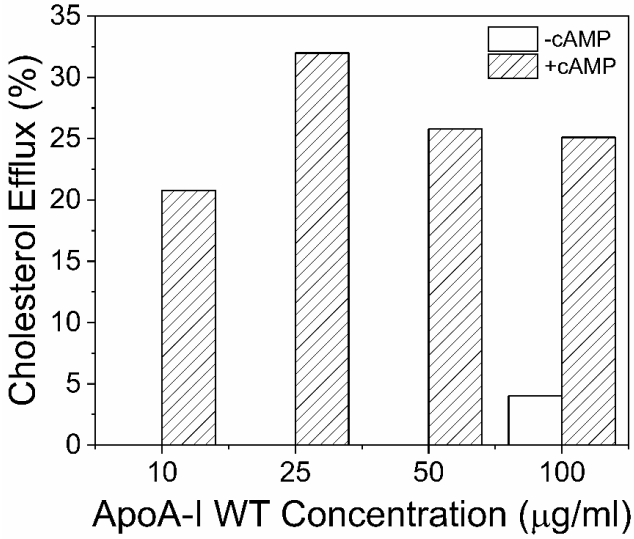

Figure 7.11. The % cholesterol efflux calculated with **Equation [18]** of BODIPY-CE from THP-1 macrophages. After loading with BODIPY-CE the cells were incubated in RPMI media containing 2 mg/mL fatty-acid free BSA, 1 μg/mL ACAT inhibitor, ±0.3 mM cAMP. Then the cells were incubated with LF apoA-I WT at 10, 25, 50, and 100 μg/mL concentrations (n = 1) for 4 hours. The cells were gated as previously described.

The establishment of controls for background cholesterol efflux was explored further. The average MFI of BODIPY-CE loaded THP-1 macrophages was measured over various time points (**Figure 7.12**) after the cells were equilibrated in media ±cAMP.

The gating strategy in flow cytometry was altered to use the gating in the FSC-width vs. FSC-A plot due to the different distribution of cells from previous P2 gating used (**Figure 7.12A**). The MFI and cholesterol efflux were determined for cells loaded with BODIPY-CE equilibrated in media ±cAMP followed by incubation in media without apoA-I WT (**Figure 7.12B-C**).

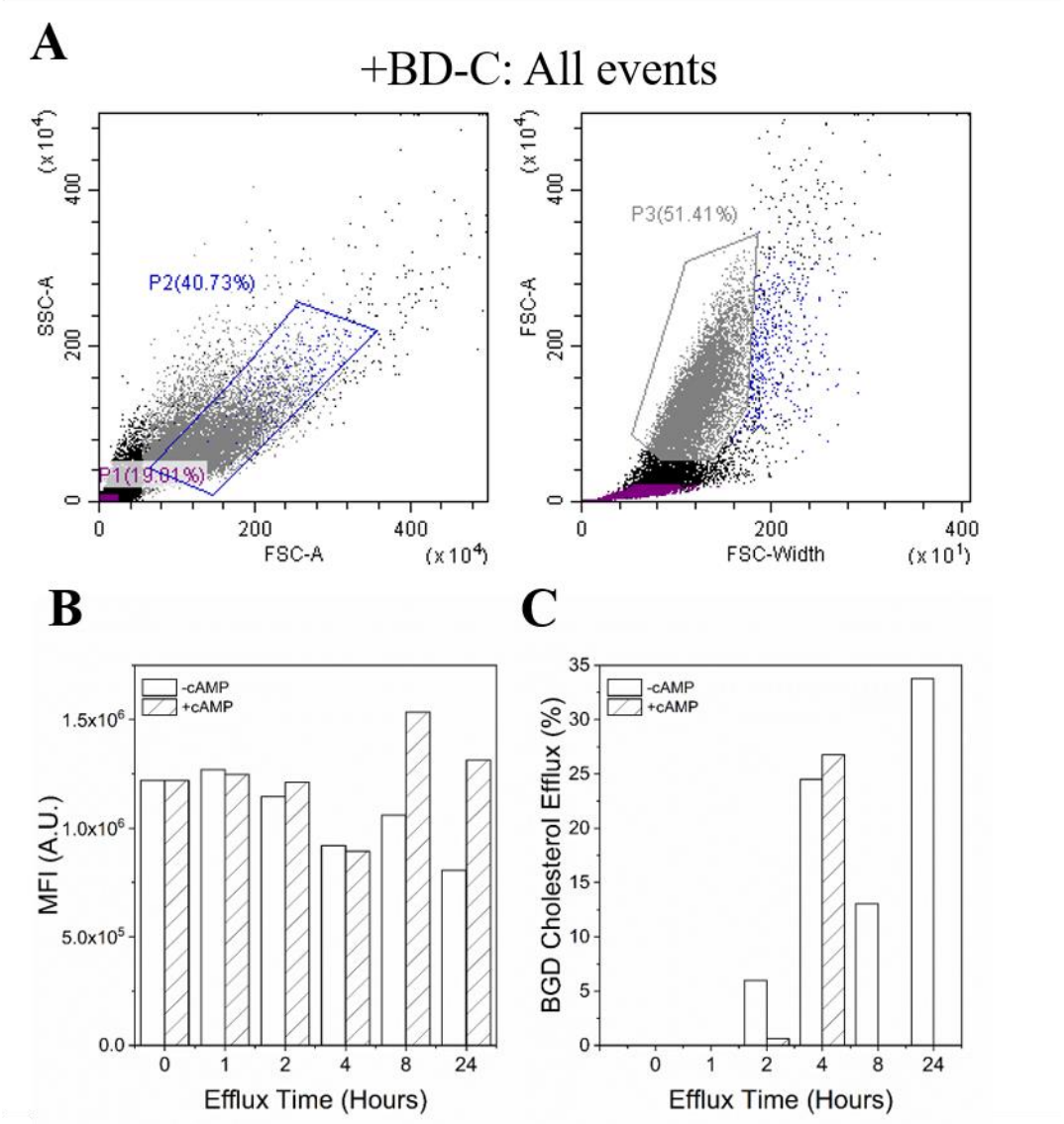

Figure 7.12. (A) An example of the flow cytometry gating used to determine the MFI of 10000 events collected in P3 (n = 1) of BODIPY-CE loaded THP-1 macrophages incubated without a cholesterol acceptor at various timepoints. At time 0 hrs the BODIPY-CE loaded THP-1 macrophages had been equilibrated for 18 hrs in media ±cAMP. The **(B)** MFI and **(C)** background efflux were calculated with **Equation [19]** for various timepoints to determine the extent of background cholesterol efflux.

The background efflux present in the THP-1 macrophages indicated the need for separate control cells for different time points. In contrast, the majority of the cells

incubated with cAMP before media only appeared to retain the BODIPY-CE overall. Therefore, the efflux experiment with apoA-I WT and the atheroprotective mutants equilibration period included cAMP and the cholesterol acceptor incubation time periods of 8 and 24 hours.

Finally, a pilot experiment of cholesterol efflux from cells incubated with apoA-I WT or the atheroprotective mutants in excess protein concentrations were tested by flow cytometry (**Figure 7.14**). The cholesterol efflux was calculated as in previous experiments with **Equation [18]** (**Figure 7.14A**), and with the background cholesterol efflux calculated separately with **Equations [19]** and **[20]**. The difference in the control samples used for calculating the cholesterol efflux in the protocol can be more clearly identified in **Figure 7.13**.

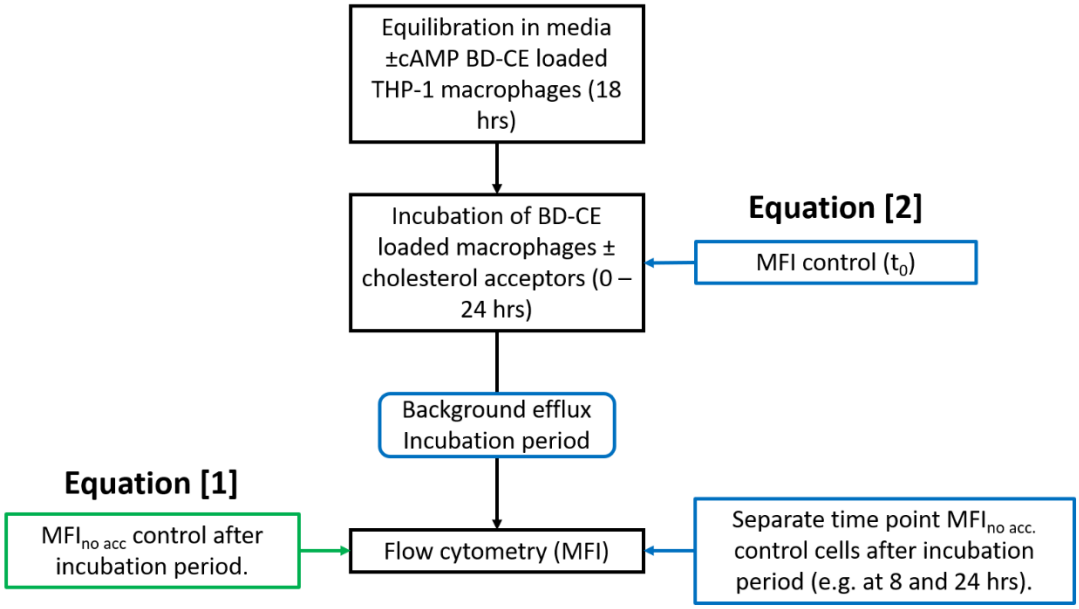

Figure 7.13. The stages of the BD-CE efflux from the THP-1 macrophages protocol. The points are identified for the control cells ($MFI_{no\ acc.}$) used to calculate the cholesterol efflux with **Equation [18]** (green), and the second approach for calculating the background cholesterol efflux with **Equation [19]** (blue).

Using **Equation [18]** to calculate the cholesterol efflux when the cells were incubated with lipid-free apoA-I WT and L144R showed cholesterol efflux, but most measurements had large standard deviations (**Figure 7.14A**). The apoA-I L144R 600 µg/mL showed similar (~18 %) cholesterol efflux at both incubation periods. This suggested the excess concentration of protein saturated the available cholesterol efflux. The difference between the 8 and 24 hr incubation apoA-I WT cholesterol efflux values, i.e., 600 µg/mL apoA-I WT at 5.7 ±12.0 % (24 hrs), 14.3 ±14.5 % (8 hrs) and 32.5 ±8.8 % at 120 µg/mL (24 hrs), suggested the results were inconsistent as both concentrations of apoA-I were in excess. Therefore, there could be discrepancies in the protocol or in the cholesterol efflux calculation.

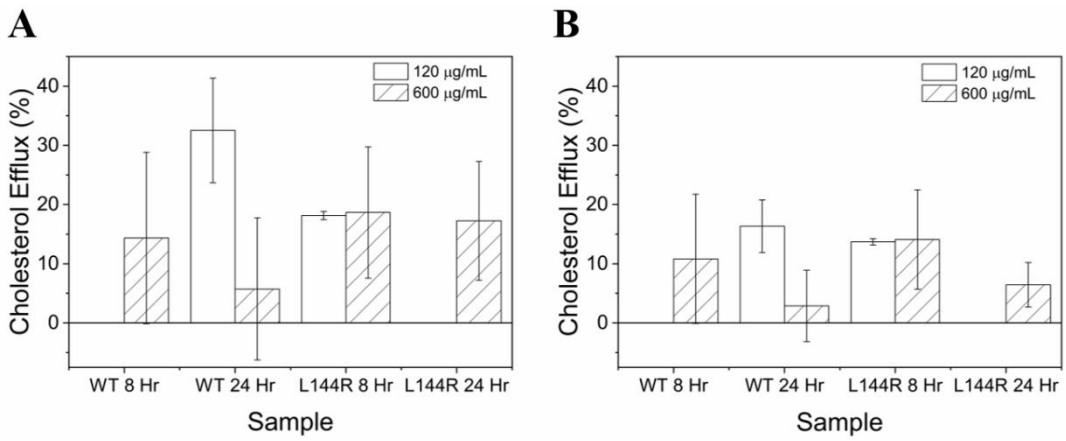

Figure 7.14. The average % cholesterol efflux ±standard deviation (n = 2) of BODIPY-CE loaded THP-1 macrophages incubated with apo WT, R173C and L144R for 8 and 24 hours. The cholesterol efflux was calculated using **(A) Equation [18]** and **(B) Equations [19]** and **[20]**. The cells were gated in flow cytometry as described (**Figure 7.12**), 10000 events were recorded in P3. Separate controls without LF apoA-I were used for the $MFI_{no\ acc.}$ at 8 and 24 hours. The apoA-I R173C samples at both concentrations and time points presented with no cholesterol efflux (not shown).

Consequently, the background cholesterol efflux was calculated separately using **Equation [19]** and the t_0 MFI was measured after the 18-hr equilibration period of the THP-1 macrophages containing the BD-CE complex (**Figure 7.13**, **Figure 7.14B**). The background efflux for the 8 and 24 hr samples incubated were relatively large at 29.9 ±22.9 % and 55.6 ±12.5 % respectively. The background efflux contradicted the previous lack of background efflux detected (**Figure 7.12C**) which suggested the background efflux was not consistent. **Equation [18]** assumed the background efflux was relatively small during the incubation period (**Figure 7.13**) which caused an overestimation of the cholesterol efflux as the background efflux of cells incubated without cholesterol acceptors was not considered (**Figure 7.14A**).

After the background efflux was subtracted, the ~16.3 ±4.4 % cholesterol efflux to apoA-I WT in the 24 hr incubated sample with lipid-free apoA-I WT was similar to the previously observed value of ~15 % [^{3}H]-cholesterol from J774 macrophages (Sankaranarayanan et al., 2011). Hence, the calculation for cholesterol efflux using **Equations [19]** and **[20]** was suitable. The large standard deviations suggested repeats were necessary.

Additionally, the background efflux was greater than the efflux observed resulting in no detection of cholesterol efflux for the samples which showed 0 % cholesterol efflux and LF apoA-I R173C (**Figure 7.14**). This suggested a shorter timeframe would be suitable for further experiments to limit the amount of background cholesterol efflux.

Overall, this suggested the methodology required further optimisation and repeats to determine if the lipid-free and rHDL-bound atheroprotective mutants have a greater capability to mediate cholesterol efflux relative to apoA-I WT.

7.3.4 ThT fluorescence assay of lipid-free apoA-I

A ThT fluorescence assay was used to determine if the lipid-free atheroprotective apoA-I mutants aggregated with and without heparin at pH 7 and 4.6. The control samples of ThT only, and each protein in the absence of ThT did not show any increase in fluorescence over the timescale observed (**Appendix 4**). Immediately after the sample conditions were acidified each protein showed an increased ThT fluorescence in the presence of heparin (**Figure 7.15A**). This suggested that amyloid fibril formation could be induced in the atheroprotective apoA-I mutants and apoA-I WT. The overall average total fluorescence was similar for each protein at ~220 – 240 A.U. (**Figure 7.15B)** which suggested the level of aggregation and ThT binding was similar for each protein.

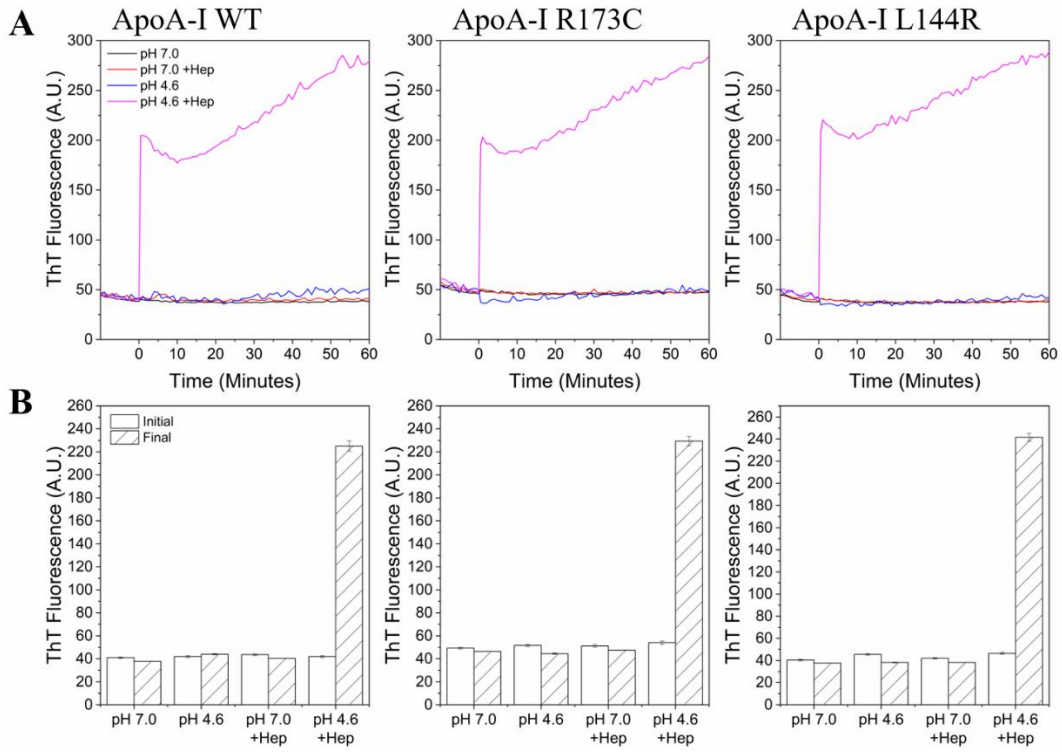

Figure 7.15. A) ThT fluorescence of 7.2 µM apoA-I WT, apoA-I R173C and apoA-I L144R in McIlvaine buffer at pH 7.0 and pH ~4.6 ± 14.4 µM heparin (n = 6). **B)** The average total fluorescence over 10 minutes (Initial) and over 60 minutes (Final).

7.4 Discussion

7.4.1 Self-assembly CGMD simulations

The CGMD simulations of the apoA-I R173C dimer and apoA-I WT Δ(1-43) monomers with POPC lipids did not produce a final HDL nanoparticle morphology similar to the "double belt" model. In this work the apoA-I R173C chain 1 and 2 N-termini helices were self-associated with the respective H1 and/or the H2/H3 of each chain (**Figure 7.6A-B**). This could have affected the propensity of the protein chain to wrap around the elongated lipid bilayer formed. In the future it could be relevant to repeat the CGMD self-assembly simulations to determine if the lipid-free apoA-I starting structure was suitable and if the protein self-association occurs in multiple repeats.

However, in the model described below of a 9.6 nm discoidal HDL R173C nanoparticle the N-termini residues 1-65 are folded back at residue G39 (Gursky et al., 2013). In this work residue G39 is in **Figure 7.6B** (grey, residues 34 – 43) and does not appear to act as a defined residue specific "hinge region" but does fold with H1 to allow the N-termini fold back and self-associate. Gursky *et al*. have produced apoA-I R173C "double-belt" discoidal HDL nanoparticle models based upon the apoA-I WT Δ(185-243) and C-terminal residues of apoA-I Δ(1-43) crystal structures combined with cross-linking data (Gursky et al., 2013). The AAMD equilibration of a preformed bilayer nanodisc of 178 POPC lipids and a "double-belt" model of the apoA-I R173C dimer remained stable throughout a 15 ns equilibration period of a 9.6 nm HDL R173C nanoparticle (Gursky et al., 2013).

Hence, the removal of the N-terminal region may not be necessary but further refinement of the starting structure of the apoA-I R173C dimer is required such as the method used by Gursky *et al*. (Gursky et al., 2013). Another aspect of their method used

a more biased starting conformation with a preformed "belt-like" structure of the apoA-I R173C dimer and lipid nanodisc (Gursky et al., 2013).

Overall, in both CGMD simulations a relatively energetically stable state was observed in the "HDL-like" nanoparticles with only minor tertiary protein conformation changes after the initial self-assembly and incorporation of the lipids into a bilayer/micellar arrangement. This occurred very early in each simulation at ~140 and ~375 ns which suggested the starting protein conformation could require further refinement. For example, utilising a model based upon the higher resolution crystal structure of apoA-I WT Δ(185-243) (Gursky et al., 2013; Mei and Atkinson, 2011). As well as, using different starting lipid conformations such as micellar, random or as a preformed nanodisc (Debnath and Schäfer, 2015; Gursky et al., 2013; Shih et al., 2006; Shih et al., 2007a; Shih et al., 2007b).

In this work the CGMD simulations demonstrated the hydrophobic effect in self-assembly of the "HDL-like" nanoparticles and the interactions between the amphipathic α-helices of the respective apoA-I proteins and the phospholipids.

During the course of this work Pourmousa *et al*. produced the multi-microsecond (10 – 20 μs) AAMD simulation models of the HDL nanoparticles containing POPC:cholesterol:apoA-I WT 200:20:2 and 160:24:2 (M/M) (**Chapter 1**, **Figure 1.15**). The atomistic definition allowed for secondary structure changes and tertiary apoA-I structural conformation rearrangements (Pourmousa et al., 2018). Importantly, the simulations required the long timescales of 10 – 20 μs to converge suggesting future AAMD simulations should use similar timescales (Pourmousa et al., 2018). Consequently, the oriented ^{31}P NMR HDL nanoparticle morphology characterisation utilised the atomistic HDL nanoparticle models (**Chapter 6**). Furthermore, some of the

details provided by the AAMD simulations are required to show the rHDL nanoparticles self-assemble.

A comparative AAMD HDL 200:20:2 nanoparticle 10 μs simulation with an initial uneven apoA-I double-belt became kinetically trapped and produced a different final HDL apoA-I conformation with a statistically equivalent average shape to the model used in **Chapter 6** (Pourmousa and Pastor, 2018). This demonstrated the starting conformation of apoA-I was highly important and suggested further research is required to produce different starting conformations of the apoA-I mutants.

Overall, due to the limited success and time available for the CGMD simulations further work was not explored. There are several enhanced sampling options discussed by Pourmousa and Pastor (Pourmousa and Pastor, 2018) available for producing different apoA-I conformations such as replica exchange MD (Sugita and Okamoto, 1999) or the use of MDSA for HDL nanoparticle simulations (Jones et al., 2011). These could be explored in future work.

Little is known about the apoA-I L144R mutant monomer or dimer arrangements in discoidal rHDL nanoparticles. The residue L144 could be mutated in both monomers of the full-length apoA-I WT dimer in the 200:20:2 HDL nanoparticle model (Pourmousa et al., 2018) to provide a framework for testing a shifted monomer to monomer registry. Furthermore, chemical cross-linking experiments combined with mass spectrometry of apoA-I L144R in discoidal rHDL nanoparticles could provide specific structural constraints to support different monomer registries such as LL5/5 or LL5/2 for apoA-I WT (Silva et al., 2005b). Overall, future AAMD simulations combined with experimental data would provide residue specific structural information.

7.4.2 Evaluation of the BODIPY-CE efflux assay

This work explored the use of BODIPY-CE to monitor efflux to ApoA-I WT and mutants from THP-1 macrophages. The use of confocal microscopy and flow cytometry to detect the fluorescently labelled BODIPY-CE inside THP-1 macrophages showed that the conditions for cellular uptake were successful (Liu et al., 2014; Sankaranarayanan et al., 2011).

Initially the cholesterol efflux was examined for LF apoA-I WT concentrations between 10 – 100 µg/mL. The efflux was mainly observed for cells equilibrated with cAMP and did not increase significantly at protein concentrations above 25 µg/mL. Previously, LF apoA-I ABCA1-mediated cholesterol efflux plateaued above ~10 µg/mL protein concentration (Sankaranarayanan et al., 2011). However, it became apparent that further controls are necessary for calculating the cholesterol efflux such as background efflux. As well as the effect of cAMP on ABCA1-mediated cholesterol efflux in THP-1 macrophages.

In the limited time available for the functional studies BODIPY-CE efflux from THP-1 macrophages was compared between LF apoA-I WT and the atheroprotective apoA-I mutants at two excess concentrations. Although efflux was observed in the apoA-I WT and L144R 8 hr incubation period samples the measurements contained large standard deviations. Furthermore, efflux was not detected for the apoA-I R173C samples which was unexpected compared to previous studies of LF apoA-I and rHDL-R173C nanoparticles (Calabresi et al., 1999; Zhu et al., 2005).

Taken together this suggested the assay conditions required further testing to produce reproducible and reliable results. In future work the cholesterol efflux calculations which included the background efflux as controls and the equilibration period t_0 MFI

(**Equations [19]-[20]**, **Figure 7.14B**) could be used to provide a more reliable efflux calculation.

Further experimental conditions were not tested due to the limited time available. However, there are several factors which require further research and understanding before examining the cholesterol efflux of different apoA-I bearing cholesterol acceptors.

Notably, the use of BODIPY-CE rather than BODIPY-cholesterol could have affected the efflux observed. Further research after experiments indicated that in macrophages CE's require hydrolysis into fatty acids and cholesterol by cholesterol ester hydrolase before free cholesterol efflux (Ghosh et al., 2010). This suggested the detection of the fluorophore in the THP-1 macrophages in the cells could be due to retained BODIPY-tagged fatty acids or BODIPY-CE molecules (Solanko et al., 2016). Additionally, the ABCA1-mediated cholesterol efflux from THP-1 macrophages can be regulated by an intracellular macrophage liver X receptor agonist not cAMP (Costet et al., 2000; Kiss et al., 2005; Yano et al., 2016).

Overall, further research was required to determine accurate cholesterol efflux values from cholesterol loaded THP-1 macrophages. An analysis of the limitations in the methodology suggested changes in the fluorophore used and ABCA1 up-regulation compound were necessary. As well as appropriate controls and cholesterol efflux calculations in the flow cytometry fluorescence detection. This is essential to compare the cholesterol efflux properties of LF or rHDL-bound apoA-I mutants in the search for clues in determining how the apoA-I mutants could be atheroprotective.

7.4.3 Amyloidogenic potential of the atheroprotective apoA-I mutants

The increased ThT fluorescence of each apoA-I protein under amyloidogenic conditions suggested the atheroprotective mutants were similarly susceptible to aggregation compared to apoA-I WT. The lack of an increase in ThT fluorescence in samples at pH 7.0 with and without heparin was similar to previous studies for apoA-I WT and R173C (Petrlova et al., 2014; Townsend et al., 2017). The apoA-I samples did not increase in fluorescence over the timescale measured (60 minutes) at pH 4.6. This difference could be due to sample incubation before fluorescence measurements were taken (Ramella et al., 2011; Townsend et al., 2017). As shown previously, aggregation is enhanced by the presence of heparin at acidic pH consistent with proinflammatory conditions.

These initial results suggest that resistance to amyloid formation is unlikely to be a major reason for the atheroprotective properties of apoA-I R173C or L144R.

8 Discussion and future work

Overall, the research in this thesis aimed to investigate the structural and functional properties of rHDL nanoparticles containing apoA-I WT, R173C or L144R, to understand how the atheroprotective apoA-I mutants could affect reverse cholesterol transport and atherosclerosis.

8.1 ApoA-I mutant protein expression

In this work the apoA-I R173C and L144R point mutations in the apoA-I WT (E2D) PNFXex vector were produced using SLIM-PCR. The recombinant atheroprotective mutants were expressed with the previously established apoA-I WT (E2D) expression methods (Oda et al., 2001; Ryan et al., 2003; Townsend, 2016). Both mutations were confirmed with gene sequencing and ESI-TOF MS confirmed the correct molecular weight for the apoA-I L144R mutant only.

A key step in the apoA-I R173C protein expression was the identification of the apoA-I C173 post-translational modification, the glutathione adduct (Sengupta and Udgaonkar, 2017). In this work, the apoA-I R173C protein after his-tag cleavage was incubated with a reducing agent (TCEP) to cleave the glutathione adduct. Upon removal of TCEP monomeric and dimeric disulphide bonded apoA-I R173C formed, and the correct MW's were confirmed by SEC separation followed by ESI-TOF MS.

Overall, the average yield of the apoA-I mutants was suitable for routine expression and formation of rHDL nanoparticles. The expression of recombinant apoA-I L144R and R173C enabled the formation of rHDL-R173C and rHDL-L144R nanoparticles for the

first direct comparison of both mutants to rHDL-WT nanoparticles. In particular, isotopically labelled [^{13}C, ^{15}N]-apoA-I WT, R173C and L144R were expressed which allowed for solid-state NMR studies in **Chapter 5**. The expression yields for the atheroprotective mutants rHDL nanoparticle production at ~32 mg/L of culture media was in excess for analysing the samples using CD and ^{31}P oriented SS NMR. However, significant scaling of the [^{13}C, ^{15}N]-labelled apoA-I R173C and WT recombinant protein expressions were required for the 2D ^{13}C-^{13}C dipolar correlation spectra analysis of lipid-bound apoA-I. It was important to establish the expression of both full-length apoA-I mutants to produce discoidal rHDL nanoparticles containing apoA-I that reflects the structural features of plasma HDL.

The primary limitation of the apoA-I R173C expression was precipitation of the protein during the removal of the glutathione moiety. Therefore, further work could explore the optimisation of the apoA-I R173C TCEP reduction protocol and subsequent apoA-I R173C dimer formation. This could be achieved by limiting the protein concentration to < 0.1 mg/mL in the TCEP reduction to prevent precipitation due to oligomerisation. As apoA-I R173C could behave similarly to apoA-I WT and form concentration dependent oligomers (Davidson et al., 1996; Giudice et al., 2017; Oda, 2017; Petrlova et al., 2016). After TCEP removal this would require subsequent concentration of the sample by spin concentration or lyophilisation. Another option would be addition of a buffer additive such as salts like 0.15 M NaCl (Bagby et al., 2001) to increase the apoA-I R173C solubility in solution during TCEP reduction and removal by dialysis.

Further work for both apoA-I L144R and R173C proteins could be to increase the expression yield (~30 mg/mL) to that of apoA-I WT, up to 100 mg/mL. This could be achieved by changing the E. *coli* competent cell type to a different strain such as

BL21(DE3) Tuner™ (Novagen) to induce IPTG concentration dependent protein expression (Khlebnikov and Keasling, 2002; Rosano and Ceccarelli, 2014).

8.2 rHDL nanoparticle production

Initially, rHDL-WT 200:2 nanoparticles were prepared using the sodium cholate dialysis method (Jonas, 1986) and two different methods for size fractionation were compared, SEC and density-based UTC. Density-based UTC was chosen as the method to isolate the major rHDL-WT nanoparticle population with a diameter between 8.6 – 9.8 nm according to NDGGE. Both types of density-based UTC fractionation separated the rHDL nanoparticles from lipid-free apoA-I and SG-UTC had the highest yield of the major rHDL-WT particles. Therefore, the rHDL nanoparticles were prepared via detergent-mediated dialysis followed by primarily SG-UTC. Importantly, this established a method for analysing the rHDL nanoparticles apoA-I secondary structure with circular dichroism and solid-state NMR.

It would be useful to optimise the yield of rHDL nanoparticle production. The yield of ~32 % was comparable to an rHDL-C purification (~33%) (Cavigiolio et al., 2008). However, this yield is below 50 % and results in apoA-I protein loss. It would be advantageous to increase the yield of rHDL nanoparticles to avoid loss of recombinant apoA-I and for further characterisation. In particular labelled protein expressions for SS NMR analyses are expensive so minimising protein loss could be included in future work.

Reconstituted HDL-R173C and L144R nanoparticles were produced at the 200:2 molar ratio for a direct comparison to the rHDL-WT nanoparticles. Reconstituted HDL-C WT nanoparticles were prepared at POPC:apoA-I WT molar ratios between 160:16:2 – 300:30:2, with respective diameter ranges according to NDGGE between 8.7 – 9.3 nm

and 9.3 – 10.1 nm. rHDL-C R173C nanoparticles were prepared at the POPC:cholesterol:apoA-I 190:10:2 molar ratio. Whilst the rHDL-C L144R nanoparticles were prepared at the 190:10:2 and 200:20:2 molar ratios.

NDGGE was used to determine the major particle population hydrodynamic diameter range of each type of rHDL, and rHDL-C nanoparticles produced. The differences between the hydrodynamic measurements according to NDGGE and DLS suggested further investigation was required to understand the rHDL nanoparticle structure, specifically, the rHDL-L144R 200:2 nanoparticles.

This work focussed on rHDL nanoparticles similar to plasma HDL nanoparticles of a similar size (**see Chapter 4**, **section 4.1.4**, **Table 4.1**, **and references therein**). The rHDL nanoparticles with and without cholesterol were produced containing apoA-I WT, R173C or L144R, with comparable major particle population diameters according to NDGGE between ~8.6 – 10.1 nm, and without the presence of lipid-free apoA-I. The production of similar size distributions of rHDL nanoparticles containing apoA-I R173C or L144R allowed for molecular level structural comparisons to rHDL-WT nanoparticles, specifically the lipid, cholesterol, and apoA-I organisation.

Regardless of producing reasonably homogeneous rHDL nanoparticle populations for structural and functional characterisation, the size fractionation of the rHDL nanoparticles could be improved. This could be achieved with more rigorous fraction selection, i.e., a smaller fraction volume, or sequential Fl-UTC followed by SG-UTC (Chen et al., 2009). Another method has used KBr ultracentrifugation to remove lipid-free apoA-I followed by size-exclusion chromatography which produced fractionated rHDL-C nanoparticle populations with a smaller SD as measured by TEM (Cavigiolio et al., 2008).

Further size measurements of rHDL nanoparticles containing apoA-I R173C and L144R with the nanodisc face perpendicular to the TEM grid are required. This could use the protocol established in this work such as the rHDL-WT 200:2 nanoparticles at the 9 μM protein concentration which suggested concentration dependent rouleaux formation, or with the optimised negative stain uranyl formate protocol (Zhang et al., 2011). It became apparent that multiple size measurement techniques are required to determine the rHDL nanoparticle size as the hydrodynamic diameter measurements differed from each other (NDGGE, DLS) or dried negatively stained nanoparticles (TEM).

8.3 rHDL nanoparticle structure

After the production of rHDL nanoparticles was established the analysis of the apoA-I secondary structure, lipid and cholesterol organisation was performed using circular dichroism and solid-state NMR.

8.3.1 The structure of apoA-I in rHDL nanoparticles

The average secondary structure and thermal stability of apoA-I in rHDL nanoparticles was determined using circular dichroism combined with secondary structure estimation. The apoA-I L144R and R173C mutants had a lower thermal stability relative to apoA-I WT in rHDL nanoparticles. The difference in melting temperatures suggested minor structural differences in the atheroprotective mutants respective secondary structures. Overall, the thermal stability and secondary structure estimations of lipid-free and rHDL-bound apoA-I proteins were similar to current literature values (**see Chapter 5**, **section 5.3.1.1**, **Table 5.4**).

The average α-helical content increased in lipid-bound apoA-I WT and R173C which has similar SSEs overall. Surprisingly, the rHDL apoA-I L144R SSE had an α-helical

content similar to lipid-free apoA-I L144R and an increased estimation of unordered content relative to apoA-I WT and R173C in rHDL. Therefore, high-resolution SS NMR spectra of isotopically labelled apoA-I in rHDL nanoparticles were obtained to further identify structural differences.

This is the first study that has directly compared the full-length protein conformations of apoA-I L144R and R173C mutants to apoA-I WT rHDL nanoparticles and the utilisation of solid-state NMR to examine structural differences in both apoA-I mutants.

The high-resolution ^{13}C-^{13}C CP MAS spectra of uniformly labelled apoA-I mutants in rHDL nanoparticles confirmed subtle structural differences between the apoA-I structure of both mutants relative to apoA-I WT and each other.

The multi-microsecond AAMD model of the nascent discoidal HDL-WT 200:20:2 nanoparticle (Pourmousa et al., 2018) was used as comparison to the rHDL nanoparticles in this work. The AAMD "double-belt" model showed the tertiary conformation of apoA-I WT was not rigidly planar when wrapped around the bilayer nanodisc, with the terminal domains moved away from being perpendicular to the nanodisc bilayer normal (Pourmousa et al., 2018).

Similarities were observed in the PEG-precipitated rHDL-WT 200:2 and simulated HDL-C WT 200:20:2 nanoparticle (Pourmousa et al., 2018) 2D ^{13}C-^{13}C dipolar correlation and the PISEMA spectra cross-peaks. This suggested the apoA-I WT conformation in the rHDL-WT nanoparticles was similar to the 200:20:2 HDL model with apoA-I predominantly perpendicular to the phospholipid bilayer nanodisc normal (Lau and Middleton, 2020). However, this requires further evidence as discussed in **Chapter 5**. To confirm the orientation of the apoA-I α-helices relative to the nanodisc

phospholipid bilayer normal a simulated PISEMA spectrum where the apoA-I helices are parallel to the bilayer normal could be produced.

The absence of large structural differences in the secondary structure of rHDL-bound apoA-I R173C and L144R did not immediately suggest why there are functional differences or lack of atherosclerosis incidence in carriers of the respective mutations.

A recent functional study showed a ~70 % and ~40 % reduction in LCAT activation and SR-B1 mediated cholesterol efflux by rHDL-C L144R 200:20:2 nanoparticles compared to rHDL-C WT nanoparticles (Gkolfinopoulou et al., 2020). This supported the reduced LCAT activation detected in a mouse model (Haase et al., 2011). Whilst the ABCG1-mediated cholesterol efflux was similar between the rHDL-C WT and L144R nanoparticles (Gkolfinopoulou et al., 2020).

Therefore, the minor structural differences detected in this work could be related to the reduced rHDL-L144R nanoparticle function in LCAT activation and SR-B1-mediated cholesterol efflux as the L144R mutation is located in helix 6, residues 143-164 which are associated with LCAT activation (Gkolfinopoulou et al., 2020; Haase et al., 2011; Sorci-Thomas et al., 1993).

Perhaps, the reduced LCAT activity in apoA-I L144R carriers is related to a shifted interhelical registry between the two monomers in discoidal HDL nanoparticles. This would be similar to the apoA-I R173C dimer shifted registry in discoidal HDL due to the intermonomer disulphide bond (Klon et al., 2000), which was suggested to contribute to reduced LCAT activation with rHDL-C R173C nanoparticles (Calabresi et al., 1997a).

Different subtle structural differences were detected when the rHDL-WT 200:2 2D ^{13}C-^{13}C dipolar correlation spectra was compared to the respective rHDL-L144R and rHDL-R173C spectrum. This suggested there are different apoA-I structural conformational changes in each apoA-I mutant relative to apoA-I WT and each other. Further experiments are suggested below that could identify the residue-specific structural differences in the apoA-I mutants with respect to apoA-I WT in rHDL nanoparticles. This would enhance our understanding of how the HDL nanoparticle functions in RCT could be affected by structural changes in the rHDL apoA-I conformation.

To resolve the subtle structural differences detected in apoA-I of the rHDL-R173C and rHDL-L144R nanoparticles further SS NMR studies to obtain residue-specific cross-peaks for secondary structure assignment in high-resolution 2D ^{13}C-^{13}C dipolar correlation spectra are required. This would require selective isotope labelling of specific residue methyl groups such as valine, leucine, and threonine, produced by expressing recombinant apoA-I in E. *coli* auxotrophs (Lin et al., 2015; Lin et al., 2011; Monneau et al., 2016).

The limitation of CD secondary structure estimation is that it addressed only average global secondary structure conformational changes. To elucidate additional lipid-bound apoA-I dimer structural information, in particular for apoA-I L144R, chemical cross-linking combined with MS could reveal inter- and intramolecular cross-links between apoA-I monomers in rHDL nanoparticles as demonstrated with discoidal rHDL-WT (Silva et al., 2005b) and rHDL-R173C nanoparticles (Bhat et al., 2010). This could provide evidence to determine if the apoA-I L144R mutant dimer retains or has a different interhelical registry compared to apoA-I WT in discoidal rHDL. This could lead to the development of a proposed model for dimeric apoA-I L144R in different

sized discoidal rHDL nanoparticles as previously demonstrated with apoA-I WT and R173C (Bhat et al., 2010; Gursky et al., 2013; Silva et al., 2005b).

8.3.1.1 rHDL nanoparticle morphology

The subtle structural differences in the rHDL apoA-I protein structure, according to CD and PEG-precipitated rHDL SSNMR spectra, suggested there could be other reasons for the functional differences observed in carriers of the apoA-I mutations. The work in **Chapter 6** described the development and optimisation of a novel technique to detect three distinct morphologies of rHDL nanoparticles using ^{31}P oriented SS NMR (Lau and Middleton, 2020). This expanded upon the theory developed by Picard *et al.* for determining the shape of an oriented phospholipid bilayer for an ellipsoid or bicelle using ^{31}P SS NMR spectra (Picard et al., 1999).

This is significant as it has provided detailed information about the surface curvature of the phospholipid headgroups, and in turn the lipid distribution in three discoidal rHDL nanoparticle morphologies. The rHDL-WT and R173C 200:2 nanoparticles had a planar disc morphology like the "double-belt" model of discoidal HDL (Segrest et al., 1999).

The "discoidal" rHDL-L144R 200:2 broad asymmetric lineshape fit the hemispheroid approximation, in which the lipid surface curvature approaches an ideal spherical particle, with a concave and convex face of the nanodisc. This is supported by the 200:20:2 AAMD HDL-C model which has concave and convex nanodisc faces (Pourmousa et al., 2018). As demonstrated by simulating lineshapes for the AAMD 200:20:2 HDL model in this work, this technique can provide an experimental detection of the rHDL morphology to compare to proposed variations of the planar "double-belt" model of nanoparticles. For example, smaller "saddle-shaped" particles at component

molar ratios <160:±24:2, which were supported by TEM only, to confirm the computational structures (Catte et al., 2006; Gu et al., 2010; Pourmousa et al., 2018).

The differences in the morphologies could explain the variation in the size measurements of the rHDL nanoparticles. The small rHDL-L144R hydrodynamic diameter (~6.5 nm) according to DLS may more accurately reflect the nanoparticle diameter due to surface curvature of the lipid nanodisc. Whereas, the planar disc rHDL-WT and R173C nanoparticle diameters could be overestimated with a spherical particle approximation (Eiser, 2014).

This is a new tool which can assess the morphological differences of rHDL nanoparticles prepared with atheroprotective apoA-I R173C or L144R. Significantly, the morphological detection technique could be used to assess the nanoparticle morphology in clinical plasma HDL samples, as demonstrated with an unfractionated plasma HDL sample.

Future work could expand to the cholesterol component of the rHDL-C nanoparticles, with isotopically [^{13}C]-labelled cholesterol to detect the orientation of cholesterol molecules in oriented rHDL-C nanoparticles to determine the cholesterol distribution. This could aid the understanding of how cholesterol is incorporated into the discoidal rHDL nanoparticles. For example, in the rHDL-C WT torus disc morphology the outer lipids are angled further from the bilayer normal due to an increased lipid and cholesterol content. It would be interesting to see if rHDL-C nanoparticles containing apoA-I L144R or R173C at similar component molar ratios showed a similar torus disc morphology. If the morphology of rHDL-C mutant particles was different this could reflect differences in lipid transfer (Lau and Middleton, 2020), enhanced

accessibility/availability of cholesterol for enzymes such as CETP or SR-B1 (Liadaki et al., 2000; Qiu et al., 2007).

The technique could be applied to the morphology of rHDL ±cholesterol and each apoA-I variant of different rHDL and plasma HDL size populations between 5 – 17 nm in diameter (Cavigiolio et al., 2008; Rosenson et al., 2011). A comprehensive comparison of various sizes and compositions would provide morphological similarities and differences between rHDL-WT, R173C and L144R nanoparticles. Future work with respect to the functional implications of structural differences is described in the following section.

8.4 Molecular dynamics, cholesterol efflux and amyloidogenicity

The future work for the computational and functional experiments were suggested in **Chapter 7**, therefore further suggestions are briefly discussed here. The conditions for self-assembly CGMD simulations containing full-length apoA-I R173C or apoA-I WT were examined and required improvement.

Further work could involve testing simulation setups such as a biased simulation setup with a preformed phospholipid nanodisc and a more planar restricted apoA-I Δ(1-43) (Borhani et al., 1997) conformation (Siuda and Tieleman, 2015). As well as, the refinement of, or alternative models of the starting full-length protein structure based upon the higher resolution apoA-I WT Δ(185-243) crystal structure (Mei and Atkinson, 2011). The molecular dynamics parameters could be tested by attempting to reproduce a control self-assembly CGMD simulation of 160 DMPC phospholipids and two apoA-I Δ(1-65) monomers (Debnath and Schäfer, 2015).

The rHDL-mediated cholesterol efflux assay required further improvements as described in **Chapter 7**. The *in vitro* cholesterol efflux could assess the cholesterol influx with HepG2 cells (Zhiping et al., 2003) from BODIPY-CE loaded rHDL nanoparticles with flow cytometry and confocal microscopy.

The ThT assay of lipid-free apoA-I WT and the atheroprotective mutants suggested the mutants were not resistant to amyloid fibril formation under conditions mimicking a proinflammatory environment. Dysfunctional HDL nanoparticles can form when apoA-I is oxidised by myeloperoxidase in atherosclerotic plaques (Nicholls et al., 2005). Specifically, apoA-I methionine oxidation of apoA-I occurs in atherogenic conditions and results in oxidised lipid-free apoA-I WT amyloid fibril formation (Townsend et al., 2017).

In rHDL containing plasma apoA-I WT nanoparticles oxidation of apoA-I methionine residues resulted in reduced particle stability (Jayaraman et al., 2008). Further experiments could compare the resistance of the apoA-I mutants to oxidation, or the stability of oxidised apoA-I mutants in rHDL nanoparticles compared to oxidised apoA-I. The rHDL nanoparticle structural stability could be determined with thermal CD and ThT assays of both lipid-free and rHDL-bound apoA-I proteins (Jayaraman et al., 2008; Townsend et al., 2017).

8.5 Summary

In conclusion, this work has compared the structure of rHDL nanoparticles containing full-length apoA-I WT, R173C or L144R with a focussed approach using circular dichroism and SS NMR to examine the protein, lipid, and cholesterol constituents. The apoA-I secondary structure characterisation of the respective apoA-I mutant nanoparticles detected structural differences compared to rHDL-WT nanoparticles.

This suggested there are structural differences in apoA-I, the major HDL protein, that could have functional consequences in RCT.

This work has established a sensitive novel method for determining three different rHDL nanoparticle morphologies using ^{31}P oriented SS NMR. This has allowed for direct experimental observation of the lipid distribution in rHDL nanoparticles which were not detected by conventional TEM. Importantly, this included a plasma HDL sample which could be fractionated in the future to analyse the morphology of clinical plasma samples.

There are many questions to be answered to gain a greater understanding of the low incidence of atherosclerosis in carriers of the mutants and inform atherosclerosis treatment, with several avenues for further structural and functional studies of rHDL nanoparticles containing apoA-I L144R or R173C.

Recent literature has suggested improvements to the approach of rHDL-infusion therapy (Darabi et al., 2016; Kingwell et al., 2014). This could include the use of rHDL nanoparticles as a molecular drug carrier for combined therapeutic treatment with rHDL containing drugs such as statins (Duivenvoorden et al., 2014; Lau et al., 2019). This could also be applied to drug molecules that can treat other diseases in the body as rHDL nanoparticles are well-tolerated in the body as demonstrated by clinical trials (Darabi et al., 2016; Kingwell et al., 2014; Simonsen, 2016). This could also include changing the lipid content to obtain protective functions such as anti-oxidative and anti-inflammatory effects (Darabi et al., 2016).

Reverse cholesterol transport is a complex system which involves a variety of cell receptors and enzymes (Fisher et al., 2012; von Eckardstein et al., 2001). Therefore, a direct comparison of the atheroprotective apoA-I mutants in rHDL with rHDL-WT

nanoparticles will require further testing to compare their interactions with enzymes in RCT, such as LCAT (Calabresi et al., 1997a; Sorci-Thomas et al., 1993), CETP (Qiu et al., 2007) and cell receptors such as ABCA1 (Sahoo et al., 2004; Sankaranarayanan et al., 2011).

9 References

Abraham, M. J., Murtola, T., Schulz, R., Páll, S., Smith, J. C., Hess, B. & Lindahl, E. (2015) GROMACS: High performance molecular simulations through multi-level parallelism from laptops to supercomputers. *SoftwareX*, 1-2, 19-25.

Alexander, E. T., Tanaka, M., Kono, M., Saito, H., Rader, D. J. & Phillips, M. C. (2009) Structural and functional consequences of the Milano mutation (R173C) in human apolipoprotein A-I. *J Lipid Res*, 50, 1409-19.

Apperley, D. C., Harris, R. K. & Hodgkinson, P. (2012) *Solid-state NMR basic principles & practice*. [[New York, N.Y.] (222 East 46th Street, New York, NY 10017): Momentum Press. Available at: http://portal.igpublish.com/iglibrary/search/MPB0000073.html.

Arciello, A., Piccoli, R. & Monti, D. M. (2016) Apolipoprotein A-I: the dual face of a protein. *FEBS Lett*, 590, 4171-4179.

Artimo, P., Jonnalagedda, M., Arnold, K., Baratin, D., Csardi, G., De Castro, E., Duvaud, S., Flegel, V., Fortier, A., Gasteiger, E., Grosdidier, A., Hernandez, C., Ioannidis, V., Kuznetsov, D., Liechti, R., Moretti, S., Mostaguir, K., Redaschi, N., Rossier, G., Xenarios, I. & Stockinger, H. (2012) ExPASy: SIB bioinformatics resource portal. *Nucleic Acids Research*, 40, W597-W603.

Asztalos, B. F., De La Llera-Moya, M., Dallal, G. E., Horvath, K. V., Schaefer, E. J. & Rothblat, G. H. (2005) Differential effects of HDL subpopulations on cellular ABCA1- and SR-BI-mediated cholesterol efflux. *J Lipid Res*, 46, 2246-53.

Asztalos, B. F., Roheim, P. S., Milani, R. L., Lefevre, M., Mcnamara, J. R., Horvath, K. V. & Schaefer, E. J. (2000) Distribution of ApoA-I-containing HDL subpopulations in patients with coronary heart disease. *Arterioscler Thromb Vasc Biol*, 20, 2670-6.

Badimon, J. J., Badimon, L. & Fuster, V. (1990) Regression of atherosclerotic lesions by high density lipoprotein plasma fraction in the cholesterol-fed rabbit. *J Clin Invest*, 85, 1234-41.

Bagby, S., Tong, K. I. & Ikura, M. (2001) [2] - Optimization of Protein Solubility and Stability for Protein Nuclear Magnetic Resonance. In: James, T. L., Dötsch, V. & Schmitz, U. (eds.) *Methods in Enzymology*. Academic Press.

Barbaras, R. (2015) Non-clinical development of CER-001. *Front Pharmacol*, 6, 220.

Barnoud, J. & Monticelli, L. (2015) Coarse-Grained Force Fields for Molecular Simulations. In: Kukol, A. (ed.) *Molecular modeling of proteins*. Second edition. ed. Totowa, NJ: Humana Press.

Barter, P. J., Nicholls, S., Rye, K. A., Anantharamaiah, G. M., Navab, M. & Fogelman, A. M. (2004) Antiinflammatory properties of HDL. *Circulation Research*, 95, 764-772.

Bayburt, T. H., Grinkova, Y. V. & Sligar, S. G. (2002) Self-assembly of discoidal phospholipid bilayer nanoparticles with membrane scaffold proteins. *Nano Letters,* 2, 853-856.

Bechinger, B., Aisenbrey, C. & Bertani, P. (2004) The alignment, structure and dynamics of membrane-associated polypeptides by solid-state NMR spectroscopy. *Biochim Biophys Acta,* 1666, 190-204.

Berendsen, H. J. C., Postma, J. P. M., Van Gunsteren, W. F., Dinola, A. & Haak, J. R. (1984) Molecular dynamics with coupling to an external bath. *The Journal of chemical physics,* 81, 3684-3690.

Bessette, P. H., Aslund, F., Beckwith, J. & Georgiou, G. (1999) Efficient folding of proteins with multiple disulfide bonds in the Escherichia coli cytoplasm. *Proc Natl Acad Sci U S A,* 96, 13703-8.

Bhat, S., Sorci-Thomas, M. G., Calabresi, L., Samuel, M. P. & Thomas, M. J. (2010) Conformation of dimeric apolipoprotein A-I milano on recombinant lipoprotein particles. *Biochemistry,* 49, 5213-24.

Biancalana, M. & Koide, S. (2010) Molecular mechanism of Thioflavin-T binding to amyloid fibrils. *Biochim Biophys Acta,* 1804, 1405-12.

Bibow, S., Polyhach, Y., Eichmann, C., Chi, C. N., Kowal, J., Albiez, S., Mcleod, R. A., Stahlberg, H., Jeschke, G., Guntert, P. & Riek, R. (2017) Solution structure of discoidal high-density lipoprotein particles with a shortened apolipoprotein A-I. *Nat Struct Mol Biol,* 24, 187-193.

Bielicki, J. K., Forte, T. M., Mccall, M. R., Stoltzfus, L. J., Chiesa, G., Sirtori, C. R., Franceschini, G. & Rubin, E. M. (1997) High density lipoprotein particle size restriction in apolipoprotein A-I(Milano) transgenic mice. *J Lipid Res,* 38, 2314-21.

Bielicki, J. K., Mccall, M. R. & Forte, T. M. (1999) Apolipoprotein A-I promotes cholesterol release and apolipoprotein E recruitment from THP-1 macrophage-like foam cells. *J Lipid Res,* 40, 85-92.

Borhani, D. W., Rogers, D. P., Engler, J. A. & Brouillette, C. G. (1997) Crystal structure of truncated human apolipoprotein A-I suggests a lipid-bound conformation. *Proc Natl Acad Sci U S A,* 94, 12291-6.

Bornhorst, J. A. & Falke, J. J. (2000) Purification of proteins using polyhistidine affinity tags. *Methods Enzymol,* 326, 245-54.

Bothwell, J. H. & Griffin, J. L. (2011) An introduction to biological nuclear magnetic resonance spectroscopy. *Biol Rev Camb Philos Soc,* 86, 493-510.

Bowry, V. W., Stanley, K. K. & Stocker, R. (1992) High-Density-Lipoprotein Is the Major Carrier of Lipid Hydroperoxides in Human Blood-Plasma from Fasting Donors. *Proceedings of the National Academy of Sciences of the United States of America,* 89, 10316-10320.

Brouillette, C. G. & Anantharamaiah, G. M. (1995) Structural models of human apolipoprotein A-I. *Biochimica et biophysica acta. Lipids and lipid metabolism,* 1256, 103-129.

Brouillette, C. G., Anantharamaiah, G. M., Engler, J. A. & Borhani, D. W. (2001) Structural models of human apolipoprotein A-I: a critical analysis and review. *Biochimica Et Biophysica Acta-Molecular and Cell Biology of Lipids,* 1531, 4-46.

Brouillette, C. G., Jones, J. L., Ng, T. C., Kercret, H., Chung, B. H. & Segrest, J. P. (1984) Structural studies of apolipoprotein A-I/phosphatidylcholine recombinants by high-field proton NMR, nondenaturing gradient gel electrophoresis, and electron microscopy. *Biochemistry,* 23, 359-67.

Bussi, G., Donadio, D. & Parrinello, M. (2007) Canonical sampling through velocity rescaling. *J Chem Phys,* 126, 014101-014101-7.

Calabresi, L., Canavesi, M., Bernini, F. & Franceschini, G. (1999) Cell cholesterol efflux to reconstituted high-density lipoproteins containing the apolipoprotein A-IMilano dimer. *Biochemistry,* 38, 16307-14.

Calabresi, L., Franceschini, G., Burkybile, A. & Jonas, A. (1997a) Activation of lecithin cholesterol acyltransferase by a disulfide-linked apolipoprotein A-I dimer. *Biochem Biophys Res Commun,* 232, 345-9.

Calabresi, L., Vecchio, G., Frigerio, F., Vavassori, L., Sirtori, C. R. & Franceschini, G. (1997b) Reconstituted high-density lipoproteins with a disulfide-linked apolipoprotein A-I dimer: evidence for restricted particle size heterogeneity. *Biochemistry,* 36, 12428-33.

Calabresi, L., Vecchio, G., Longhi, R., Gianazza, E., Palm, G., Wadensten, H., Hammarström, A., Olsson, A., Karlström, A. & Sejlitz, T. (1994) Molecular characterization of native and recombinant apolipoprotein A-IMilano dimer. The introduction of an interchain disulfide bridge remarkably alters the physicochemical properties of apolipoprotein A-I. *J Biol Chem,* 269, 32168-32174.

Calkin, A. C., Drew, B. G., Ono, A., Duffy, S. J., Gordon, M. V., Schoenwaelder, S. M., Sviridov, D., Cooper, M. E., Kingwell, B. A. & Jackson, S. P. (2009) Reconstituted High-Density Lipoprotein Attenuates Platelet Function in Individuals With Type 2 Diabetes Mellitus by Promoting Cholesterol Efflux. *Circulation,* 120, 2095-U60.

Caparon, M. H., Rust, K. J., Hunter, A. K., Mclaughlin, J. K., Thomas, K. E., Herberg, J. T., Shell, R. E., Lanter, P. B., Bishop, B. F., Dufield, R. L., Wang, X. & Ho, S. V. (2010) Integrated solution to purification challenges in the manufacture of a soluble recombinant protein in E. coli. *Biotechnol. Bioeng,* 105, 239-249.

Casu, B., Naggi, A. & Torri, G. (2015) Re-visiting the structure of heparin. *Carbohydr Res,* 403, 60-8.

Catte, A., Patterson, J. C., Jones, M. K., Jerome, W. G., Bashtovyy, D., Su, Z., Gu, F., Chen, J., Aliste, M. P., Harvey, S. C., Li, L., Weinstein, G. & Segrest, J. P. (2006) Novel changes in discoidal high density lipoprotein morphology: a molecular dynamics study. *Biophys J,* 90, 4345-60.

Cavigiolio, G., Shao, B., Geier, E. G., Ren, G., Heinecke, J. W. & Oda, M. N. (2008) The interplay between size, morphology, stability, and functionality of high-density lipoprotein subclasses. *Biochemistry,* 47, 4770-4779.

Chapman, M. J., Goldstein, S., Lagrange, D. & Laplaud, P. M. (1981) A density gradient ultracentrifugal procedure for the isolation of the major lipoprotein classes from human serum. *J Lipid Res,* 22, 339-58.

Chen, B., Ren, X., Neville, T., Jerome, W. G., Hoyt, D. W., Sparks, D., Ren, G. & Wang, J. (2009) Apolipoprotein AI tertiary structures determine stability and phospholipid-binding activity of discoidal high-density lipoprotein particles of different sizes. *Protein Sci,* 18, 921-35.

Chen, K. & Tjandra, N. (2012) The use of residual dipolar coupling in studying proteins by NMR. *Top Curr Chem,* 326, 47-67.

Chen, W., Cormode, D. P., Vengrenyuk, Y., Herranz, B., Feig, J. E., Klink, A., Mulder, W. J. M., Fisher, E. A. & Fayad, Z. A. (2013) Collagen-Specific Peptide Conjugated HDL Nanoparticles as MRI Contrast Agent to Evaluate Compositional Changes in Atherosclerotic Plaque Regression. *Jacc-Cardiovascular Imaging,* 6, 373-384.

Chen, Z., O'neill, E. A., Meurer, R. D., Gagen, K., Luell, S., Wang, S. P., Ichetovkin, M., Frantz-Wattley, B., Eveland, S., Strack, A. M., Fisher, T. S., Johns, D. G., Sparrow, C. P., Wright, S. D., Hubbard, B. K. & Carballo-Jane, E. (2012) Reconstituted HDL Elicits Marked Changes in Plasma Lipids Following Single-Dose Injection in C57Bl/6 Mice. *Journal of Cardiovascular Pharmacology and Therapeutics,* 17, 315-323.

Chetty, P. S., Mayne, L., Lund-Katz, S., Stranz, D., Englander, S. W. & Phillips, M. C. (2009) Helical structure and stability in human apolipoprotein A-I by hydrogen exchange and mass spectrometry. *Proceedings of the National Academy of Sciences of the United States of America,* 106, 19005-19010.

Chetty, P. S., Ohshiro, M., Saito, H., Dhanasekaran, P., Lund-Katz, S., Mayne, L., Englander, W. & Phillips, M. C. (2012) Effects of the Iowa and Milano mutations on apolipoprotein A-I structure and dynamics determined by hydrogen exchange and mass spectrometry. *Biochemistry,* 51, 8993-9001.

Chiu, J., March, P. E., Lee, R. & Tillett, D. (2004) Site-directed, Ligase-Independent Mutagenesis (SLIM): a single-tube methodology approaching 100% efficiency in 4 h. *Nucleic Acids Research,* 32.

Cho, K. H. & Kim, J. R. (2009) A reconstituted HDL containing V156K or R173C apoA-I exhibited anti-inflammatory activity in apo-E deficient mice and showed resistance to myeloperoxidase-mediated oxidation. *Exp Mol Med,* 41, 417-28.

Chroni, A., Liu, T., Gorshkova, I., Kan, H. Y., Uehara, Y., Von Eckardstein, A. & Zannis, V. I. (2003) The central helices of ApoA-I can promote ATP-binding cassette transporter A1 (ABCA1)-mediated lipid efflux. Amino acid residues 220-231 of the wild-type ApoA-I are required for lipid efflux in vitro and high density lipoprotein formation in vivo. *J Biol Chem,* 278, 6719-30.

Cohlberg, J. A., Li, J., Uversky, V. N. & Fink, A. L. (2002) Heparin and other glycosaminoglycans stimulate the formation of amyloid fibrils from alpha-synuclein in vitro. *Biochemistry,* 41, 1502-11.

Costet, P., Luo, Y., Wang, N. & Tall, A. R. (2000) Sterol-dependent transactivation of the ABC1 promoter by the liver X receptor/retinoid X receptor. *J Biol Chem,* 275, 28240-5.

Dalla-Riva, J., Lagerstedt, J. O. & Petrlova, J. (2015) Structural and Functional Analysis of the ApolipoproteinA-I A164S Variant. *Plos One,* 10.

Daniil, G., Zannis, V. I. & Chroni, A. (2013) Effect of apoA-I Mutations in the Capacity of Reconstituted HDL to Promote ABCG1-Mediated Cholesterol Efflux. *PLoS One,* 8, e67993.

Darabi, M., Guillas-Baudouin, I., Le Goff, W., Chapman, M. J. & Kontush, A. (2016) Therapeutic applications of reconstituted HDL: When structure meets function. *Pharmacol Ther,* 157, 28-42.

Das, N., Murray, D. T. & Cross, T. A. (2013) Lipid bilayer preparations of membrane proteins for oriented and magic-angle spinning solid-state NMR samples. *Nature Protocols,* 8, 2256-2270.

Davidson, W. S., Hazlett, T., Mantulin, W. W. & Jonas, A. (1996) The role of apolipoprotein AI domains in lipid binding. *Proc Natl Acad Sci U S A,* 93, 13605-10.

De Jong, D. H., Baoukina, S., Ingólfsson, H. I. & Marrink, S. J. (2016) Martini straight: Boosting performance using a shorter cutoff and GPUs. *Computer physics communications,* 199, 1-7.

De Jong, D. H., Singh, G., Bennett, W. F. D., Arnarez, C., Wassenaar, T. A., Schäfer, L. V., Periole, X., Tieleman, D. P. & Marrink, S. J. (2013) Improved Parameters for the Martini Coarse-Grained Protein Force Field. *Journal of Chemical Theory and Computation,* 9, 687-697.

Debnath, A. & Schäfer, L. V. (2015) Structure and Dynamics of Phospholipid Nanodiscs from All-Atom and Coarse-Grained Simulations. *The Journal of Physical Chemistry B,* 119, 6991-7002.

Del Giudice, R., Arciello, A., Itri, F., Merlino, A., Monti, M., Buonanno, M., Penco, A., Canetti, D., Petruk, G., Monti, S. M., Relini, A., Pucci, P., Piccoli, R. & Monti, D. M. (2016) Protein conformational perturbations in hereditary amyloidosis: Differential impact of single point mutations in ApoAI amyloidogenic variants. *Biochim Biophys Acta,* 1860, 434-44.

Del Giudice, R., Arciello, A., Monti, D. M., De Marco, N. & Piccoli, R. (2011) Amyloidoses associated to apolipoprotein A-I: The intriguing case of a natively unfolded protein fragment. *Febs Journal,* 278, 125-125.

Del Giudice, R., Domingo-Espin, J., Iacobucci, I., Nilsson, O., Monti, M., Monti, D. M. & Lagerstedt, J. O. (2017) Structural determinants in ApoA-I amyloidogenic variants explain improved cholesterol metabolism despite low HDL levels. *Biochim Biophys Acta Mol Basis Dis,* 1863, 3038-3048.

Del Giudice, R. & Lagerstedt, J. O. (2018) High-efficient bacterial production of human ApoA-I amyloidogenic variants. *Protein Sci,* 27, 2101-2109.

Derman, A. I., Prinz, W. A., Belin, D. & Beckwith, J. (1993) Mutations that allow disulfide bond formation in the cytoplasm of Escherichia coli. *Science,* 262, 1744-7.

Desjardins, P., Hansen, J. B. & Allen, M. (2009) Microvolume protein concentration determination using the NanoDrop 2000c spectrophotometer. *J Vis Exp*.

Di Bartolo, B. A., Psaltis, P. J., Bursill, C. A. & Nicholls, S. J. (2018) Translating Evidence of HDL and Plaque Regression. *Arterioscler Thromb Vasc Biol,* 38, 1961-1968.

Diditchenko, S., Gille, A., Pragst, I., Stadler, D., Waelchli, M., Hamilton, R., Leis, A. & Wright, S. D. (2013) Novel formulation of a reconstituted high-density lipoprotein (CSL112) dramatically enhances ABCA1-dependent cholesterol efflux. *Arterioscler Thromb Vasc Biol,* 33, 2202-11.

Duer, M. J. (2004) *Introduction to solid-state NMR spectroscopy.* Oxford, UK ; Malden, MA: Blackwell.

Duivenvoorden, R., Tang, J., Cormode, D. P., Mieszawska, A. J., Izquierdo-Garcia, D., Ozcan, C., Otten, M. J., Zaidi, N., Lobatto, M. E., Van Rijs, S. M., Priem, B., Kuan, E. L., Martel, C., Hewing, B., Sager, H., Nahrendorf, M., Randolph, G. J., Stroes, E. S., Fuster, V., Fisher, E. A., Fayad, Z. A. & Mulder, W. J. (2014) A statin-loaded reconstituted high-density lipoprotein nanoparticle inhibits atherosclerotic plaque inflammation. *Nat Commun,* 5, 3065.

Duong, P. T., Collins, H. L., Nickel, M., Lund-Katz, S., Rothblat, G. H. & Phillips, M. C. (2006) Characterization of nascent HDL particles and microparticles formed by ABCA1-mediated efflux of cellular lipids to apoA-I. *J Lipid Res,* 47, 832-43.

Duong, P. T., Weibel, G. L., Lund-Katz, S., Rothblat, G. H. & Phillips, M. C. (2008) Characterization and properties of pre beta-HDL particles formed by ABCA1-mediated cellular lipid efflux to apoA-I. *Journal of Lipid Research,* 49, 1006-1014.

Easton, R., Gille, A., D'andrea, D., Davis, R., Wright, S. D. & Shear, C. (2014) A multiple ascending dose study of CSL112, an infused formulation of ApoA-I. *J Clin Pharmacol,* 54, 301-10.

Eiser, E. (2014) Multi Length-Scale Characterisation. New York, UNITED KINGDOM: John Wiley & Sons, Incorporated.

Essmann, U. & Berkowitz, M. L. (1999) Dynamical Properties of Phospholipid Bilayers from Computer Simulation. *Biophys J,* 76, 2081-2089.

Fang, Y., Gursky, O. & Atkinson, D. (2003a) Lipid-binding studies of human apolipoprotein A-I and its terminally truncated mutants. *Biochemistry,* 42, 13260-8.

Fang, Y., Gursky, O. & Atkinson, D. (2003b) Structural studies of N- and C-terminally truncated human apolipoprotein A-I. *Biochemistry,* 42, 6881-90.

Favari, E., Gomaraschi, M., Zanotti, I., Bernini, F., Lee-Rueckert, M., Kovanen, P. T., Sirtori, C. R., Franceschini, G. & Calabresi, L. (2007) A unique protease-sensitive high density lipoprotein particle containing the apolipoprotein A-I(Milano) dimer effectively promotes ATP-binding Cassette A1-mediated cell cholesterol efflux. *J Biol Chem,* 282, 5125-32.

Fiddyment, S., Barcelo-Batllori, S., Pocovi, M. & Garcia-Otin, A. L. (2011) Expression and purification of recombinant apolipoprotein A-I Zaragoza (L144R) and formation of reconstituted HDL particles. *Protein Expr Purif,* 80, 110-6.

Fielding, C. J. & Fielding, P. E. (1995) Molecular Physiology of Reverse Cholesterol Transport. *Journal of Lipid Research,* 36, 211-228.

Fisher, E. A., Feig, J. E., Hewing, B., Hazen, S. L. & Smith, J. D. (2012) High-Density Lipoprotein Function, Dysfunction, and Reverse Cholesterol Transport. *Arteriosclerosis Thrombosis and Vascular Biology,* 32, 2813-2820.

Forte, T. M., Bielicki, J. K., Goth-Goldstein, R., Selmek, J. & Mccall, M. R. (1995) Recruitment of cell phospholipids and cholesterol by apolipoproteins A-II and A-I: formation of nascent apolipoprotein-specific HDL that differ in size, phospholipid composition, and reactivity with LCAT. *J Lipid Res,* 36, 148-57.

Franceschini, G., Calabresi, L., Tosi, C., Sirtori, C. R., Fragiacomo, C., Noseda, G., Gong, E., Blanche, P. & Nichols, A. V. (1987) Apolipoprotein A-IMilano. Correlation between high density lipoprotein subclass distribution and triglyceridemia. *Arteriosclerosis,* 7, 426-35.

Franceschini, G., Frosi, T. G., Manzoni, C., Gianfranceschi, G. & Sirtori, C. R. (1982) High density lipoprotein-3 heterogeneity in subjects with the apo-AIMilano variant. *J Biol Chem,* 257, 9926-30.

Franceschini, G., Sirtori, C. R., Capurso, A., 2nd, Weisgraber, K. H. & Mahley, R. W. (1980) A-IMilano apoprotein. Decreased high density lipoprotein cholesterol levels with significant lipoprotein modifications and without clinical atherosclerosis in an Italian family. *J Clin Invest,* 66, 892-900.

Fukuda, I. & Nakamura, H. (2012) Non-Ewald methods: theory and applications to molecular systems. *Biophys Rev,* 4, 161-170.

Fung, B. M., Khitrin, A. K. & Ermolaev, K. (2000) An improved broadband decoupling sequence for liquid crystals and solids. *J Magn Reson,* 142, 97-101.

Galkina, E. & Ley, K. (2009) Immune and Inflammatory Mechanisms of Atherosclerosis. *Annual Review of Immunology,* 27, 165-197.

Ge, M. & Freed, J. H. (2011) Two Conserved Residues Are Important for Inducing Highly Ordered Membrane Domains by the Transmembrane Domain of Influenza Hemagglutinin. *Biophys J,* 100, 90-97.

Genscript (2019) *Codon Usage Frequency Table* Available at: https://www.genscript.com/tools/codon-frequency-table.

Ghosh, S., Zhao, B., Bie, J. & Song, J. (2010) Macrophage cholesteryl ester mobilization and atherosclerosis. *Vascul Pharmacol,* 52, 1-10.

Gibson, C. M., Kerneis, M., Yee, M. K., Daaboul, Y., Korjian, S., Mehr, A. P., Tricoci, P., Alexander, J. H., Kastelein, J. J. P., Mehran, R., Bode, C., Lewis, B. S., Mehta, R., Duffy, D., Feaster, J., Halabi, M., Angiolillo, D. J., Duerschmied, D., Ophuis, T. O. & Merkely, B. (2019) The CSL112-2001 trial: Safety and tolerability of multiple doses of CSL112 (apolipoprotein A-I [human]), an intravenous formulation of plasma-derived apolipoprotein A-I, among subjects with moderate renal impairment after acute myocardial infarction. *Am Heart J,* 208, 81-90.

Gibson, C. M., Korjian, S., Tricoci, P., Daaboul, Y., Yee, M., Jain, P., Alexander, J. H., Steg, P. G., Lincoff, A. M., Kastelein, J. J. P., Mehran, R., D'andrea, D. M., Deckelbaum, L. I., Merkely, B., Zarebinski, M., Ophuis, T. O. & Harrington, R. A. (2016) Safety and Tolerability of CSL112, a Reconstituted, Infusible, Plasma-Derived

Apolipoprotein A-I, After Acute Myocardial Infarction The AEGIS-I Trial (ApoA-I Event Reducing in Ischemic Syndromes I). *Circulation,* 134, 1918-+.

Gille, A., D'andrea, D., Tortorici, M. A., Hartel, G. & Wright, S. D. (2018) CSL112 (Apolipoprotein A-I [Human]) Enhances Cholesterol Efflux Similarly in Healthy Individuals and Stable Atherosclerotic Disease Patients. *Arterioscler Thromb Vasc Biol,* 38, 953-963.

Gille, A., Duffy, D., Tortorici, M. A., Wright, S. D., Deckelbaum, L. I. & D'andrea, D. M. (2019) Moderate Renal Impairment Does Not Impact the Ability of CSL112 (Apolipoprotein A-I [Human]) to Enhance Cholesterol Efflux Capacity. *J Clin Pharmacol,* 59, 427-436.

Gille, A., Easton, R., D'andrea, D., Wright, S. D. & Shear, C. L. (2014) CSL112 enhances biomarkers of reverse cholesterol transport after single and multiple infusions in healthy subjects. *Arterioscler Thromb Vasc Biol,* 34, 2106-14.

Gimbrone, M. A. (1999) Vascular endothelium, hemodynamic forces, and atherogenesis. *American Journal of Pathology,* 155, 1-5.

Giudice, R. D., Nilsson, O., Domingo-Espin, J. & Lagerstedt, J. O. (2017) Synchrotron radiation circular dichroism spectroscopy reveals structural divergences in HDL-bound apoA-I variants. *Sci Rep,* 7, 13540.

Gkolfinopoulou, C., Soukou, F., Dafnis, I., Kellici, T. F., Sanoudou, D., Mavromoustakos, T., Stratikos, E. & Chroni, A. (2020) Structure-function analysis of naturally occurring apolipoprotein A-I L144R, A164S and L178P mutants provides insight on their role on HDL levels and cardiovascular risk. *Cell Mol Life Sci*.

Gogonea, V. (2016) Structural Insights into High Density Lipoprotein: Old Models and New Facts. *Front Pharmacol,* 6, 318.

Gogonea, V., Gerstenecker, G. S., Wu, Z., Lee, X., Topbas, C., Wagner, M. A., Tallant, T. C., Smith, J. D., Callow, P., Pipich, V., Malet, H., Schoehn, G., Didonato, J. A. & Hazen, S. L. (2013) The low-resolution structure of nHDL reconstituted with DMPC with and without cholesterol reveals a mechanism for particle expansion. *J Lipid Res,* 54, 966-83.

Gogonea, V., Wu, Z., Lee, X., Pipich, V., Li, X. M., Ioffe, A. I., Didonato, J. A. & Hazen, S. L. (2010) Congruency between biophysical data from multiple platforms and molecular dynamics simulation of the double-super helix model of nascent high-density lipoprotein. *Biochemistry,* 49, 7323-43.

Gottesman, S. (1996) Proteases and their targets in Escherichia coli. *Annual Review of Genetics,* 30, 465-506.

Greenfield, N. & Fasman, G. D. (1969) Computed circular dichroism spectra for the evaluation of protein conformation. *Biochemistry,* 8, 4108-16.

Greenfield, N. J. (2006a) Using circular dichroism collected as a function of temperature to determine the thermodynamics of protein unfolding and binding interactions. *Nature Protocols,* 1, 2527-2535.

Greenfield, N. J. (2006b) Using circular dichroism spectra to estimate protein secondary structure. *Nature Protocols,* 1, 2876-2890.

Grodberg, J. & Dunn, J. J. (1988) Ompt Encodes the Escherichia-Coli Outer-Membrane Protease That Cleaves T7-Rna Polymerase during Purification. *Journal of Bacteriology,* 170, 1245-1253.

Gu, F., Jones, M. K., Chen, J., Patterson, J. C., Catte, A., Jerome, W. G., Li, L. & Segrest, J. P. (2010) Structures of discoidal high density lipoproteins: a combined computational-experimental approach. *J Biol Chem,* 285, 4652-65.

Gualandri, V., Franceschini, G., Sirtori, C. R., Gianfranceschi, G., Orsini, G. B., Cerrone, A. & Menotti, A. (1985) AIMilano apoprotein identification of the complete kindred and evidence of a dominant genetic transmission. *Am J Hum Genet,* 37, 1083-97.

Gursky, O. (2013) Crystal structure of Delta(185-243)ApoA-I suggests a mechanistic framework for the protein adaptation to the changing lipid load in good cholesterol: from flatland to sphereland via double belt, belt buckle, double hairpin and trefoil/tetrafoil. *J Mol Biol,* 425, 1-16.

Gursky, O. & Atkinson, D. (1996) Thermal unfolding of human high-density apolipoprotein A-1: implications for a lipid-free molten globular state. *Proc Natl Acad Sci U S A,* 93, 2991-5.

Gursky, O., Jones, M. K., Mei, X., Segrest, J. P. & Atkinson, D. (2013) Structural basis for distinct functions of the naturally occurring Cys mutants of human apolipoprotein A-I. *J Lipid Res,* 54, 3244-57.

Haase, C. L., Frikke-Schmidt, R., Nordestgaard, B. G., Kateifides, A. K., Kardassis, D., Nielsen, L. B., Andersen, C. B., Kober, L., Johnsen, A. H., Grande, P., Zannis, V. I. & Tybjaerg-Hansen, A. (2011) Mutation in APOA1 predicts increased risk of ischaemic heart disease and total mortality without low HDL cholesterol levels. *J Intern Med,* 270, 136-46.

Hagn, F., Etzkorn, M., Raschle, T. & Wagner, G. (2013) Optimized phospholipid bilayer nanodiscs facilitate high-resolution structure determination of membrane proteins. *J Am Chem Soc,* 135, 1919-25.

Han, B., Liu, Y., Ginzinger, S. W. & Wishart, D. S. (2011) SHIFTX2: significantly improved protein chemical shift prediction. *Journal of Biomolecular NMR,* 50, 43.

Han, J. M., Jeong, T. S., Lee, W. S., Choi, I. & Cho, K. H. (2005) Structural and functional properties of V156K and A158E mutants of apolipoprotein A-I in the lipid-free and lipid-bound states. *J Lipid Res,* 46, 589-96.

Hansen, S. K., Bertelsen, K., Paaske, B., Nielsen, N. C. & Vosegaard, T. (2015) Solid-state NMR methods for oriented membrane proteins. *Prog Nucl Magn Reson Spectrosc,* 88-89, 48-85.

Hartmann, S. R. & Hahn, E. L. (1962) Nuclear Double Resonance in the Rotating Frame. *Physical Review,* 128, 2042-2053.

Haynes, W. M. (2010) *CRC handbook of chemistry and physics : a ready-reference book of chemical and physical data.* 91st ed. Boca Raton, Fla.: CRC Press.

Holzwarth, G. & Doty, P. (1965) THE ULTRAVIOLET CIRCULAR DICHROISM OF POLYPEPTIDES. *J Am Chem Soc,* 87, 218-28.

Huang, R., Silva, R. A., Jerome, W. G., Kontush, A., Chapman, M. J., Curtiss, L. K., Hodges, T. J. & Davidson, W. S. (2011) Apolipoprotein A-I structural organization in high-density lipoproteins isolated from human plasma. *Nat Struct Mol Biol,* 18, 416-22.

Hughes, E. & Middleton, D. A. (2014) Comparison of the structure and function of phospholamban and the arginine-14 deficient mutant associated with dilated cardiomyopathy. *PLoS One,* 9, e106746.

Humphrey, W., Dalke, A. & Schulten, K. (1996) VMD: visual molecular dynamics. *J Mol Graph,* 14, 33-8, 27-8.

Hussain, R., Benning, K., Myatt, D., Javorfi, T., Longo, E., Rudd, T. R., Pulford, B. & Siligardi, G. (2015) CDApps: integrated software for experimental planning and data processing at beamline B23, Diamond Light Source (vol 22, pg 465, 2015). *Journal of Synchrotron Radiation,* 22, 862-862.

Huster, D. (2014) Solid-state NMR spectroscopy to study protein–lipid interactions. *Biochimica et Biophysica Acta (BBA) - Molecular and Cell Biology of Lipids,* 1841, 1146-1160.

Ibanez, B., Giannarelli, C., Cimmino, G., Santos-Gallego, C. G., Alique, M., Pinero, A., Vilahur, G., Fuster, V., Badimon, L. & Badimon, J. J. (2012) Recombinant HDL(Milano) exerts greater anti-inflammatory and plaque stabilizing properties than HDL(wild-type). *Atherosclerosis,* 220, 72-7.

Ibanez, B., Vilahur, G., Cimmino, G., Speidl, W. S., Pinero, A., Choi, B. G., Zafar, M. U., Santos-Gallego, C. G., Krause, B., Badimon, L., Fuster, V. & Badimon, J. J. (2008) Rapid change in plaque size, composition, and molecular footprint after recombinant apolipoprotein A-I Milano (ETC-216) administration: magnetic resonance imaging study in an experimental model of atherosclerosis. *J Am Coll Cardiol,* 51, 1104-9.

Islam, R. M., Pourmousa, M., Sviridov, D., Gordon, S. M., Neufeld, E. B., Freeman, L. A., Perrin, J. B. S., Pastor, R. W. & Remaley, A. T. (2018) Structural properties of apolipoprotein A-I mimetic peptides that promote ABCA1-dependent cholesterol efflux. *Sci Rep,* 8, 2956-15.

Jayaraman, S., Gantz, D. L. & Gursky, O. (2008) Effects of Protein Oxidation on the Structure and Stability of Model Discoidal High-Density Lipoproteins. *Biochemistry,* 47, 3875-3882.

Jonas, A. (1986) Reconstitution of high-density lipoproteins. *Methods Enzymol,* 128, 553-82.

Jonas, A., Kezdy, K. E. & Wald, J. H. (1989) Defined apolipoprotein A-I conformations in reconstituted high density lipoprotein discs. *J Biol Chem,* 264, 4818-24.

Jonas, A., Sweeny, S. A. & Herbert, P. N. (1984) Discoidal Complexes of a and C Apolipoproteins with Lipids and Their Reactions with Lecithin - Cholesterol Acyltransferase. *Journal of Biological Chemistry,* 259, 6369-6375.

Jonas, A., Wald, J. H., Toohill, K. L. H., Krul, E. S. & Kezdy, K. E. (1990) Apolipoprotein A-I Structure and Lipid Properties in Homogeneous, Reconstituted Spherical and Discoidal High-Density-Lipoproteins. *Journal of Biological Chemistry,* 265, 22123-22129.

Jones, M. K., Gu, F., Catte, A., Li, L. & Segrest, J. P. (2011) "Sticky" and "promiscuous", the yin and yang of apolipoprotein A-I termini in discoidal high-density lipoproteins: a combined computational-experimental approach. *Biochemistry,* 50, 2249-63.

Jones, M. K., Zhang, L., Catte, A., Li, L., Oda, M. N., Ren, G. & Segrest, J. P. (2010) Assessment of the validity of the double superhelix model for reconstituted high density lipoproteins: a combined computational-experimental approach. *J Biol Chem,* 285, 41161-71.

Joosten, R. P., Te Beek, T. A., Krieger, E., Hekkelman, M. L., Hooft, R. W., Schneider, R., Sander, C. & Vriend, G. (2011) A series of PDB related databases for everyday needs. *Nucleic Acids Res,* 39, D411-9.

Kabsch, W. & Sander, C. (1983) Dictionary of Protein Secondary Structure - Pattern Recognition of Hydrogen-bonded and Geometrical Features *Biopolymers,* 22, 2577-2637.

Kallend, D. G., Reijers, J. a. A., Bellibas, S. E., Bobillier, A., Kempen, H., Burggraaf, J., Moerland, M. & Wijngaard, P. L. J. (2016) A single infusion of MDCO-216 (ApoA-1 Milano/POPC) increases ABCA1-mediated cholesterol efflux and pre-beta 1 HDL in healthy volunteers and patients with stable coronary artery disease. *European Heart Journal-Cardiovascular Pharmacotherapy,* 2, 23-29.

Karalis, I. & Jukema, J. W. (2018) HDL Mimetics Infusion and Regression of Atherosclerosis: Is It Still Considered a Valid Therapeutic Option? *Curr Cardiol Rep,* 20, 66.

Keeler, J. (2010) *Understanding NMR spectroscopy.* 2nd ed. Chichester, U.K.: John Wiley and Sons.

Kelley, J. L. & Kruski, A. W. (1986) Density gradient ultracentrifugation of serum lipoproteins in a swinging bucket rotor. *Methods Enzymol,* 128, 170-81.

Kempen, H. J., Asztalos, B. F., Moerland, M., Jeyarajah, E., Otvos, J., Kallend, D. G., Bellibas, S. E. & Wijngaard, P. L. J. (2016a) High-Density Lipoprotein Subfractions and Cholesterol Efflux Capacities After Infusion of MDCO-216 (Apolipoprotein A-IMilano/Palmitoyl-Oleoyl-Phosphatidylcholine) in Healthy Volunteers and Stable Coronary Artery Disease Patients. *Arteriosclerosis Thrombosis and Vascular Biology,* 36, 736-742.

Kempen, H. J., Gomaraschi, M., Bellibas, S. E., Plassmann, S., Zerler, B., Collins, H. L., Adelman, S. J., Calabresi, L. & Wijngaard, P. L. J. (2013) Effect of repeated apoA-IMilano/POPC infusion on lipids, (apo)lipoproteins, and serum cholesterol efflux capacity in cynomolgus monkeys. *Journal of Lipid Research,* 54, 2341-2353.

Kempen, H. J., Gomaraschi, M., Simonelli, S., Calabresi, L., Moerland, M., Otvos, J., Jeyarajah, E., Kallend, D. & Wijngaard, P. L. J. (2016b) Persistent changes in lipoprotein lipids after a single infusion of ascending doses of MDCO-216 (apoA-IMilano/POPC) in healthy volunteers and stable coronary artery disease patients. *Atherosclerosis,* 255, 17-24.

Khlebnikov, A. & Keasling, J. D. (2002) Effect of lacY expression on homogeneity of induction from the P(tac) and P(trc) promoters by natural and synthetic inducers. *Biotechnol Prog,* 18, 672-4.

Khurana, R., Coleman, C., Ionescu-Zanetti, C., Carter, S. A., Krishna, V., Grover, R. K., Roy, R. & Singh, S. (2005) Mechanism of thioflavin T binding to amyloid fibrils. *J Struct Biol,* 151, 229-38.

Kijac, A. Z., Li, Y., Sligar, S. G. & Rienstra, C. M. (2007) Magic-Angle Spinning Solid-State NMR Spectroscopy of Nanodisc-Embedded Human CYP3A4. *Biochemistry,* 46, 13696-13703.

Kingwell, B. A., Chapman, M. J., Kontush, A. & Miller, N. E. (2014) HDL-targeted therapies: progress, failures and future. *Nat Rev Drug Discov,* 13, 445-64.

Kiss, R. S., Maric, J. & Marcel, Y. L. (2005) Lipid efflux in human and mouse macrophagic cells: evidence for differential regulation of phospholipid and cholesterol efflux. *J Lipid Res,* 46, 1877-87.

Klauda, J. B., Roberts, M. F., Redfield, A. G., Brooks, B. R. & Pastor, R. W. (2008) Rotation of lipids in membranes: molecular dynamics simulation, 31P spin-lattice relaxation, and rigid-body dynamics. *Biophys J,* 94, 3074-83.

Klon, A. E., Jones, M. K., Segrest, J. P. & Harvey, S. C. (2000) Molecular belt models for the apolipoprotein A-I Paris and Milano mutations. *Biophys J,* 79, 1679-85.

Komar, A. A. (2016) The Yin and Yang of codon usage. *Hum Mol Genet,* 25, R77-R85.

Kontush, A., Lhomme, M. & Chapman, M. J. (2013) Unraveling the complexities of the HDL lipidome. *J Lipid Res,* 54, 2950-63.

Kucerka, N., Tristram-Nagle, S. & Nagle, J. F. (2005) Structure of fully hydrated fluid phase lipid bilayers with monounsaturated chains. *J Membr Biol,* 208, 193-202.

Lagerstedt, J. O., Budamagunta, M. S., Liu, G. S., Devalle, N. C., Voss, J. C. & Oda, M. N. (2012) The "beta-clasp" model of apolipoprotein A-I--a lipid-free solution structure determined by electron paramagnetic resonance spectroscopy. *Biochim Biophys Acta,* 1821, 448-55.

Lau, S. & Middleton, D. A. (2020) Sensitive morphological characterization of oriented high-density lipoprotein nanoparticles using 31P NMR spectroscopy. *Angew Chem Int Ed Engl*.

Lau, S., Stanhope, N., Griffin, J., Hughes, E. & Middleton, D. A. (2019) Drug orientations within statin-loaded lipoprotein nanoparticles by (19)F solid-state NMR. *Chem Commun (Camb),* 55, 13287-13290.

Law, S. W. & Brewer, H. B., Jr. (1984) Nucleotide sequence and the encoded amino acids of human apolipoprotein A-I mRNA. *Proc Natl Acad Sci U S A,* 81, 66-70.

Lee, J. M., Robson, M. D., Yu, L. M., Shirodaria, C. C., Cunnington, C., Kylintireas, I., Digby, J. E., Bannister, T., Handa, A., Wiesmann, F., Durrington, P. N., Channon, K. M., Neubauer, S. & Choudhury, R. P. (2009) Effects of high-dose modified-release nicotinic acid on atherosclerosis and vascular function: a randomized, placebo-controlled, magnetic resonance imaging study. *J Am Coll Cardiol,* 54, 1787-94.

Lee, M. & Goldburg, W. I. (1965) Nuclear-Magnetic-Resonance Line Narrowing by a Rotating rf Field. *Physical Review,* 140, A1261-A1271.

Levine, H., 3rd (1993) Thioflavine T interaction with synthetic Alzheimer's disease beta-amyloid peptides: detection of amyloid aggregation in solution. *Protein Sci,* 2, 404-10.

Lewis, G. F. & Rader, D. J. (2005) New insights into the regulation of HDL metabolism and reverse cholesterol transport. *Circulation Research,* 96, 1221-1232.

Li, L., Chen, J., Mishra, V. K., Kurtz, J. A., Cao, D., Klon, A. E., Harvey, S. C., Anantharamaiah, G. M. & Segrest, J. P. (2004) Double belt structure of discoidal high density lipoproteins: molecular basis for size heterogeneity. *J Mol Biol,* 343, 1293-311.

Li, L., Li, S. L., Jones, M. K. & Segrest, J. P. (2012) Rotational and hinge dynamics of discoidal high density lipoproteins probed by interchain disulfide bond formation. *Biochimica Et Biophysica Acta-Molecular and Cell Biology of Lipids,* 1821, 481-489.

Li, T., Jiang, S., Ni, B., Cui, Q., Liu, Q. & Zhao, H. (2019) Discontinued Drugs for the Treatment of Cardiovascular Disease from 2016 to 2018. *Int J Mol Sci,* 20.

Li, W. H., Tanimura, M., Luo, C. C., Datta, S. & Chan, L. (1988) The apolipoprotein multigene family: biosynthesis, structure, structure-function relationships, and evolution. *J Lipid Res,* 29, 245-71.

Li, Y., Kijac, A. Z., Sligar, S. G. & Rienstra, C. M. (2006) Structural analysis of nanoscale self-assembled discoidal lipid bilayers by solid-state NMR spectroscopy. *Biophys J,* 91, 3819-28.

Liadaki, K. N., Liu, T., Xu, S., Ishida, B. Y., Duchateaux, P. N., Krieger, J. P., Kane, J., Krieger, M. & Zannis, V. I. (2000) Binding of high density lipoprotein (HDL) and discoidal reconstituted HDL to the HDL receptor scavenger receptor class B type I. Effect of lipid association and APOA-I mutations on receptor binding. *J Biol Chem,* 275, 21262-71.

Libby, P., Ridker, P. M. & Hansson, G. K. (2011) Progress and challenges in translating the biology of atherosclerosis. *Nature,* 473, 317-325.

Lin, M. T., Fukazawa, R., Miyajima-Nakano, Y., Matsushita, S., Choi, S. K., Iwasaki, T. & Gennis, R. B. (2015) Escherichia coli auxotroph host strains for amino acid-selective isotope labeling of recombinant proteins. *Methods Enzymol,* 565, 45-66.

Lin, M. T., Sperling, L. J., Frericks Schmidt, H. L., Tang, M., Samoilova, R. I., Kumasaka, T., Iwasaki, T., Dikanov, S. A., Rienstra, C. M. & Gennis, R. B. (2011) A rapid and robust method for selective isotope labeling of proteins. *Methods,* 55, 370-378.

Liu, Z., Thacker, S. G., Fernandez-Castillejo, S., Neufeld, E. B., Remaley, A. T. & Bittman, R. (2014) Synthesis of cholesterol analogues bearing BODIPY fluorophores by Suzuki or Liebeskind-Srogl cross-coupling and evaluation of their potential for visualization of cholesterol pools. *Chembiochem,* 15, 2087-96.

Luckey, M. (2014) Membrane Structural Biology: With Biochemical and Biophysical Foundations, Second Edition. *Membrane Structural Biology: With Biochemical and Biophysical Foundations, Second Edition,* 1-399.

Lusis, A. J. (2000) Atherosclerosis. *Nature,* 407, 233-241.

Macdonald, P. M., Saleem, Q., Lai, A. & Morales, H. H. (2013) NMR methods for measuring lateral diffusion in membranes. *Chem Phys Lipids,* 166, 31-44.

Malvern Instruments Ltd (2011) Dynamic Light Scattering Common Terms Defined. *https://www.malvernpanalytical.com/en/products/technology/light-scattering/dynamic-light-scattering*.

Marassi, F. M. & Crowell, K. J. (2003) Hydration-optimized oriented phospholipid bilayer samples for solid-state NMR structural studies of membrane proteins. *Journal of Magnetic Resonance,* 161, 64-69.

Marassi, F. M., Ma, C., Gratkowski, H., Straus, S. K., Strebel, K., Oblatt-Montal, M., Montal, M. & Opella, S. J. (1999) Correlation of the structural and functional domains in the membrane protein Vpu from HIV-1. *Proc Natl Acad Sci U S A,* 96, 14336-41.

Marassi, F. M. & Opella, S. J. (2000) A Solid-State NMR Index of Helical Membrane Protein Structure and Topology. *Journal of Magnetic Resonance,* 144, 150-155.

Marassi, F. M., Ramamoorthy, A. & Opella, S. J. (1997) Complete resolution of the solid-state NMR spectrum of a uniformly ^{15}N-labeled membrane protein in phospholipid bilayers. *Proceedings of the National Academy of Sciences,* 94, 8551-8556.

Marrink, S. J., Risselada, H. J., Yefimov, S., Tieleman, D. P. & De Vries, A. H. (2007) The MARTINI force field: coarse grained model for biomolecular simulations. *J Phys Chem B,* 111, 7812-24.

Marrink, S. J. D. V., A. H.; Mark, A.E.; (2004) Coarse Grained Model for Semiquantitative Lipid Simulations. *J. Phys. Chem. B,* 108, 750-760.

Martin, D. D., Budamagunta, M. S., Ryan, R. O., Voss, J. C. & Oda, M. N. (2006) Apolipoprotein A-I assumes a "looped belt" conformation on reconstituted high density lipoprotein. *J Biol Chem,* 281, 20418-26.

Martin, S. S., Jones, S. R. & Toth, P. P. (2014) High-density lipoprotein subfractions: current views and clinical practice applications. *Trends in Endocrinology and Metabolism,* 25, 329-336.

Matlahov, I. & Van Der Wel, P. C. A. (2018) Hidden motions and motion-induced invisibility: Dynamics-based spectral editing in solid-state NMR. *Methods,* 148, 123-135.

Matz, C. E. & Jonas, A. (1982) Micellar Complexes of Human Apolipoprotein A-I with Phosphatidylcholines and Cholesterol Prepared from Cholate-Lipid Dispersions. *J. Biol. Chem. ,* 257, 4535-4540.

Mckinnon, K. M. (2018) Flow Cytometry: An Overview. *Curr Protoc Immunol,* 120, 5 1 1-5 1 11.

Mclaurin, J., Franklin, T., Zhang, X., Deng, J. & Fraser, P. E. (1999) Interactions of Alzheimer amyloid-beta peptides with glycosaminoglycans effects on fibril nucleation and growth. *Eur J Biochem,* 266, 1101-10.

Mei, X. & Atkinson, D. (2011) Crystal structure of C-terminal truncated apolipoprotein A-I reveals the assembly of high density lipoprotein (HDL) by dimerization. *J Biol Chem,* 286, 38570-82.

Miyazaki, M., Nakano, M., Fukuda, M. & Handa, T. (2009) Smaller discoidal high-density lipoprotein particles form saddle surfaces, but not planar bilayers. *Biochemistry,* 48, 7756-63.

Mlynarik, V. (2017) Introduction to nuclear magnetic resonance. *Anal Biochem,* 529, 4-9.

Monneau, Y. R., Ishida, Y., Rossi, P., Saio, T., Tzeng, S.-R., Inouye, M. & Kalodimos, C. G. (2016) Exploiting E. coli auxotrophs for leucine, valine, and threonine specific methyl labeling of large proteins for NMR applications. *J Biomol NMR,* 65, 99-108.

Monticelli, L., Kandasamy, S. K., Periole, X., Larson, R. G., Tieleman, D. P. & Marrink, S. J. (2008) The MARTINI Coarse-Grained Force Field: Extension to Proteins. *J Chem Theory Comput,* 4, 819-34.

Morrisett, J. D., David, J. S., Pownall, H. J. & Gotto, A. M., Jr. (1973) Interaction of an apolipoprotein (apoLP-alanine) with phosphatidylcholine. *Biochemistry,* 12, 1290-9.

Mors, K., Roos, C., Scholz, F., Wachtveitl, J., Dotsch, V., Bernhard, F. & Glaubitz, C. (2013) Modified lipid and protein dynamics in nanodiscs. *Biochimica Et Biophysica Acta-Biomembranes,* 1828, 1222-1229.

Mucchiano, G. I., Haggqvist, B., Sletten, K. & Westermark, P. (2001) Apolipoprotein A-1-derived amyloid in atherosclerotic plaques of the human aorta. *J Pathol,* 193, 270-5.

Nagao, K., Hata, M., Tanaka, K., Takechi, Y., Nguyen, D., Dhanasekaran, P., Lund-Katz, S., Phillips, M. C. & Saito, H. (2014) The roles of C-terminal helices of human apolipoprotein A-I in formation of high-density lipoprotein particles. *Biochim Biophys Acta,* 1841, 80-7.

Naito, A. (2009) Structure elucidation of membrane-associated peptides and proteins in oriented bilayers by solid-state NMR spectroscopy. *Solid State Nucl Magn Reson,* 36, 67-76.

Nakamura, Y., Gojobori, T. & Ikemura, T. (1999) Codon usage tabulated from the international DNA sequence databases; its status 1999. *Nucleic Acids Res,* 27, 292.

Nakazawa, Y., Suzuki, Y., Williamson, M. P., Saitô, H. & Asakura, T. (2009) The interaction of amyloid Aβ(1–40) with lipid bilayers and ganglioside as studied by 31P solid-state NMR. *Chemistry and Physics of Lipids,* 158, 54-60.

Nath, A., Atkins, W. M. & Sligar, S. G. (2007) Applications of phospholipid bilayer nanodiscs in the study of membranes and membrane proteins. *Biochemistry,* 46, 2059-69.

Navab, M., Imes, S. S., Hama, S. Y., Hough, G. P., Ross, L. A., Bork, R. W., Valente, A. J., Berliner, J. A., Drinkwater, D. C., Laks, H. & Fogelman, A. M. (1991) Monocyte Transmigration Induced by Modification of Low-Density-Lipoprotein in Cocultures of Human Aortic-Wall Cells Is Due to Induction of Monocyte Chemotactic Protein-1 Synthesis and Is Abolished by High-Density-Lipoprotein. *Journal of Clinical Investigation,* 88, 2039-2046.

Nicholls, S. J., Puri, R., Ballantyne, C. M., Jukema, J. W., Kastelein, J. J. P., Koenig, W., Wright, R. S., Kallend, D., Wijngaard, P., Borgman, M., Wolski, K. & Nissen, S. E. (2018) Effect of Infusion of High-Density Lipoprotein Mimetic Containing Recombinant Apolipoprotein A-I Milano on Coronary Disease in Patients With an

Acute Coronary Syndrome in the MILANO-PILOT Trial A Randomized Clinical Trial. *Jama Cardiology,* 3, 806-814.

Nicholls, S. J., Zheng, L. & Hazen, S. L. (2005) Formation of Dysfunctional High-Density Lipoprotein by Myeloperoxidase. *Trends Cardiovasc Med,* 15, 212-219.

Nichols, A. V., Krauss, R. M. & Musliner, T. A. (1986) Nondenaturing polyacrylamide gradient gel electrophoresis. *Methods Enzymol,* 128, 417-31.

Nicholson, L. K., Moll, F., Mixon, T. E., Lograsso, P. V., Lay, J. C. & Cross, T. A. (1987) Solid-state 15N NMR of oriented lipid bilayer bound gramicidin A'. *Biochemistry,* 26, 6621-6.

Nissen, S. E., Tsunoda, T., Tuzcu, E. M., Schoenhagen, P., Cooper, C. J., Yasin, M., Eaton, G. M., Lauer, M. A., Sheldon, W. S., Grines, C. L., Halpern, S., Crowe, T., Blankenship, J. C. & Kerensky, R. (2003) Effect of recombinant ApoA-I Milano on coronary atherosclerosis in patients with acute coronary syndromes - A randomized controlled trial. *Jama-Journal of the American Medical Association,* 290, 2292-2300.

Nolte, R. T. & Atkinson, D. (1992) Conformational analysis of apolipoprotein A-I and E-3 based on primary sequence and circular dichroism. *Biophys J,* 63, 1221-39.

Oas, T. G., Griffin, R. G. & Levitt, M. H. (1988) Rotary resonance recoupling of dipolar interactions in solid-state nuclear magnetic resonance spectroscopy. *The Journal of Chemical Physics,* 89, 692-695.

Oda, M. N. (2017) Lipid-free apoA-I structure - Origins of model diversity. *Biochimica Et Biophysica Acta-Molecular and Cell Biology of Lipids,* 1862, 221-233.

Oda, M. N., Bielicki, J. K., Berger, T. & Forte, T. M. (2001) Cysteine substitutions in apolipoprotein A-I primary structure modulate paraoxonase activity. *Biochemistry,* 40, 1710-1718.

Oda, M. N., Budamagunta, M. S., Borja, M. S., Petrlova, J., Voss, J. C. & Lagerstedt, J. O. (2013) The secondary structure of apolipoprotein A-I on 9.6-nm reconstituted high-density lipoprotein determined by EPR spectroscopy. *FEBS J,* 280, 3416-24.

Oda, M. N., Forte, T. M., Ryan, R. O. & Voss, J. C. (2003) The C-terminal domain of apolipoprotein A-I contains a lipid-sensitive conformational trigger. *Nat Struct Biol,* 10, 455-60.

Okura, H., Yamashita, S., Ohama, T., Saga, A., Yamamoto-Kakuta, A., Hamada, Y., Sougawa, N., Ohyama, R., Sawa, Y. & Matsuyama, A. (2010) HDL/Apolipoprotein A-I Binds to Macrophage-Derived Progranulin and Suppresses its Conversion into Proinflammatory Granulins. *Journal of Atherosclerosis and Thrombosis,* 17, 568-577.

Pan, L. & Segrest, J. P. (2016) Computational studies of plasma lipoprotein lipids. *Biochim Biophys Acta,* 1858, 2401-2420.

Panagotopulos, S. E., Witting, S. R., Horace, E. M., Nicholas Maiorano, J. & Sean Davidson, W. (2002) Bacterial expression and characterization of mature apolipoprotein A-I. *Protein Expr Purif,* 25, 353-361.

Park, S. H., Berkamp, S., Cook, G. A., Chan, M. K., Viadiu, H. & Opella, S. J. (2011) Nanodiscs versus Macrodiscs for NMR of Membrane Proteins. *Biochemistry,* 50, 8983-8985.

Park, S. H., Das, B. B., Casagrande, F., Tian, Y., Nothnagel, H. J., Chu, M., Kiefer, H., Maier, K., De Angelis, A. A., Marassi, F. M. & Opella, S. J. (2012) Structure of the chemokine receptor CXCR1 in phospholipid bilayers. *Nature,* 491, 779-783.

Patel, S., Drew, B. G., Nakhla, S., Duffy, S. J., Murphy, A. J., Barter, P. J., Rye, K. A., Chin-Dusting, J., Hoang, A., Sviridov, D., Celermajer, D. S. & Kingwell, B. A. (2009) Reconstituted high-density lipoprotein increases plasma high-density lipoprotein anti-inflammatory properties and cholesterol efflux capacity in patients with type 2 diabetes. *J Am Coll Cardiol,* 53, 962-71.

Petrlova, J., Dalla-Riva, J., Morgelin, M., Lindahl, M., Krupinska, E., Stenkula, K. G., Voss, J. C. & Lagerstedt, J. O. (2014) Secondary structure changes in ApoA-I Milano (R173C) are not accompanied by a decrease in protein stability or solubility. *PLoS One,* 9, e96150.

Petrlova, J., Hilt, S., Budamagunta, M., Domingo-Espin, J., Voss, J. C. & Lagerstedt, J. O. (2016) Molecular crowding impacts the structure of apolipoprotein A-I with potential implications on in vivo metabolism and function. *Biopolymers,* 105, 683-92.

Phillips, J. C., Wriggers, W., Li, Z., Jonas, A. & Schulten, K. (1997) Predicting the structure of apolipoprotein A-I in reconstituted high-density lipoprotein disks. *Biophys J,* 73, 2337-46.

Picard, F., Paquet, M. J., Levesque, J., Belanger, A. & Auger, M. (1999) 31P NMR first spectral moment study of the partial magnetic orientation of phospholipid membranes. *Biophys J,* 77, 888-902.

Pollard, R. D., Fulp, B., Samuel, M. P., Sorci-Thomas, M. G. & Thomas, M. J. (2013) The conformation of lipid-free human apolipoprotein A-I in solution. *Biochemistry,* 52, 9470-81.

Pourmousa, M. & Pastor, R. W. (2018) Molecular dynamics simulations of lipid nanodiscs. *Biochim Biophys Acta Biomembr,* 1860, 2094-2107.

Pourmousa, M., Song, H. D., He, Y., Heinecke, J. W., Segrest, J. P. & Pastor, R. W. (2018) Tertiary structure of apolipoprotein A-I in nascent high-density lipoproteins. *Proc Natl Acad Sci U S A,* 115, 5163-5168.

Pownall, H. J., Massey, J. B., Kusserow, S. K. & Gotto, A. M. (1978) Kinetics of Lipid-Protein Interactions - Interaction of Apolipoprotein a-I from Human-Plasma High-Density Lipoproteins with Phosphatidylcholines. *Biochemistry,* 17, 1183-1188.

Prinz, W. A., Åslund, F., Holmgren, A. & Beckwith, J. (1997) The role of the thioredoxin and glutaredoxin pathways in reducing protein disulfide bonds in the Escherichia coli cytoplasm. *Journal of Biological Chemistry,* 272, 15661-15667.

Provencher, S. W. & Gloeckner, J. (1981) Estimation of globular protein secondary structure from circular dichroism. *Biochemistry,* 20, 33-37.

Puppato, A., Dupré, D. B., Stolowich, N. & Yappert, M. C. (2007) Effect of temperature and pH on 31P nuclear magnetic resonances of phospholipids in cholate micelles. *Chem Phys Lipids,* 150, 176-185.

Pyle, L. E., Sawyer, W. H., Fujiwara, Y., Mitchell, A. & Fidge, N. H. (1996) Structural and Functional Properties of Full-Length and Truncated Human Proapolipoprotein AI Expressed in Escherichia coli. *Biochemistry,* 35, 12046-12052.

Qiu, X., Mistry, A., Ammirati, M. J., Chrunyk, B. A., Clark, R. W., Cong, Y., Culp, J. S., Danley, D. E., Freeman, T. B., Geoghegan, K. F., Griffor, M. C., Hawrylik, S. J., Hayward, C. M., Hensley, P., Hoth, L. R., Karam, G. A., Lira, M. E., Lloyd, D. B., Mcgrath, K. M., Stutzman-Engwall, K. J., Subashi, A. K., Subashi, T. A., Thompson, J. F., Wang, I. K., Zhao, H. & Seddon, A. P. (2007) Crystal structure of cholesteryl ester transfer protein reveals a long tunnel and four bound lipid molecules. *Nat Struct Mol Biol,* 14, 106-13.

Ramamoorthy, A., Wu, C. H. & Opella, S. J. (1999) Experimental Aspects of Multidimensional Solid-State NMR Correlation Spectroscopy. *Journal of Magnetic Resonance,* 140, 131-140.

Ramella, N. A., Rimoldi, O. J., Prieto, E. D., Schinella, G. R., Sanchez, S. A., Jaureguiberry, M. S., Vela, M. E., Ferreira, S. T. & Tricerri, M. A. (2011) Human apolipoprotein A-I-derived amyloid: its association with atherosclerosis. *PLoS One,* 6, e22532.

Recalde, D., Velez-Carrasco, W., Civeira, F., Cenarro, A., Gomez-Coronado, D., Ordovas, J. M. & Pocovi, M. (2001) Enhanced fractional catabolic rate of apo A-I and apo A-II in heterozygous subjects for apo A-I-Zaragoza (L144R). *Atherosclerosis,* 154, 613-623.

Reijers, J. a. A., Kallend, D. G., Malone, K. E., Jukema, J. W., Wijngaard, P. L. J., Burggraaf, J. & Moerland, M. (2017) MDCO-216 Does Not Induce Adverse Immunostimulation, in Contrast to Its Predecessor ETC-216. *Cardiovascular Drugs and Therapy,* 31, 381-389.

Rigotti, A. & Krieger, M. (1999) Getting a handle on "good" cholesterol with the high-density lipoprotein receptor. *N Engl J Med,* 341, 2011-3.

Roberts, L. M., Ray, M. J., Shih, T. W., Hayden, E., Reader, M. M. & Brouillette, C. G. (1997) Structural analysis of apolipoprotein A-I: limited proteolysis of methionine-reduced and -oxidized lipid-free and lipid-bound human apo A-I. *Biochemistry,* 36, 7615-24.

Rocken, C., Tautenhahn, J., Buhling, F., Sachwitz, D., Vockler, S., Goette, A. & Burger, T. (2006) Prevalence and pathology of amyloid in atherosclerotic arteries. *Arterioscler Thromb Vasc Biol,* 26, 676-7.

Rogers, D. P., Brouillette, C. G., Engler, J. A., Tendian, S. W., Roberts, L., Mishra, V. K., Anantharamaiah, G. M., Lundkatz, S., Phillips, M. C. & Ray, M. J. (1997) Truncation of the amino terminus of human apolipoprotein A-I substantially alters only the lipid-free conformation. *Biochemistry,* 36, 288-300.

Rogers, D. P., Roberts, L. M., Lebowitz, J., Datta, G., Anantharamaiah, G. M., Engler, J. A. & Brouillette, C. G. (1998a) The lipid-free structure of apolipoprotein A-I: effects of amino-terminal deletions. *Biochemistry,* 37, 11714-25.

Rogers, D. P., Roberts, L. M., Lebowitz, J., Engler, J. A. & Brouillette, C. G. (1998b) Structural analysis of apolipoprotein A-I: effects of amino- and carboxy-terminal deletions on the lipid-free structure. *Biochemistry,* 37, 945-55.

Rosano, G. L. & Ceccarelli, E. A. (2014) Recombinant protein expression in Escherichia coli: advances and challenges. *Frontiers in Microbiology,* 5.

Rosano, G. L., Morales, E. S. & Ceccarelli, E. A. (2019) New tools for recombinant protein production in Escherichia coli: A 5-year update. *Protein Sci,* 28, 1412-1422.

Rosenson, R. S., Brewer, H. B., Jr., Chapman, M. J., Fazio, S., Hussain, M. M., Kontush, A., Krauss, R. M., Otvos, J. D., Remaley, A. T. & Schaefer, E. J. (2011) HDL measures, particle heterogeneity, proposed nomenclature, and relation to atherosclerotic cardiovascular events. *Clin Chem,* 57, 392-410.

Ryan, R. O., Forte, T. M. & Oda, M. N. (2003) Optimized bacterial expression of human apolipoprotein A-I. *Protein Expression and Purification,* 27, 98-103.

Rzepiela, A. J., Schäfer, L. V., Goga, N., Risselada, H. J., De Vries, A. H. & Marrink, S. J. (2010) Reconstruction of atomistic details from coarse-grained structures. *J Comput Chem,* 31, 1333-1343.

Sahoo, D., Trischuk, T. C., Chan, T., Drover, V. a. B., Ho, S., Chimini, G., Agellon, L. B., Agnihotri, R., Francis, G. A. & Lehner, R. (2004) ABCA1-dependent lipid eff lux to apolipoprotein A-1 mediates HDL particle formation and decreases VLDL secretion from murine hepatocytes. *Journal of Lipid Research,* 45, 1122-1131.

Saito, H., Dhanasekaran, P., Nguyen, D., Deridder, E., Holvoet, P., Lund-Katz, S. & Phillips, M. C. (2004) Alpha-helix formation is required for high affinity binding of human apolipoprotein A-I to lipids. *J Biol Chem,* 279, 20974-81.

Saito, H., Dhanasekaran, P., Nguyen, D., Holvoet, P., Lund-Katz, S. & Phillips, M. C. (2003) Domain structure and lipid interaction in human apolipoproteins A-I and E, a general model. *J Biol Chem,* 278, 23227-32.

Salnikov, E. S., Friedrich, H., Li, X., Bertani, P., Reissmann, S., Hertweck, C., O'neil, J. D., Raap, J. & Bechinger, B. (2009) Structure and alignment of the membrane-associated peptaibols ampullosporin A and alamethicin by oriented 15N and 31P solid-state NMR spectroscopy. *Biophys J,* 96, 86-100.

Samuelson, J. C. (2011) Recent Developments in Difficult Protein Expression: A Guide to *E. coli* Strains, Promoters, and Relevant Host Mutations. In: Evans Jr., T. C. & Xu, M.-Q. (eds.) *Heterologous Gene Expression in E. coli Methods and Protocols.* Totowa, NJ: Humana Press.

Sanderson, J. M. (2012) Resolving the kinetics of lipid, protein and peptide diffusion in membranes. *Mol Membr Biol,* 29, 118-143.

Sankaranarayanan, S., Kellner-Weibel, G., De La Llera-Moya, M., Phillips, M. C., Asztalos, B. F., Bittman, R. & Rothblat, G. H. (2011) A sensitive assay for ABCA1-mediated cholesterol efflux using BODIPY-cholesterol. *J Lipid Res,* 52, 2332-40.

Schindelin, J., Arganda-Carreras, I., Frise, E., Kaynig, V., Longair, M., Pietzsch, T., Preibisch, S., Rueden, C., Saalfeld, S., Schmid, B., Tinevez, J. Y., White, D. J., Hartenstein, V., Eliceiri, K., Tomancak, P. & Cardona, A. (2012) Fiji: an open-source platform for biological-image analysis. *Nature Methods,* 9, 676-682.

Schmidt, H. H. J., Remaley, A. T., Stonik, J. A., Ronan, R., Wellmann, A., Thomas, F., Zech, L. A., Brewer, H. B. & Hoeg, J. M. (1995) Carboxyl-terminal Domain Truncation Alters Apolipoprotein A-I in Vivo Catabolism (∗). *J Biol Chem,* 270, 5469-5475.

Schrodinger, Llc (2015) The PyMOL Molecular Graphics System, Version 1.8.

Schumaker, V. N. & Puppione, D. L. (1986) Sequential flotation ultracentrifugation. *Methods Enzymol,* 128, 155-70.

Schwendeman, A., Sviridov, D. O., Yuan, W., Guo, Y., Morin, E. E., Yuan, Y., Stonik, J., Freeman, L., Ossoli, A., Thacker, S., Killion, S., Pryor, M., Chen, Y. E., Turner, S. & Remaley, A. T. (2015) The effect of phospholipid composition of reconstituted HDL on its cholesterol efflux and anti-inflammatory properties. *J Lipid Res,* 56, 1727-37.

Seddon, A. M., Curnow, P. & Booth, P. J. (2004) Membrane proteins, lipids and detergents: not just a soap opera. *Biochim Biophys Acta,* 1666, 105-17.

Segrest, J. P., Jackson, R. L., Morrisett, J. D. & Gotto, A. M., Jr. (1974) A molecular theory of lipid-protein interactions in the plasma lipoproteins. *FEBS Lett,* 38, 247-58.

Segrest, J. P., Jones, M. K. & Catte, A. (2013) MD simulations suggest important surface differences between reconstituted and circulating spherical HDL. *J Lipid Res,* 54, 2718-32.

Segrest, J. P., Jones, M. K., De Loof, H., Brouillette, C. G., Venkatachalapathi, Y. V. & Anantharamaiah, G. M. (1992) The amphipathic helix in the exchangeable apolipoproteins: a review of secondary structure and function. *J Lipid Res,* 33, 141-66.

Segrest, J. P., Jones, M. K., Klon, A. E., Sheldahl, C. J., Hellinger, M., De Loof, H. & Harvey, S. C. (1999) A detailed molecular belt model for apolipoprotein A-I in discoidal high density lipoprotein. *J Biol Chem,* 274, 31755-8.

Segrest, J. P., Jones, M. K., Shao, B. & Heinecke, J. W. (2014) An experimentally robust model of monomeric apolipoprotein A-I created from a chimera of two X-ray structures and molecular dynamics simulations. *Biochemistry,* 53, 7625-40.

Sengupta, I. & Udgaonkar, J. B. (2017) Expression and purification of single cysteine-containing mutant variants of the mouse prion protein by oxidative refolding. *Protein Expression and Purification,* 140, 1-7.

Sharma, M., Yi, M., Dong, H., Qin, H., Peterson, E., Busath, D. D., Zhou, H. X. & Cross, T. A. (2010) Insight into the mechanism of the influenza A proton channel from a structure in a lipid bilayer. *Science,* 330, 509-12.

Shaw, J. A., Bobik, A., Murphy, A., Kanellakis, P., Blombery, P., Mukhamedova, N., Woollard, K., Lyon, S., Sviridov, D. & Dart, A. M. (2008) Infusion of Reconstituted High-Density Lipoprotein Leads to Acute Changes in Human Atherosclerotic Plaque. *Circulation Research,* 103, 1084-1091.

Shen, M. Y. & Sali, A. (2006) Statistical potential for assessment and prediction of protein structures. *Protein Sci,* 15, 2507-24.

Shen, W. J., Azhar, S. & Kraemer, F. B. (2018) SR-B1: A Unique Multifunctional Receptor for Cholesterol Influx and Efflux. *Annu Rev Physiol,* 80, 95-116.

Shih, A. Y., Arkhipov, A., Freddolino, P. L. & Schulten, K. (2006) Coarse grained protein-lipid model with application to lipoprotein particles. *J Phys Chem B,* 110, 3674-84.

Shih, A. Y., Arkhipov, A., Freddolino, P. L., Sligar, S. G. & Schulten, K. (2007a) Assembly of lipids and proteins into lipoprotein particles. *J Phys Chem B,* 111, 11095-104.

Shih, A. Y., Freddolino, P. L., Arkhipov, A. & Schulten, K. (2007b) Assembly of lipoprotein particles revealed by coarse-grained molecular dynamics simulations. *J Struct Biol,* 157, 579-92.

Shih, A. Y., Sligar, S. G. & Schulten, K. (2008) Molecular models need to be tested: the case of a solar flares discoidal HDL model. *Biophys J,* 94, L87-9.

Silva, R. A., Hilliard, G. M., Fang, J., Macha, S. & Davidson, W. S. (2005a) A three-dimensional molecular model of lipid-free apolipoprotein A-I determined by cross-linking/mass spectrometry and sequence threading. *Biochemistry,* 44, 2759-69.

Silva, R. A., Hilliard, G. M., Li, L., Segrest, J. P. & Davidson, W. S. (2005b) A mass spectrometric determination of the conformation of dimeric apolipoprotein A-I in discoidal high density lipoproteins. *Biochemistry,* 44, 8600-7.

Silva, R. A., Huang, R., Morris, J., Fang, J., Gracheva, E. O., Ren, G., Kontush, A., Jerome, W. G., Rye, K. A. & Davidson, W. S. (2008) Structure of apolipoprotein A-I in spherical high density lipoproteins of different sizes. *Proc Natl Acad Sci USA,* 105, 12176-81.

Simonsen, J. B. (2016) Evaluation of reconstituted high-density lipoprotein (rHDL) as a drug delivery platform – a detailed survey of rHDL particles ranging from biophysical properties to clinical implications. *Nanomedicine,* 12, 2161-2179.

Siuda, I. & Tieleman, D. P. (2015) Molecular Models of Nanodiscs. *J. Chem. Theory Comput,* 11, 4923-4932.

Sivashanmugam, A., Murray, V., Cui, C., Zhang, Y., Wang, J. & Li, Q. (2009) Practical protocols for production of very high yields of recombinant proteins using Escherichia coli. *Protein Sci,* 18, 936-948.

Solanko, K. A., Modzel, M., Solanko, L. M. & Wüstner, D. (2016) Fluorescent Sterols and Cholesteryl Esters as Probes for Intracellular Cholesterol Transport. *Lipid insights,* 8, 95-114.

Sorci-Thomas, M., Kearns, M. W. & Lee, J. P. (1993) Apolipoprotein A-I domains involved in lecithin-cholesterol acyltransferase activation. Structure:function relationships. *J Biol Chem,* 268, 21403-9.

Sparks, D. L., Lund-Katz, S. & Phillips, M. C. (1992a) The charge and structural stability of apolipoprotein A-I in discoidal and spherical recombinant high density lipoprotein particles. *J Biol Chem,* 267, 25839-47.

Sparks, D. L., Phillips, M. C. & Lund-Katz, S. (1992b) The conformation of apolipoprotein A-I in discoidal and spherical recombinant high density lipoprotein particles. 13C NMR studies of lysine ionization behavior. *J Biol Chem,* 267, 25830-8.

Sreerama, N. & Woody, R. W. (2000) Estimation of protein secondary structure from circular dichroism spectra: comparison of CONTIN, SELCON, and CDSSTR methods with an expanded reference set. *Anal Biochem,* 287, 252-60.

Sreerama, N. & Woody, R. W. (2004a) Computation and Analysis of Protein Circular Dichroism Spectra. *Methods in Enzymology.* Academic Press.

Sreerama, N. & Woody, R. W. (2004b) On the analysis of membrane protein circular dichroism spectra. *Protein Sci,* 13, 100-112.

Stetefeld, J., Mckenna, S. A. & Patel, T. R. (2016) Dynamic light scattering: a practical guide and applications in biomedical sciences. *Biophys Rev,* 8, 409-427.

Stewart, E. J., Aslund, F. & Beckwith, J. (1998) Disulfide bond formation in the Escherichia coli cytoplasm: an in vivo role reversal for the thioredoxins. *EMBO J,* 17, 5543-50.

Studier, F. W., Rosenberg, A. H., Dunn, J. J. & Dubendorff, J. W. (1990) Use of T7 Rna-Polymerase to Direct Expression of Cloned Genes. *Methods in Enzymology,* 185, 60-89.

Sud, M., Fahy, E., Cotter, D., Brown, A., Dennis, E. A., Glass, C. K., Merrill, A. H., Jr., Murphy, R. C., Raetz, C. R., Russell, D. W. & Subramaniam, S. (2007) LMSD: LIPID MAPS structure database. *Nucleic Acids Res,* 35, D527-32.

Sugita, Y. & Okamoto, Y. (1999) Replica-exchange molecular dynamics method for protein folding. *Chemical Physics Letters,* 314, 141-151.

Suurkuusk, M. & Singh, S. K. (2000) Formation of HDL-like complexes from apolipoprotein A-I-M and DMPC. *International Journal of Pharmaceutics,* 194, 21-38.

Tabas, I. (2005) Consequences and therapeutic implications of macrophage apoptosis in atherosclerosis - The importance of lesion stage and phagocytic efficiency. *Arteriosclerosis Thrombosis and Vascular Biology,* 25, 2255-2264.

Tabas, I. (2010) Macrophage death and defective inflammation resolution in atherosclerosis. *Nature Reviews Immunology,* 10, 36-46.

Tabas, I., Williams, K. J. & Boren, J. (2007) Subendothelial lipoprotein retention as the initiating process in atherosclerosis - Update and therapeutic implications. *Circulation,* 116, 1832-1844.

Takegoshi, K., Nakamura, S. & Terao, T. (2001) C-13-H-1 dipolar-assisted rotational resonance in magic-angle spinning NMR. *Chemical Physics Letters,* 344, 631-637.

Tanford, C. (1973) *The hydrophobic effect: formation of micelles and biological membranes.* New York,: Wiley.

Tardif, J. C., Ballantyne, C. M., Barter, P., Dasseux, J. L., Fayad, Z. A., Guertin, M. C., Kastelein, J. J., Keyserling, C., Klepp, H., Koenig, W., L'allier, P. L., Lesperance, J., Luscher, T. F., Paolini, J. F., Tawakol, A., Waters, D. D. & Can, H. D. L. I. S. Q. a. R. I. (2014) Effects of the high-density lipoprotein mimetic agent CER-001 on coronary atherosclerosis in patients with acute coronary syndromes: a randomized trial. *Eur Heart J,* 35, 3277-86.

Tardif, J. C., Gregoire, J., L'allier, P. L., Ibrahim, R., Lesperance, J., Heinonen, T. M., Kouz, S., Berry, C., Basser, R., Lavoie, M. A., Guertin, M. C., Rodes-Cabau, J. & Investigators, E. (2007) Effects of reconstituted high-density lipoprotein infusions on coronary atherosclerosis - A randomized controlled trial. *Jama-Journal of the American Medical Association,* 297, 1675-1682.

Teoh, C. L., Griffin, M. D. & Howlett, G. J. (2011) Apolipoproteins and amyloid fibril formation in atherosclerosis. *Protein Cell,* 2, 116-27.

Townsend, D. (2016) *Molecular level characterisation of apolipoprotein A-I aggregation leading to fibrils comprising of both α-helical and β-sheet structures.* Lancaster University.

Townsend, D., Hughes, E., Hussain, R., Siligardi, G., Baldock, S., Madine, J. & Middleton, D. A. (2017) Heparin and Methionine Oxidation Promote the Formation of

Apolipoprotein A-I Amyloid Comprising alpha-Helical and beta-Sheet Structures. *Biochemistry,* 56, 1632-1644.

Traaseth, N. J., Buffy, J. J., Zamoon, J. & Veglia, G. (2006) Structural dynamics and topology of phospholamban in oriented lipid bilayers using multidimensional solid-state NMR. *Biochemistry,* 45, 13827-34.

Tricerri, M. A., Behling Agree, A. K., Sanchez, S. A., Bronski, J. & Jonas, A. (2001) Arrangement of apolipoprotein A-I in reconstituted high-density lipoprotein disks: an alternative model based on fluorescence resonance energy transfer experiments. *Biochemistry,* 40, 5065-74.

Tricoci, P., D'andrea, D. M., Gurbel, P. A., Yao, Z. L., Cuchel, M., Winston, B., Schott, R., Weiss, R., Blazing, M. A., Cannon, L., Bailey, A., Angiolillo, D. J., Gille, A., Shear, C. L., Wright, S. D. & Alexander, J. H. (2015) Infusion of Reconstituted High-Density Lipoprotein, CSL112, in Patients With Atherosclerosis: Safety and Pharmacokinetic Results From a Phase 2a Randomized Clinical Trial. *Journal of the American Heart Association,* 4.

Tripathi, N. K. & Shrivastava, A. (2019) Recent Developments in Bioprocessing of Recombinant Proteins: Expression Hosts and Process Development. *Front Bioeng Biotechnol,* 7, 420-420.

Ulrich, E. L., Akutsu, H., Doreleijers, J. F., Harano, Y., Ioannidis, Y. E., Lin, J., Livny, M., Mading, S., Maziuk, D., Miller, Z., Nakatani, E., Schulte, C. F., Tolmie, D. E., Kent Wenger, R., Yao, H. & Markley, J. L. (2007) BioMagResBank. *Nucleic Acids Research,* 36, D402-D408.

Vance, D. E. & Vance, J. E. (2002) *Biochemistry of lipids, lipoproteins, and membranes.* 4th ed. Amsterdam: Elsevier.

Von Eckardstein, A., Nofer, J.-R. & Assmann, G. (2001) High Density Lipoproteins and Arteriosclerosis Role of Cholesterol Efflux and Reverse Cholesterol Transport. *Arteriosclr. Thromb. Vasc. Biol.* , 21, 13-27.

Wald, J. H., Coormaghtigh, E., De Meutter, J., Ruysschaert, J. M. & Jonas, A. (1990) Investigation of the lipid domains and apolipoprotein orientation in reconstituted high density lipoproteins by fluorescence and IR methods. *J Biol Chem,* 265, 20044-50.

Wallace, B. A. & Janes, R. W. (2009) *Modern techniques for circular dichroism and synchrotron radiation circular dichroism spectroscopy*. [Amsterdam: IOS Press.

Walter, A., Vinson, P. K., Kaplun, A. & Talmon, Y. (1991) Intermediate Structures in the Cholate-Phosphatidylcholine Vesicle Micelle Transition. *Biophysical Journal,* 60, 1315-1325.

Wang, Y. & Jardetzky, O. (2002) Probability-based protein secondary structure identification using combined NMR chemical-shift data. *Protein science : a publication of the Protein Society,* 11, 852-861.

Ward, N. C., Watts, G. F. & Eckel, R. H. (2019) Statin Toxicity: Mechanistic Insights and Clinical Implications. *Circulation research,* 124, 328-350.

Wassenaar, T. A., Ingólfsson, H. I., Böckmann, R. A., Tieleman, D. P. & Marrink, S. J. (2015) Computational Lipidomics with insane: A Versatile Tool for Generating

Custom Membranes for Molecular Simulations. *Journal of Chemical Theory and Computation,* 11, 2144-2155.

Webb, B. & Sali, A. (2016) Comparative Protein Structure Modeling Using MODELLER. *Curr Protoc Bioinformatics,* 54, 5 6 1-5 6 37.

Weisgraber, K. H., Bersot, T. P., Mahley, R. W., Franceschini, G. & Sirtori, C. R. (1980) A-Imilano Apoprotein - Isolation and Characterization of a Cysteine-Containing Variant of the a-I Apoprotein from Human High-Density Lipoproteins. *Journal of Clinical Investigation,* 66, 901-907.

Weisgraber, K. H., Rall, S. C., Jr., Bersot, T. P., Mahley, R. W., Franceschini, G. & Sirtori, C. R. (1983) Apolipoprotein A-IMilano. Detection of normal A-I in affected subjects and evidence for a cysteine for arginine substitution in the variant A-I. *J Biol Chem,* 258, 2508-13.

Whitmore, L. & Wallace, B. A. (2008) Protein secondary structure analyses from circular dichroism spectroscopy: methods and reference databases. *Biopolymers,* 89, 392-400.

Wiesner, P., Leidl, K., Boettcher, A., Schmitz, G. & Liebisch, G. (2009) Lipid profiling of FPLC-separated lipoprotein fractions by electrospray ionization tandem mass spectrometry. *J Lipid Res,* 50, 574-85.

Wong, Y. Q., Binger, K. J., Howlett, G. J. & Griffin, M. D. (2010) Methionine oxidation induces amyloid fibril formation by full-length apolipoprotein A-I. *Proc Natl Acad Sci U S A,* 107, 1977-82.

Wu, C. H., Ramamoorthy, A. & Opella, S. J. (1994) High-resolution heteronuclear dipolar solid-state NMR spectroscopy. *Journal of Magnetic Resonance Series A,* 109, 270-272.

Wu, Z., Gogonea, V., Lee, X., May, R. P., Pipich, V., Wagner, M. A., Undurti, A., Tallant, T. C., Baleanu-Gogonea, C., Charlton, F., Ioffe, A., Didonato, J. A., Rye, K. A. & Hazen, S. L. (2011) The low resolution structure of ApoA1 in spherical high density lipoprotein revealed by small angle neutron scattering. *J Biol Chem,* 286, 12495-508.

Wu, Z., Gogonea, V., Lee, X., Wagner, M. A., Li, X. M., Huang, Y., Undurti, A., May, R. P., Haertlein, M., Moulin, M., Gutsche, I., Zaccai, G., Didonato, J. A. & Hazen, S. L. (2009) Double superhelix model of high density lipoprotein. *J Biol Chem,* 284, 36605-19.

Wu, Z., Wagner, M. A., Zheng, L., Parks, J. S., Shy, J. M., 3rd, Smith, J. D., Gogonea, V. & Hazen, S. L. (2007) The refined structure of nascent HDL reveals a key functional domain for particle maturation and dysfunction. *Nat Struct Mol Biol,* 14, 861-8.

Xu, S., Laccotripe, M., Huang, X., Rigotti, A., Zannis, V. I. & Krieger, M. (1997) Apolipoproteins of HDL can directly mediate binding to the scavenger receptor SR-BI, an HDL receptor that mediates selective lipid uptake. *J Lipid Res,* 38, 1289-98.

Yamamoto, K., Lee, D. K. & Ramamoorthy, A. (2005) Broadband-PISEMA solid-state NMR spectroscopy. *Chemical Physics Letters,* 407, 289-293.

Yano, K., Ohkawa, R., Sato, M., Yoshimoto, A., Ichimura, N., Kameda, T., Kubota, T. & Tozuka, M. (2016) Cholesterol Efflux Capacity of Apolipoprotein A-I Varies with the Extent of Differentiation and Foam Cell Formation of THP-1 Cells. *J Lipids,* 2016, 9891316.

Yoshida, H. & Kisugi, R. (2010) Mechanisms of LDL oxidation. *Clin Chim Acta,* 411, 1875-1882.

Yvan-Charvet, L., Wang, N. & Tall, A. R. (2010) Role of HDL, ABCA1, and ABCG1 transporters in cholesterol efflux and immune responses. *Arterioscler Thromb Vasc Biol,* 30, 139-43.

Zhang, L., Song, J., Cavigiolio, G., Ishida, B. Y., Zhang, S., Kane, J. P., Weisgraber, K. H., Oda, M. N., Rye, K. A., Pownall, H. J. & Ren, G. (2011) Morphology and structure of lipoproteins revealed by an optimized negative-staining protocol of electron microscopy. *J Lipid Res,* 52, 175-84.

Zhang, Z., Schwartz, S., Wagner, L. & Miller, W. (2000) A greedy algorithm for aligning DNA sequences. *Journal of Computational Biology,* 7, 203-214.

Zhiping, H., Akihiro, I., Masa-Aki, K., Atsushi, N., Toshinori, H. & Hiroshi, M. (2003) Dual effects on HDL metabolism by cholesteryl ester transfer protein inhibition in HepG2 cells. *Am J Physiol Endocrinol Metab,* 284, 1210-1219.

Zhou, L. Y., Li, C. C., Gao, L. & Wang, A. H. (2015) High-density lipoprotein synthesis and metabolism (Review). *Molecular Medicine Reports,* 12, 4015-4021.

Zhu, X., Wu, G., Zeng, W., Xue, H. & Chen, B. (2005) Cysteine mutants of human apolipoprotein A-I: a study of secondary structural and functional properties. *J Lipid Res,* 46, 1303-11.

Appendices

Appendix 1

The cDNA and amino acid sequences of recombinant human apoA-I. **A)** The his_6-tag (purple) and first 3 amino acid residues of the apoA-I sequence without the E2D mutation (Oda et al., 2001), the ellipses refer to the continued sequence in (B) from the 4^{th} residue. The 2^{nd} amino acid residue is indicated in green. **B**) The apoA-I (E2D) sequence (Ryan et al., 2003), adapted from (Townsend, 2016). The E2D mutated residue and formic acid his-tag cleavage site (D/P) (green), L144 (blue), R173C (red), underlined new restriction endonuclease sites (solid), and optimised *E. coli* abundance codons (dashed). The superscript numbers indicate the amino acid residue number in the full-length apoA-I WT protein.

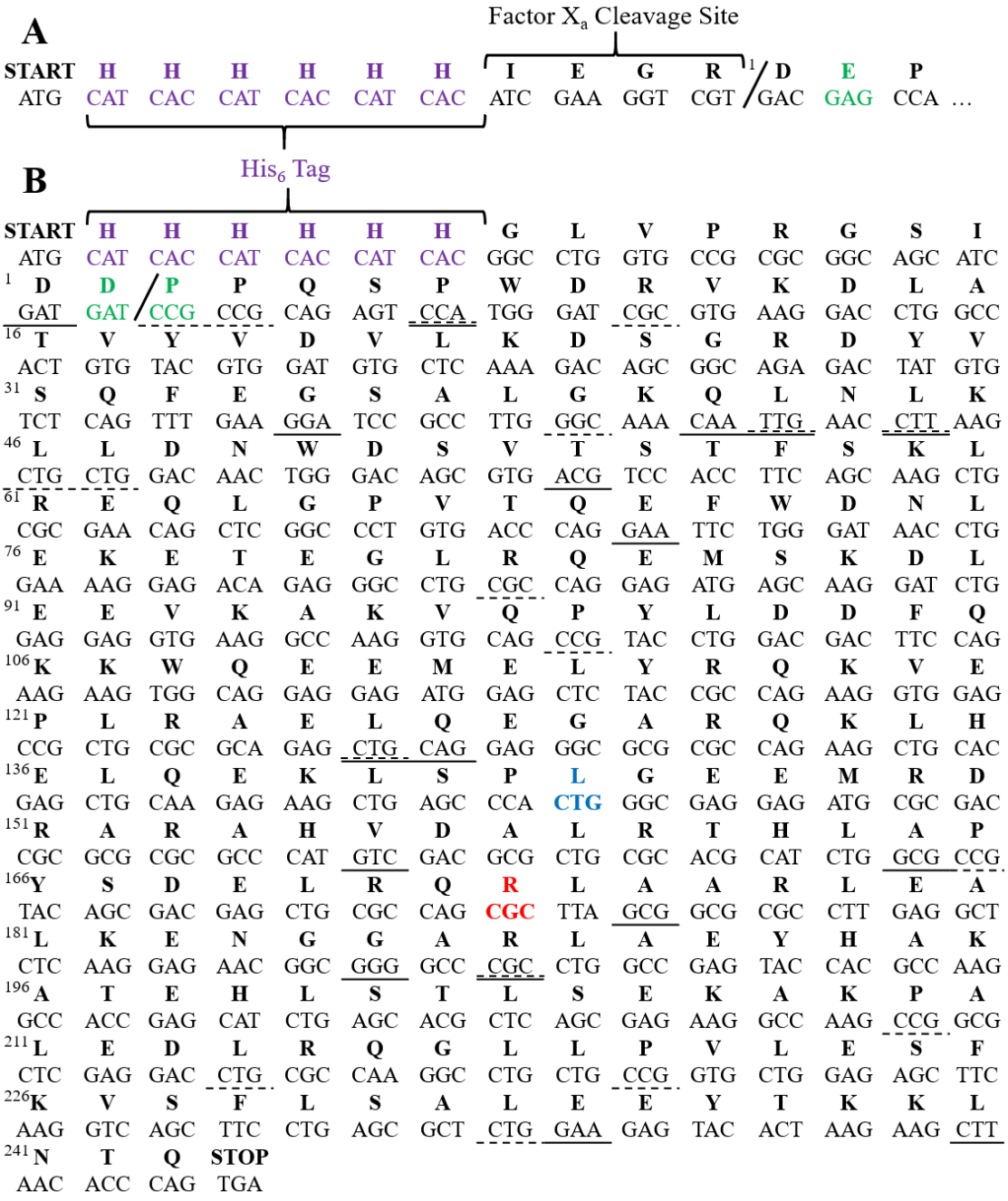
A
Factor X_a Cleavage Site
START H H H H H H I E G R 1 D E P
ATG CAT CAC CAT CAC CAT CAC ATC GAA GGT CGT GAC GAG CCA …
B
His_6 Tag
START H H H H H H G L V P R G S I
ATG CAT CAC CAT CAC CAT CAC GGC CTG GTG CCG CGC GGC AGC ATC
1 D D P P Q S P W D R V K D L A
GAT GAT CCG CCG CAG AGT CCA TGG GAT CGC GTG AAG GAC CTG GCC
16 T V Y V D V L K D S G R D Y V
ACT GTG TAC GTG GAT GTG CTC AAA GAC AGC GGC AGA GAC TAT GTG
31 S Q F E G S A L G K Q L N L K
TCT CAG TTT GAA GGA TCC GCC TTG GGC AAA CAA TTG AAC CTT AAG
46 L L D N W D S V T S T F S K L
CTG CTG GAC AAC TGG GAC AGC GTG ACG TCC ACC TTC AGC AAG CTG
61 R E Q L G P V T Q E F W D N L
CGC GAA CAG CTC GGC CCT GTG ACC CAG GAA TTC TGG GAT AAC CTG
76 E K E T E G L R Q E M S K D L
GAA AAG GAG ACA GAG GGC CTG CGC CAG GAG ATG AGC AAG GAT CTG
91 E E V K A K V Q P Y L D D F Q
GAG GAG GTG AAG GCC AAG GTG CAG CCG TAC CTG GAC GAC TTC CAG
106 K K W Q E E M E L Y R Q K V E
AAG AAG TGG CAG GAG GAG ATG GAG CTC TAC CGC CAG AAG GTG GAG
121 P L R A E L Q E G A R Q K L H
CCG CTG CGC GCA GAG CTG CAG GAG GGC GCG CGC CAG AAG CTG CAC
136 E L Q E K L S P L G E E M R D
GAG CTG CAA GAG AAG CTG AGC CCA CTG GGC GAG GAG ATG CGC GAC
151 R A R A H V D A L R T H L A P
CGC GCG CGC GCC CAT GTC GAC GCG CTG CGC ACG CAT CTG GCG CCG
166 Y S D E L R Q R L A A R L E A
TAC AGC GAC GAG CTG CGC CAG CGC TTA GCG GCG CGC CTT GAG GCT
181 L K E N G G A R L A E Y H A K
CTC AAG GAG AAC GGC GGG GCC CGC CTG GCC GAG TAC CAC GCC AAG
196 A T E H L S T L S E K A K P A
GCC ACC GAG CAT CTG AGC ACG CTC AGC GAG AAG GCC AAG CCG GCG
211 L E D L R Q G L L P V L E S F
CTC GAG GAC CTG CGC CAA GGC CTG CTG CCG GTG CTG GAG AGC TTC
226 K V S F L S A L E E Y T K K L
AAG GTC AGC TTC CTG AGC GCT CTG GAA GAG TAC ACT AAG AAG CTT
241 N T Q STOP
AAC ACC CAG TGA

The pBluescript KS (+) plasmid (2958 bp) was discontinued (Addgene), therefore the pBluescript II KS (+) plasmid map (2961 bp) obtained from Addgene is shown with the cloning/expression region (bp 598-826) obtained from Agilent.

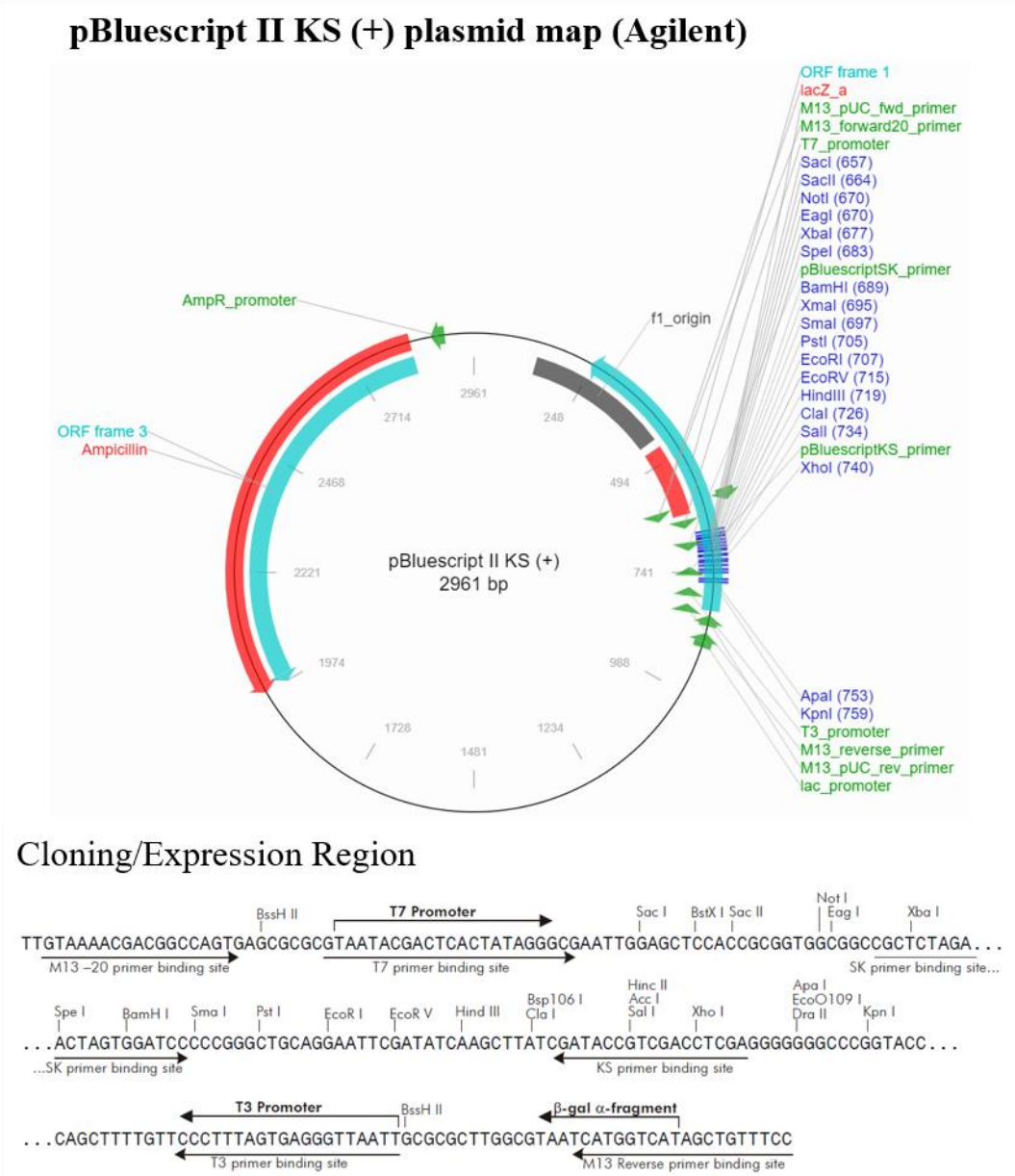

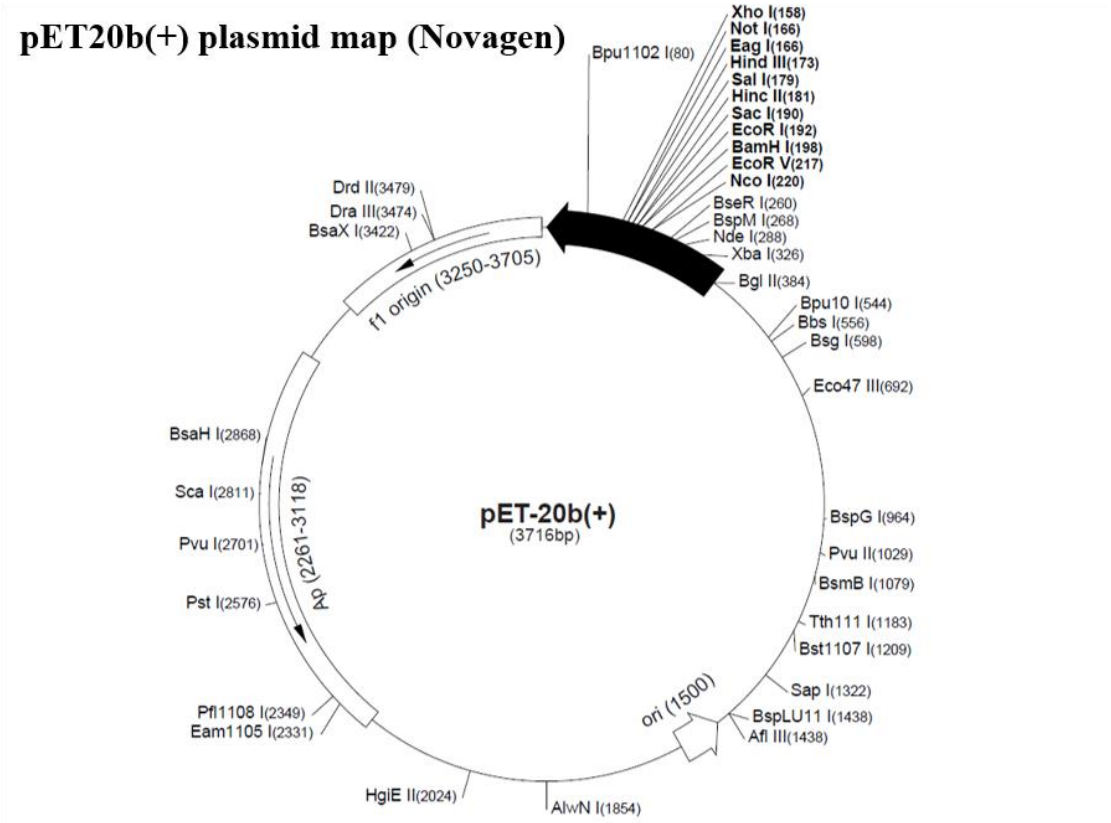

Cloning/Expression Region

Original gene sequencing data before translation to amino acid sequence using ExPASy translate tool.

The re-isolated and sequenced apoA-I R173C plasmid from (Townsend, 2016). Nucleotide BLAST® results compared to apoA-I WT (E2D) sequence 477/579 identities (82%).

NNNNNNNNNNNNNNNNNNNNNNNNNNNNNNGNNTNTTCCTATGCNTNACCATTCCATC
NNNNNNNNNNNNNNCGCGGCATCATCNATGATCCGCCNNANAGTNNTNNGGATCNNGTG
AAGGANCTGGCCACTGTGTACGTGGATGTGCTCAAAAACAGCGGNNGNNNTNATGTGTCT
CANTTTGAATGATCCGCCTTGGGCAAACAATTGAACCTTAAGCTGCTGGACAACTGGGAC
AACGTGACGTCCACCTTCATNAGCTGCGCGAACANGTCGGCCCTGTGACCCACNAATTCTG
GGATAACCTGGAAAATGAGACAGAAGGCCTGCGCCCGAGATGAGCAAGGATCTGGAGGA
NGTGAAGGCCCCGGTGCANNNNNNCCTGGGCNACTTCCNCAAAAANTGGCAGGAGGAGA
TGGAGCTCTACCGCCACAAAGTGGANNCGCTGCGCGCACANATNCACGAGGGCGCGCGCC
ACANACTGCACNANCTGNANNAGAAACTGAGCCCACNCNGCGAGAAGATGCGCGACCGC
GCGCGCGCCCTTGTNTACGCGCTGCGCTNCTTCTGGGGGNCNTACANNNNCNANATGCGA
CCCCGCTTANAGCGCGCCCTTTNGCTCTCATGGAGAACGGCGGTGGCCCGCCCTGCGGNA
GNATACGGCATGAGTCNCTGA

ApoA-I R173C – 776/777 identities (99%)

NNNGAANATTTTGTTTACTTTAAGAAGGAGATATACATATGCATCACCATCACCATCACGG
CCTGGTGCCGCGCGGCAGCATCGATGATCCGCCGCAGAGTCCATGGGATCGCGTGAAGGA
CCTGGCCACTGTGTACGTGGATGTGCTCAAAGACAGCGGCAGAGACTATGTGTCTCAGTTT
GAAGGATCCGCCTTGGGCAAACAATTGAACCTTAAGCTGCTGGACAACTGGGACAGCGTG
ACGTCCACCTTCAGCAAGCTGCGCGAACAGCTCGGCCCTGTGACCCAGGAATTCTGGGAT
AACCTGGAAAAGGAGACAGAGGGCCTGCGCCAGGAGATGAGCAAGGATCTGGAGGAGGT
GAAGGCCAAGGTGCAGCCGTACCTGGACGACTTCCAGAAGAAGTGGCAGGAGGAGATGG
AGCTCTACCGCCAGAAGGTGGAGCCGCTGCGCGCAGAGCTGCAGGAGGGCGCGCGCCAG
AAGCTGCACGAGCTGCAAGAGAAGCTGAGCCCACTGGGCGAGGAGATGCGCGACCGCGC
GCGCGCCCATGTCGACGCGCTGCGCACGCATCTGGCGCCGTACAGCGACGAGCTGCGCCA
GTGCTTAGCGGCGCGCCTTGAGGCTCTCAAGGAGAACGGCGGGGCCCGCCTGGCCGAGTA
CCACGCCAAGGCCACCGAGCATCTGAGCACGCTCAGCGAGAAGGCCAAGCCGGCGCTCGA
GGACCTGCGCCAAGGCCTGCTGCCGGTGCTGGAGAGCTTCAAGGTCAGCTTCCTGAGCGC
TCTGGAAGAGTACACTAAGAAGCTTAACACCCAGTGATCAGCTCTAGAACTAGTAGATCT
GCGGCCGCACTCGAGCACCACCACCACCACCACTGAGATCCGGCTGCTAACAAAGCCCGA
AAGGAAGCTGAGTTGGCTGCTGCCACCGCTGANCAATAACTAGCATAACCCCTTGGGGCC
TCTAAACGGGTCTTGNAGGGGGTTTTTTTGCTGAAAG

ApoA-I L144R - 775/777 identities (99%)

NNNNANATTTTGTTTACTTTAAGAAGGAGATATACATATGCATCACCATCACCATCACGGC
CTGGTGCCGCGCGGCAGCATCGATGATCCGCCGCAGAGTCCATGGGATCGCGTGAAGGAC
CTGGCCACTGTGTACGTGGATGTGCTCAAAGACAGCGGCAGAGACTATGTGTCTCAGTTTG
AAGGATCCGCCTTGGGCAAACAATTGAACCTTAAGCTGCTGGACAACTGGGACAGCGTGA
CGTCCACCTTCAGCAAGCTGCGCGAACAGCTCGGCCCTGTGACCCAGGAATTCTGGGATA
ACCTGGAAAAGGAGACAGAGGGCCTGCGCCAGGAGATGAGCAAGGATCTGGAGGAGGTG
AAGGCCAAGGTGCAGCCGTACCTGGACGACTTCCAGAAGAAGTGGCAGGAGGAGATGGA
GCTCTACCGCCAGAAGGTGGAGCCGCTGCGCGCAGAGCTGCAGGAGGGCGCGCGCCAGA
AGCTGCACGAGCTGCAAGAGAAGCTGAGCCCACGCGGCGAGGAGATGCGCGACCGCGCG
CGCGCCCATGTCGACGCGCTGCGCACGCATCTGGCGCCGTACAGCGACGAGCTGCGCCAG
CGCTTAGCGGCGCGCCTTGAGGCTCTCAAGGAGAACGGCGGGGCCCGCCTGGCCGAGTAC
CACGCCAAGGCCACCGAGCATCTGAGCACGCTCAGCGAGAAGGCCAAGCCGGCGCTCGA
GGACCTGCGCCAAGGCCTGCTGCCGGTGCTGGAGAGCTTCAAGGTCAGCTTCCTGAGCGC
TCTGGAAGAGTACACTAAGAAGCTTAACACCCAGTGATCAGCTCTAGAACTAGTAGATCT
GCGGCCGCACTCGAGCACCACCACCACCACCACTGAGATCCGGCTGCTAACAAAGCCCGA
AAGGAAGCTGANTTGGCTGCTGCCACCGCTGAGCAATAACTAGCATAACCCCTTGGGGCC
TCTAAACGGGTCTTGGAGGGGGTTTTTTTGCTGAAN

The pre- and post- his-tag cleavage gels for apoA-I R173C and L144R showing the cropped, duplicate sample and empty lanes removed.

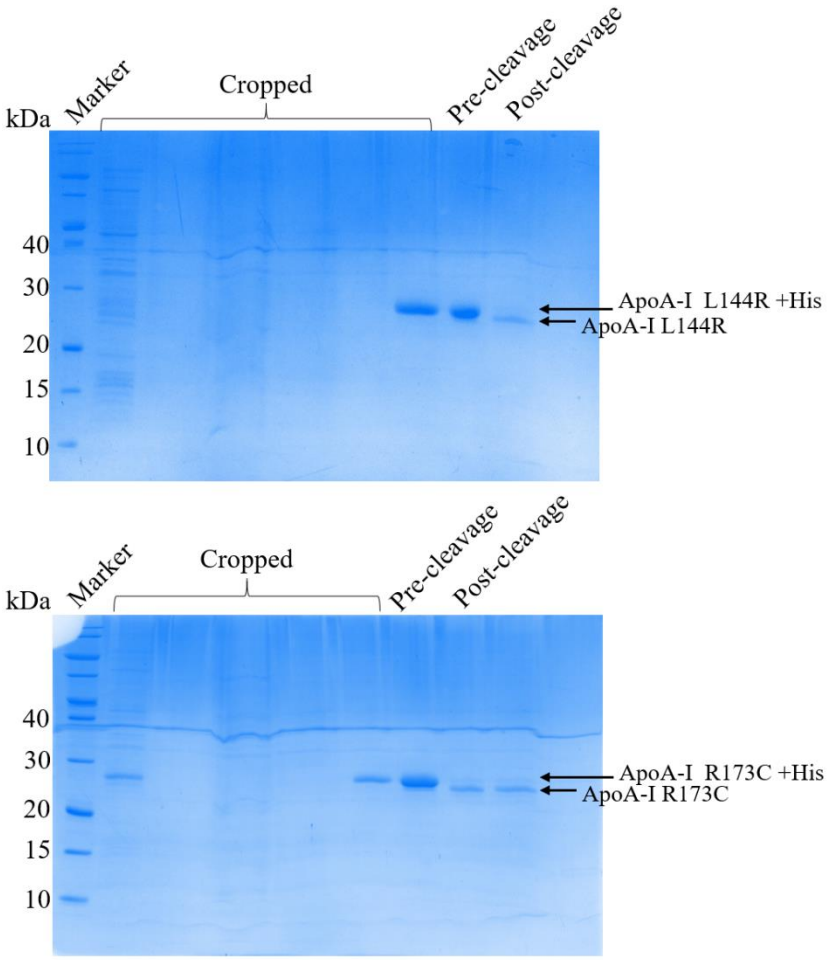

Appendix 2

Original data of mass % of NaBr in solution and the corresponding densities (g/mL) from the Handbook of Chemistry and Physics (Haynes, 2010).

Mass (%)	Density (g/mL)	Mass (%)	Density (g/mL)
0.5	1.0021	16	1.1352
1	1.006	18	1.1546
2	1.0139	20	1.1745
3	1.0218	22	1.1951
4	1.0298	24	1.2163
5	1.038	26	1.2382
6	1.0462	28	1.2608
7	1.0546	30	1.2842
8	1.063	32	1.3083
9	1.0716	34	1.3333
10	1.0803	36	1.3592
12	1.0981	38	1.386
14	1.1164	40	1.4138

The NaBr mass (%) and the corresponding density (g/mL) original data (Haynes, 2010) and linearly interpolated values using Origin 2018 software.

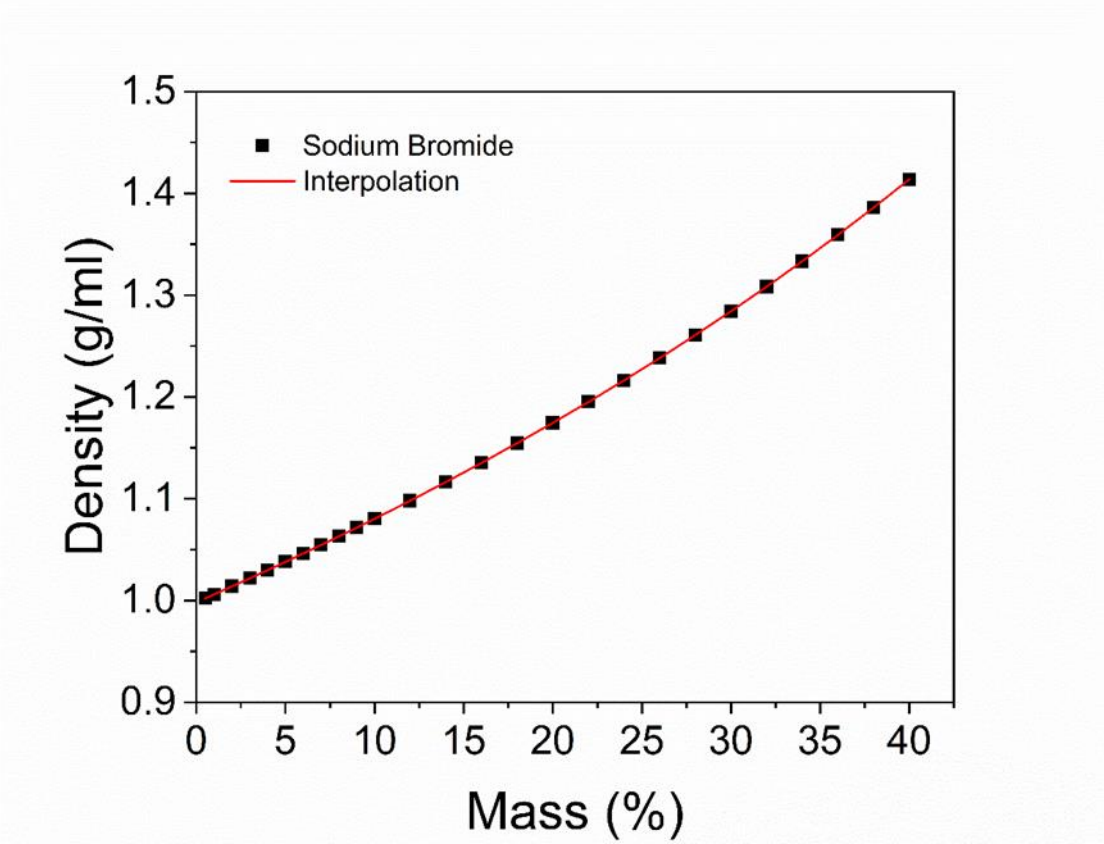

NaBr SG-UTC density solutions (g/mL) and the corresponding mass (%) and mass in grams for a 10 mL total volume.

Density (g/mL)	NaBr Mass (%)	NaBr Mass (g)
1.0404	5.2879	0.5288
1.0952	11.6717	1.1672
1.1513	17.6566	1.7657
1.2125	23.6414	2.3641
1.3037	31.6212	3.1621

Appendix 3

The average chemical shifts of amino acids by secondary structure. Data obtained and table adapted from (Wang and Jardetzky, 2002). β-strand (β), random coil (RC), α-helix (α). $^{13}C_{\alpha}$ and $^{13}C_{\beta}$, and $^{13}C'$ are the labelled carbon atoms in the amino acid R group, and the polypeptide backbone, respectively.

Amino acid	$^{13}C_{\alpha}$			$^{13}C_{\beta}$			$^{13}C'$		
	β	RC	α	β	RC	α	β	RC	α
Ala (A)	50.86 ±1.28	52.67 ±1.76	54.89 ±0.94	21.72 ±1.77	19.03 ±1.27	18.27 ±1.08	175.3 ±1.61	177.39 ±1.45	179.58 ±1.39
Gly (G)	45.08 ±1.20	45.34 ±1.17	47.02 ±0.90				173.01 ±2.59	174.30 ±1.80	176.31 ±1.50
Leu (L)	53.94 ±1.19	54.85 ±1.79	57.54 ±0.98	44.02 ±1.99	41.87 ±1.70	41.40 ±1.11	175.16 ±1.31	176.61 ±1.77	178.42 ±1.70
Pro(P)	62.79 ±1.22	63.53 ±1.26	65.52 ±1.01	32.45 ±0.93	31.87 ±0.96	31.08 ±0.84	176.41 ±1.50	176.91 ±1.72	178.34 ±1.53
Ser (S)	57.14 ±1.11	58.35 ±1.78	60.86 ±1.27	65.39 ±1.48	63.88 ±1.24	62.81 ±0.58	173.52 ±1.55	174.33 ±1.22	176.51 ±1.40
Thr (T)	61.10 ±1.71	61.59 ±2.04	65.89 ±1.55	70.82 ±2.11	69.75 ±1.29	68.64 ±0.98	173.47 ±1.39	174.62 ±1.45	176.62 ±1.24
Val (V)	60.72 ±1.59	61.80 ±2.25	65.96 ±1.39	33.81 ±1.79	32.68 ±1.76	31.41 ±0.74	174.66 ±1.36	175.76 ±1.63	177.75 ±1.49

Appendix 4

ApoA-I R173C dimer RMSD CGMD ~6.6 μs **(A)** RMSD of the protein backbone with a least-squares fit to the equilibrated protein backbone. **(B)** The radius of gyration of the protein in the CGMD simulation.

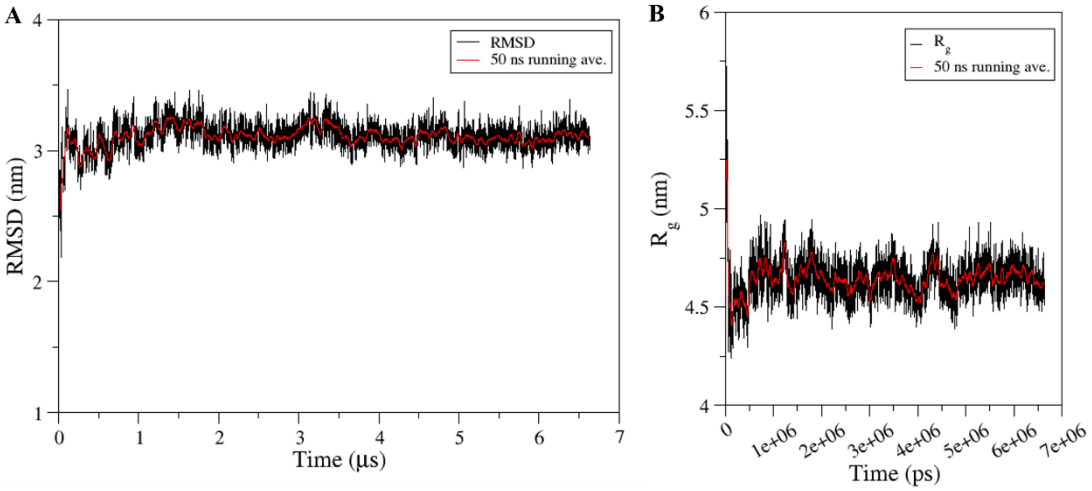

ApoA-I WT Δ(1-43) chains A and B RMSD CGMD ~8.9 μs **(A)** RMSD of the protein backbone with a least-squares fit to the equilibrated protein backbone. **(B)** The radius of gyration of the protein in the CGMD simulation.

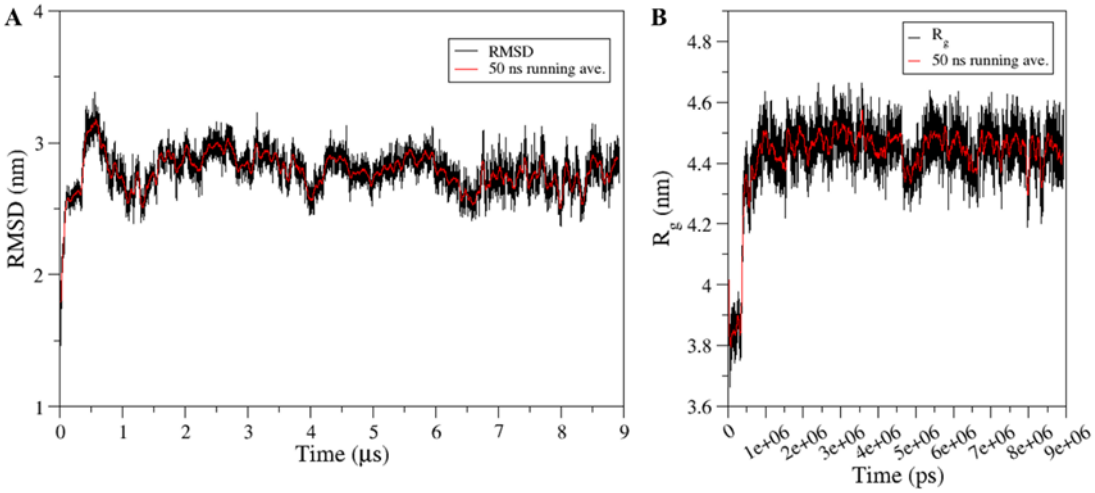

ThT Fluorescence assay controls: ThT only, apoA-I WT, R173C and L144R without ThT in McIlvaine buffer, pH 7.0.